University at Buffalo
The State University of New York

Mid-height Seismic Isolation of Tall, Slender Equipment in Advanced Nuclear Power Plants

by
Kaivalya M. Lal, Andrew S. Whittaker
and Michael C. Constantinou

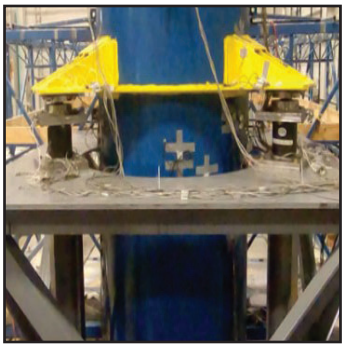

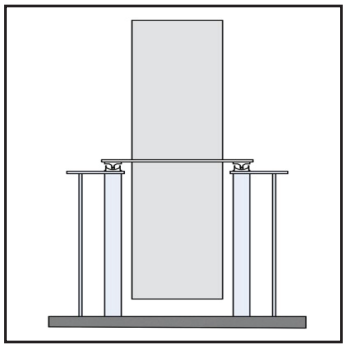
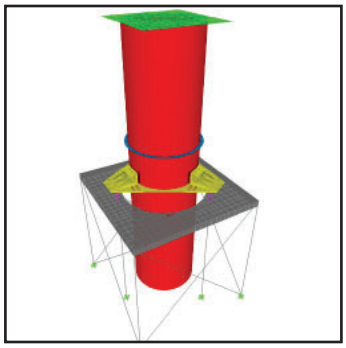

Technical Report MCEER-23-0001

February 4, 2023

NOTICE

This report was prepared by the University at Buffalo, State University of New York, as a result of research sponsored by the Advanced Research Projects Agency - Energy (ARPA-E) under award number DE-AR0000978. Neither MCEER, associates of MCEER, its sponsors, University at Buffalo, State University of New York, nor any person acting on their behalf:

a. makes any warranty, express or implied, with respect to the use of any information, apparatus, method, or process disclosed in this report or that such use may not infringe upon privately owned rights; or

b. assumes any liabilities of whatsoever kind with respect to the use of, or the damage resulting from the use of, any information, apparatus, method, or process disclosed in this report.

Any opinions, findings, and conclusions or recommendations expressed in this publication are those of the author(s) and do not necessarily reflect the views of MCEER, the Advanced Research Projects Agency, or other sponsors.

University at Buffalo
The State University of New York

Mid-height Seismic Isolation of Tall, Slender Equipment in Advanced Nuclear Power Plants

by

Kaivalya M. Lal,[1] Andrew S. Whittaker[2] and Michael C. Constantinou[2]

Publication Date: February 4, 2023
Submittal Date: January 11, 2023

Technical Report MCEER-23-0001

Advanced Research Projects Agency – Energy
Award Number DE-AR0000978

1. Graduate Student, Department of Civil, Structural and Environmental Engineering, University at Buffalo, The State University of New York
2 SUNY Distinguished Professor, Department of Civil, Structural and Environmental Engineering, University at Buffalo, The State University of New York

MCEER: Earthquake Engineering to Extreme Events
University at Buffalo, The State University of New York
212 Ketter Hall, Buffalo, NY 14260
buffalo.edu/mceer

Preface

MCEER was originally established by the National Science Foundation in 1986 at the University at Buffalo, The State University of New York, as the first National Center for Earthquake Engineering Research (NCEER). In 1998, it became known as the Multidisciplinary Center for Earthquake Engineering Research (MCEER), from which the current name, MCEER, evolved.

Comprising a consortium of researchers and industry partners from numerous disciplines and institutions throughout the United States, MCEER's mission expanded in the early 2000s from its original focus on earthquake engineering to one which addresses the technical and socioeconomic impacts of a variety of hazards, both natural and man-made, on critical infrastructure, facilities, and society.

This report describes a non-traditional seismic isolation solution for designers of safety-class equipment in advanced nuclear reactors. The test specimen considered herein was a tall, slender carbon steel vessel that could represent a steam generator, a reactor vessel, or a heat exchanger. The vessel was supported at its mid-height, near its center of gravity, on a steel frame and isolated using spherical sliding bearings. The isolated vessel was tested using a six degrees-of-freedom earthquake simulator at the University at Buffalo. Numerical models were benchmarked using the experiment data and utilized to quantify the benefits of mid-height seismic isolation. Analysis and design recommendations for equipment isolation in nuclear facilities are provided.

ABSTRACT

The use of seismic isolation could substantially reduce earthquake demands on safety-class equipment and is being considered for application to some advanced nuclear reactors. The conventional implementation involves isolating a reactor building at its base. An alternate approach, when building isolation is not practical, involves isolating equipment inside a reactor building. Mid-height seismic isolation of equipment is the focus of this report: an application not studied previously and considered here to expand the range of options available to designers of safety-class equipment in advanced reactors.

The experimental program described herein examined a mid-height seismic isolation solution for a tall, slender cylindrical vessel, which could represent a reactor vessel, a steam generator, or a heat exchanger in an advanced nuclear power plant. The carbon steel test article was 240 inches tall with an outer diameter of 60 inches and a wall thickness of 1 inch. It was supported near its center of gravity (at its mid-height) on a *stiff* steel frame using three radial mounts. Three configurations of the vessel were tested: non-isolated, isolated using single Friction Pendulum (SFP) bearings, and isolated using triple Friction Pendulum (TFP) bearings. The vessel was subjected to three component ground motions using a 6 degrees-of-freedom earthquake simulator. The vessel was filled with water during testing to simulate in-service conditions.

A direct comparison of responses of the non-isolated vessel and the isolated vessels was not possible because the amplitudes of the seismic inputs were not identical. However, test results demonstrated that mid-height seismic isolation generally enables a very significant reduction in horizontal spectral accelerations at the top and bottom of the vessel, where other safety-related equipment would be attached. In the non-isolated configuration, the peak horizontal accelerations were greater than 1 g at the top and the bottom of the vessel for moderate-to-high seismic inputs. In the isolated configurations, the peak horizontal accelerations at the top and the bottom of the vessel were less than 0.5 g for intensities of shaking substantially greater than those input to the non-isolated vessel.

Numerical models of the non-isolated and isolated vessel were developed in SAP2000 and benchmarked using the experiment data. These models were used to a) confirm the utility of mid-height isolation for various stiffnesses of the frame supporting the vessel, isolation system properties, and ground motions, b) quantify the benefits of mid-height seismic isolation, c) investigate the feasibility of base isolation for tall, slender vessels, and d) provide analysis and design recommendations for isolation of equipment in nuclear facilities.

Results from the numerical analysis confirm that mid-height seismic isolation is effective at reducing horizontal spectral accelerations with respect to those in a non-isolated vessel for a range of support structure stiffnesses, isolation-system properties, and ground motions. Importantly, the reductions in horizontal spectral accelerations (with respect to those in the non-isolated configuration) enabled by mid-height seismic isolation were not significantly affected by the stiffness of the support frame. Base isolation, although viable, may not be a practical choice for tall, slender equipment because rocking of the vessel may lead to significant changes in axial load on the bearings and possibly axial tension (or uplift in the case of spherical sliding isolators). Mid-height isolation virtually eliminated the rocking response, and with it, the large changes in axial load.

ACKNOWLEDGMENTS

The work presented in this report was funded by the Advanced Research Projects Agency – Energy (ARPA-E), U.S. Department of Energy, under Award Number DE-AR0000978. This financial support is gratefully acknowledged. The views and opinions of the authors expressed herein do not necessarily state or reflect those of the U.S. Government or any agency thereof.

The experiments described in this report were conducted at the Structural Engineering and Earthquake Simulation Laboratory (SEESL) at the University at Buffalo. The authors acknowledge the technical support provided by the SEESL staff in executing experiments, including Messrs. Mark Pitman, Scot Weinreber, Robert Staniszewski, Christopher Budden, Michael Branch, Jeffrey Cizdziel, and Louis Moretta.

The authors thank the researchers and technical personnel who provided valuable inputs and ideas over the course of this research project, including Professor Mettupalayam V. Sivaselvan, Mr. Sai Sharath Parsi, Mr. Faizan Ul-Haq Mir, and Dr. Ching Ching Yu at the University at Buffalo. The authors acknowledge the support of Earthquake Protection Systems, Vallejo, CA, who provided the Friction Pendulum bearings used for the experimental program at no cost.

TABLE OF CONTENTS

LIST OF FIGURES

LIST OF TABLES

SECTION 1
INTRODUCTION

1.1 Background

Numerous studies have identified the important role of nuclear energy in decarbonizing the global economy, mitigating climate change, and meeting future energy demands (e.g., Buongiorno *et al.* (2018), IEA (2019), Partanen *et al.* (2019), IAEA (2020c; 2020b; 2020a), Ingersoll and Gogan (2020)). Major impediments to the widespread deployment of new nuclear power plants (NPPs) are high overnight capital cost (OCC) and time required to analyze, design, review, license, construct, and commission them. Nuclear energy can only compete with other energy sources, including renewables, measured here using capital cost normalized by kWe generated, by significantly reducing OCC and time for deployment.

Standardizing reactor buildings and their equipment might be the only pathway to deploy NPPs with substantially lower capital cost and a much shorter deployment duration: time from project start to grid connection, including Front-End Engineering Design (FEED) studies, analysis, design, equipment qualification, regulatory review, licensing, and construction. (For reference, the expected deployment duration for Units 3 and 4 at Plant Vogtle is approximately 18 years, with pre-construction work lasting 7 years and construction 11 years.) The seismic load case is a key contributor to the capital cost of an NPP (Lal *et al.*, 2022) and thwarts deployment of standardized reactors as the near-surface geology and seismic hazard are never identical at any two sites. Site-specific soil-structure-interaction analysis, design, equipment qualification, regulatory review, licensing, and construction will be required if conventional construction is employed. Site-independent, certified NPP designs could possibly be used at multiple sites if sufficient conservatism is introduced but that adds to OCC. Front-End Engineering Design studies, analysis, design, regulatory review, and perhaps equipment qualification, would still be needed to demonstrate the acceptability of the certified design for the proposed site.

Seismic isolation is a proven, mature technology that offers a means to minimize the effects of earthquake shaking and can enable deployment of standardized NPPs (Parsi *et al.*, 2022). The implementation of seismic isolation and standardized NPPs would substantially de-scope the pre-construction activities and simplify the construction, reducing capital cost and time to deploy.

1.2 Seismic isolation of nuclear power plants

Seismic isolation has been applied to more than 10,000 structures worldwide in the past three decades. Examples include hospitals, data centers, buildings of cultural importance, bridges, and emergency operations facilities. Applications of isolation to non-nuclear infrastructure include liquefied natural gas tanks, offshore oil and gas platforms, port facilities, container cranes, and electrical substations and power distribution systems.

Although the benefits of seismically isolating NPPs, in terms of reduced seismic demands and risk, are well established (e.g., Tajirian *et al.* (1989), Tajirian (1992), Tajirian and Patel (1993), Clark *et al.* (1995), Aiken *et al.* (2002), Huang *et al.* (2008; 2009; 2011a; 2011b), Kumar *et al.* (2015; 2017a; 2017b), Bolisetti *et al.* (2016), Yu *et al.* (2018), Parsi *et al.* (2022)), seismic isolation has yet to be applied to an NPP (or a nuclear facility) in the United States.

Outside the U.S., two NPPs, in Cruas, France and Koeberg, South Africa, were seismically isolated in the early 1980s to enable the re-use of a certified plant design developed for a site of lower seismic hazard. Seismic isolation has also been implemented in other nuclear facilities outside the U.S., including the International Thermonuclear Experimental Reactor (ITER), the Jules Horowitz (research) Reactor (JHR), the La Hague spent fuel storage pool, and the Georges Besse II uranium enrichment facility, all in France, with ITER and JHR under construction at the time of this writing. In Japan, electric utilities have seismically isolated emergency operations buildings at the sites of NPPs (e.g., Kashiwazaki-Kariwa, Fukushima Daiichi, Fukushima Daini, and Onagawa) with the objective of ensuring the availability of emergency equipment and management capacity in the aftermath of an earthquake. The isolated buildings at Fukushima Daiichi, Fukushima Daini, and Onagawa experienced significant shaking during the 2011 East Japan Earthquake and performed well, with no substantial damage reported (EPRI, 2013).

The global pursuit of clean energy has driven interest in advanced or Generation IV[1] nuclear reactors, with seismic isolation being considered as an integral design feature for some of them. The traditional

[1] The deployment of nuclear reactors is often described in terms of four generations, with each having improved safety and performance over the prior generation. Early prototype reactors were Generation I. Early commercial reactors were Generation II. Generation III and III+ are Gen II reactors with design enhancements. Generation IV reactors are under development at the time of this writing, and a number of them utilize non-water coolants such as liquid sodium, molten salt, and helium.

implementation of seismic isolation involves installation of horizontally flexible and vertically stiff bearings (or isolators) at the base of a building, that is, base isolation: Figure 1-1a. An alternate implementation, that could be considered where base isolation is impractical (e.g., a deeply embedded reactor building), is to isolate safety-class equipment at their supports inside the nuclear facility: see Figure 1-1b.

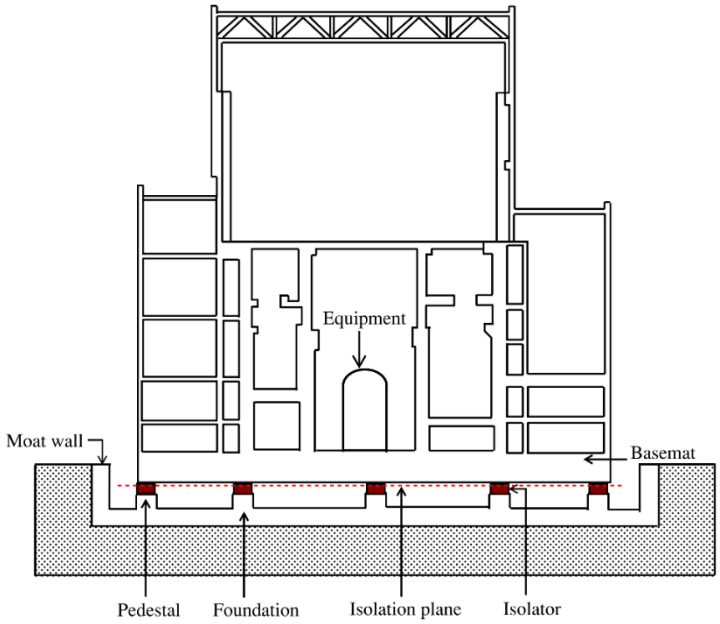

a) building isolation

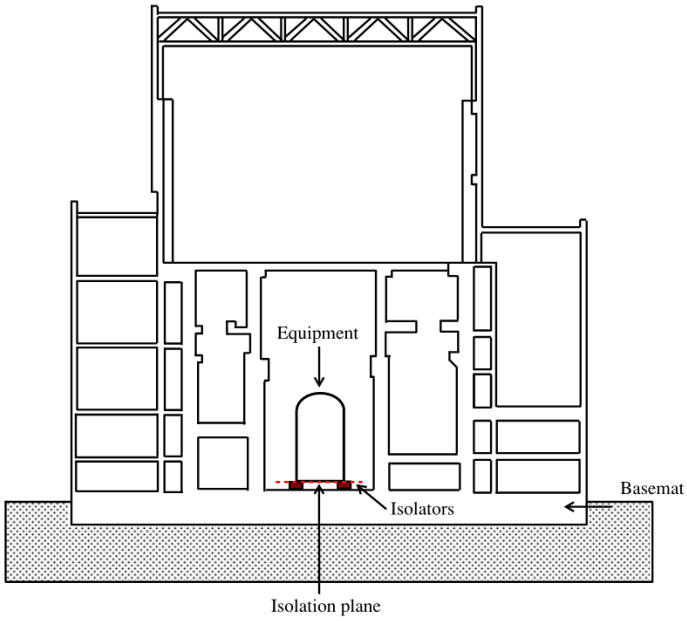

b) equipment isolation

Figure 1-1. Seismic isolation of nuclear power plants (adapted from Kammerer *et al.* (2019))

The U.S. Department of Energy (DOE) and the U.S. Nuclear Regulatory Commission (NRC) funded several projects between 2008 and 2018 to develop tools and guidelines for base isolation of large light water reactors. Consensus standards, ASCE/SEI 4-16 (ASCE, 2017) and ASCE/SEI 43-19 (ASCE, 2021), now include analysis and design criteria for base-isolated, safety-related nuclear facilities. Technical reports on the analysis and design of seismically isolated NPPs have been published by the NRC: 1) NUREG/CR-7253, Technical considerations for seismic isolation of nuclear facilities (Kammerer *et al.*, 2019), 2) NUREG/CR-7254, Seismic isolation of nuclear power plants using sliding bearings (Kumar *et al.*, 2019a), and 3) NUREG/CR-7255, Seismic isolation of nuclear power plants using elastomeric bearings (Kumar *et al.*, 2019b). The cost benefits of base isolating advanced reactors have been characterized recently (Lal *et al.*, 2022).

Herein, this prior work is extended to address seismic isolation of safety-class equipment inside nuclear reactor buildings, to enable standardization, albeit not at the scale enabled by building isolation.

1.3 Objectives of the study

The overarching goal of this report is to provide equipment isolation solutions for the designers of safety-class equipment in advanced nuclear power plants. The goal is achieved by meeting the following objectives:

1. Demonstrate experimentally the feasibility of a mid-height seismic isolation system for a tall, slender vessel that could represent a reactor vessel, a steam generator, or a heat exchanger in an advanced NPP.
2. Numerically explore base isolation of tall, slender vessels.
3. Provide recommendations for analysis and design of isolated equipment suitable for inclusion in the next revision of ASCE/SEI Standards 4 and 43.

1.4 Organization of the report

This report is organized into seven sections and three appendices as described below:

Section 2 *Literature review*

Reviews prior research and applications of equipment isolation.

Section 3 *Description and testing of Friction Pendulum bearings*

Describes the Friction Pendulum (FP) bearings utilized for mid-height seismic isolation of a tall, slender vessel. Summary results from the testing of individual bearings are presented to characterize their behavior.

Section 4 *Earthquake-simulator experiments*

Describes the earthquake-simulator experiments of a tall, slender vessel, including the components and instrumentation of the test specimen, data acquisition system, and input motions. Key results are presented to enable a qualitative comparison of the response between the non-isolated and isolated vessels and demonstrate the concept of a mid-height seismic isolation system.

Section 5 *Numerical modeling and response-history analyses of mid-height and base isolated tall, slender vessels*

Presents the numerical models, and their benchmarking, for the test specimen of Section 4. Investigates the utility and quantifies the benefits of mid-height seismic isolation of tall, slender vessels using the benchmarked numerical models. Base isolation of tall, slender vessels is also explored numerically.

Section 6 *Summary, conclusions, and recommendations*

Summarizes the report, presents conclusions, and provides analysis and design recommendations for isolation of equipment in a nuclear facility.

Section 7 *References*

This section presents a list of references used in the report.

Appendix A *Test data for SFP and TFP bearings*

Presents all results from the bearing characterization tests summarized in Section 3.

Appendix B *Fabrication drawings*

Presents the fabrication drawings for the test specimen (vessel, frame, gasket, and bearings) of Section 4.

Appendix C *Vertical accelerations in SFP bearings*

Investigates the change in height and the resulting vertical acceleration of single Friction Pendulum bearing as a function of horizontal displacement, and offers practical solutions to account for it in response-history analysis.

SECTION 2
LITERATURE REVIEW

2.1 Introduction

The concept of isolating equipment from steady-state and transient vibrations is more than 100 years old. The goal was, and is, to reduce the vibration response of the asset through the strategic installation of devices at reaction points. Most vibration-mitigation devices must also provide gravity-load support of the asset.

Seismic isolation is a specific application of vibration isolation where an equipment or a structure is isolated to protect it against the effects of strong earthquake shaking. Seismic isolation has been used in non-nuclear sectors as an engineered solution since the 1970s to substantially reduce the impact of the earthquake load case on buildings and other infrastructure. Only two nuclear power plants have been isolated at the time of this writing, one in Cruas, France and the other in Koeberg, South Africa. Both power plants were constructed in the 1980s. Whittaker *et al.* (2018) presents a history of seismic isolation, identifies the research that led to the first implementation of base isolation for buildings and bridges, summarizes the first applications of the technology to nuclear facilities, and describes important research and developments that led to the development of tools and guidelines for base isolation of large light water reactors.

An alternative to base isolation of buildings is the protection of individual pieces of equipment or clusters of equipment. There are only a few applications of isolation to equipment and few studies reported in the literature. Those studies relevant to this report are presented next.

2.2 Seismic isolation of equipment

The California Department of Water Resources sponsored a program in the late 1970s to seismically protect electrical equipment in the switchyards of power and pumping plants. Kircher *et al.* (1979) conducted tests on a base-isolated 230 kV circuit breaker at Stanford University. Those circuit breakers had fragile porcelain insulators that are susceptible to earthquake shaking. The circuit breaker was tested using three types of GAPEC (elastomeric) isolators with different horizontal and vertical stiffnesses. The tests demonstrated that the isolators reduced accelerations of the circuit breaker by a factor of between 4 and 5. Following these tests, a circuit breaker was protected using GAPEC isolators in Southern California, which is considered to be the first engineered application of seismic isolation in the United States.

Kelly (1983) conducted earthquake-simulator tests at the University of California, Berkeley to investigate the use of base isolation as a retrofit strategy for large components in existing nuclear power plants. The test specimen was a one-third scale, 206-inch tall cylindrical steam generator vessel, with a wall thickness of 3/8 inch. The vessel was supported by a five-story, three-bay steel frame as shown in elevation in Figure 2-1. The vessel was filled with water to increase its weight, and was isolated at its base using one elastomeric bearing. The isolated vessel was stabilized using four prestressed coil springs attached to the top of the vessel and the steel frame. The total weight of the vessel was 11.4 kips and that of the support frame was 64.5 kips. Unidirectional (horizontal) and bi-directional (horizontal and vertical) earthquake shaking tests were performed. A comparison of results from tests in the fixed-base (i.e., non-isolated) and base-isolated configurations showed significantly lower accelerations for the latter support condition.

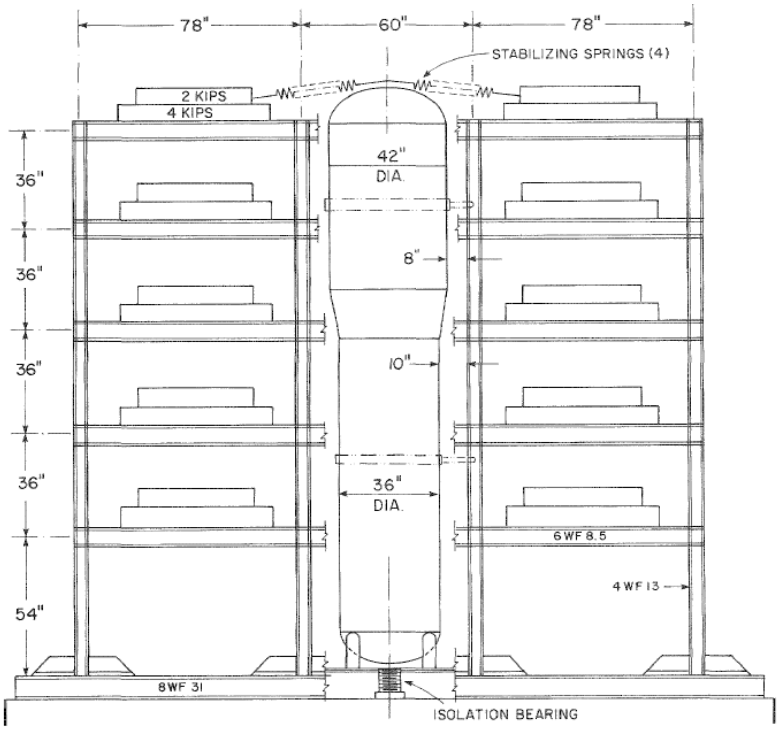

Figure 2-1. Elevation of a base-isolated steam generator model (Kelly, 1983)

In the late 1980s, the Mark II Detector, a component of the Linear Collider at Stanford University, was isolated using four lead-rubber bearings (Buckle and Mayes, 1990; Tajirian, 1998). The detector was approximately 30 ft tall, with plan dimensions of 25 ft × 34.4 ft; it weighed 3,200 kips. The isolators were designed to resist the effects of shaking characterized by a RG 1.60 spectrum (USNRC, 1973) scaled to peak ground acceleration of 0.6g. A Liquid Argon Calorimeter was later isolated at Stanford University.

The Bucharest FN tandem accelerator, commissioned in 1973, was used for nuclear physics research. It was damaged by strong earthquakes in 1977 (Richter M7.2) and 1986 (M6.8) and substantial repairs were required after both events. Subsequently, a GERB seismic isolation system was developed for the accelerator. Four GERB isolators, which consist of helical steel springs and a viscous damper (Dobrescu and Marinescu, 2005; Marinescu *et al.*, 1993), isolated this asset. Figure 2-2 is an elevation of the isolated accelerator. Figure 2-3 is a photograph of one installed isolator and damper. The isolated accelerator had horizontal and vertical frequencies of 0.5 Hz and 0.9 Hz, respectively. The maximum horizontal (vertical) displacement of the isolators was 7 inches (2 inches) and the devices (e.g., protection gate valves and aluminum tubes in Figure 2-2) connected to the accelerator were upgraded to accommodate these relative displacements (with respect to the accelerator supports). Each isolator was equipped with a mechanical fuse that unlocked automatically at a threshold seismic motion.

1. Tank; 2. GERB isolators; 3. Tank supports; 4. Mechanical fuses; 5. Protection gate vales; 6. Aluminum tubes.

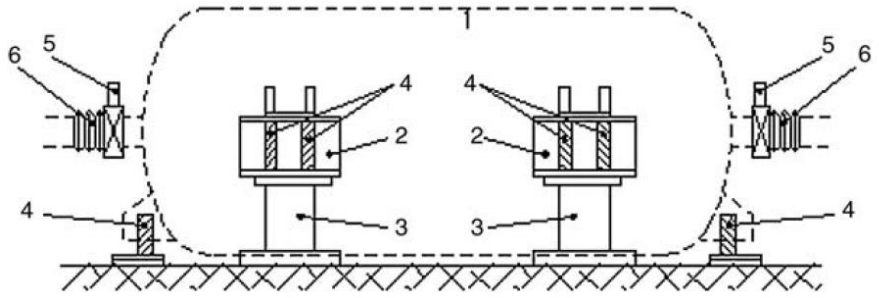

Figure 2-2. Elevation of the isolated Bucharest tandem accelerator (Dobrescu and Marinescu, 2005)

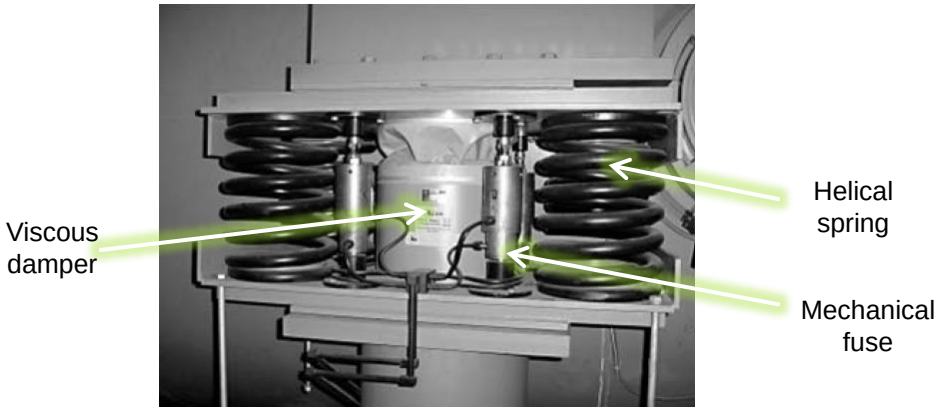

Figure 2-3. Photograph of a GERB isolator and damper under the Bucharest tandem accelerator (Dobrescu and Marinescu, 2005)

Spring and viscous damper devices, such as the GERB isolators, have been used to seismically protect components in nuclear power plants. For example, the GERB isolators were used to seismically upgrade steam generators and safety-related piping in some WWER power plants in the Czech Republic, the Slovak Republic, and Hungary (Masopust *et al.*, 1993; Pecínka *et al.*, 2001). Figure 2-4 presents a photograph of the installed GERB isolators beneath a steam generator at the Bohunice nuclear power plant (NPP) in the Slovak Republic. Figure 2-5 presents a photograph of a motor-operated valve isolated using GERB isolators in a WWER power plant.

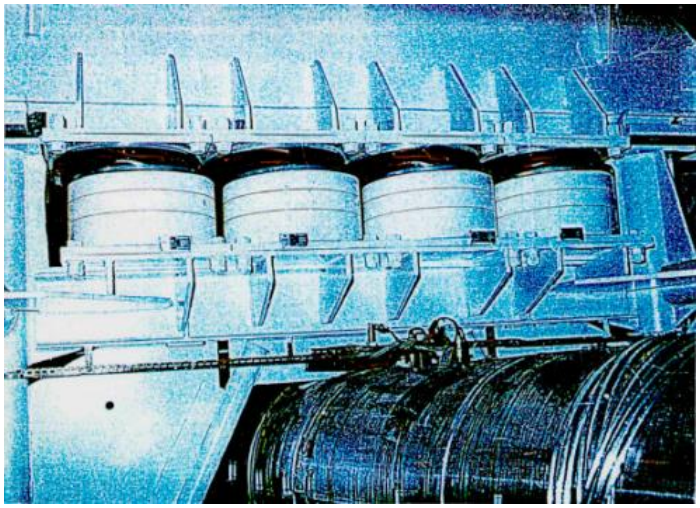

Figure 2-4. Photograph of the GERB isolators underneath a steam generator at the Bohunice NPP in the Slovak Republic (Pecínka *et al.*, 2001)

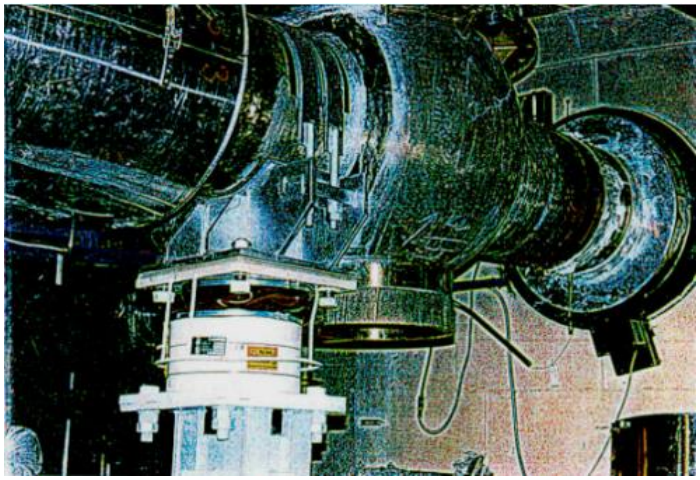

Figure 2-5. Photograph of a GERB isolator underneath a motor-operated valve in an NPP in the Slovak Republic (Pecínka *et al.*, 2001)

Chalhoub and Kelly (1988) performed earthquake-simulator tests on two fluid-filled tanks: one attached directly to an earthquake-simulator, representing a fixed-base tank, and the other mounted on the first floor of an isolated nine-story steel frame. The steel frame, representing a 1/4 length scaled building, was isolated using eight elastomeric bearings. Tests were conducted using unidirectional seismic inputs and sinusoids. The test data showed that isolation reduced accelerations, displacements, and hydrodynamic pressure on the tank wall. Kelly and Mayes (1989) proposed to seismically isolate fluid-containing tanks supported on a large concrete basemat. Both Tajirian (1993) and Zayas and Low (1995) extended the study and analyzed the response of Liquified Natural Gas (LNG) tanks isolated using rubber bearings and Friction Pendulum bearings, respectively. Not unexpectedly, these authors concluded that base isolation enabled significantly lower seismic demands in LNG tanks. Others have numerically simulated the behavior of base-isolated fluid-filled tanks; information is summarized in Mir *et al.* (2022b). Calugaru and Mahin (2009) conducted earthquake-simulator tests on a cylindrical fluid-filled tank. The tank was 6 ft tall with a diameter of 6 ft and was tested in two configurations: 1) non-isolated, and 2) base isolated using Triple Friction Pendulum (TFP) bearings. Figure 2-6 is a photograph of the isolated tank. Tri-directional seismic inputs were imposed. Similar to the findings of other researchers, these authors concluded that seismic demands on the tank were significantly smaller when it was base isolated.

Figure 2-6. Photograph of an isolated fluid-filled tank (Calugaru and Mahin, 2009)

The application of seismic base isolation to critical electrical equipment, such as power transformers and disconnect switches, has been studied extensively in the past two decades. Ersoy *et al.* (2001) performed analytical and experimental studies on an 8.9 ft tall power transformer model with plan dimensions of 7.9 ft × 7.2 ft. A 11.5 ft tall bushing was installed atop the transformer model that was supported on four single

Friction Pendulum (SFP) bearings. Earthquake tests were conducted at the National Center of Research for Earthquake Engineering (NCREE) in Taiwan. Figure 2-7 is a photograph of the test setup. Isolation of the transformer reduced its response by 60% on average. Murota *et al.* (2005) tested a similar power transformer model (and its bushing) at NCREE using two isolation systems: 1) a hybrid sliding and low-damping rubber bearing system in which sliding bearings were installed at the four corners of the transformer and two rubber bearings were placed at its center, and 2) segmented (or multi-stage) high-damping rubber bearings, consisting of three stacks of four rubber bearings, installed at the corners of the transformer model. The introduction of the hybrid isolation system, which is not permitted in US practice because of the incompatibility of the vertical deflections of sliding and rubber isolators, was not beneficial and some acceleration responses were amplified. The multi-stage rubber bearing isolation system reduced accelerations in the bushings.

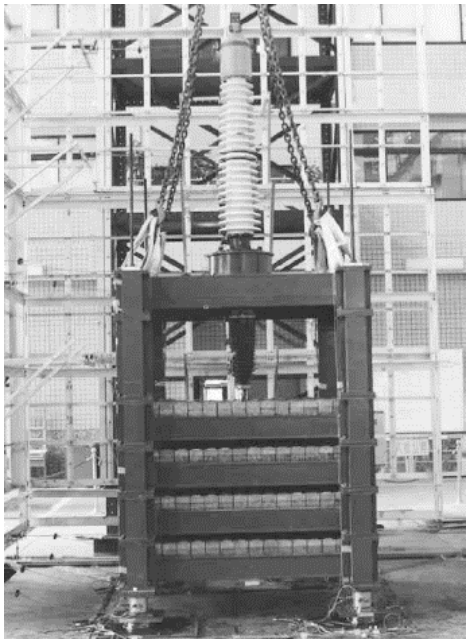

Figure 2-7. Photograph of a power transformer model and its bushing at NCREE (Ersoy *et al.*, 2001)

In the mid-2000s, a multi-stage linear rubber bearing isolation system, equipped with fluid viscous dampers, was used by ExxonMobil as a tuned mass damper (TMD) to seismically protect the drilling derrick on the Sakhalin I Orlan oil and gas platform (Constantinou and Whittaker, 2022). Figure 2-8, courtesy of ExxonMobil and Motioneering, presents a photograph identifying the location of the TMD atop the drilling derrick, and an isometric drawing of the TMD.

a) Sakhalin I Orlan platform (courtesy of ExxonMobil)

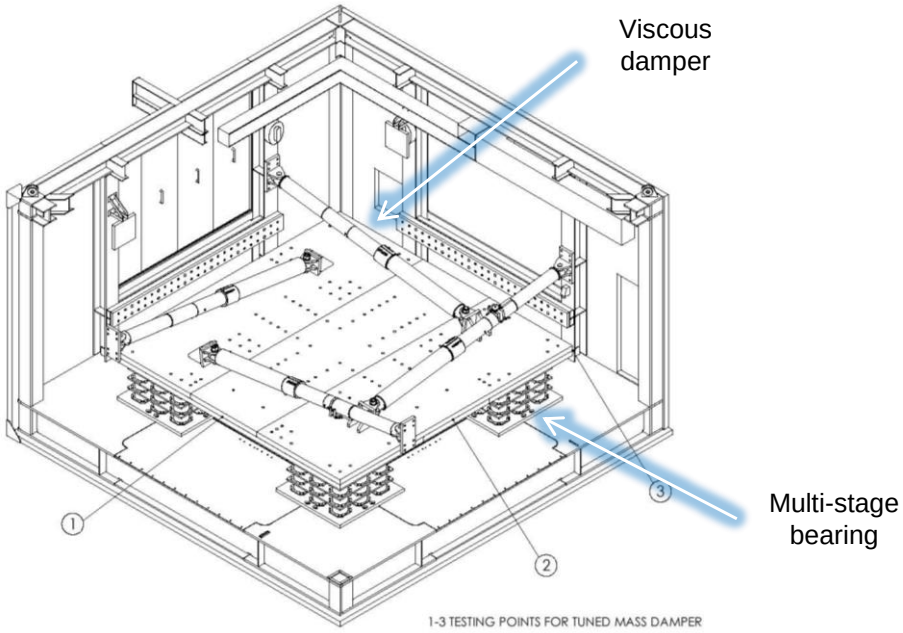

b) TMD isometric showing multi-stage bearings (courtesy of Motioneering)

Figure 2-8. Earthquake protection of the Sakhalin I drilling derrick

Kong (2010) studied the response of a 230 kV disconnect switch using experiments and simulations and proposed retrofitting strategies using wire rope isolators and Friction Pendulum bearings. Figure 2-9 presents the test setup mounted on the earthquake simulator at the University at Buffalo. Accelerations and

base shears were substantially reduced when the disconnect switch was base isolated. The use of isolation increased the total displacement of the switch, which must be addressed in the design of interconnections (Kong, 2010).

Figure 2-9. A 230 kV disconnect switch installed on the earthquake-simulator at the University at Buffalo (Kong, 2010)

Oikonomou *et al*. (2012; 2016) conducted a series of earthquake-simulator tests on a one-third length scale model of a transformer with a porcelain bushing installed on its roof. Steel plates were used to add mass to the model, which had a total weight of 47 kips. Three base isolation systems were considered for the experiments: 1) lead-rubber bearings, 2) scaled TFP bearings, and 3) full scale TFP bearings. Bearings were installed at the four corners of the model. Seven three-component earthquake records were used to represent a uniform hazard response spectrum developed for a site in California. Tests were performed for various configurations of the model wherein symmetric and asymmetric distributions of mass were simulated by changing the positions of the steel plates. Figure 2-10 presents a photograph of the model with an asymmetric distribution of mass, wherein the steel plates were installed on two of the four sides. The placement of the bushing on the roof of the transformer was also varied to study its response for symmetric and asymmetric configurations. Accelerations were significantly reduced in all isolated configurations. The successful outcomes of the Oikonomou *et al.* studies led Bonneville Power Administration to base isolate an existing high voltage transformer in 2013 and Seattle City Light to base isolate a new high voltage power transformer in 2014 (Cochran, 2015). Both applications used triple Friction Pendulum bearings.

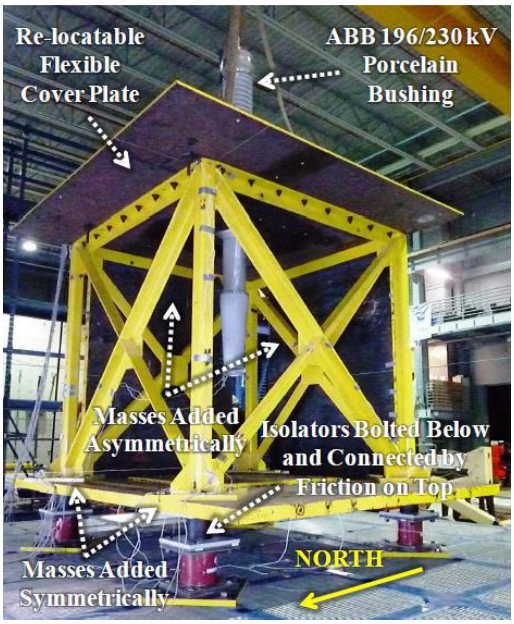

Figure 2-10. A base-isolated transformer model assembled on the earthquake-simulator at the University at Buffalo (Kong, 2010)

Lee and Constantinou (2017; 2018) tested a transformer model similar to that of Oikonomou *et al*. (2012; 2016), but focused on developing a passive three-dimensional (3D) seismic isolation system, which consisted of TFP bearings providing horizontal isolation, supported atop spring-damper devices for vertical isolation. The model was tested at the University at Buffalo using three-component earthquake records. Test results demonstrated that this 3D seismic isolation system was generally effective in reducing the vertical and horizonal accelerations in the model and the bushings.

Parsi *et al.* (2022) numerically demonstrated the benefits of seismically isolating safety-class equipment in advanced nuclear power plants. Two reactor buildings were considered, one housing a molten salt reactor and the other a high temperature gas reactor. Reactor vessels and steam generators were isolated at their points of the attachment to the reactor buildings. Two benefits were observed: 1) peak horizontal accelerations were reduced by a factor of between 3 and 12 in the isolated vessels, and 2) equipment designed for a site of low seismic hazard could be deployed for sites of higher seismic hazard when isolated, enabling standardization.

Mir *et al.* (2022a) conducted earthquake-simulator experiments of a base-isolated model of a fluoride-salt cooled high temperature reactor. The model was a 6.5 ft tall cylindrical tank with an outer diameter of 5 ft and involved representations of a prototype reactor vessel, a core barrel, reflector blocks in the vessel, a

fluid coolant, and spherical fuel pebbles. Figure 2-11 presents a photograph of the vessel (without the vessel head) and the reflector blocks being assembled at the University at Buffalo. The benefits of base isolation, namely, reduction in horizontal accelerations in the reactor components, were demonstrated using SFP and TFP bearings.

Figure 2-11. A base-isolated fluoride-salt cooled high temperature reactor vessel model at the University at Buffalo (Mir *et al.*, 2022a)

SECTION 3
DESCRIPTION AND TESTING OF FRICTION PENDULUM BEARINGS

3.1 Introduction

This section describes and characterizes the Friction Pendulum bearings used to demonstrate the feasibility of a mid-height seismic isolation system for a tall, slender vessel. Two types of Friction Pendulum (FP) bearings were used to seismically isolate the vessel: 1) Single Friction Pendulum bearings, and 2) Triple Friction Pendulum bearings. The bearings were tested individually to characterize their force-displacement behavior in the horizontal and vertical directions.

Section 3.2 describes the Friction Pendulum bearings. Section 3.3 presents the instrumentation and the data acquisition system. The inputs and test sequences for the testing of the FP bearings are presented in Section 3.4. Section 3.5 presents the procedures used to determine the coefficients of sliding friction and summarizes the test data. Section 3.6 characterizes the vertical stiffness of Friction Pendulum bearings.

3.2 Description of bearings

3.2.1 Single Friction Pendulum bearing

A Single Friction Pendulum (SFP) bearing consists of an articulated slider coated with a PTFE-type composite, a sliding surface of polished stainless steel, and a housing plate. Figures 3-1 and 3-2 present the elevation and cross section, and internal construction, respectively, of the SFP bearings. Fabrication drawings for the SFP bearings are presented in Appendix B.

The idealized force-displacement relationship of an SFP bearing is characterized by two parameters: 1) coefficient of friction at the sliding surface (μ), and 2) radius of curvature of the sliding surface (R). Figure 3-3 presents an idealized force-displacement relationship for an SFP bearing. The characteristic strength (Q) and post-elastic sliding stiffness (K_s) are defined as:

$$Q = \mu W \tag{3-1}$$

$$K_s = \frac{W}{R} \tag{3-2}$$

where μ and R were defined previosly and W is the instantaneous axial load on the bearing. The radius of curvature of the concave surface is a geometric property of the SFP bearing and a known quantity. The coefficient of friction, which is a function of the velocity of the sliding surface, axial load on the bearing,

and the temperature of the sliding surface, is a material parameter that is determined by testing. As the temperature of the sliding surface increases during motion, the coefficient of friction reduces. The dependence of the coefficient of friction on the sliding velocity and the axial (or normal) load for a PTFE-type composite and polished stainless-steel interface is illustrated in Figure 3-4. The breakaway friction (μ_B) is the value at which sliding starts (when the velocity is very small). Immediately after the initiation of sliding, the coefficient of friction drops to its minimum value ($\mu_{\min}$), and increases as the velocity increases. At high velocities, the coefficient of friction attains its maximum value ($\mu_{\max}$) and remains constant thereafter. An increase in normal pressure reduces the coefficient of friction.

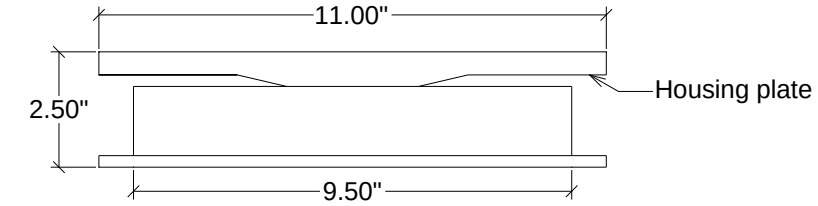

a) elevation

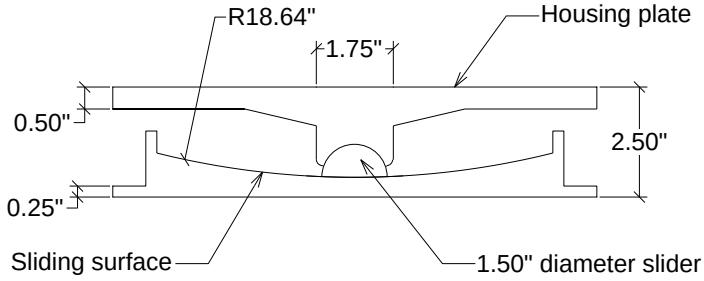

b) cross section

Figure 3-1. Geometric properties of the SFP bearing

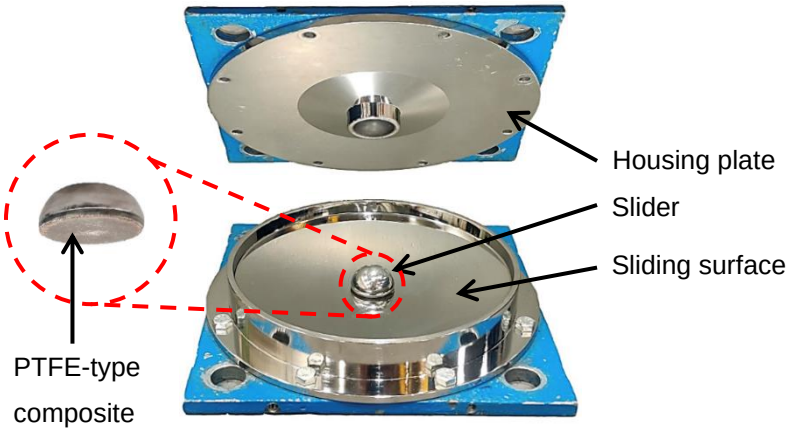

Figure 3-2. Internal construction of SFP bearing

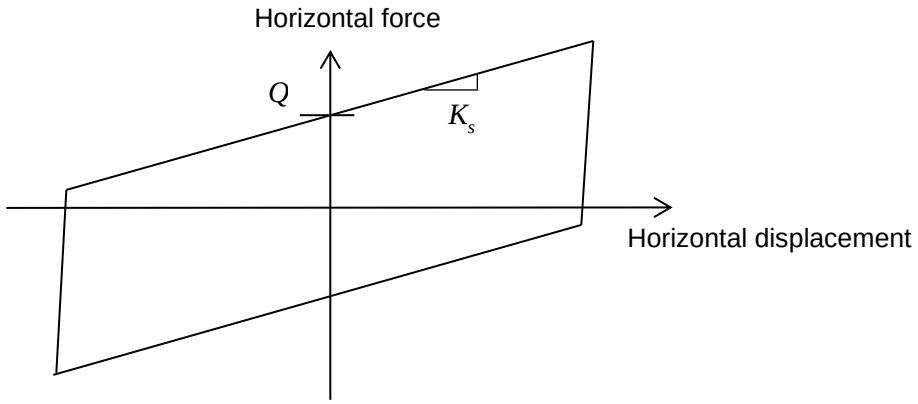

Figure 3-3. Horizontal force-displacement behavior of an SFP bearing

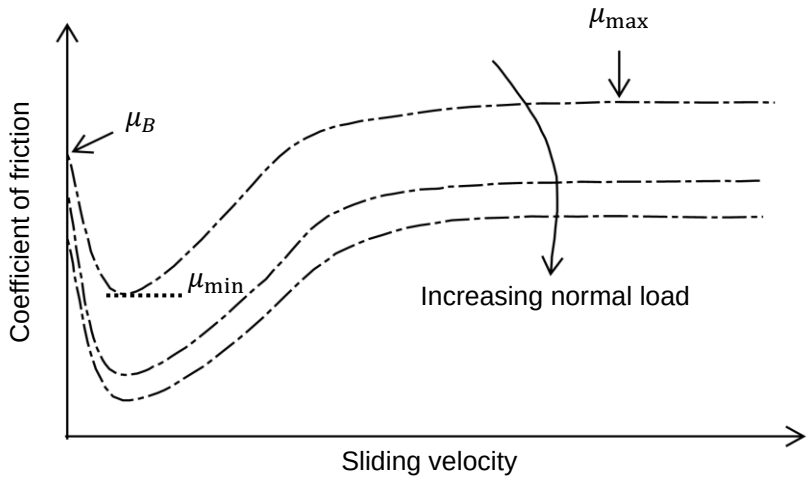

Figure 3-4. Dependence of coefficient of friction of PTFE-polished stainless steel interface on velocity of sliding and axial load (Constantinou *et al.*, 2007)

3.2.2 Triple Friction Pendulum bearing

A Triple Friction Pendulum bearing consists of two concave plates and a nested slider assembly. The slider assembly consists of two concave slide plates separated by a rigid slider and is enclosed by a rubber seal. The surfaces of the slide plates in contact with the outer concave plates and the two surfaces of the rigid slider are coated with a PTFE-type material. Sliding is permitted on all four concave surfaces, which are made of polished stainless steel. Figures 3-5 and 3-6 present the elevation and cross section, and internal construction, respectively, of the TFP bearings. The concave surfaces in the TFP bearing are numbered 1 through 4, as identified in Figure 3-5b. Fabrication drawings for the TFP bearings are presented in Appendix B.

The horizontal force-displacement relationship of a TFP bearing is characterized by: 1) radii of curvature of the concave plates, 2) radii of curvature of the slide plates, and 3) coefficients of friction at each of the four sliding surfaces. Figure 3-7 presents the idealized force-displacement loops of a TFP bearing. Depending on where the sliding occurs during motion, a TFP bearing exhibits different force-displacement relationships depicted by Regimes I to V in Figure 3-7. The mathematical formulation of the force-displacement relationship of a TFP bearing is presented in Fenz and Constantinou (2008a) and not repeated here. The radius of curvature of each of the concave surfaces is known a priori. The coefficients of friction, which are a function of the velocity of the sliding surface, axial load on the bearing, and the temperature of the sliding surface, are determined by testing.

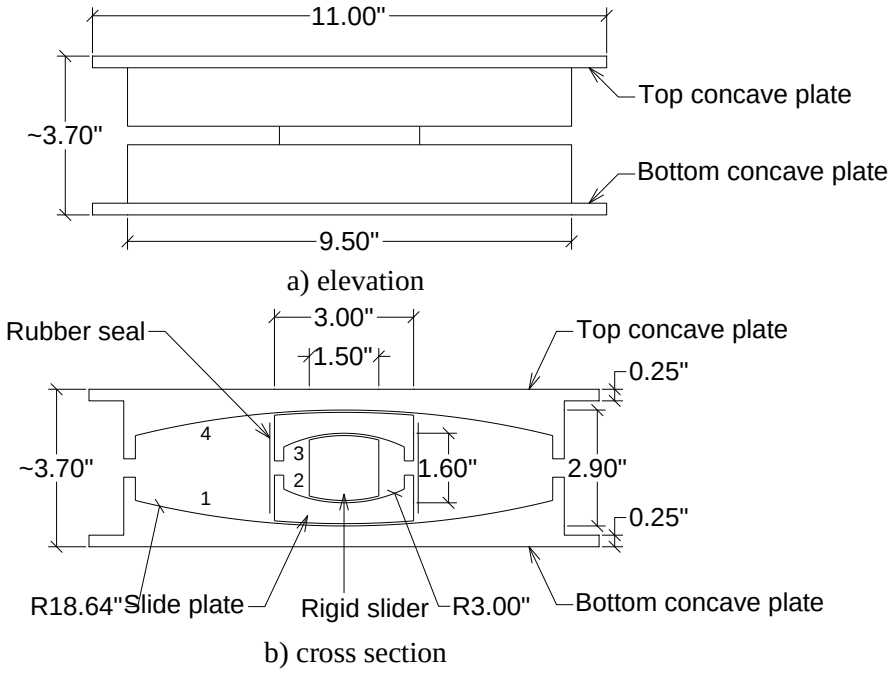

Figure 3-5. Geometric properties of the TFP bearing

3.3 Instrumentation and data acquisition

3.3.1 Single bearing testing machine

The Friction Pendulum bearings were tested in the single bearing testing machine (SBTM) at the University at Buffalo. This machine can impose combinations of axial and unidirectional shear loads and/or displacements on an individual bearing. The SBTM consists of a pedestal frame, a reaction frame, a loading beam, a horizontal actuator, two vertical actuators, and a reaction load cell. The horizontal and vertical

actuators transmit the loads and/or displacements to the bearing via a loading beam. Figure 3-8 presents a schematic diagram of the SBTM, including approximate dimensions. Figure 3-9 is a photograph of the SBTM. The maximum displacement, velocity, and force capacities of the actuators in SBTM are presented in Table 3-1.

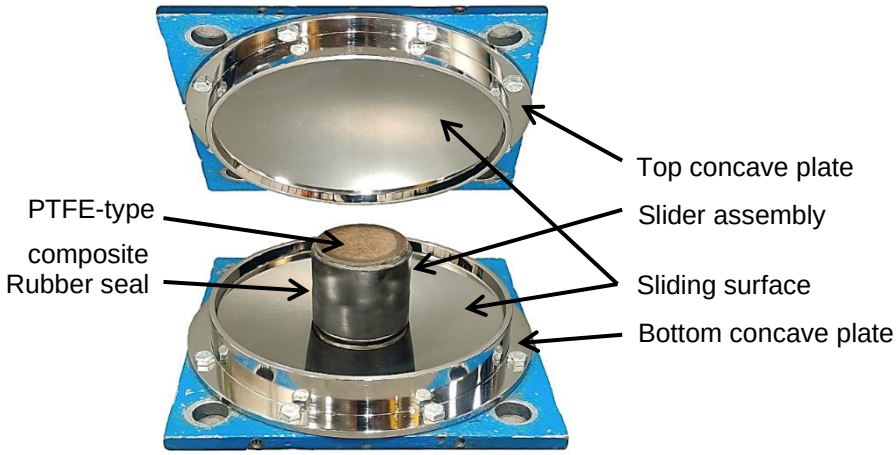

Figure 3-6. Internal construction of TFP bearing

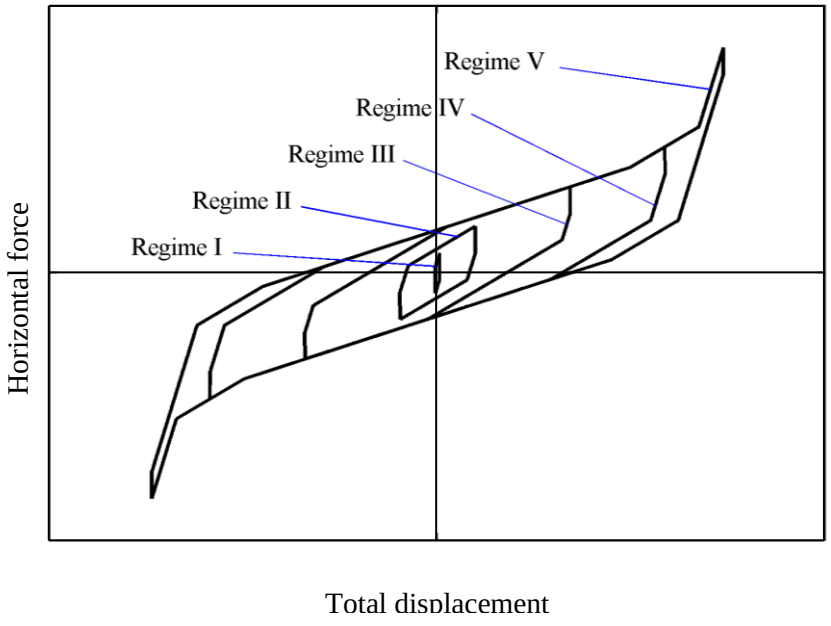

Figure 3-7. Force-displacement behavior of a TFP bearing (adapted from Fenz and Constantinou (2008a))

Each Friction Pendulum bearing was tested under combined axial and unidirectional shear loads to characterize horizontal force-displacement behavior. The vertical actuators were run under force control to

accommodate changes in bearing height but maintain a predefined (constant) axial load. The horizontal actuator was run under displacement control to impose predefined displacement histories; see Section 3.4.

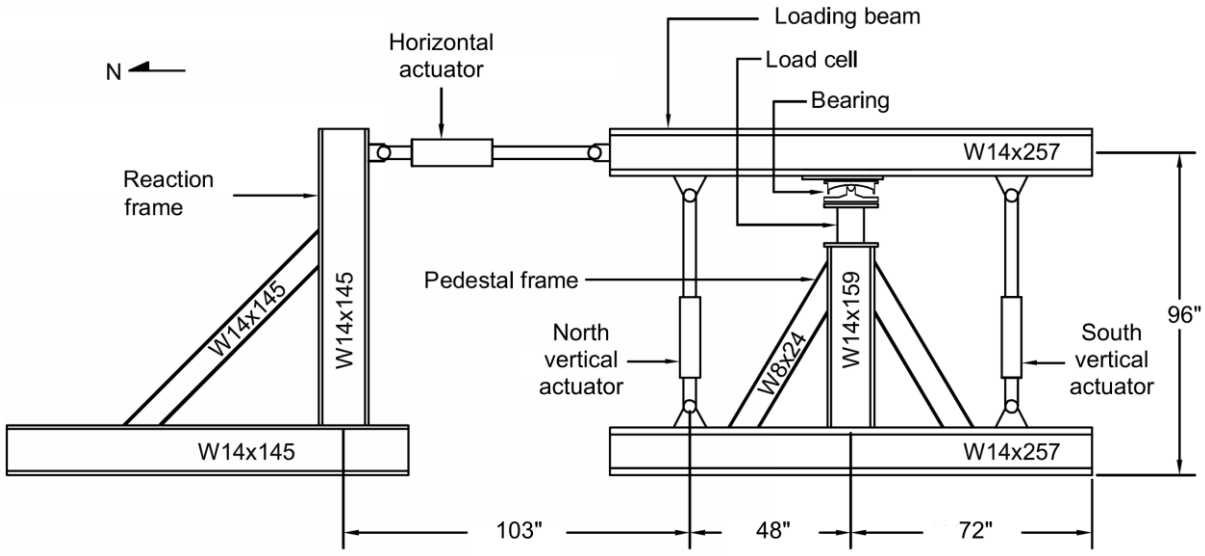

Figure 3-8. Schematic diagram of single bearing testing machine (adapted from Warn and Whittaker (2006))

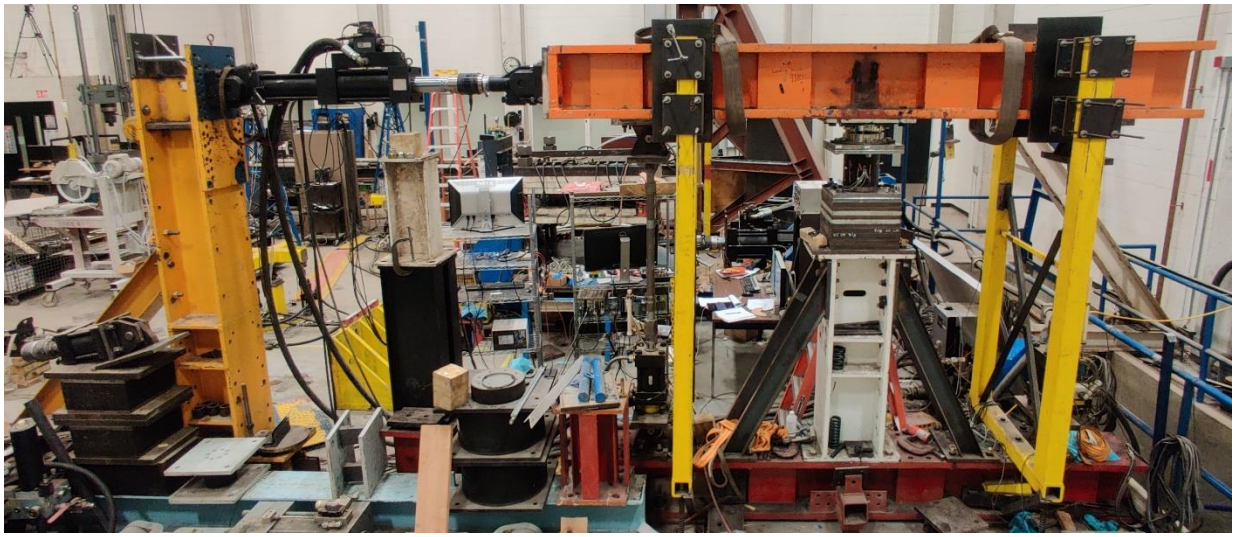

Figure 3-9. Photograph of the single bearing testing machine

3.3.2 Load cell

A five-channel load cell was placed beneath the bearings to measure the horizontal and vertical forces from the bearing characterization tests; see Figure 3-8. Placing the load cell in this location permits accurate

measurements of the reaction forces beneath the bearing and excludes the inertia force of the beam. (The forces in the actuators are affected by the inertia of the loading beam, especially for tests with high velocities where the acceleration of the beam generates an inertia force comparable to the shear force in the bearings.)

Table 3-1. Single bearing testing machine actuator capacities

Actuator	Displacement (in)	Velocity (in/sec)	Force (kip)
Horizontal	± 6.5	17.7	55
North vertical	± 2.0	2.0	71 (compression), 67 (tension)
South vertical	± 2.0	2.0	71 (compression), 67 (tension)

The five-channel load cell is capable of measuring axial load, shear force in two horizontal directions (S_x and S_y), and moment about two horizontal axes (M_x and M_y). The geometry of the load cell is shown in Figure 3-10. Since the bearing tests were conducted for unidirectional shear and axial loads, only one shear force channel (S_x) and the axial load channel were utilized.

The five-channel load cell was calibrated against a National Institute of Standards and Technology (NIST) approved reference load cell using a Tinius Olsen tension-compression machine. Two configurations were used for calibration, one for shear and the other for axial load. The shear force channel was calibrated using a two-point loading arrangement shown in Figure 3-11, wherein two identical load cells were bolted together and loaded in shear. A known axial load (P), measured using the reference load cell, was applied to the assembly resulting in shear force of magnitude $P/2$ in each load cell. An output gain of 10 V was set equal to 20 kip of shear. For the axial load channel, the reference load cell was stacked on top of the five-channel load cell, as shown in Figure 3-12. An output gain of 10 V was set equal to 50 kip of axial load.

3.3.3 Data acquisition

A total of eleven data channels were used to record the response of the SBTM actuators and the reaction load cell. The horizontal actuator contains an in-line uniaxial load cell and an internal linear variable displacement transducer (LVDT) to measure axial load and displacement, respectively. Each vertical actuator includes an in-line uniaxial load cell and externally attached transducer to record axial load and displacement, respectively. An accelerometer was mounted on the loading beam to record its acceleration to compute inertial effects. Table 3-2 summarizes the engineering quantities recorded using the eleven data channels.

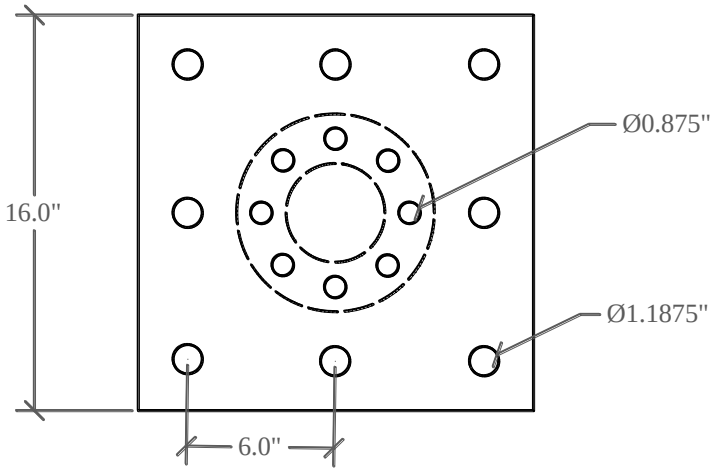

a) plan

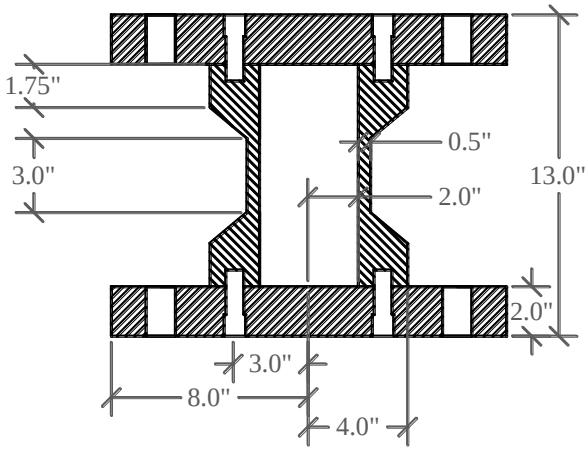

b) elevation

Figure 3-10. Plan and elevation of five-channel load cell (Mir *et al.*, 2022b)

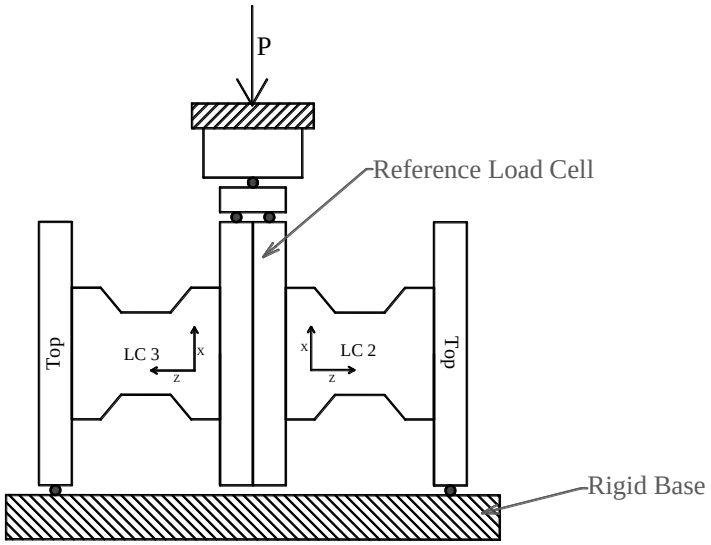

Figure 3-11. Calibration setup for shear channel

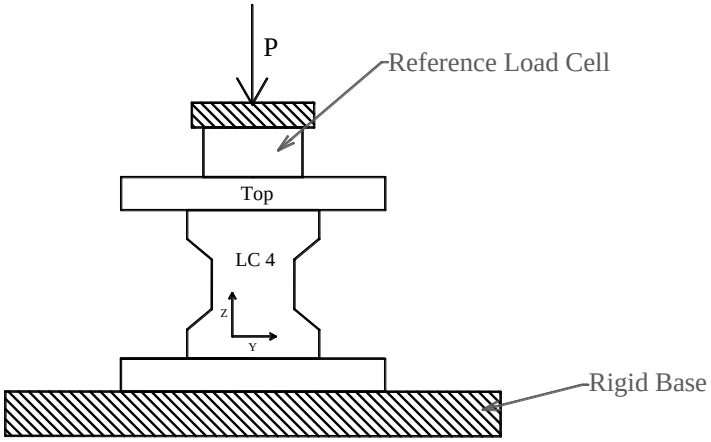

Figure 3-12. Calibration setup for axial load channel

Table 3-2. Engineering quantities measured in the bearing tests

Channel #	Recorded engineering quantity
1	Time
2	Displacement command for horizontal actuator
3	Displacement of horizontal actuator
4	Axial load in horizontal actuator
5	Acceleration of loading beam
6	Axial load in load cell
7	Shear force in load cell
8	Axial load in north vertical actuator
9	Axial load in south vertical actuator
10	Displacement of north vertical actuator
11	Displacement of south vertical actuator

3.4 Characterizing the sliding bearings

3.4.1 Introduction

A test program was developed to characterize the horizontal force-displacement behavior of the SFP (TFP) bearings, which are characterized by the radius (radii) of curvature of the sliding surface (surfaces) and the coefficients of friction at the sliding surface (surfaces). The radii of curvature of the sliding surfaces were known from the construction drawings provided by Earthquake Protection System (EPS), which are reproduced in Figures 3-1 and 3-5. The coefficients of friction were determined by testing individual bearings. The objectives of the test program were to determine:

1. Minimum ($\mu_{\min}$) and maximum ($\mu_{\max}$) values of the coefficient of friction.
2. Dependence of coefficient of friction on velocity of sliding.

The three SFP and TFP bearings were each assigned numbers 1 through 3, namely, SF1, SF2, SF3, and TF1, TF2, TF3. An axial load of 14 kips (approximately a third of 40 kips, the weight of the vessel including water, head, and internals; see Section 4) was imposed on the bearings. The bearing testing program is described next.

3.4.2 SFP bearings

Table 3-3 presents the test program for the SFP bearings. The low velocity (quasi-static) tests S1 and S4 utilized the three-cycle sinusoidal displacement history shown in Figure 3-13. The low velocity tests provide hysteresis loops with clearly defined transition points. The tests at higher velocities utilized a displacement history proposed by Constantinou *et al.* (2007), which is presented in Figure 3-14. The displacement history (termed cosine hereafter) starts with an idle time of 2 seconds during which the data acquisition begins and before the horizontal displacement history is imposed, to ensure that data is recorded in the event of unforeseen movement of the actuator. A build-up time of 60 to 180 seconds follows, during which the displacement is increased very slowly to a maximum value (u_o) at a velocity of less than 0.05 in/sec. This part of the motion allows calculation of the minimum coefficient of friction ($\mu_{\min}$) under nearly quasi-static conditions (i.e., velocity of sliding is essentially zero). An idle time of 10 seconds is then imposed to allow the temperature at the sliding surface to stabilize. The idle time is followed by 3.25 cycles of harmonic displacement, which allows calculation of the maximum coefficient of friction ($\mu_{\max}$). (To characterize the effects of frictional heating on the coefficient of friction, the temperature of the sliding surface must be measured. The temperature of the sliding surface was not recorded and the effects of heating on the coefficient of friction could not be characterized.)

Table 3-3. Test program for SFP bearings

Test	Signal	Pressure on slider (ksi)[1]	Displacement amplitude (in)	Frequency (Hz)	Maximum velocity of horizontal actuator (in/sec)	Build up time (sec)
S1	Sine	7.9	1.0	0.01	0.06	-
S2	Cosine	7.9	1.0	0.30	1.9	60
S3	Cosine	7.9	1.0	2.00	12.6	60
S4	Sine	7.9	3.3	0.005	0.1	-
S5	Cosine	7.9	3.3	0.10	0.1	180
S6	Cosine	7.9	3.3	0.60	12.3	180

1. Calculated as 14 kips divided by the area of the slider = 1.77 square inches.

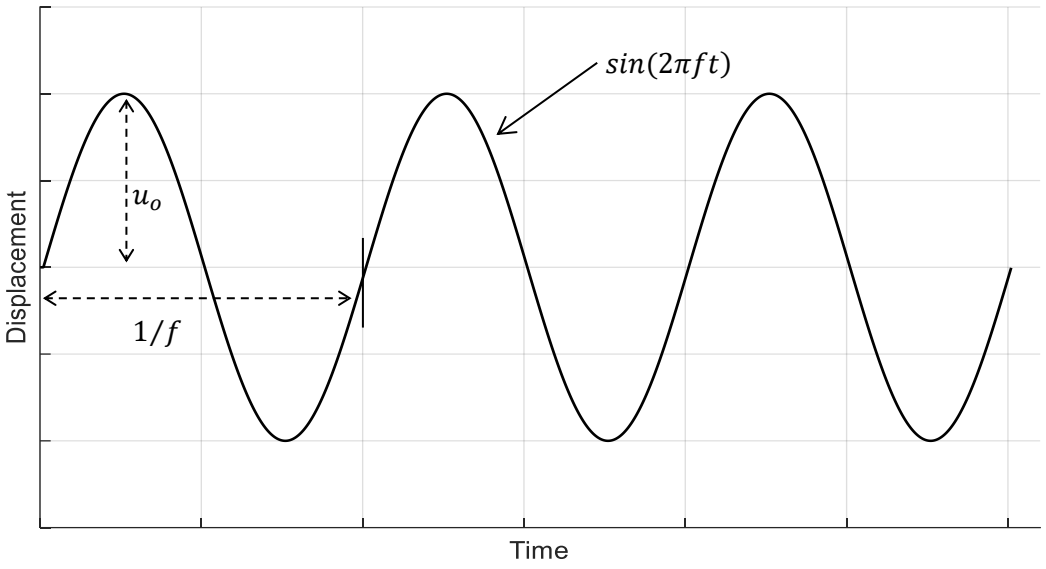

Figure 3-13. Sinusoidal displacement history for the low velocity tests of the SFP bearings

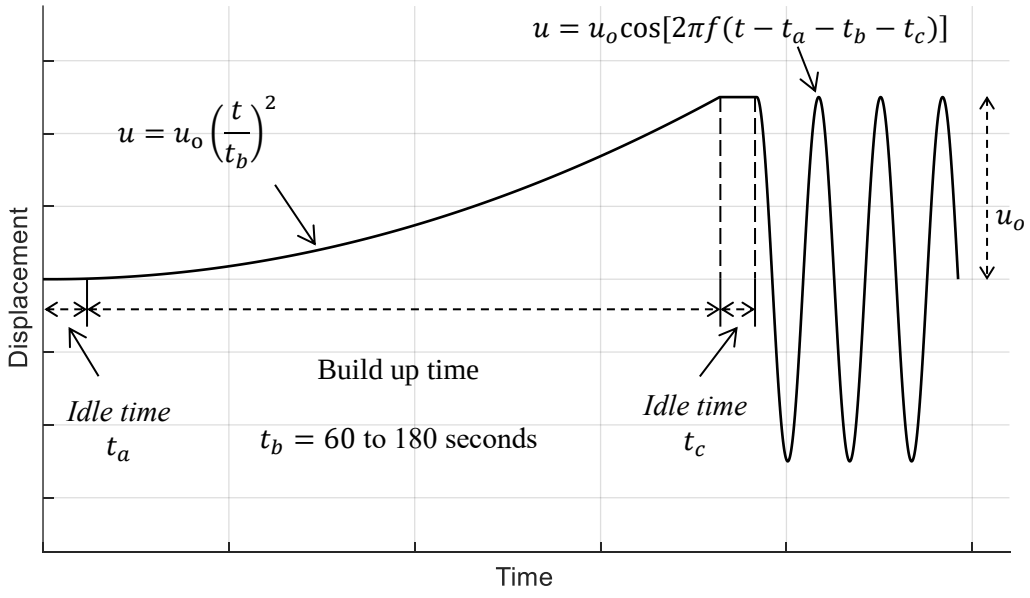

Figure 3-14. Displacement history for high velocity tests (adapted from Constantinou *et al.* (2007))

3.4.3 TFP bearings

Table 3-4 presents details of the displacement histories used for testing the TFP bearings. The low velocity tests of the TFP bearings, T1 and T4, utilized the triangular displacement history (having a constant velocity) of Figure 3-15 to characterize the changes in stiffness in the force-displacement behavior. The high velocity tests of the TFP bearings utilized the displacement history of Figure 3-14.

Table 3-4. Test program for TFP bearings

Test	Signal	Pressure on slider (ksi)		Displacement amplitude (in)	Frequency (Hz) or Velocity (in/sec)	Maximum velocity of horizontal actuator (in/sec)	Build up time (sec)
		Inner[1]	Outer[2]				
T1	Triangular	7.9	2.0	1.00	0.05 in/sec	0.05	-
T2	Cosine	7.9	2.0	1.00	0.30 Hz	1.9	60
T3	Cosine	7.9	2.0	1.00	2.00 Hz	12.6	60
T4	Triangular	7.9	2.0	5.00	0.05 in/sec	0.05	-
T5	Cosine	7.9	2.0	5.00	0.06 Hz	1.9	180
T6	Cosine	7.9	2.0	5.00	0.40 Hz	12.6	180

1. Pressure on the surfaces of the rigid slider
2. Pressure on the surfaces of the slide plates in contact with the outer concave plates

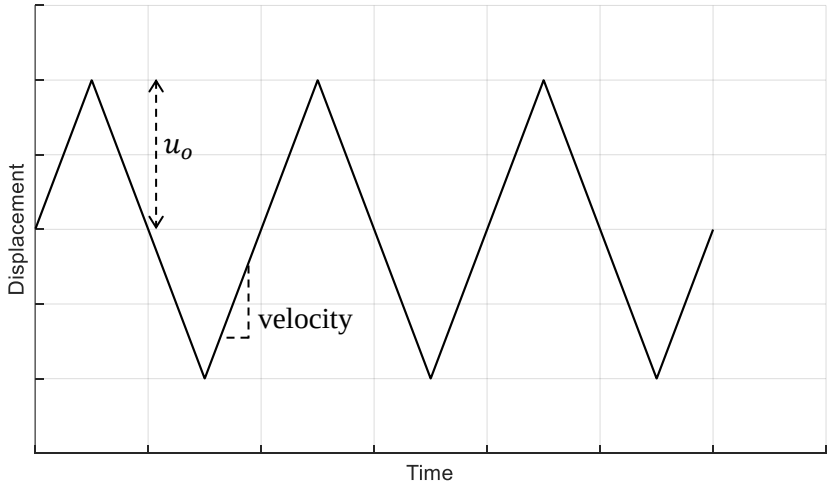

Figure 3-15. Triangular displacement history for the low velocity tests of the TFP bearings

3.5 Determining the coefficients of friction using test data

3.5.1 Introduction

Normalized horizontal force-displacement loops, wherein the horizontal force is normalized by the instantaneous axial load on the bearing, were used to determine the coefficients of friction at the sliding surfaces. The procedure used to determine the coefficients of friction for SFP and TFP bearings is described in Sections 3.5.2 and 3.5.3, respectively.

Shear (or horizontal) force and axial load from the five-channel load cell were utilized to obtain the normalized force-displacement loops. To confirm the accuracy of the load-cell data, the shear force was compared to that obtained from the horizontal actuator for the slow tests of the SFP bearings (S1 and S4 in Table 3-3), wherein the accelerations of and the corresponding inertial forces from the loading beam are negligible. The force from the horizontal actuator was corrected for the effects of the change in inclination of the horizontal and vertical actuators using the procedure outlined in Section 3.5 of Cilsalar and Constantinou (2019). Figure 3-16 presents the shear force from the load cell and the corrected force from the horizontal actuator for test S4 of the three SFP bearings. The close agreement between the two readings confirms the accuracy of the load cell data.

3.5.2 SFP bearings

Constantinou *et al.* (2007) outlines a procedure to determine the coefficient of friction for an SFP bearing. Figure 3-17 presents the normalized force-displacement loop for test S3 of SF1 bearing. The minimum value of friction ($\mu_{\min}$) occurs immediately after the initiation of sliding (when the sliding velocity is essentially zero) as illustrated in Figure 3-17. The maximum value of friction ($\mu_{\max}$) occurs at the first instant the largest sliding velocity is attained, that is, at zero displacement in the first loading cycle. In subsequent cycles, the coefficient of friction is reduced due to frictional heating (associated with an increase in temperature) of the sliding surface, as can be observed from Figure 3-17. (The effects of heating on the coefficient of friction are not characterized here. Kumar *et al.* (2019a) presents details for characterizing the effects of frictional heating on the coefficient of friction.) Figure 3-18 presents the snapshots of bearing SF1 at zero and maximum displacement (= 3.3 inches) during test S5. Normalized force-displacement loops for the six tests of the three SFP bearings are presented in Appendix A.

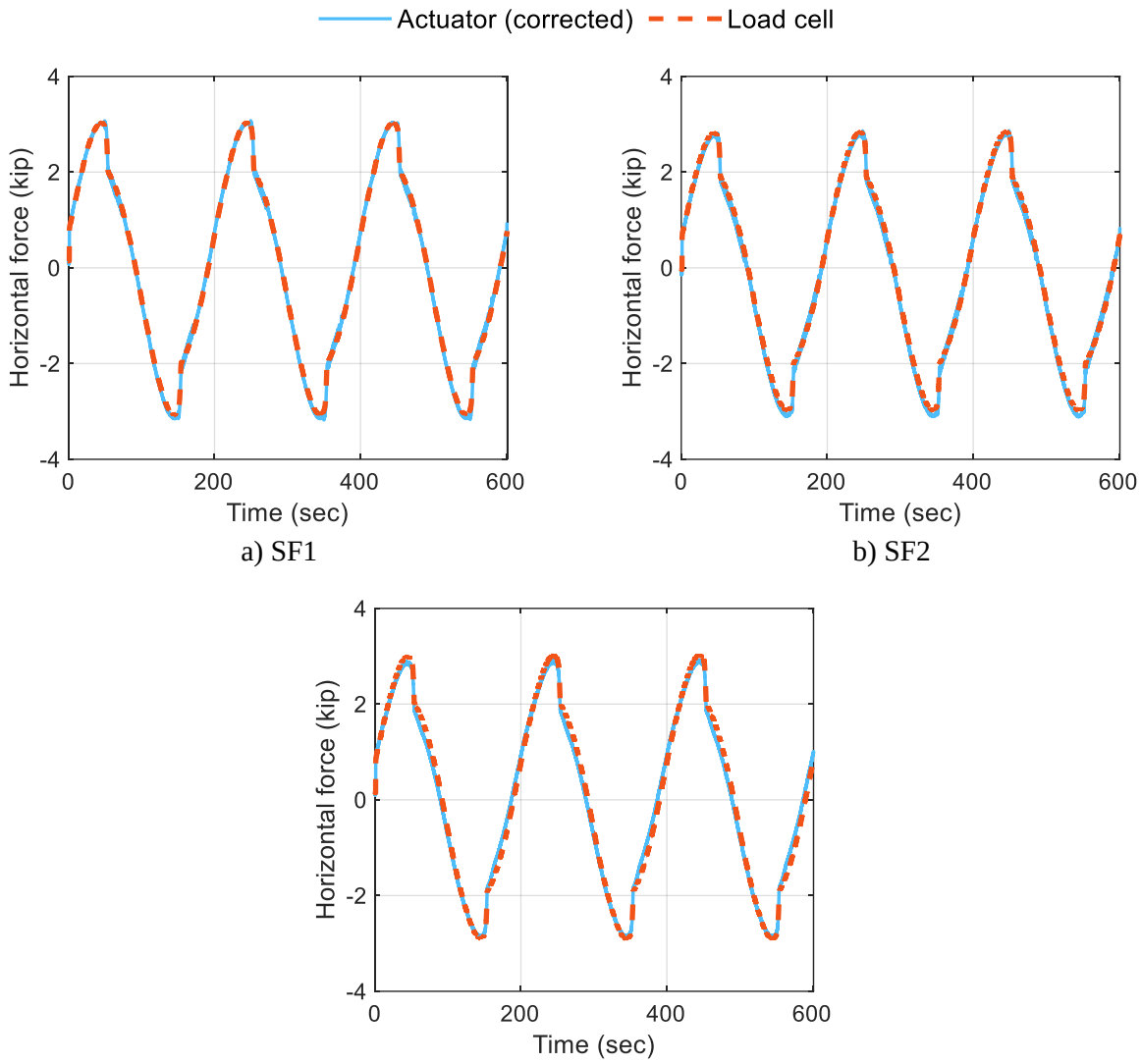

Figure 3-16. Shear force from the five-channel load cell and the actuator force from test S4 of SFP bearings

Table 3-5 presents the coefficients of sliding friction for the three SFP bearings. The values are reported for a normal pressure of 7.9 ksi (axial load of 14 kip on a 1.5-inch diameter slider) and an ambient temperature of approximately 70°F. Data from tests S2, S3, S5, and S6 were utilized to determine the minimum and maximum values of friction. Coefficients of friction from tests S1 and S4 are for intermediate velocities and were used to determine the velocity dependence of friction. The variability in the friction values in Table 3-5 is typical at both model and prototype scales (e.g., Sarlis *et al.* (2013), McVitty and Constantinou (2015), and Lee and Constantinou (2017)) and average values can be used as representative

estimates of friction. The average μ_{min} and μ_{max} for the three SFP bearings were 2.8% and 7.8%, respectively.

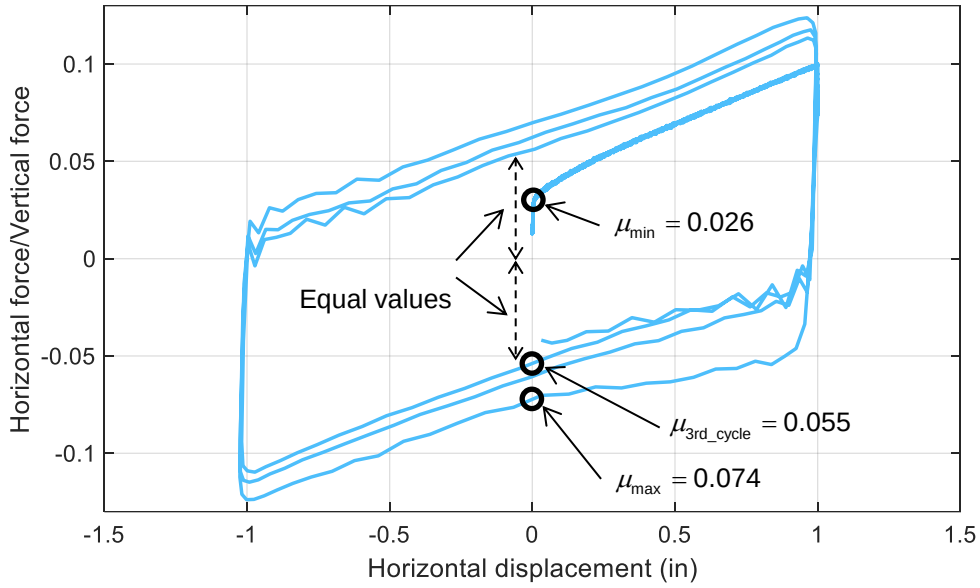

Figure 3-17. Determination of coefficients of friction for an SFP bearing

a) zero displacement b) maximum displacement

Figure 3-18. Snapshots from test S5 of bearing SF1

For a constant normal load on a Friction Pendulum bearing, Constantinou *et al.* (1990) describe the dependence of the coefficient of sliding friction on velocity of sliding (V) as:

$$\mu = \mu_{max} - (\mu_{max} - \mu_{min})e^{-aV} \tag{3-3}$$

where μ_{min}, μ_{max}, and V were defined previously and a is a rate parameter that controls the variation of the coefficient of friction with velocity. Four pairs of friction and velocity were utilized to determine the

rate parameter for each SFP bearing: 1) minimum value of friction when the sliding velocity is essentially zero, taken as the average of the μ_{min} from tests S2, S3, S5, and S6, 2) coefficient of friction from test S1, having a maximum sliding velocity of 0.06 inch/sec, 3) coefficient of friction from test S4, having a maximum sliding velocity of 0.1 inch/sec, and 4) maximum value of friction, calculated as the average of the μ_{max} from tests S2, S3, S5, and S6. Figure 3-19 presents plots for the coefficients of friction versus sliding velocity from the test data and the best-fit curves per Equation 3-3. The average rate parameter for the three SFP bearings was 8 sec/in.

Table 3-5. Coefficients of friction (%) for the SFP bearings

Test	S1	S4		S2	S3	S5	S6	Avg.
SF1	4.9	5.3	μ_{min}	3.2	2.6	2.8	2.7	2.8
			μ_{max}	7.9	7.4	7.8	7.4	7.6
SF2	4.9	5.3	μ_{min}	2.8	2.8	2.6	2.5	2.7
			μ_{max}	7.7	7.5	7.7	7.4	7.6
SF3	5.1	5.6	μ_{min}	3.2	3.2	3.1	2.5	3.0
			μ_{max}	8.5	8.5	8.2	8.4	8.4

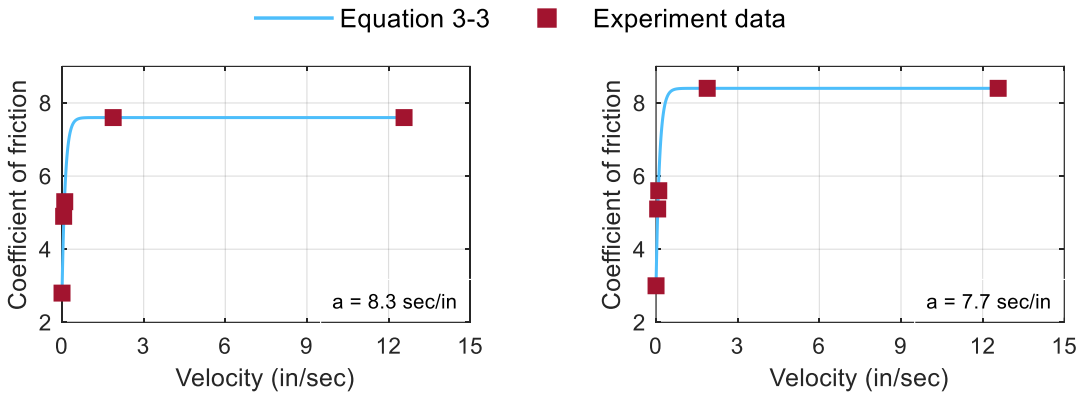

a) SF1 and SF2 b) SF3

Figure 3-19. Coefficient of friction (%) as a function of velocity for the SFP bearings

3.5.3 TFP bearings

Unlike SFP bearings wherein the slider is articulated on the housing plate, the slider assembly in a TFP bearing moves along the concave plate and results in the normal load acting eccentrically on the five-channel load cell. This is illustrated in Figure 3-20 that presents the snapshots of bearing TF1 at zero and maximum displacement (= 5.0 inches) during test T5. The slider assembly is enclosed by the open red rectangle in Figure 3-20. The green solid line represents the center of the load cell beneath the bearing and the yellow arrow the line of action of the normal load.

a) zero displacement b) maximum displacement

Figure 3-20. Snapshots from test T5 of bearing TF1

Eccentric normal load leads to an overturning moment on the load cell and induces crosstalk between the axial, shear, and moment channels. Crosstalk can lead to errors in the recorded shear (or horizontal) force, and thus the computed coefficient of friction. To check for such errors, the post-elastic stiffness of the normalized force-displacement loops were compared with the theoretical stiffness. The error in the post-elastic stiffness increased with displacement (i.e., increasing overturning moment on the load cell). To determine the coefficients of friction, the normalized loops were corrected per Equation 3-4 such that the post-elastic stiffness from the test data matched the theoretical stiffness.

$$(H/V)_{corrected} = (H/V)_{recorded} - 0.006 \times D_H \tag{3-4}$$

where H is the horizontal force, V is the vertical force, and D_H is the horizontal displacement. Figure 3-21 presents the as-recorded and corrected force-displacement loops for test T13 of bearing TF1, along with the theoretical post-elastic stiffness.

For the reduced-scale TFP bearings used herein, the coefficients of friction on the four surfaces can be determined by either decomposing the force-displacement loops for each sliding interface or by comparing the analytical force-displacement loops with those from test data. (A procedure to determine the coefficients

of friction for TFP bearings at the prototype scale is described in McVitty and Constantinou (2015).) To obtain decomposed force-displacements loops, the motion of the internal components of a TFP bearing must be monitored (e.g., see Sarlis *et al.* (2013)). For the tests herein, the internals components were not tracked and the coefficients of friction were determined by comparing the test data with analytical force-displacement loops obtained using the theory presented in Fenz and Constantinou (2008a). Figure 3-22 presents the analytical and corrected experimental force-displacement loops for test T13 of bearing TF1, wherein the coefficients of friction were determined such that the analytical loop matched the test data. The corrected normalized force-displacement loops for the three TFP bearings are presented in Appendix A.

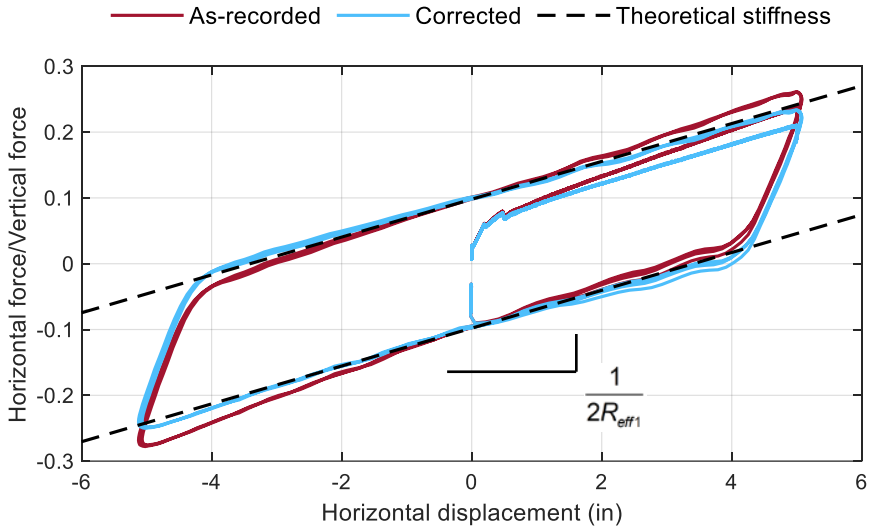

Figure 3-21. As-recorded and corrected force-displacement loops for test T13 of bearing TF1

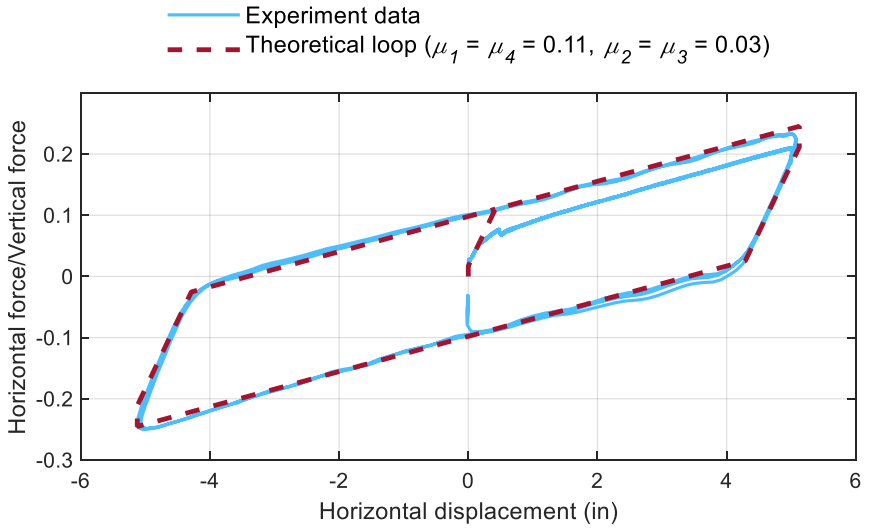

Figure 3-22. Analytical and experimental force-displacement loops for test T13 of bearing TF1

Table 3-6 presents the coefficients of sliding friction for the three TFP bearings. The values of friction are for a normal pressure of 7.9 ksi on the inner rigid slider (axial load of 14 kip on a 1.5-inch diameter slider) and 2 ksi on the outer concave slide plates (axial load of 14 kip on a 3-inch diameter slide plate). The ambient temperature during the tests was approximately 70°F. Identical to the SFP bearings, the variability in the coefficients of friction in Table 3-6 is typical at both model and prototype scales.

Table 3-6. Coefficients of friction (%) for the TFP bearings

	Test	T1	T2	T3	T4	T5	T6	Minimum	Maximum
TF1	$\mu_1 = \mu_4$	6.5	9.0	11.0	7.0	10.0	11.0	6.8	11.0
	$\mu_2 = \mu_3$	0.8	1.5	1.8	1.4	1.8	2.0	1.6	2.5
TF2	$\mu_1 = \mu_4$	6.0	9.0	11.5	6.5	9.8	11.5	6.3	11.5
	$\mu_2 = \mu_3$	0.5	1.2	1.5	0.5	1.5	1.3	1.1	2.0
TF3	$\mu_1 = \mu_4$	7.8	9.0	11.5	6.4	9.5	11.0	7.1	11.3
	$\mu_2 = \mu_3$	1.0	1.6	2.0	1.0	1.6	1.6	1.5	2.3

The TFP bearings tested here had coefficients of friction such that: 1) sliding friction on the two outer surfaces, and on the two inner surfaces are equal, and 2) friction on the outer surfaces is greater than on the inner surfaces, that is, $\mu_1 = \mu_4 > \mu_2 = \mu_3$. This is common in practice. For the outer surfaces, the minimum coefficient of friction was determined as the average of the friction values from tests T1 and T4 for a sliding velocity of 0.025 in/sec (essentially zero velocity) for each surface. (The maximum sliding velocity for each surface is one-half of the values presented in Table 3-4 because the two outer and the two inner surfaces have identical coefficients of friction and hence the sliding motion is divided equally between the surfaces, depending on the sliding regime.) The maximum coefficient of friction for the outer surfaces was determined as the average of the friction values from tests T3 and T6 for a sliding velocity of 6.3 inch/sec for each surface. The average $\mu_{\min}$ and $\mu_{\max}$ for the outer surfaces were 6.7% and 11.3%, resepctively. Data from tests T2 and T5 are for an intermediate velocity (= 0.95 in/sec) and were used to determine the rate parameter for the outer surfaces. Figure 3-23 plots the coefficient of friction versus sliding velocity for

the outer surfaces and the best-fit curves using Equation 3-3. The average rate parameter for the outer surfaces was 1 sec/in.

The minimum coefficient of friction for the two inner surfaces is one-half of the drop in the normalized horizontal force when velocity reverses sign, that is, at the maximum displacement. The velocity is essentially zero at maximum displacement, making it difficult to identify the maximum coffiecients of friction for the inner surfaces. The average of the friction values determined from tests T1 through T6 were utilized as the minimum coefficient of friction. Approximate values were assigned to the maximum cofficient of fricion for the inner surfaces. This is because the cofficients of friction for the inner surfaces are of secondary importance as the majority of the displacements and high velocities occur on the outer surfaces, and the force-displacement behavior of a TFP bearing is governed by the friction coefficients for the outer surfaces (McVitty and Constantinou, 2015). The average $\mu_{\min}$ and $\mu_{\max}$ for the inner surfaces were determined as 1.4% and 2.3%, respectively. The rate parameter for the inner surfaces was assumed to be identical to that for the outer surfaces.

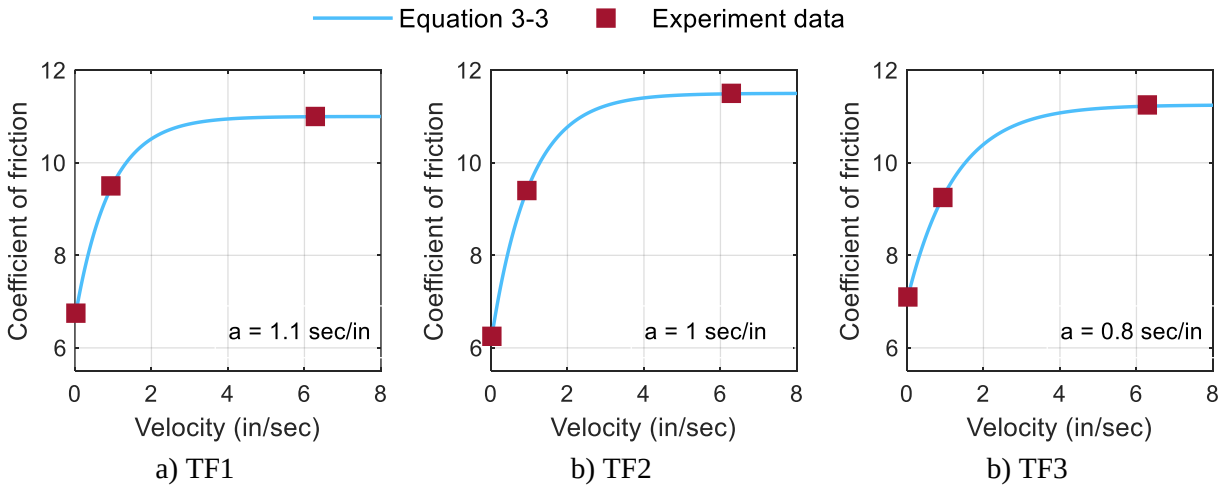

Figure 3-23. Coefficient of friction (%) as a function of velocity for the TFP bearings

3.6 Vertical stiffness of Friction Pendulum bearings

The vertical stiffness of an FP bearing can be characterized for the purpose of analysis as a fraction of the elastic axial stiffness of a carbon steel cylinder of height L (= height of the bearing), cross-sectional area A (= area of the slider), and modulus of elasticity E, namely, $\alpha(EA/L)$ where α is determined by physical testing. Much of the flexibility in the slider is associated with the composite that lines the sliding surfaces: in the concave housing for the slider (for SFP bearings) and on the surfaces of the slider: see Figures 3-2

and 3-6. Figure 3-24 presents an axial force-displacement relationship for an FP bearing in compression, which is based on testing of small and large bearings in compression.

The vertical stiffnesses for the SFP and TFP bearings herein were determined using the procedure outlined in Appendix D of Mir *et al.* (2022b). The bearings were tested in the MTS tension-compression machine at the University at Buffalo. The loading history of Figure 3-25 was utilized, wherein a pre-load of approximately 1 kip was applied before the start of data acquisition, followed by a ramp up to a load of 14 kips at a constant velocity and 2.75 cycles of ±2 kips at 0.1 Hz. Figures 3-26 and 3-27 present the axial load-displacement plots for the SFP and TFP bearings, respectively. The average vertical stiffness for the SFP (TFP) bearings was 2,370 (2,080) kip/in and approximately 12% (15%) of *EA/L*. (For the SFP bearings: A = 1.77 in^2 (area of the slider), L = 2.5 in (height of the bearing, see Figure 3-1), E = 29,000 kip/in, and EA/L = 20,500 kip/in. For the TFP bearings, A = 1.77 in^2 (area of the inner rigid slider); L = 3.7 in (height of the bearing, see Figure 3-5), and EA/L = 13,850 kip/in.) The expected axial stiffness of production FP bearings is between 0.1 and 0.2 times EA/L (Constantinou, 2022).

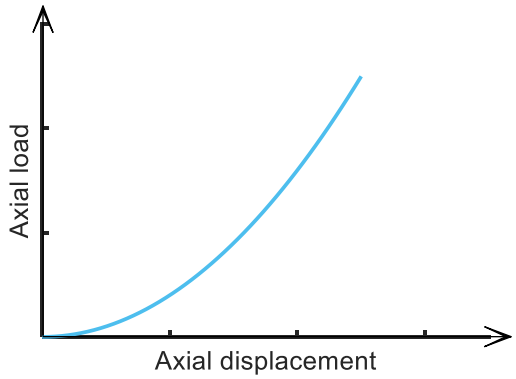

Figure 3-24. Force-displacement behavior of a FP bearing in compression

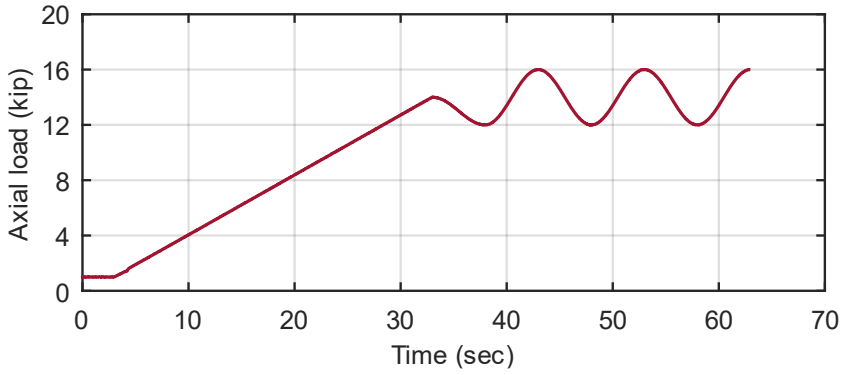

Figure 3-25. Loading history utilized to characterize the vertical stiffness of FP bearings

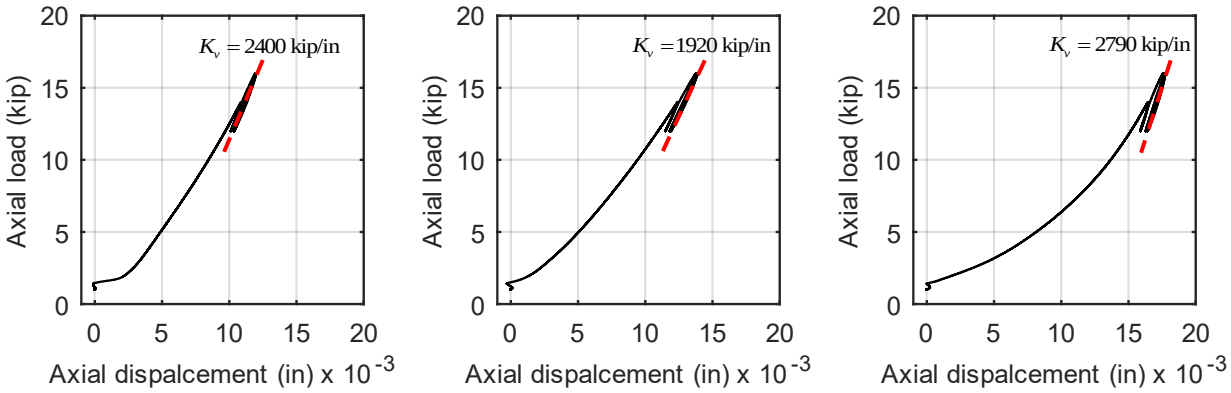

a) SF1 b) SF2 b) SF3

Figure 3-26. Axial load-displacement plots for SFP bearings

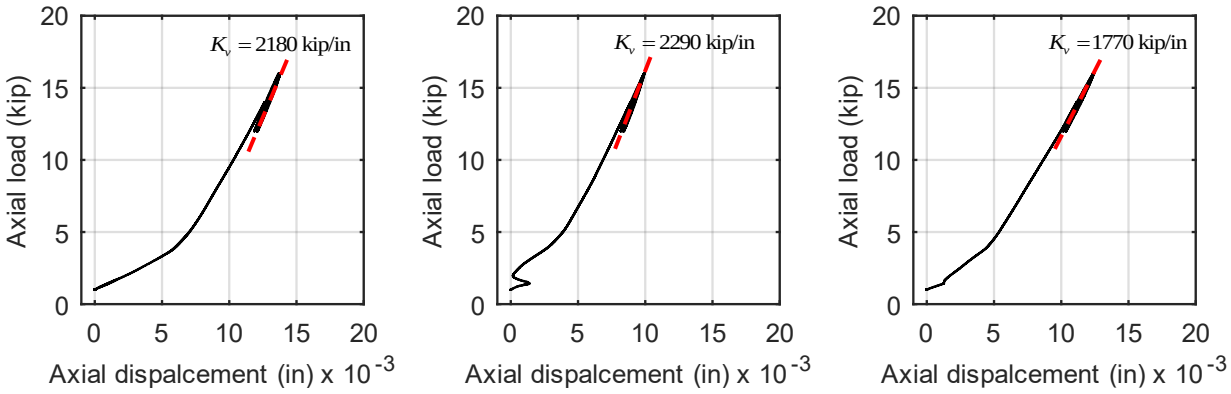

a) TF1 b) TF2 b) TF3

Figure 3-27. Axial load-displacement plots for TFP bearings

SECTION 4
EARTHQUAKE-SIMULATOR EXPERIMENTS

4.1 Introduction

This section describes earthquake-simulator experiments of a tall, slender vessel that could represent a reactor vessel, a steam generator, or a heat exchanger in a nuclear power plant. The vessel was seismically isolated using the Friction Pendulum bearings described in Section 3. The goals of the experiments were to 1) demonstrate the concept of mid-height seismic isolation, and 2) build a dataset to support validation of numerical models.

Section 4.2 describes the test specimen including the vessel, its internals, and its supporting frame. Section 4.3 presents the instrumentation and the data acquisition system. Ground motions and test sequences for the earthquake-simulator tests are presented in Section 4.4. System identification and selected test results are presented in Section 4.5. Section 4.6 presents a summary and discussion on the results.

4.2 Test specimen

4.2.1 Vessel and support frame

The test specimen was a half-length scale, cylindrical, carbon steel (ASTM A36) vessel with an outer diameter of 60 inches, a height of 240 inches, and a wall thickness of 1 inch. The length scale of 0.5 is based on the physical sizes of a proposed high temperature gas reactor and a proposed steam generator. The vessel was fabricated in two pieces, one 150 inches tall and the other 90 inches tall. The lower 150-inch tall section had a 1-inch thick end plate welded at its bottom and a 1-inch thick flange welded at its top. The upper 90-inch tall section was a cylinder and 1-inch thick flanges were welded at both its ends. Twenty-four equally spaced holes were drilled in the flanges to enable a bolted connection between the two sections of the vessel. A 1/8-inch thick EPDM rubber gasket was installed between the two sections to prevent loss of water. The vessel was supported at its mid-height on a stiff steel frame by three equally spaced mounts. The mounts were welded to the vessel wall and connected to each other via shaped plates to achieve diaphragm action at the isolation plane. Bending of the support mounts was prevented using 1-inch thick stiffener plates (see panels c and d of Figure B-2).

The steel frame had plan dimensions of 116 in $\times$ 116 in and was 121 inches tall. The frame had four W10 $\times$22 corner columns concentrically braced with $6\times6\times1$ angles to provide lateral stiffness, and three W8$\times$

58 interior columns, one beneath each support mount, to provide vertical support to the vessel. The corner columns were joined by 6-inch deep by 1-inch thick plates, welded to a 1-inch thick mounting plate with a central 76-inch diameter hole. The steel frame was bolted directly to the earthquake simulator. Fabrication drawings for the support frame, vessel, and rubber gasket are provided in Appendix B. Figure 4-1 shows the test assembly installed on the earthquake simulator.

The vessel was filled with water to indirectly account for the fluid and internal equipment inside a prototype vessel. A rectangular plate, identified as Vessel head in Figure 4-1, was bolted to the top flange of the 90-inch tall upper section to attach sample internals. To prevent loss of water during testing, a 1/8-inch thick EPDM rubber gasket was installed between the rectangular plate and the vessel flange. The weight of the vessel including water, head, and internals was 39.3 kips. The total weight of the specimen and the steel frame was 49.3 kips. (The weight of the empty vessel, including the head and the internals, was 16.3 kips. The weight of the support frame was 10 kips. The weight of water inside the vessel was 23 kips.)

Three configurations of the specimen were tested: 1) non-isolated, wherein load cells were installed atop the steel frame and the vessel was bolted to the load cells via the three support mounts, 2) isolated using three single Friction Pendulum (SFP) bearings (described in Section 3.2.1), wherein bearings were installed above the load cells and beneath the support mounts of the vessel, and 3) isolated using three Triple Friction Pendulum (TFP) bearings (described in Section 3.2.2), wherein bearings were installed between the load cells and the support mounts. Figure 4-2 presents photographs of the installed bearings. Bearings numbered 1, 2, and 3, (see Section 3) were placed beneath the support mounts of the vessel on west, south-east, and north-east sides, respectively. (The bearings used in the experiments did not include a perimeter strip of cover rubber, which is used for field applications to prevent the ingress of moisture, dust, and debris. The perimeter strip of cover rubber offers no significant lateral resistance and is torn upon significant movement of a bearing, requiring replacement after significant shaking.)

4.2.2 Internals

Two internals were attached to the vessel head: 1) a 6-ft long aluminum tube with a 3-inch outer diameter, a wall thickness of 0.125 in, and first mode frequency of about 7 Hz in air (Mir *et al.*, 2022b), and 2) a 6-ft long rectangular carbon steel plate with plan dimensions of 0.5 in × 6 in and a first mode frequency of about 3 Hz in air (Mir *et al.*, 2022b). Figure 4-3 is a photograph of the installed internals on the vessel head.

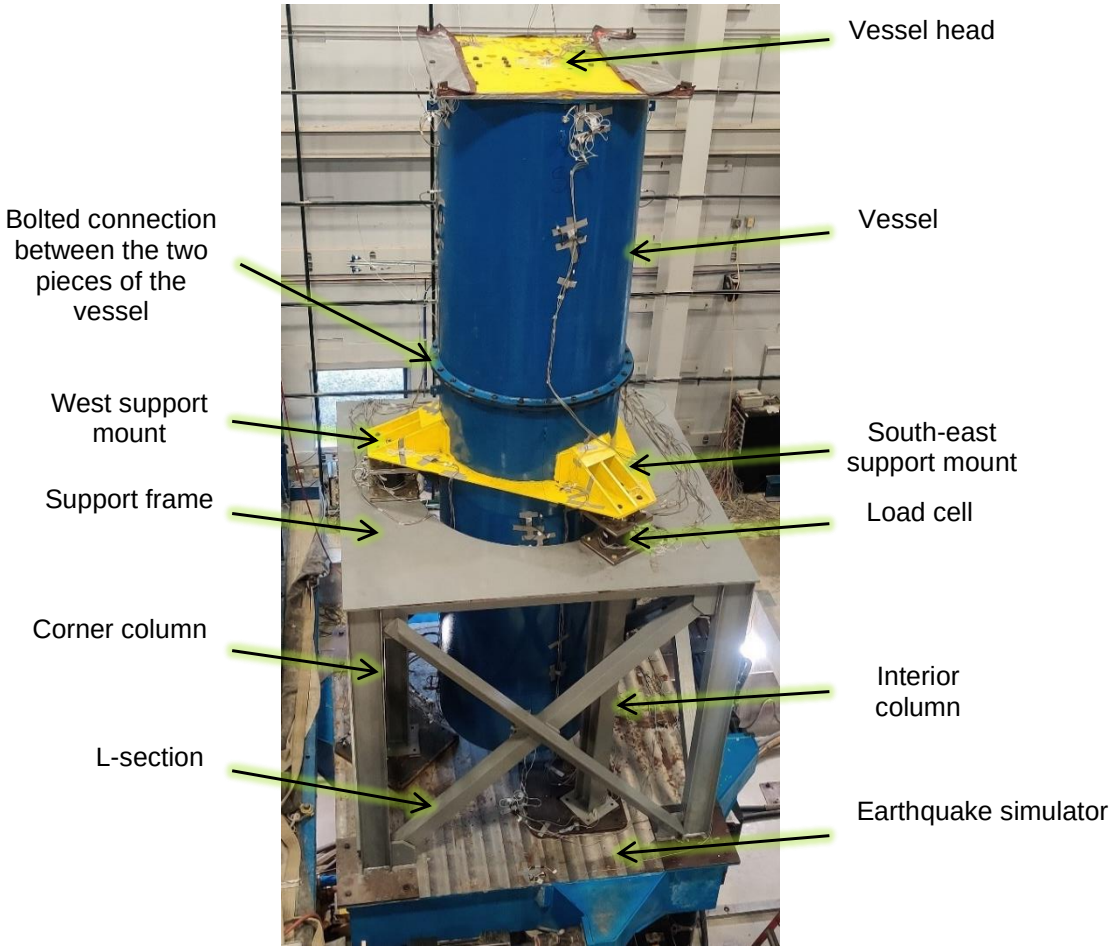

Figure 4-1. SFP-isolated vessel on the earthquake-simulator

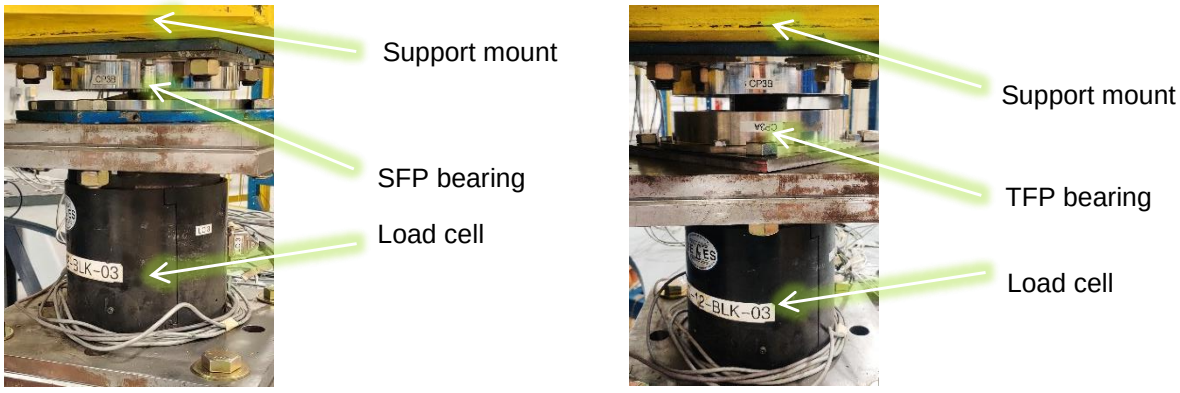

a) SFP bearing b) TFP bearing

Figure 4-2. Installed bearings in the isolated configurations of the vessel

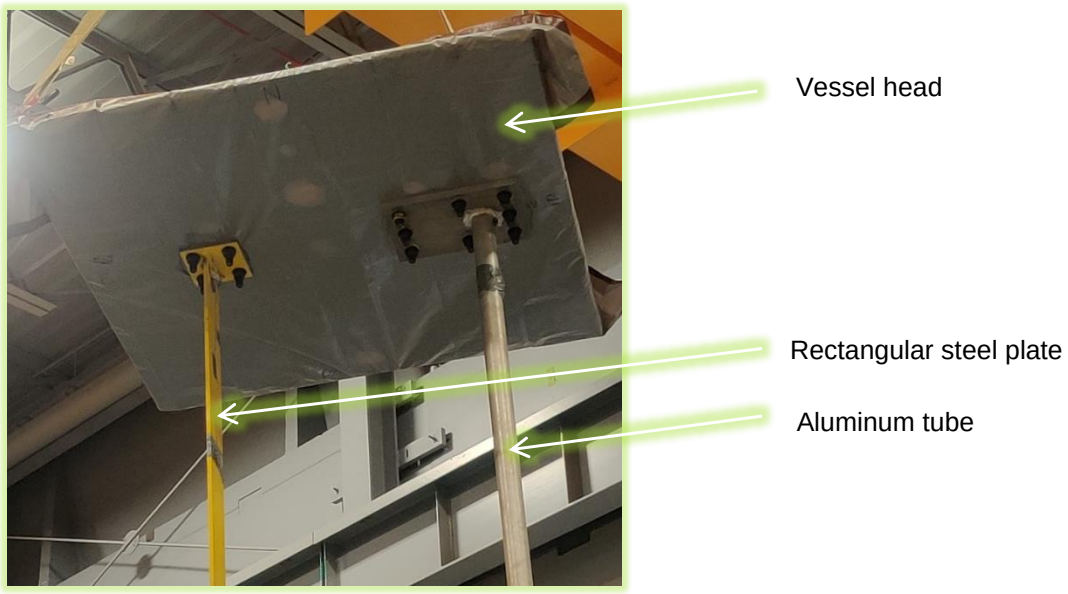

Figure 4-3. Installed internals

4.3 Instrumentation and data acquisition

The response of the test specimen was analyzed using time series of accelerations, hydrodynamic pressures, and horizonal displacements at different elevations on the vessel, forces and displacements in the bearings, and strains and accelerations in the internals. Figure 4-4 locates the instruments on the vessel and provides some key dimensions. Accelerometers were placed at the top and bottom of the vessel, and at its mid-height on the support mounts. String potentiometers measured horizontal displacements at the top, bottom, and mid-height of the vessel with respect to a reference frame on the ground. Hydrodynamic pressures on the vessel wall were measured using pressure gages, placed in arrays of four at three elevations. Two internals, shaded in green in Figure 4-4, were mounted on the vessel head. Figure 4-5 presents the locations of instruments on the two internals. For each internal, waterproofed accelerometers were installed at the mid-height and the bottom. Strains near the points of attachment of the internals were measured using waterproofed strain gages.

Figure 4-6 locates instruments on the earthquake-simulator and the support frame, and provides some key dimensions. Accelerometers were installed on the earthquake-simulator to measure the applied seismic inputs. Accelerometers were also installed at the load cell-bearing interfaces to measure accelerations below the isolation system and atop the steel frame. The forces in the bearings were measured using calibrated five-channel load cells, placed beneath the bearings (see Figure 4-2). The displacements of the bearings

were measured using string potentiometers. String potentiometers were also installed at the load cell-bearing interfaces to measure the displacements at that level with respect to the ground. Table 4-1 lists the channels used to record the response of the test specimen and the earthquake-simulator. A total of 109 channels of data were collected.

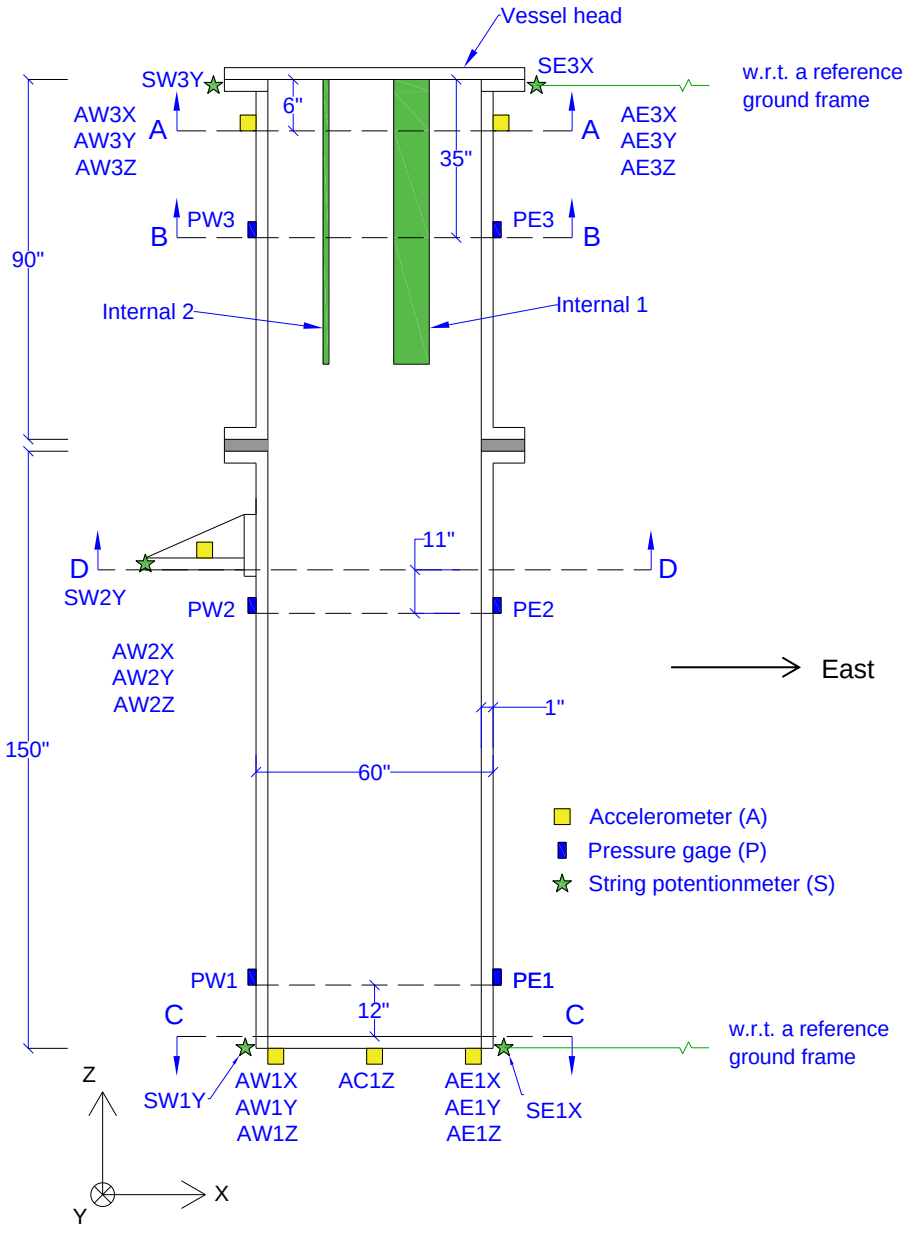

a) elevation

Figure 4-4. Overall dimensions and instrumentation of the vessel

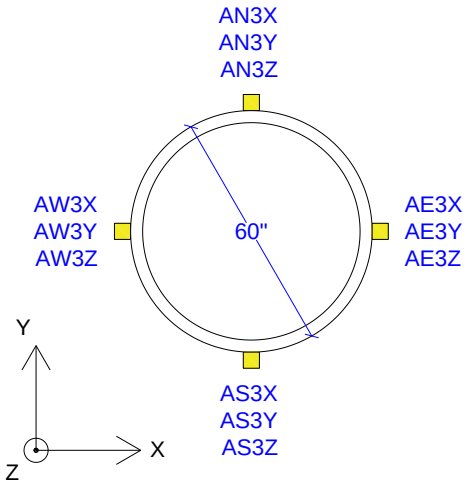

b) section A-A

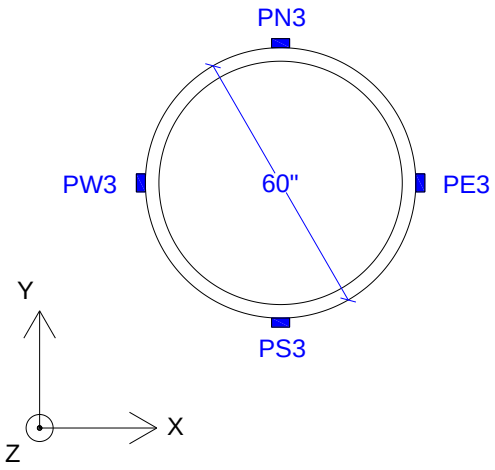

c) section B-B

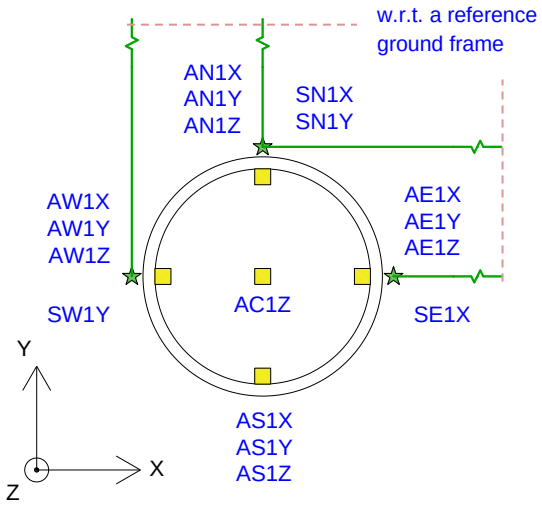

d) section C-C

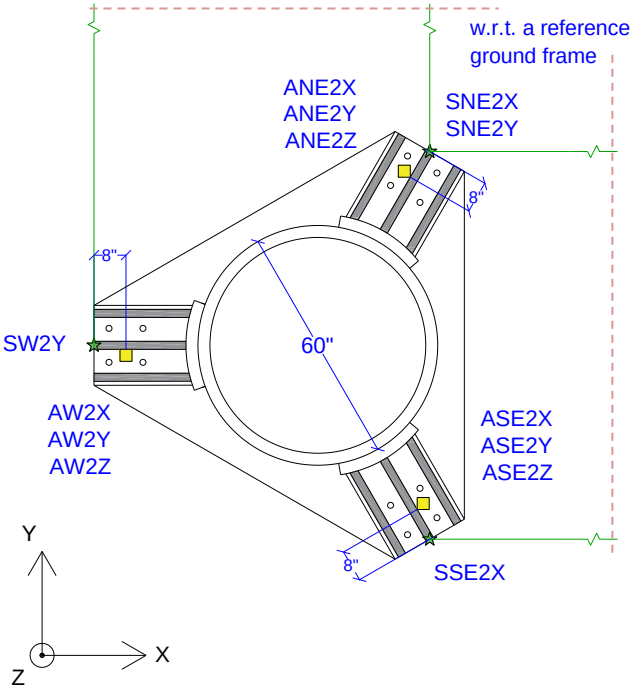

e) section D-D

Figure 4-4. Overall dimensions and instrumentation of the vessel (cont.)

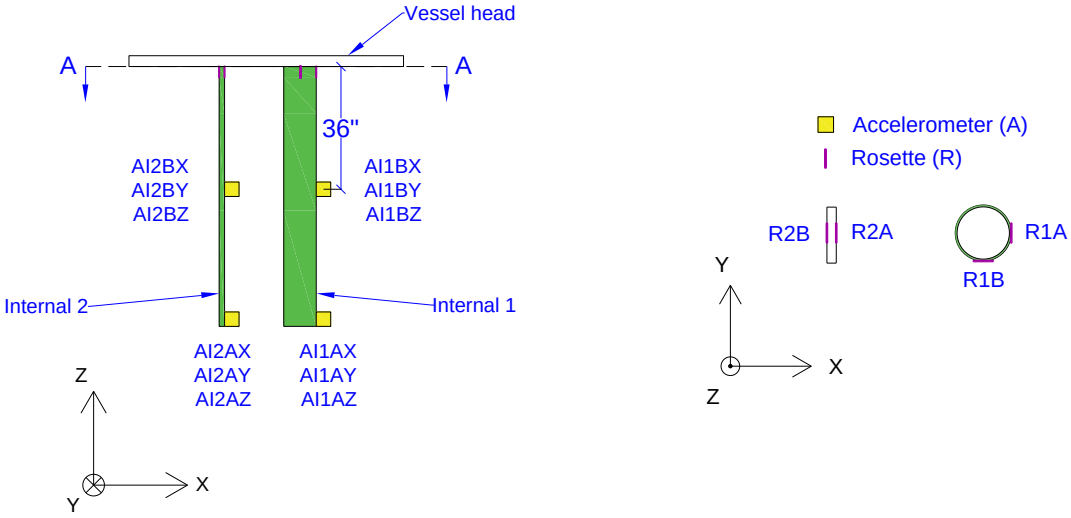

a) elevation b) section A-A

Figure 4-5. Instrumentation of internals

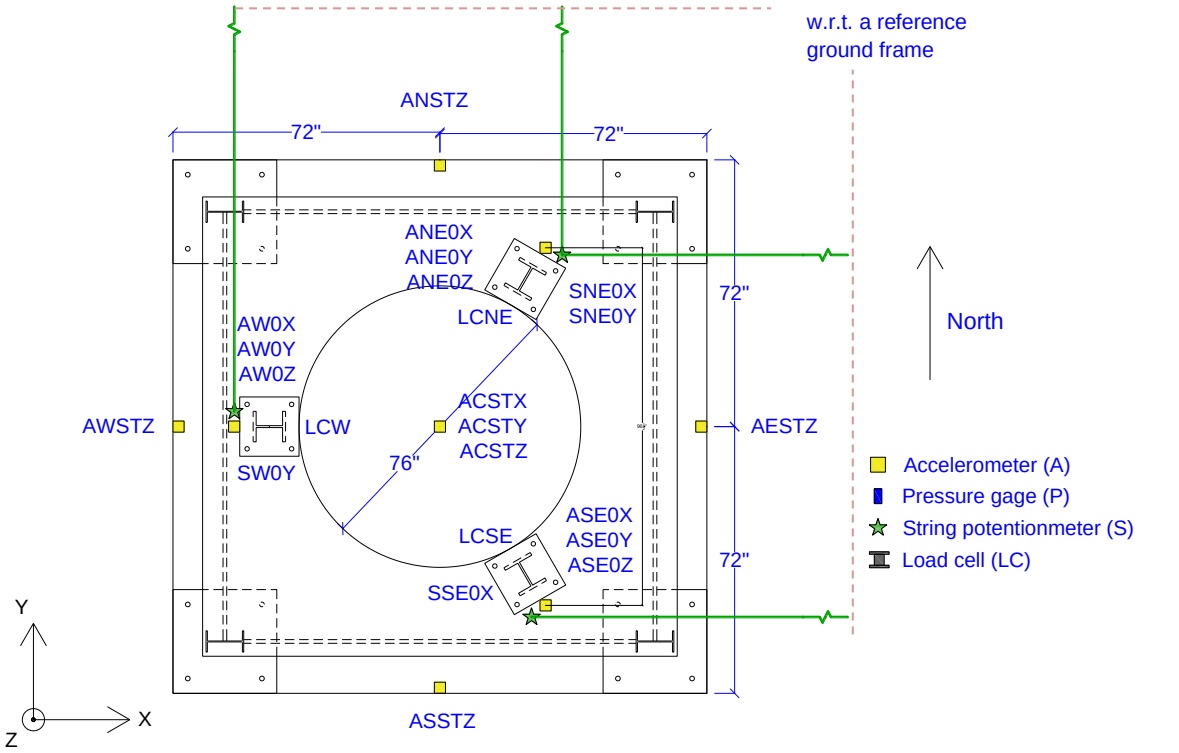

a) plan

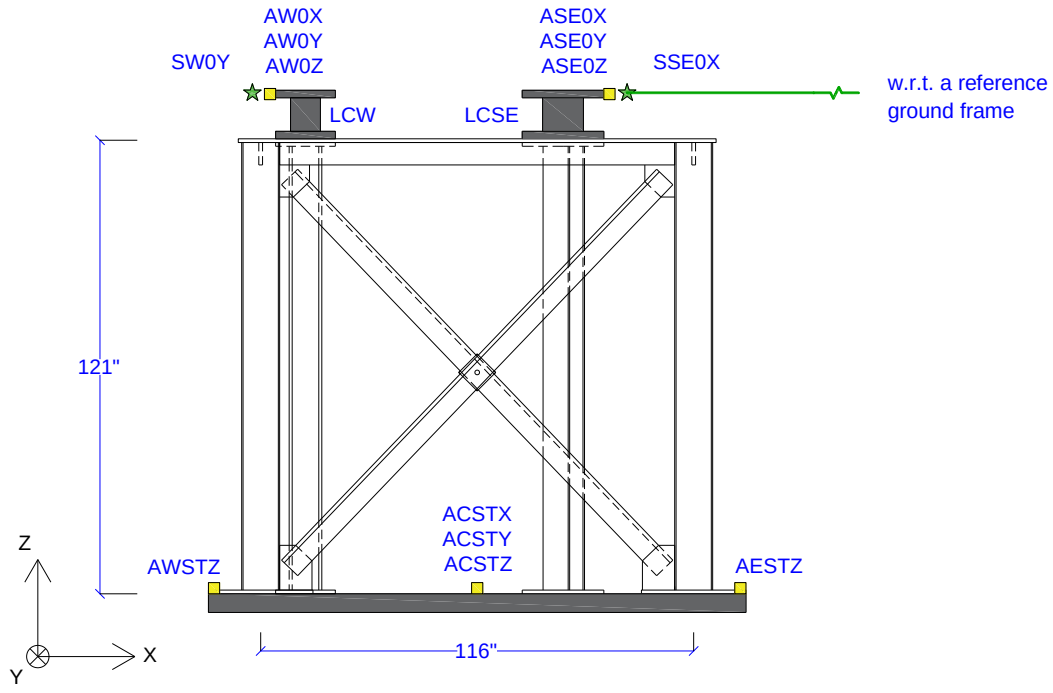

b) south elevation

Figure 4-6. Dimensions, and instrumentation of the support frame and the earthquake-simulator

Table 4-1. Channels used for the earthquake-simulator tests

	Vessel	Internals	Frame	Earthquake simulator	
Accelerometers	34	12	9	7	
String pots	12	0	4	0	
Strain gages	0	4	0	0	
Pressure gages	12	0	0	0	
Load cell	0	0	15	0	
Total channels	58	16	28	7	109

4.4 Ground motions for testing

Three ground motions from the Pacific Earthquake Engineering Research (PEER) NGA-West 2 ground motion database were used for the earthquake-simulator tests. The motions were selected to have a broad range of frequency content: from approximately 0.2 Hz to 45 Hz in the two horizontal directions and 0.2 Hz to 70 Hz in the vertical direction. The as-recorded characteristics of the three ground motions are listed in Table 4-2. The time scale of all three components of the ground motions was reduced by a factor of 0.71, consistent with the assumed length scale of 0.5. Figure 4-7 presents 5% damped acceleration response spectra of the time-scaled ground motions.

The ground motions were amplitude scaled to achieve different intensities of shaking. The maximum values of the scale factors were determined so as to not exceed:

1) The displacement, velocity, and acceleration capacities of the horizontal and vertical actuators of the earthquake simulator.
2) The displacement capacities of the SFP (= 3.5 inches) and TFP bearings (≈ 6 inches prior to the initiation of stiffening).
3) A stress in the wall and support mounts of the vessel, in the non-isolated configuration, of 36 ksi (i.e., the yield strength of the ASTM A36 carbon steel).

To estimate bearing displacements and stresses in the wall and support mounts of the vessel, response-history analyses were performed using a preliminary model of the test specimen in the computer program SAP2000 (CSI, 2019). The vessel and the support frame were modelled using frame and shell elements.

The SFP and TFP bearings were modelled using *Friction Isolator* and *Triple Pendulum Isolator* elements, respectively, with the coefficients of friction and rate parameter as determined in Section 3. Numerical modeling of the test specimen and its benchmarking is discussed in detail in Section 5.

The test sequences for the non-isolated, SFP-isolated, and TFP-isolated configurations are presented in Tables 4-3, 4-4, and 4-5, respectively. Different amplitude scale factors were used for the isolated and non-isolated configurations. Multisine excitation (see Section 4 of Parsi (2022) for a description) with a frequency range of 0.25 to 100 Hz and an amplitude of 0.1 g was imposed on the non-isolated test specimen prior to earthquake testing, to identify its modal properties.

Table 4-2. As-recorded characteristics of the ground motions used for the earthquake-simulator testing

	Record sequence number (RSN)	**Earthquake**	**Magnitude**	**Rrup (km)**	**Component1**	**Peak ground values**		
						Accel. (g)	**Vel. (in/sec)**	**Disp. (in)**
GM1	587	1987 New Zealand-02	6.6	16.1	H1	0.28	25.7	7.4
					H2	0.24	21.2	8.7
					V	0.14	9.7	6.6
GM2	728	1987 Superstition Hills-02	6.54	13.0	H1	0.17	23.5	15.0
					H2	0.21	32.3	22.3
					V	0.23	8.7	4.3
GM3	796	1989 Loma Prieta	6.93	77.3	H1	0.10	12.9	4.7
					H2	0.20	32.8	6.0
					V	0.06	11.5	3.3

1. H1 and H2 are the two orthogonal horizontal components; V is the vertical component

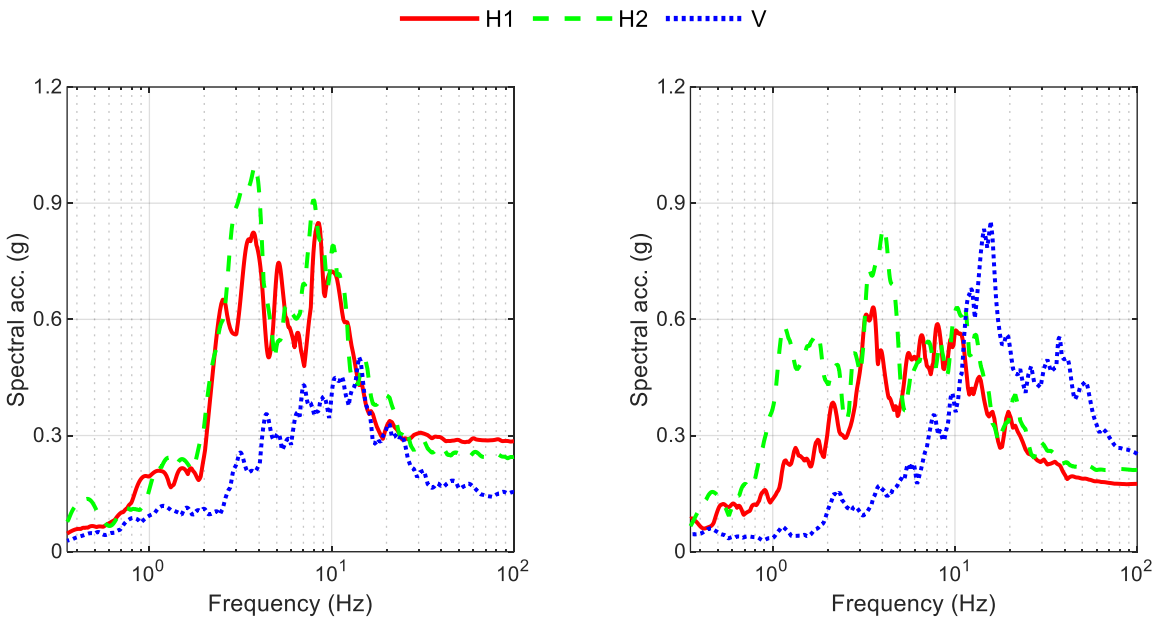

a) GM1

b) GM2

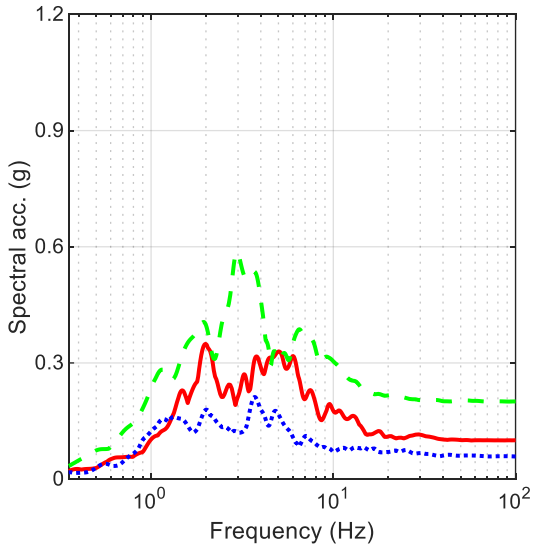

c) GM3

Figure 4-7. Acceleration response spectra of the time-scaled ground motions, 5% damping

Table 4-3. Testing sequence for the non-isolated configuration

#	Test	Input motion			Geomean horizontal PGA (g)[1,2]	Vertical PGA (g)
		X	Y	Z		
1	FBMS-X	MS	-	-	0.1	-
2	FBMS-Y	-	MS	-	0.1	-
3	FBMS-Z	-	-	MS	-	0.1
4	FB1-X	GM1_X	-	-	0.43	-
5	FB1-Y	-	GM1_Y	-	0.37	-
6	FB1-Z	-	-	GM1_Z	-	0.22
7	FB1A-2D	GM1_X	GM1_Y	-	0.20	-
8	FB1B-2D	GM1_X	GM1_Y	-	0.40	-
9	FB1A-3D	GM1_X	GM1_Y	GM1_Z	0.20	0.11
10	FB1B-3D	GM1_X	GM1_Y	GM1_Z	0.40	0.22
11	FB2-X	GM2_X	-	-	0.27	-
12	FB2-Y	-	GM2_Y	-	0.33	-
13	FB2-Z	-	-	GM2_Z	-	0.37
14	FB2A-2D	GM2_X	GM2_Y	-	0.20	-
15	FB2B-2D	GM2_X	GM2_Y	-	0.35	-
16	FB2A-3D	GM2_X	GM2_Y	GM2_Z	0.20	0.25
17	FB2B-3D	GM2_X	GM2_Y	GM2_Z	0.35	0.43
18	FB3-X	GM3_X	-	-	0.14	-
19	FB3-Y	-	GM3_Y	-	0.28	-
20	FB3-Z	-	-	GM3_Z	-	0.08
21	FB3A-2D	GM3_X	GM3_Y	-	0.10	-
22	FB3B-2D	GM3_X	GM3_Y	-	0.25	-
23	FB3A-3D	GM3_X	GM3_Y	GM3_Z	0.10	0.04
24	FB3B-3D	GM3_X	GM3_Y	GM3_Z	0.25	0.10

1. Geomean horizontal PGA = $\sqrt{\text{PGA of H1} \times \text{PGA of H2}}$
2. For unidirectional inputs, the PGA of the single ground motion component is listed

Table 4-4. Testing sequence for the SFP-isolated configuration

#	Test	Input motion			Geomean horizontal PGA (g)[1,2]	Vertical PGA (g)
		X	Y	Z		
1	SF1-X	GM1_X	-	-	0.43	-
2	SF1-Y	-	GM1_Y	-	0.37	-
3	SF1A-2D	GM1_X	GM1_Y	-	0.20	-
4	SF1B-2D	GM1_X	GM1_Y	-	0.60	-
5	SF1A-3D	GM1_X	GM1_Y	GM1_Z	0.20	0.11
6	SF1B-3D	GM1_X	GM1_Y	GM1_Z	0.60	0.33
7	SF2-X	GM2_X	-	-	0.27	-
8	SF2-Y	-	GM2_Y	-	0.33	-
9	SF2A-2D	GM2_X	GM2_Y	-	0.20	-
10	SF2B-2D	GM2_X	GM2_Y	-	0.35	-
11	SF2A-3D	GM2_X	GM2_Y	GM2_Z	0.20	0.25
12	SF2B-3D	GM2_X	GM2_Y	GM2_Z	0.35	0.43
13	SF3-X	GM3_X	-	-	0.14	-
14	SF3-Y	-	GM3_Y	-	0.28	-
15	SF3A-2D	GM3_X	GM3_Y	-	0.10	-
16	SF3B-2D	GM3_X	GM3_Y	-	0.25	-
17	SF3A-3D	GM3_X	GM3_Y	GM3_Z	0.10	0.04
18	SF3B-3D	GM3_X	GM3_Y	GM3_Z	0.25	0.1

1. Geomean horizontal PGA = $\sqrt{\text{PGA of H1} \times \text{PGA of H2}}$
2. For unidirectional inputs, the PGA of the single ground motion component is listed

Table 4-5. Testing sequence for the TFP-isolated configuration

#	Test	Input motion			Geomean horizontal PGA (g)[1,2]	Vertical PGA (g)
		X	Y	Z		
1	TF1-X	GM1_X	-	-	0.65	-
2	TF1A-3D	GM1_X	GM1_Y	GM1_Z	0.20	0.11
3	TF1B-3D	GM1_X	GM1_Y	GM1_Z	0.60	0.33
4	TF2-X	GM2_X	-	-	0.45	-
5	TF2A-3D	GM2_X	GM2_Y	GM2_Z	0.20	0.25
6	TF2B-3D	GM2_X	GM2_Y	GM2_Z	0.50	0.61
7	TF3-Y	-	GM3_Y	-	0.43	-
8	TF3A-3D	GM3_X	GM3_Y	GM3_Z	0.10	0.04
9	TF3B-3D	GM3_X	GM3_Y	GM3_Z	0.30	0.12

1. Geomean horizontal PGA = $\sqrt{\text{PGA of H1} \times \text{PGA of H2}}$
2. For unidirectional inputs, the PGA of the single ground motion component is listed

4.5 Test results

4.5.1 Introduction

Earthquake-simulator tests were performed using unidirectional (1D), bi-directional (2D), and tri-directional (3D) inputs. This section presents test results for the 3D tests of Tables 4-3, 4-4, and 4-5. Data from the 1D and 2D tests is archived at DesignSafe (Lal *et al.*, 2023). The amplitudes of the seismic inputs and simulator-specimen interaction were different for the non-isolated and isolated configurations. Accordingly, only a qualitative comparison of specimen responses in the non-isolated and isolated configurations is presented in Section 4.6 to demonstrate the feasibility of mid-height seismic isolation. A quantitative comparison, utilizing numerical simulations of validated models, is presented in Section 5. The solid pink circles in Figure 4-8 identify locations on the test specimen and the earthquake simulator where results are reported.

The test results presented in this section include:

1. Horizontal and vertical acceleration response spectra and peak accelerations:
    a) At the center of the earthquake-simulator platform (location *C1* in Figure 4-8).

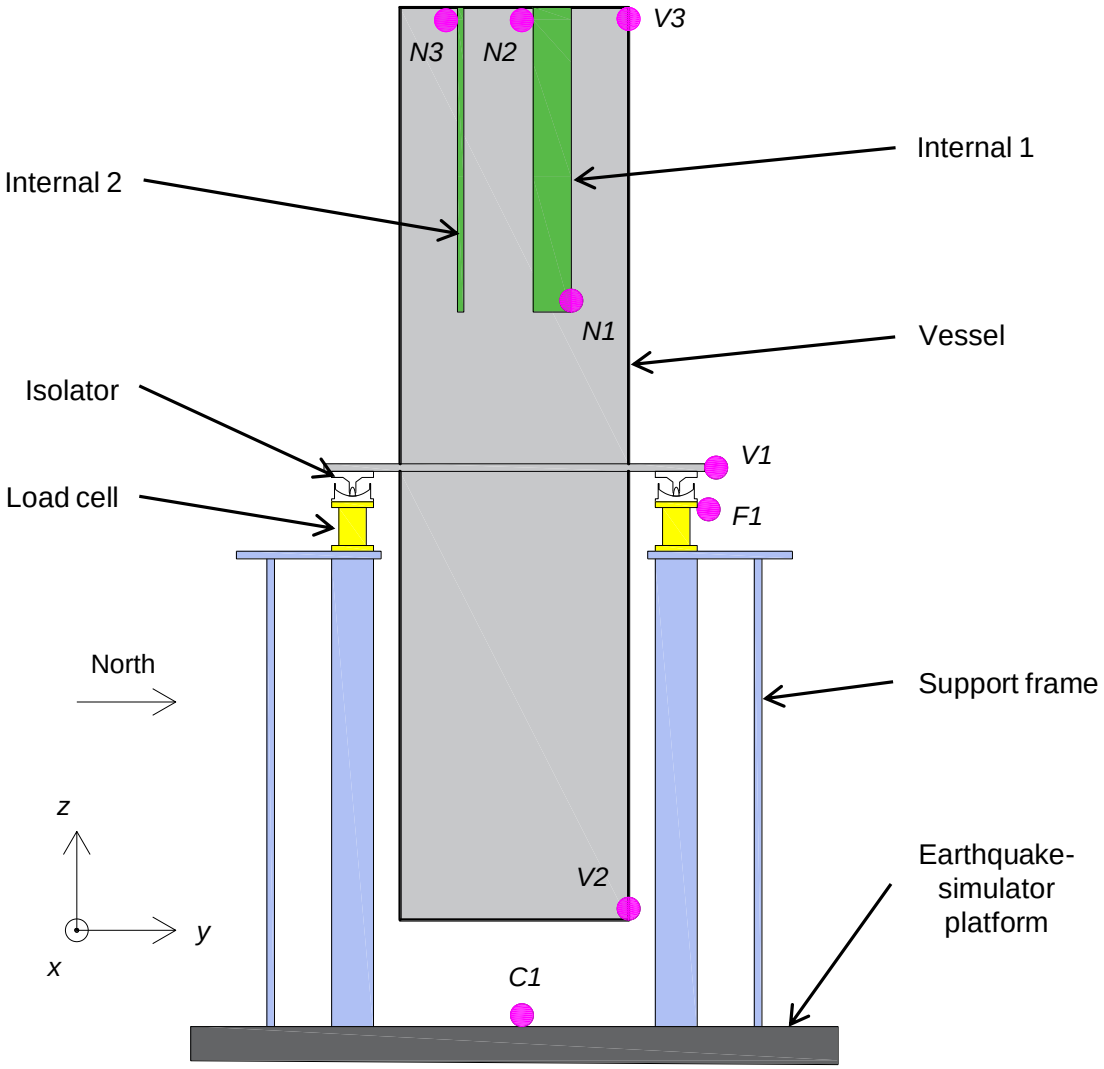

Figure 4-8. Locations for presenting earthquake-simulator test results

b) Atop the load cell on the north-east side (location *F1*). It represents the acceleration response at the mid-height of the vessel, at the level of support mounts, for the non-isolated configuration, and directly below the isolation plane for the isolated configurations. (North is defined in Figures 4-6 and 4.8.)

c) On the north-east support mount of the vessel for the isolated configurations (location *V1*), representing the acceleration response directly above the isolation plane.

d) At the top and bottom of the vessel on the north face (locations *V2* and *V3*).

2. Rocking acceleration spectra about the two horizontal axes:

   a) At the center of the earthquake-simulator. (There were no rocking inputs to the earthquake simulator, but rocking resulted from simulator-specimen interaction and compliance between the simulator's horizontal and vertical actuators.)

   b) At the top and bottom of the vessel.

3. Peak accelerations at the bottom of internal 1 (location *N1*).

4. Peak axial strains in the submerged internals (locations *N2* and *N3*).

5. Normalized force-displacement loops of the isolation system.

Identical acceleration histories were recorded in each direction on a) the north-east, south-east, and west load cells, b) the north-east, south-east, and west support mounts and c) the north, east, west, and south faces of the vessel at its top and bottom. (Strain gage R1A on internal 1 and the accelerometers on internal 2 were discovered to be faulty while processing data after the testing was completed.)

Rocking acceleration histories about the *x*- and *y*-axes were determined by calculating the difference in vertical (*z*) acceleration responses and dividing by the distance between the accelerometers: see Figure 4-6 for the global co-ordinate system. For example, the rocking accelerations (in rad/sec^2) about the *x* and *y* axes, at the center of earthquake simulator were calculated as:

$$R_x = (\text{ANSTZ} - \text{ASSTZ})/L \tag{4-1}$$

$$R_y = (\text{AWSTZ} - \text{AESTZ})/L \tag{4-2}$$

where ANSTZ, AESTZ, ASSTZ, and AWSTZ are the vertical acceleration histories (in inch/sec^2) at the north, east, south, and west sides of the earthquake-simulator, respectively (see Figure 4-6); *L* (= 136 inches)

is the distance between the north and south, and the east and west accelerometers on the earthquake simulator. The same approach was utilized to calculate rocking accelerations at the top and bottom of the vessel.

The force-displacement loops for the isolation systems were derived by normalizing the total instantaneous horizontal force in each direction by the total instantaneous normal load on the bearings. The total horizontal (normal) force is the sum of the shear (axial) forces in the load cells mounted beneath the bearings. Displacement histories were recorded at the top of the load cells, just below the isolators, and at the level of the supporting mounts of the vessel, just above the isolators. Isolator displacements were calculated as the difference between the displacement histories above and below the bearings. Displacement was measured at two locations in each direction: for the north-east and south-east bearings in the *x* direction, and the north-east and west bearings in the *y* direction, as identified in Figure 4-4e. The isolated vessel did not rotate about its longitudinal axis, as established by comparing the isolator displacement histories from the two sets of recordings in each direction. The *x*- and *y*-direction isolator displacement histories for the north-east bearing were used to generate the normalized force-displacement loops presented in Section 4.5.5.

4.5.2 Processing the test data

Prior to executing the tests, trials were performed to tune the earthquake simulator so as to accurately reproduce the target accelerations in the two horizontal and vertical directions. Figure 4-9 presents vertical response spectra for the recorded acceleration histories at the center of the earthquake simulator with the targets identified for tests FB1B-3D, FB2B-3D, and FB3B-3D in the non-isolated configuration. Amplification was observed at frequencies near 30 Hz and 50 Hz: see the red dashed lines in Figure 4-9. The inability to match the target spectra is a result of significant simulator-specimen interaction associated with the large relative weight of the specimen (= 50 kips versus the simulator platform weight of 24 kips), the high center-of-mass of the specimen with respect to the platform (= 124 inches), and cross talk between the simulator's vertical and horizontal actuators. To eliminate the effects of these simulator-related amplifications on the response of the specimen, the recorded acceleration histories (on the earthquake-simulator platform and the specimen) were processed using a band-stop filter in the frequency ranges of 28 Hz to 35 Hz and 48 Hz to 54 Hz. The green dashed lines in Figure 4-9 present the vertical response spectra of the *filtered* acceleration histories.

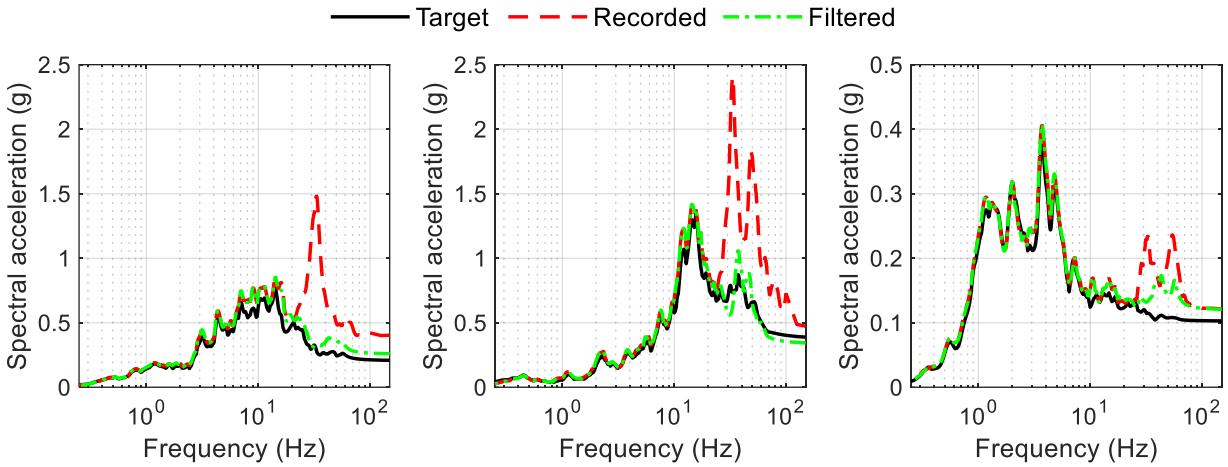

a) FB1B-3D b) FB2B-3D c) FB3B-3D

Figure 4-9. Vertical acceleration response spectra on the earthquake-simulator for the non-isolated configuration, 5% damping

4.5.3 System identification

The modal properties of the test specimen, namely, its frequencies and damping ratios, were derived using frequency response functions (FRFs) from multisine tests in the non-isolated configuration. The FRFs were generated using acceleration histories measured at the top and bottom of the vessel and at the center of the earthquake simulator. Figure 4-10 presents the FRFs for the north, south, east, and west faces at the top and bottom of the vessel in the *x*, *y*, and *z* directions (see Figure 4-4 for the global co-ordinate system). Figure 4-11 presents the FRFs for the rocking accelerations along the *x* and *y* axes.

The modal frequencies in the vertical direction were 17 Hz and 45 Hz: see panels e and f of Figure 4-10. The interior columns, load cells, and vessel support mounts contribute to the vertical flexibility of the specimen. The peaks in the FRFs in the *x*- and *y*-directions (see panels a through d of Figure 4-10) were at 11 Hz and correspond to the rocking of the vessel, as confirmed by the peaks observed at 11 Hz in the rotational FRFs of Figure 4-11. The horizontal modes of response of the support frame and of the vessel are not identified in these FRFs because their horizontal stiffness is very high.

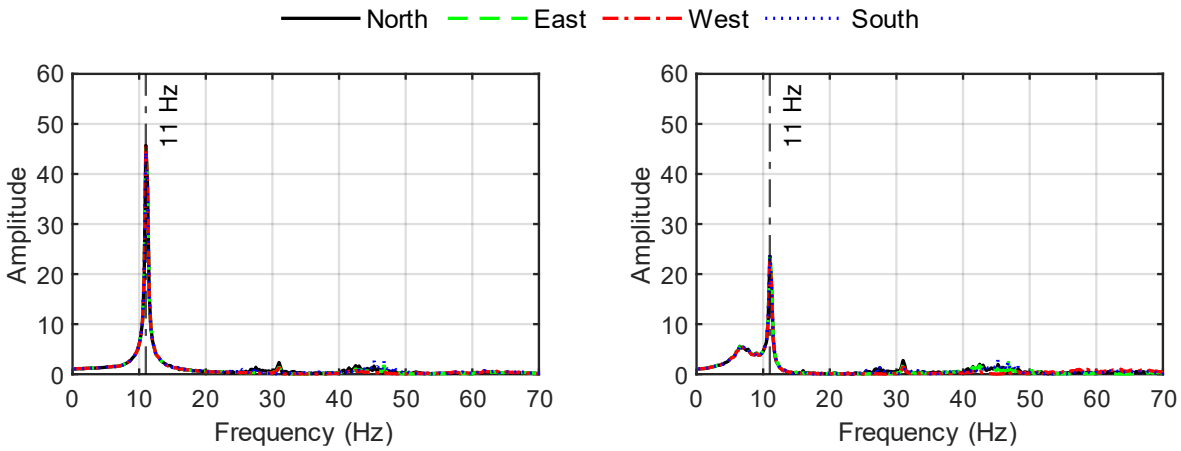

a) *x* direction, vessel bottom

b) *x* direction, vessel top

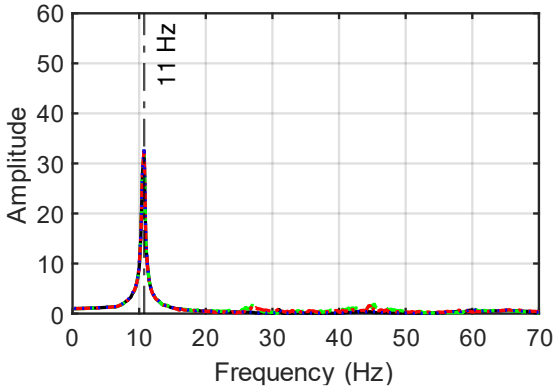

c) *y* direction, vessel bottom

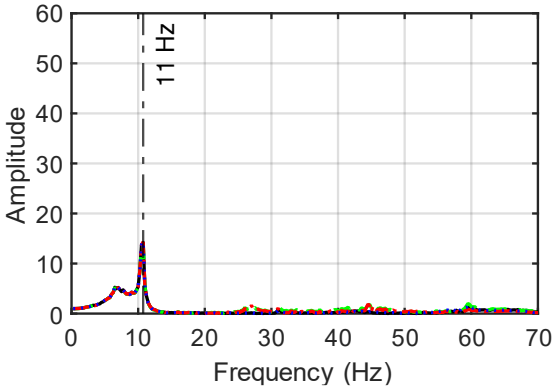

d) *y* direction, vessel top

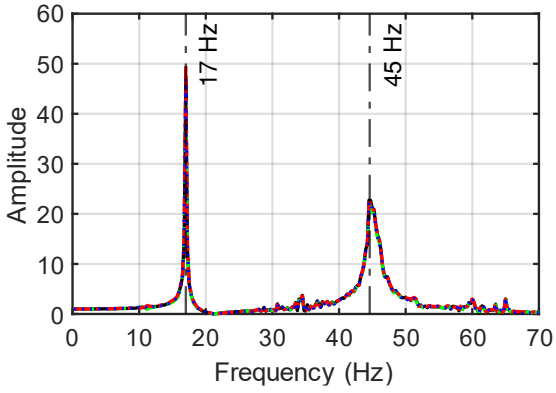

e) *z* direction, vessel bottom

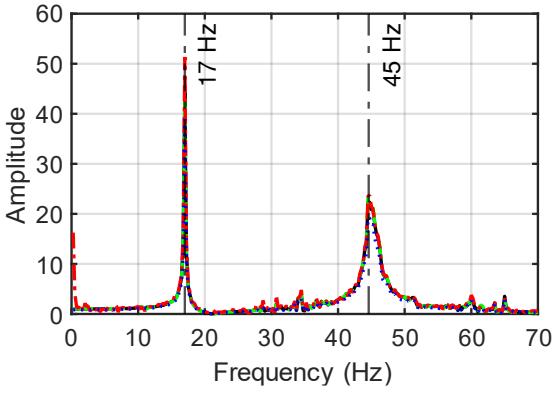

f) *z* direction, vessel top

Figure 4-10. Amplitude of frequency response functions for the test specimen in the *x*, *y*, and *z* directions of the non-isolated configuration

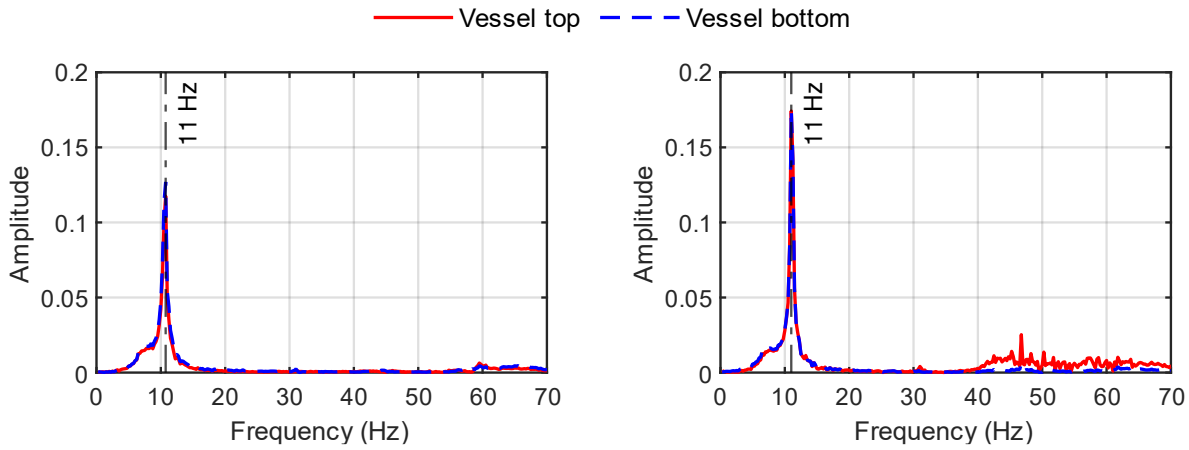

a) R_x direction a) R_y direction

Figure 4-11. Amplitude of frequency response functions for the test specimen about the *x* and *y* axes in the non-isolated configuration

To determine damping ratios, the test specimen was assumed to be a single degree-of-freedom (SDOF) system, uncoupled along each translational axis. The damping ratio of a SDOF system can be estimated using the amplitude of the FRF at the resonant frequency. Figure 4-12 presents an example FRF for an SDOF system having a resonant frequency f_R and a damping ratio ξ. The FRF amplitude at the resonant frequency, FRF_{f_R}, for the acceleration response of an SDOF system is presented in Chopra (2007) as:

$$\text{FRF}_{f_R} = \frac{1}{2\xi\sqrt{1-\xi^2}} \tag{4-3}$$

where all the terms were defined previously. For lightly damped systems ($\xi^2 \ll 1$), the damping ratio can be estimated as:

$$\xi = \frac{1}{2\text{TF}_{f_R}} \tag{4-4}$$

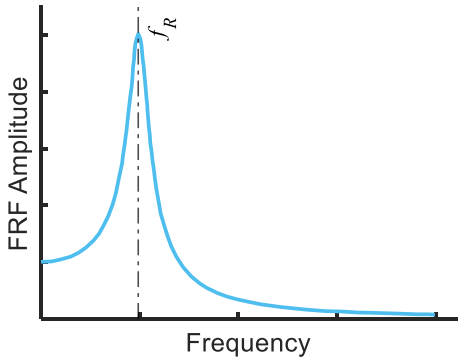

Figure 4-12. Idealized frequency response function for an SDOF system

Table 4-6 presents the amplitudes of the FRF for the test specimen at the resonant frequencies at the top and bottom of the vessel. In the vertical direction, the test specimen was idealized as an SDOF system with $f_R = 17$ Hz and the average of the amplitudes of the FRF at the top and bottom of the vessel was utilized to estimate the damping ratio of 1% of critical:

$$\xi_z = \frac{1}{2 \times 0.5 \times (44 + 47)} = 0.011 \tag{4-5}$$

Table 4-6. Frequency response function amplitudes for the test specimen at its resonant frequencies in the *x*, *y*, and *z* directions

TF amplitude	Vessel top					Vessel Bottom				
	North	East	West	South	Avg.	North	East	West	South	Avg.
x direction	24	25	23	24	24	46	46	46	44	46
y direction	14	14	14	14	14	32	32	33	33	33
z direction[1]	44	43	51	39	44	46	44	50	47	47

1. Amplitude of FRF for the vertical mode at 17 Hz

In the *x* and *y* directions, the test specimen was idealized as a SDOF system for damping calculations, using a two-step procedure. In the first step, the test specimen was reduced to a two degree-of-freedom (TDOF) system with the top and bottom halves of the vessel lumped at their respective centers of mass (COMs): see blue solid circles in panel a of Figure 4-13. The amplitudes of the FRFs at the respective COMs were assumed to be one-half of those at the top and bottom of the vessel: see panel b of Figure 4-13. (The mass of the filled vessel was uniformly distributed along its height.) In the second step, the TDOF system was reduced to an SDOF system with an FRF amplitude equal to the average of those from step one: see panel c of Figure 4-13. The damping ratios in the horizontal directions were estimated as:

$$\xi_x = \frac{1}{2 \times \frac{1}{2} \times \left(\frac{24}{2} + \frac{46}{2} \right)} = 0.028 \tag{4-6}$$

$$\xi_y = \frac{1}{2 \times \frac{1}{2} \times \left(\frac{14}{2} + \frac{33}{2} \right)} = 0.043 \tag{4-7}$$

These horizontal damping ratios were greater than those expected in a steel structure due to significant simulator-specimen interaction. The damping in the oil columns of the earthquake-simulator's actuators affect the dynamics of the test specimen (Sivaselvan, 2022).

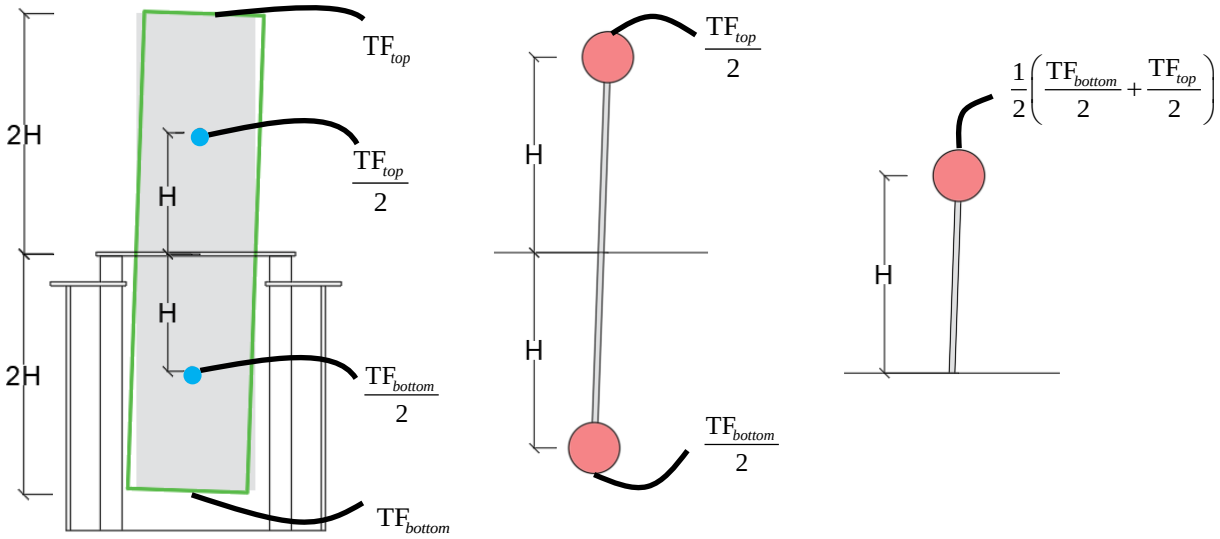

a) test specimen b) idealized TDOF c) idealized SDOF

Figure 4-13. Equivalent SDOF system of the test specimen for estimating damping ratios in the horizontal directions

4.5.4 Non-isolated configuration

Figures 4-14 through 4-19 present 5% damped acceleration response spectra for the six 3D motions of Table 4-3, at the locations identified in Section 4.5.1 and Figure 4-8. Table 4-7 presents the corresponding peak accelerations, calculated here as spectral acceleration at 100 Hz. Accelerations from the center of the earthquake simulator[1] were amplified by the support frame to the support mounts of the vessel, from location *C1* to *V1* in Figure 4-8[2]: compare the green dashed and black solid lines in panels a through c of Figures 4-14 through 4-19. The peak horizontal (vertical) accelerations were amplified by the support frame by a factor of between 1.4 (1.2) and 1.8 (2.9)[3].

[1] Accelerations at the center of the earthquake-simulator platform were used instead of the input motions of Section 4.4 because of differences due to specimen-structure interaction (see Section 4.5.2).

[2] The vessel was bolted directly to the load cells in the non-isolated configuration, for which the acceleration histories at locations *V1* and *F1* in Figure 4-8 will be identical.

[3] Significant variation was expected because of differences in the frequency content of the input motions.

The peak accelerations at top of the load cells (location *V1* in Figure 4-8*)* were amplified to the top and the bottom of the vessel (locations *V2* and *V3*), by a factor of between 1.2 (1.6) and 2.2 (1.9) in the horizontal (vertical) direction[1]. The vertical response of the vessel was driven by its vertical modes at 17 Hz and 45 Hz, and its horizontal response by rocking at 11 Hz, as explained in Section 4.5.3. The rocking of the vessel was amplified by the rocking of the earthquake-simulator platform due to simulator-specimen interaction.

At the bottom of internal 1, the peak accelerations were amplified by a factor of between 1.9 (1.1) and 2.4 (1.4) in the horizontal (vertical) direction with respect to the top of the vessel (from location *V3* to *N1* in Figure 4-8). Table 4-8 presents peak axial strains in the two internals, measured near their points of attachments to the vessel head, at locations *N2* and *N3* in Figure 4-8, where maximum strains (and corresponding stresses) were expected. The peak strains in both the internals were between 5% and 22% of the corresponding yield strain. (Internal 1 was constructed of aluminum, and internal 2 from carbon steel. The specified minimum yield stress and the elastic modulus for the aluminum internal were 40 ksi and 10,000 ksi, respectively, with a corresponding yield strain of 4000 μS. The specified minimum yield stress and the elastic modulus for the carbon steel internal were 36 ksi and 29,000 ksi, respectively, with a yield strain of 1240 μS.)

[1] Significant variation was expected because of differences in the frequency content of the input motions.

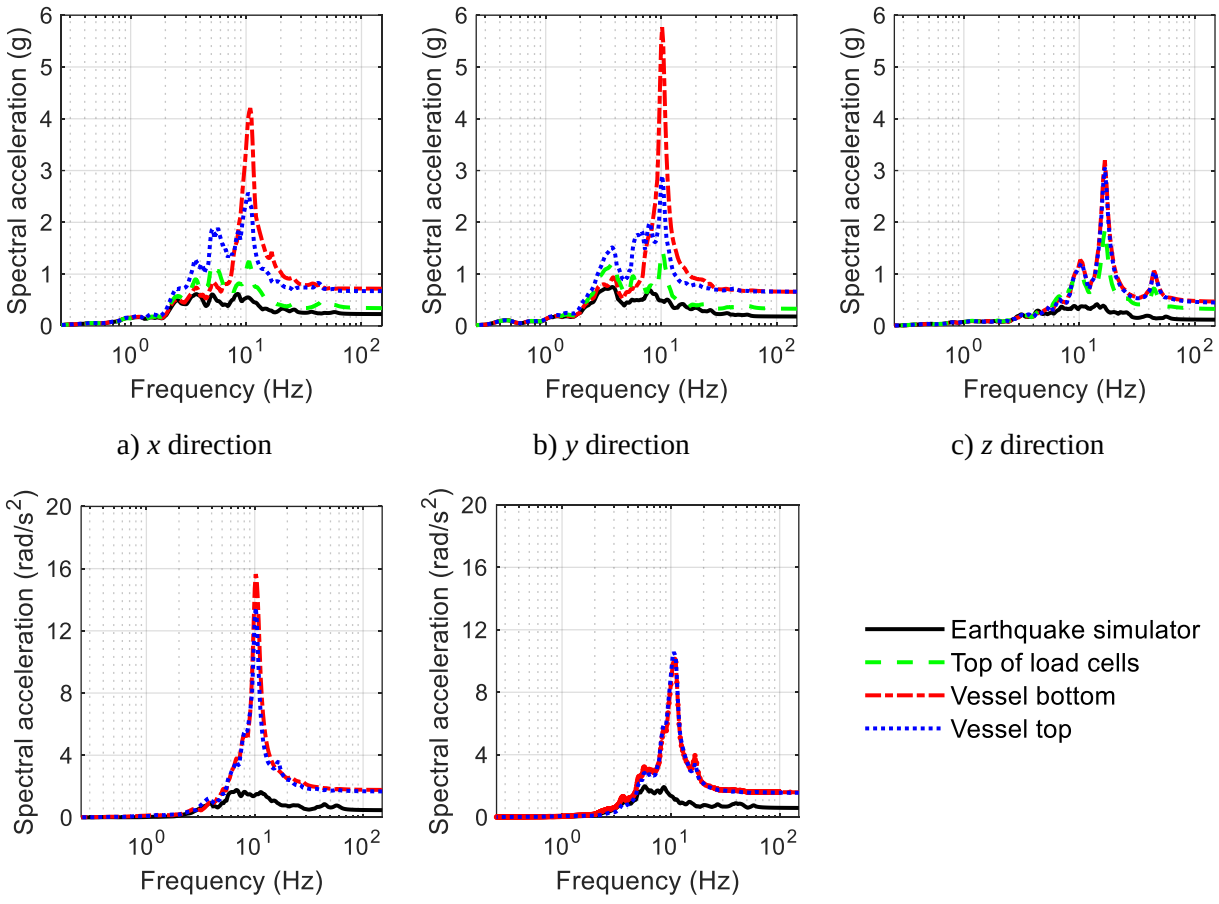

a) *x* direction b) *y* direction c) *z* direction

d) rocking about *x* axis e) rocking about *y* axis

Figure 4-14. Acceleration response spectra at the top and bottom of the vessel, test FB1A-3D, 5% damping

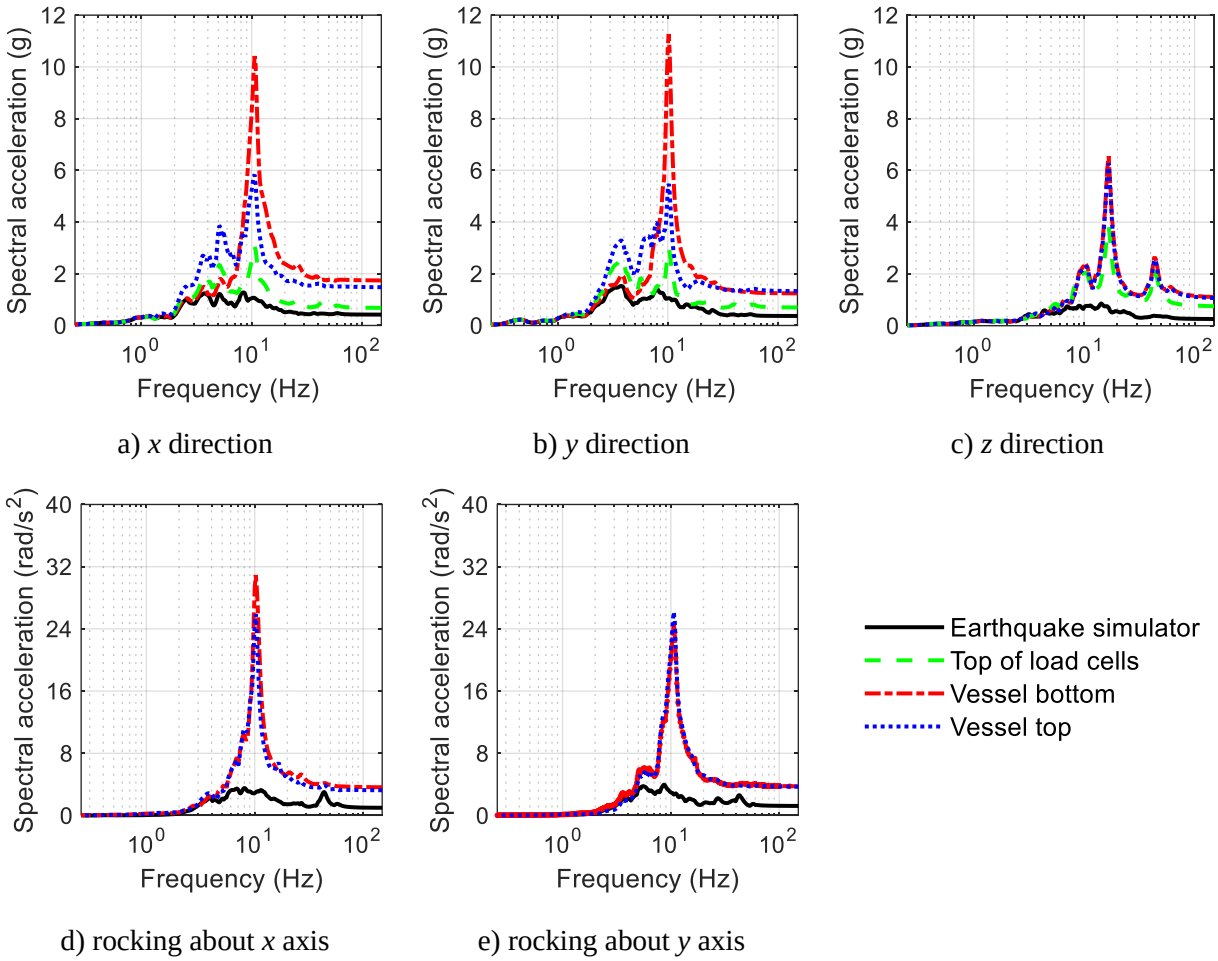

a) *x* direction b) *y* direction c) *z* direction

d) rocking about *x* axis e) rocking about *y* axis

Figure 4-15. Acceleration response spectra at the top and bottom of the vessel, test FB1B-3D, 5% damping

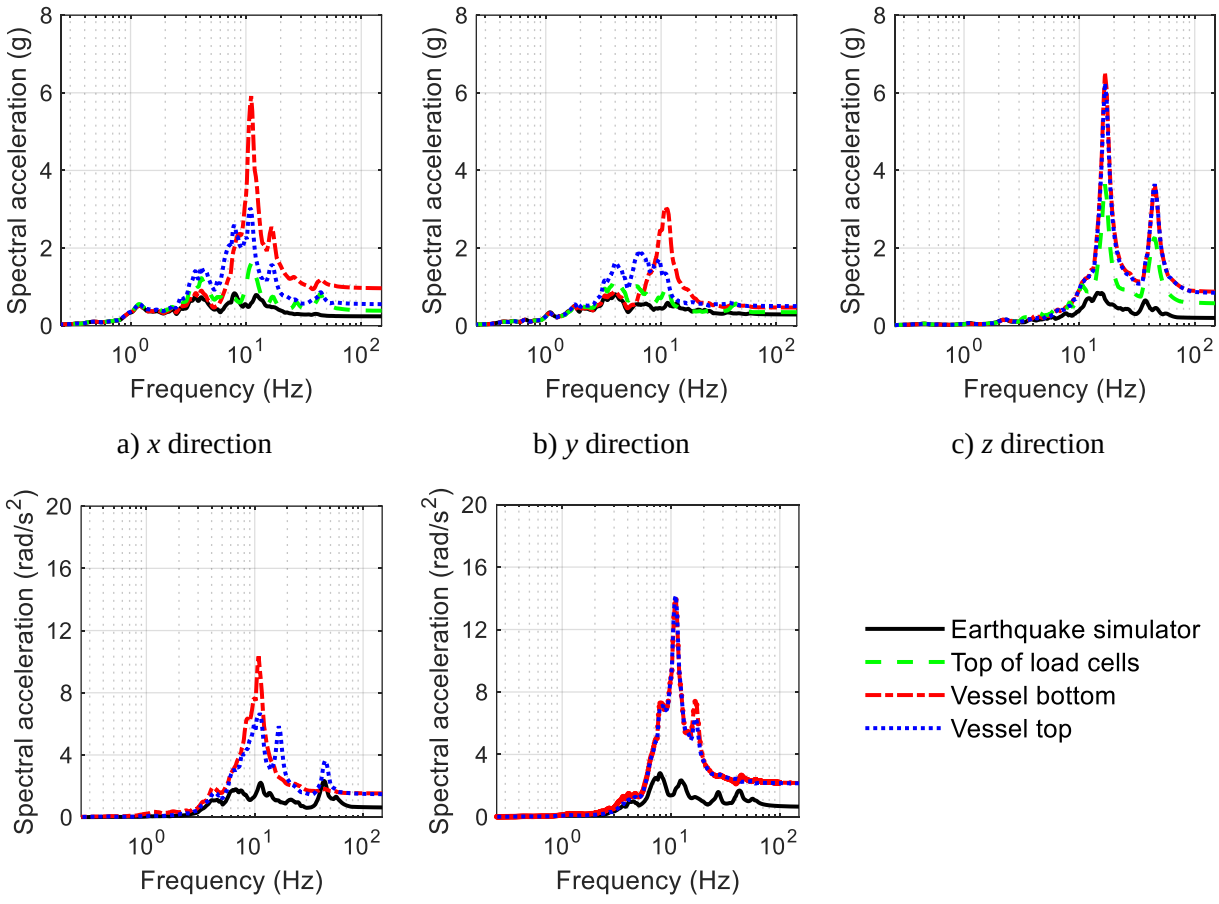

a) *x* direction b) *y* direction c) *z* direction

d) rocking about *x* axis e) rocking about *y* axis

Figure 4-16. Acceleration response spectra at the top and bottom of the vessel, test FB2A-3D, 5% damping

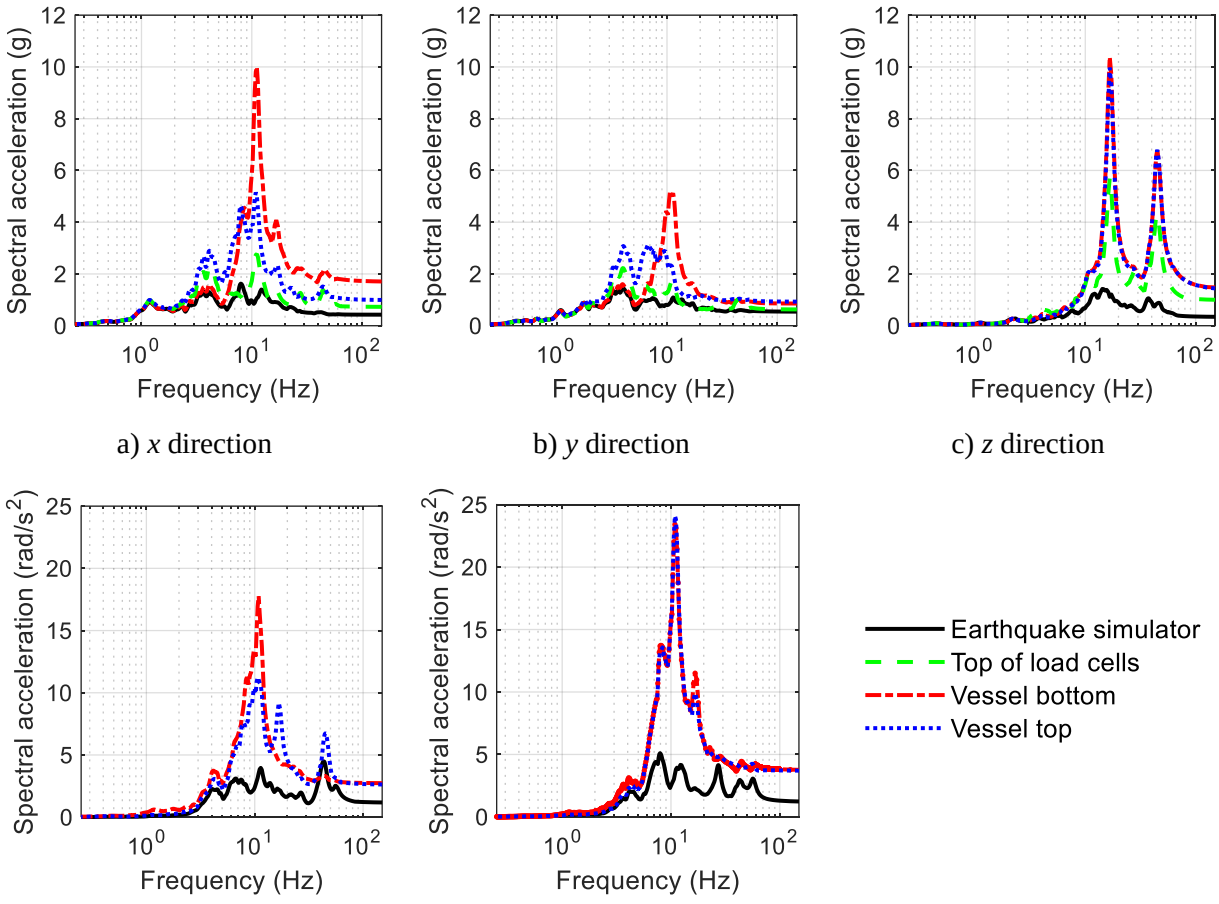

a) *x* direction b) *y* direction c) *z* direction

d) rocking about *x* axis e) rocking about *y* axis

Figure 4-17. Acceleration response spectra at the top and bottom of the vessel, test FB2B-3D, 5% damping

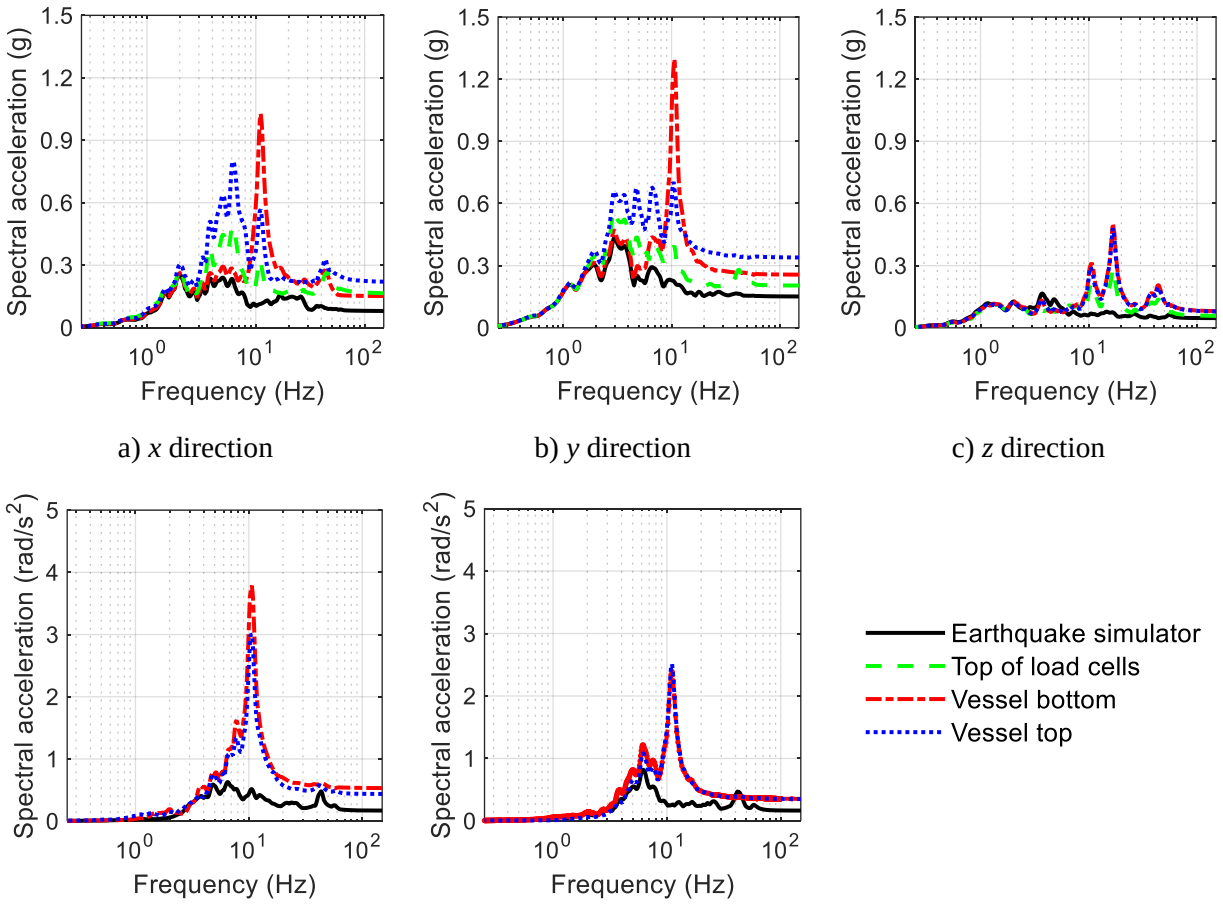

a) *x* direction b) *y* direction c) *z* direction

d) rocking about *x* axis e) rocking about *y* axis

Figure 4-18. Acceleration response spectra at the top and bottom of the vessel, test FB3A-3D, 5% damping

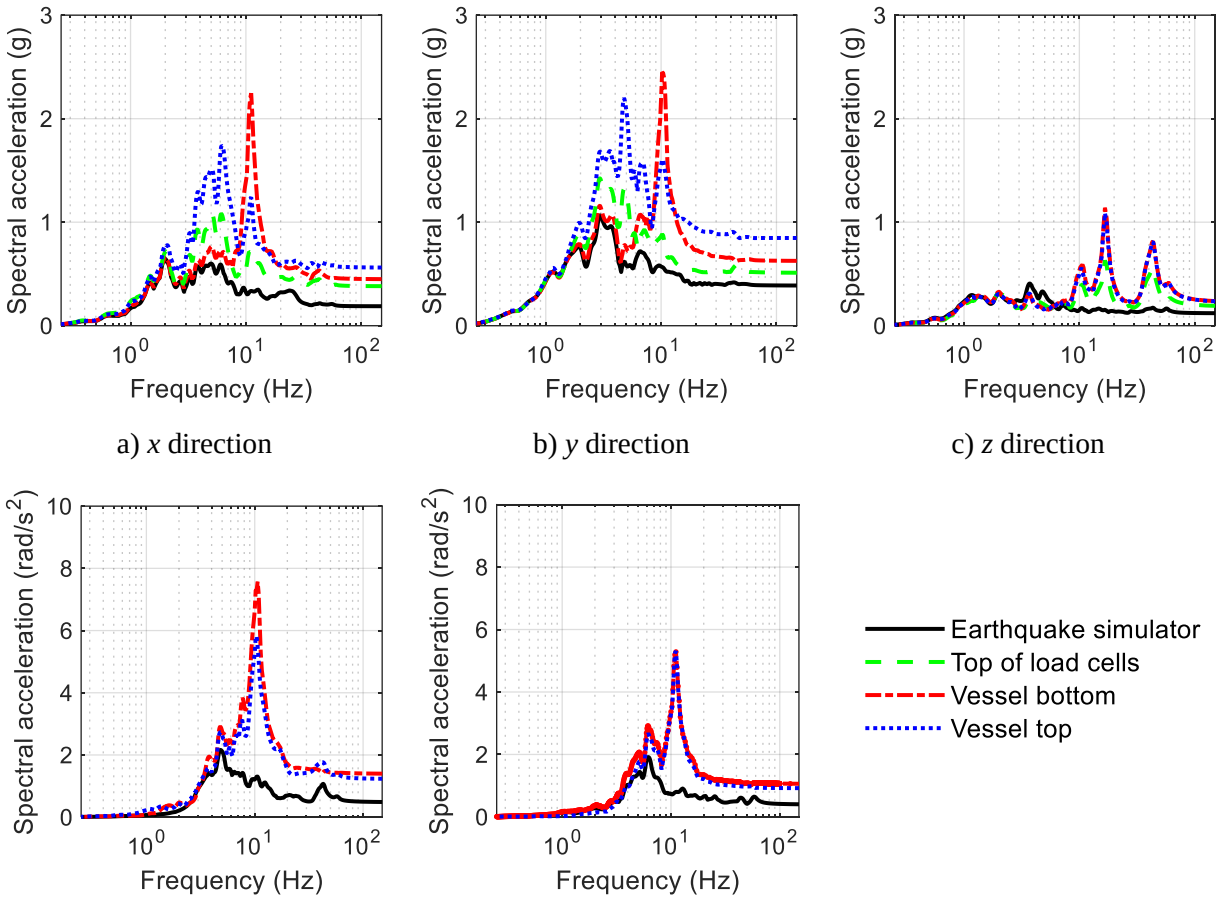

a) *x* direction b) *y* direction c) *z* direction

d) rocking about *x* axis e) rocking about *y* axis

Figure 4-19. Acceleration response spectra at the top and bottom of the vessel, test FB3B-3D, 5% damping

Table 4-7. Peak accelerations[1] (g) for the 3D tests of the non-isolated configuration, *x*, *y*, and *z* directions[2]

Test	Earthquake simulator			Atop load cells			Vessel bottom			Vessel top			Internal 1 bottom		
	x	***y***	***z***	***x***	***y***	***z***	***x***	***y***	***z***	***x***	***y***	***z***	***x***	***y***	***z***
FB1A-3D	0.23	0.18	0.12	0.34	0.33	0.32	0.72	0.65	0.46	0.67	0.66	0.44	2.20	0.93	0.53
FB1B-3D	0.42	0.37	0.26	0.68	0.69	0.73	1.73	1.24	1.07	1.47	1.32	1.04	3.73	1.83	1.25
FB2A-3D	0.24	0.29	0.20	0.39	0.35	0.57	0.96	0.47	0.86	0.55	0.5	0.83	1.47	0.89	1.05
FB2B-3D	0.42	0.54	0.34	0.72	0.63	0.98	1.69	0.85	1.44	0.98	0.93	1.39	2.55	1.46	1.88
FB3A-3D	0.08	0.15	0.05	0.16	0.2	0.06	0.16	0.26	0.08	0.22	0.34	0.08	0.58	0.49	0.08
FB3B-3D	0.19	0.39	0.12	0.38	0.51	0.18	0.45	0.63	0.23	0.56	0.85	0.22	1.51	1.27	0.26

1. Peak acceleration calculated as spectral acceleration at 100 Hz
2. See Figure 4-4 for the global co-ordinate system

Table 4-8. Peak axial strains (μS) in internals for the 3D tests of the non-isolated configuration[1]

Test	Internal 1	Internal 2	
	R1B	**R2A**	**R2B**
FB1A-3D	427	140	141
FB1B-3D	749	231	231
FB2A-3D	373	185	189
FB2B-3D	569	268	273
FB3A-3D	206	123	125
FB3B-3D	486	235	236

1. For reference, the yield strain in internal 1 (internal 2) is approximately 4000 (1240) μS

4.5.5 Isolated configurations

4.5.5.1 SFP-isolated

Figures 4-20 through 4-37 present processed data for the six 3D motions of Table 4-4 and images from testing. The input motions had different frequency contents and amplitudes (see Section 4.4) and the *y*-axis scale in the figures presenting acceleration response spectra is different for each motion.

Figures 4-20, 4-23, 4-26, 4-29, 4-32, and 4-35 present 5% damped acceleration response spectra (generated from the recorded acceleration histories) directly above and below the isolation plane (locations *V1* and *F1* in Figure 4-8). The vertical thin blue lines in these figures at a frequency of 0.72 Hz correspond to the sliding period (1.38 seconds) of the SFP bearings (see Section 3). The support frame amplified the motions at the center of the earthquake simulator (location *C1*) to the underside of the isolation plane for frequencies greater than 10 Hz (compare the black solid lines and red dashed lines in these figures), with increases in peak accelerations by a factor of between 1.1 (1.0) and 1.6 (1.5) in the horizontal (vertical) direction. For frequencies greater than 3 Hz (of interest for the vessel and its internals), the horizontal spectral accelerations above the isolation plane were generally substantially smaller than those below the isolation plane. The peak horizontal accelerations above the isolation plane were reduced by a factor of between 1.9 and 3.4 with respect to those below the isolation plane[1].

Figures 4-21, 4-24, 4-27, 4-30, 4-33, and 4-36 present normalized horizontal force-displacement loops for the SFP isolation system. (Section 4.5.1 describes the derivation of the normalized force-displacement loops.) For the smaller amplitude motions (tests SF1A, SF2A, and SF3A in Table 4-4), the displacement of the isolation system was between 10% and 20% of its capacity (= 3.5 inches), and the corresponding reduction in the spectral accelerations above the isolation plane (and at the top and bottom of the vessel) was smaller than for the larger amplitude motions: see Figures 4-20, 4-26, and 4-32. The fluctuation in the coefficient of friction in the normalized loops is due to a) its dependence on the sliding velocity, as characterized in Section 3, b) its dependence on the contact pressure on the slider (see Constantinou *et al.* (2007)), and c) rotation of the concave plates of the bearings, attached to the support mounts of the vessel (see Fenz and Constantinou (2008a)). Figure 4-38 present snapshots of the mid-height of the vessel from

[1] Significant variation in the percent change due to isolation was expected because of differences in the frequency content and the amplitude of the input motions.

test SFP2B-3D, wherein the south-east (left) and north-east (right) SFP bearings are at the at-rest position and the maximum displacement (= 2.4 inches).

Figures 4-22, 4-25, 4-28, 4-31, 4-34, and 4-37 present acceleration response spectra at the top and the bottom of the vessel (locations *V2* and *V3* in Figure 4-8). For the larger amplitude motions (tests SF1B, SF2B, and SF3B in Table 4-4), the SFP bearings generally enabled a significant reduction in horizontal spectral accelerations at the top and the bottom of the vessel for frequencies greater than 3 Hz. For the smaller amplitude motions (tests SF1A, SF2A, and SF3A in Table 4-4), wherein the SFP bearings operated primarily in the elastic range, the benefit of isolation is small. The response of the vessel in the vertical direction was driven by the vertical modes of the frame-bearing-vessel system with modal frequencies at 14 Hz and 38 Hz (see panel c of Figures 4-22, 4-25, 4-28, 4-31, 4-34, and 4-37). The modal frequency for rocking of the vessel about the *x* and *y* axes was 8 Hz (see panels d and e of Figures 4-22, 4-25, 4-28, 4-31, 4-34, and 4-37). Rocking of the vessel was amplified by the rotation of the earthquake-simulator platform.

Table 4-9 presents the peak accelerations at the locations identified in Section 4.5.1. The peak horizontal accelerations at the top and the bottom of the vessel for the larger amplitude motions were reduced by a factor of between 1.4 (1.2) and 2.5 (2.2) with respect to those below the isolation plane (at the center of the earthquake simulator). The peak vertical accelerations were 1.1 (1.1) to 2.2 (3.1) times greater than those at the underside of the isolation plane (the center of the earthquake simulator).

The peak accelerations at the bottom of internal 1 (location *N1* in Figure 4-8) were amplified by a factor of between 2.5 (1.2) and 3.4 (2.2) in the horizontal (vertical) directions with respect to the top of the vessel (location *V3*). Table 4-10 presents peak axial strains in the two internals, at locations *N2* and *N3* in Figure 4-8, with values of between 3% and 10% of the corresponding yield strains.

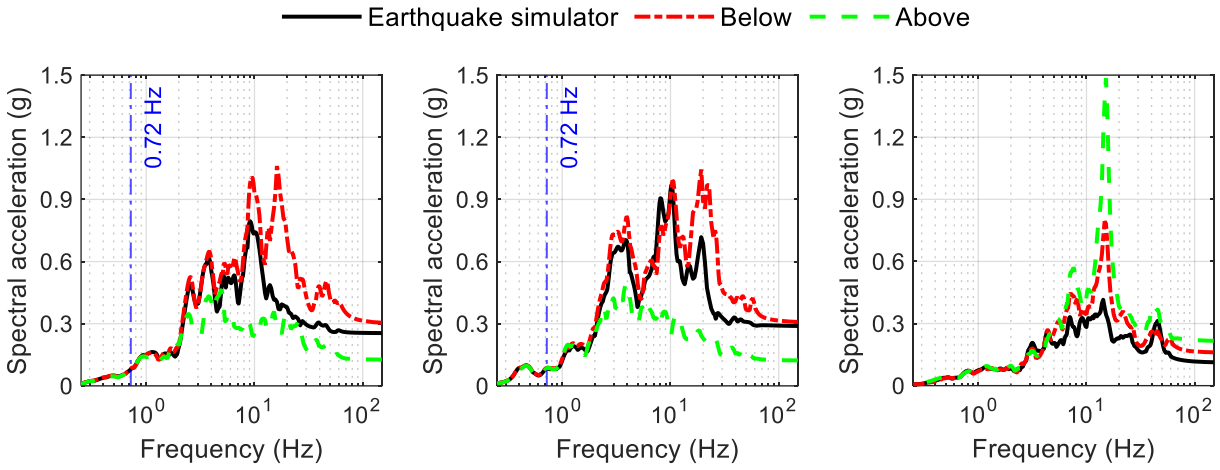

a) *x* direction b) *y* direction c) *z*-direction

Figure 4-20. Acceleration response spectra directly above and below the isolation plane, test SF1A-3D, 5% damping

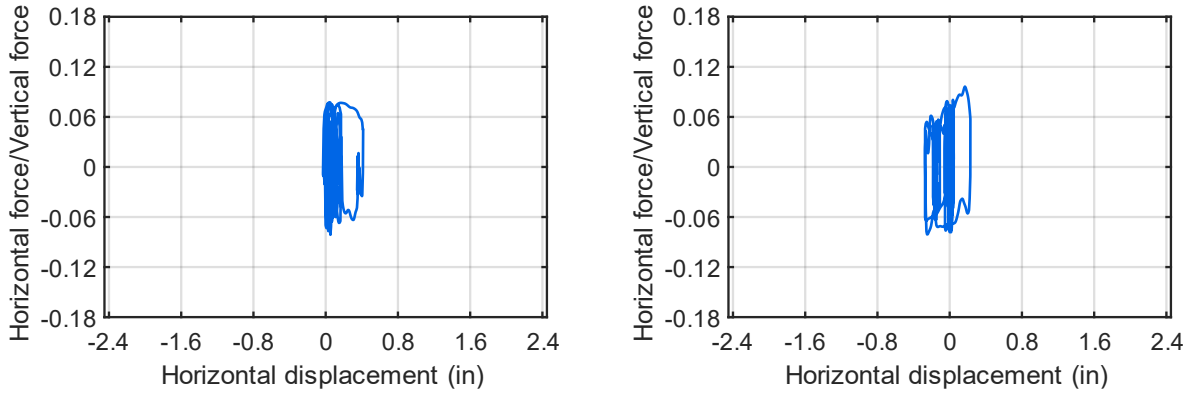

a) *x* direction b) *y* direction

Figure 4-21. Normalized force-displacement loops for the isolation system, test SF1A-3D

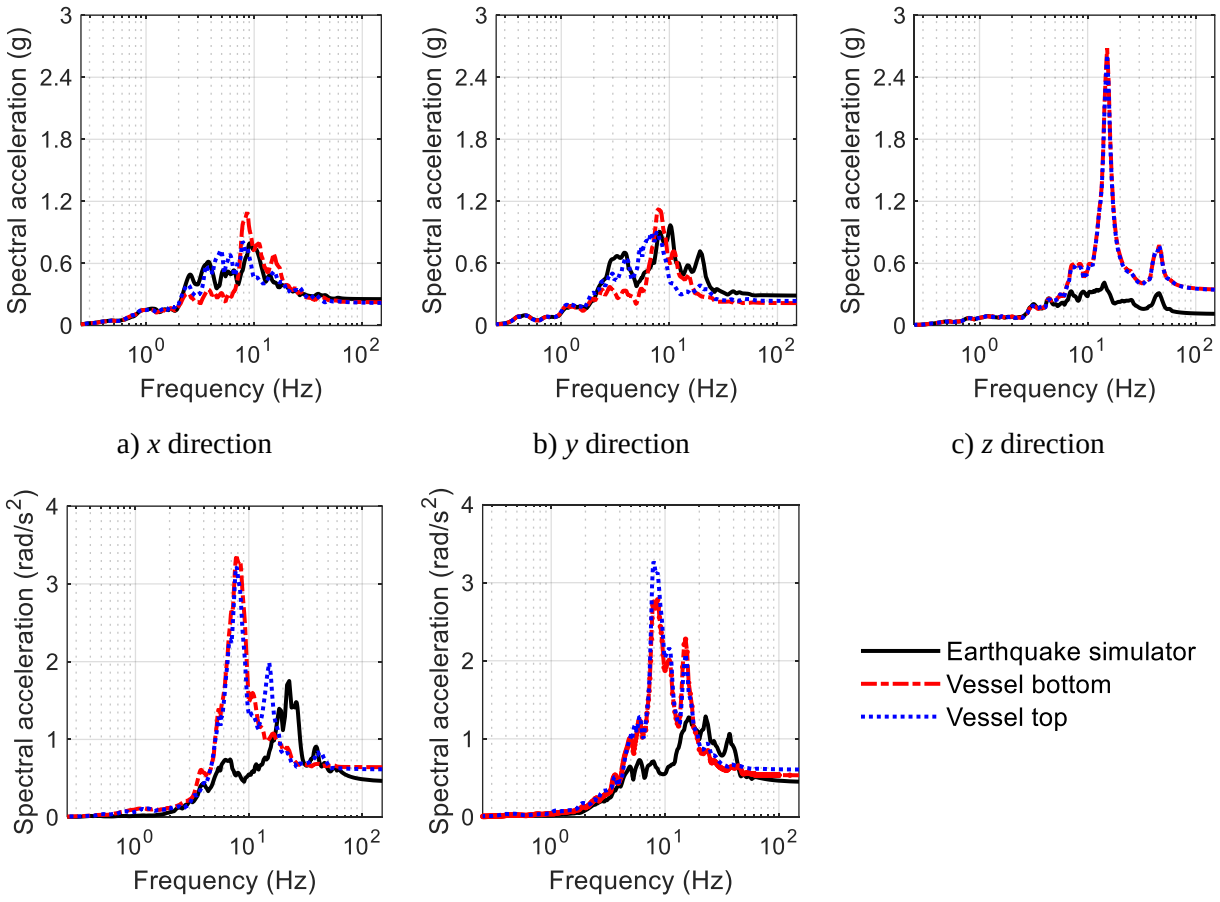

a) *x* direction b) *y* direction c) *z* direction

d) rocking about *x* axis e) rocking about *y* axis

Figure 4-22. Acceleration response spectra at the top and bottom of the vessel, test SF1A-3D, 5% damping

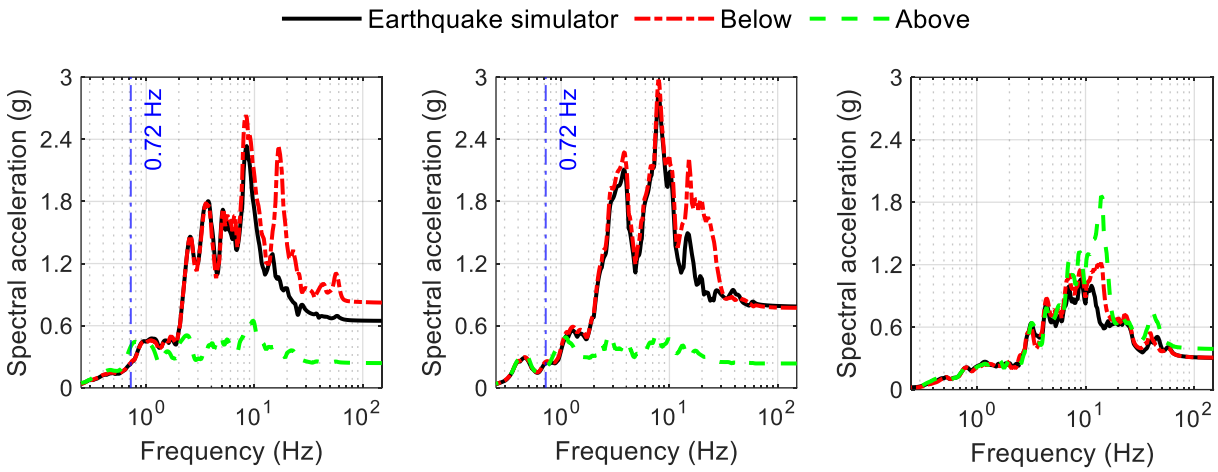

a) *x* direction b) *y* direction c) *z* direction

Figure 4-23. Acceleration response spectra directly above and below the isolation plane, test SF1B-3D, 5% damping

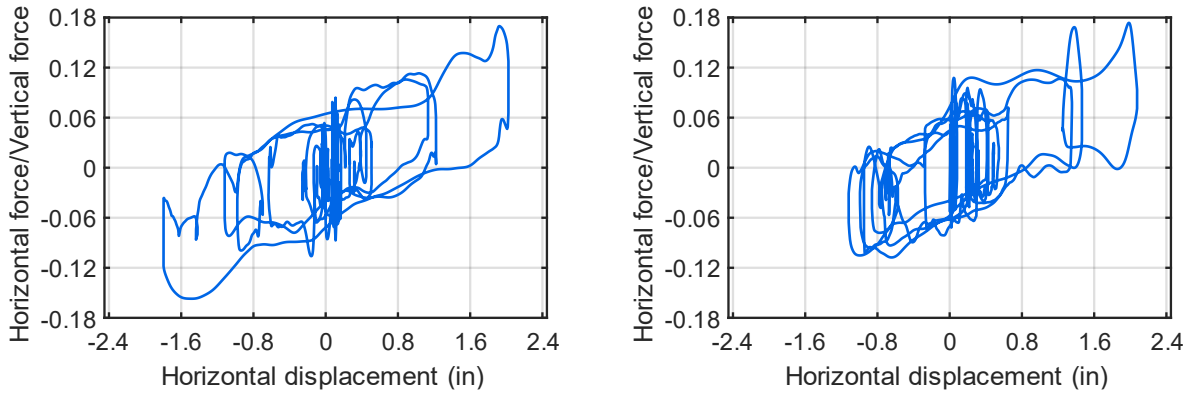

a) *x* direction b) *y* direction

Figure 4-24. Normalized force-displacement loops for the isolation system, test SF1B-3D

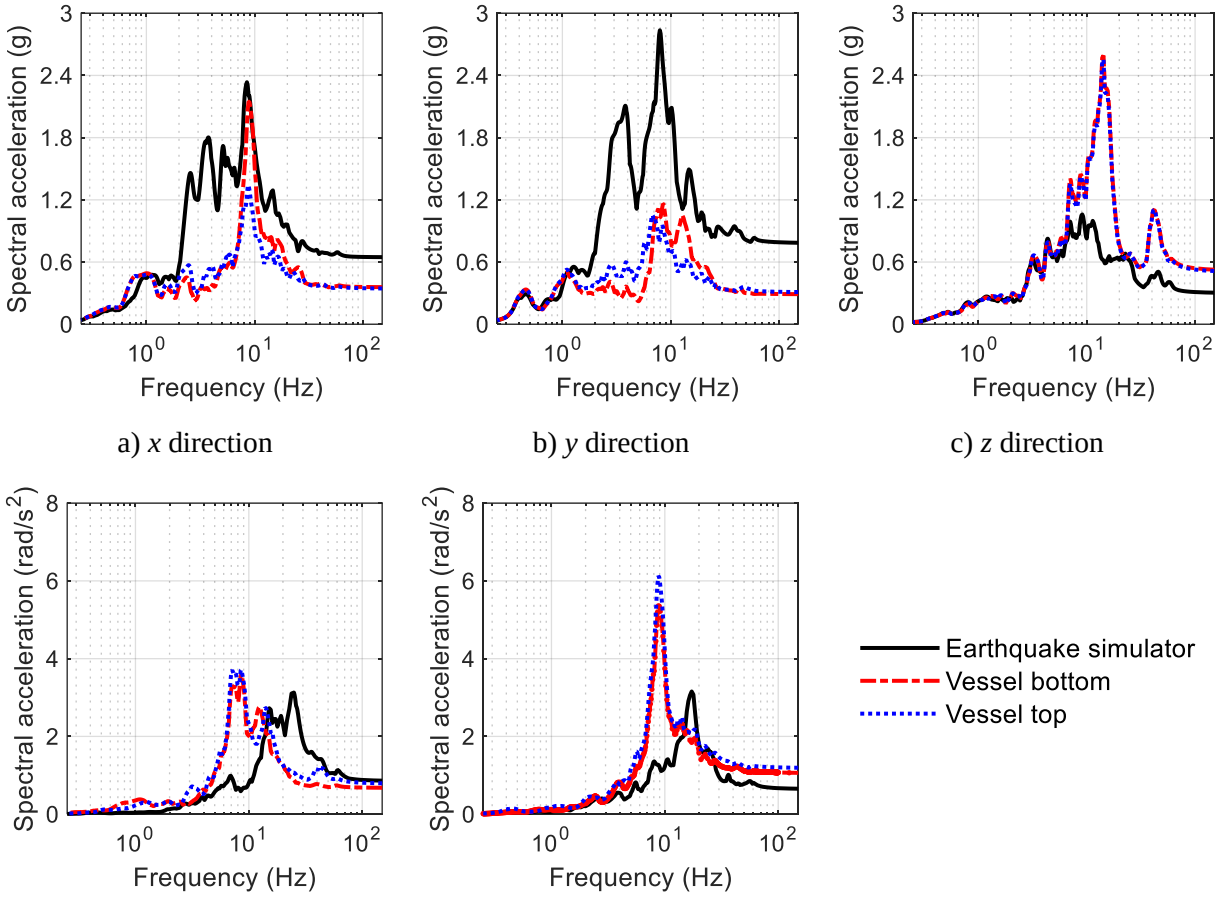

a) *x* direction b) *y* direction c) *z* direction

d) rocking about *x* axis e) rocking about *y* axis

Figure 4-25. Acceleration response spectra at the top and bottom of the vessel, test SF1B-3D, 5% damping

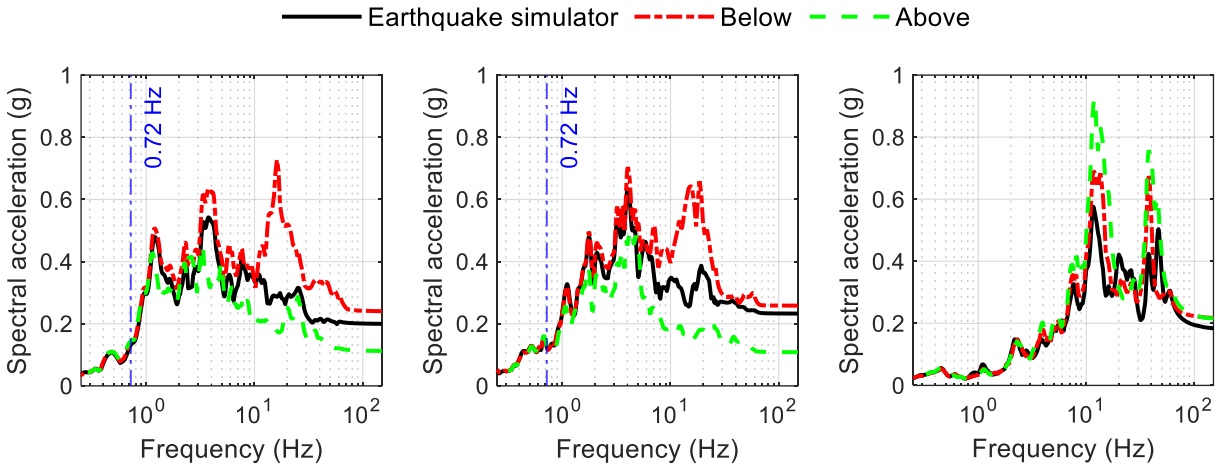

a) *x* direction b) *y* direction c) *z* direction

Figure 4-26. Acceleration response spectra directly above and below the isolation plane, test SF2A-3D, 5% damping

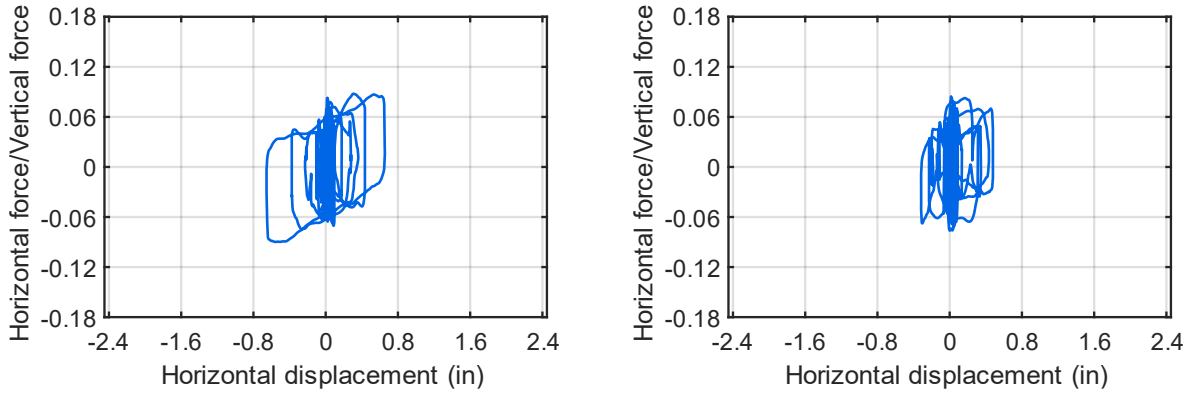

a) *x* direction b) *y* direction

Figure 4-27. Normalized force-displacement loops for the isolation system, test SF2A-3D

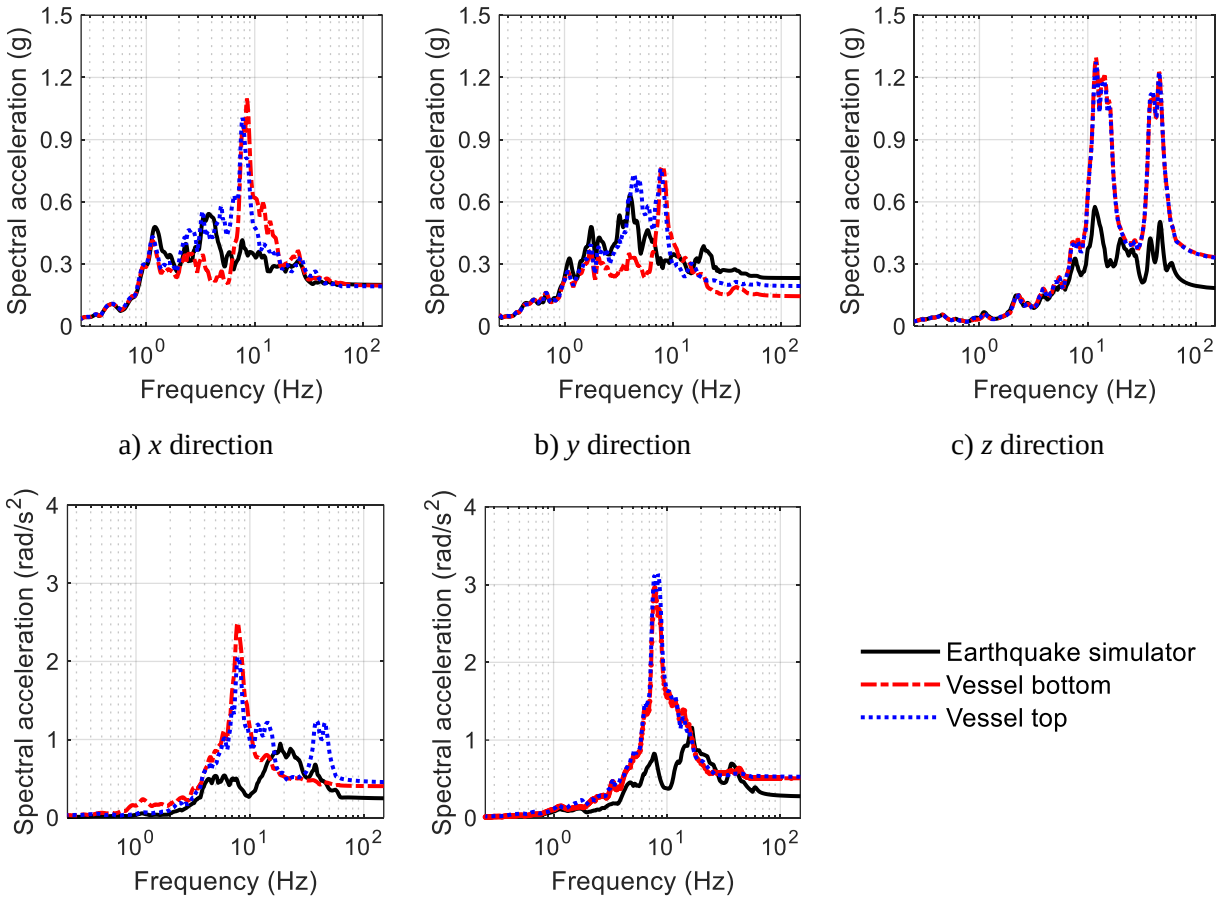

a) *x* direction b) *y* direction c) *z* direction

d) rocking about *x* axis e) rocking about *y* axis

Figure 4-28. Acceleration response spectra at the top and bottom of the vessel, test SF2A-3D, 5% damping

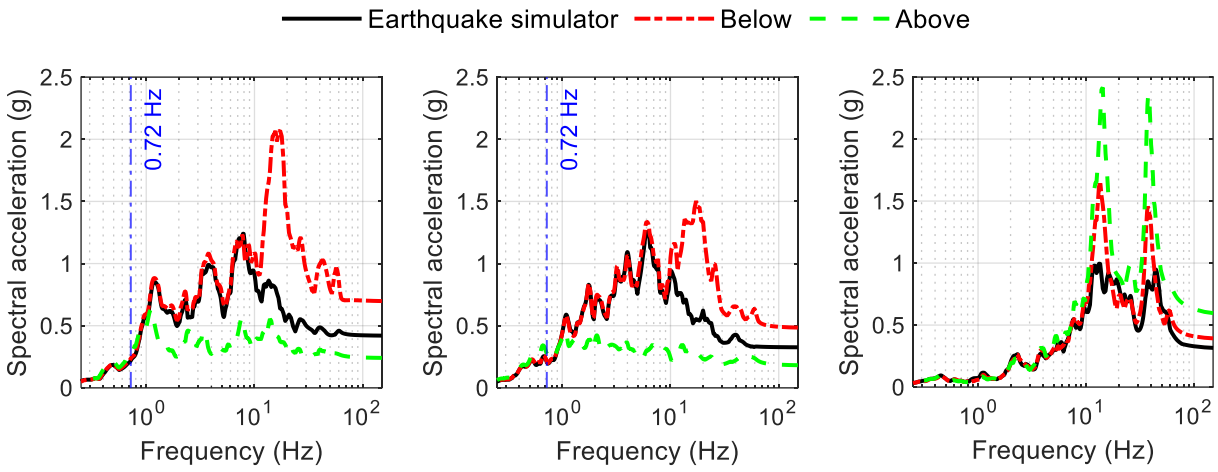

a) *x* direction b) *y* direction c) *z* direction

Figure 4-29. Acceleration response spectra directly above and below the isolation plane, test SF2B-3D, 5% damping

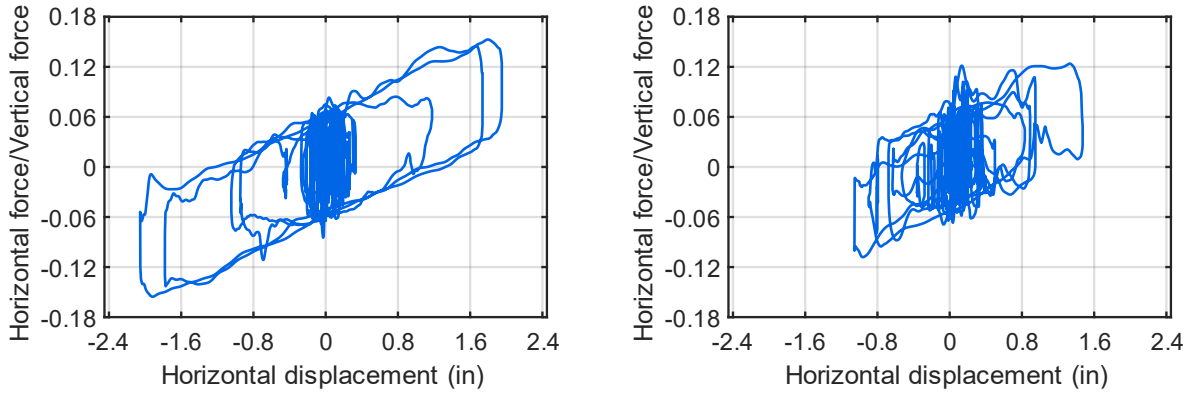

a) *x* direction b) *y* direction

Figure 4-30. Normalized force-displacement loops for the isolation system, test SF2B-3D

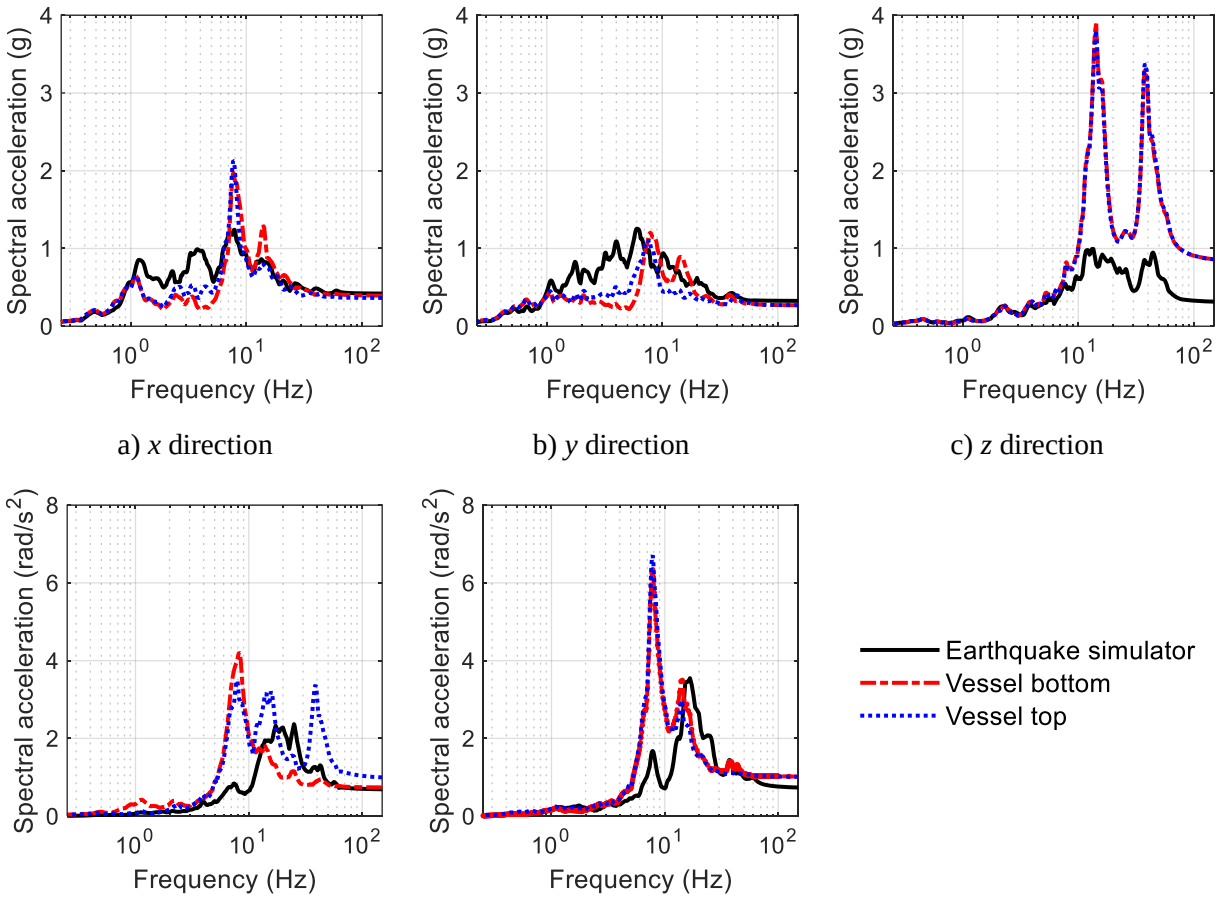

a) *x* direction b) *y* direction c) *z* direction

d) rocking about *x* axis e) rocking about *y* axis

Figure 4-31. Acceleration response spectra at the top and bottom of the vessel, test SF2B-3D, 5% damping

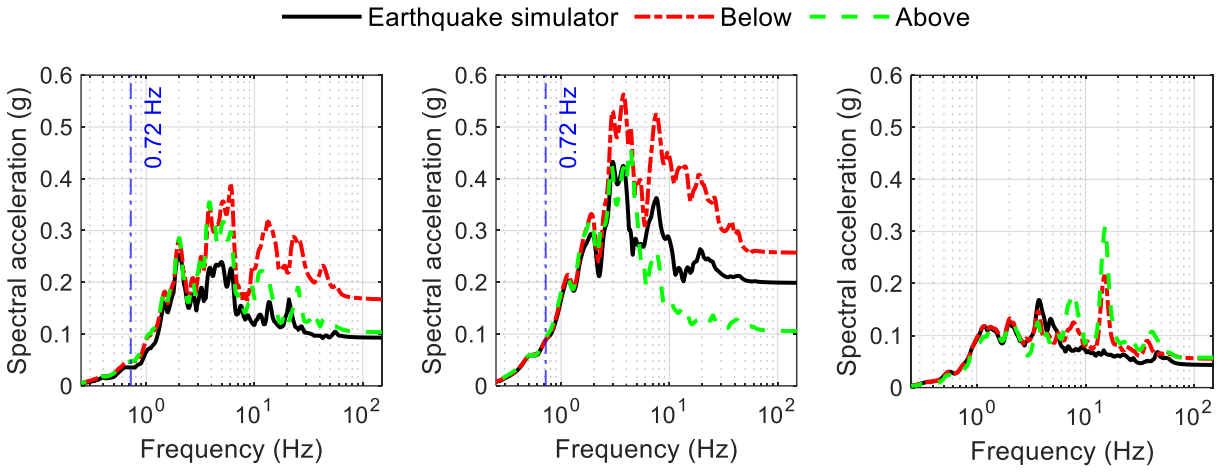

a) *x* direction b) *y* direction c) *z* direction

Figure 4-32. Acceleration response spectra directly above and below the isolation plane, test SF3A-3D, 5% damping

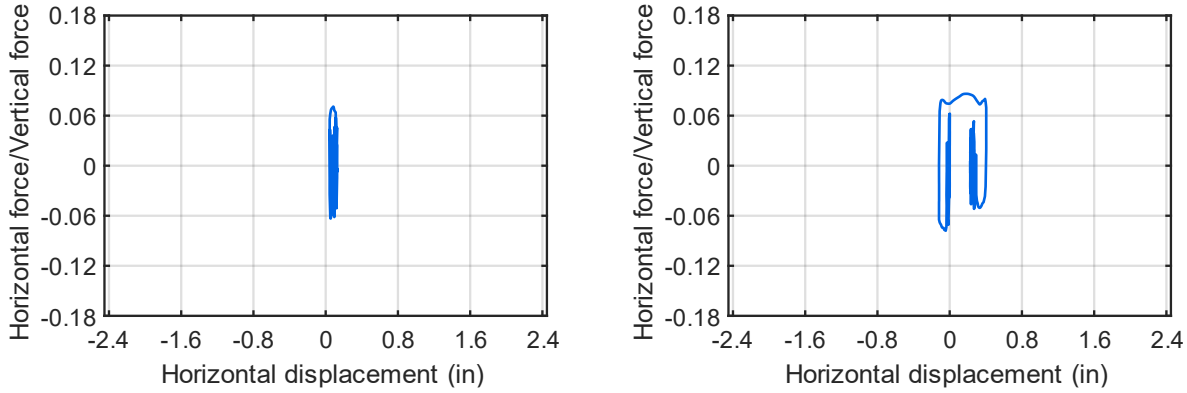

a) *x* direction b) *y* direction

Figure 4-33. Normalized force-displacement loops for the isolation system, test SF3A-3D

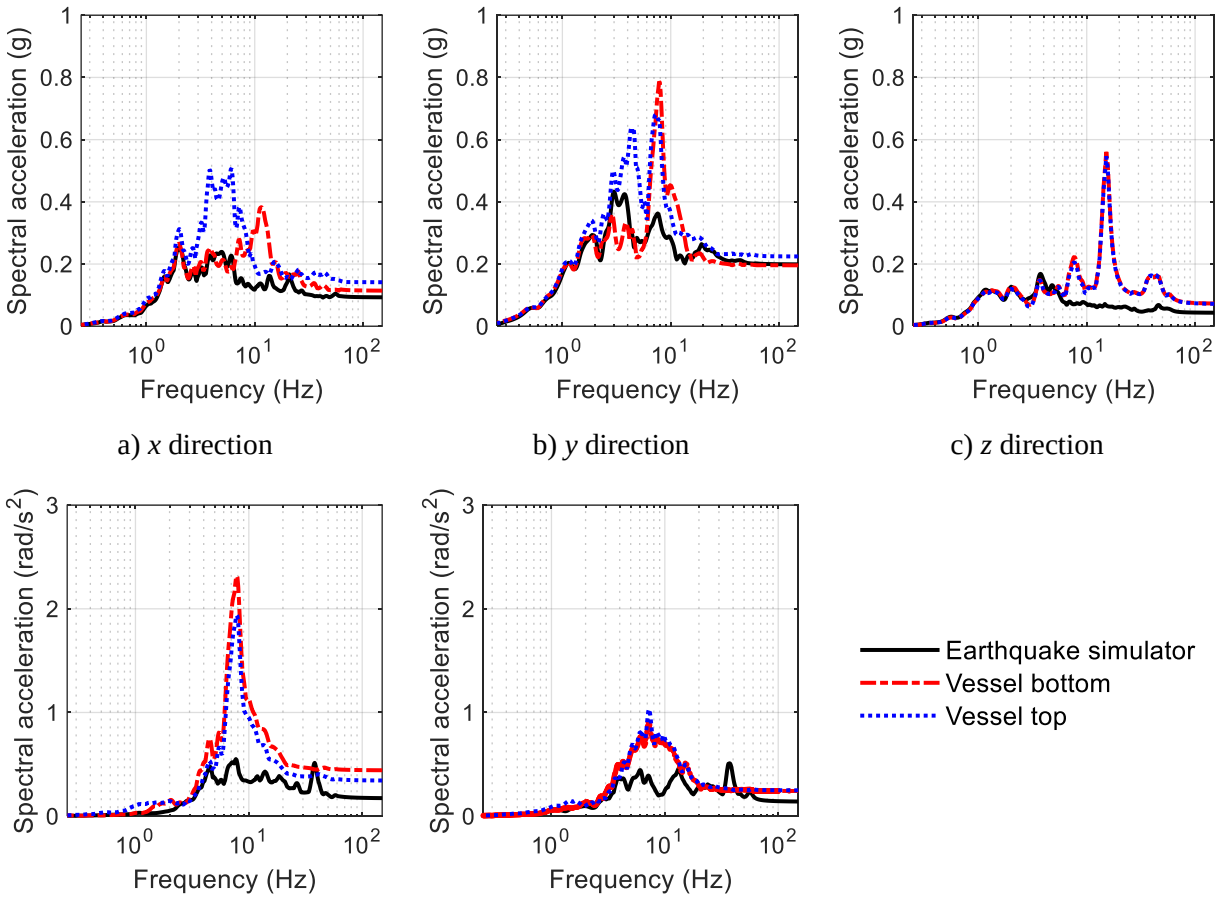

a) *x* direction b) *y* direction c) *z* direction

d) rocking about *x* axis e) rocking about *y* axis

Figure 4-34. Acceleration response spectra at the top and bottom of the vessel, test SF3A-3D, 5% damping

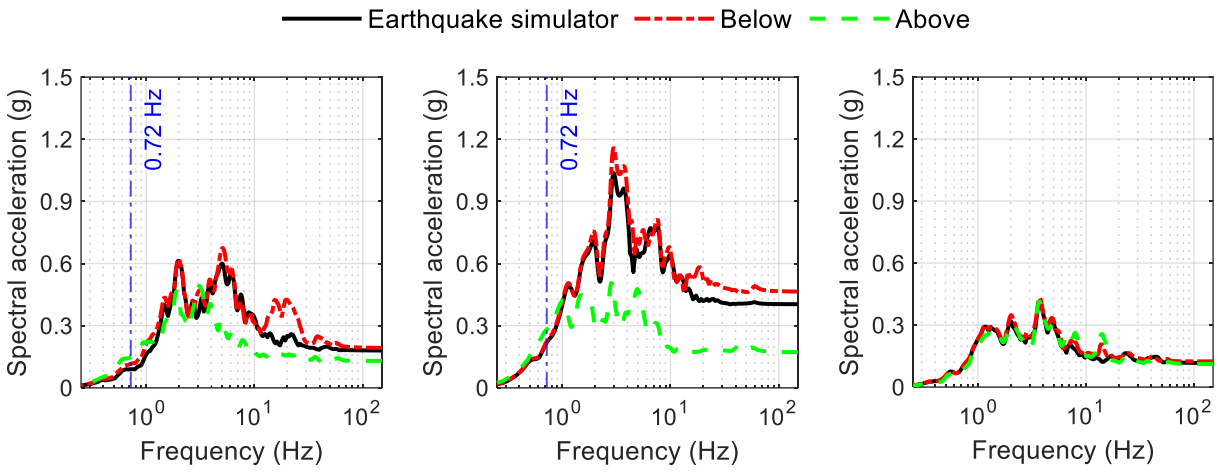

a) *x* direction b) *y* direction c) *z* direction

Figure 4-35. Acceleration response spectra directly above and below the isolation plane, test SF3B-3D, 5% damping

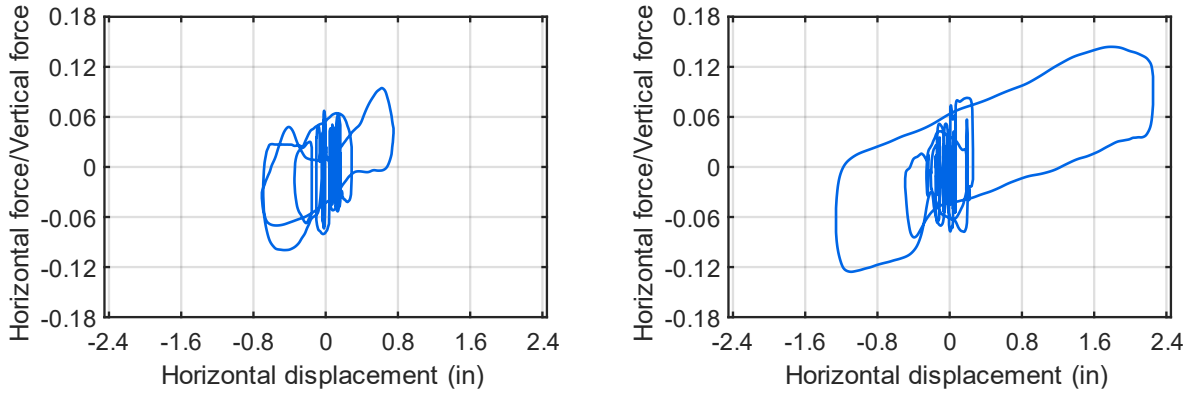

a) *x* direction b) *y* direction

Figure 4-36. Normalized force-displacement loops for the isolation system, test SF3B-3D

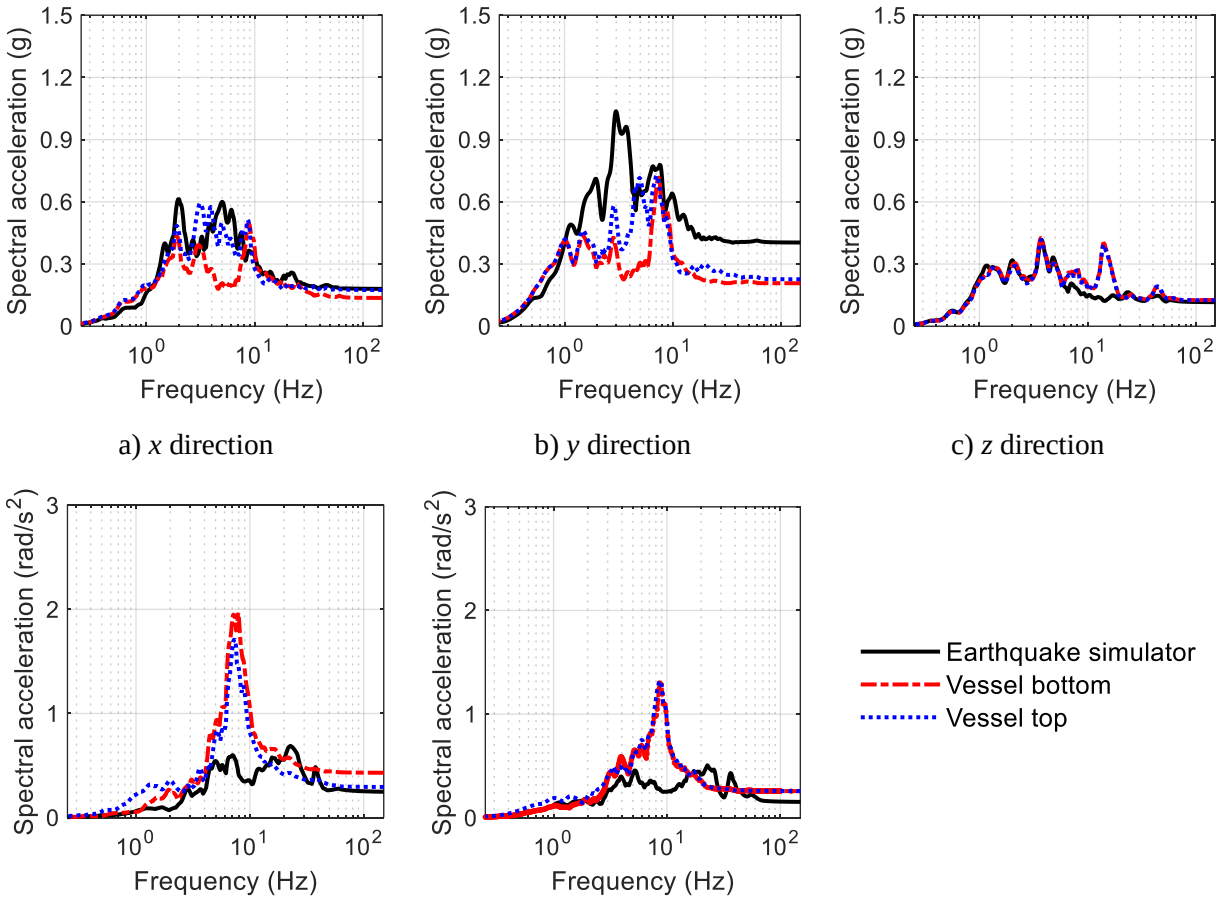

a) *x* direction b) *y* direction c) *z* direction

d) rocking about *x* axis e) rocking about *y* axis

Figure 4-37. Acceleration response spectra at the top and bottom of the vessel, test SF3B-3D, 5% damping

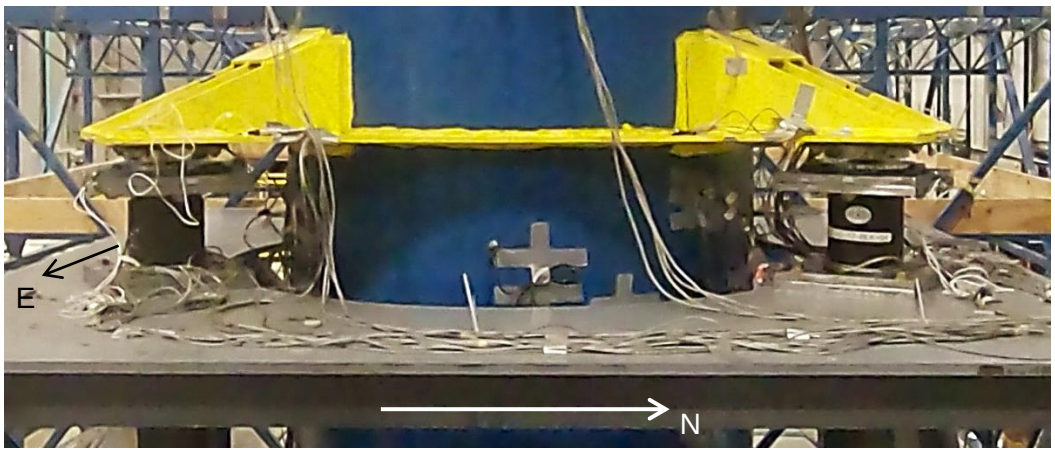

a) at-rest

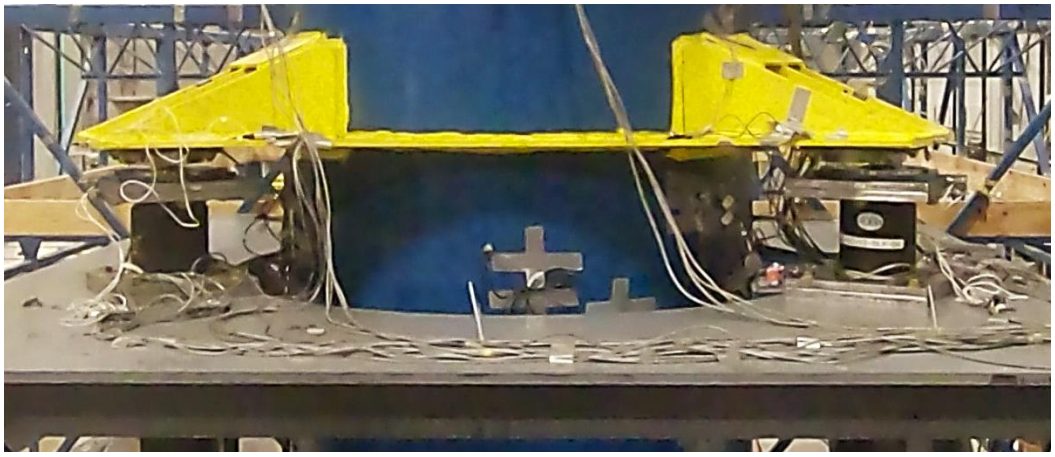

b) at maximum isolator displacement (= 2.4 inches)

Figure 4-38. Snapshots from test SF2B-3D at the mid-height of the vessel

Table 4-9. Peak acceleration[1] (g) for the 3D tests of the SFP-isolated configuration, *x*, *y*, and *z* directions[2]

Test	Earthquake simulator			Directly above (below) the isolation plane			Vessel bottom			Vessel top			Internal 1 bottom		
	x	***y***	***z***	***x***	***y***	***z***	***x***	***y***	***z***	***x***	***y***	***z***	***x***	***y***	***z***
SF1A-3D	0.25	0.29	0.11	0.13 (0.30)	0.12 (0.30)	0.21 (0.16)	0.22	0.22	0.34	0.22	0.24	0.34	0.75	0.71	0.43
SF1B-3D	0.65	0.78	0.30	0.24 (0.82)	0.23 (0.77)	0.39 (0.30)	0.36	0.29	0.52	0.34	0.31	0.50	1.06	0.62	0.68
SF2A-3D	0.20	0.23	0.18	0.11 (0.24)	0.11 (0.26)	0.21 (0.20)	0.20	0.14	0.32	0.19	0.19	0.32	NR[3]	0.61	0.5
SF2B-3D	0.42	0.33	0.31	0.24 (0.69)	0.18 (0.48)	0.57 (0.38)	0.39	0.27	0.83	0.36	0.27	0.83	NR[3]	0.74	1.84
SF3A-3D	0.09	0.20	0.04	0.10 (0.16)	0.11 (0.25)	0.06 (0.05)	0.11	0.20	0.07	0.14	0.22	0.07	0.46	0.46	0.09
SF3B-3D	0.18	0.40	0.12	0.13 (0.19)	0.17 (0.46)	0.11 (0.10)	0.14	0.21	0.13	0.17	0.23	0.13	0.59	0.76	0.16

1. Peak acceleration calculated as spectral acceleration at 100 Hz

2. See Figure 4-4 for the global co-ordinate system

3. Not recorded

Table 4-10. Peak strain (μS) in internals for the 3D tests of the SFP-isolated configuration

Test	Internal 1	Internal 2	
	R1B	**R2A**	**R2B**
SF1A-3D	208	74	74
SF1B-3D	172	117	114
SF2A-3D	179	97	97
SF2B-3D	226	107	107
SF3A-3D	137	80	80
SF3B-3D	213	95	95

4.5.5.2 TFP-isolated

Figures 4-39 through 4-56 present processed data for the six 3D motions of Table 4-5 and images from testing. The input motions had different frequency contents and amplitudes (see Section 4.4) and the *y*-axis scale in the figures presenting acceleration response spectra is different for each motion. A video recording of the test TF2B-3D can be viewed here. Table 4-11 presents the peak accelerations at the locations identified in Section 4.5.1.

Figures 4-39, 4-42, 4-45, 4-48, 4-51, and 4-54 present 5% damped acceleration response spectra (derived using the recorded acceleration histories) directly above and below the isolation plane (locations *V1* and *F1* in Figure 4-8). The vertical thin blue lines in these figures at a frequency of 0.51 Hz correspond to the sliding period (1.95 seconds) of the outer two surfaces of the TFP bearings (see Section 3). The amplification by the support frame (from location *C1* to *F1* in Figure 4-8) was similar to that in the SFP-isolated configuration. The spectral accelerations above the isolation plane, for frequencies greater than 3 Hz, were generally substantially smaller than those below the isolation plane, with reductions in peak accelerations (i.e., spectral accelerations at 100 Hz) by a factor of between 1.5 and 4.2[1].

The percentage reduction was generally higher than in the SFP-isolated configuration because of the adaptive behavior of TFP bearings, that is, sliding on multiple concave surfaces (Fenz and Constantinou, 2008b). For a small amplitude shaking, sliding occurs on the inner surfaces where the coefficients of friction are lower than for the outer surfaces (see Section 3).

Figures 4-40, 4-43, 4-46, 4-49, 4-52, and 4-55 present normalized force-displacement loops for the TFP isolation system. (Section 4.5.1 describes the derivation of the normalized force-displacement loops.) Similar to the correction of force-displacement loops from the testing of individual TFP bearings (see Section 3.5.3), the loops for the earthquake-simulator tests of the TFP-isolated vessel were corrected for cross talk between the axial, shear, and moment channels of the load cells.) The fluctuation in the coefficients of friction in the normalized loops is explained in Section 4.5.5.1. Figure 4-57 presents snapshots at the mid-height of the vessel from test TFP2B-3D, wherein the south-east (left) and north-east (right) TFP bearings are at the at-rest position and the maximum displacement (= 3.5 inches).

[1] Significant variation in the percent reduction due isolation was expected because of differences in the frequency content and the amplitude of the input motions.

Acceleration response spectra at the top and the bottom of the vessel (locations *V2* and *V3* in Figure 4-8), are presented in Figures 4-41, 4-44, 4-47, 4-50, 4-53, and 4-56. The TFP bearings generally enabled a significant reduction in horizontal spectral accelerations with respect to the underside of the isolation plane (the center of the earthquake simulator), with decreases in peak accelerations by a factor of between 1.1 (1.1) and 3.3 (2.9). The spectral accelerations in the vertical direction at the top and the bottom of the vessel were amplified, similar to that observed in the SFP-isolated configuration.

At the bottom of internal 1 (location *N1* in Figure 4-8), the peak horizontal (vertical) accelerations were amplified by a factor of between 1.5 (1.2) and 2.9 (2.3) with respect to the top of vessel (location *V3*). Peak axial strains in the internals (at locations *N2* and *N3*), reported in Table 4-12, were between 2% and 12% of the corresponding yield strains.

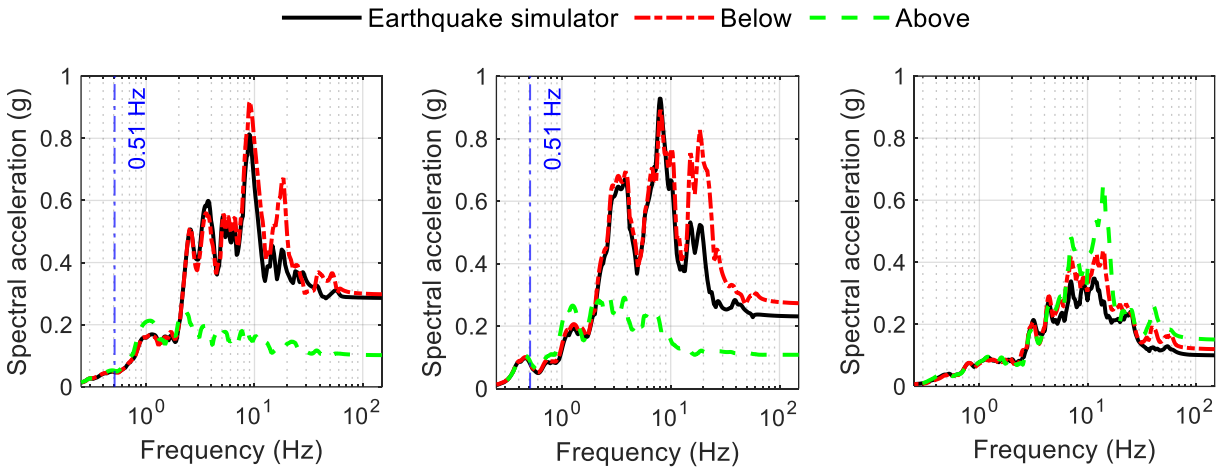

a) *x* direction b) *y* direction c) *z* direction

Figure 4-39. Acceleration response spectra directly above and below the isolation plane, test TF1A-3D, 5% damping

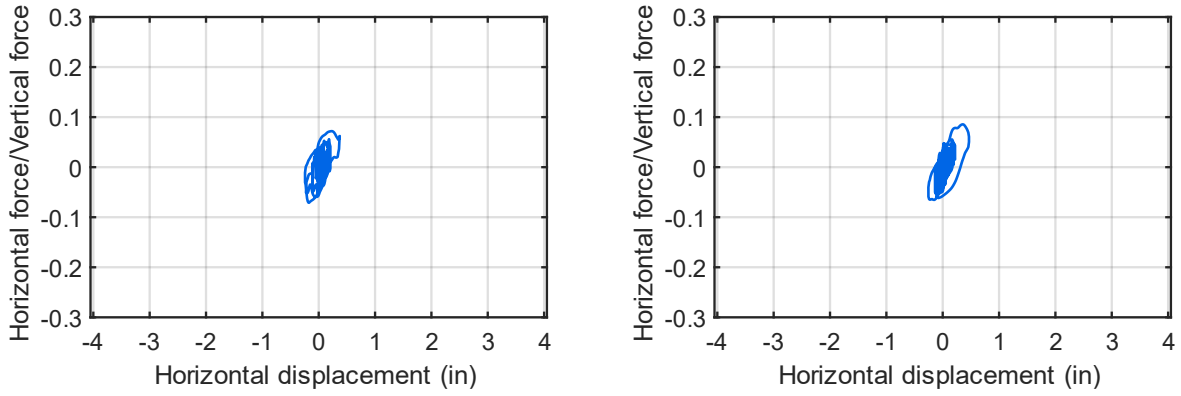

a) *x* direction b) *y* direction

Figure 4-40. Normalized force-displacement loops for the isolation system, test TF1A-3D

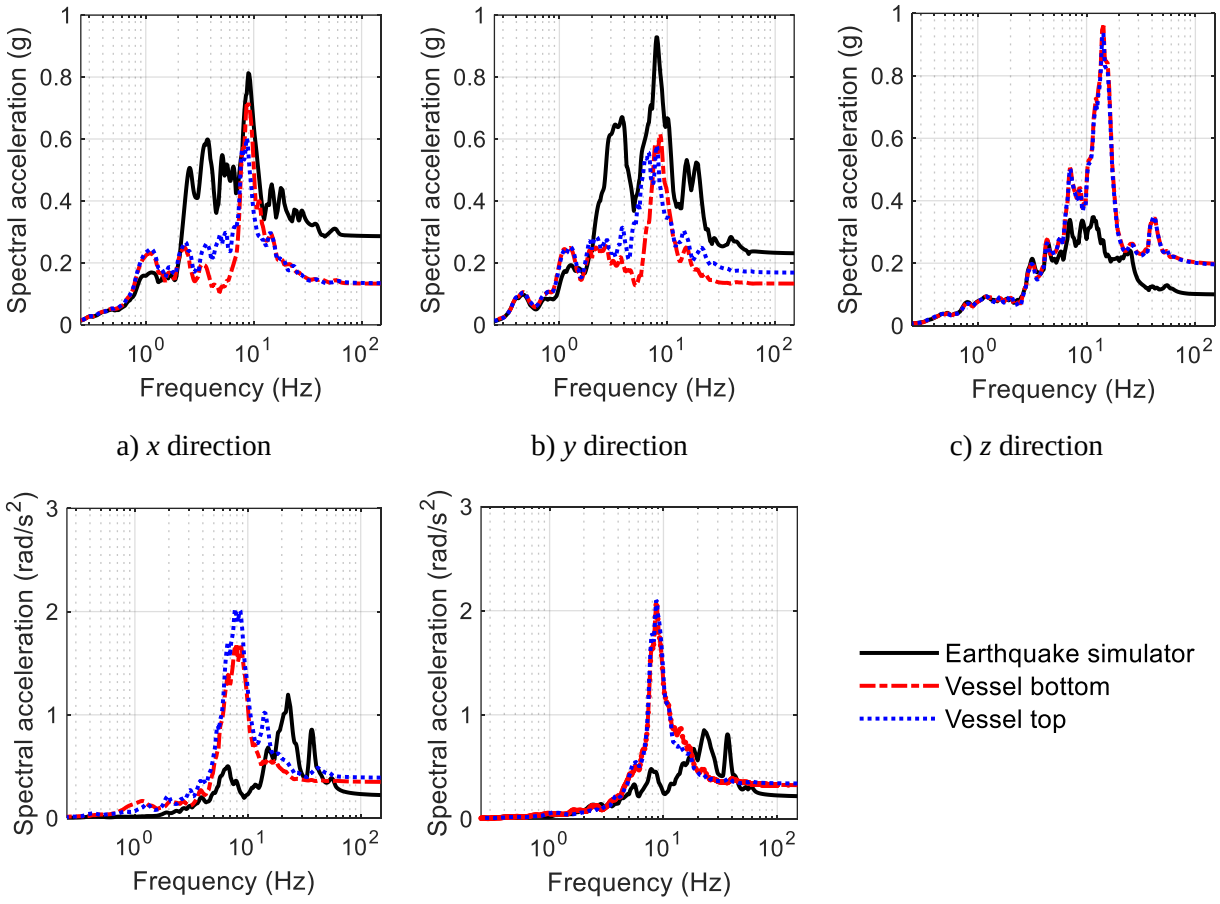

a) *x* direction b) *y* direction c) *z* direction

d) rocking about *x* axis e) rocking about *y* axis

Figure 4-41. Acceleration response spectra at the top and bottom of the vessel, test TF1A-3D, 5% damping

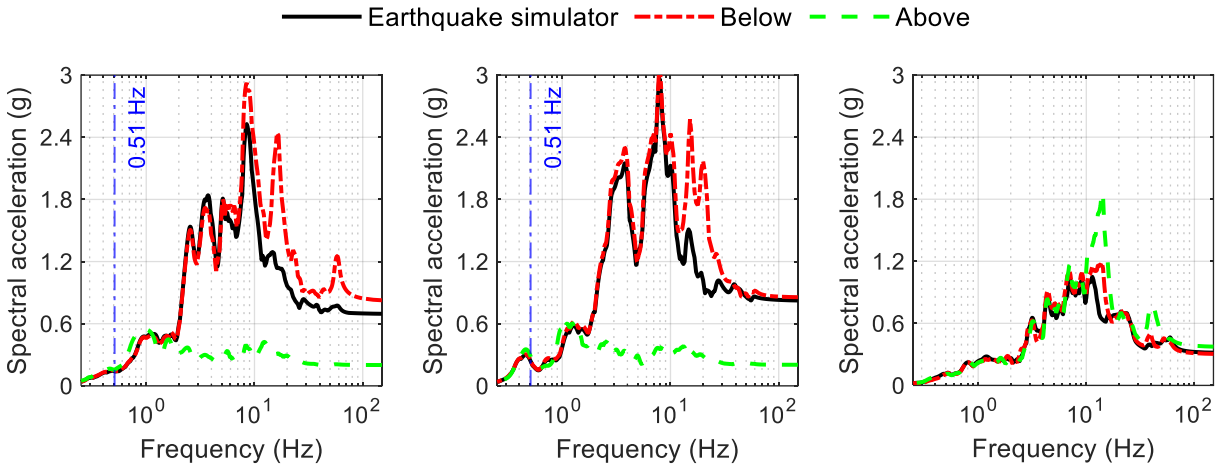

a) *x* direction b) *y* direction c) *z* direction

Figure 4-42. Acceleration response spectra directly above and below the isolation plane, test TF1B-3D, 5% damping

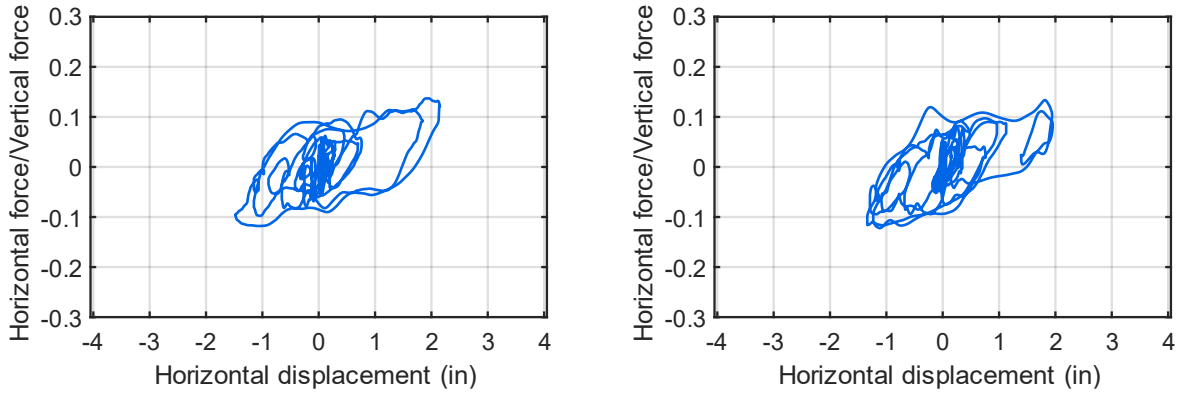

a) *x* direction b) *y* direction

Figure 4-43. Normalized force-displacement loops for the isolation system, test TF1B-3D

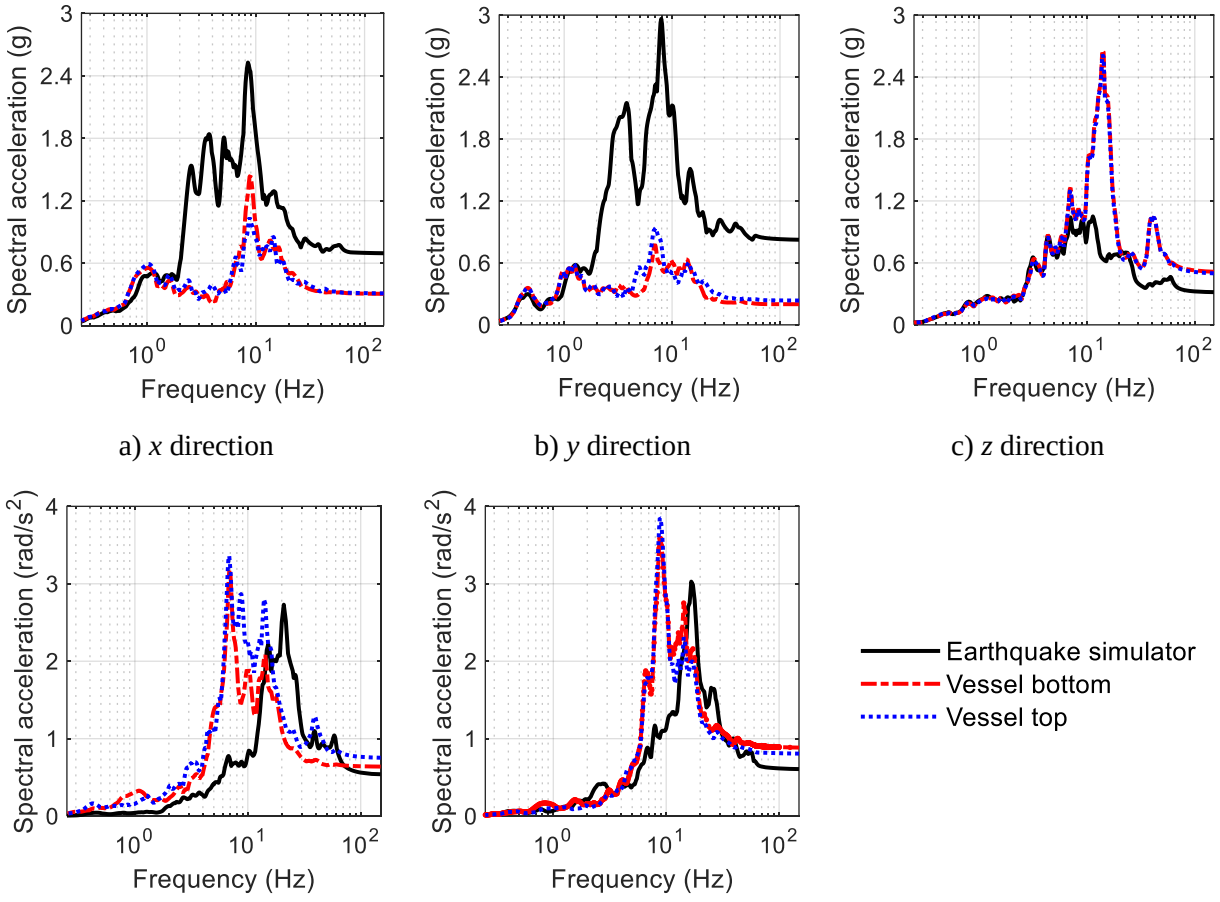

a) *x* direction b) *y* direction c) *z* direction

d) rocking about *x* axis e) rocking about *y* axis

Figure 4-44. Acceleration response spectra at the top and bottom of the vessel, test TF1B-3D, 5% damping

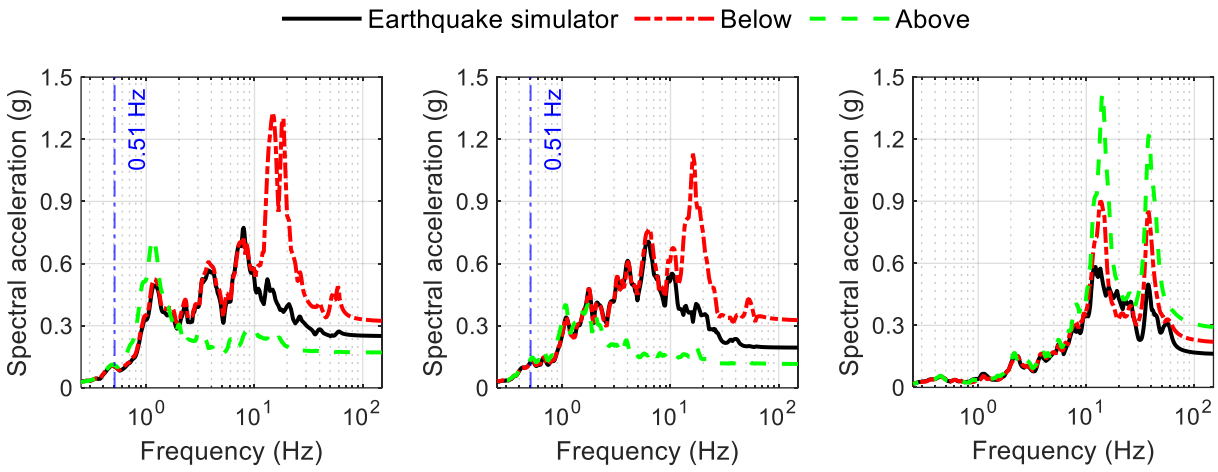

a) *x* direction b) *y* direction c) *z* direction

Figure 4-45. Acceleration response spectra directly above and below the isolation plane, test TF2A-3D, 5% damping

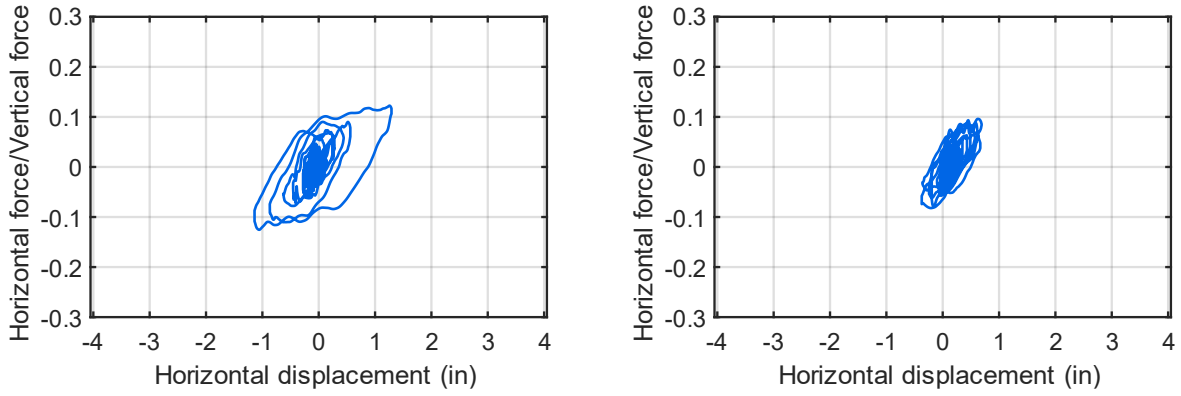

a) *x* direction b) *y* direction

Figure 4-46. Normalized force-displacement loops for the isolation system, test TF2A-3D

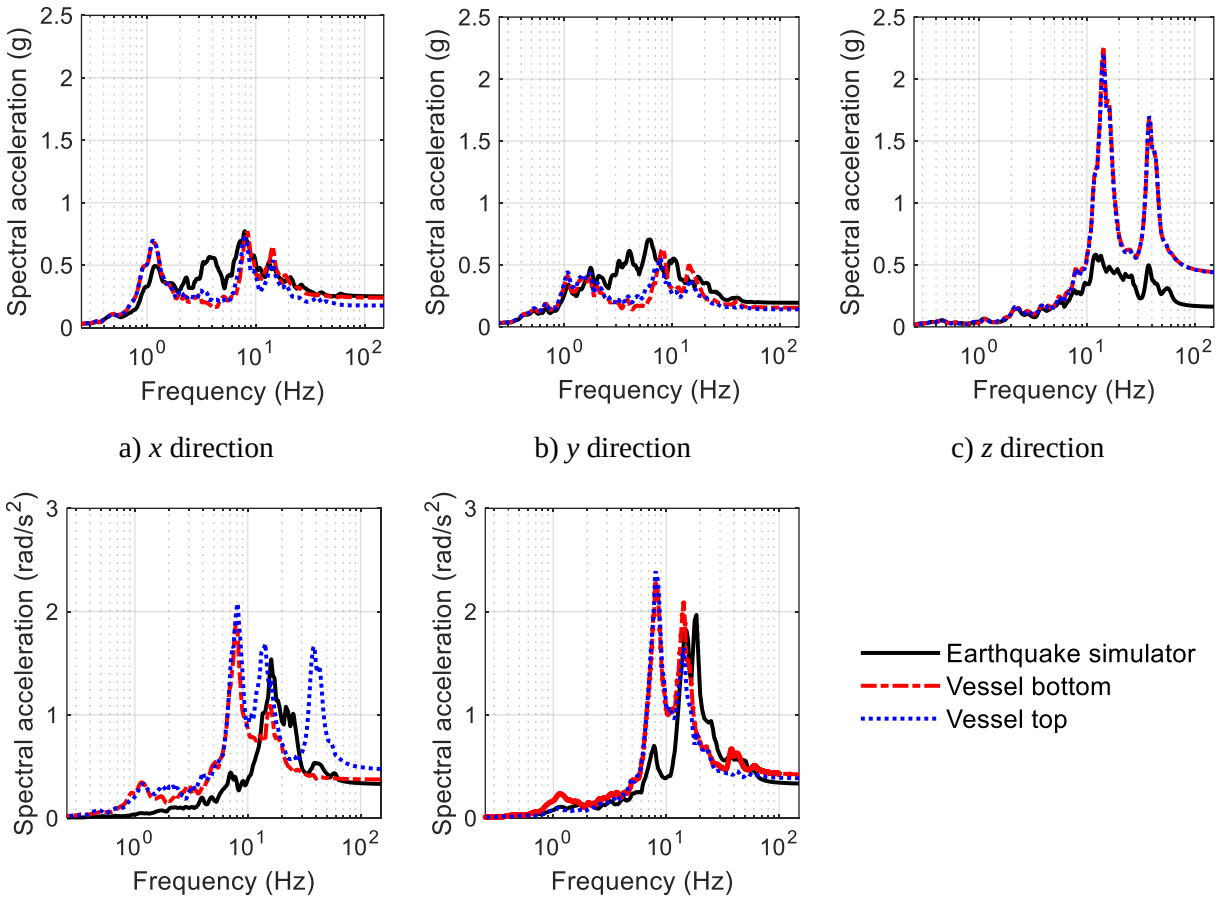

a) *x* direction b) *y* direction c) *z* direction

d) rocking about *x* axis e) rocking about *y* axis

Figure 4-47. Acceleration response spectra at the top and bottom of the vessel, test TF2A-3D, 5% damping

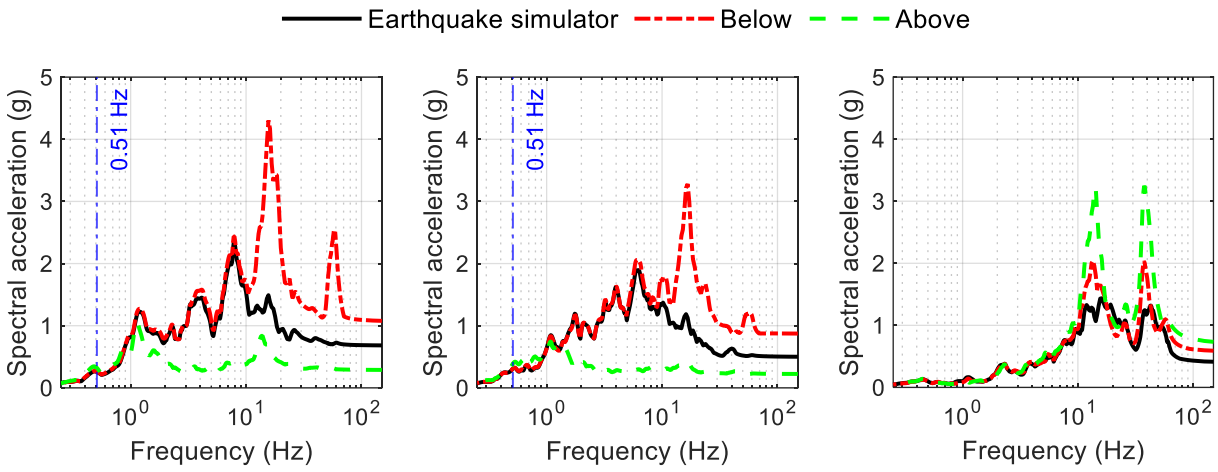

a) *x* direction b) *y* direction c) *z* direction

Figure 4-48. Acceleration response spectra directly above and below the isolation plane, test TF2B-3D, 5% damping

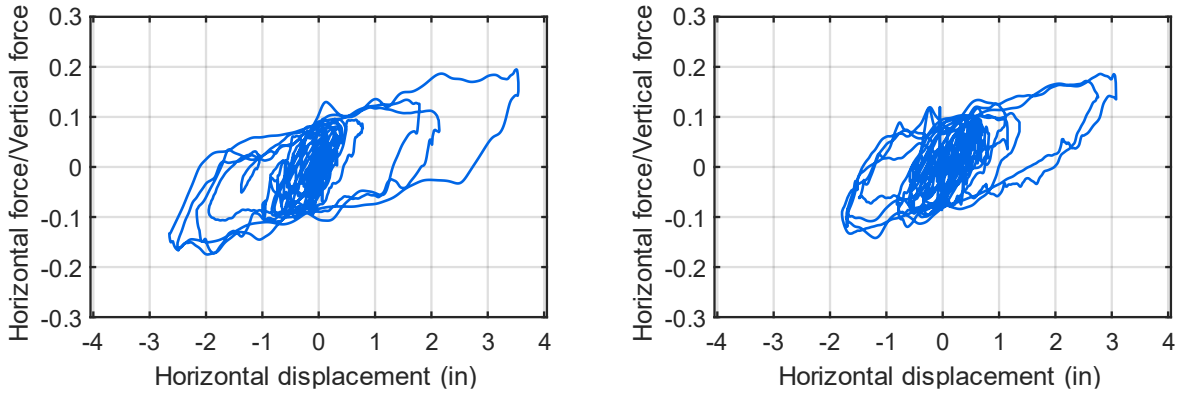

a) *x* direction b) *y* direction

Figure 4-49. Normalized force-displacement loops for the isolation system, test TF2B-3D

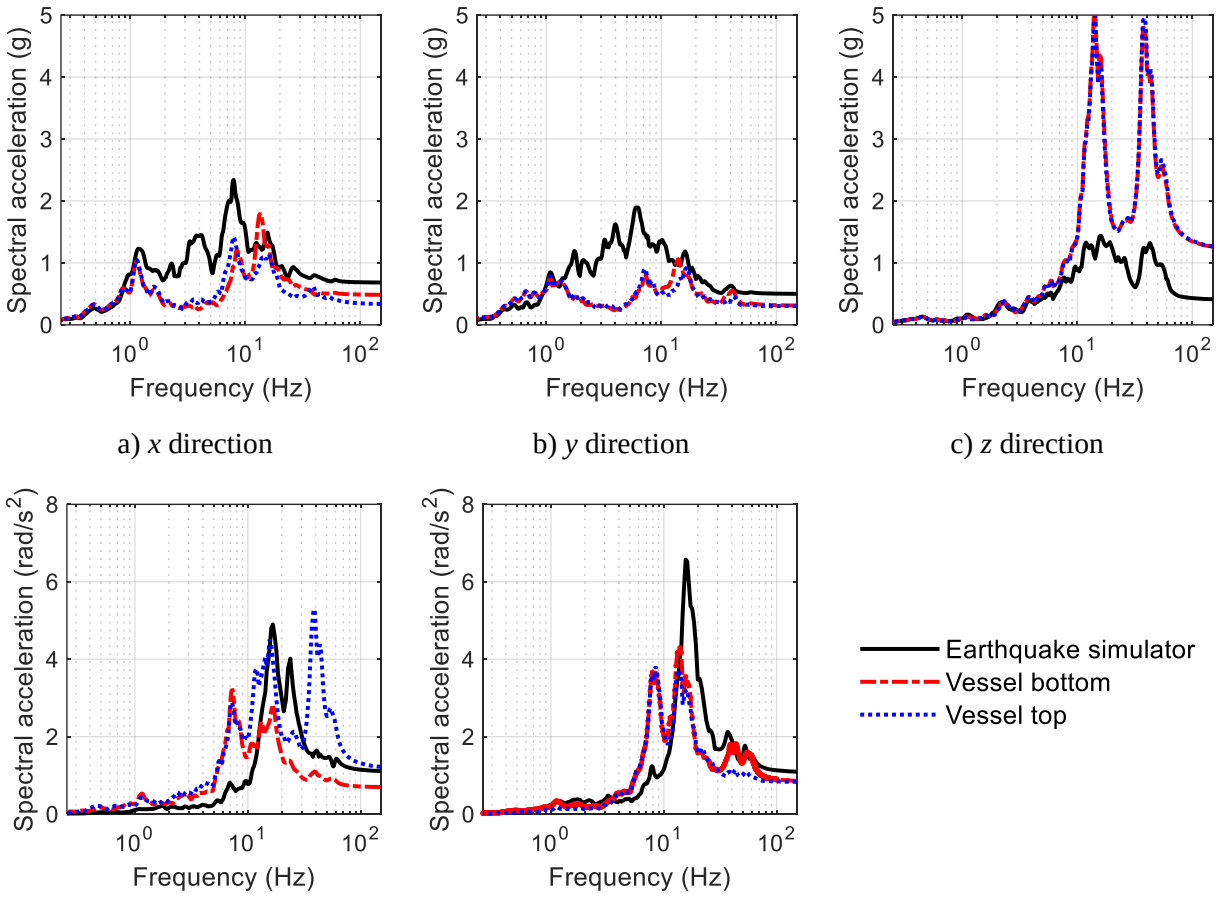

a) *x* direction b) *y* direction c) *z* direction

d) rocking about *x* axis e) rocking about *y* axis

Figure 4-50. Acceleration response spectra at the top and bottom of the vessel, test TF2B-3D, 5% damping

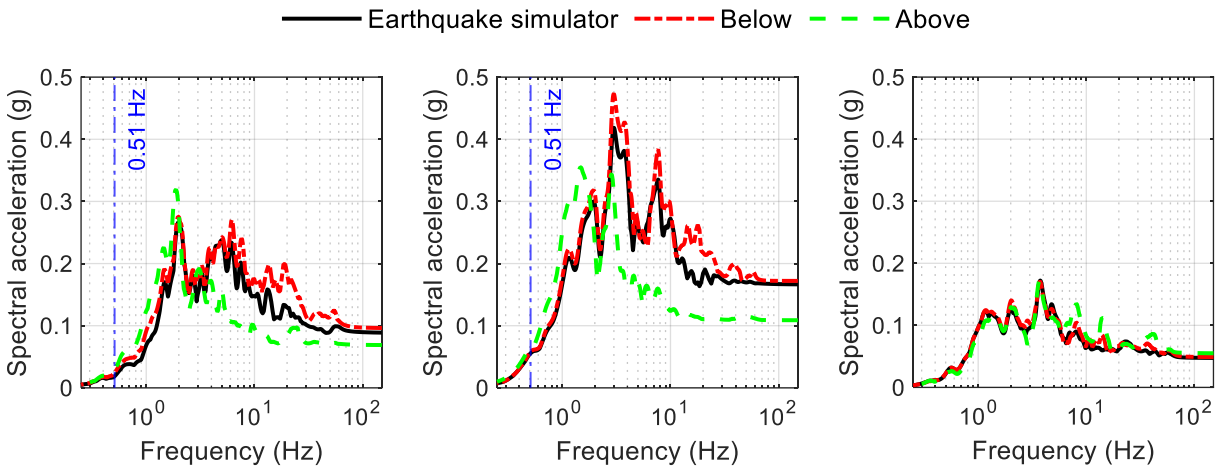

a) *x* direction b) *y* direction c) *z* direction

Figure 4-51. Acceleration response spectra directly above and below the isolation plane, test TF3A-3D, 5% damping

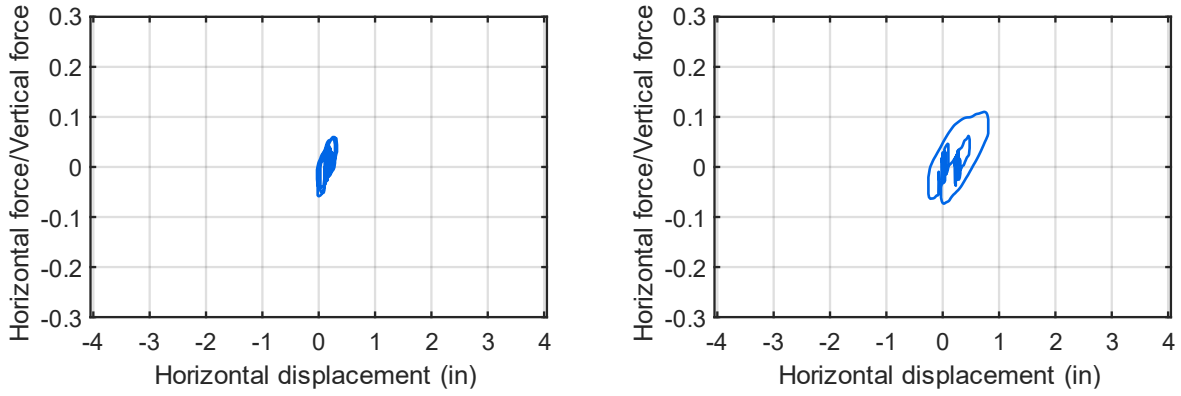

a) *x* direction b) *y* direction

Figure 4-52. Normalized force-displacement loops for the isolation system, test TF3A-3D

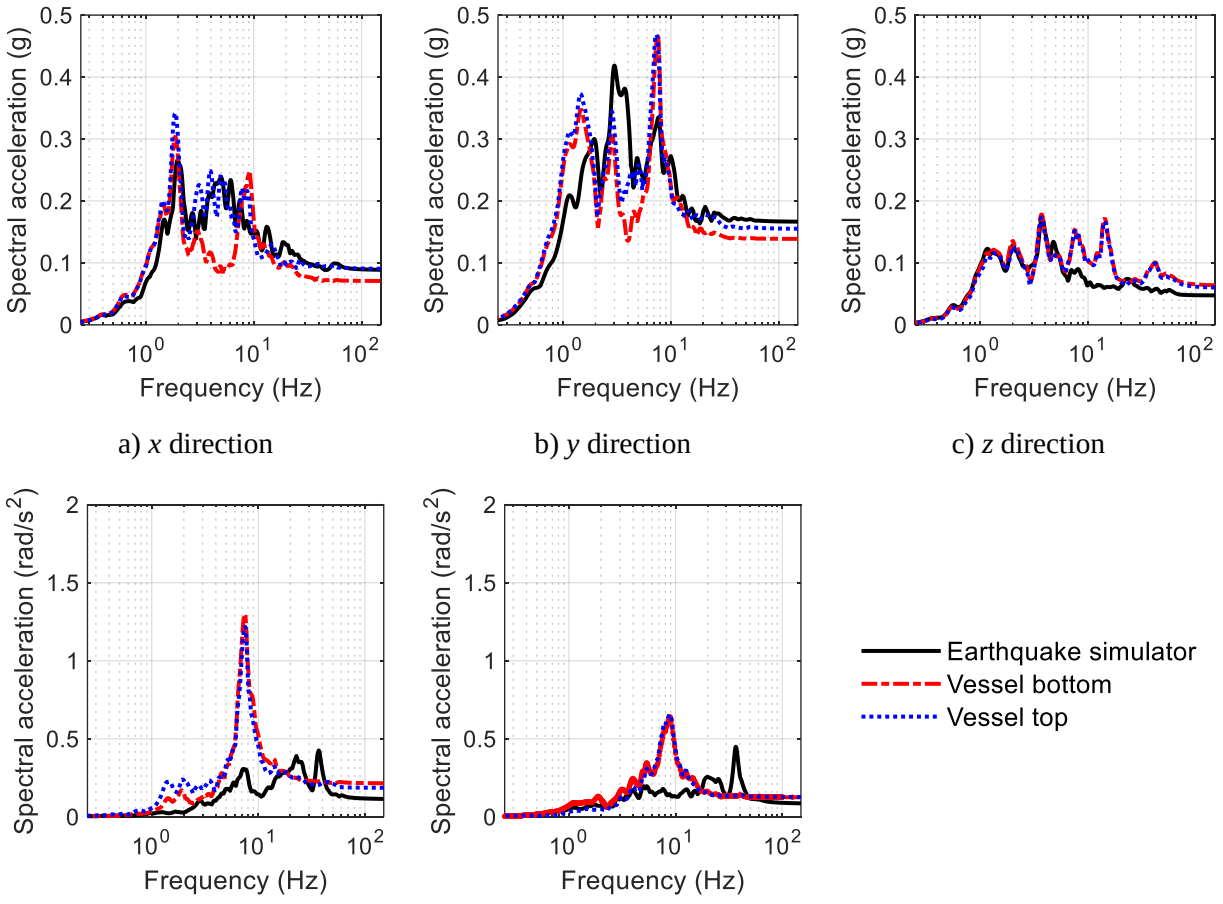

a) *x* direction b) *y* direction c) *z* direction

d) rocking about *x* axis e) rocking about *y* axis

Figure 4-53. Acceleration response spectra at the top and bottom of the vessel, test TF3A-3D, 5% damping

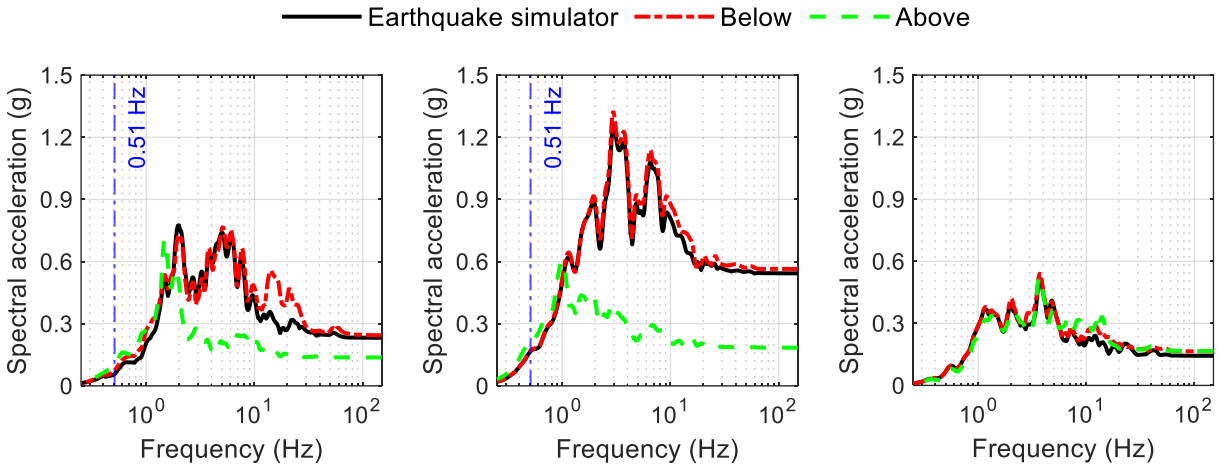

a) *x* direction b) *y* direction c) *z* direction

Figure 4-54. Acceleration response spectra directly above and below the isolation plane, test TF3B-3D, 5% damping

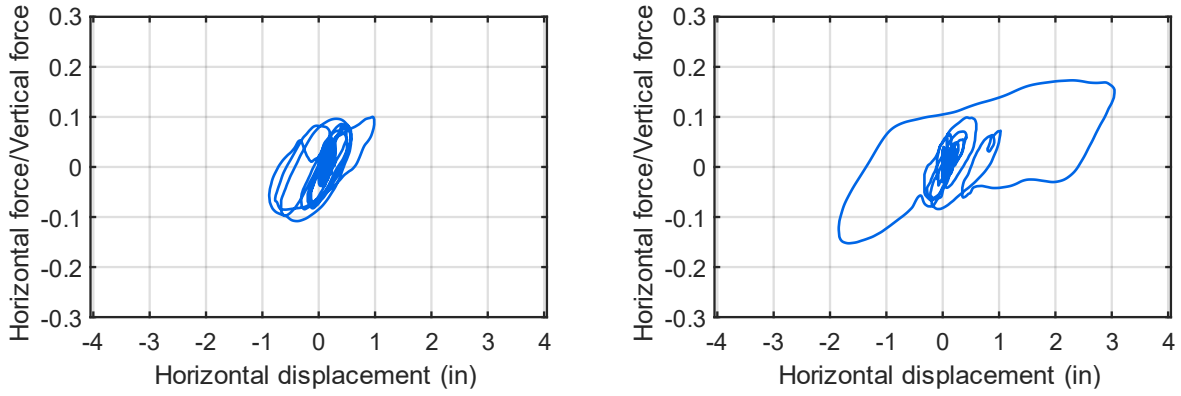

a) *x* direction b) *y* direction

Figure 4-55. Normalized force-displacement loops for the isolation system, test TF3B-3D

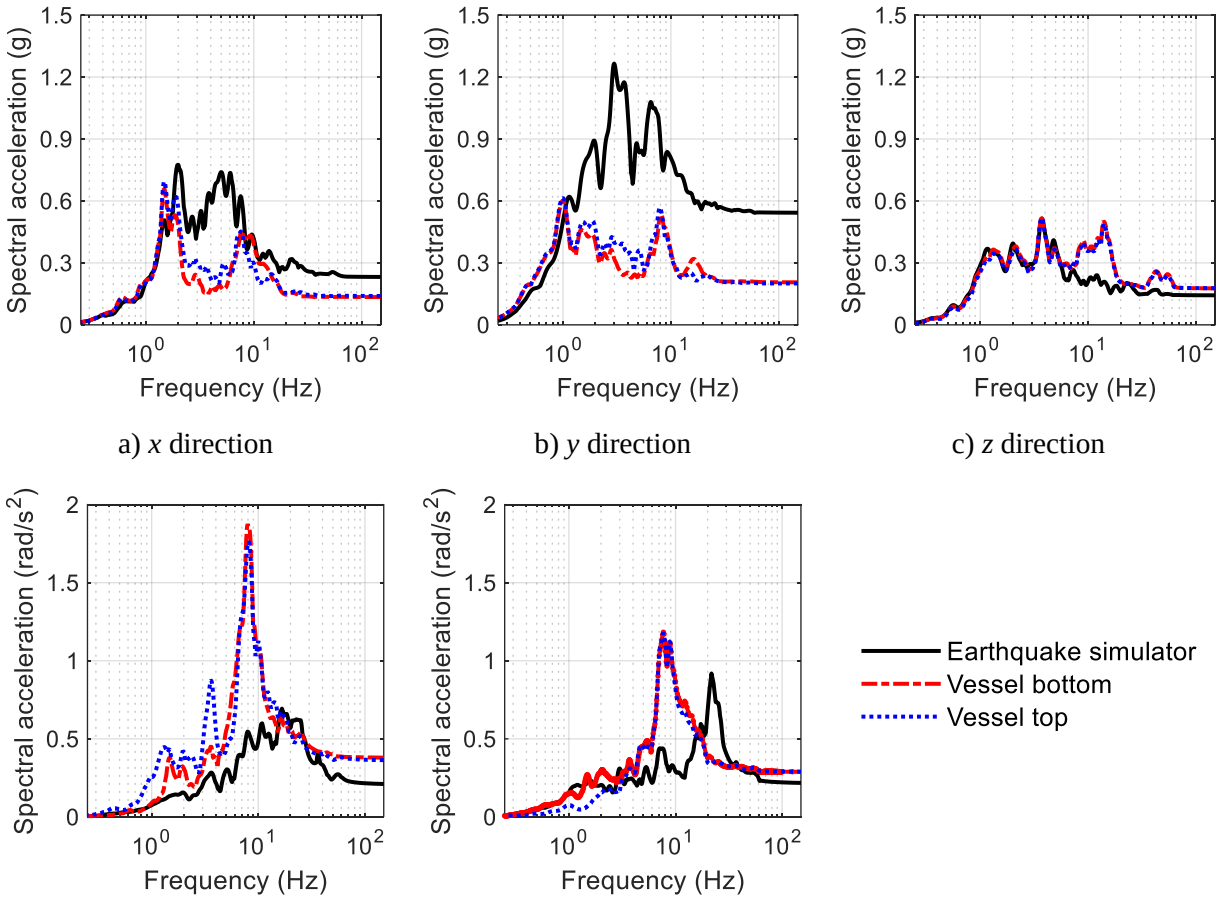

a) *x* direction b) *y* direction c) *z* direction

d) rocking about *x* axis e) rocking about *y* axis

Figure 4-56. Acceleration response spectra at the top and bottom of the vessel, test TF3B-3D, 5% damping

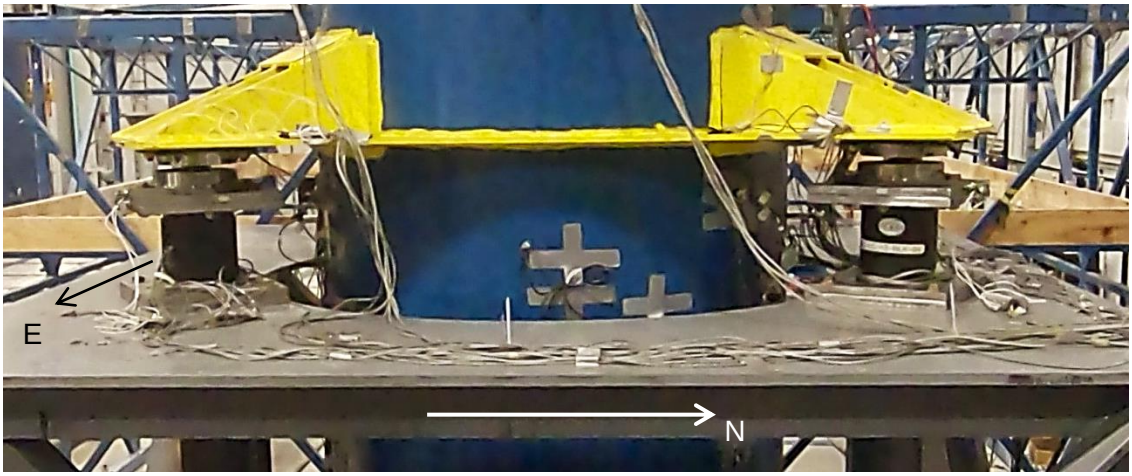

a) at-rest

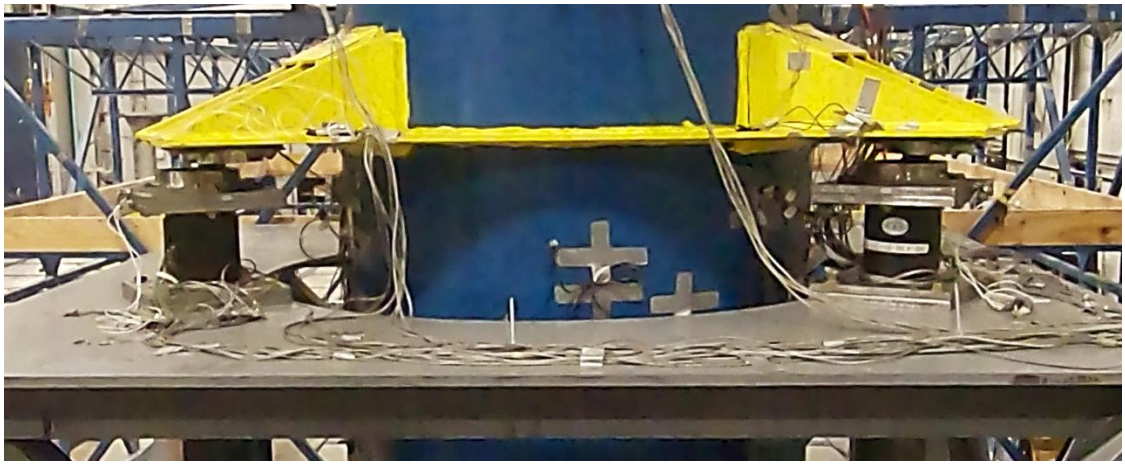

b) at maximum isolator displacement (= 3.5 inches)

Figure 4-57. Snapshots from test TF2B-3D at the mid-height of the vessel

Table 4-11. Peak acceleration[1] (g) for the 3D tests of the TFP-isolated configuration, *x*, *y*, and *z* directions[2]

Test	Earthquake simulator			Directly above (below) the isolation plane			Vessel bottom			Vessel top			Internal 1 bottom		
	x	***y***	***z***	***x***	***y***	***z***	***x***	***y***	***z***	***x***	***y***	***z***	***x***	***y***	***z***
TF1A-3D	0.29	0.23	0.10	0.10 (0.30)	0.11 (0.27)	0.15 (0.12)	0.13	0.13	0.19	0.13	0.17	0.19	0.44	0.32	0.24
TF1B-3D	0.69	0.82	0.31	0.20 (0.81)	0.20 (0.85)	0.37 (0.31)	0.30	0.20	0.50	0.31	0.23	0.49	0.74	0.40	0.61
TF2A-3D	0.25	0.19	0.16	0.17 (0.32)	0.12 (0.32)	0.28 (0.21)	0.24	0.15	0.43	0.18	0.14	0.42	NR[3]	0.37	0.83
TF2B-3D	0.68	0.50	0.41	0.29 (1.07)	0.22 (0.87)	0.70 (0.58)	0.48	0.31	1.20	0.33	0.3	1.21	NR[3]	0.45	2.71
TF3A-3D	0.09	0.17	0.05	0.07 (0.11)	0.11 (0.18)	0.05 (0.05)	0.07	0.14	0.06	0.09	0.15	0.06	0.31	0.35	0.07
TF3B-3D	0.23	0.54	0.14	0.14 (0.24)	0.18 (0.56)	0.17 (0.14)	0.13	0.21	0.18	0.14	0.2	0.18	0.41	0.48	0.17

1. Peak acceleration calculated as spectral acceleration at 100 Hz
2. See Figure 4-4 for the global co-ordinate system
3. Not recorded

Table 4-12. Peak strain (μS) in internals for the 3D tests of the TFP-isolated configuration

Test	Internal 1	Internal 2	
	R1B	**R2A**	**R2B**
TF1A-3D	98	67	67
TF1B-3D	94	110	108
TF2A-3D	95	90	92
TF2B-3D	99	146	145
TF3A-3D	94	72	69
TF3B-3D	141	119	118

4.6 Summary and discussion

The earthquake-simulator experiments described in this section were designed to assess the feasibility of mid-height seismic isolation of tall vessels. A 240-inch tall vessel with an outer diameter of 60 inches and a wall thickness of 1-inch was utilized for the experiments. Two internals were attached to the vessel head as described in Section 4.2.2. Three configurations of the vessel were tested: 1) non-isolated, 2) SFP-isolated, and 3) TFP-isolated. The characterization of the Friction Pendulum bearings is presented in Section 3. Ground motions with a broad range of frequency content and different amplitudes were utilized for the earthquake-simulator tests (see Section 4.4)

In the non-isolated configuration, the peak accelerations at the top of the load cells (location *F1* in Figure 4-8) were amplified by a factor of between 1.2 (1.6) and 2.2 (1.9) to the top and the bottom of the vessel (locations *V2* and *V3*) in the horizontal (vertical) directions. The horizontal response of the vessel was driven by its rocking at 11 Hz (see Figures 4-10 and 4-11), which was amplified by the rocking of the earthquake-simulator platform due to simulator-specimen interaction. The frequencies of the vertical modes, driving the vessel's vertical response, were 17 Hz and 45 Hz (see panels e and f of Figure 4-10). For moderate-to-high seismic inputs such as those in tests FB1B-3D and FB2B-3D, peak horizontal accelerations greater than 1 g were observed at the top and the bottom of the vessel: see columns 8, 9, 11, and 12 in Table 4-7.

Mid-height seismic isolation using SFP and TFP bearings generally enabled a significant reduction in the horizontal spectral accelerations above the isolation plane (location *V1*) and at the top and the bottom of the vessel (locations *V2* and *V3*), with peak horizontal accelerations lower than those at the center of the earthquake-simulator platform in most cases (see Tables 4-9 and 4-11). For moderate-to-high seismic inputs, and intensities greater than those in tests FB1B-3D and FB2B-3D of the non-isolated configuration, the peak horizontal accelerations at the top and the bottom of the isolated vessel were less than 0.5 g (see Tables 4-9 and 4-11). The efficacy of the isolation systems and the corresponding reduction in the peak horizontal accelerations was a function of the frequency content and the amplitude of the input motions. For design of isolated safety-class equipment in nuclear power plants, an isolation system could be tuned for the reactor- and site-specific seismic hazard (that is, the frequency content and the amplitude of shaking) to enable significant reductions in horizontal spectral accelerations: the isolation systems tested herein were not optimized across multiple ranges of frequency content and amplitude of seismic input.

Although rocking of the vessel was observed in both isolated configurations, it was smaller than in the non-isolated configuration as evident from the peak rocking accelerations (at 100 Hz) at the top and the bottom of the vessel. For example, compare the peak rocking accelerations in panel d of Figures 4-14 and 4-22, having identical values at the center of the earthquake simulator for the non-isolated and SFP-isolated configurations (0.56 rad/sec^2) with corresponding values of 1.8 rad/sec^2 (non-isolated) and 0.6 rad/sec^2 (SFP-isolated) at the top of the vessel. The rocking modal frequency at 8 Hz in the isolated configurations was lower than in the non-isolated configuration (at 11 Hz) because of the vertical flexibility of the bearings (characterized in Section 3). In the vertical direction, the amplification of spectral accelerations from the top of the load cells (location *F1*) to the top and the bottom of the vessel (locations *V2* and *V3*) was similar in the non-isolated and isolated configurations.

Even though the amplitude of shaking was larger in the isolated configurations, the peak axial strains (at locations *N2* and *N3*) and the peak horizontal accelerations (at location *N1*) in the internals were smaller than in non-isolated configuration. Maximum peak axial strain values were 10% (12%) of the yield strain in the SFP- (TFP-) isolated vessel and 22% in the non-isolated vessel: compare the values in Tables 4-8, 4-10, and 4-12. Peak horizontal accelerations (at location *N1*) greater than 1.5 g were observed in the non-isolated configuration but smaller than 1 g in the isolated configurations: compare the values in columns 14 and 15 of Tables 4-7, 4-9, and 4-11.

The results from the earthquake-simulator tests of the vessel and its internals, summarized above, enable a qualitative comparison of the responses in the isolated and non-isolated configurations. Mid-height seismic isolation is beneficial and practical for tall vessels. The experimental results are used to benchmark numerical models of the test specimen, described in Section 5, that is utilized to compare responses in the non-isolated and isolated configurations for identical inputs, and investigate other seismic isolation strategies for tall, slender vessels.

SECTION 5
NUMERICAL MODELING AND RESPONSE-HISTORY ANALYSES OF MID-HEIGHT AND BASE ISOLATED TALL, SLENDER VESSELS

5.1 Introduction

This section describes the numerical modeling of the mid-height supported vessel described in Section 4, investigation of the utility of mid-height seismic isolation, and quantification of its benefits. (A qualitative comparison of response for the isolated and non-isolated vessel is presented in Section 4.) The feasibility of base isolation for a tall, slender vessel is also investigated. Numerical models were constructed for six configurations of the vessel: non-isolated at the mid-height, non-isolated at the base, mid-height isolated using single Friction Pendulum (SFP) bearings, mid-height isolated using Triple Friction Pendulum (TFP) bearings, base isolated using SFP bearings, base isolated using SFP bearings with extended support mounts. The goals of the modeling were to 1) investigate the utility and quantify the benefits of mid-height seismic isolation, 2) investigate the feasibility of base isolation for a tall, slender vessel, and 3) provide analysis and design recommendations for seismic isolation of safety-class equipment.

Section 5.2 presents the numerical modeling and modal analysis results. Section 5.3 enables a comparison of and discusses predicted and experimentally measured responses. Section 5.4 investigates the utility and quantifies the benefits of mid-height seismic isolation using the (benchmarked) numerical models of Section 5.2. Section 5.5 explores base isolation of a tall, slender vessel and Section 5.6 presents a summary and discussion.

5.2 Numerical modelling

5.2.1 Introduction

Numerical models of the test specimen were developed in the computer program SAP2000 (CSI, 2021). Figure 5-1a presents an isometric view of the non-isolated numerical model. The vessel (red in Figure 5-1a), its flanges (blue), support mounts and the shaped plates (yellow), vessel head (green), and the mounting plate of the support frame (grey) were modelled using shell elements with appropriate thicknesses (see Section 4). The columns and angles of the support frame were modelled using beam elements with appropriate section properties (see Section 4).

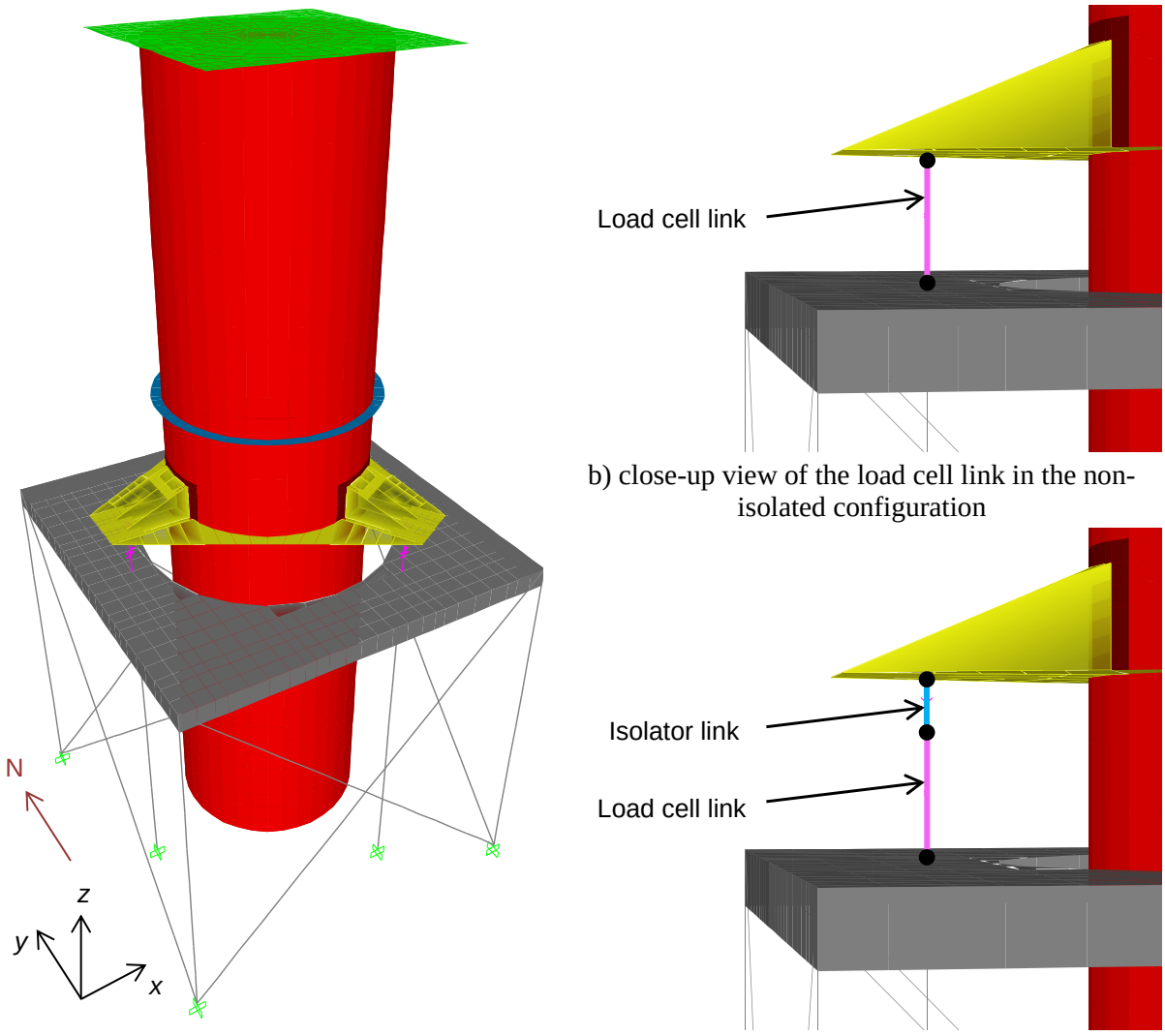

a) isometric view

b) close-up view of the load cell link in the non-isolated configuration

c) close-up view of the load cell and isolator links in the isolated configurations

Figure 5-1. Numerical model of the test specimen in SAP2000

Mechanical properties consistent with carbon steel, and listed in Table 5-1, were assigned to the shell and the beam elements. The bottom nodes of the columns and angles, where the support frame was bolted to the earthquake-simulator platform, were assigned the *fixed* joint restraint in all six degrees-of-freedom. The SAP2000 model was calibrated to the measured rocking frequencies (see Section 5.2.2) by reducing a) the stiffness of the columns, angles, and plates of the support frame by 15% (to account for the flexibility of the connections between the members of the support frame), and b) membrane, bending, and shear stiffnesses of the support mounts and the shaped plates by 15% (to account for the flexibility of the welded connections).

Table 5-1. Mechanical properties of carbon steel

Property	Value
Minimum yield stress	36 ksi
Density	0.29 lb/in^3
Elastic modulus	29000 ksi
Poisson's ratio	0.3

The measured weight of the empty vessel, including the head and internals was 16.3 kips (see Section 4). The corresponding weight computed by SAP2000 was within 1% of the measured value: 16.2 kips. For testing, the vessel was filled full of water to simulate in-service condition, eliminating sloshing of the fluid. In this case, the fluid response is treated as impulsive[1], and interaction of the fluid and the surrounding structure (vessel) was ignored for the purpose of benchmarking numerical models of the isolation systems and the mid-height supported vessel. The weight of the water (= 23 kips) was distributed uniformly along the height of the vessel wall (red in Figure 5-1a) using area mass for shell elements in SAP2000[2].

The five-channel load cells and the Friction Pendulum (FP) bearings were modelled using two joint links. The *Linear Spring* element was assigned to the load cell links, with horizontal and vertical stiffnesses per Appendix A of Mir *et al.* (2022b). The rotational degrees of freedom for the load cell links were *fixed* as they have high rotational stiffness. The load cell links were 13 inches tall (= height of the load cells, see Figure 3-10) with their bottom node connected to the mounting plate of the support frame, directly above the beam elements for the interior columns. The *Friction Isolator* and *Triple Pendulum Isolator* elements were assigned to the bearing links for modelling single and triple FP isolators, respectively, with the radius of curvature, coefficients of friction, rate parameter, and axial stiffness per Section 3. Table 5-2 lists the parameters assigned to the SFP and TFP elements in SAP2000.

[1] Studies on fluid-structure-interaction parse hydrodynamic response of a fluid in a dynamically excited vessel into impulsive and convective components. The impulsive response is from the part of the fluid that moves (and accelerates) with the vessel. The convective response is from the part of the fluid that oscillates and forms waves on the free surface (sloshing).

[2] At the time of this writing, SAP2000 does not have the ability to explicitly model fluid-structure-interaction, for which other finite element programs (e.g., LS-DYNA and ABAQUS) can be used (see Yu and Whittaker (2020) and Mir et al., (2022b))

Table 5-2. Parameters for modelling Friction Pendulum bearings in SAP2000

	SFP bearings	TFP bearings	
Supported weight per bearing, W (kip)[1]	13.2	13.2	
Element height, h (in)[2]	4	4	
Shear deformation location (in)	2	2	
Effective radius, R_{eff} (in)[2]	18.64	$R_{eff\,1} = R_{eff\,4}$	17.2
		$R_{eff\,2} = R_{eff\,3}$	2.2
Friction coefficient slow, μ_{slow} [2]	0.028	$\mu_1 = \mu_4$	0.067
		$\mu_2 = \mu_3$	0.014
Friction coefficient fast, μ_{fast} [2]	0.078	$\mu_1 = \mu_4$	0.113
		$\mu_2 = \mu_3$	0.023
Rate parameter (sec/in)[2]	8	1	
Axial stiffness (kip/in)[2]	2,370	2,080	
Elastic stiffness (kip/in)[3]	104.4	$K_{e1} = K_{e4}$	151
		$K_{e2} = K_{e3}$	26.8
Post-elastic stiffness (kip/in)[4]	0.709	0.383	
Rotational inertia (kip-in-sec^2)[5]	0.071	0.133	
Rotational/torsional stiffness[5]	0	0	

1. A third of the weight of the vessel, including water, head, and internals (see Section 4)
2. See Section 3
3. Stiffness prior to the initiation of sliding, $\mu_{fast} W / Y$, where Y is yield displacement (= 0.01" per Section 3)
4. Stiffness corresponding to sliding
5. Rotational mass moment of inertia, $m_{isolator}(D_R^{\,2} + h^2)/12$ where $m_{isolator}$ is the mass of the bearing, and D_R is the diameter of slider (inner rigid slider for TFP bearings)
6. Friction Pendulum bearings have negligible resistance to rotation and torsion

Three numerical models were developed, one each for the non-isolated, SFP-isolated, and TFP-isolated configuration. In the non-isolated configuration, the top nodes of the load cell links were connected to the underside of the support mounts of the vessel: see panel b of Figure 5-1. In the isolated configurations, the isolator links were modelled atop the load cells links: see panel c of Figure 5-1.

5.2.2 Modal analysis

Modal analysis of the numerical models was performed to compare predicted and measured (Section 4) resonant frequencies. Table 5-3 presents results. Translational modal frequencies in the *x* and *y* directions could not be clearly identified from the experimental data because rocking of the table (and hence the vessel) dominated the translational response of the vessel. In the *z* direction, the SAP2000 model overestimated the first translational frequency in all three configurations (non-isolated, SFP-isolated, and TFP-isolated): the sources of the difference could not be clearly identified but are attributed to connections, including those associated with the support mounts. The close agreement between the predicted and measured rocking frequencies is an outcome of the calibration exercise described previously (in Section 5.2.1).

Table 5-3. Resonant frequencies from the SAP2000 model and test data[1]

	x and *y* directions[2]		R_x and R_y directions[2]		*z* direction[2]	
	SAP2000	Test data	SAP2000	Test data	SAP2000	Test data
Non-isolated	14 Hz[3]	NA[4]	10.4 Hz	11 Hz	27 Hz	17 Hz
SFP-isolated	0.72 Hz[5]	NA[6]	8.4 Hz[7]	8 Hz[7]	20 Hz	15.3 Hz
TFP-isolated	0.53 Hz[8]	NA[6]	8.3 Hz[7]	8 Hz[7]	19.6 Hz	15.5 Hz

1. Measured frequencies for the non-isolated vessel were derived from low-amplitude system identification tests using multisine excitation. Frequencies for the isolated vessels were derived by analysis of data from the seismic tests.
2. See Figure 5-1 for the global coordinate system
3. Corresponds to the horizontal modes of the support frame
4. Could not be clearly identified as the behavior of the test specimen was driven by the rocking of the vessel
5. Corresponds to the sliding period of the SFP bearings of 1.38 seconds
6. Could not be identified from the test data
7. Lower than in the non-isolated configuration because of the added flexibility of the bearings
8. Corresponds to the sliding period of the TFP bearings of 1.95 seconds

5.2.3 Response-history analyses and damping specifications

Response-history analyses were performed using the Fast Nonlinear Analysis (FNA) method in SAP2000, with the only nonlinear elements being the isolator links. The acceleration histories recorded at the center of the earthquake simulator platform during the experiments were used as inputs to the numerical models. Rocking acceleration inputs for the models were derived as described in Section 4.5.1. (There were no rocking inputs to the earthquake simulator but rocking of the platform resulted from simulator-specimen interaction and compliance in the simulator's horizontal and vertical actuators.) Prior to the start of a response-history analysis, the models were subjected to a vertical acceleration of 1 g to develop gravity load on the isolators, applied gradually over a period of 10 seconds, and followed by an idle time of 5 seconds for the load to stabilize.

Damping in the SAP2000 model was specified using the *Constant Damping with Override* option. This option enables the analyst to select a baseline damping ratio (e.g., 1.5% of critical) for all modes bar some for which an alternate value is specified (i.e., the override). Herein, a constant damping ratio of 1.5% was specified as the baseline value based on analysis of data from tests of the non-isolated configuration. Exceptions to the baseline value were based on the system identification results in Section 4.5.3 and analysis of data from the seismic tests: 1) in the non-isolated configuration, an override of 2.5% (4.6%)[1] was applied to the rocking of the vessel about the x (y) axis; 2) in the isolated configurations, a) an override of 0% was specified for the isolated modes because the energy dissipation in those modes is hysteretic (see Sarlis and Constantinou (2010)), and b) an override of 4.6%[2] was applied to the rocking of the vessel about both x and y axes. A calibration exercise was not performed to determine damping ratios for each seismic input and intensity. Rather a single set of values were used to predict responses for all tests such that the rocking responses were recovered reasonably well by the SAP2000 models across a wide range of intensities.

Because the mass of the water was distributed on the vessel wall, breathing of the vessel wall was observed at approximately 40 Hz: see Figure 5-2. Breathing would occur at much higher frequencies if fluid (water

[1] Damping for rocking about the x and y axis is associated with the oil columns in the simulator's actuators and varies with the intensity of the seismic input. The chosen values enabled the rocking responses to be recovered by the SAP2000 model.

[2] The chosen values for the isolated configurations enabled the rocking responses to be recovered by the SAP2000 model.

herein) is explicitly modeled. For all analyses herein, the breathing modes were assigned a damping override of 95% to eliminate its effect on the response of the isolators and the vessel.

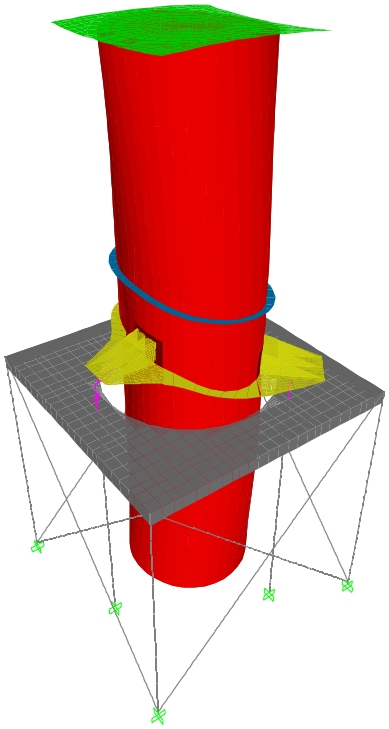

Figure 5-2. Breathing of the vessel wall

5.3 Comparison of analytical and experimental results

5.3.1 Introduction

The numerical models were benchmarked by comparing predicted results with experiment data. Results extracted from the numerical models include:

1. Acceleration time series in the *x*, *y*, and *z* directions (global coordinate system is defined in Figure 5-1):

    a) Atop the load cells on the north-east side (location *F1* in Figure 4-8), representing acceleration response at the mid-height of the vessel for the non-isolated configuration and directly below the isolation plane for the isolated configurations. (North is defined in Figure 5-1a.)

    b) On the north-east support mount of the vessel (location *V1*), representing acceleration response directly above the isolation plane.

c) At the top and the bottom of the vessel on the north face (locations *V2* and *V3*).

2. Isolation-system displacement and force histories. The normalized force-displacement loops were derived by normalizing the total horizontal force in the three isolator links by the total instantaneous normal load at the same time step. Identical displacement histories were obtained for the three isolator links, and the *x*- and *y*-direction histories for the north-east link were utilized for generating the force-displacement loops.

Rocking accelerations about the *x*- and *y*-axis at the top and the bottom of the vessel were derived by calculating the difference in the vertical (*z*) acceleration responses and dividing by the horizontal distance between the output stations in SAP2000. Sections 5.3.2, 5.3.3, and 5.3.4 below present predicted (SAP2000) and measured (test) responses. Section 5.3.5 presents a discussion of the predicted and measured results.

5.3.2 Non-isolated configuration

Figures 5-3 through 5-14 enable a comparison of predicted and measured (after processing) acceleration spectra at the top and the bottom of the vessel for the six 3D motions of Table 4-3. Table 5-4 presents the peak accelerations, derived as spectral acceleration at 100 Hz[1], at the top, bottom, and mid-height of the vessel, and the absolute percentage difference between the numerical and experimental values. Peak acceleration is used here as a measure of seismic input to safety-related equipment at the head and the base of the vessel.

The acceleration responses predicted by the numerical model in the two horizontal directions and for rocking about the *x*- and *y*-axis are in good agreement with the test data, with an average difference of 13% (range: 0% to 35%) in the peak horizontal accelerations. Greater differences are seen in the peak vertical accelerations, equal to 24% on average (range: 0% to 48%), due in large part to the significant differences between the measured and predicted frequencies in the *z* direction (see Section 5.2.2).

[1] Acceleration time series from SAP2000 were processed with a low-pass filter at 100 Hz and so peak accelerations were taken as spectral acceleration at 100 Hz.

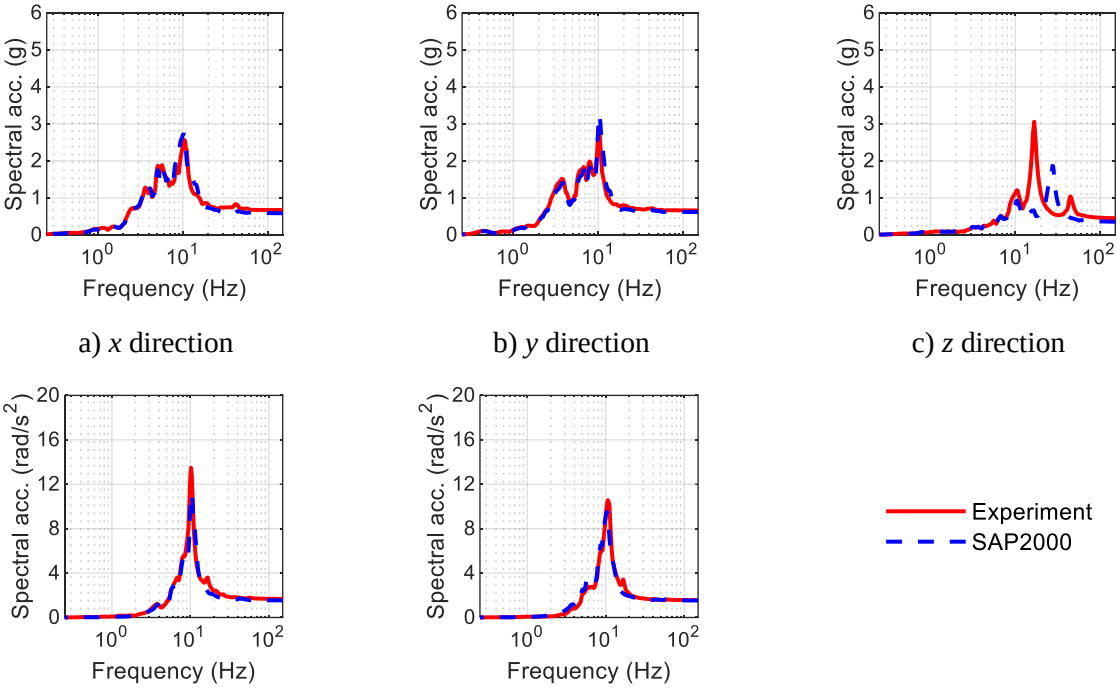

a) *x* direction b) *y* direction c) *z* direction

d) rocking about *x* axis e) rocking about *y* axis

Figure 5-3. Acceleration response spectra at the top of the vessel, test FB1A-3D

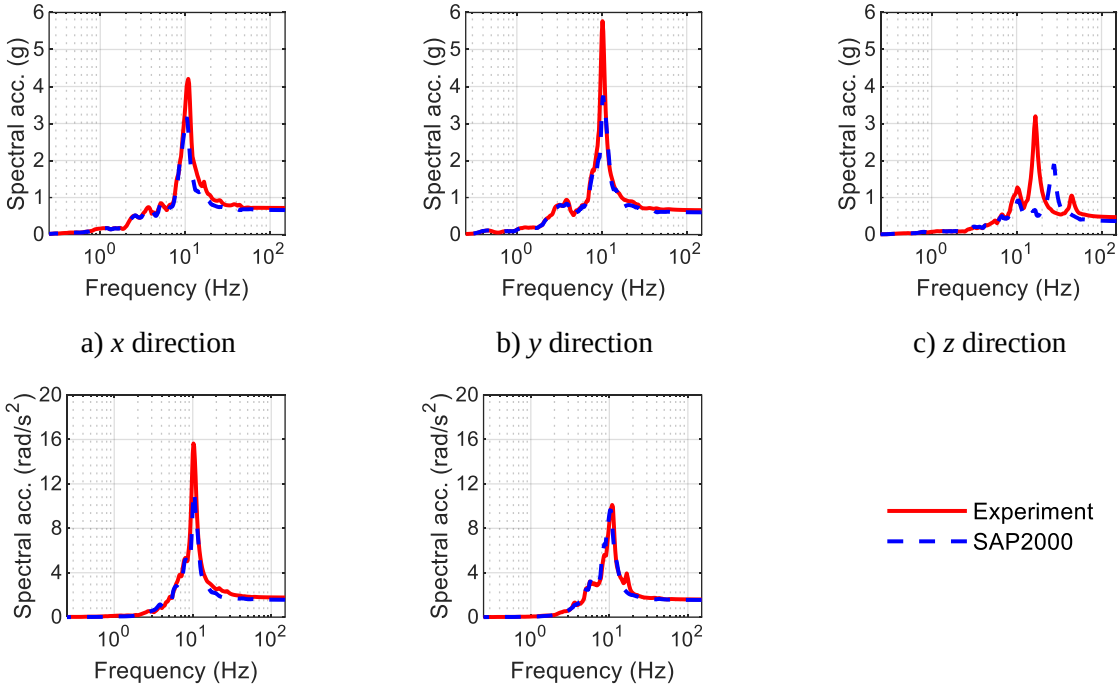

a) *x* direction b) *y* direction c) *z* direction

d) rocking about *x* axis e) rocking about *y* axis

Figure 5-4. Acceleration response spectra at the bottom of the vessel, test FB1A-3D

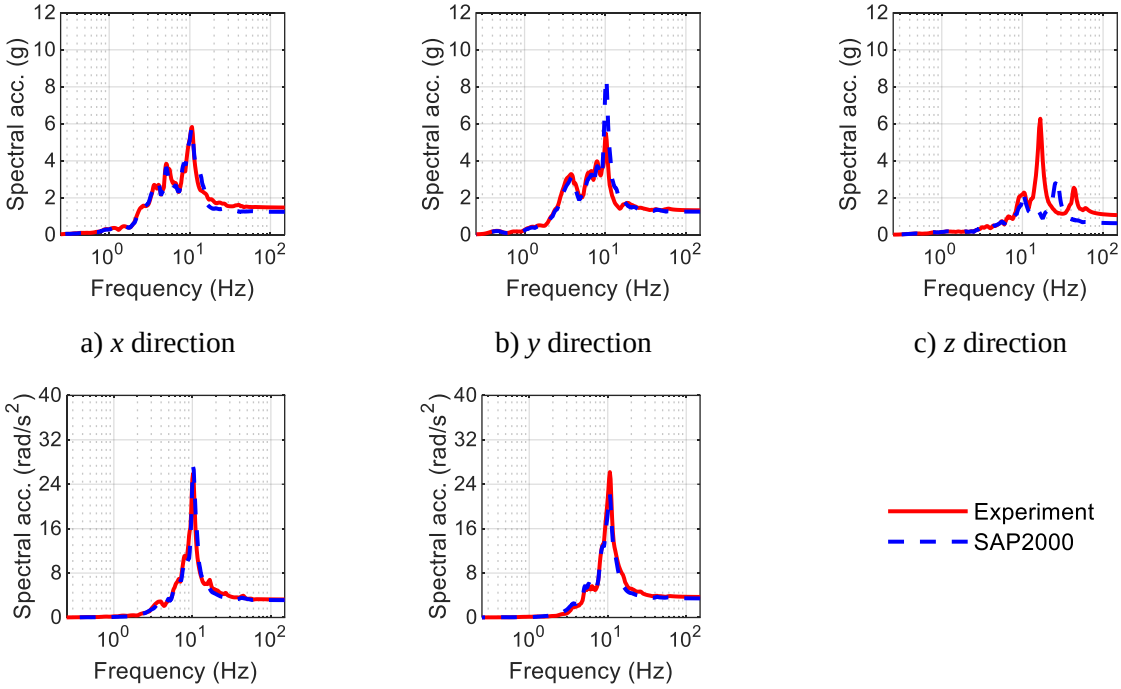

Figure 5-5. Acceleration response spectra at the top of the vessel, test FB1B-3D

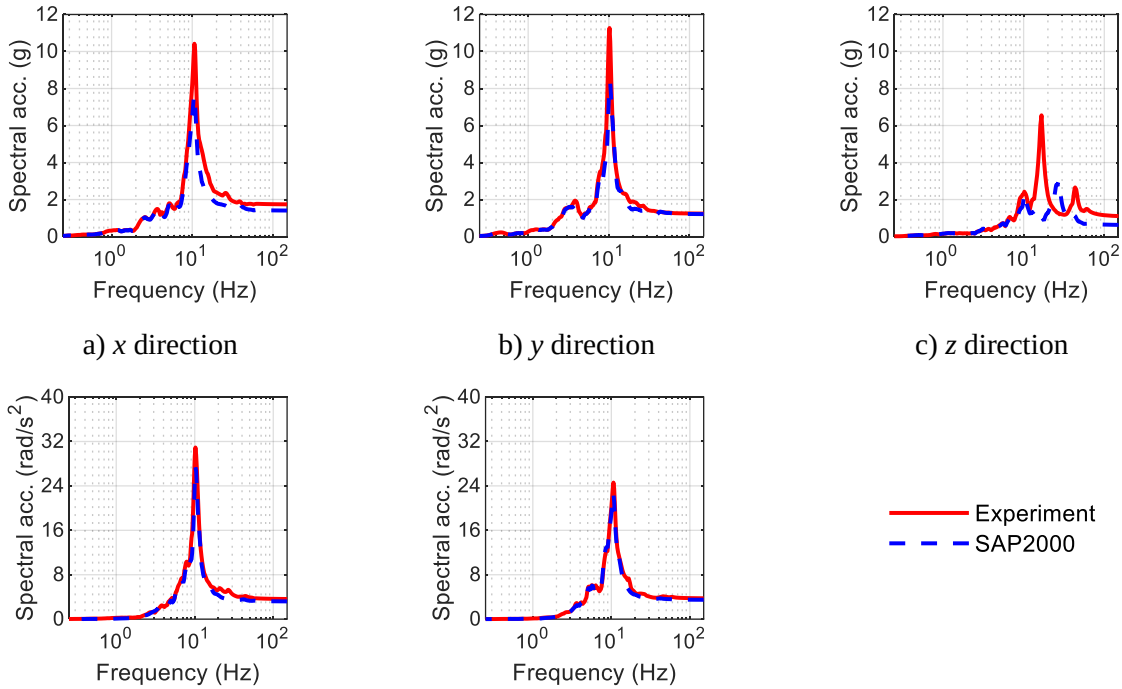

Figure 5-6. Acceleration response spectra at the bottom of the vessel, test FB1B-3D

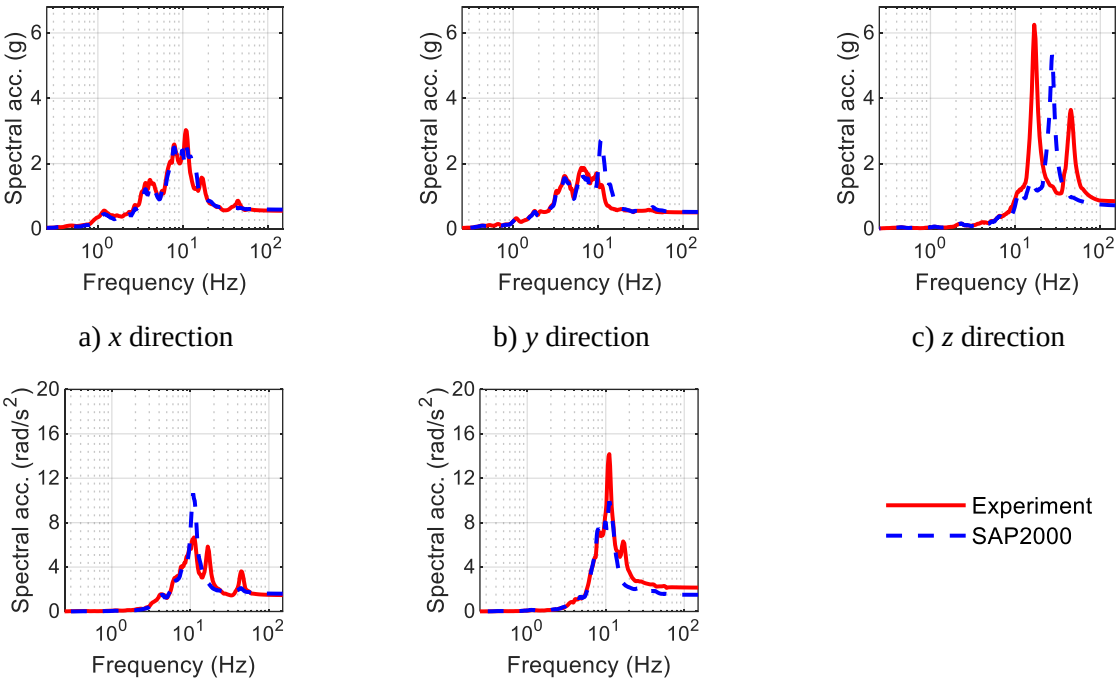

a) *x* direction b) *y* direction c) *z* direction

d) rocking about *x* axis e) rocking about *y* axis

Figure 5-7. Acceleration response spectra at the top of the vessel, test FB2A-3D

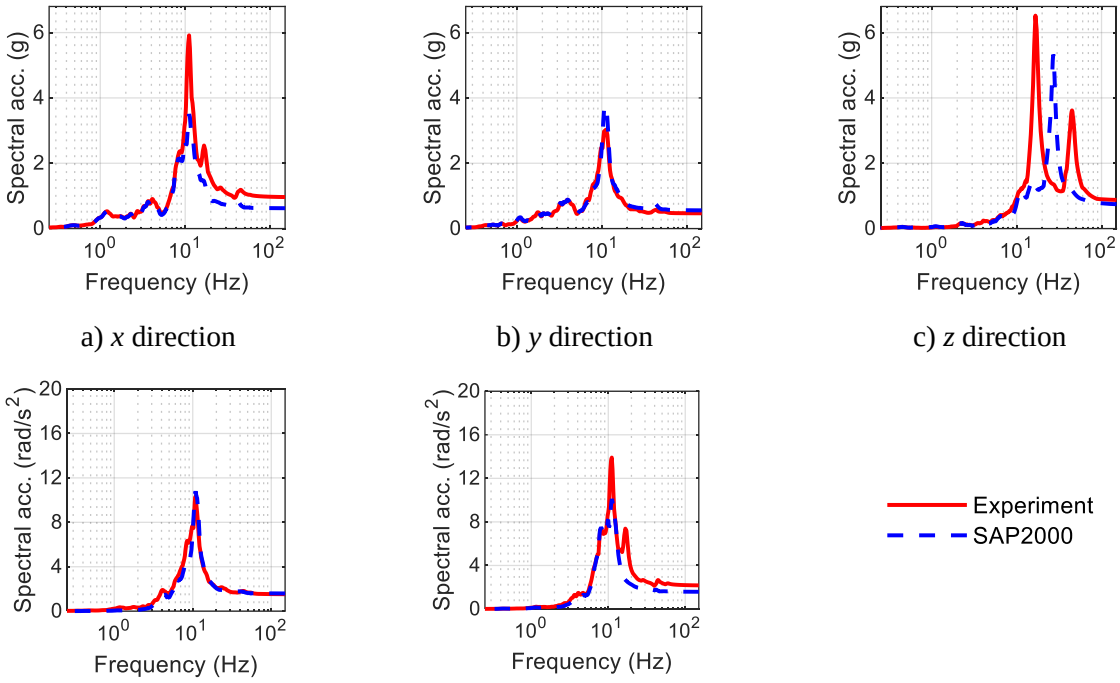

a) *x* direction b) *y* direction c) *z* direction

d) rocking about *x* axis e) rocking about *y* axis

Figure 5-8. Acceleration response spectra at the bottom of the vessel, test FB2A-3D

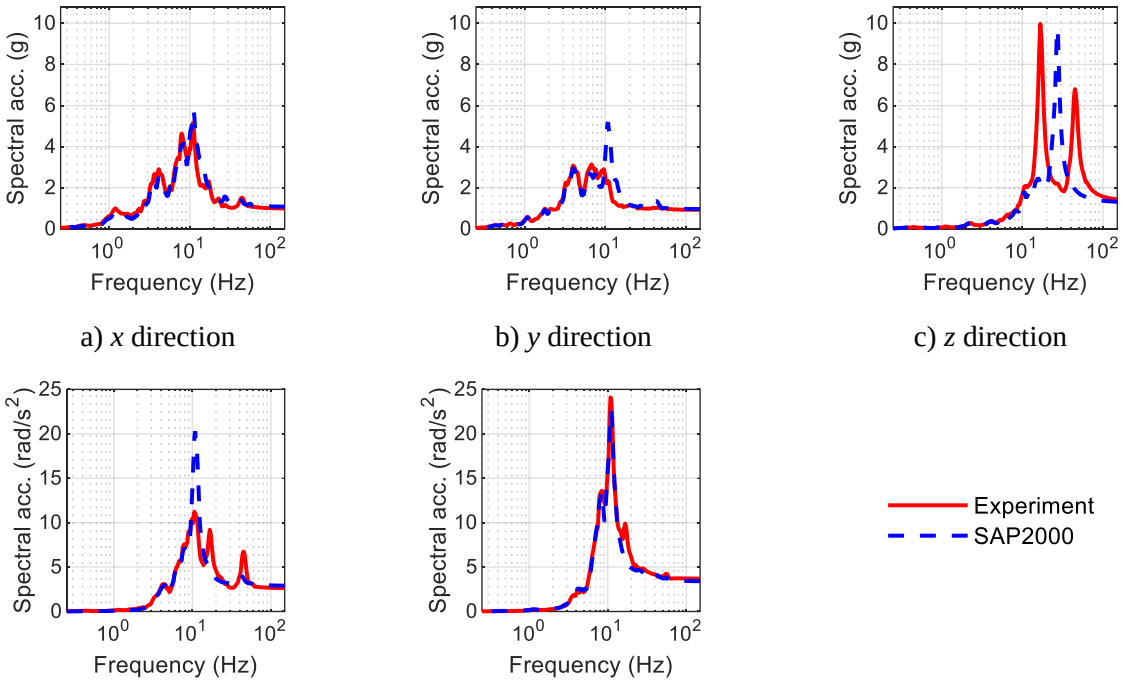

a) *x* direction b) *y* direction c) *z* direction

d) rocking about x axis e) rocking about y axis

Figure 5-9. Acceleration response spectra at the top of the vessel, test FB2B-3D

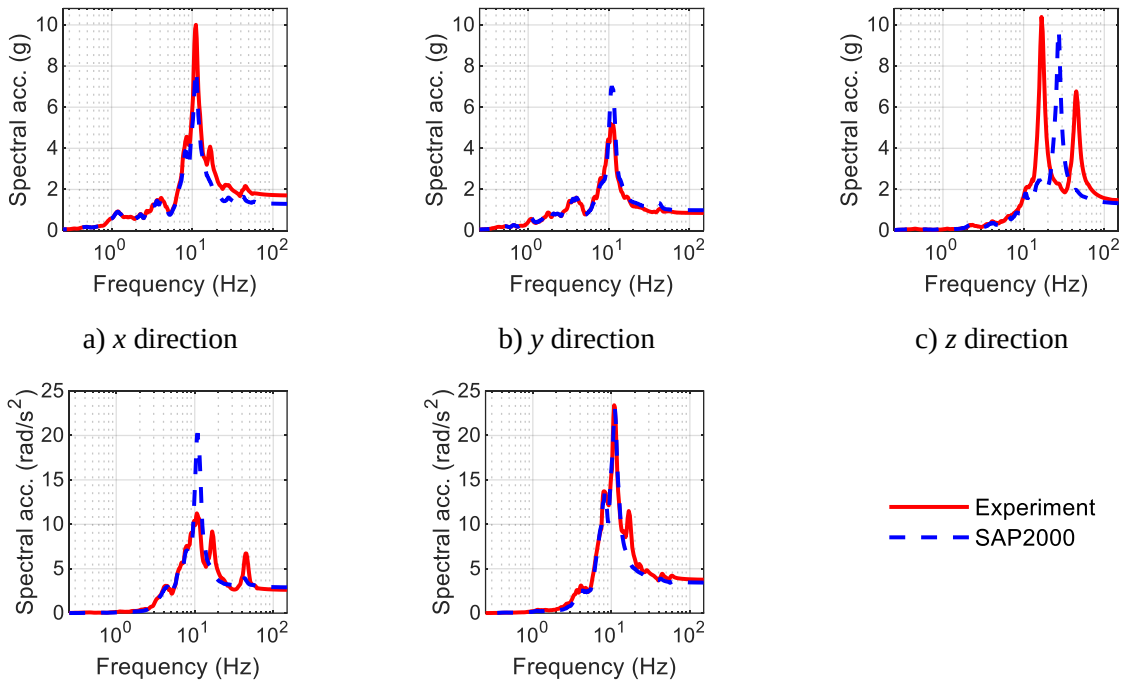

a) *x* direction b) *y* direction c) *z* direction

d) rocking about *x* axis e) rocking about *y* axis

Figure 5-10. Acceleration response spectra at the bottom of the vessel, test FB2B-3D

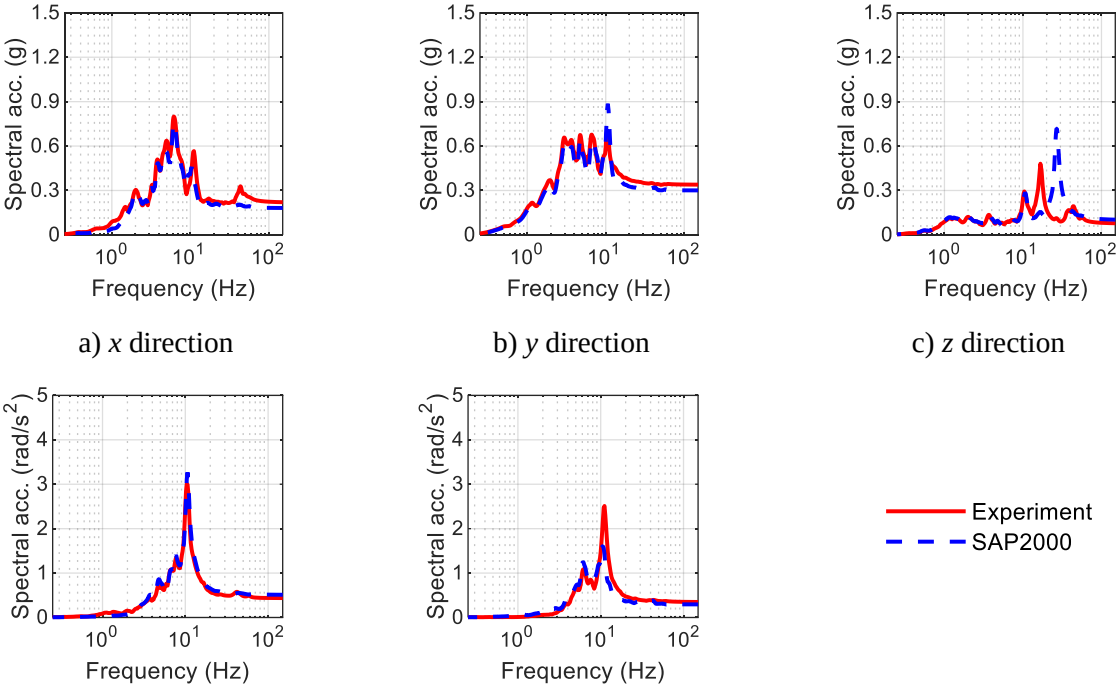

a) *x* direction b) *y* direction c) *z* direction

d) rocking about *x* axis e) rocking about *y* axis

Figure 5-11. Acceleration response spectra at the top of the vessel, test FB3A-3D

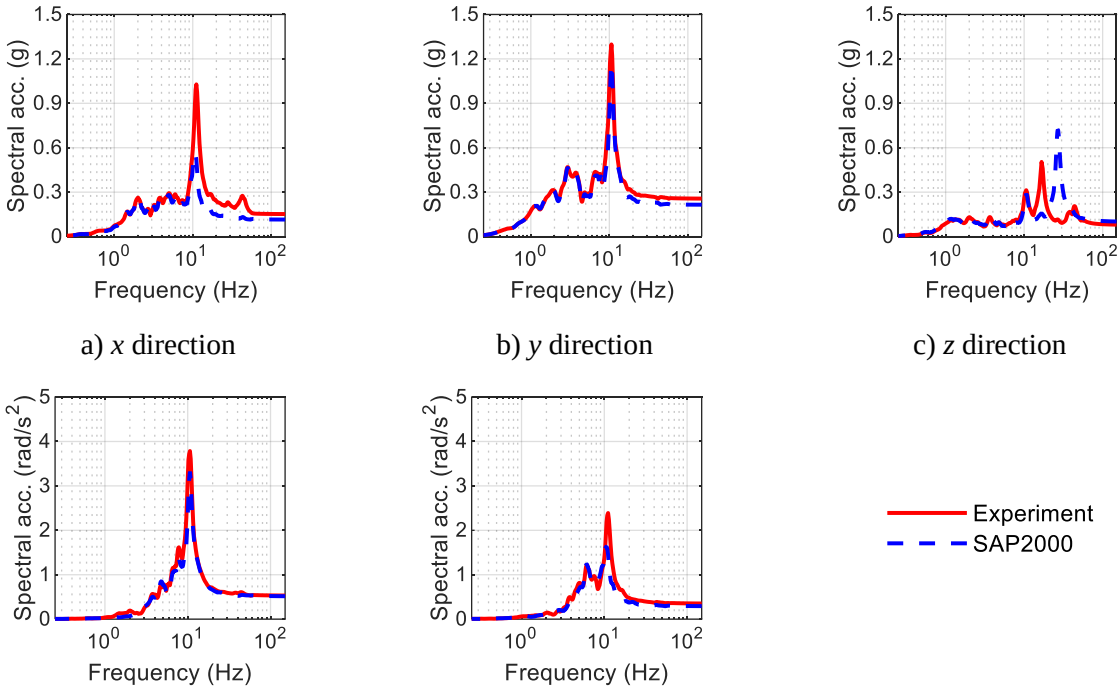

a) *x* direction b) *y* direction c) *z* direction

d) rocking about *x* axis e) rocking about *y* axis

Figure 5-12. Acceleration response spectra at the bottom of the vessel, test FB3A-3D

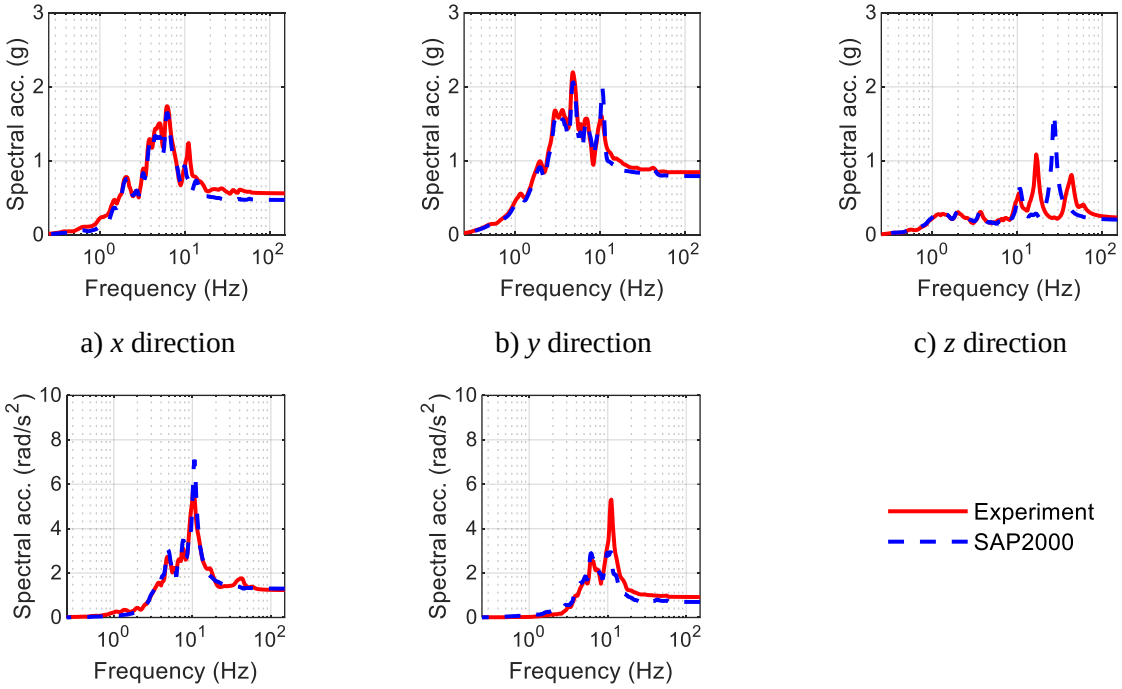

a) *x* direction b) *y* direction c) *z* direction

d) rocking about *x* axis e) rocking about *y* axis

Figure 5-13. Acceleration response spectra at the top of the vessel, test FB3B-3D

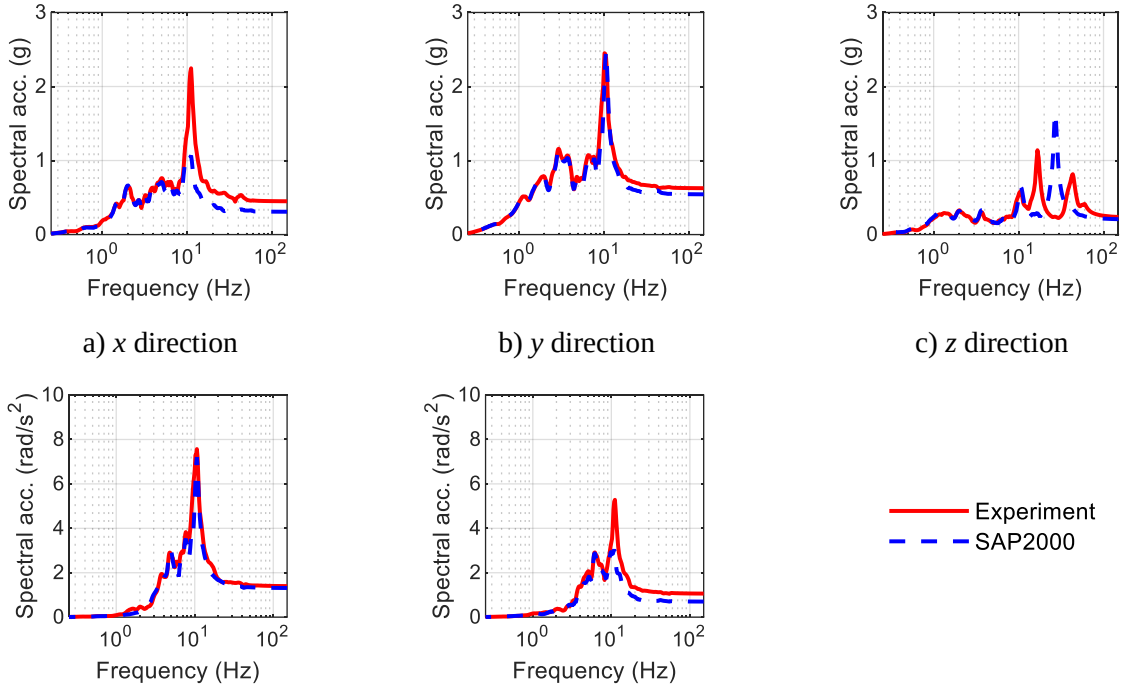

a) *x* direction b) *y* direction c) *z* direction

d) rocking about *x* axis e) rocking about *y* axis

Figure 5-14. Acceleration response spectra at the bottom of the vessel, test FB3B-3D

Table 5-4. Peak accelerations[1] (g) for the 3D tests in the non-isolated configuration, *x*, *y*, and *z* directions

Test		Mid-height of vessel			Vessel bottom			Vessel top		
		x	***y***	***z***	***x***	***y***	***z***	***x***	***y***	***z***
FB1A-3D	Experiment	0.34	0.33	0.32	0.72	0.65	0.46	0.67	0.66	0.44
	SAP2000	0.34	0.30	0.20	0.66	0.60	0.36	0.58	0.62	0.35
	Diff (%)	0	9	38	8	8	22	13	6	20
FB1B-3D	Experiment	0.68	0.69	0.73	1.73	1.24	1.07	1.47	1.32	1.04
	SAP2000	0.64	0.63	0.38	1.40	1.21	0.62	1.24	1.25	0.62
	Diff (%)	6	9	48	19	2	42	16	5	40
FB2A-3D	Experiment	0.39	0.35	0.57	0.96	0.47	0.86	0.55	0.50	0.83
	SAP2000	0.35	0.40	0.35	0.62	0.56	0.72	0.59	0.52	0.70
	Diff (%)	10	14	39	35	19	16	7	4	16
FB2B-3D	Experiment	0.72	0.63	0.98	1.69	0.85	1.44	0.98	0.93	1.39
	SAP2000	0.61	0.79	0.62	1.29	0.99	1.29	1.08	0.96	1.28
	Diff (%)	15	25	37	24	16	10	10	3	8
FB3A-3D	Experiment	0.16	0.20	0.06	0.16	0.26	0.08	0.22	0.34	0.08
	SAP2000	0.13	0.20	0.06	0.11	0.21	0.10	0.18	0.30	0.10
	Diff (%)	19	0	0	31	19	25	18	12	25
FB3B-3D	Experiment	0.38	0.51	0.18	0.45	0.63	0.23	0.56	0.85	0.22
	SAP2000	0.34	0.54	0.14	0.31	0.54	0.20	0.47	0.79	0.20
	Diff (%)	11	6	22	31	14	13	16	7	9

1. Peak acceleration calculated as spectral acceleration at 100 Hz

5.3.3 SFP-isolated configuration

Figures 5-15 through 5-50 enable a comparison of numerical and experimental results for the six 3D motions (see Table 4-4) in the SFP-isolated configuration. Because the acceleration response of the isolated vessel in the two horizontal directions was substantially smaller than in the vertical direction, the *y*-axis range for the *x*- and *y*-direction spectra is different than in the *z* direction. Table 5-5 presents the peak accelerations at the locations identified in Section 5.3.1 and the absolute percentage difference between the numerical response and the test data. The maximum isolator displacements and normalized forces are presented in Table 5-6.

The predicted horizontal and rocking acceleration responses are in good agreement with the experiment data. Differences in the vertical accelerations are attributed to the higher vertical mode frequency of the SAP2000 model: see Section 5.2.2. The percentage difference in the peak horizontal accelerations directly above and below the isolation plane, and at the top and the bottom of the vessel is nearly identical to that in the non-isolated configuration: 15% on average (range: 0% to 65%). The difference in the peak vertical accelerations is 32% on average (range: 0% to 106%).

The global response of the SFP isolation system is examined using normalized force-displacement loops, maximum horizontal displacements, and peak normalized forces, defined as the ratio of the horizontal force in the isolation system to the instantaneous axial force on it. The agreement between the predicted and recorded normalized force-displacement loops, maximum horizontal displacements, and peak normalized forces is excellent for the larger amplitude motions (SF1B-3D, SF2B-3D, SF3B-3D), producing larger isolation-system displacements. The agreement was poorer for the low amplitude motions, resulting in small isolation-system displacements.

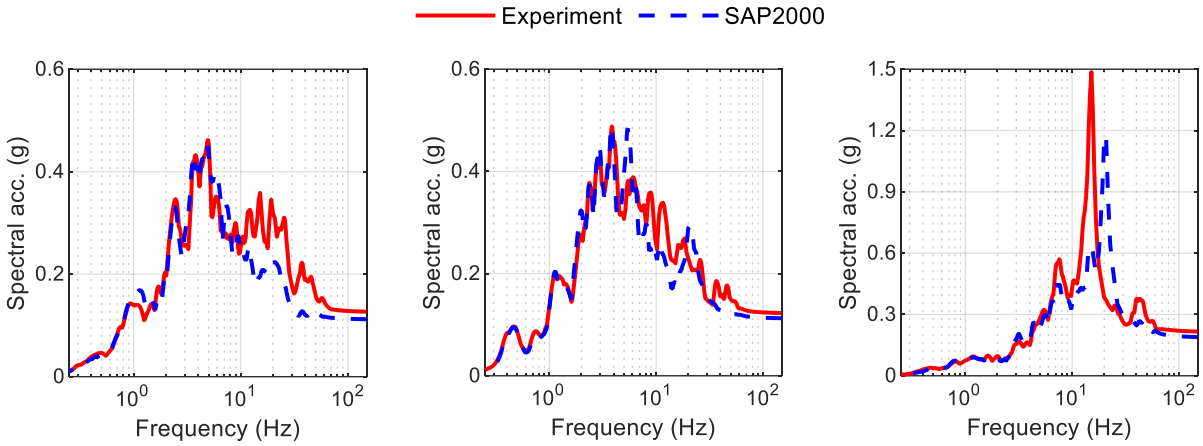

a) *x* direction b) *y* direction c) *z* direction

Figure 5-15. Acceleration response spectra directly above the isolation plane, test SF1A-3D

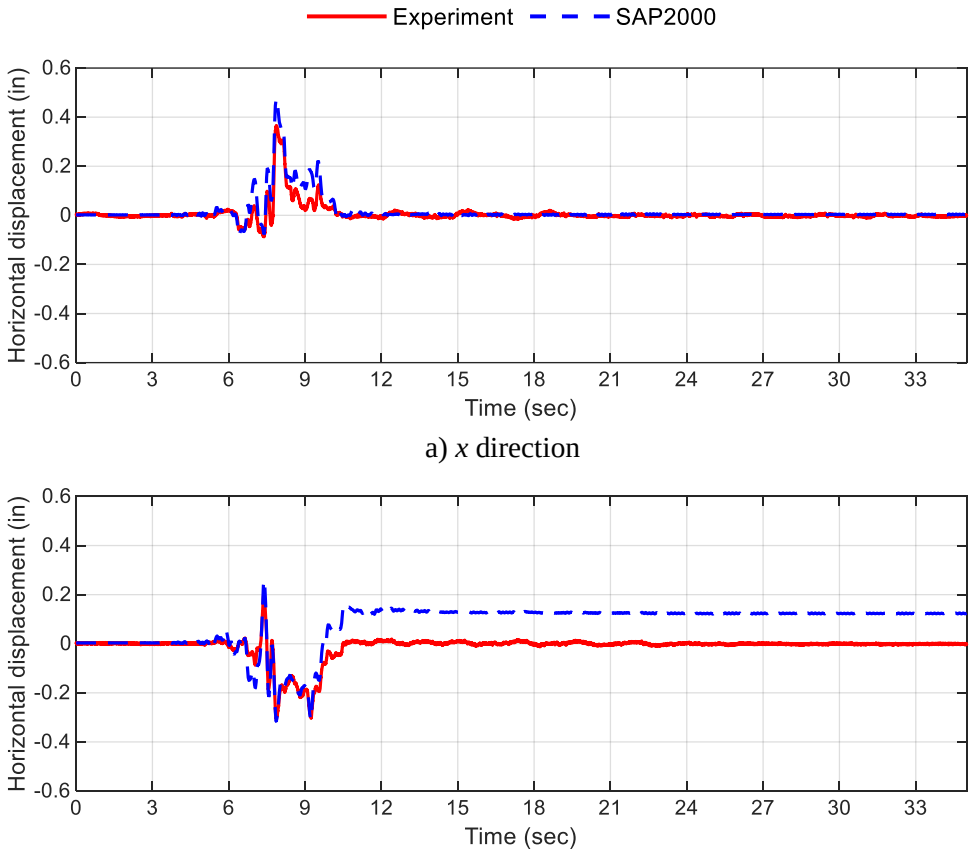

a) *x* direction

b) *y* direction

Figure 5-16. Isolation system displacements, test SF1A-3D

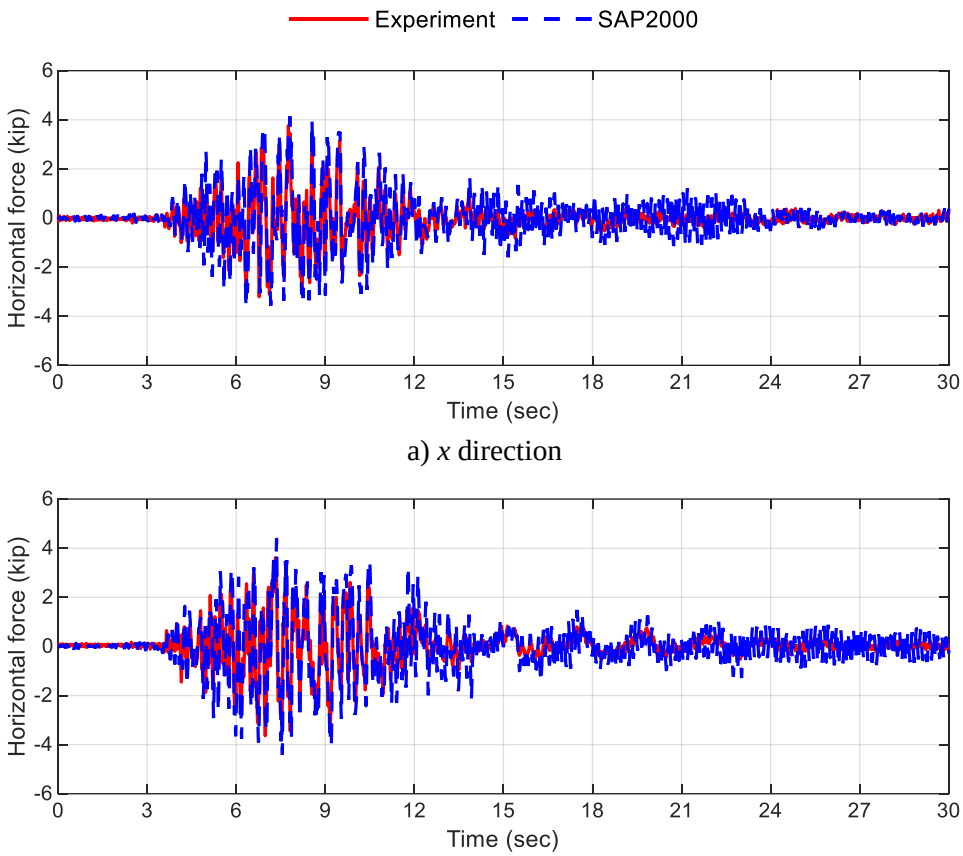

a) *x* direction

b) *y* direction

Figure 5-17. Isolation system forces, test SF1A-3D

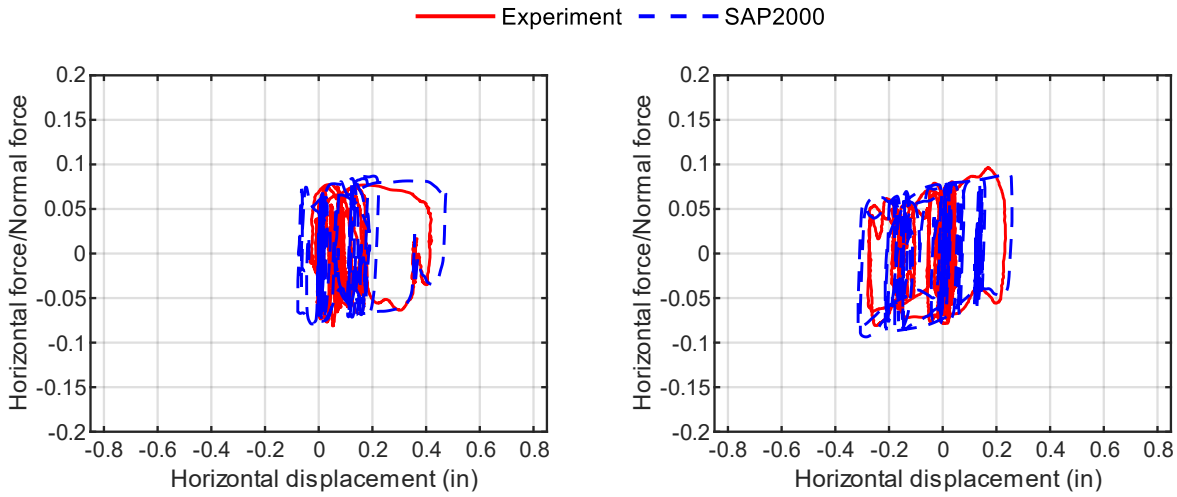

a) *x* direction

b) *y* direction

Figure 5-18. Normalized force-displacement loops for the isolation system, test SF1A-3D

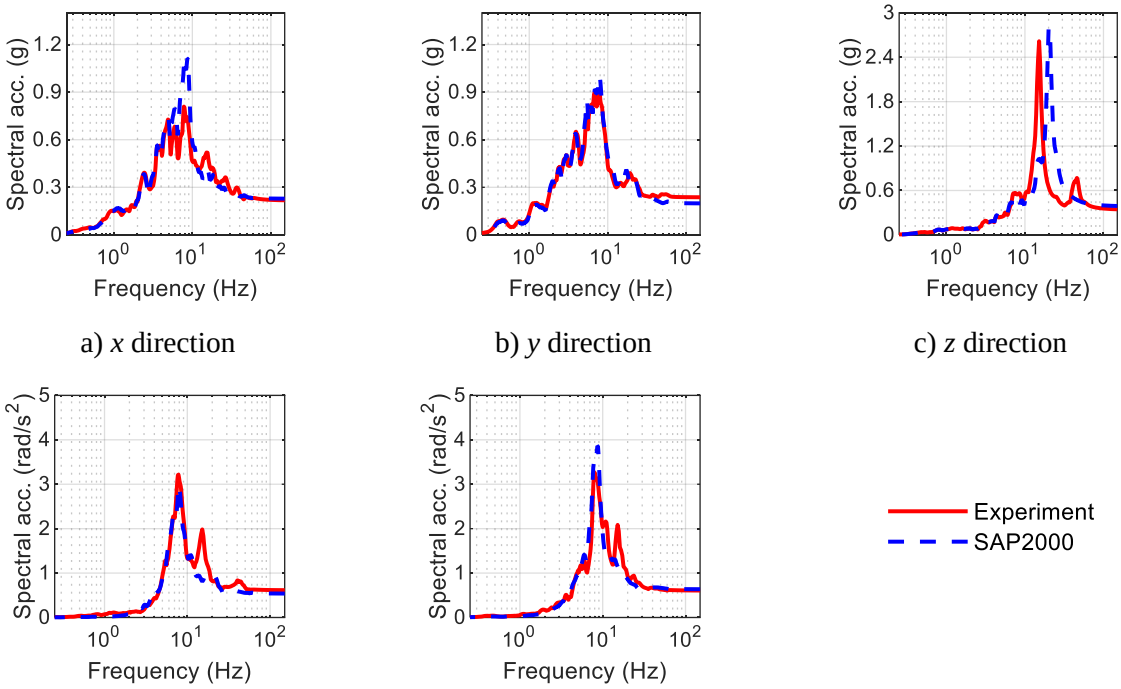

a) *x* direction b) *y* direction c) *z* direction

d) rocking about *x* axis e) rocking about *y* axis

Figure 5-19. Acceleration response spectra at the top of the vessel, test SF1A-3D

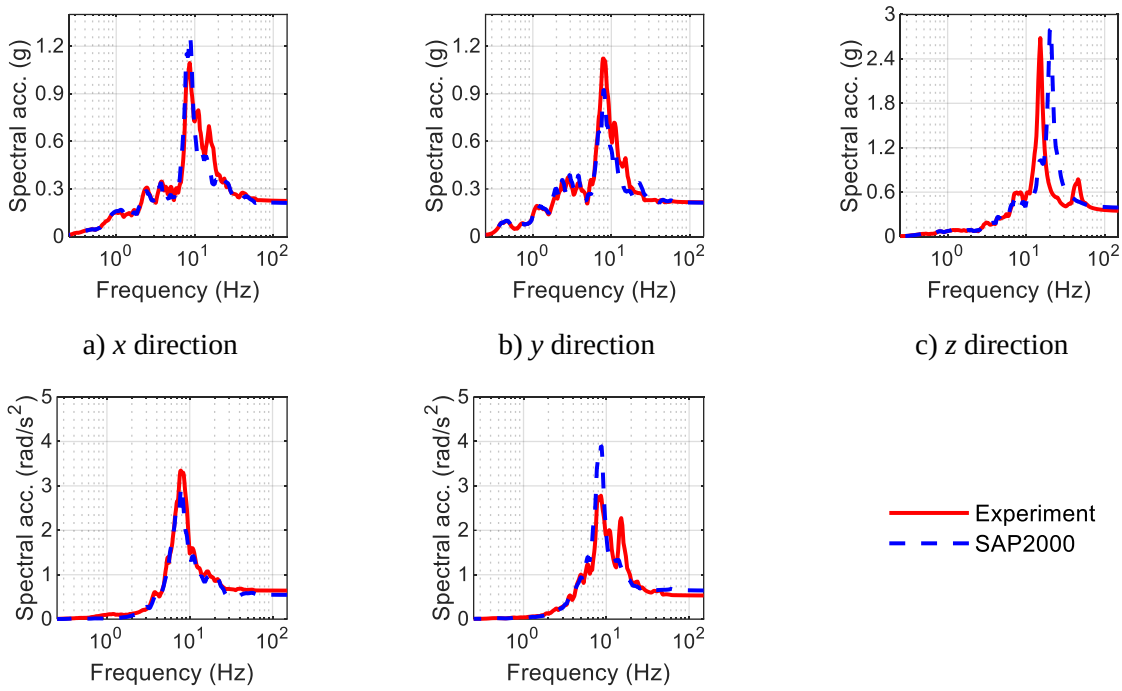

a) *x* direction b) *y* direction c) *z* direction

d) rocking about *x* axis e) rocking about *y* axis

Figure 5-20. Acceleration response spectra at the bottom of the vessel, test SF1A-3D

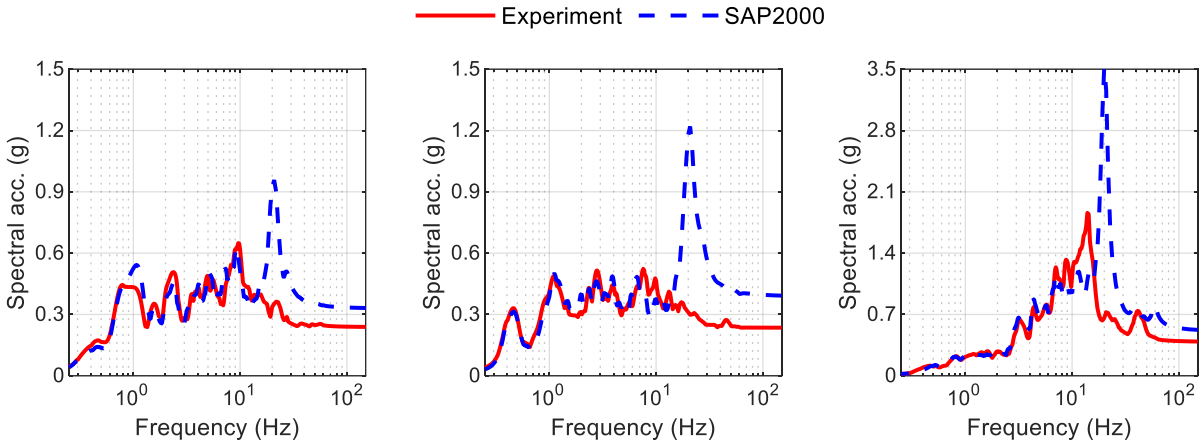

a) *x* direction b) *y* direction c) *z* direction

Figure 5-21. Acceleration response spectra directly above the isolation plane, test SF1B-3D

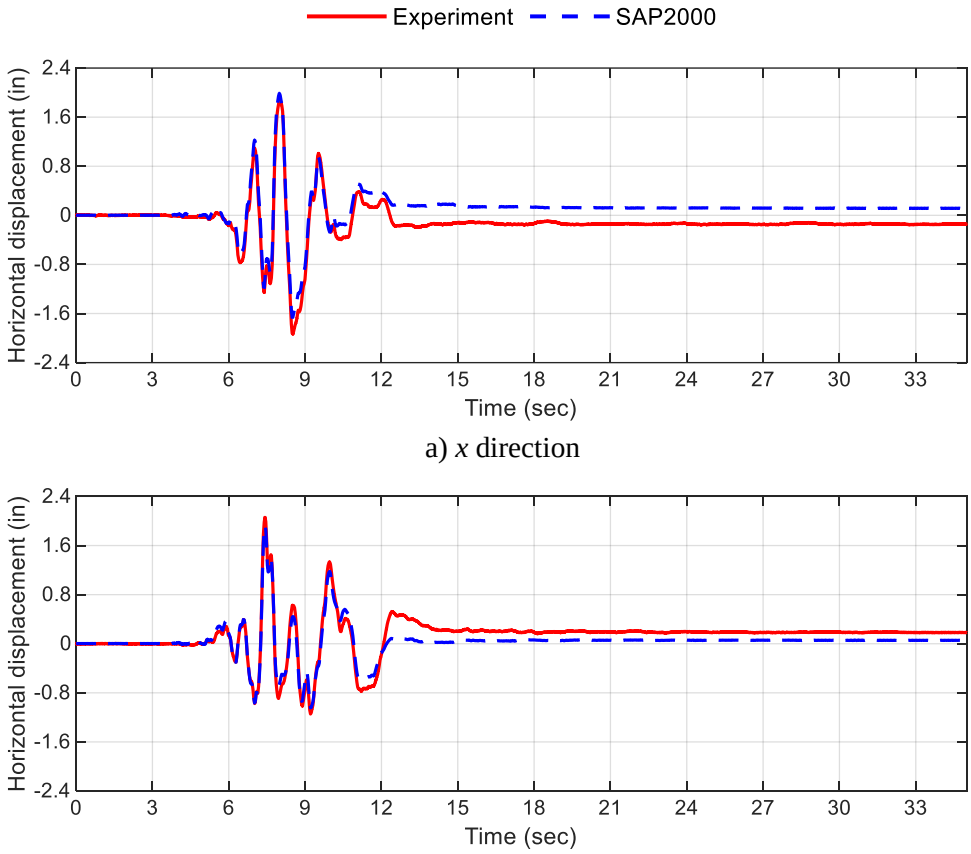

a) *x* direction

b) *y* direction

Figure 5-22. Isolation system displacements, test SF1B-3D

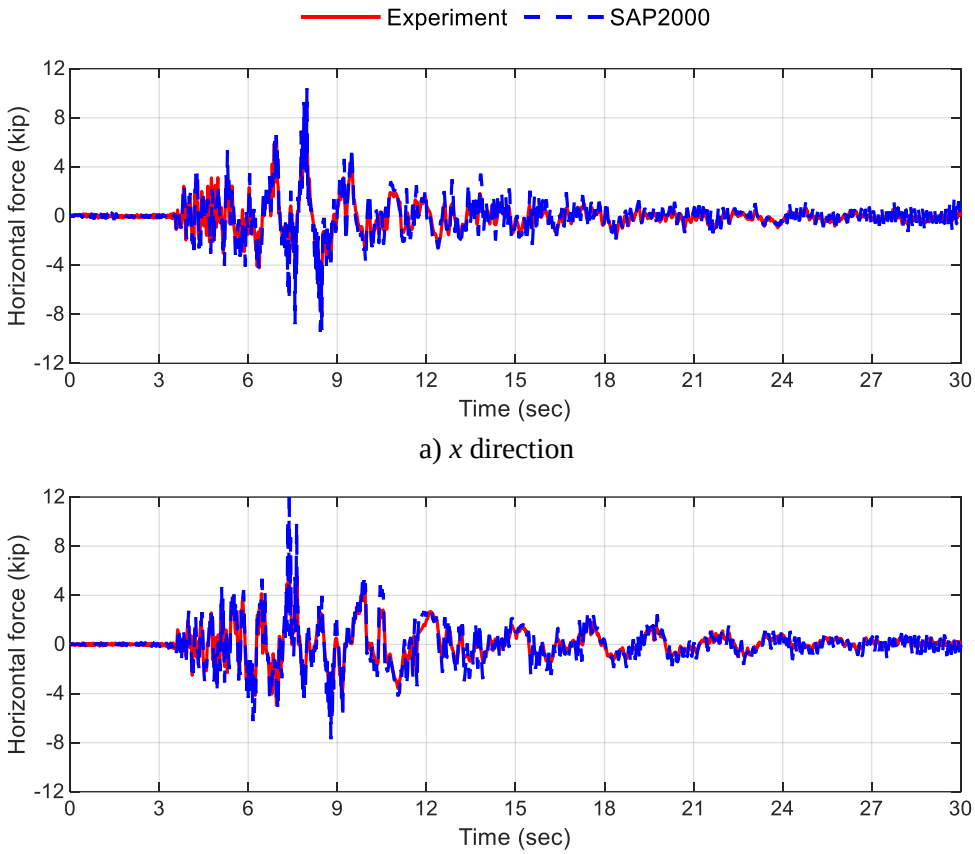

a) *x* direction

b) *y* direction

Figure 5-23. Isolation system forces, test SF1B-3D

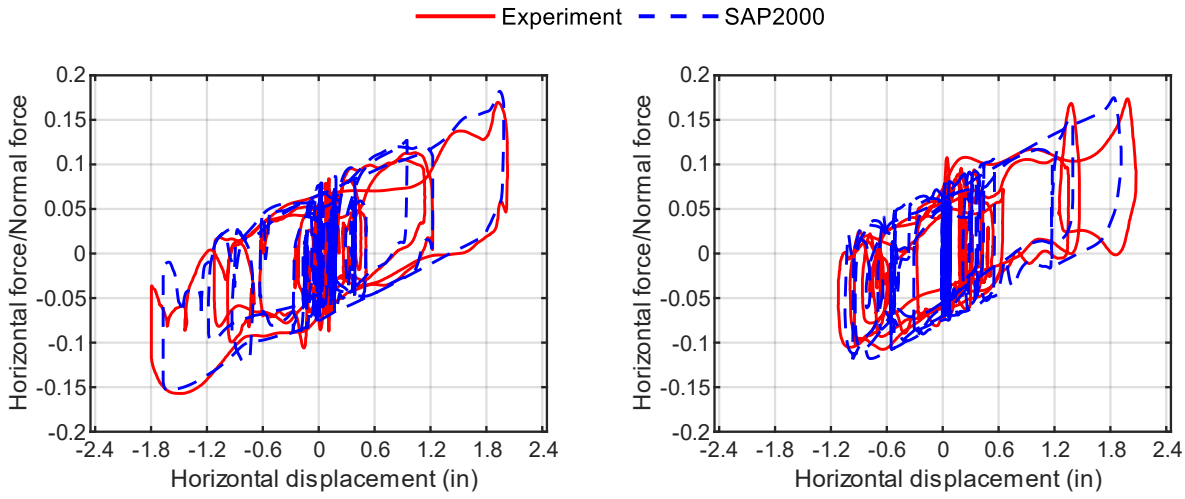

a) *x* direction

b) *y* direction

Figure 5-24. Normalized force-displacement loops for the isolation system, test SF1B-3D

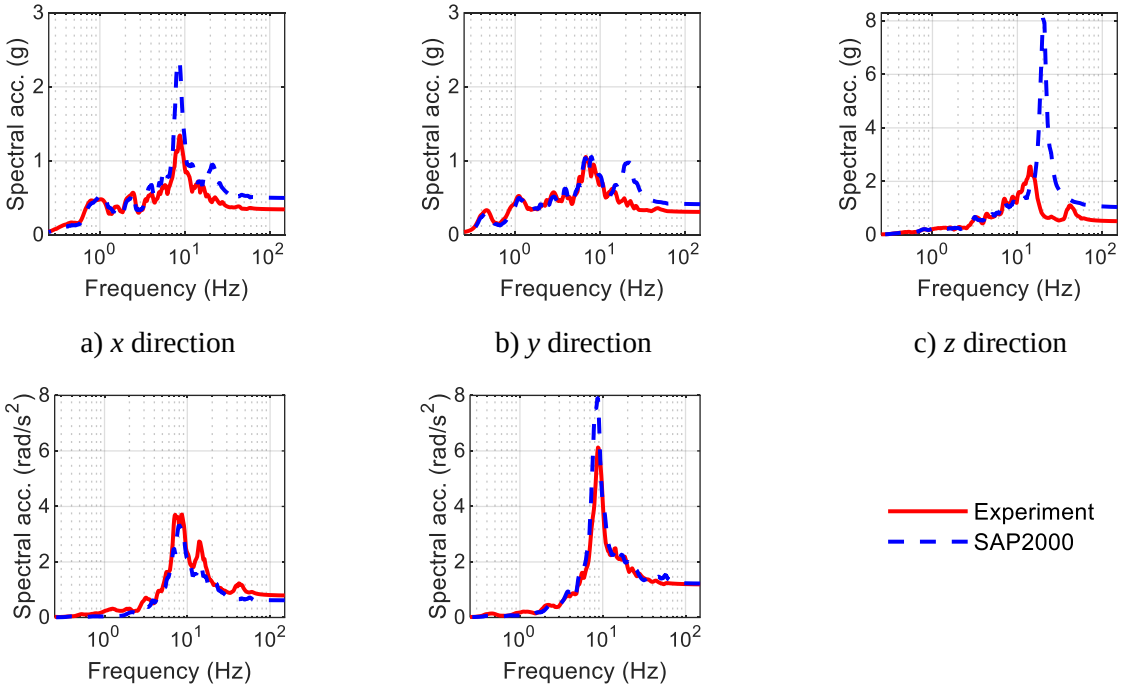

a) *x* direction b) *y* direction c) *z* direction

d) rocking about *x* axis e) rocking about *y* axis

Figure 5-25. Acceleration response spectra at the top of the vessel, test SF1B-3D

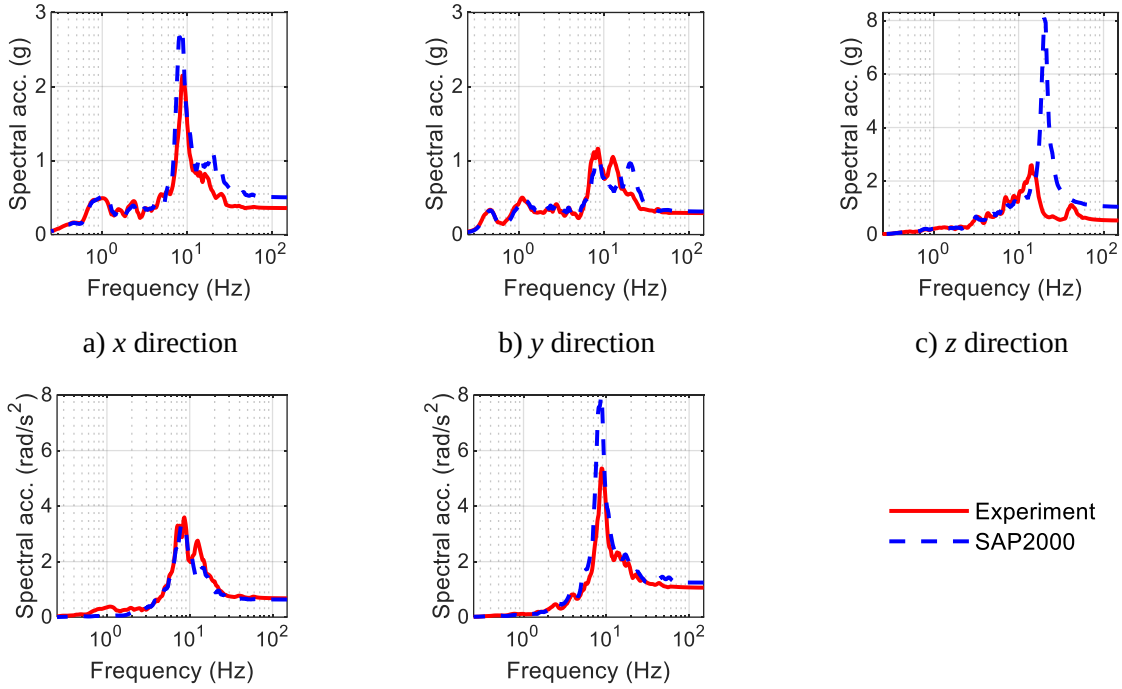

a) *x* direction b) *y* direction c) *z* direction

d) rocking about *x* axis e) rocking about *y* axis

Figure 5-26. Acceleration response spectra at the bottom of the vessel, test SF1B-3D

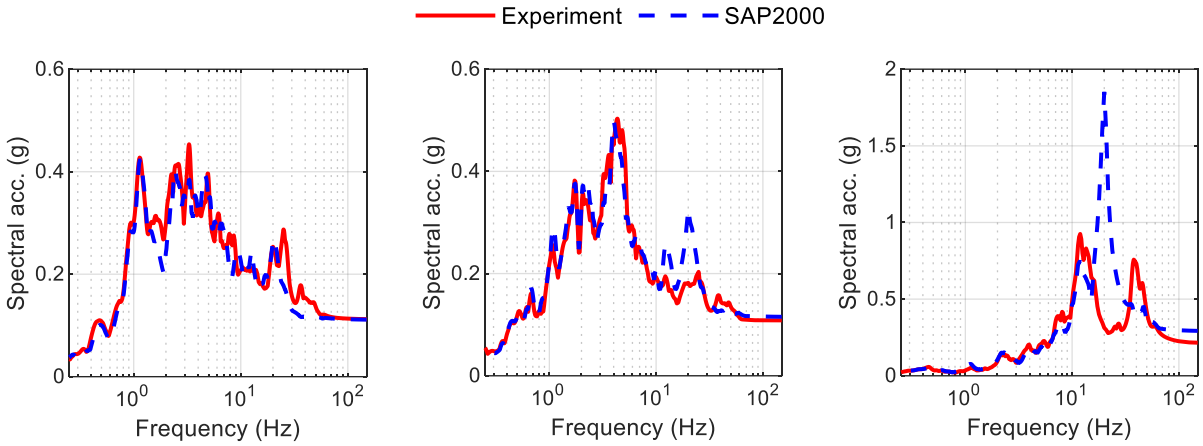

a) *x* direction b) *y* direction c) *z* direction

Figure 5-27. Acceleration response spectra directly above the isolation plane, test SF2A-3D

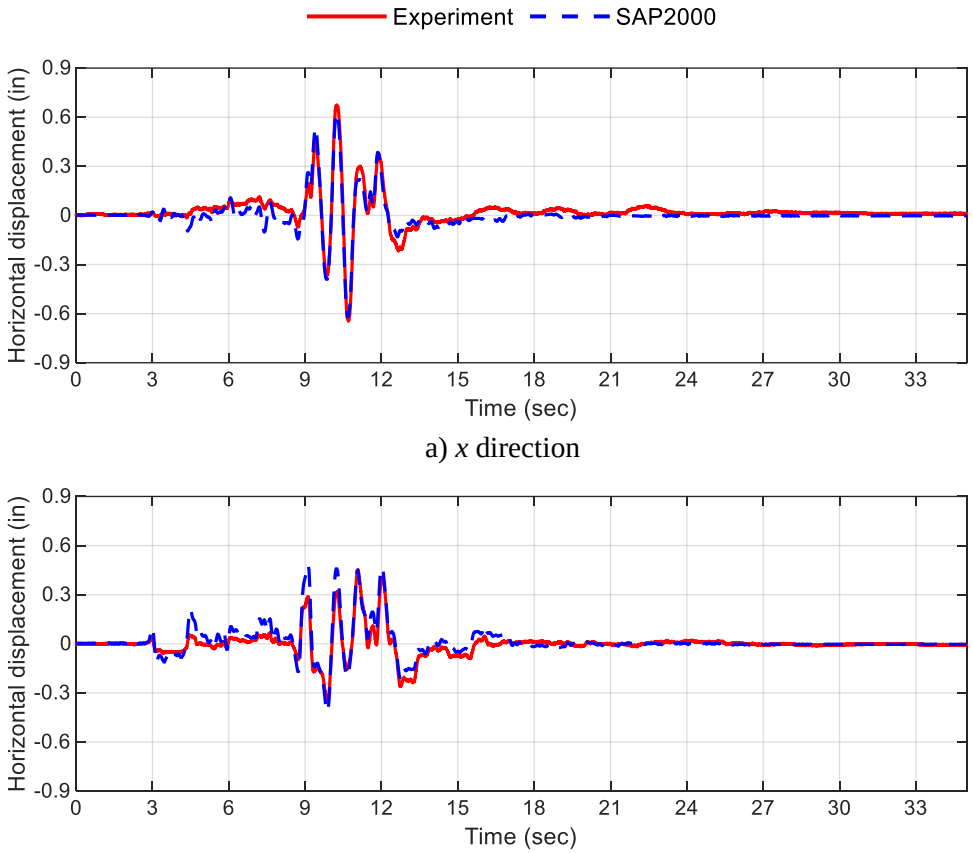

a) *x* direction

b) *y* direction

Figure 5-28. Isolation system displacements, test SF2A-3D

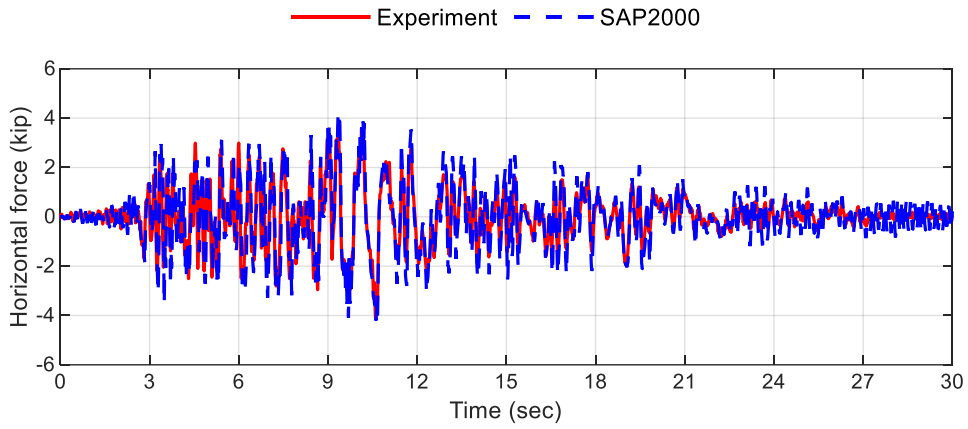

a) *x* direction

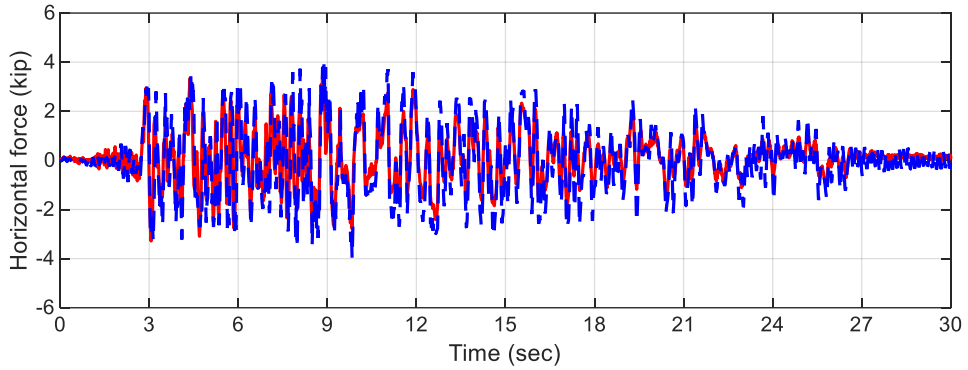

b) *y* direction

Figure 5-29. Isolation system forces, test SF2A-3D

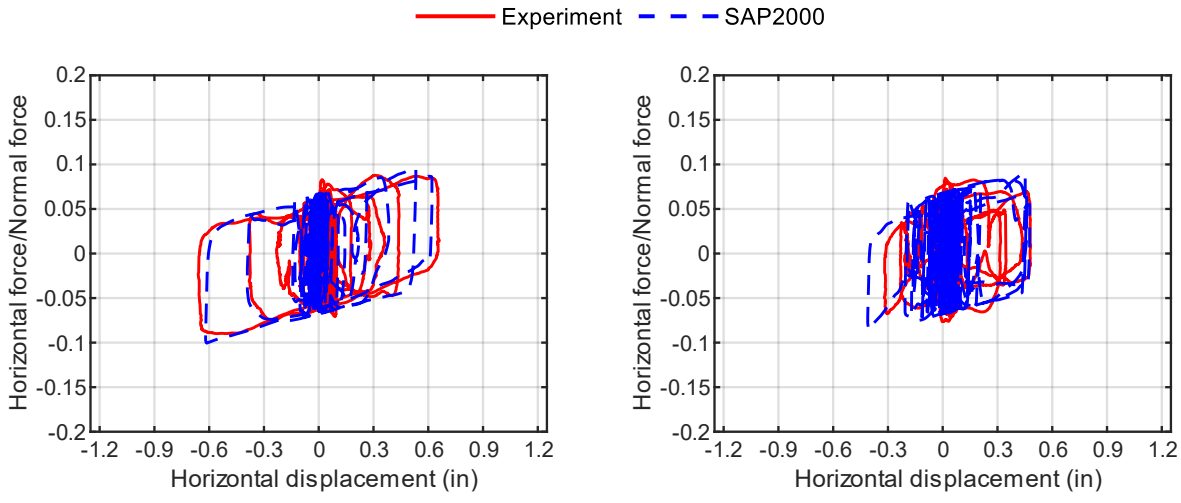

a) *x* direction

b) *y* direction

Figure 5-30. Normalized force-displacement loops for the isolation system, test SF2A-3D

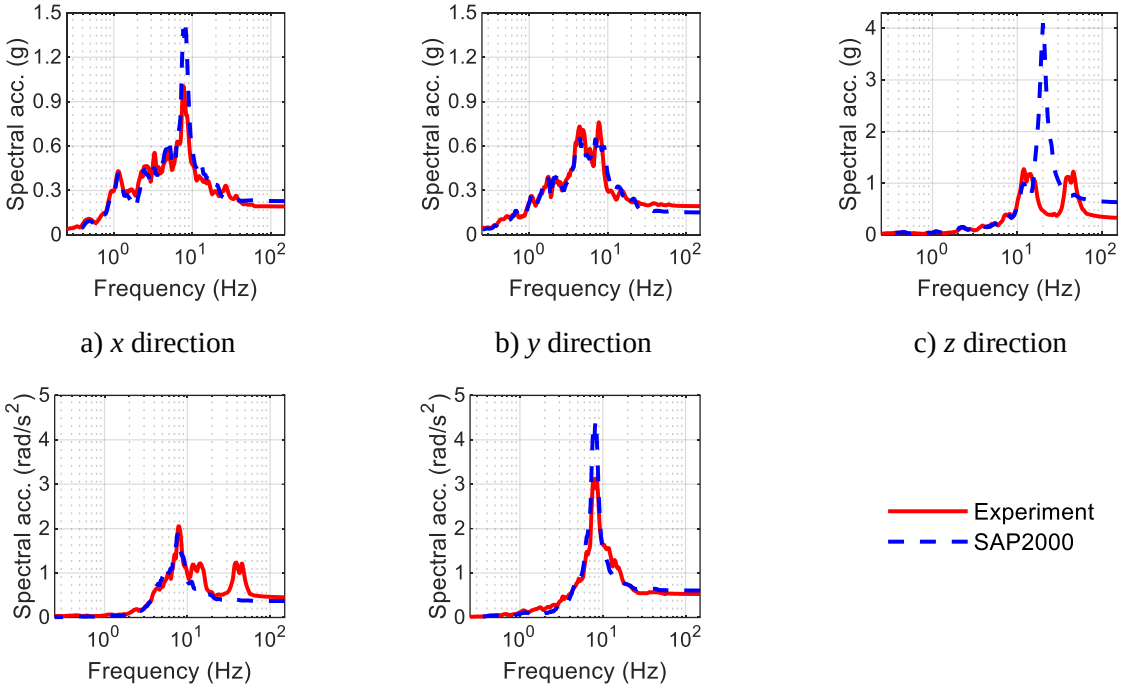

a) *x* direction b) *y* direction c) *z* direction

d) rocking about *x* axis e) rocking about *y* axis

Figure 5-31. Acceleration response spectra at the top of the vessel, test SF2A-3D

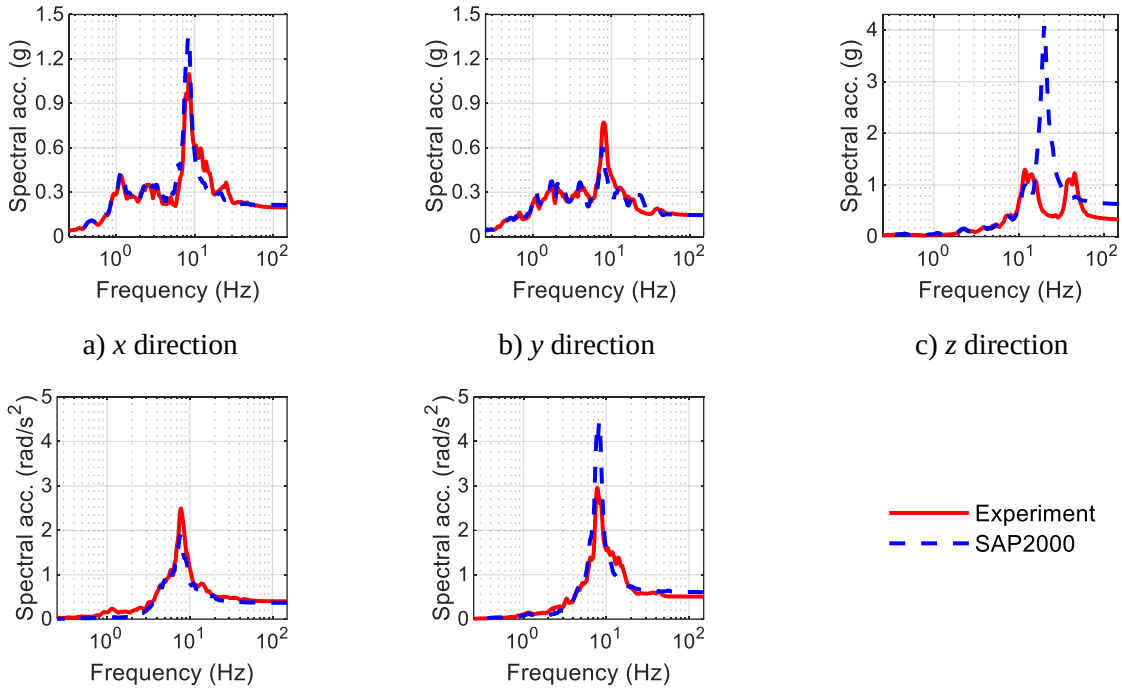

a) *x* direction b) *y* direction c) *z* direction

d) rocking about *x* axis e) rocking about *y* axis

Figure 5-32. Acceleration response spectra at the bottom of the vessel, test SF2A-3D

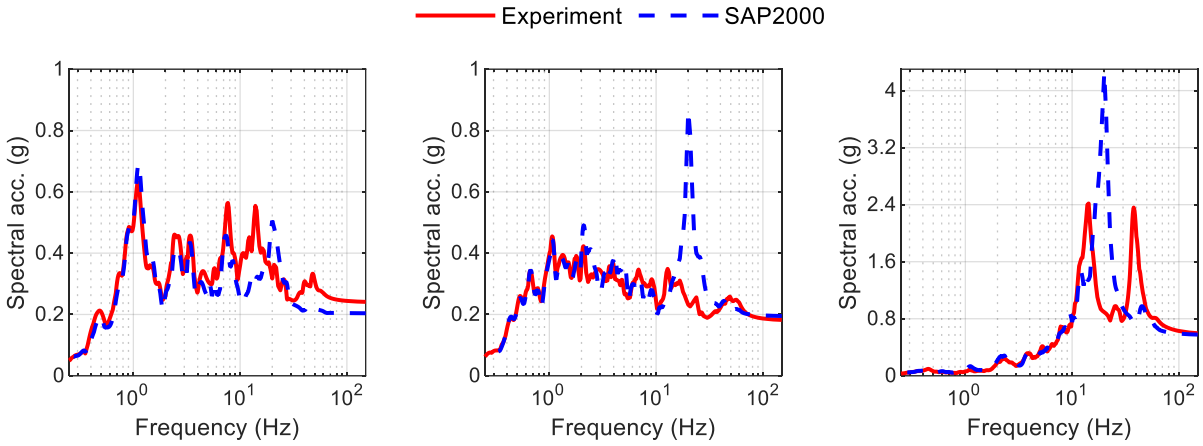

a) *x* direction b) *y* direction c) *z* direction

Figure 5-33. Acceleration response spectra directly above the isolation plane, test SF2B-3D

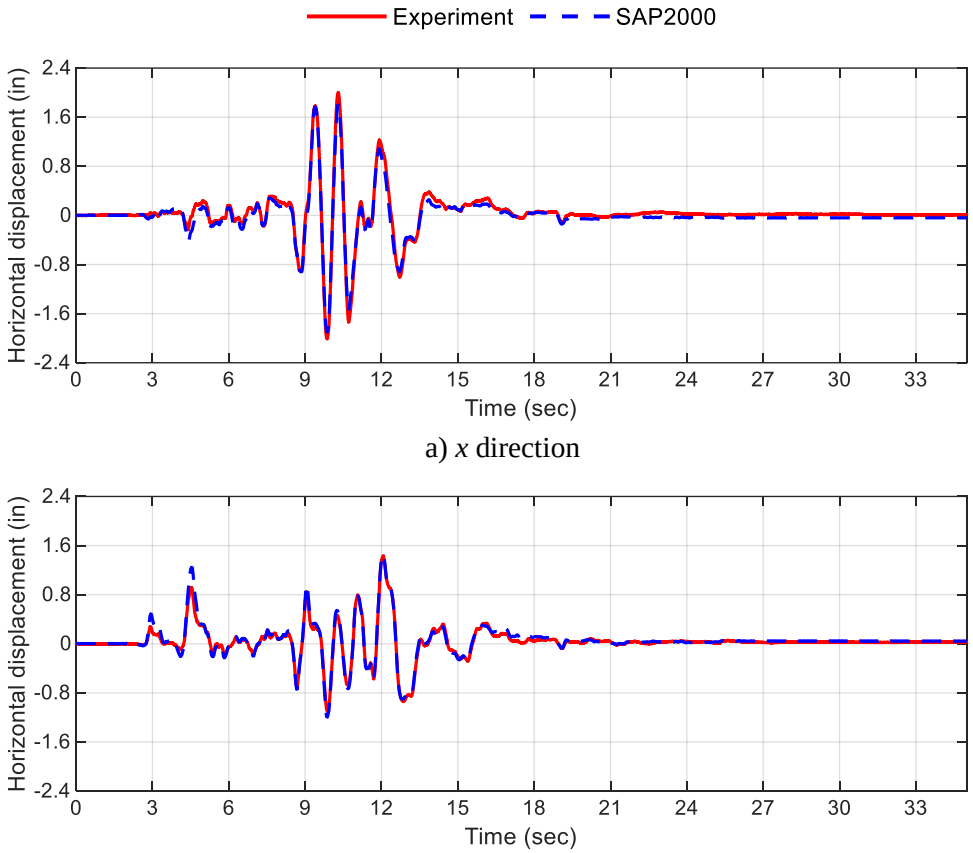

a) *x* direction

b) *y* direction

Figure 5-34. Isolation system displacements, test SF2B-3D

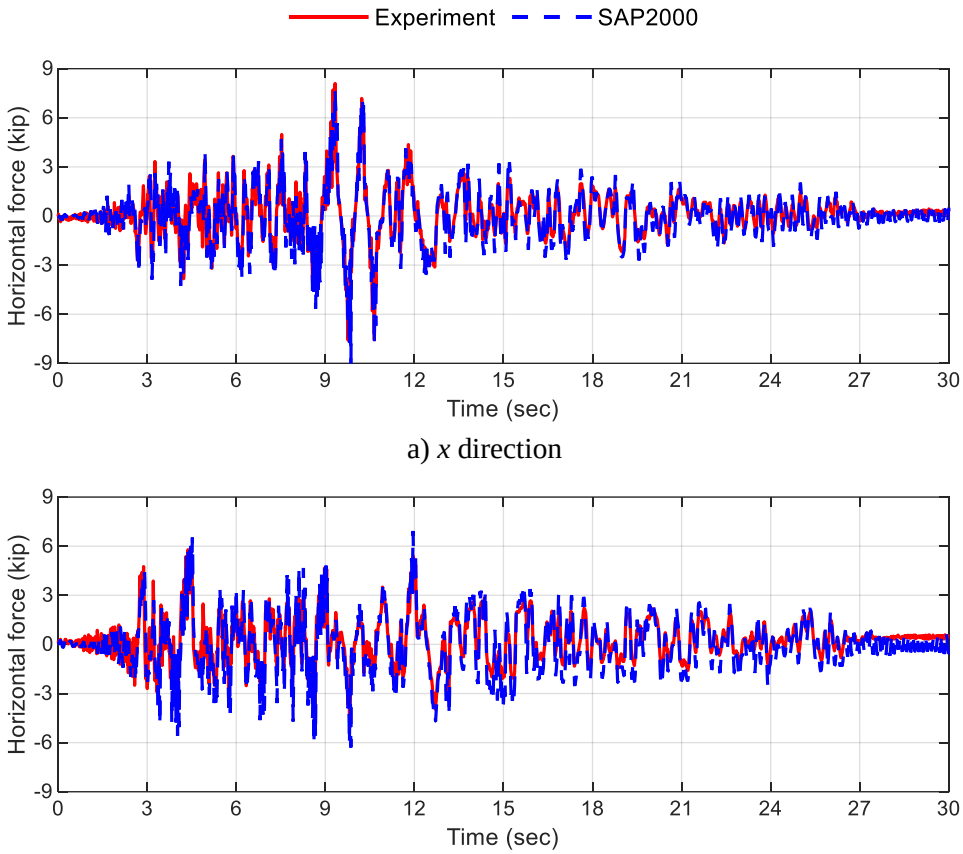

a) *x* direction

b) *y* direction

Figure 5-35. Isolation system forces, test SF2B-3D

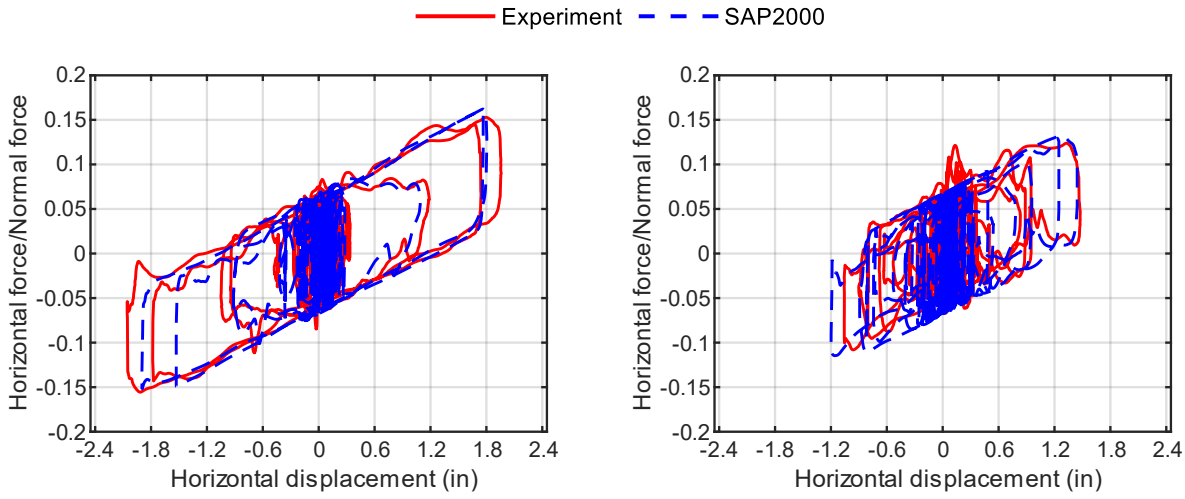

a) *x* direction

b) *y* direction

Figure 5-36. Normalized force-displacement loops for the isolation system, test SF2B-3D

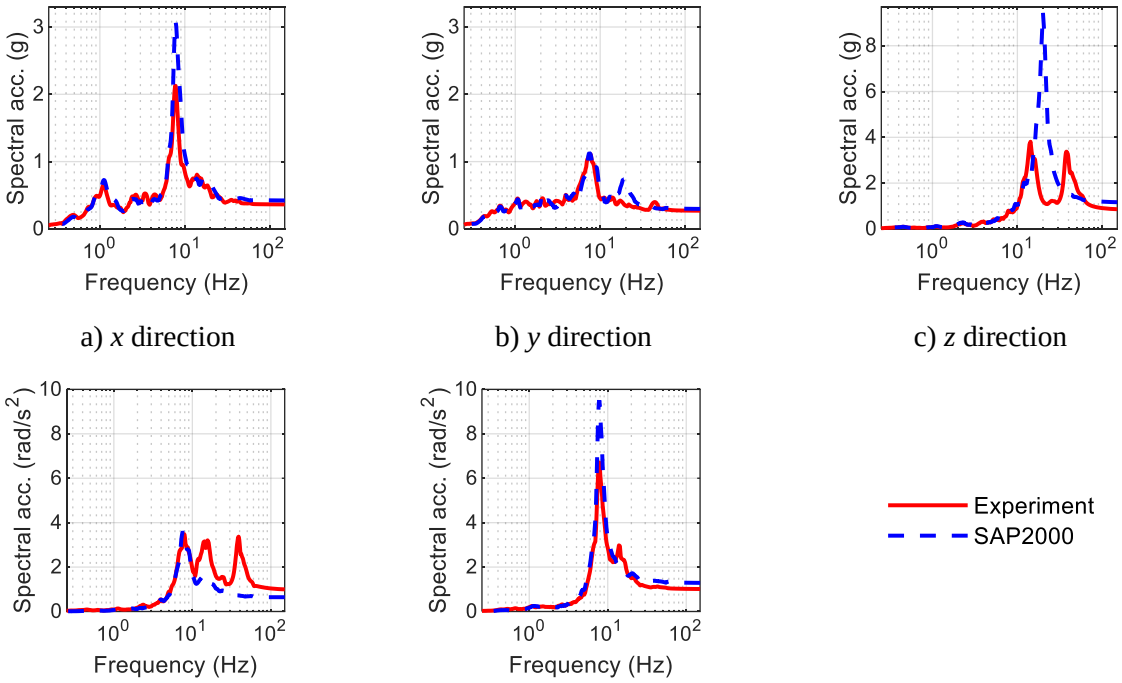

a) *x* direction b) *y* direction c) *z* direction

d) rocking about *x* axis e) rocking about *y* axis

Figure 5-37. Acceleration response spectra at the top of the vessel, test SF2B-3D

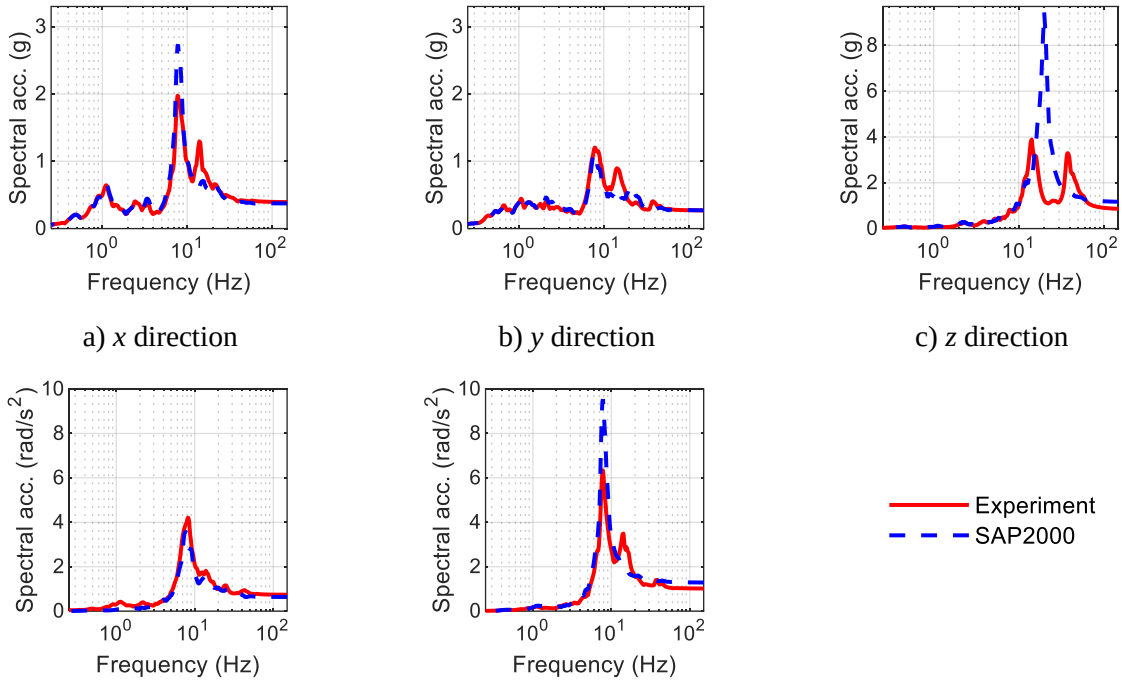

a) *x* direction b) *y* direction c) *z* direction

d) rocking about *x* axis e) rocking about *y* axis

Figure 5-38. Acceleration response spectra at the bottom of the vessel, test SF2B-3D

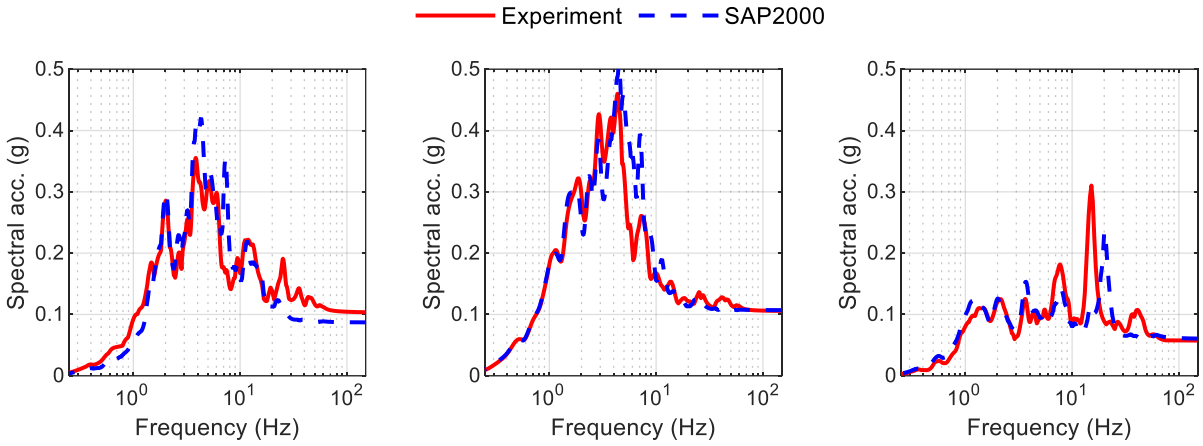

a) *x* direction b) *y* direction c) *z* direction

Figure 5-39. Acceleration response spectra directly above the isolation plane, test SF3A-3D

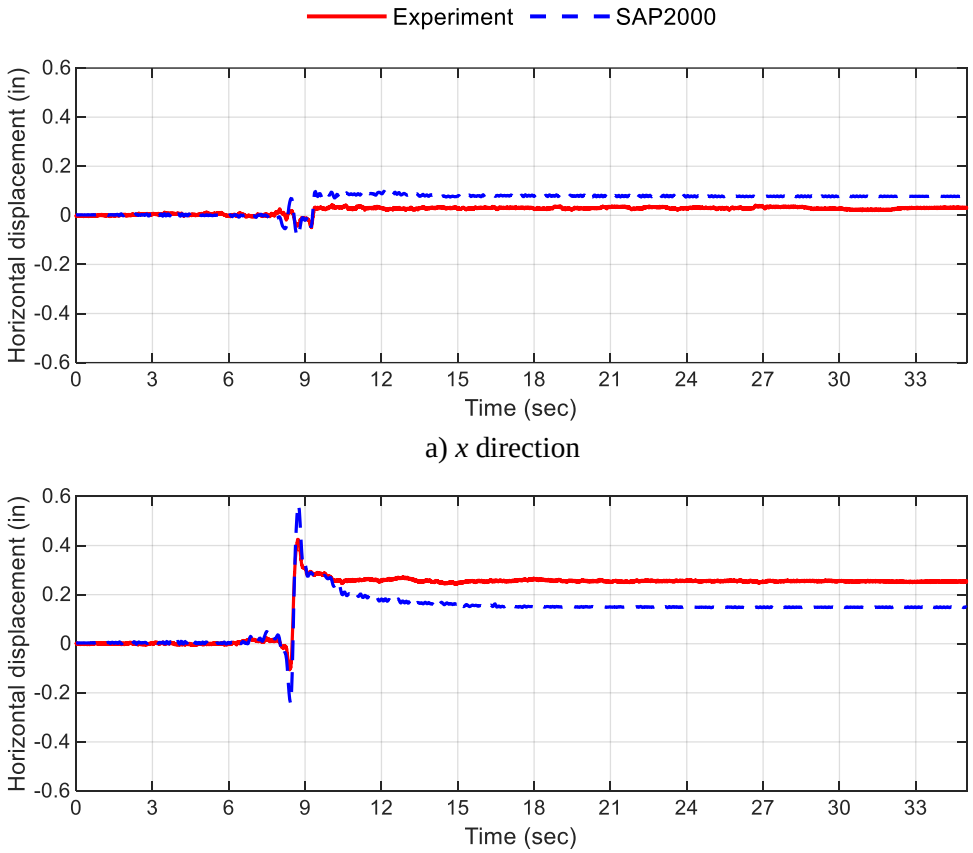

a) *x* direction

b) *y* direction

Figure 5-40. Isolation system displacements, test SF3A-3D

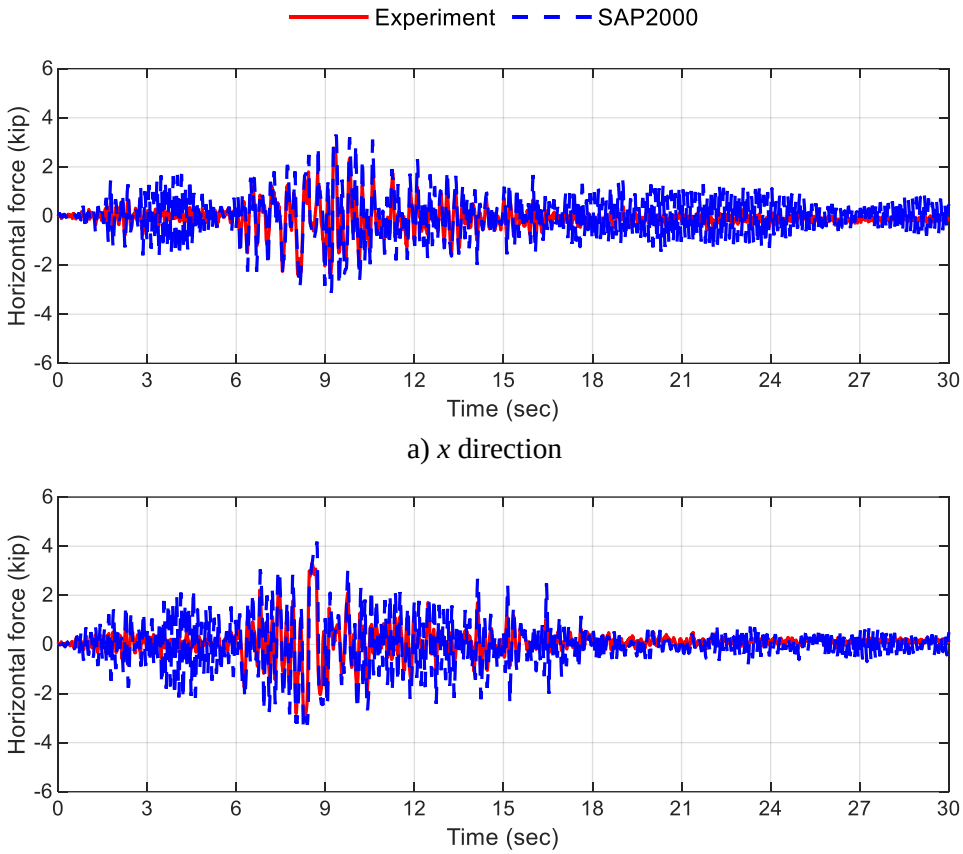

a) *x* direction

b) *y* direction

Figure 5-41. Isolation system forces, test SF3A-3D

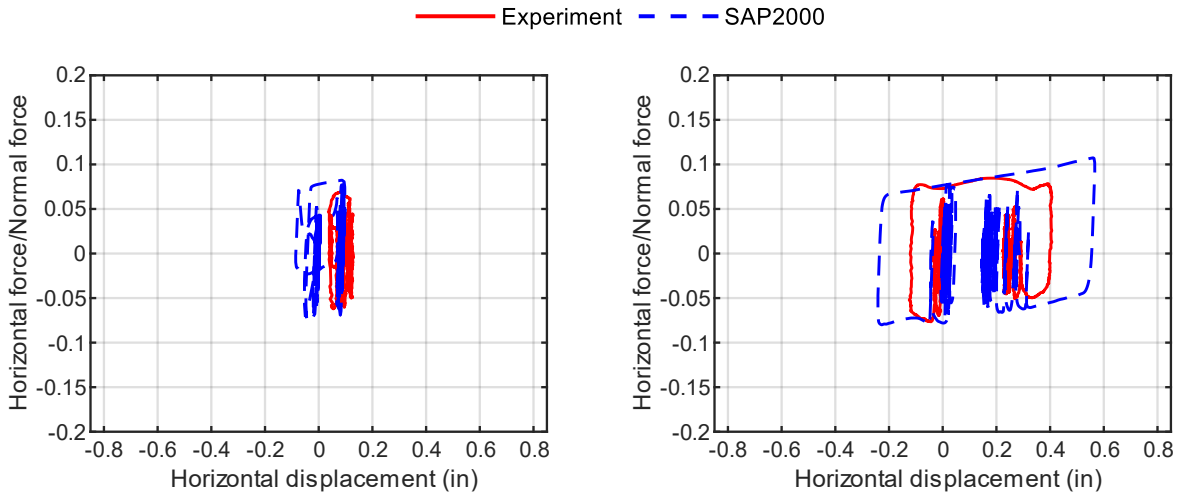

a) *x* direction

b) *y* direction

Figure 5-42. Normalized force-displacement loops for the isolation system, test SF3A-3D

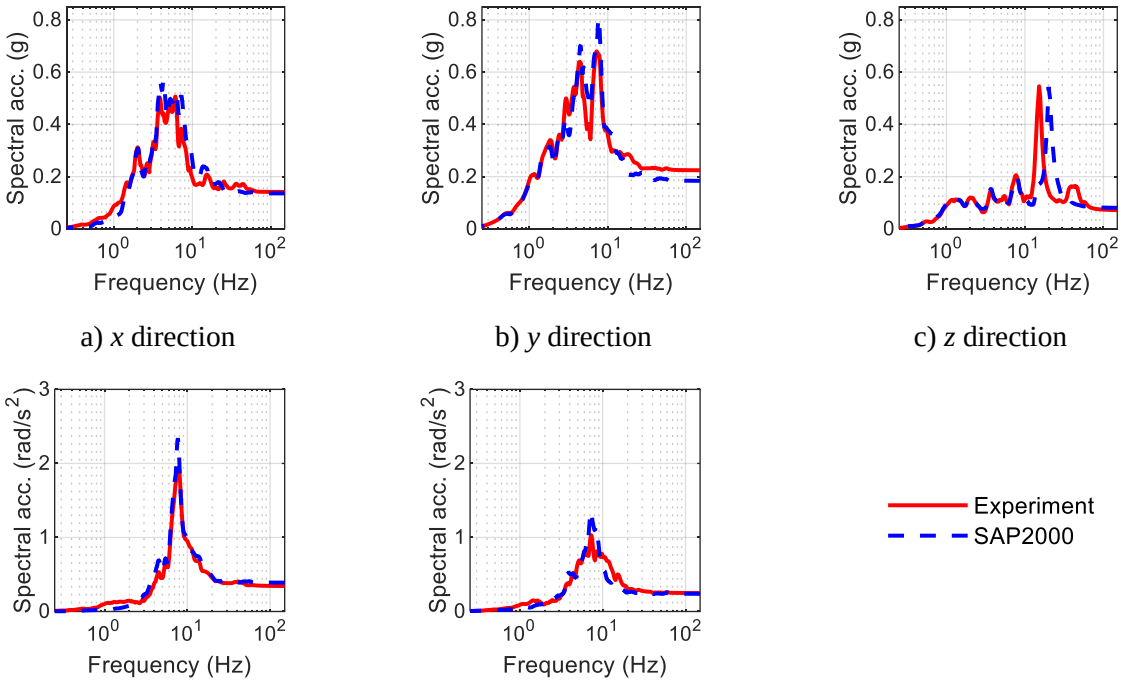

a) *x* direction b) *y* direction c) *z* direction

d) rocking about *x* axis e) rocking about *y* axis

Figure 5-43. Acceleration response spectra at the top of the vessel, test SF3A-3D

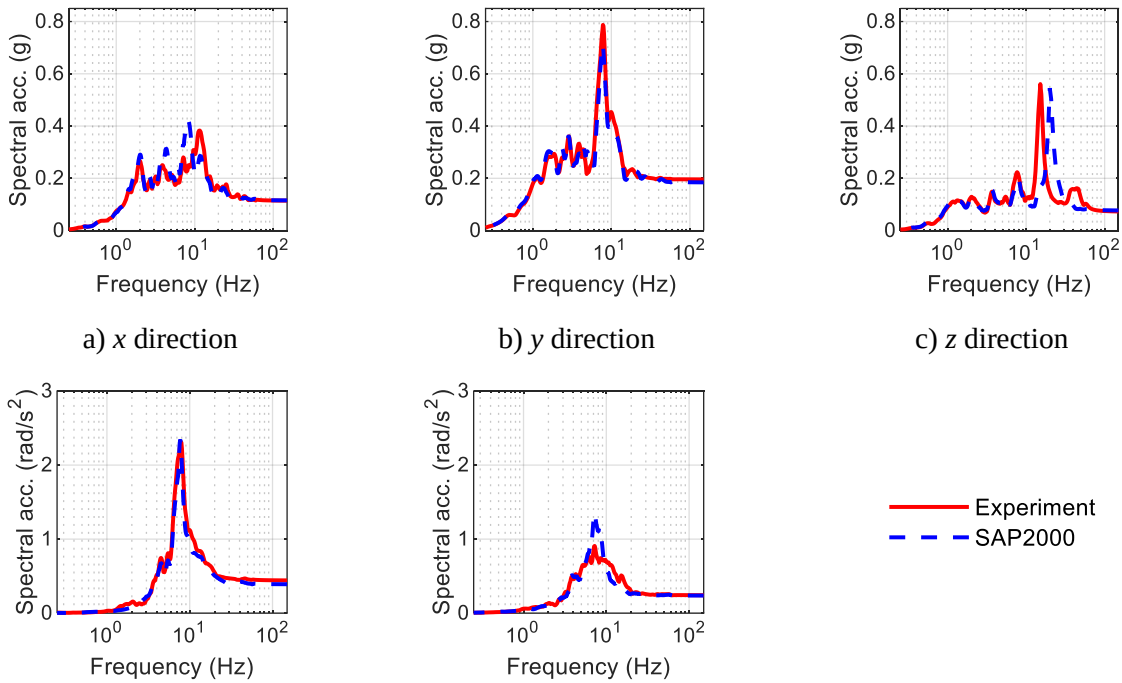

a) *x* direction b) *y* direction c) *z* direction

d) rocking about *x* axis e) rocking about *y* axis

Figure 5-44. Acceleration response spectra at the bottom of the vessel, test SF3A-3D

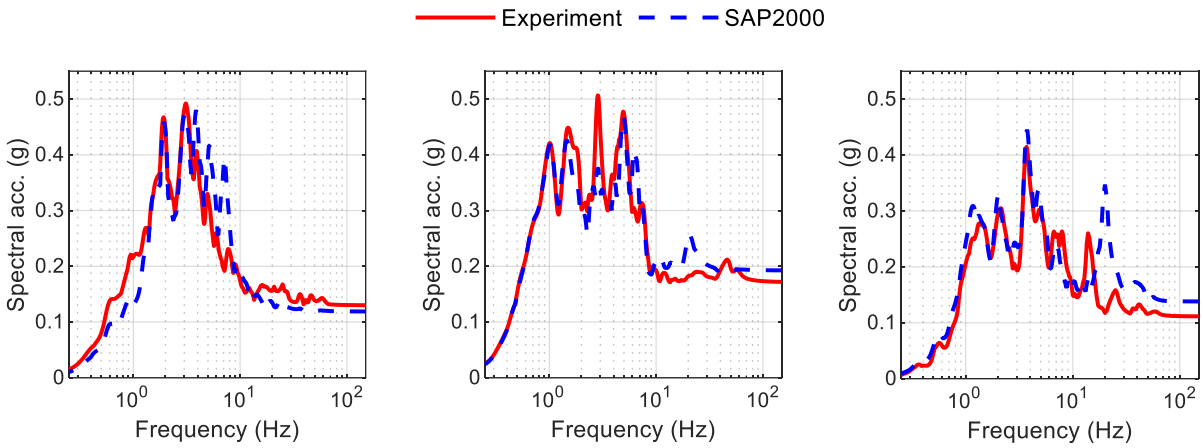

a) *x* direction b) *y* direction c) *z* direction

Figure 5-45. Acceleration response spectra directly above the isolation plane, test SF3B-3D

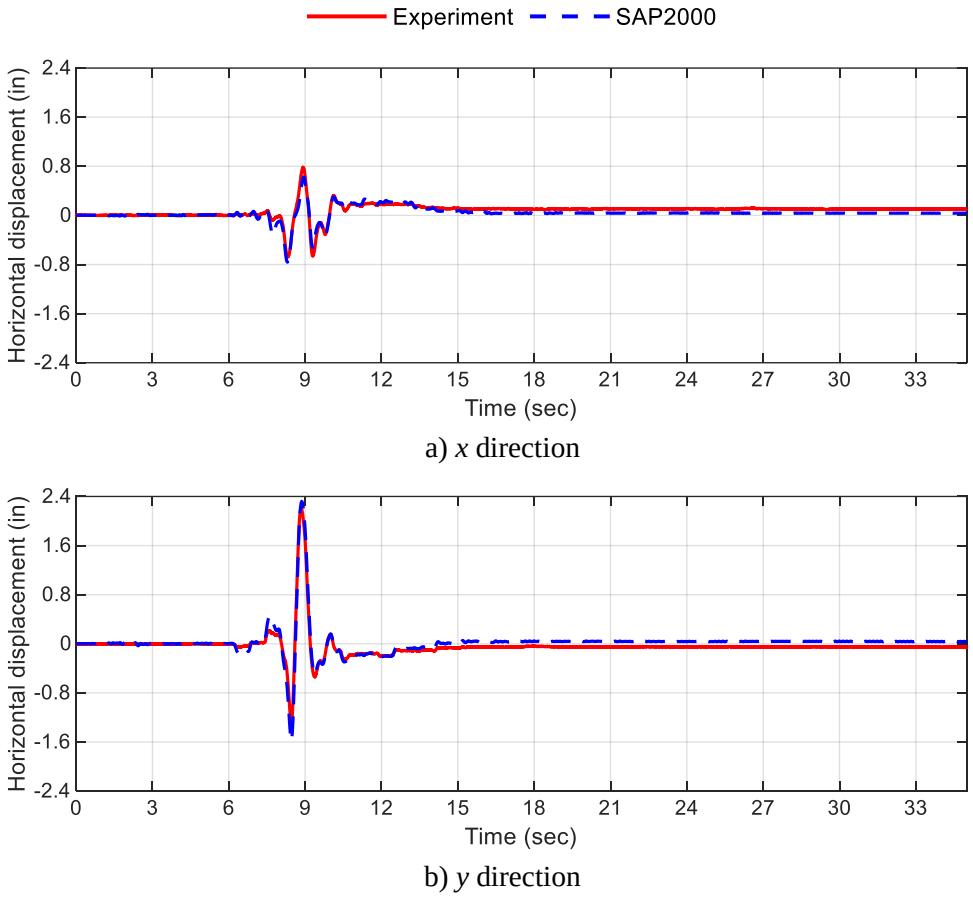

a) *x* direction

b) *y* direction

Figure 5-46. Isolation system displacements, test SF3B-3D

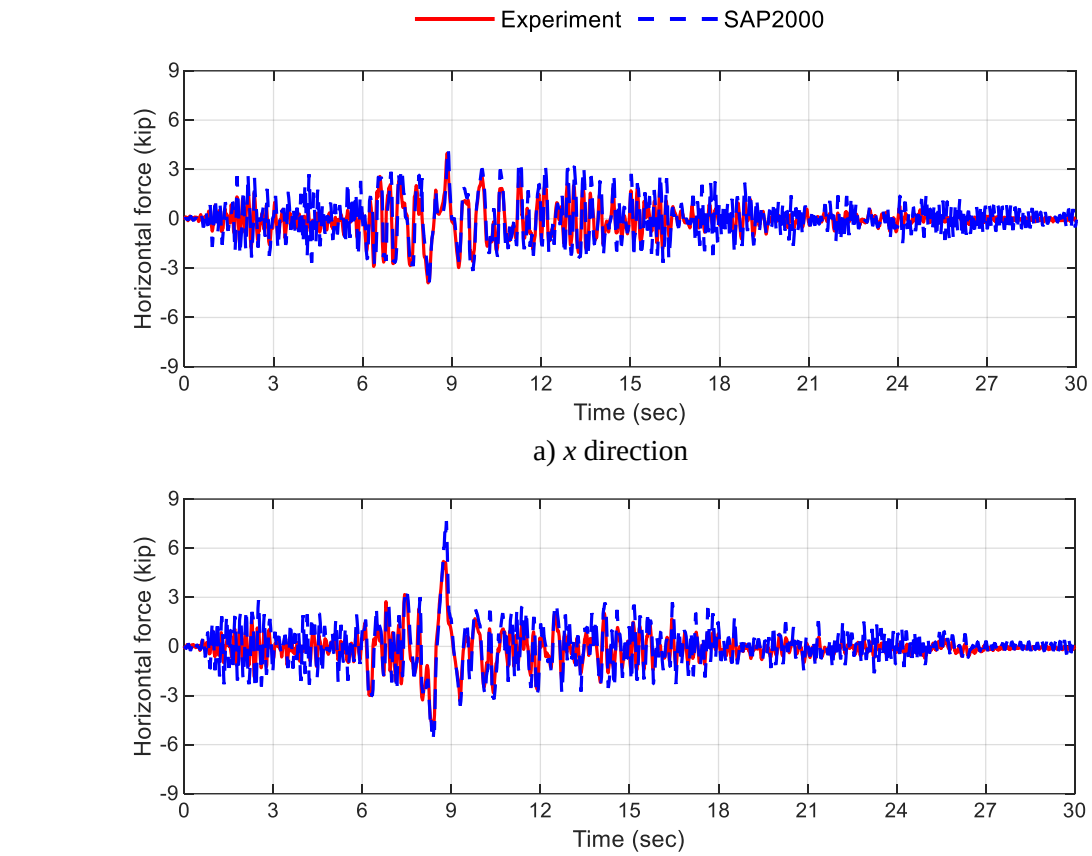

a) *x* direction

b) *y* direction

Figure 5-47. Isolation system forces, test SF3B-3D

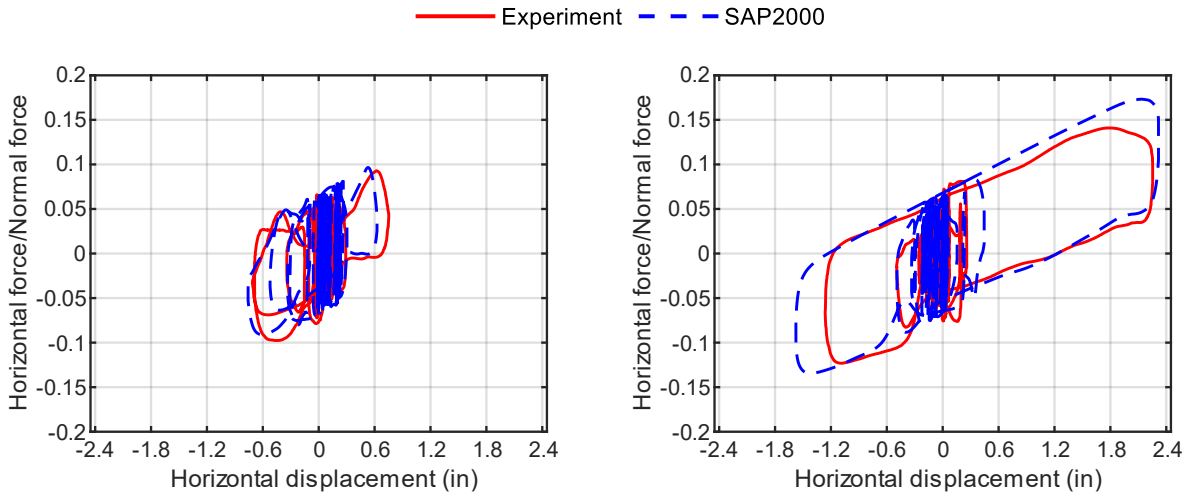

a) *x* direction

b) *y* direction

Figure 5-48. Normalized force-displacement loops for the isolation system, test SF3B-3D

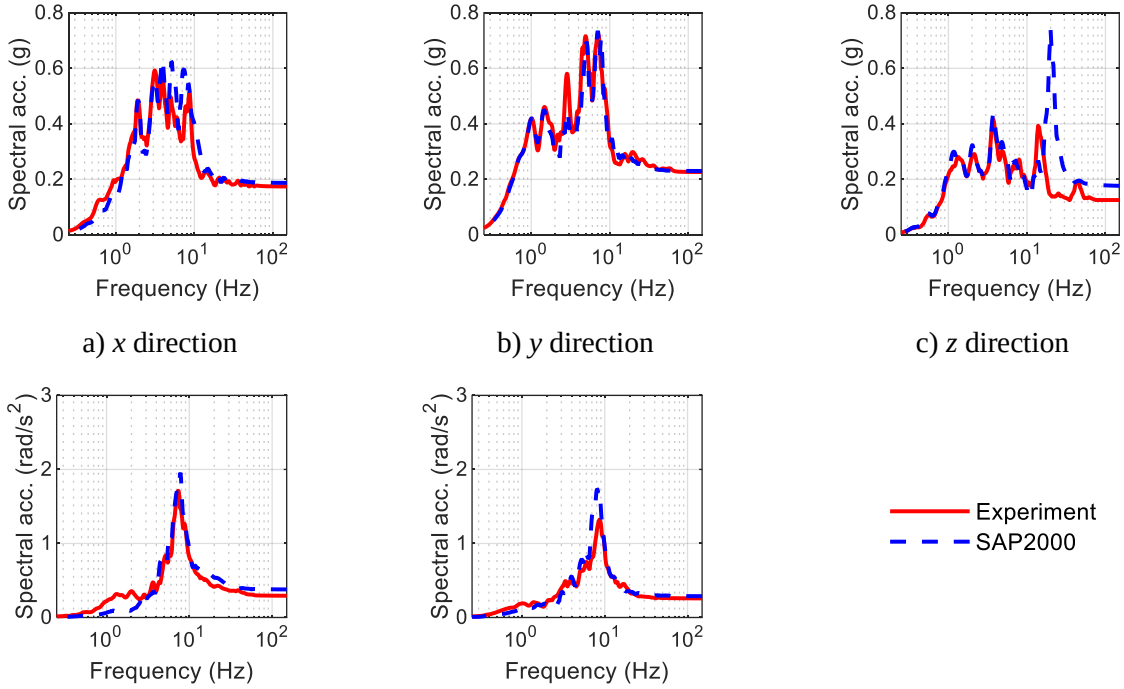

a) *x* direction b) *y* direction c) *z* direction

d) rocking about *x* axis e) rocking about *y* axis

Figure 5-49. Acceleration response spectra at the top of the vessel, test SF3B-3D

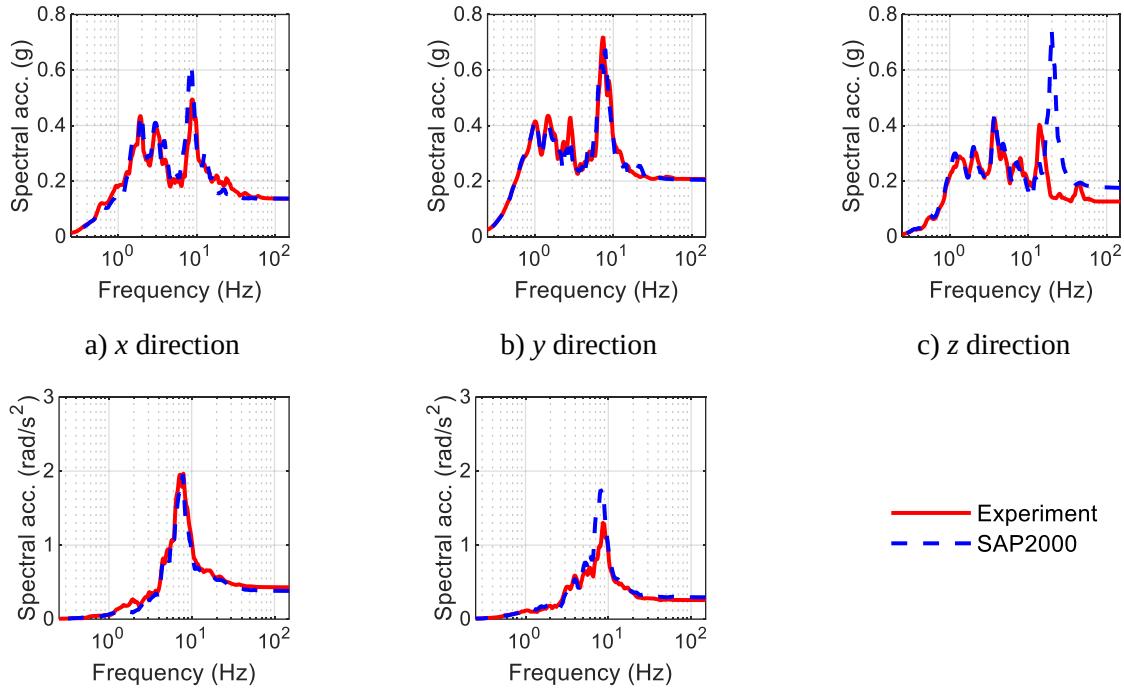

a) *x* direction b) *y* direction c) *z* direction

d) rocking about *x* axis e) rocking about *y* axis

Figure 5-50. Acceleration response spectra at the bottom of the vessel, test SF3B-3D

Table 5-5. Peak accelerations[1] (g) for the 3D tests in the SFP-isolated configuration, *x*, *y*, and *z* directions

Test		Below isolation plane			Above isolation plane			Vessel bottom			Vessel top		
		x	***y***	***z***	***x***	***y***	***z***	***x***	***y***	***z***	***x***	***y***	***z***
SF1A-3D	Experiment	0.30	0.30	0.16	0.13	0.12	0.21	0.22	0.22	0.34	0.22	0.24	0.34
	SAP2000	0.42	0.47	0.13	0.11	0.11	0.19	0.21	0.21	0.39	0.23	0.20	0.38
	Diff (%)	40	57	19	15	8	10	5	5	15	5	17	12
SF1B-3D	Experiment	0.82	0.77	0.30	0.24	0.23	0.39	0.36	0.29	0.52	0.34	0.31	0.50
	SAP2000	0.76	0.80	0.37	0.33	0.38	0.51	0.50	0.30	1.02	0.50	0.42	1.03
	Diff (%)	7	4	23	38	65	31	39	3	96	47	35	106
SF2A-3D	Experiment	0.24	0.26	0.20	0.11	0.11	0.21	0.20	0.14	0.32	0.19	0.19	0.32
	SAP2000	0.25	0.39	0.21	0.11	0.11	0.29	0.21	0.14	0.62	0.23	0.16	0.62
	Diff (%)	4	50	5	0	0	38	5	0	94	21	16	94
SF2B-3D	Experiment	0.69	0.48	0.38	0.24	0.18	0.57	0.39	0.27	0.83	0.36	0.27	0.83
	SAP2000	0.68	0.66	0.40	0.20	0.19	0.57	0.37	0.27	1.15	0.42	0.29	1.15
	Diff (%)	1	38	5	17	6	0	5	0	39	17	7	39
SF3A-3D	Experiment	0.16	0.25	0.05	0.10	0.11	0.06	0.11	0.20	0.07	0.14	0.22	0.07
	SAP2000	0.17	0.37	0.05	0.09	0.11	0.06	0.12	0.18	0.08	0.14	0.18	0.08
	Diff (%)	6	48	0	10	0	0	9	10	14	0	18	14
SF3B-3D	Experiment	0.19	0.46	0.10	0.13	0.17	0.11	0.14	0.21	0.13	0.17	0.23	0.13
	SAP2000	0.18	0.42	0.13	0.12	0.19	0.14	0.14	0.20	0.17	0.19	0.23	0.18
	Diff (%)	5	9	30	8	12	27	0	5	31	12	0	38

1. Peak acceleration calculated as spectral acceleration at 100 Hz

Table 5-6. Peak isolator displacements and normalized forces for the 3D tests of the SFP-isolated configuration

		Displacement (in)		Normalized force	
Test		***x* direction**	***y* direction**	***x* direction**	***y* direction**
SF1A-3D	Experiment	0.4	0.3	0.08	0.10
	SAP2000	0.5	0.3	0.09	0.09
	Diff (%)	25	0	13	10
SF1B-3D	Experiment	1.9	2.1	0.17	0.17
	SAP2000	2.0	1.9	0.18	0.17
	Diff (%)	5	10	6	0
SF2A-3D	Experiment	0.7	0.5	0.09	0.08
	SAP2000	0.6	0.5	0.10	0.09
	Diff (%)	14	0	11	13
SF2B-3D	Experiment	2.0	1.4	0.16	0.12
	SAP2000	1.9	1.5	0.16	0.13
	Diff (%)	5	7	0	8
SF3A-3D	Experiment	0.1	0.4	0.07	0.08
	SAP2000	0.1	0.6	0.08	0.10
	Diff (%)	0	50	14	25
SF3B-3D	Experiment	0.8	2.2	0.10	0.14
	SAP2000	0.8	2.3	0.10	0.17
	Diff (%)	0	5	0	21

5.3.4 TFP-isolated configuration

Figures 5-51 through 5-86 present the responses of the numerical analysis of TFP-isolated model and the experiment data for the six 3D motions of Table 4-5. The peak accelerations at the locations identified previously and the absolute percentage difference between the predicted and experimental values are presented in Table 5-7. Companion results for maximum isolation system displacements and normalized forces are presented in Table 5-8. The *y*-axis range for the acceleration response spectra in the *x*- and *y*-directions is different than in the *z* direction: see Section 5.3.3.

The agreement between the numerically predicted and experimentally recorded accelerations for the horizontal and rocking responses of the vessel is reasonable. The agreement in the vertical direction is poorer with differences due to the higher vertical frequency of the SAP2000 model (see Section 5.2.2). The average difference in the peak horizontal (vertical) accelerations directly above and below the isolation, and at the top and bottom of the vessel is 21% (40%), with a range of 0% (0%) to 70% (129%). In some cases, analysis of the SAP2000 model over predicted the amplitude of spectral acceleration at the rocking frequency (e.g., Figures 5-61a, 5-61e, 5-62a, and 5-62e) because the damping ratios in the rocking modes were not calibrated for specific seismic inputs and a single damping value was used for rocking about both the *x* and *y* axes: see Section 5.2.3.

Identical to the SFP-isolated configuration, the predicted normalized force-displacement loops (maximum isolation-system displacements and peak normalized forces) of the TFP isolation system are in excellent agreement with the test data for the larger amplitude motions.

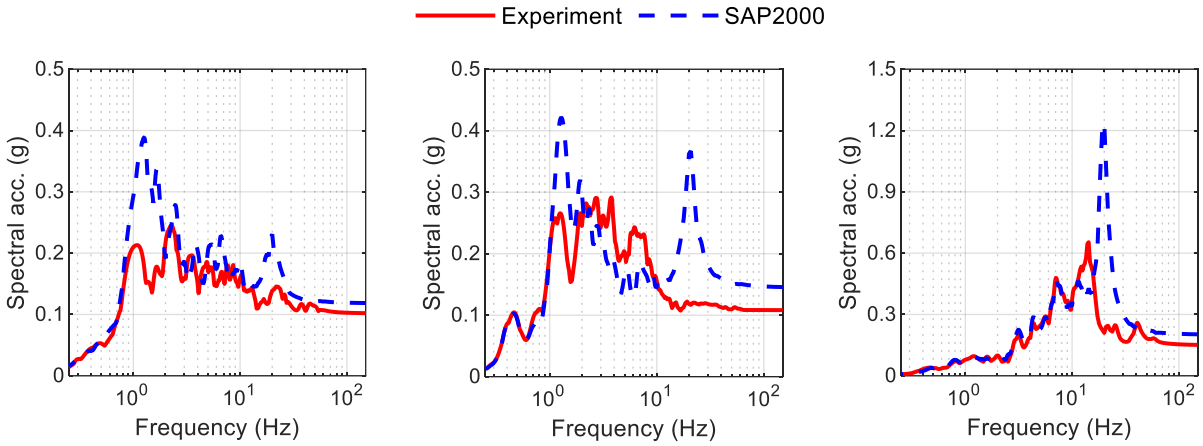

a) *x* direction b) *y* direction c) *z* direction

Figure 5-51. Acceleration response spectra directly above the isolation plane, test TF1A-3D

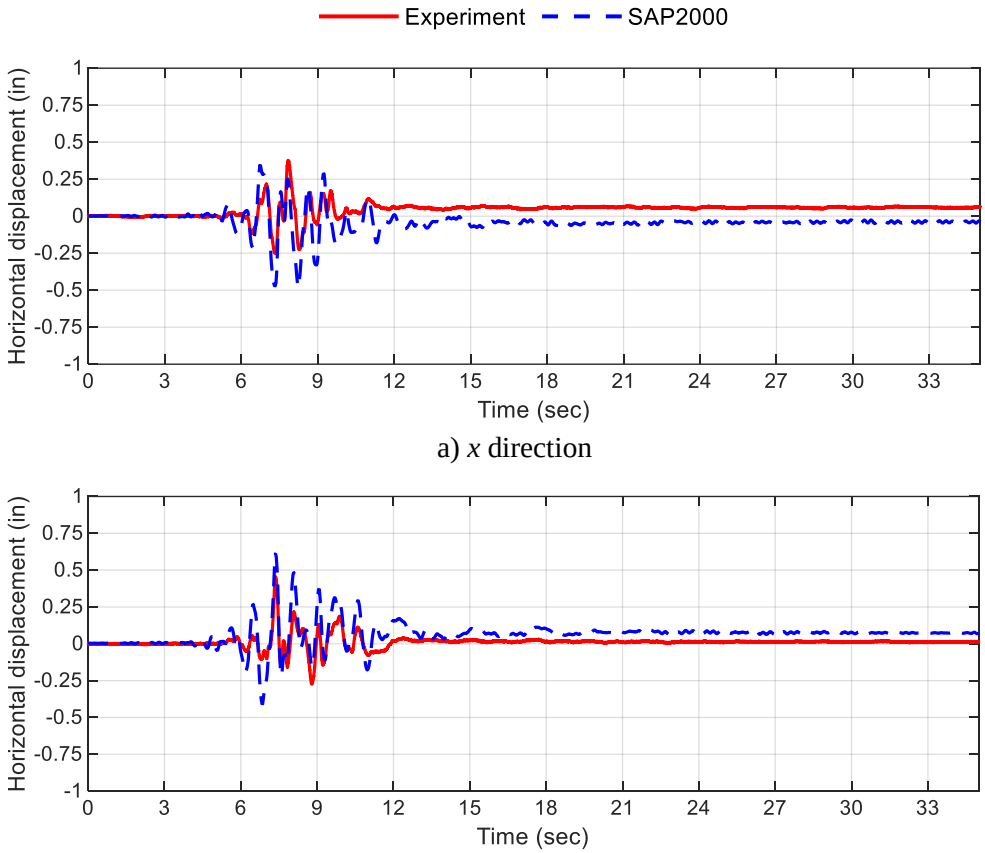

a) *x* direction

b) *y* direction

Figure 5-52. Isolation system displacements, test TF1A-3D

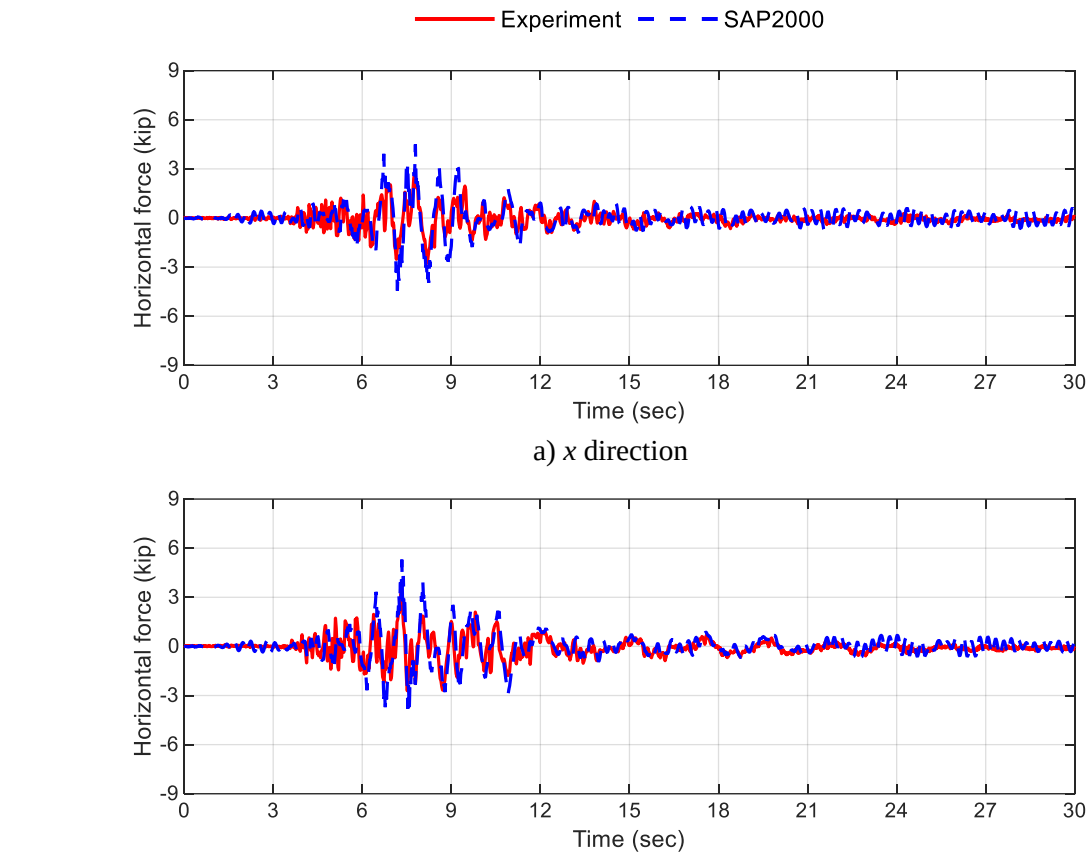

a) *x* direction

b) *y* direction

Figure 5-53. Isolation system forces, test TF1A-3D

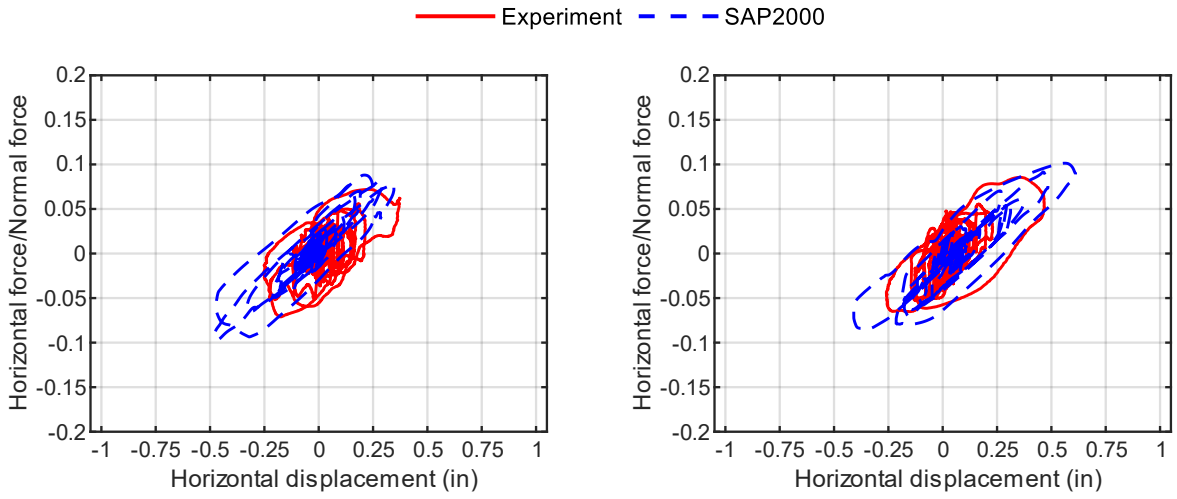

a) *x* direction

b) *y* direction

Figure 5-54. Normalized force-displacement loops for the isolation system, test TF1A-3D

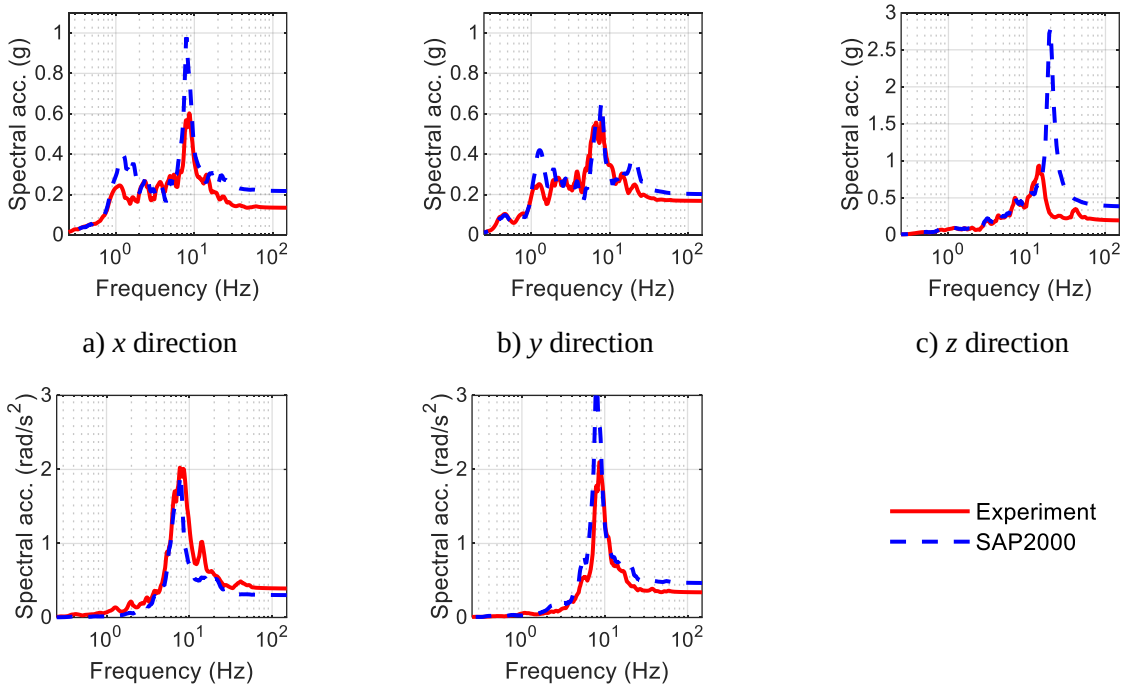

a) *x* direction b) *y* direction c) *z* direction

d) rocking about *x* axis e) rocking about *y* axis

Figure 5-55. Acceleration response spectra at the top of the vessel, test TF1A-3D

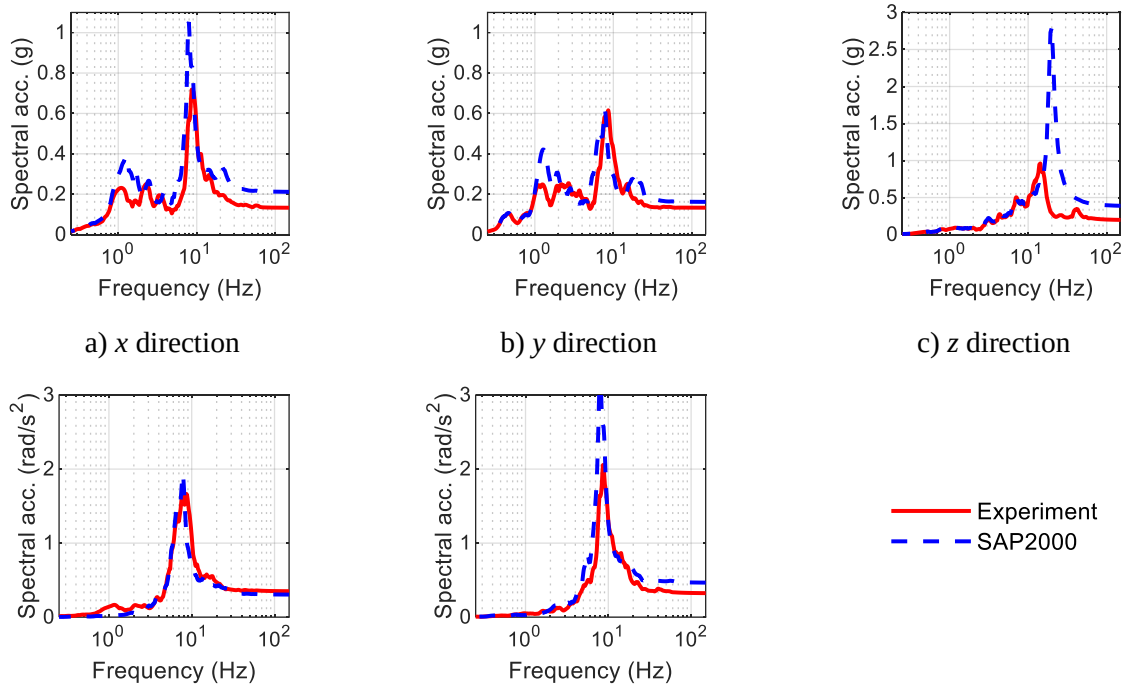

a) *x* direction b) *y* direction c) *z* direction

d) rocking about *x* axis e) rocking about *y* axis

Figure 5-56. Acceleration response spectra at the bottom of the vessel, test TF1A-3D

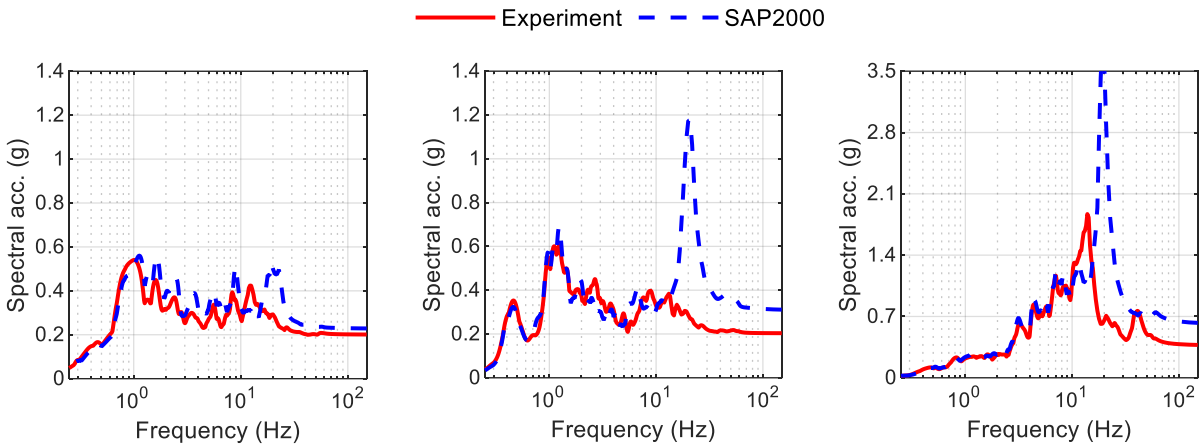

a) *x* direction b) *y* direction c) *z* direction

Figure 5-57. Acceleration response spectra directly above the isolation plane, test TF1B-3D

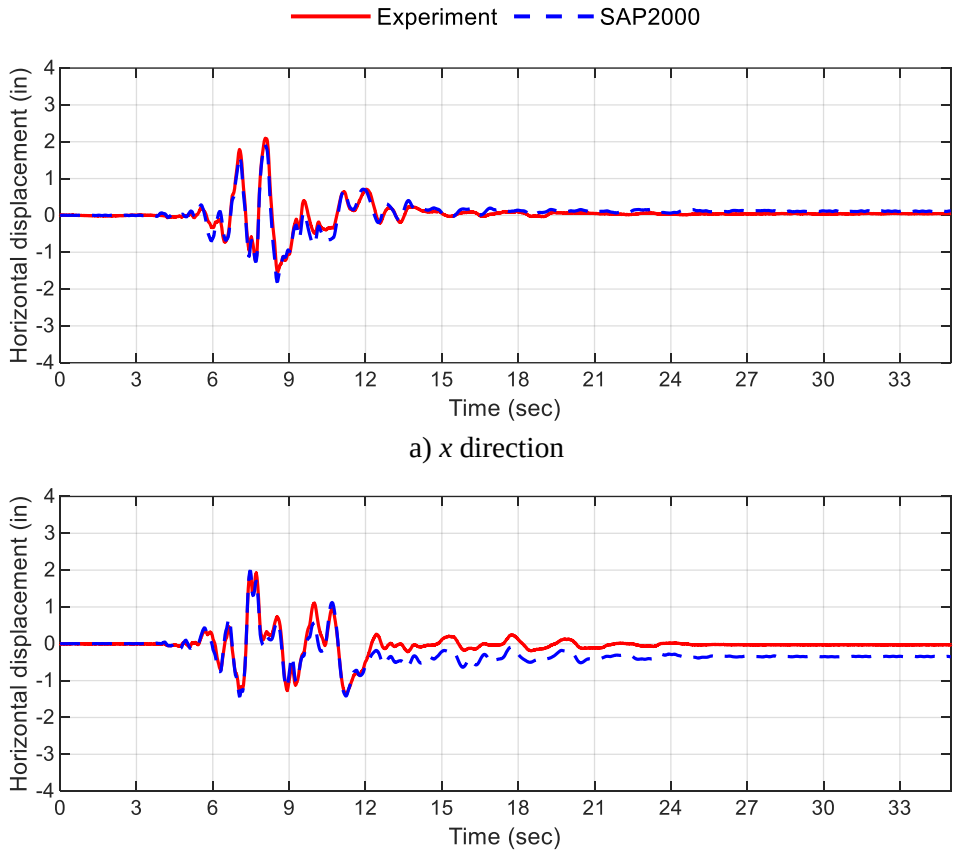

a) *x* direction

b) *y* direction

Figure 5-58. Isolation system displacements, test TF1B-3D

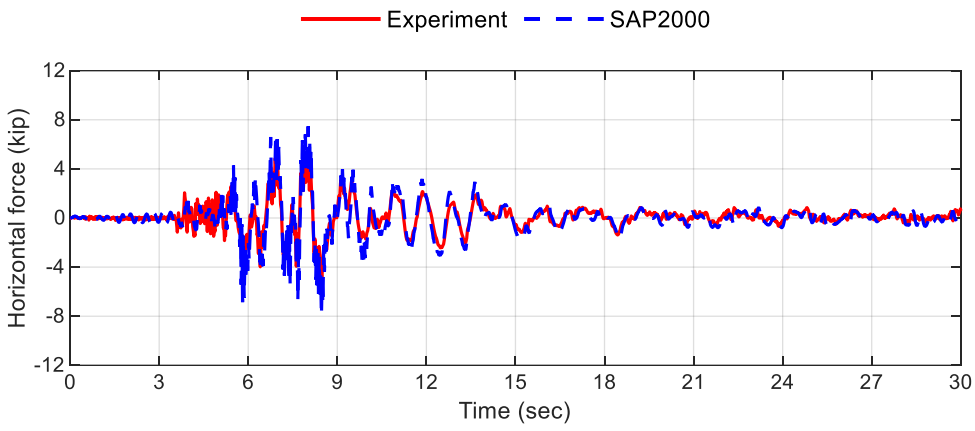

a) *x* direction

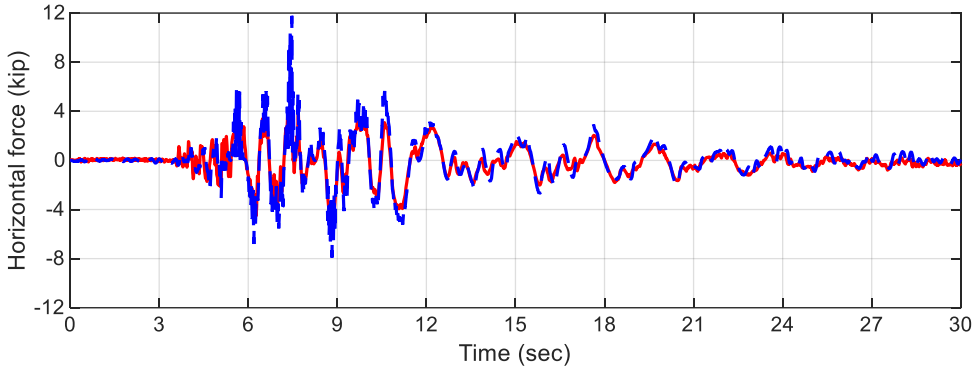

b) *y* direction

Figure 5-59. Isolation system forces, test TF1B-3D

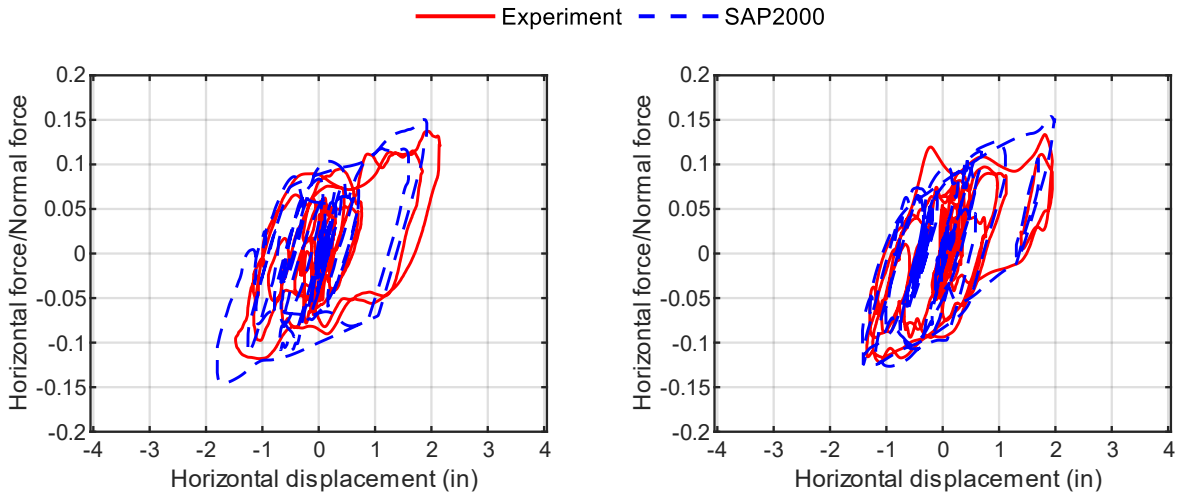

a) *x* direction b) *y* direction

Figure 5-60. Normalized force-displacement loops for the isolation system, test TF1B-3D

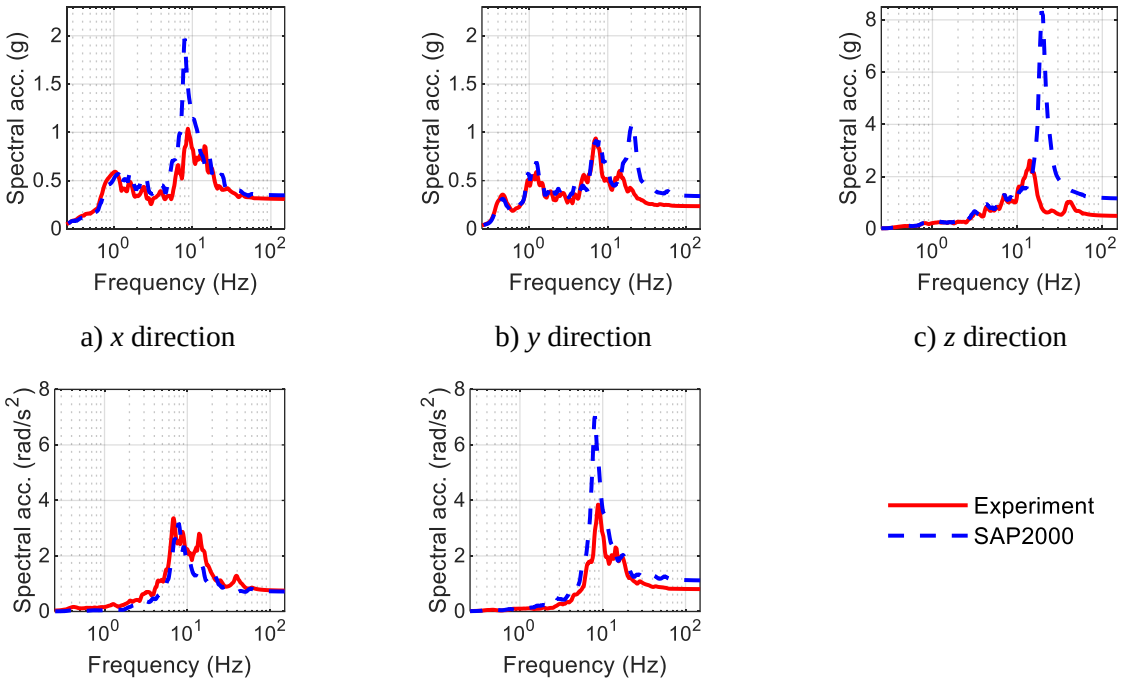

a) *x* direction b) *y* direction c) *z* direction

d) rocking about *x* axis e) rocking about *y* axis

Figure 5-61. Acceleration response spectra at the top of the vessel, test TF1B-3D

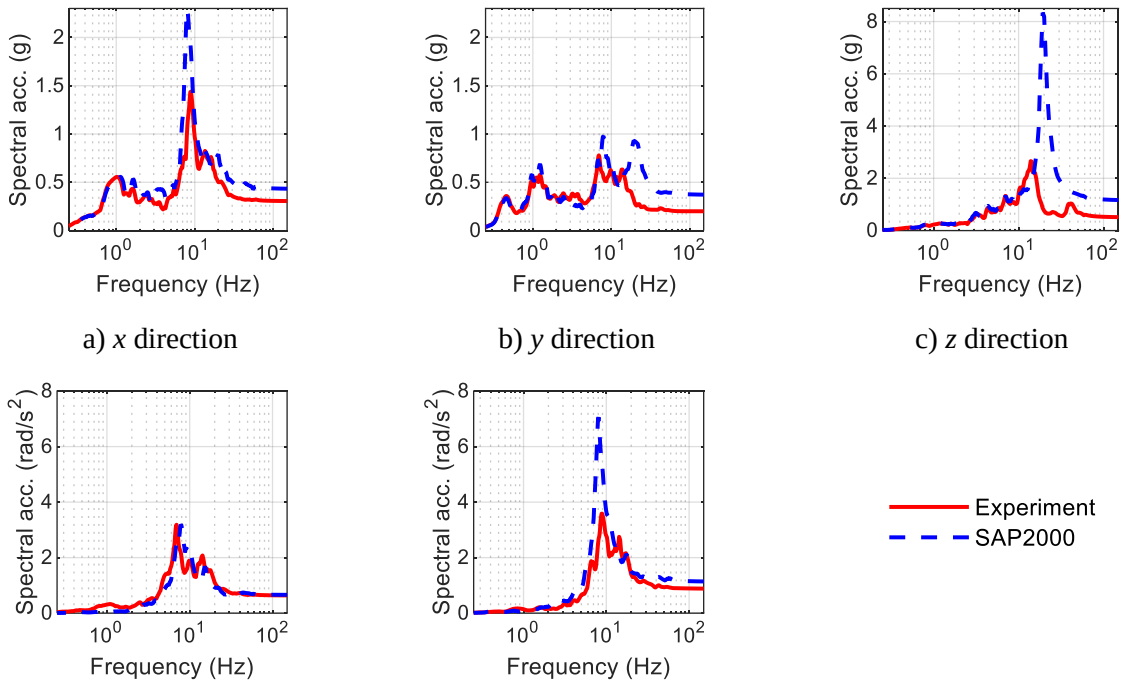

a) *x* direction b) *y* direction c) *z* direction

d) rocking about *x* axis e) rocking about *y* axis

Figure 5-62. Acceleration response spectra at the bottom of the vessel, test TF1B-3D

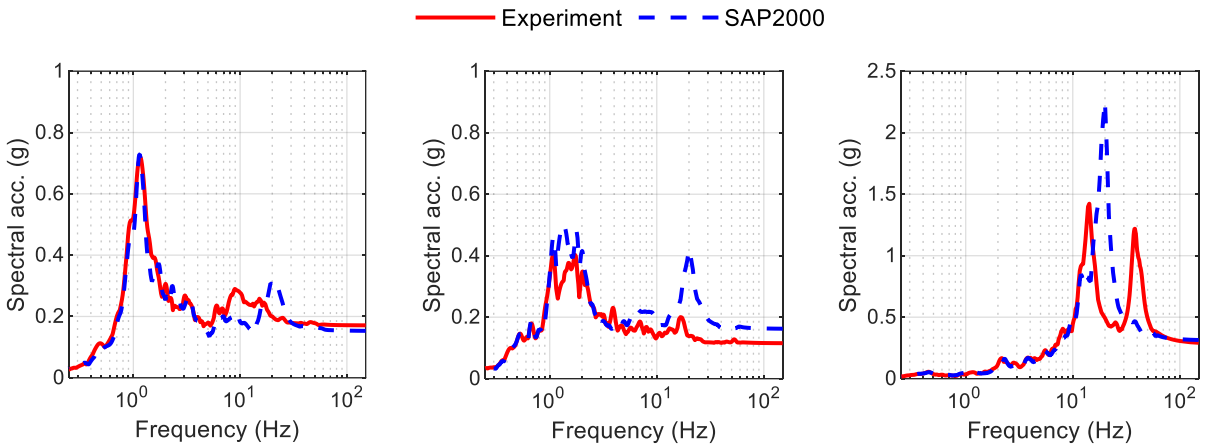

a) *x* direction b) *y* direction c) *z* direction

Figure 5-63. Acceleration response spectra directly above the isolation plane, test TF2A-3D

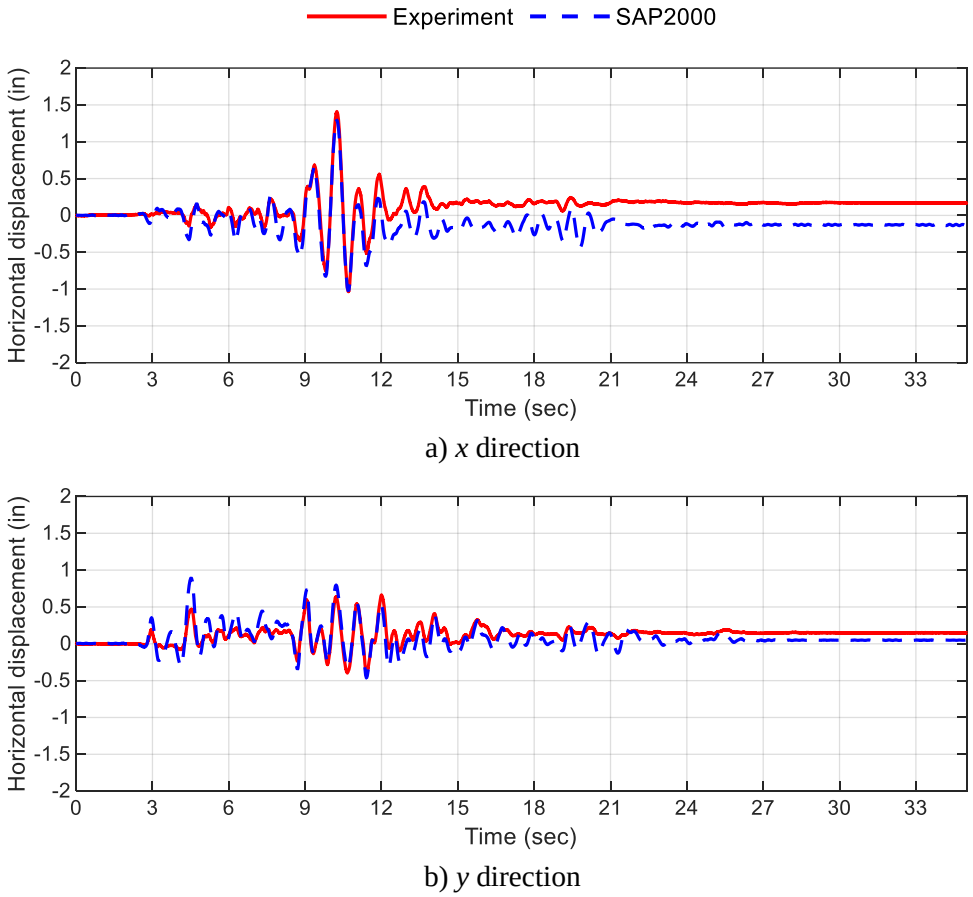

a) *x* direction

b) *y* direction

Figure 5-64. Isolation system displacements, test TF2A-3D

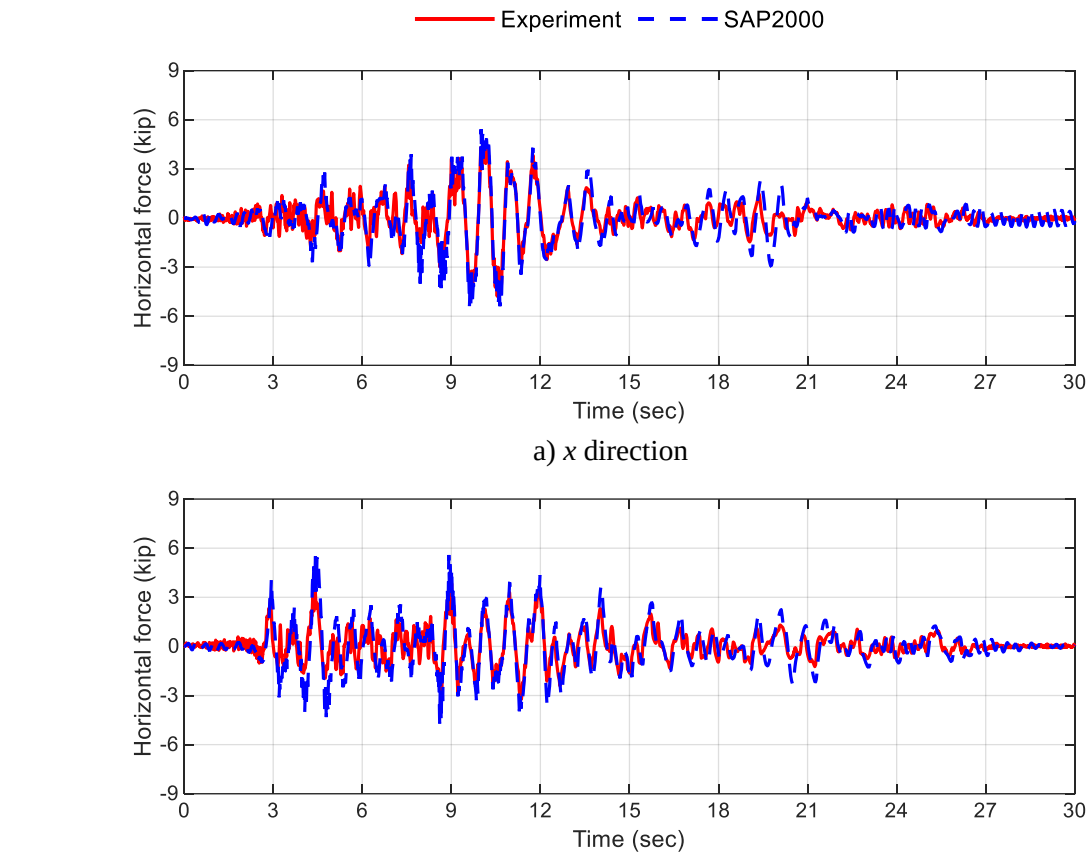

a) *x* direction

b) *y* direction

Figure 5-65. Isolation system forces, test TF2A-3D

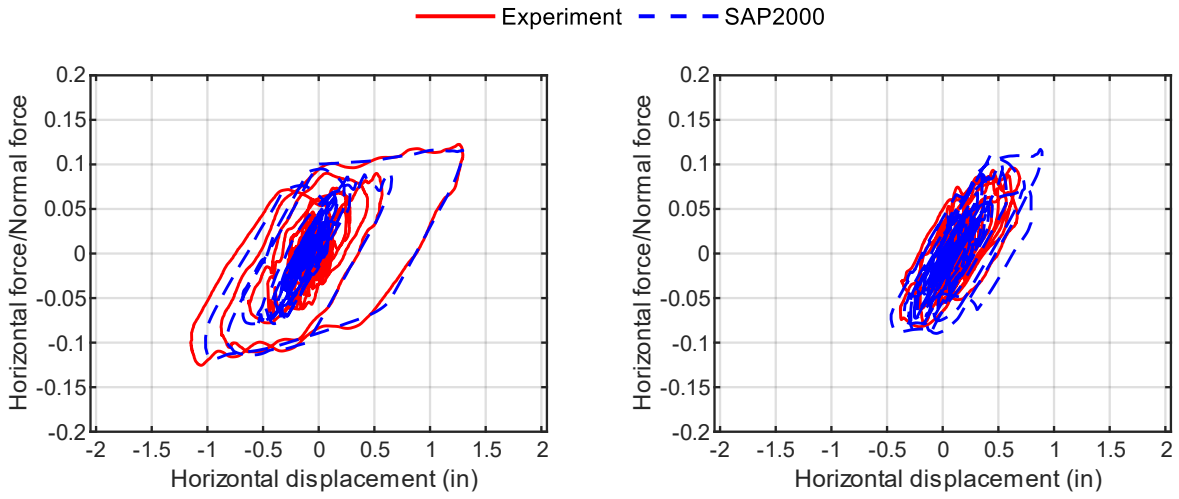

a) *x* direction

b) *y* direction

Figure 5-66. Normalized force-displacement loops for the isolation system, test TF2A-3D

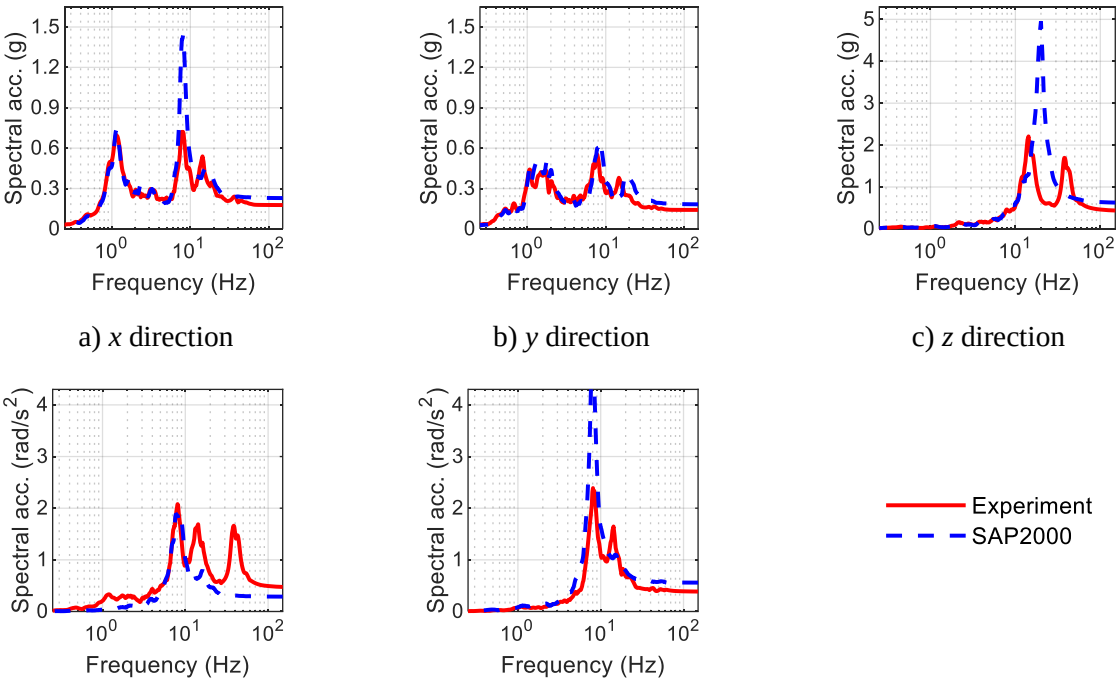

a) *x* direction b) *y* direction c) *z* direction

d) rocking about *x* axis e) rocking about *y* axis

Figure 5-67. Acceleration response spectra at the top of the vessel, test TF2A-3D

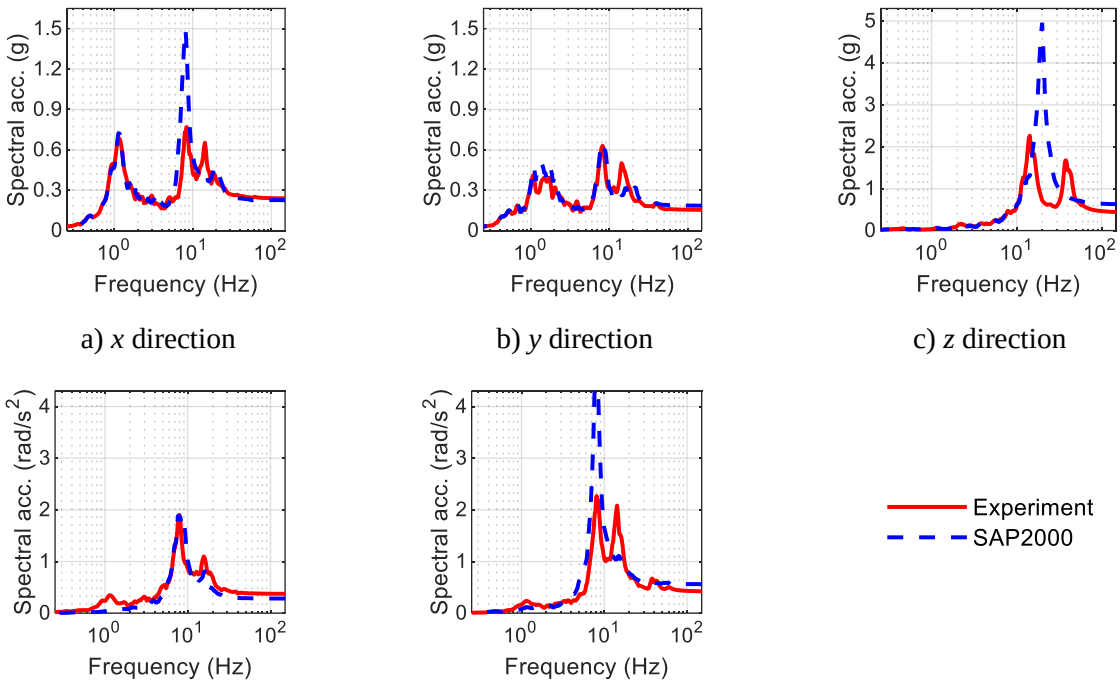

a) *x* direction b) *y* direction c) *z* direction

d) rocking about *x* axis e) rocking about *y* axis

Figure 5-68. Acceleration response spectra at the bottom of the vessel, test TF2A-3D

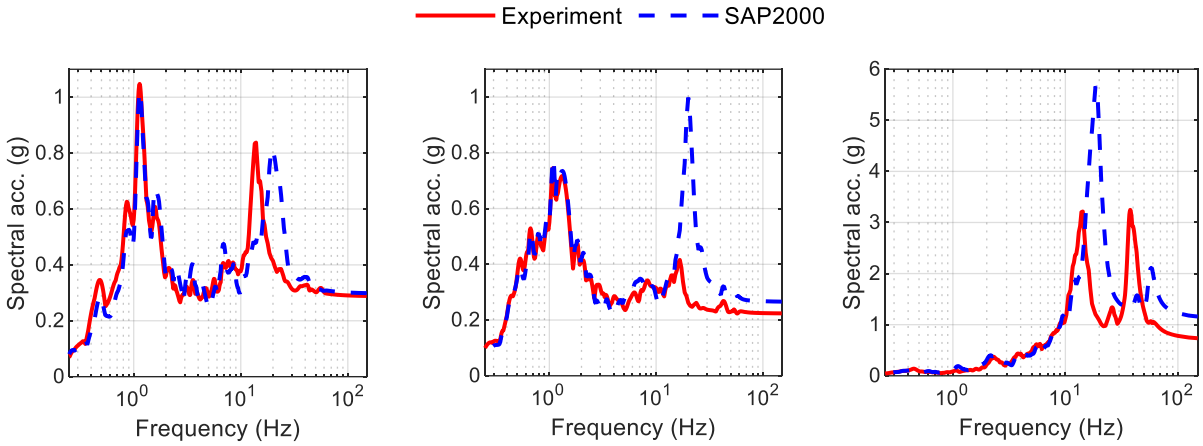

a) *x* direction b) *y* direction c) *z* direction

Figure 5-69. Acceleration response spectra directly above the isolation plane, test TF2B-3D

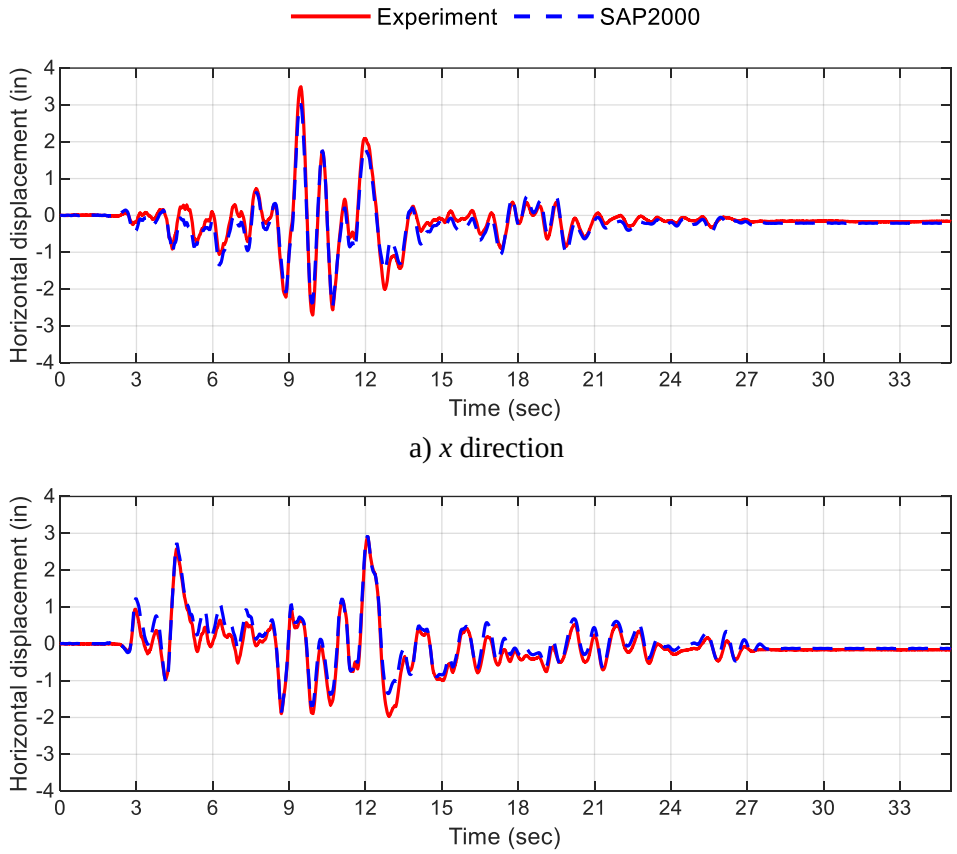

a) *x* direction

b) *y* direction

Figure 5-70. Isolation system displacements, test TF2B-3D

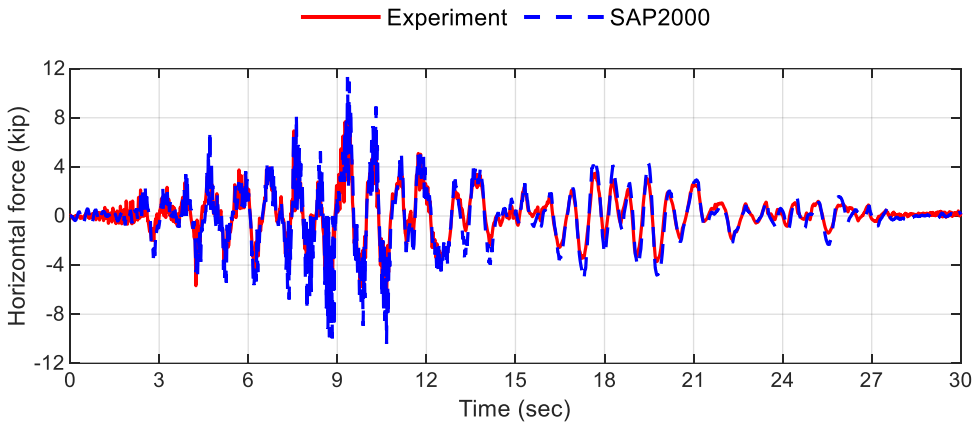

a) *x* direction

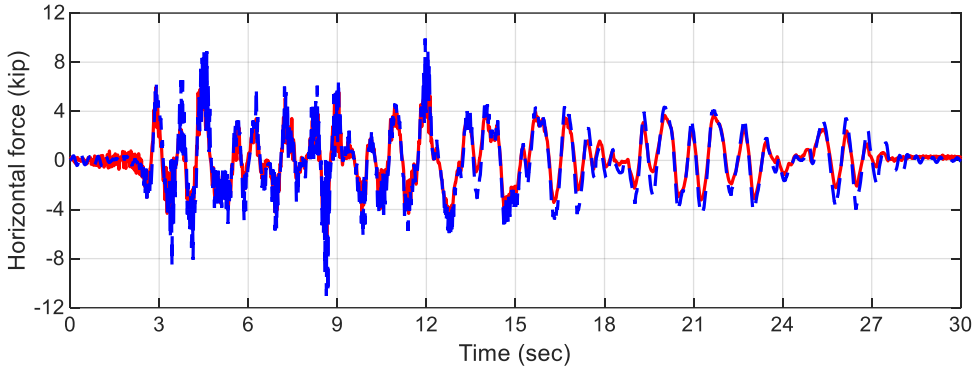

b) *y* direction

Figure 5-71. Isolation system forces, test TF2B-3D

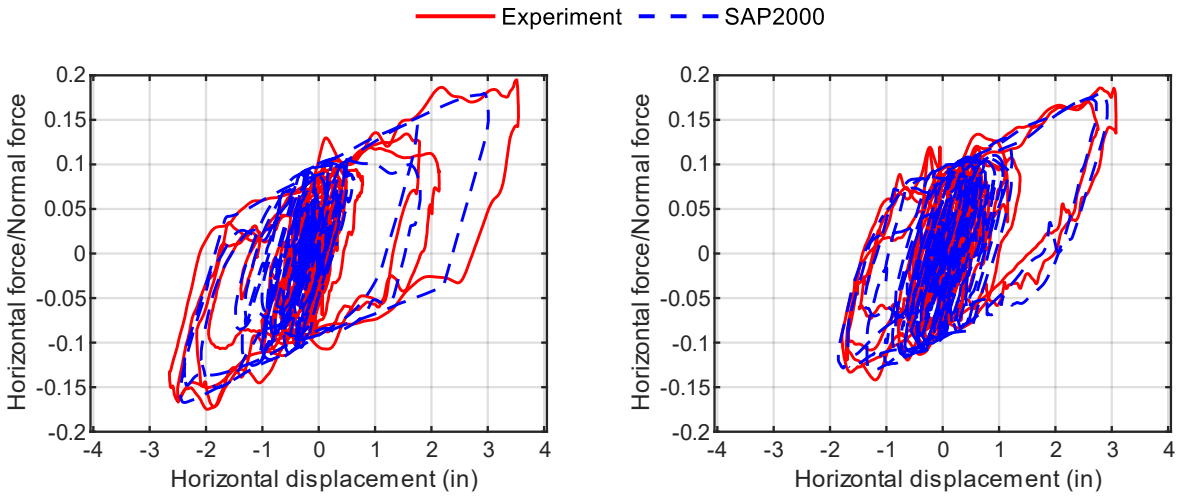

a) *x* direction

b) *y* direction

Figure 5-72. Normalized force-displacement loops for the isolation system, test TF2B-3D

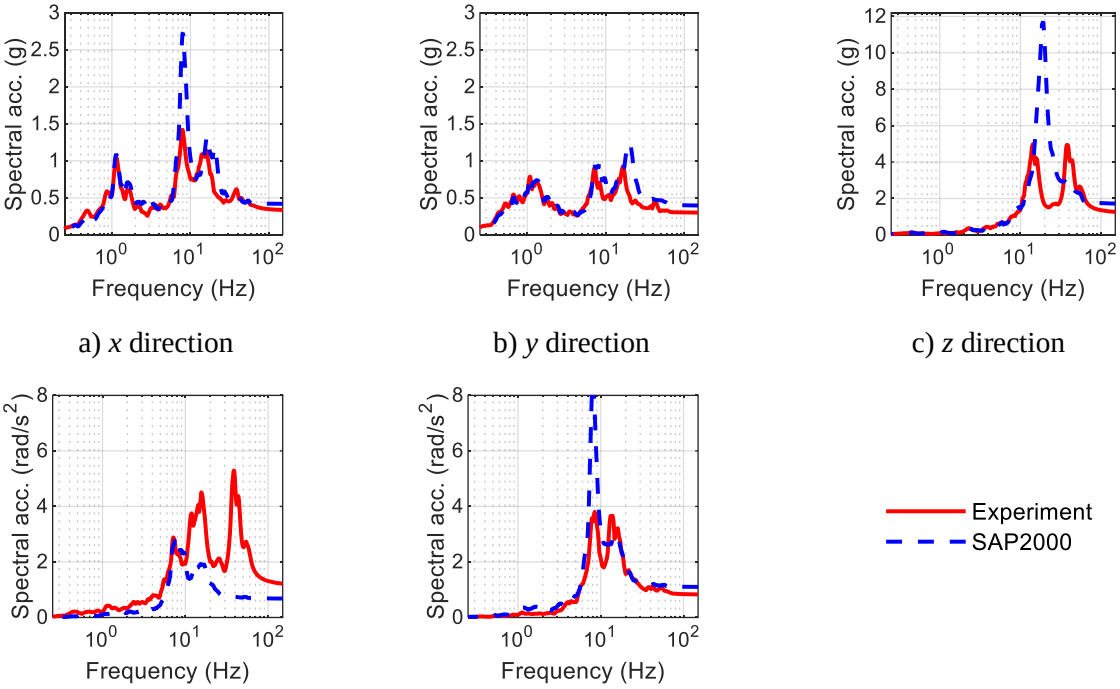

a) *x* direction b) *y* direction c) *z* direction

d) rocking about *x* axis e) rocking about *y* axis

Figure 5-73. Acceleration response spectra at the top of the vessel, test TF2B-3D

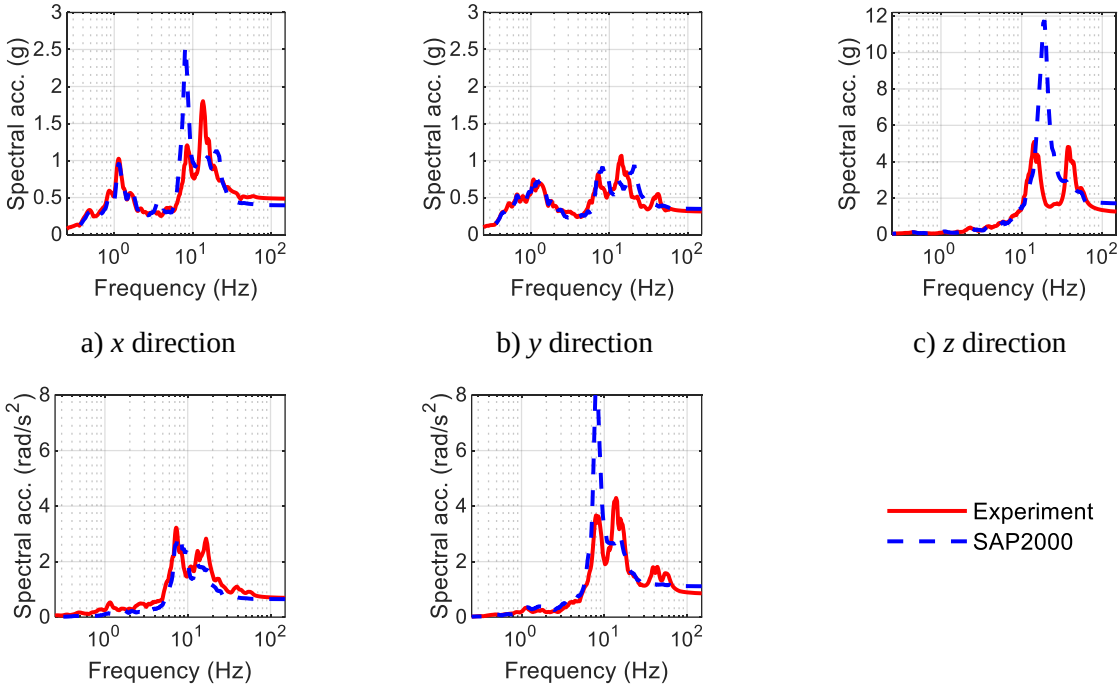

a) *x* direction b) *y* direction c) *z* direction

d) rocking about *x* axis e) rocking about *y* axis

Figure 5-74. Acceleration response spectra at the bottom of the vessel, test TF2B-3D

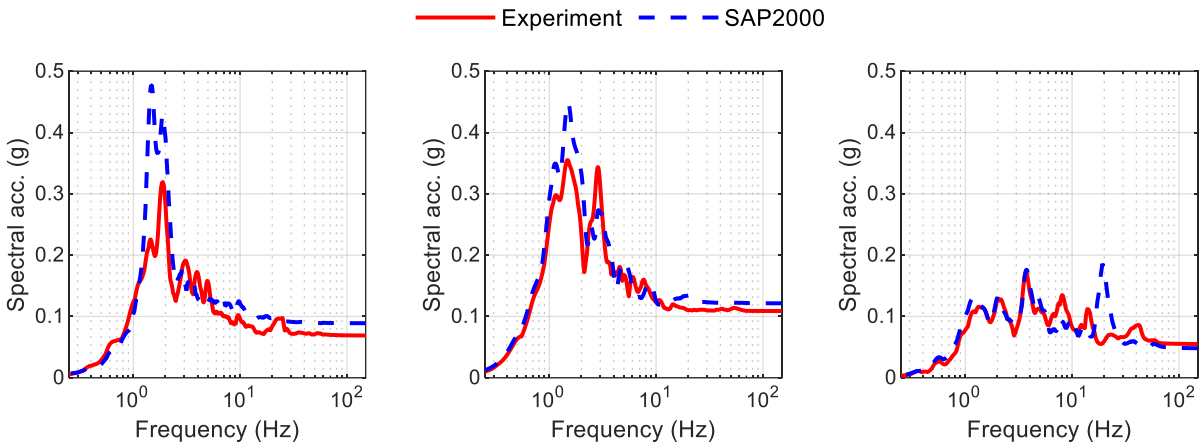

a) *x* direction b) *y* direction c) *z* direction

Figure 5-75. Acceleration response spectra directly above the isolation plane, test TF3A-3D

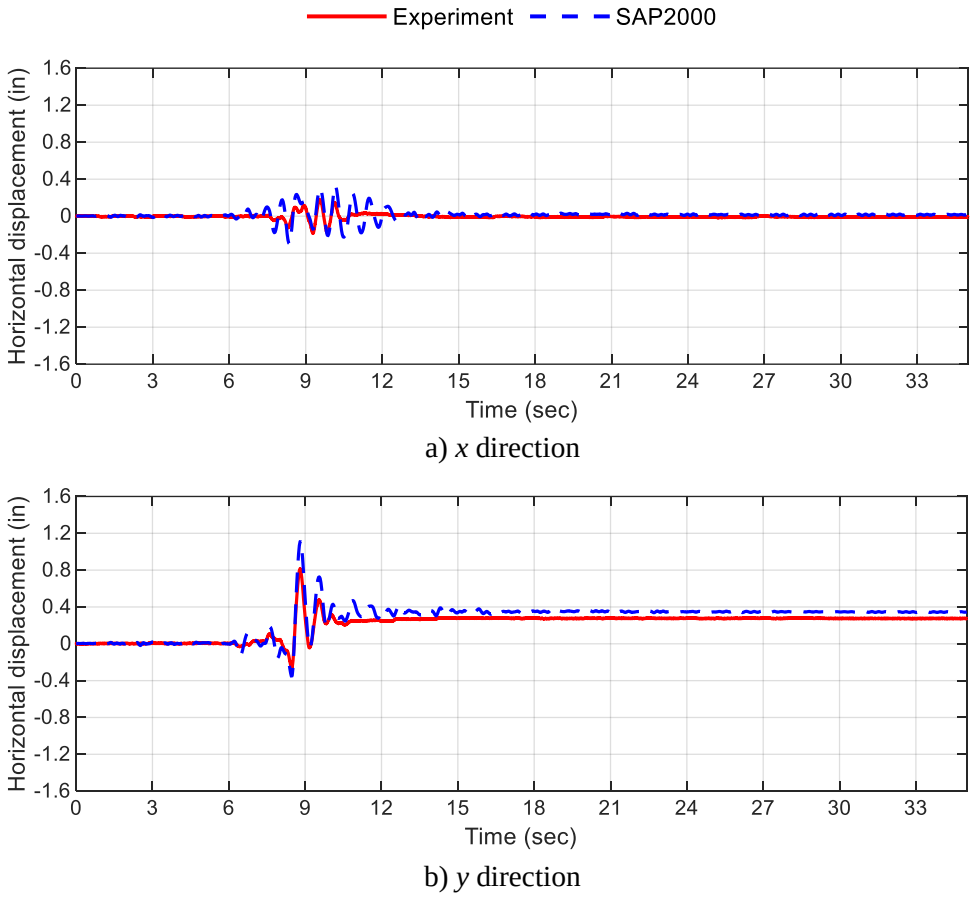

a) *x* direction

b) *y* direction

Figure 5-76. Isolation system displacements, test TF3A-3D

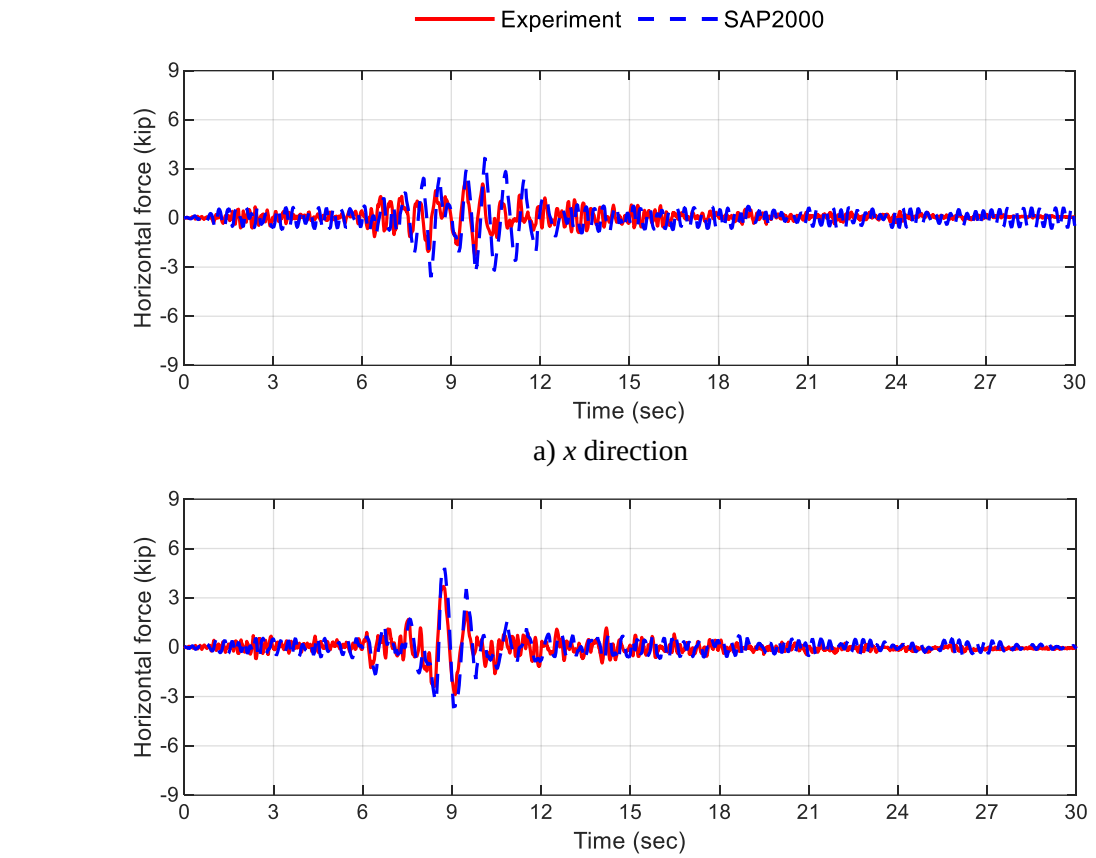

a) *x* direction

b) *y* direction

Figure 5-77. Isolation system forces, test TF3A-3D

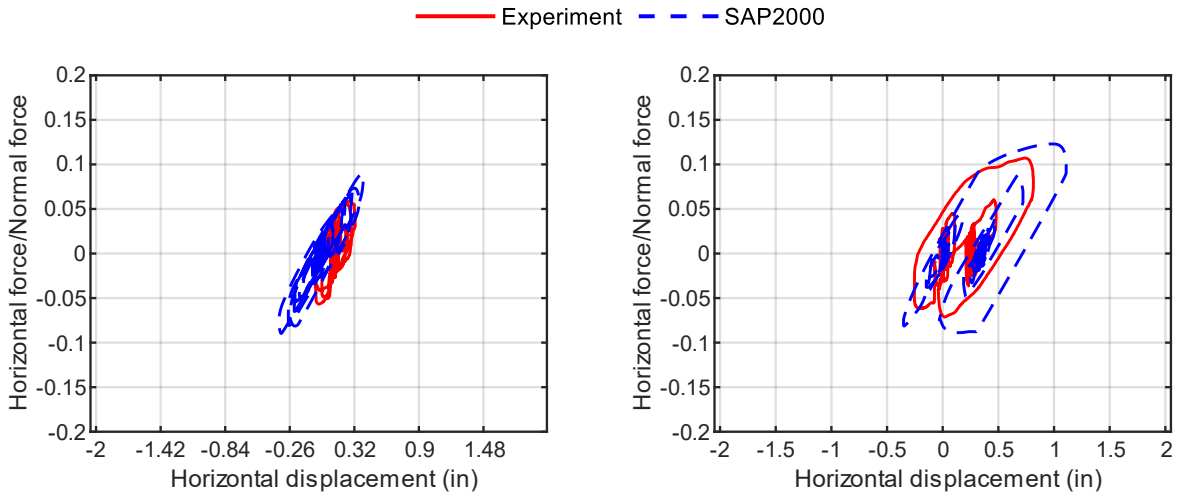

a) *x* direction

b) *y* direction

Figure 5-78. Normalized force-displacement loops for the isolation system, test TF3A-3D

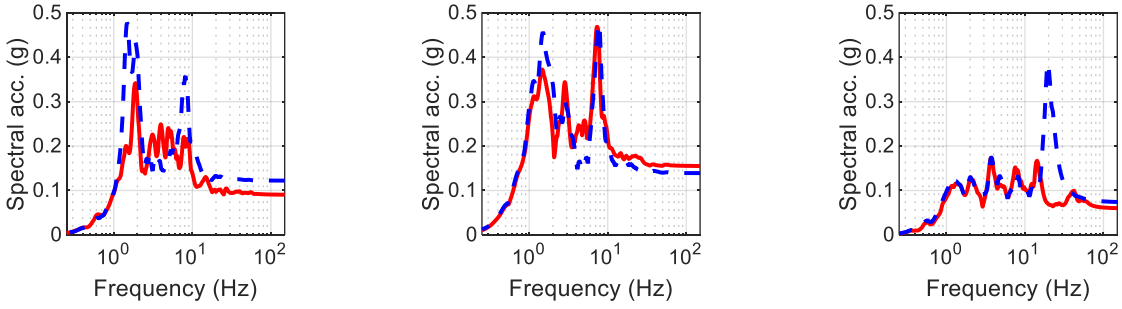

a) *x* direction b) *y* direction c) *z* direction

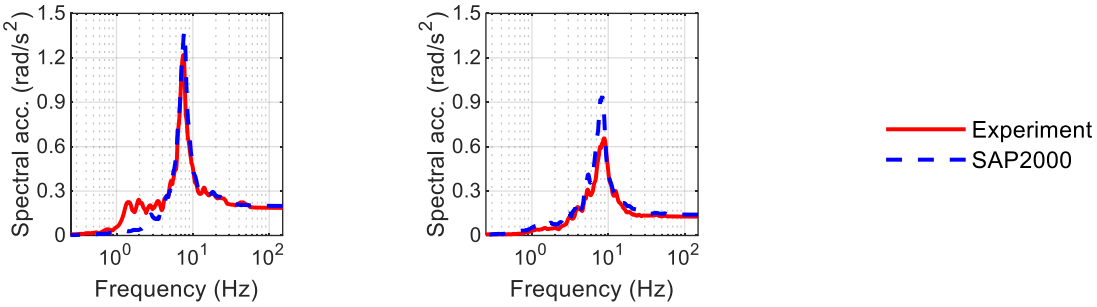

d) rocking about *x* axis e) rocking about *y* axis

Figure 5-79. Acceleration response spectra at the top of the vessel, test TF3A-3D

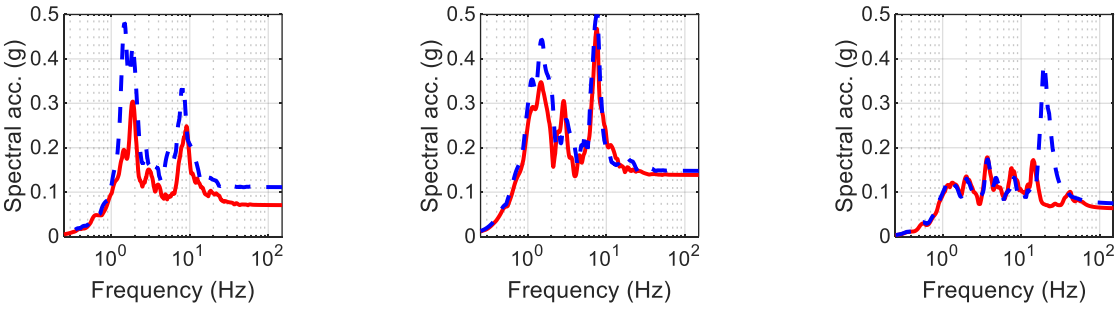

a) *x* direction b) *y* direction c) *z* direction

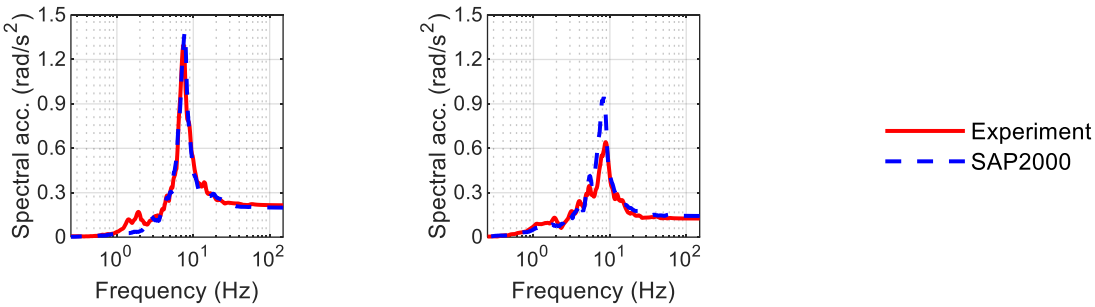

d) rocking about *x* axis e) rocking about *y* axis

Figure 5-80. Acceleration response spectra at the bottom of the vessel, test TF3A-3D

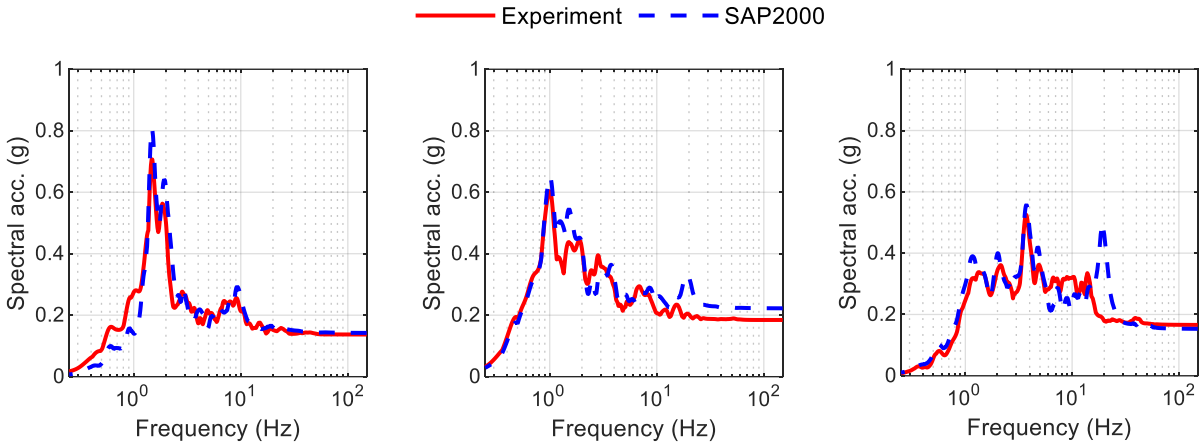

a) *x* direction b) *y* direction c) *z* direction

Figure 5-81. Acceleration response spectra directly above the isolation plane, test TF3B-3D

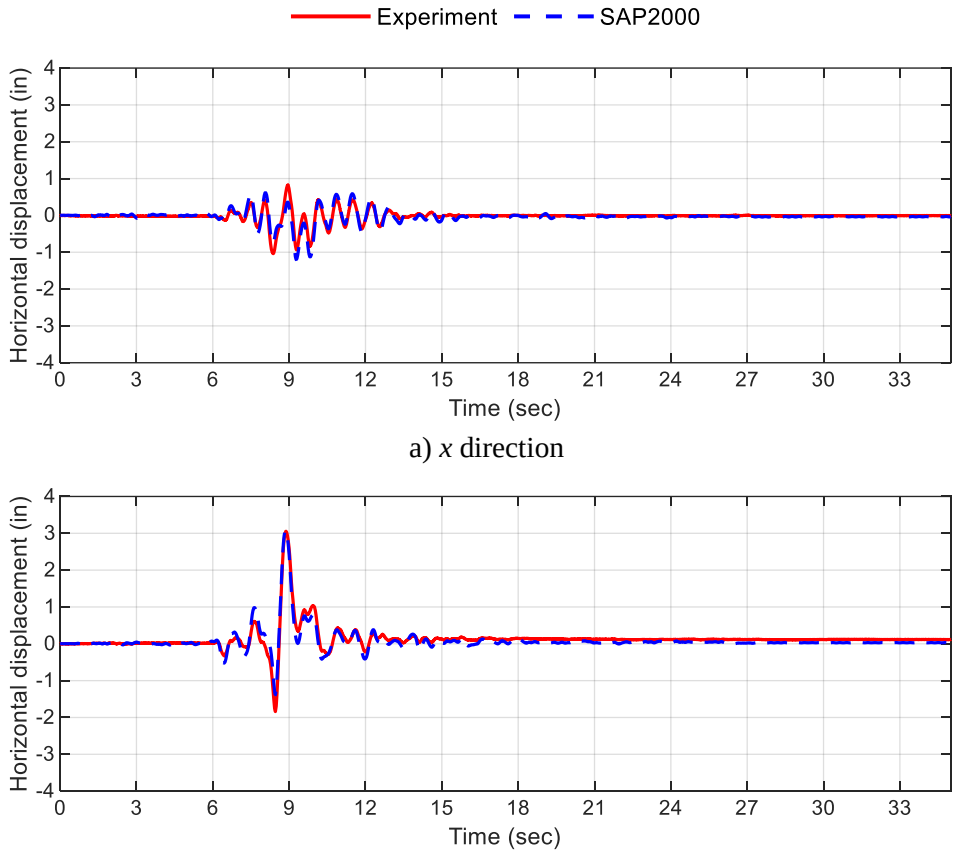

a) *x* direction

b) *y* direction

Figure 5-82. Isolation system displacements, test TF3B-3D

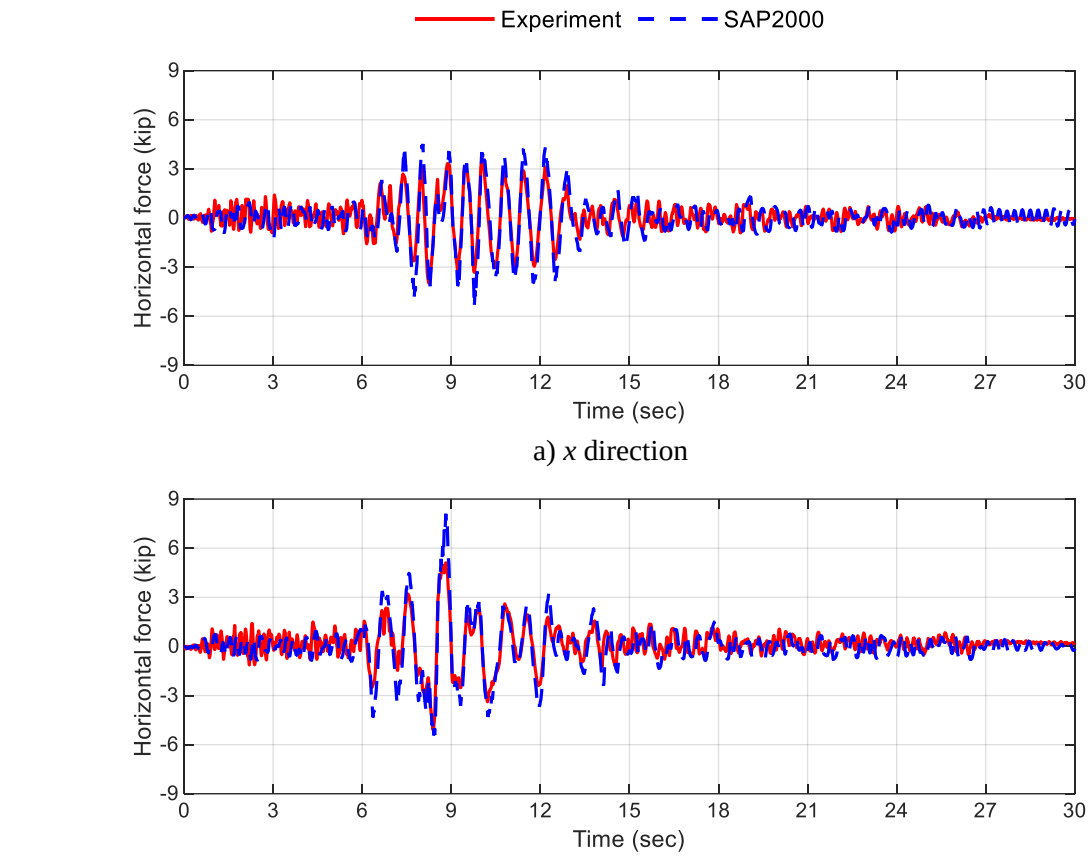

a) *x* direction

b) *y* direction

Figure 5-83. Isolation system forces, test TF3B-3D

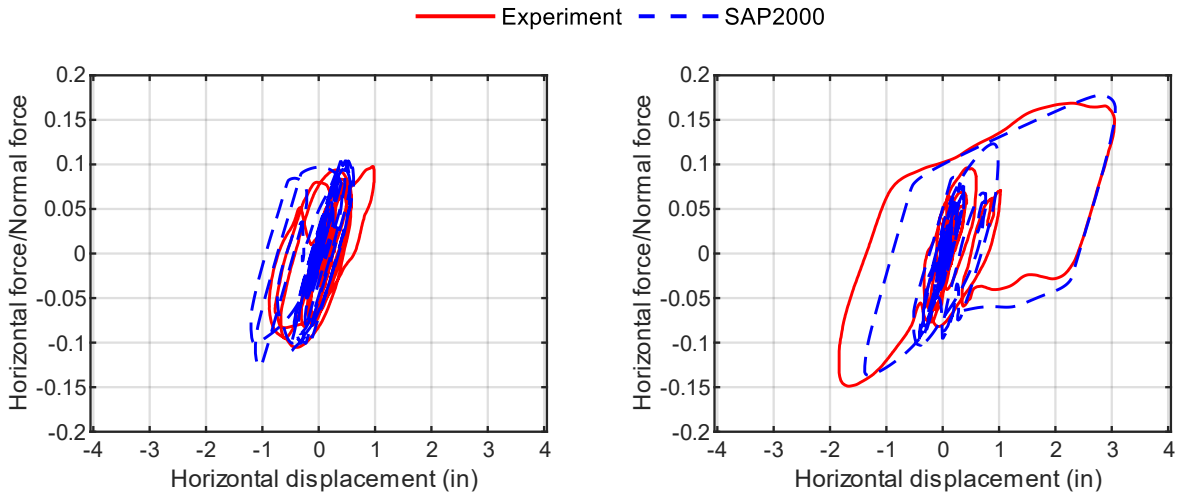

a) *x* direction

b) *y* direction

Figure 5-84. Normalized force-displacement loops for the isolation system, test TF3B-3D

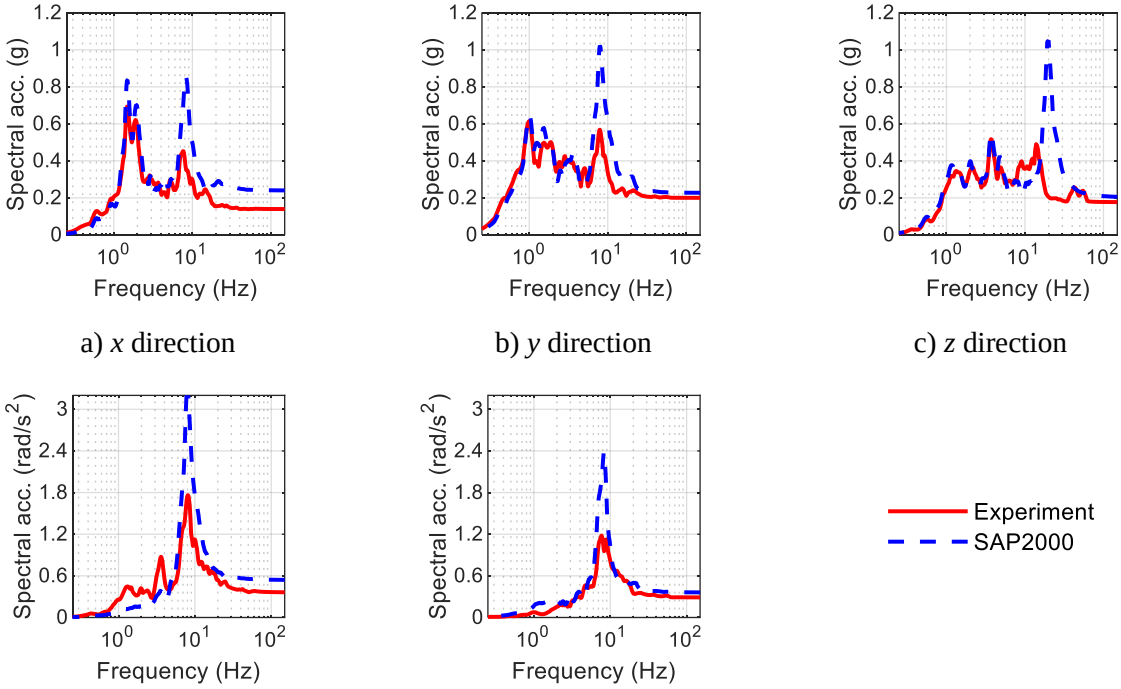

a) *x* direction b) *y* direction c) *z* direction

d) rocking about *x* axis e) rocking about *y* axis

Figure 5-85. Acceleration response spectra at the top of the vessel, test TF3B-3D

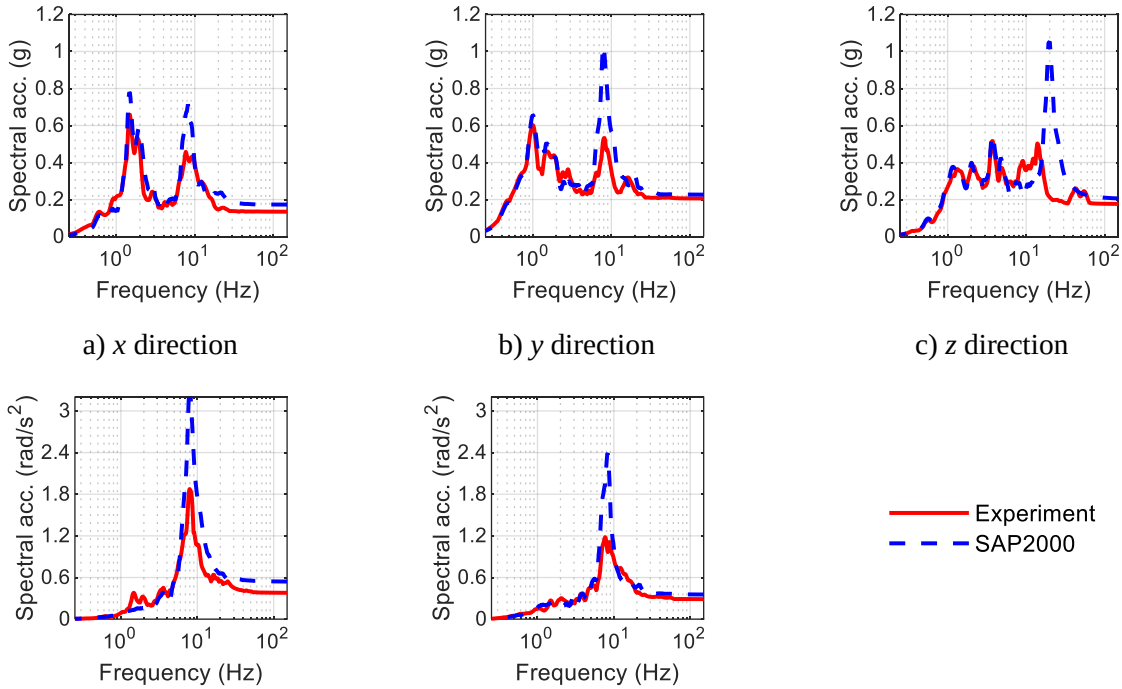

a) *x* direction b) *y* direction c) *z* direction

d) rocking about *x* axis e) rocking about *y* axis

Figure 5-86. Acceleration response spectra at the bottom of the vessel, test TF3B-3D

Table 5-7. Peak accelerations[1] (g) for the 3D tests of the TFP-isolated configuration, *x*, *y*, and *z* directions

Test		Below isolation plane			Above isolation plane			Vessel bottom			Vessel top		
		x	***y***	***z***	***x***	***y***	***z***	***x***	***y***	***z***	***x***	***y***	***z***
TF1A-3D	Experiment	0.30	0.27	0.12	0.10	0.11	0.15	0.13	0.13	0.19	0.13	0.17	0.19
	SAP2000	0.30	0.24	0.15	0.12	0.14	0.20	0.20	0.16	0.37	0.21	0.20	0.37
	Diff (%)	0	11	25	20	27	33	54	23	95	62	18	95
TF1B-3D	Experiment	0.81	0.85	0.31	0.20	0.20	0.37	0.30	0.20	0.50	0.31	0.23	0.49
	SAP2000	0.80	0.88	0.42	0.23	0.31	0.61	0.43	0.34	1.12	0.35	0.34	1.12
	Diff (%)	1	4	35	15	55	65	43	70	124	13	48	129
TF2A-3D	Experiment	0.32	0.32	0.21	0.17	0.12	0.28	0.24	0.15	0.43	0.18	0.14	0.42
	SAP2000	0.31	0.30	0.20	0.15	0.16	0.31	0.23	0.18	0.62	0.23	0.18	0.62
	Diff (%)	3	6	5	12	33	11	4	20	44	28	29	48
TF2B-3D	Experiment	1.07	0.87	0.58	0.29	0.22	0.70	0.48	0.31	1.20	0.33	0.30	1.21
	SAP2000	0.90	0.81	0.53	0.30	0.26	1.12	0.39	0.35	1.69	0.42	0.39	1.70
	Diff (%)	16	7	9	3	18	60	19	13	41	27	30	40
TF3A-3D	Experiment	0.11	0.18	0.05	0.07	0.11	0.05	0.07	0.14	0.06	0.09	0.15	0.06
	SAP2000	0.10	0.16	0.04	0.09	0.12	0.05	0.11	0.15	0.07	0.12	0.14	0.07
	Diff (%)	9	11	20	29	9	0	57	7	17	33	7	17
TF3B-3D	Experiment	0.24	0.56	0.14	0.14	0.18	0.17	0.13	0.21	0.18	0.14	0.20	0.18
	SAP2000	0.24	0.52	0.15	0.14	0.22	0.15	0.17	0.23	0.20	0.21	0.23	0.20
	Diff (%)	0	7	7	0	22	12	31	10	11	50	15	11

1. Peak acceleration calculated as spectral acceleration at 100 Hz

Table 5-8. Peak isolator displacements and normalized forces for the 3D tests of the TFP-isolated configuration

		Displacement (in)		Normalized force	
Test		***x* direction**	***y* direction**	***x* direction**	***y* direction**
	Experiment	0.4	0.5	0.07	0.09
TF1A-3D	SAP2000	0.5	0.6	0.10	0.10
	Diff (%)	25	20	43	11
	Experiment	2.1	1.9	0.14	0.13
TF1B-3D	SAP2000	1.9	2.0	0.15	0.15
	Diff (%)	10	5	7	15
	Experiment	1.4	0.7	0.13	0.10
TF2A-3D	SAP2000	1.3	0.9	0.12	0.12
	Diff (%)	7	29	8	20
	Experiment	3.5	2.9	0.19	0.19
TF2B-3D	SAP2000	3.0	2.9	0.18	0.18
	Diff (%)	14	0	5	5
	Experiment	0.2	0.8	0.06	0.11
TF3A-3D	SAP2000	0.3	1.1	0.09	0.12
	Diff (%)	50	38	50	9
	Experiment	1.0	3.1	0.11	0.17
TF3B-3D	SAP2000	1.1	3.1	0.13	0.18
	Diff (%)	10	0	18	6

5.3.5 Summary and discussion

The results in Section 5.3.2, 5.3.3, and 5.3.4 above demonstrate that the behavior of a mid-height isolated vessel and its isolation system is predictable. The predicted acceleration response of the vessel in the two horizontal directions was in good agreement with the test data for the non-isolated, SFP-isolated, and TFP-configurations, with an average difference in the peak values of 13% (range: 0% to 35%), 15% (range: 0% to 57%), and 21% (range: 0% to 70%), respectively. The rocking response of the vessel was also captured well by the numerical models. The larger differences in the vertical acceleration response were due to the differences in the predicted and measured vertical mode frequencies. The predicted normalized force-displacement loops of the isolation systems were in excellent agreement with the experimental data for the larger amplitude motions.

The error thresholds for validation of a numerical model are problem- and response-specific (Doulgerakis *et al.*, 2021). Ipek *et al.* (2021) presents a validation exercise for a seismically isolated six-story building model tested on an earthquake simulator using unidirectional inputs. Differences of 35% and 65% of the recorded response were reported for the numerically predicted peak isolator displacements and floor accelerations, respectively. Given the complexity of the test specimen herein and the use of 3D seismic inputs (and the rocking of the earthquake-simulator platform, see Section 4), the numerical models are considered benchmarked and are utilized next to investigate the utility and quantify the benefits of mid-height seismic isolation.

5.4 Investigating the utility and quantifying the benefits of mid-seismic isolation

5.4.1 Introduction

A qualitative comparison of the responses in the non-isolated and isolated configurations of the tall, slender vessel of Section 4 demonstrated the feasibility of mid-height seismic isolation. In this section, the numerical models of Section 5.2 are used to perform response-history analyses to further investigate the utility of mid-height seismic isolation and to quantify its benefits. Various stiffnesses for the support frame of the vessel, isolation system properties, and ground motions were considered to answer the following three questions:

1. Is mid-height seismic isolation feasible and beneficial if the support frame of the vessel is stiff or flexible?
2. Is mid-height seismic isolation beneficial for a range of isolation-system properties and seismic inputs?
3. Are more onerous testing requirements needed for seismic isolators used for equipment protection?

5.4.2 Support structure stiffnesses

Two support conditions were considered for the vessel by modifying the stiffness of the frame of Figure 5-1 in SAP2000:

1. *Near rigid*, achieved by increasing the elastic modulus of the frame material by a factor of 10, to model a piece of equipment supported on or near the basemat of a reactor building, wherein the ground motions are not (significantly) filtered by the building response and the seismic inputs at the points of attachment of equipment are broad banded.
2. *Flexible*, achieved by reducing elastic modulus of the frame material by a factor of 4, to model a piece of equipment supported above the basemat of a reactor building, wherein the ground motions from the basemat to the point of attachment of the equipment are amplified and filtered by the building response and the seismic inputs (for the equipment) are narrow banded, with spectral peaks near the modal frequencies of the building. (See for example the HTGR building in Figure 4 of Parsi *et al.* (2022) where the steam generator and the reactor vessel are supported on a floor slab approximately 40 ft above the basemat.)

5.4.3 Isolation systems

Six isolation systems (IS) were utilized for the study, all consisting of SFP bearings but with different isolation periods and coefficients of friction, with the properties listed in Table 5-9. At the assumed model length scale of 0.5 for the cylindrical vessel herein, isolation periods of 1.06, 1.5, and 2.12 seconds were considered. (At the prototype scale, these would correspond to isolation periods of 1.5, 2.12, and 3 seconds, respectively.) A more flexible isolation system (with a larger isolation period) generally enables a larger reduction in accelerations, but the tradeoff is larger displacements in the bearings and on umbilical lines crossing the isolation interface. This is discussed in more detail in Section 5.4.6.3. Coefficients of friction of 6% and 10% were utilized: representing values achieved with different axial pressures on the articulated slider. (See Constantinou *et al.* (2007) or Kumar *et al.* (2019a) for a discussion of the relationship between coefficient of friction and axial pressure on a Friction Pendulum bearing.)

Table 5-9. Isolation system properties

	Sliding period[1]	Radius of curvature (R) [1,2]	Coefficient of friction		Axial stiffness[3,4]
			μ_{max}	μ_{min}	
IS1	1.06 second	11 inches	0.06	0.03	3075 kip/in^2
IS2	1.06 second	11 inches	0.10	0.05	
IS3	1.5 second	22 inches	0.06	0.03	
IS4	1.5 second	22 inches	0.10	0.05	
IS5	2.12 second	44 inches	0.06	0.03	
IS6	2.12 second	44 inches	0.10	0.05	

1. At the assumed model length scale of 0.5
2. The SFP bearings and its sliders were assumed to be of the same height and diameter, respectively, as those in Section 3, for which the effective radius of curvature (R_{eff}) was equal to the radius of curvature (R)
3. The axial stiffness of Friction Pendulum bearings must be modeled and should be characterized experimentally, see Section 3
4. The axial stiffness was assumed to be $0.15 \times EA / L$ (see Section 3), where E = 29,000, A = 1.77 in^2, and L = 2.5 in

5.4.4 Seismic inputs

Two ground motions having a broad range of frequency content were utilized for the response-history analyses. Ground motions with record sequence numbers (RSN) 587 and 728 were selected from the PEER NGA-West2 database and are described in Section 4.4. The time scale of all three components of the ground motions was reduced by a factor of 0.71, consistent with the assumed length scale of 0.5 for the vessel. Rotational ground motion inputs were not considered. To investigate the effectiveness of mid-height seismic isolation at different intensities of shaking, the ground motions were amplitude scaled to have geomean horizontal peak accelerations of 0.2 g, 0.4 g, and 0.6 g. Table 5-10 presents nomenclature for the six seismic inputs (2 ground motions, 3 intensities each).

Table 5-10. Nomenclature for the six seismic inputs

	Geomean horizontal PGA (g)	Vertical PGA (g)
GM1A[1]	0.20	0.11
GM1B	0.40	0.22
GM1C	0.60	0.33
GM2A[1]	0.20	0.24
GM2B	0.40	0.49
GM2C	0.60	0.73

1. GM1 is RSN 587; GM2 is RSN 728

5.4.5 Modal analysis

Analysis of the isolated and non-isolated configurations was performed to determine the modal frequencies of the vessel supported on the *flexible* and *rigid* frames. Table 5-11 lists the modal frequencies.

5.4.6 Response-history analyses

5.4.6.1 Introduction

Response-history analyses were performed for the non-isolated and isolated configurations of the vessel using the numerical models of Section 5.2. A total of 84 cases were analyzed: 12 for the non-isolated

configuration (2 support conditions, 6 seismic inputs) and 72 for the isolated vessel (2 support conditions, 6 isolation systems, 6 seismic inputs). The results extracted from the analyses include:

1. Acceleration histories at the top of the support frame on the north-east side. See location *F1* marked by the solid pink circle in Figure 5-87.
2. Acceleration histories at the top (location *V3*) and the bottom (location *V2*) of the vessel on the north face and at the mid-height of the vessel (location *V1*) on the north-east side.
3. Displacement histories for the SFP bearings. Identical displacement histories were obtained for the three isolator links; the *x*- and *y*-direction histories for the north-east link were utilized.

Table 5-11. Modal analysis results for the isolated and non-isolated configurations (Hz)

	Non-isolated		**Isolated**	
	***Rigid* frame**	***Flexible* frame**	***Rigid* frame**	***Flexible* frame**
Rocking of vessel (about *x* and *y* axes)	12.4	8.3	9.5[1]	7.4[1]
Horizontal modes (*x* and *y* directions)	26	9.6	0.47/0.66/0.94[2]	0.47/0.66/0.94[2]
Vertical mode (*z* direction)	33	21	22.5[1]	17.5[1]

1. These values are lower than the corresponding frequencies in the non-isolated configuration due to the added vertical flexibility from the SFP bearings (see Section 4)
2. Corresponds to the isolated modes of the vessel with isolation periods of 2.12, 1.5, and 1.06 seconds

5.4.6.2 Maximum isolation-system displacements

Table 5-12 presents maximum horizontal isolation-system displacements, calculated as a vector sum, time step by time step. The displacements in the cells highlighted in red in the table cannot be realized. Consider seismic input GM2C, and IS1 and IS2, which correspond to isolation systems with a radius of curvature of 11 inches.

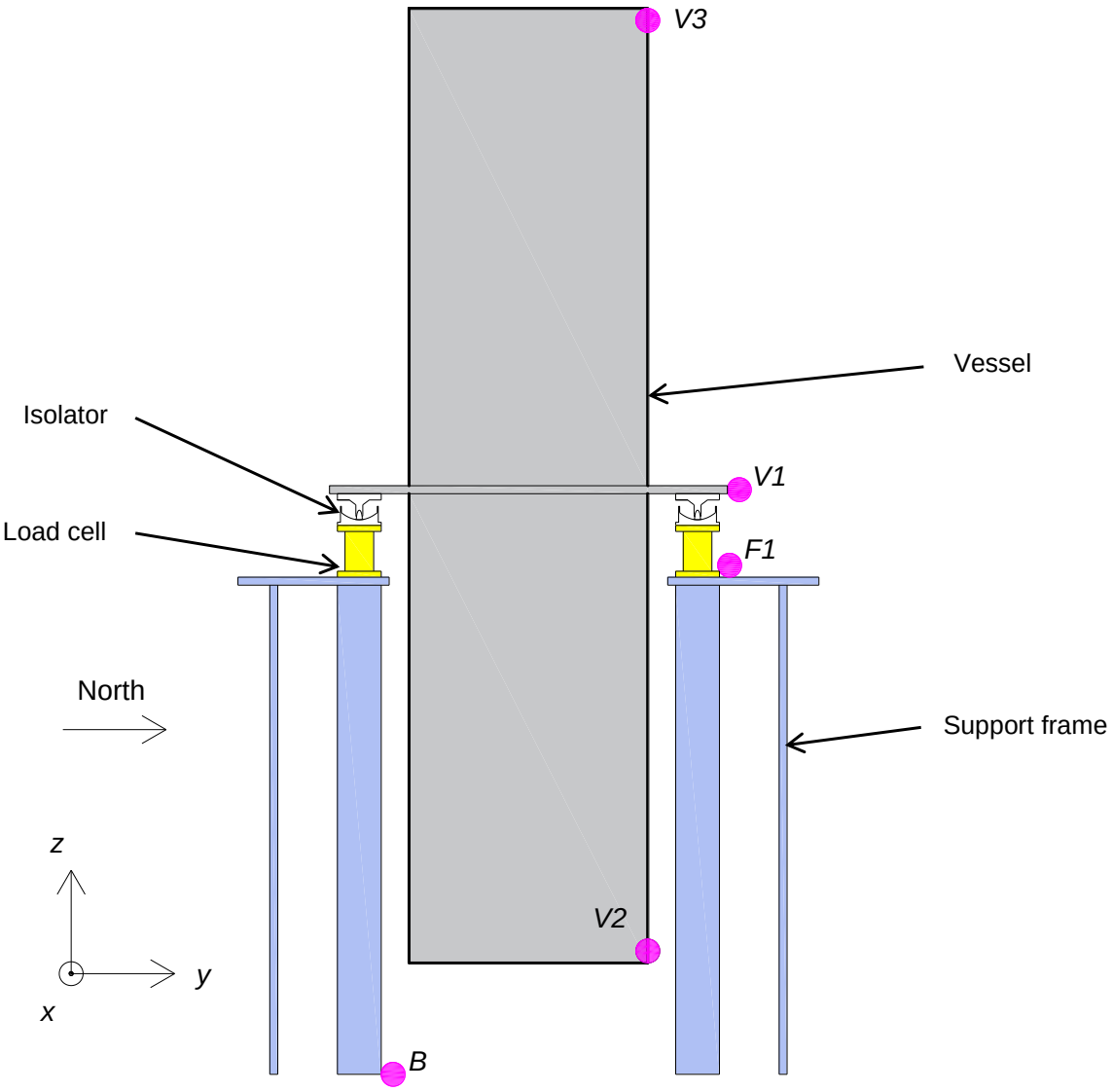

Figure 5-87. Locations for extracting results from response-history analyses

Table 5-12. Peak isolation-system displacements

Isolation system	Support frame	GM1A	GM1B	GM1C	GM2A	GM2B	GM2C
IS1	*Rigid*	0.5	1.4	3.6[1]	2.0	7.0	12.5[2]
	Flexible	0.5	1.4	3.6	2.0	7.0	12.7
IS2	*Rigid*	0.3	1.0	2.0	0.7	4.6	9.7
	Flexible	0.2	1.0	1.9	0.6	4.8	10.0
IS3	*Rigid*	0.5	1.5	2.9	1.3	4.2	8.0
	Flexible	0.5	1.4	2.9	1.3	4.2	8.0
IS4	*Rigid*	0.3	1.1	2.0	0.9	2.8	5.9
	Flexible	0.2	1.1	2.0	0.8	2.8	5.9
IS5	*Rigid*	0.6	1.7	3.1	1.6	4.6	11.7
	Flexible	0.5	1.7	3.1	1.5	4.6	11.7
IS6	*Rigid*	0.3	1.4	2.5	1.1	3.6	6.6
	Flexible	0.3	1.3	2.4	1.0	3.5	6.6

1. Displacements in the cells highlighted in yellow exceed the *soft* limit of 0.2*R*; see Appendix C.
2. Displacements in the cells highlighted in red cannot be realized.

It is not physically possible to achieve the horizontal displacements of 12.4, 12.7, 9.7, and 10 inches (the cells highlighted in red) for an isolation system with an 11-inch radius of curvature[1,2].

Horizontal displacement of the slider in an SFP bearing is accompanied by its vertical displacement (i.e., increase in bearing height) and acceleration. A reasonable *soft* limit on the maximum horizontal displacement in an SFP isolator is 0.2*R*. Although SAP2000 does not calculate the increase in bearing height, capping the horizontal displacement at 0.2*R* limits the vertical displacement of the slider and the corresponding accelerations. See Appendix C. The cells highlighted in yellow in Table 5-12 identify maximum isolation-system displacement greater than 0.2*R*. The next section presents computed accelerations at the top and the bottom of the vessel for all combinations listed in Table 5-12 except for the cases highlighted in red and yellow.

5.4.6.3 Acceleration response at the top and the bottom of the vessel

To answer the first question of Section 5.4.1, acceleration response spectra at the top of the isolated vessel[3] (location *V3* in Figure 5-87) are plotted for IS1 through IS6 for GM1B[4] in Figures 5-88 through 5-93 and IS3 through IS6 for GM2B[2] in Figures 5-94 through 5-97. The corresponding acceleration spectra for the non-isolated vessel are plotted in Figures 5-98 and 5-99. Tables 5-13 through 5-18 present the peak accelerations (spectral acceleration at 100 Hz) at the top and the bottom of the vessel (location *V2*) for the non-isolated and isolated configurations for the six seismic inputs of Section 5.4.4.

In the non-isolated configuration, the horizontal response of the vessel at its top is significantly greater when supported on the *flexible* frame: compare the red and green dashed lines in panels a and b of Figures 5-98 and 5-99. The peak horizontal accelerations at the top and the bottom of the non-isolated vessel supported on the *flexible* frame are greater by a factor of between 1.8 and 4.1 compared to those for the *rigid* frame. The seismic inputs are significantly amplified by the support frame (from location *B* to *F1*)

---

[1] Although it is physically not possible to achieve these displacements in IS1 and IS2, SAP2000 executes the response-history analyses for these cases as it does not limit horizontal isolator displacements based on the geometry (radius of curvature) of an SFP bearing.

[2] The larger peak horizontal displacements in the stiffest (1.06 second) isolation systems (IS1 and IS2) for GM2A, GM2B, and GM2C are due to spectral shape: see the red solid and green dashed lines in Figure 4-7b.

[3] Similar trends in results were observed at the bottom of the vessel, and so only the spectra at the top are presented.

[4] Similar trends were observed for the other seismic inputs and are not presented.

when it is *flexible*, with further amplification by the vessel (from location *F1* to *V2*/*V3*). Amplification of the seismic inputs by the *rigid* support frame (from location *B* to *F1*) is negligible and is due primarily to the vessel (from location *F1* to *V2*/*V3*). The horizontal responses of the isolated vessel supported on the *flexible* and *rigid* frames are virtually identical: compare the red and green dashed lines in panels a and b of Figures 5-88 through 5-97. This observation is confirmed by analysis of a) maximum isolation-system displacements for the vessel supported on the *flexible* and *rigid* frames presented in Table 5-12 (in Section 5.4.6.2), and b) peak horizontal accelerations at the top and the bottom of the isolated vessel in Tables 5-13 through 5-18. This outcome is expected because the flexibility afforded by the isolators is more than an order of magnitude greater than that of the support frames.

Mid-height seismic isolation is effective at reducing horizontal spectral accelerations in equipment with respect to their non-isolated counterparts for a range of support stiffnesses. Importantly, horizontal spectral accelerations enabled by mid-height seismic isolation are not significantly affected by the support stiffness. The seismic qualification of equipment is a significant contributor to capital cost Lal *et al.*, (2020; 2022). The response reductions afforded by mid-height isolation will simplify the qualification calculations for the vessel and its internals, assuming qualification is based primarily on analysis. Importantly, the seismic spectral demands in the isolated configuration are by-and-large independent of support configuration, meaning that the vessel could be seismically qualified once but for multiple support conditions.

The vertical response of the vessel is a function of the frequency content of the input motion and the modal frequencies of the vessel-frame system in the *z* direction. For example, in the non-isolated configuration the peak vertical accelerations at the top of the vessel for GM1A, GM1B, and GM1C are greater in the case of a *flexible* frame than for a *rigid* frame, whereas they are similar for GM2A, GM2B, and GM2C. The peaks in spectral accelerations for the non-isolated (isolated) vessel represent the vertical modes at frequencies of 21 Hz (17.5 Hz) and 33 Hz (22.5 Hz) for the *flexible* and *rigid* frames, respectively, as identified in Table 5-11.

To answer the second question of Section 5.4.1 and to quantify the benefits of mid-height isolation for the vessel studied herein, ratios of peak geomean horizontal accelerations at the top of the non-isolated vessel to those in the isolated vessel, termed as an acceleration reduction factor (ARF), are presented in Tables 5-19 (*rigid* frame) and 5-20 (*flexible* frame). The corresponding maximum isolation-system displacements are also reported. Mid-height seismic isolation can reduce horizontal spectral accelerations in equipment across a range of isolation-system properties and seismic inputs. The peak accelerations at the top of the

isolated vessel are smaller by a factor of between 1.5 and 6 (5 and 20) with respect to those on the non-isolated vessel supported on the *rigid* (*flexible*) frame. The maximum isolation-system displacements are between 0.2 inch and 6.6 inches.

For the same coefficient of friction, the ARF is generally greater for the more flexible isolation system, but the tradeoff is larger displacements in the bearings and across the isolation interface. For example, compare the ARFs and maximum isolation-system displacements for IS2 (1.06 sec, 10%) and IS6 (2.12 sec, 10%) for seismic input GM1C in Table 5-19: the ARF increased from 2.4 to 3.9 as the maximum isolator displacement increased from 1.9 inches to 2.4 inches. Although a smaller peak horizontal acceleration is beneficial for equipment design, safety-related umbilicals crossing the isolation plane will have to be designed and qualified to accommodate larger displacements.

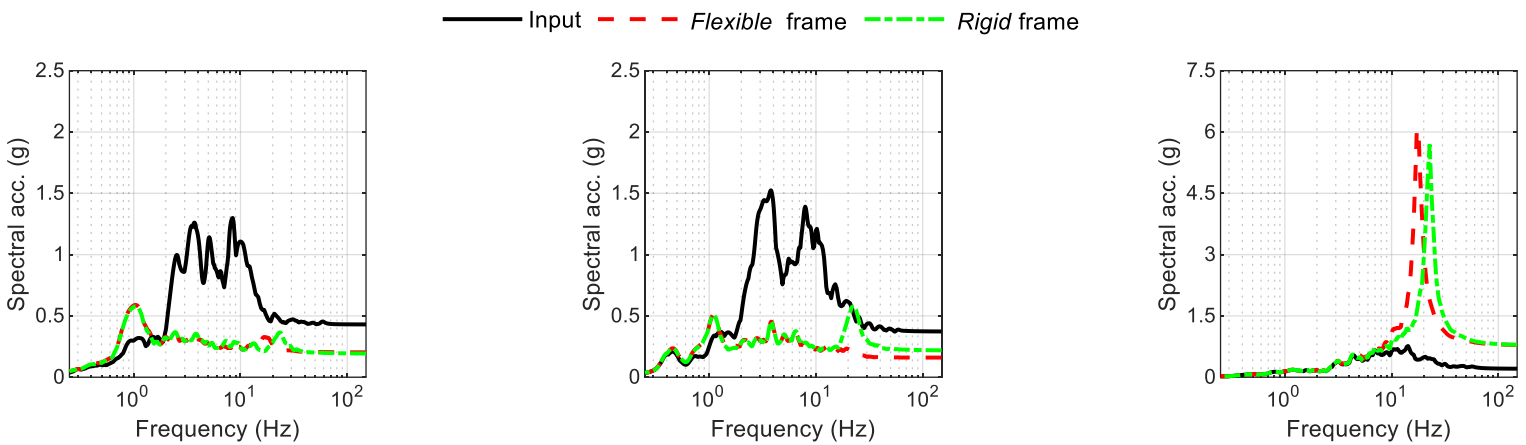

a) x direction b) y direction c) z direction

Figure 5-88. Acceleration response spectra at the top of the vessel, IS1 isolated, GM1B, 5% damping

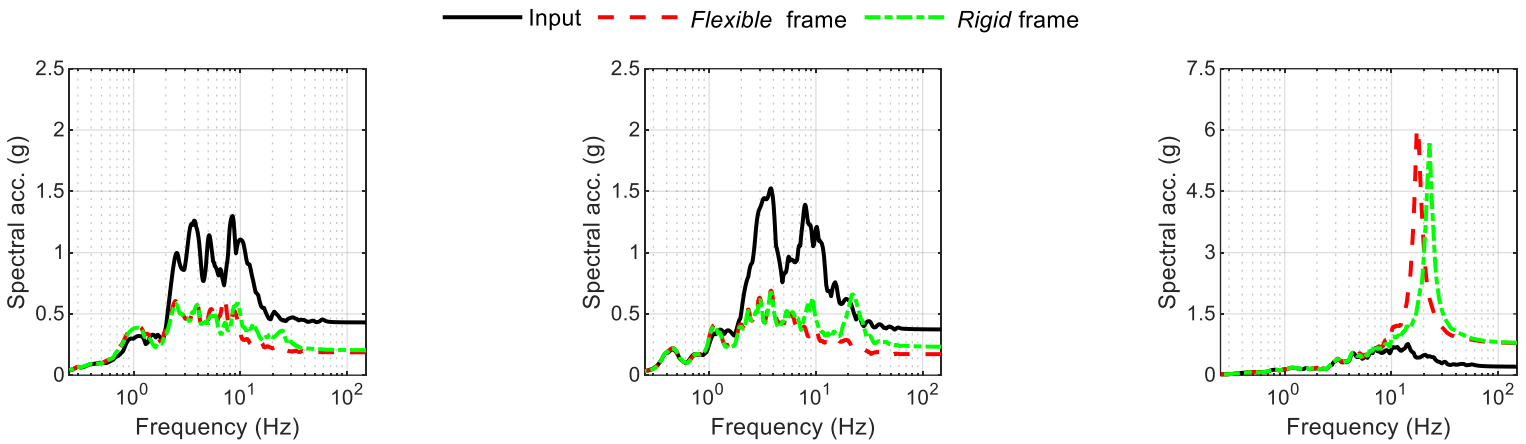

a) *x* direction b) *y* direction c) *z* direction

Figure 5-89. Acceleration response spectra at the top of the vessel, IS2 isolated, GM1B, 5% damping

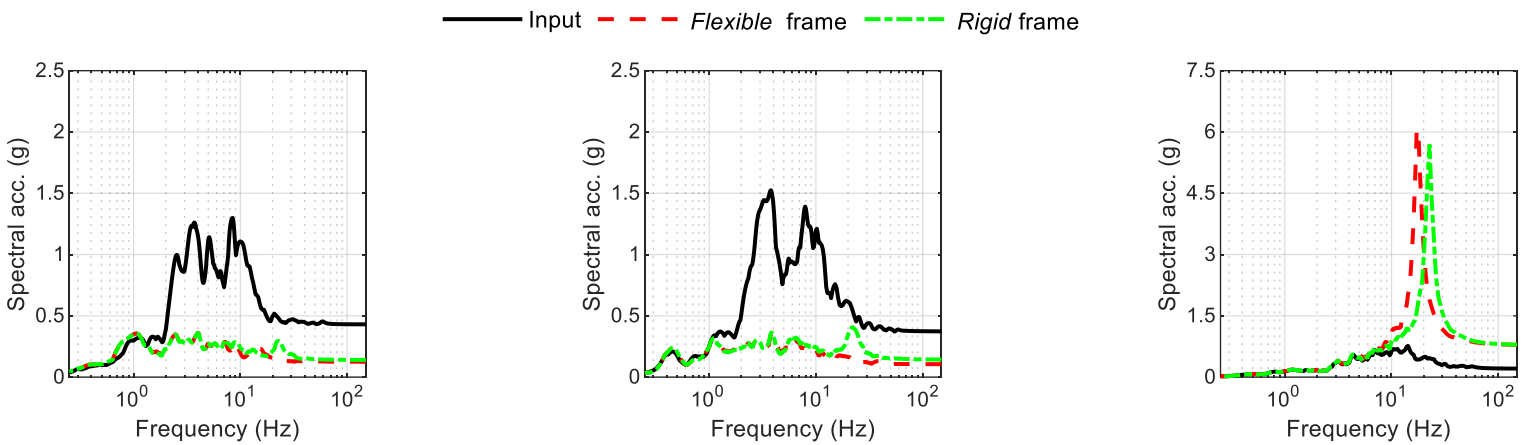

a) *x* direction b) *y* direction c) *z* direction

Figure 5-90. Acceleration response spectra at the top of the vessel, IS3 isolated, GM1B, 5% damping

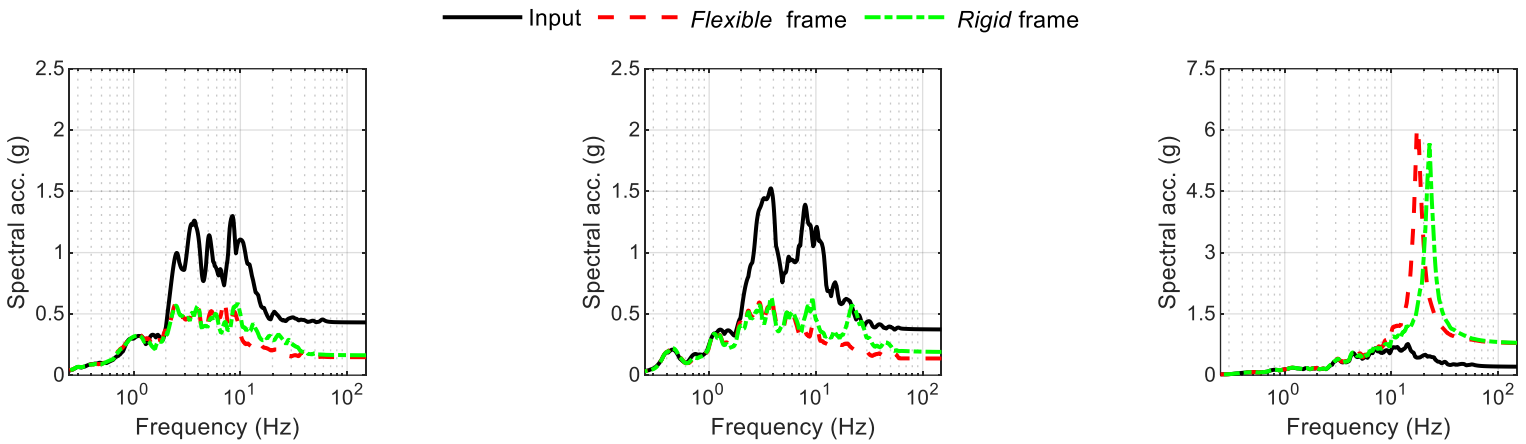

a) *x* direction b) *y* direction c) *z* direction

Figure 5-91. Acceleration response spectra at the top of the vessel, IS4 isolated, GM1B, 5% damping

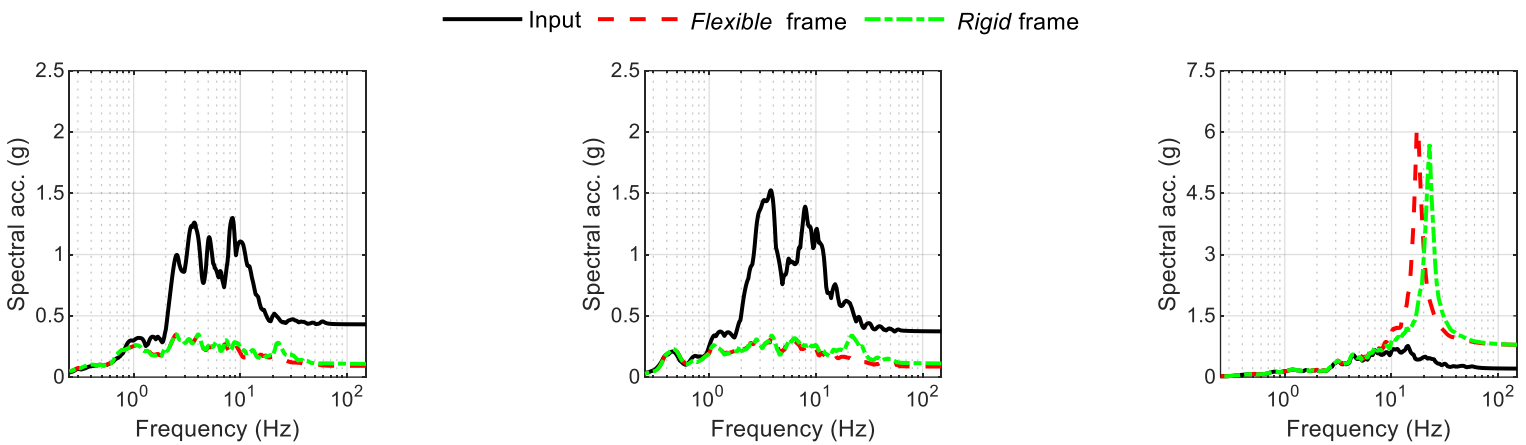

a) *x* direction b) *y* direction c) *z* direction

Figure 5-92. Acceleration response spectra at the top of the vessel, IS5 isolated, GM1B, 5% damping

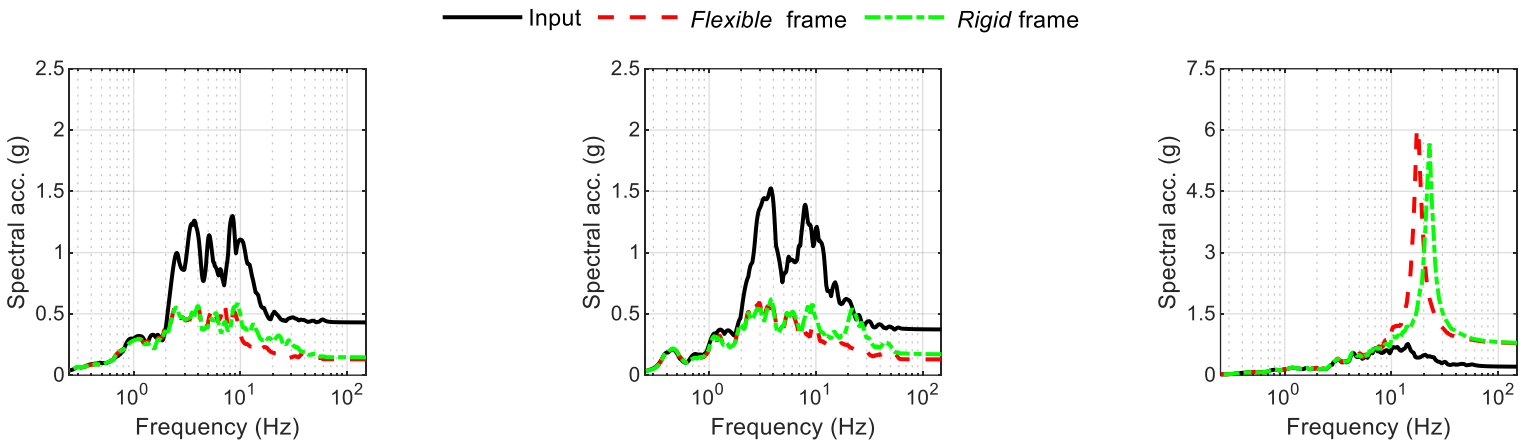

a) *x* direction b) *y* direction c) *z* direction

Figure 5-93. Acceleration response spectra at the top of the vessel, IS6 isolated, GM1B, 5% damping

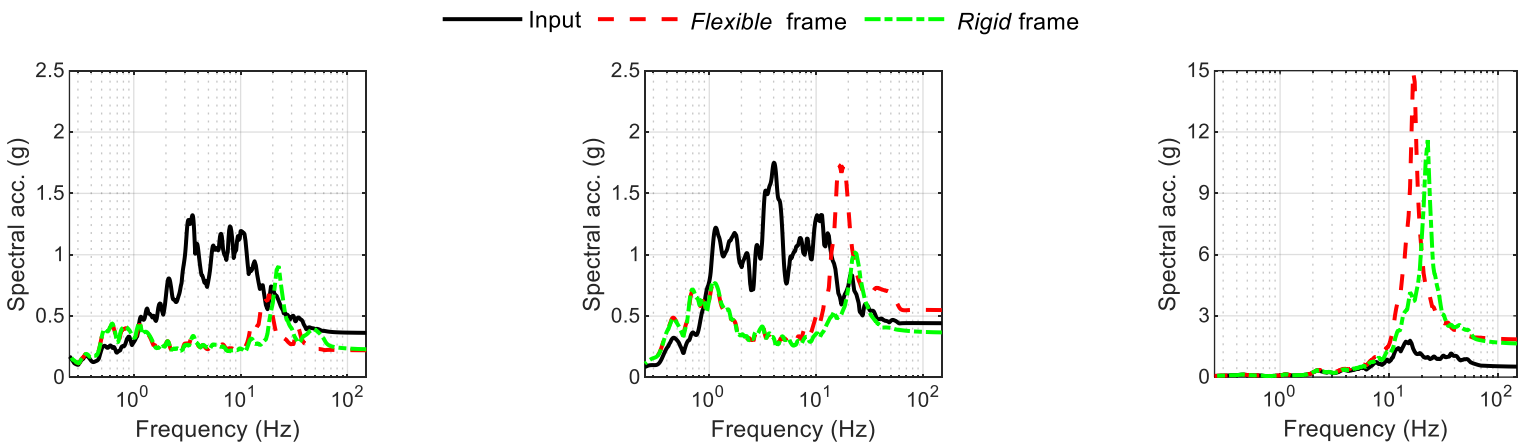

a) *x* direction b) *y* direction c) *z* direction

Figure 5-94. Acceleration response spectra at the top of the vessel, IS3 isolated, GM2B, 5% damping

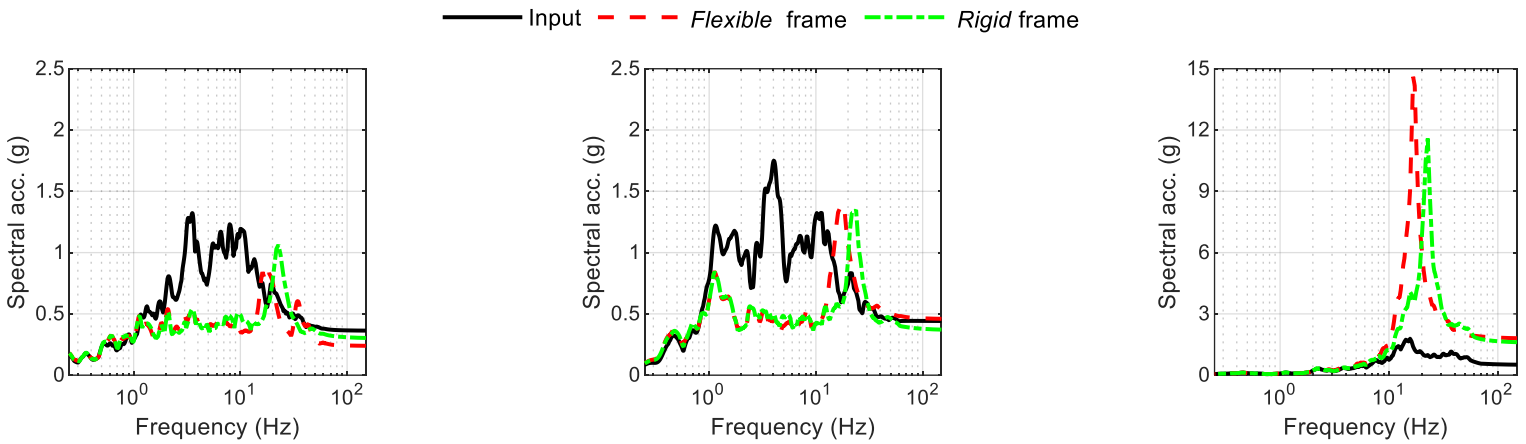

a) *x* direction b) *y* direction c) *z* direction

Figure 5-95. Acceleration response spectra at the top of the vessel, IS4 isolated, GM2B, 5% damping

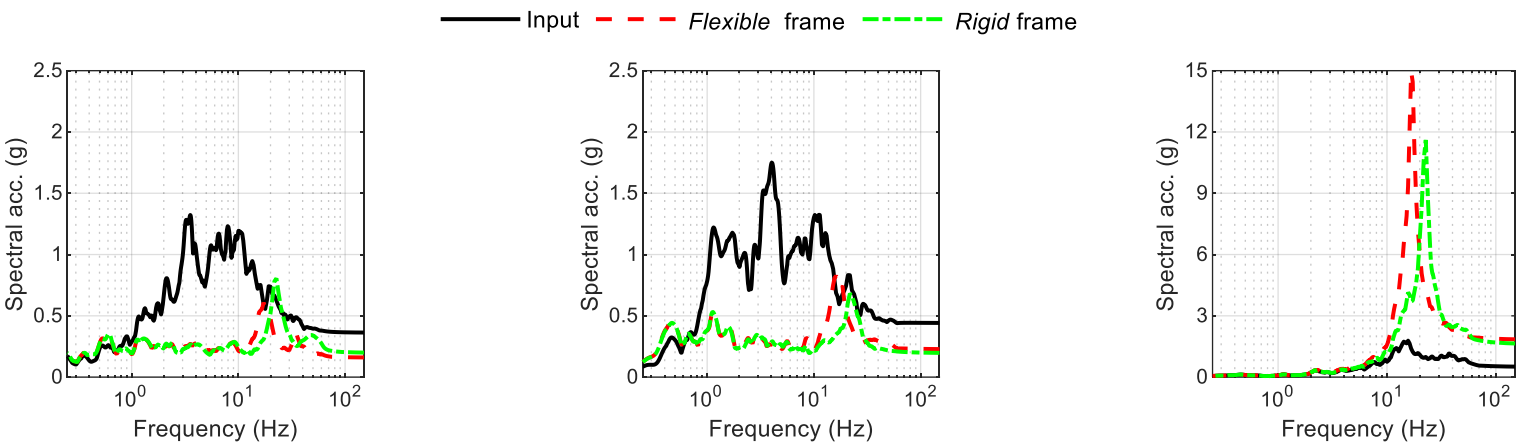

a) *x* direction b) *y* direction c) *z* direction

Figure 5-96. Acceleration response spectra at the top of the vessel, IS5 isolated, GM2B, 5% damping

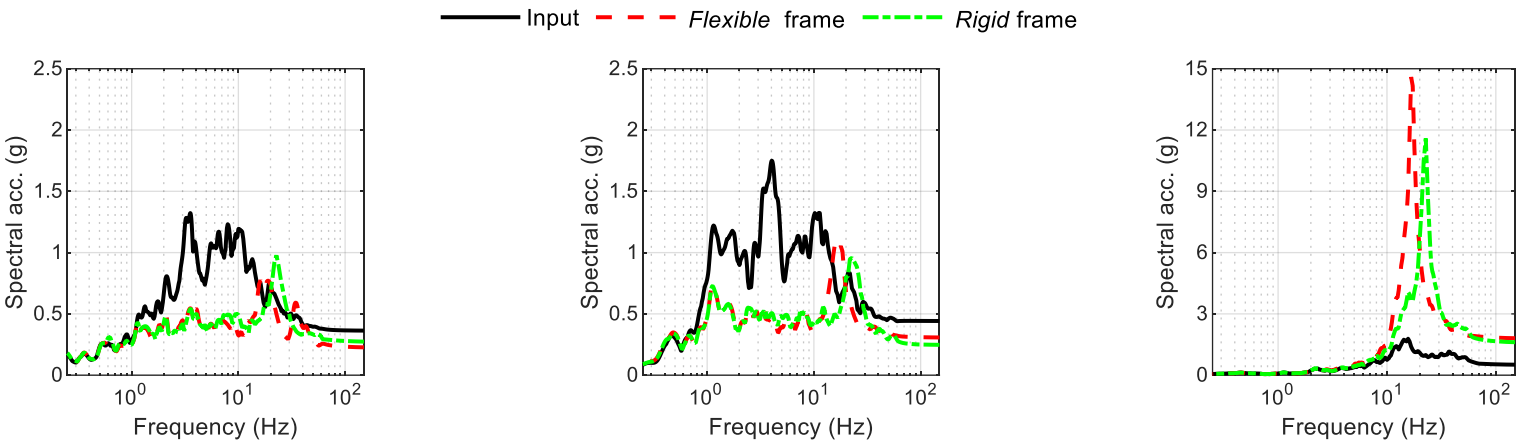

a) *x* direction b) *y* direction c) *z* direction

Figure 5-97. Acceleration response spectra at the top of the vessel, IS6 isolated, GM2B, 5% damping

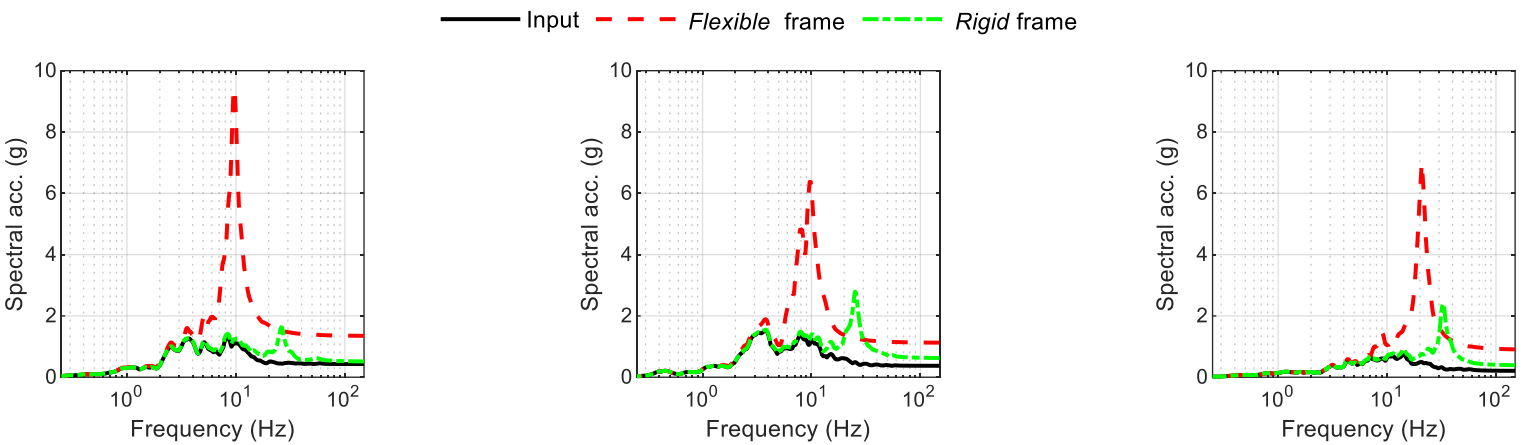

a) *x* direction b) *y* direction c) *z* direction

Figure 5-98. Acceleration response spectra at the top of the vessel, non-isolated, GM1B, 5% damping

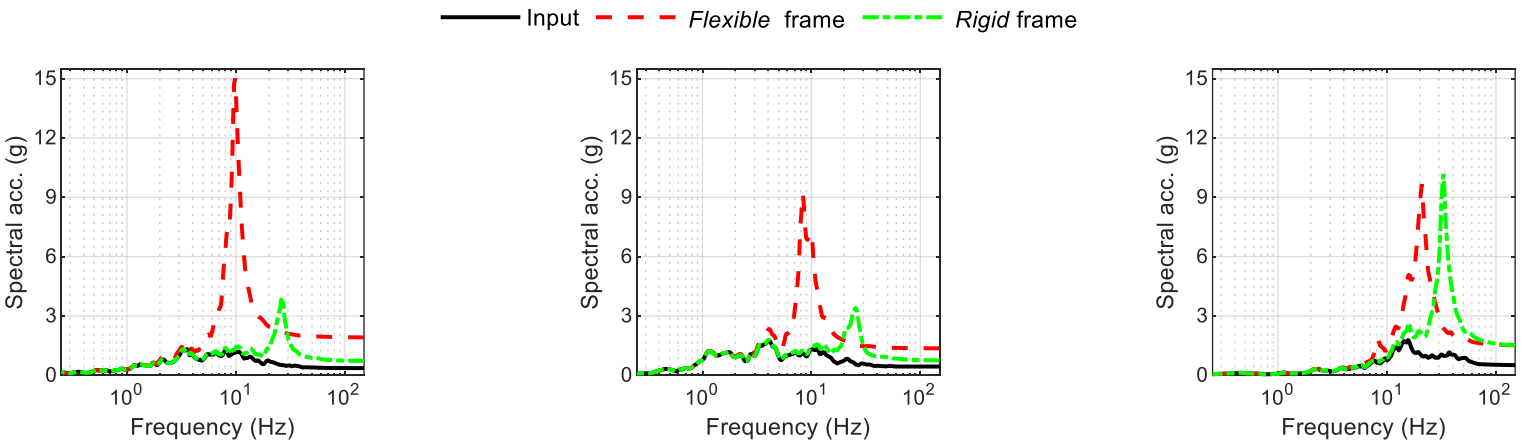

a) *x* direction b) *y* direction c) *z* direction

Figure 5-99. Acceleration response spectra at the top of the vessel, non-isolated, GM2B, 5% damping

Table 5-13. Peak accelerations at the top of the vessel (g), GM1A

	Support frame	Input			Top of the vessel			Bottom of the vessel		
		x	***y***	***z***	***x***	***y***	***z***	***x***	***y***	***z***
Non-isolated	*Rigid*	0.22	0.19	0.10	0.26	0.31	0.20	0.25	0.31	0.19
	Flexible				1.06	0.74	0.44	0.67	0.56	0.45
IS1 isolated	*Rigid*	0.22	0.19	0.10	0.10	0.10	0.39	0.10	0.10	0.39
	Flexible				0.10	0.09	0.39	0.10	0.09	0.39
IS2 isolated	*Rigid*	0.22	0.19	0.10	0.13	0.13	0.39	0.13	0.14	0.39
	Flexible				0.12	0.12	0.39	0.13	0.13	0.39
IS3 isolated	*Rigid*	0.22	0.19	0.10	0.08	0.09	0.39	0.08	0.09	0.39
	Flexible				0.08	0.07	0.39	0.08	0.07	0.39
IS4 isolated	*Rigid*	0.22	0.19	0.10	0.12	0.13	0.39	0.12	0.13	0.39
	Flexible				0.12	0.12	0.39	0.12	0.13	0.39
IS5 isolated	*Rigid*	0.22	0.19	0.10	0.07	0.08	0.39	0.07	0.08	0.39
	Flexible				0.07	0.07	0.39	0.07	0.07	0.39
IS6 isolated	*Rigid*	0.22	0.19	0.10	0.12	0.13	0.39	0.12	0.13	0.39
	Flexible				0.12	0.12	0.39	0.12	0.12	0.39

Table 5-14. Peak accelerations at the top of the vessel (g), GM1B

	Support frame	Input			Top of the vessel			Bottom of the vessel		
		x	***y***	***z***	***x***	***y***	***z***	***x***	***y***	***z***
Non-isolated	*Rigid*	0.43	0.37	0.21	0.52	0.62	0.39	0.51	0.62	0.38
	Flexible				2.12	1.47	0.89	1.35	1.12	0.89
IS1 isolated	*Rigid*	0.43	0.37	0.21	0.20	0.22	0.78	0.19	0.22	0.78
	Flexible				0.20	0.16	0.78	0.20	0.16	0.78
IS2 isolated	*Rigid*	0.43	0.37	0.21	0.20	0.23	0.77	0.20	0.23	0.78
	Flexible				0.19	0.17	0.77	0.19	0.17	0.78
IS3 isolated	*Rigid*	0.43	0.37	0.21	0.14	0.14	0.78	0.14	0.14	0.78
	Flexible				0.13	0.11	0.78	0.13	0.11	0.78
IS4 isolated	*Rigid*	0.43	0.37	0.21	0.16	0.19	0.77	0.16	0.19	0.78
	Flexible				0.15	0.13	0.77	0.15	0.14	0.78
IS5 isolated	*Rigid*	0.43	0.37	0.21	0.10	0.12	0.78	0.11	0.11	0.78
	Flexible				0.10	0.09	0.78	0.09	0.09	0.78
IS6 isolated	*Rigid*	0.43	0.37	0.21	0.15	0.18	0.77	0.15	0.17	0.78
	Flexible				0.14	0.13	0.77	0.13	0.13	0.78

Table 5-15. Peak accelerations at the top of the vessel (g), GM1C

	Support frame	Input			Top of the vessel			Bottom of the vessel		
		x	***y***	***z***	***x***	***y***	***z***	***x***	***y***	***z***
Non-isolated	*Rigid*	0.65	0.56	0.31	0.78	0.93	0.59	0.76	0.93	0.57
	Flexible				3.18	2.21	1.33	2.02	1.69	1.34
IS1 isolated	*Rigid*	0.65	0.56	0.31	Isolation-system displacements exceed the *soft* limit of 0.2*R*; see Section 5.4.6.2 and Appendix C.					
	Flexible									
IS2 isolated	*Rigid*	0.65	0.56	0.31	0.32	0.39	1.16	0.31	0.39	1.15
	Flexible				0.27	0.26	1.16	0.27	0.25	1.16
IS3 isolated	*Rigid*	0.65	0.56	0.31	0.25	0.23	1.17	0.24	0.22	1.16
	Flexible				0.21	0.17	1.17	0.20	0.16	1.16
IS4 isolated	*Rigid*	0.65	0.56	0.31	0.24	0.27	1.16	0.24	0.26	1.15
	Flexible				0.21	0.18	1.16	0.20	0.17	1.16
IS5 isolated	*Rigid*	0.65	0.56	0.31	0.15	0.16	1.17	0.14	0.15	1.16
	Flexible				0.13	0.14	1.17	0.13	0.14	1.16
IS6 isolated	*Rigid*	0.65	0.56	0.31	0.21	0.23	1.16	0.21	0.23	1.15
	Flexible				0.18	0.15	1.16	0.17	0.15	1.16

Table 5-16. Peak accelerations at the top of the vessel (g), GM2A

	Support frame	Input			Top of the vessel			Bottom of the vessel		
		x	***y***	***z***	***x***	***y***	***z***	***x***	***y***	***z***
Non-isolated	*Rigid*	0.18	0.22	0.25	0.37	0.38	0.73	0.36	0.37	0.72
	Flexible				1.42	0.93	0.74	0.95	0.68	0.74
IS1 isolated	*Rigid*	0.18	0.22	0.25	0.15	0.31	0.78	0.16	0.31	0.78
	Flexible				0.15	0.32	0.90	0.15	0.32	0.89
IS2 isolated	*Rigid*	0.18	0.22	0.25	0.15	0.21	0.78	0.14	0.21	0.78
	Flexible				0.14	0.23	0.89	0.14	0.23	0.89
IS3 isolated	*Rigid*	0.18	0.22	0.25	0.12	0.14	0.78	0.12	0.14	0.78
	Flexible				0.09	0.17	0.90	0.09	0.17	0.89
IS4 isolated	*Rigid*	0.18	0.22	0.25	0.14	0.18	0.78	0.14	0.17	0.78
	Flexible				0.14	0.20	0.89	0.13	0.20	0.89
IS5 isolated	*Rigid*	0.18	0.22	0.25	0.12	0.10	0.78	0.12	0.11	0.77
	Flexible				0.09	0.13	0.90	0.09	0.13	0.89
IS6 isolated	*Rigid*	0.18	0.22	0.25	0.14	0.16	0.78	0.14	0.16	0.78
	Flexible				0.13	0.19	0.89	0.13	0.19	0.89

Table 5-17. Peak accelerations at the top of the vessel (g), GM2B

	Support frame	Input			Top of the vessel			Bottom of the vessel		
		x	***y***	***z***	***x***	***y***	***z***	***x***	***y***	***z***
Non-isolated	*Rigid*	0.36	0.44	0.50	0.74	0.75	1.45	0.71	0.74	1.45
	Flexible				2.85	1.86	1.48	1.91	1.36	1.49
IS1 isolated	*Rigid*	0.36	0.44	0.50	Isolation-system displacements exceed the *soft* limit of 0.2*R*; see Section 5.4.6.2 and Appendix C.					
	Flexible									
IS2 isolated	*Rigid*	0.36	0.44	0.50						
	Flexible									
IS3 isolated	*Rigid*	0.36	0.44	0.50	0.22	0.37	1.60	0.23	0.36	1.61
	Flexible				0.23	0.54	1.85	0.22	0.55	1.83
IS4 isolated	*Rigid*	0.36	0.44	0.50	0.29	0.36	1.56	0.30	0.37	1.58
	Flexible				0.26	0.46	1.81	0.24	0.46	1.79
IS5 isolated	*Rigid*	0.36	0.44	0.50	0.19	0.20	1.60	0.20	0.20	1.61
	Flexible				0.17	0.23	1.85	0.16	0.23	1.83
IS6 isolated	*Rigid*	0.36	0.44	0.50	0.27	0.25	1.56	0.27	0.25	1.58
	Flexible				0.25	0.31	1.81	0.22	0.31	1.79

Table 5-18. Peak accelerations at the top of the vessel (g), GM2C

	Support frame	Input			Top of the vessel			Bottom of the vessel		
		x	***y***	***z***	***x***	***y***	***z***	***x***	***y***	***z***
Non-isolated	*Rigid*	0.54	0.66	0.75	1.11	1.13	2.18	1.07	1.11	2.17
	Flexible				4.27	2.80	2.21	2.86	2.04	2.23
IS1 isolated	*Rigid*	0.54	0.66	0.75	Isolation-system displacements exceed the *soft* limit of 0.2*R*; see Section 5.4.6.2 and Appendix C.					
	Flexible									
IS2 isolated	*Rigid*	0.54	0.66	0.75						
	Flexible									
IS3 isolated	*Rigid*	0.54	0.66	0.75						
	Flexible									
IS4 isolated	*Rigid*	0.54	0.66	0.75						
	Flexible									
IS5 isolated	*Rigid*	0.54	0.66	0.75						
	Flexible									
IS6 isolated	*Rigid*	0.54	0.66	0.75	0.39	0.39	2.40	0.38	0.38	2.40
	Flexible				0.43	0.46	3.47	0.39	0.47	3.43

Table 5-19. Acceleration reduction factors[1] (ARF) and maximum isolation-system displacements (inches) for the vessel supported on the *rigid* frame

Isolation system		GM1A	GM1B	GM1C	GM2A	GM2B	GM2C
IS1 isolated (1.06 sec, 6%)	ARF	2.8	2.7	[2]	1.7		
	Maximum isolation-system displacement	0.5	1.4		2.0		
IS2 isolated (1.06 sec, 10%)	ARF	2.2	2.6	2.4	2.1		
	Maximum isolation-system displacement	0.2	1.0	1.9	0.6		
IS3 isolated (1.5 sec, 6%)	ARF	3.3	4.1	3.6	2.9	2.6	
	Maximum isolation-system displacement	0.5	1.4	2.9	1.3	4.2	
IS4 isolated (1.5 sec, 10%)	ARF	2.3	3.3	3.3	2.4	2.3	
	Maximum isolation-system displacement	0.2	1.1	2.1	0.8	2.8	
IS5 isolated (2.12 sec, 6%)	ARF	3.8	5.2	5.5	3.4	3.8	
	Maximum isolation-system displacement	0.5	1.7	3.1	1.5	4.6	
IS6 isolated (2.12 sec, 10%)	ARF	2.3	3.5	3.9	2.5	2.9	2.9
	Maximum isolation - system displacement	0.3	1.3	2.4	1.0	3.5	6.6

1. Ratio of peak geomean horizontal acceleration at the top of the non-isolated vessel to that in the isolated vessel
2. Results are not reported for the cells highlighted in red because the maximum isolation-system displacements exceed the *soft* limit of 0.2*R*; see Section 5.4.6.2 and Appendix C

Table 5-20. Acceleration reduction factors[1] (ARF) and maximum isolation-system displacements (inches) for the vessel supported on the *flexible* frame

Isolation system		GM1A	GM1B	GM1C	GM2A	GM2B	GM2C
IS1 isolated (1.06 sec, 6%)	ARF	9.3	9.9	[2]	5.2		
	Maximum isolation-system displacement	0.5	1.4		1.7		
IS2 isolated (1.06 sec, 10%)	ARF	7.4	9.8	10.0	6.4		
	Maximum isolation-system displacement	0.3	1.0	2.0	0.7		
IS3 isolated (1.5 sec, 6%)	ARF	11.8	14.8	14.0	9.3	6.5	
	Maximum isolation-system displacement	0.5	1.5	2.9	1.3	4.2	
IS4 isolated (1.5 sec, 10%)	ARF	7.4	12.6	13.6	6.9	6.7	
	Maximum isolation-system displacement	0.3	1.1	2.1	0.9	2.8	
IS5 isolated (2.12 sec, 6%)	ARF	12.7	18.6	19.7	10.6	11.6	
	Maximum isolation-system displacement	0.6	1.7	3.2	1.6	4.6	
IS6 isolated (2.12 sec, 10%)	ARF	7.4	13.1	16.1	7.3	8.3	7.8
	Maximum isolation-system displacement	0.3	1.3	2.4	1.0	3.5	6.6

1. Ratio of peak geomean horizontal acceleration at the top of the non-isolated vessel to that in the isolated vessel
2. Results are not reported for the cells highlighted in red because the maximum isolation-system displacements exceed the *soft* limit of 0.2*R*; see Section 5.4.6.2 and Appendix C

5.4.6.4 Energy demands on isolators

Consensus standards ASCE/SEI 4-16 (ASCE, 2017) and ASCE/SEI 43-19 (ASCE, 2021) present requirements for prototype and production testing of seismic isolators. Five fully reversed cycles of loading to user-specified displacements for design-basis and beyond-design-basis shaking are the key seismic tests, where five is based on normalized dissipated energy calculations presented in Warn and Whittaker (2007) for base-isolated structures.

To examine if five fully reversed cycles is also sufficient for testing isolators used for equipment protection, calculations were performed for the six isolation systems of Section 5.4.3, the six ground motions of Section 5.4.4, and the two support conditions of Section 5.4.2 (i.e., *rigid* frame and *flexible* frame). Results are presented in Table 5-21 as normalized energy dissipated (NED) per Warn and Whittaker (2007), namely, the ratio of the total energy dissipated by an isolator during one ground motion to the energy dissipated in one fully reversed cycle of loading to the maximum displacement computed for that ground motion. Values of NED are presented for the north-east isolator, noting that the values for the west and south-east isolators were essentially identical. The range for NED is between 2.1 and 5.1, confirming that five fully reversed cycles of loading is sufficient for testing isolators used to protect both structures and equipment: answering the third question of Section 5.4.1.

Table 5-21. Normalized energy dissipated in the north-east isolator

		GM1A	GM1B	GM1C	GM2A	GM2B	GM2C
IS1	*Rigid* frame	2.9	3.6	[1]	3.6		
	Flexible frame	2.9	3.6		3.6		
IS2	*Rigid* frame	3.1	3.1	3.5	3.9		
	Flexible frame	3.1	3.1	3.5	4.1		
IS3	*Rigid* frame	2.6	3.3	3.5	4.1	5.1	
	Flexible frame	2.7	3.3	3.6	4.2	5.1	
IS4	*Rigid* frame	2.9	2.6	3.1	2.9	4.4	
	Flexible frame	2.9	2.7	3.3	3.0	4.5	
IS5	*Rigid* frame	2.3	2.6	3.5	3.1	4.6	
	Flexible frame	2.3	2.7	3.5	3.2	4.6	
IS6	*Rigid* frame	2.8	2.1	2.5	2.6	3.2	4.0
	Flexible frame	2.8	2.2	2.5	2.3	3.3	4.1

1. Results are not reported for the cells highlighted in red because the maximum isolation-system displacements exceed the *soft* limit of 0.2*R*; see Section 5.4.6.2 and Appendix C.

5.5 Feasibility of base isolation for a tall, slender vessel

5.5.1 Introduction

The utility and benefits of mid-height seismic isolation of a tall, slender vessel were characterized in the previous section. This section examines whether such a vessel could be base isolated and if so, to quantify the advantages and disadvantages of doing so. To support this study, four models of the vessel were analyzed in SAP2000 using the six seismic inputs of Section 5.4.4:

1. Model 1 (M1): The support mounts of the SFP-isolated vessel of Section 5.2 were moved to the bottom of the vessel, see Figure 5-100a, and their thickness (including the shaped plates, see Section 4) was increased to 4 inches. The elastic modulus of the steel support mounts was increased so as to provide a *stiff* base. The total weight of the base, including the support mounts and bottom plate of the vessel was 6.3 kips, approximately one-sixth of the total weight of the vessel (including water) of 37.4 kips. The isolation system IS3 from Table 5-9 (1.5 second sliding period, 6% friction) was installed beneath the base. The top nodes of the bearings were connected to the underside of the support mounts and the bottom nodes were assigned a *fixed* joint restraint in all six degrees of freedom. The center of each bearing was 45 inches from the center of the vessel: see Figure 5-100b wherein the red solid circles identify the locations of the centers of the isolators.

2. Model 2 (M2): The model 1 base was extended such that the center of each bearing was 90 inches from the center of the vessel: see Figure 5-101. Isolation system IS3 was installed beneath the base. The bearings were moved outwards so as to increase the lever arm for resisting the overturning moment (see Section 5.5.3.2 for details) and to reduce the resulting axial forces, tensile and compressive, in the bearings. (Single Friction pendulum bearings have zero stiffness in tension and uplift will occur if the axial force due to overturning and vertical shaking exceeds the gravity load on the bearing.) Similar to model 1, the elastic modulus of the extended support mounts was increased to provide a *stiff* base. Because the base was *stiff*, moving the isolators outwards increased the rocking frequency of the isolation system. The total weight of the base of model 2 was 17.7 kips: approximately one-half of the total weight of the vessel. The additional weight of the extended base increases the gravity load on the bearings.

3. Model 3 (M3): The mid-height isolated vessel of Section 5.2 (see Figure 5-1) configured with IS3.

4. Model 4 (M4): A conventional (fixed base) vessel. The joints on the circumference of the vessel at its bottom were assigned a *fixed* joint restraint in the three translational degrees of freedom: see Figure 5-102 wherein the green triangles represent the *fixed* joint restraints.

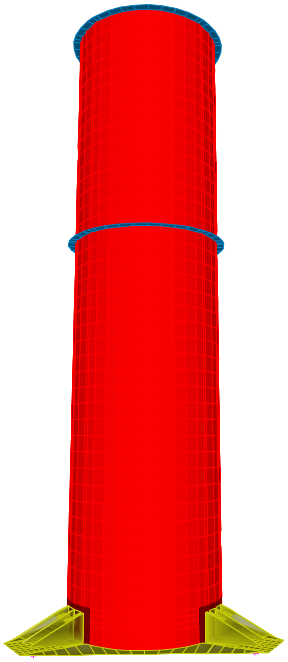

a) isometric view

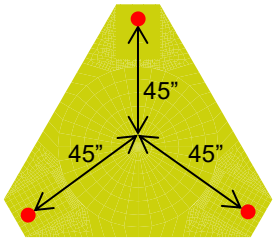

b) plan view of the base showing isolator locations

Figure 5-100. Model 1 in SAP2000

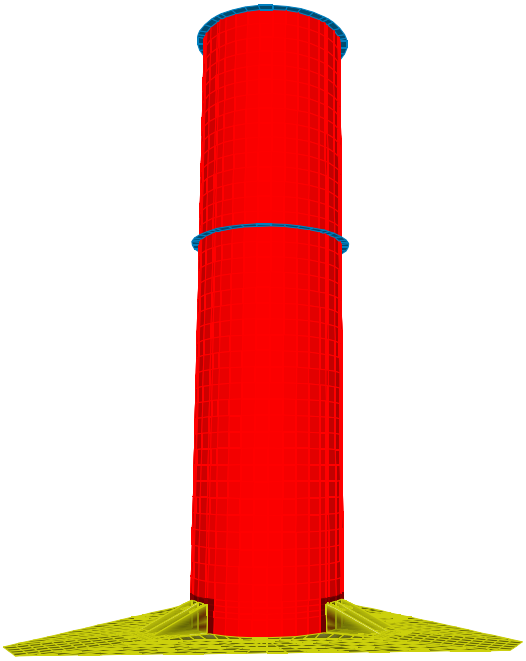

a) isometric view

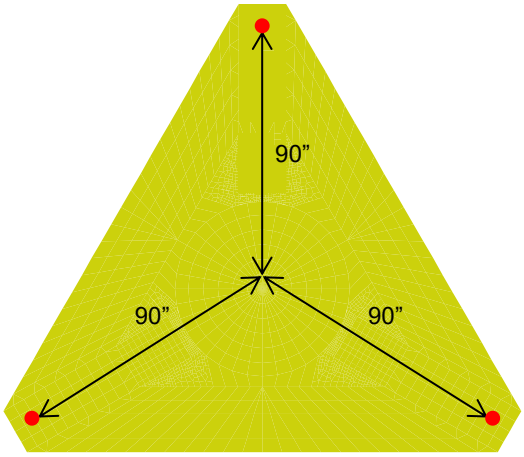

b) plan view of the base showing isolator locations

Figure 5-101. Model 2 in SAP2000

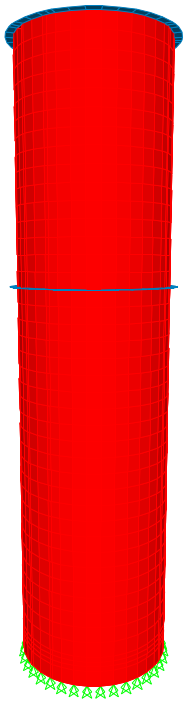

Figure 5-102. Model 4 in SAP2000

5.5.2 Modal analysis

The modal frequencies of models 1 through 4 are listed in Table 5-22. Vertical frequencies are reported in the table but are of secondary importance for this study. The rocking mode shape of the base-isolated vessels is presented in Figure 5-103: rotation about the center of mass and horizontal displacement of the isolators. Moving the isolators outwards in model 2 increased the rocking frequency of the vessel from 14.9 Hz (model 1) to 20.3 Hz.

5.5.3 Response-history analyses

5.5.3.1 Introduction

Results extracted from the response-history analysis using the six seismic inputs of Section 5.4.4 include:

1. Axial load histories in the isolators.
2. Horizontal acceleration histories directly above the isolation plane, at the bottom of the vessel, on the north-east side: location *V2* marked by the solid pink circle in Figure 5-104.
3. Horizontal acceleration histories at the top (location *V3*) and the mid-height (location *V1*) of the vessel on the north face.

Table 5-22. Modal analysis results

	Model 1 (base isolated)	Model 2 (base isolated, extended foundation)	Model 3 (mid-height isolated)	Model 4 (fixed based)
Rocking of vessel (about *x* and *y* axes)	14.9 Hz	20.3 Hz	8.7 Hz	--
Horizontal modes (*x* and *y* directions)	0.67 Hz[1]	0.67 Hz[1]	0.67 Hz[1]	20.4 Hz
Vertical mode (*z* direction)	42 Hz[2]	39 Hz[2]	20.5 Hz[3]	[4]

1. Corresponds to the 1.5 second sliding period of the IS3 isolation system
2. Higher than model 3 because a) the flexible support frame is omitted, and b) the elastic modulus of the steel support mounts was increased to provide a *stiff* base. Vertical flexibility primarily from the isolators.
3. The sources of vertical flexibility are the isolators (see Section 3), the interior columns of the support frame (see Section 4), and bending of the support mounts and the vessel wall
4. The vessel has 1-inch-thick walls, with a vertical mode at a frequency higher than 100 Hz

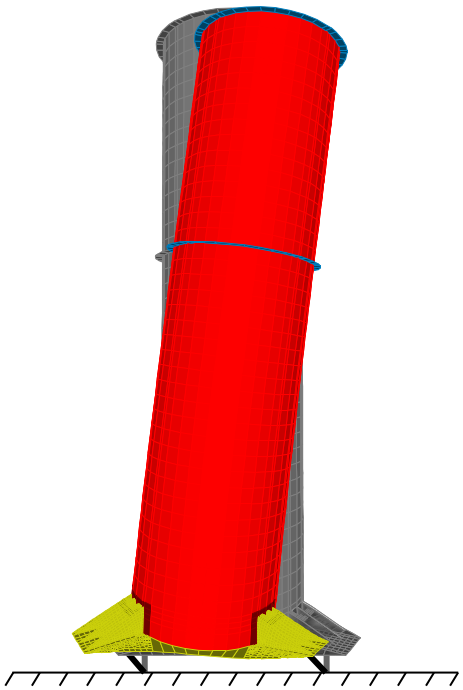

Figure 5-103. Rocking of base-isolated vessels

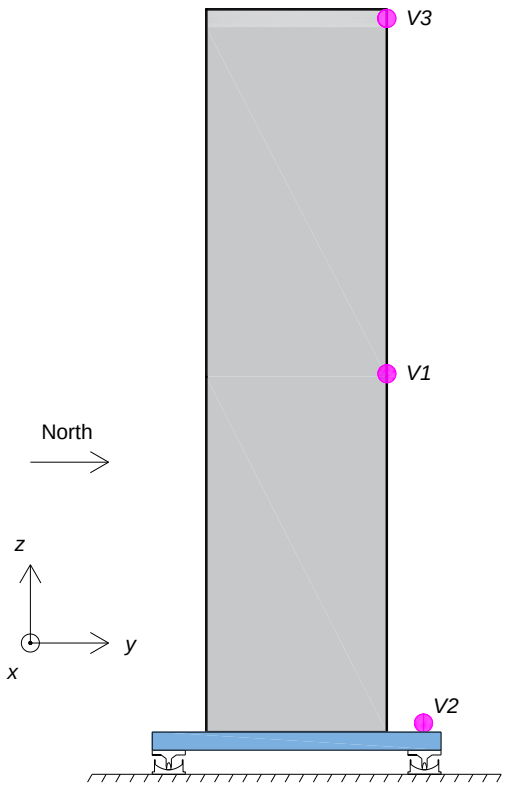

Figure 5-104. Monitoring locations for outputting results of response-history analyses

5.5.3.2 Results and discussion

Figures 5-105 through 5-109 present the geomean horizontal acceleration response spectra at the mid-height and the top of the vessel. Spectra are plotted for a) base-isolated vessel using model 1, blue dashed line, b) base isolated vessel using model 2, pink dashed line, c) mid-height isolated vessel (M3), green dashed line, and d) non-isolated vessel (M4), red solid line. Spectra are not presented for GM2C as the maximum horizontal isolation-system displacement exceeded the proposed soft limit of 0.2*R* of Section 5.4.6.2 and Appendix C.

For frequencies higher than 2 Hz (1.4 Hz) at the model (prototype) scale, base isolation reduced the horizontal spectral accelerations with respect to those in the non-isolated vessel: compare the red solid line with the blue and pink dashed lines in Figures 5-105 through 5-109. (In the non-isolated vessel (M4), the peak at 20 Hz corresponds to its horizontal mode, see Table 5-22). Rocking of the base-isolated vessels (M1 and M2) contributed to the horizontal response at their top and bottom: see the peaks near 15 Hz and 20 Hz for the blue and pink dashed lines, respectively, in panel b of Figures 5-105 through 5-109. These

peaks are not present in the spectra at the mid-height, as the vessel rocks about its center of gravity, which is near the mid-height: see Figure 5-103. Rocking did not contribute to the horizontal response at the top and the bottom of the mid-height isolated vessel (M3), noting again that the center of gravity of the vessel is at its mid-height. (The peak near 20 Hz for the mid-height isolated vessel (M3) corresponds to its vertical mode, see Table 5-21. This is because the horizontal and vertical responses of a spherical sliding bearing are coupled. The peaks for the vertical modes of M1 and M2 are near 40 Hz, as seen in results for GM2A and GM2B: see the blue and pink lines in Figures 5-107 and 5-108. These peaks weren't observed in the results for GM1A, GM1B, and GM1C because the vertical component of these motions did not have significant frequency content beyond 30 Hz.)

Figure 5-110 presents axial load histories on the three SFP bearings for models 1, 2 and 3 for the first 15 seconds of GM2A[1], wherein the axial load is normalized by the gravity load on the bearings. A time window of normalized axial load, from 9 to 12 seconds, is presented in Figure 5-111. The variation in the normalized axial load between the three isolators is greatest for model 1. The periodicity in the variation of axial load is associated with the overturning moment induced by sliding of the vessel on the bearings. See Figure 5-112 wherein the horizontal force (F_I) in the bearings, due to sliding, acts at the center of mass of the vessel (red solid circle) as an inertial force and induces an overturning moment ($F_I \times H$) that generates a tensile force in the bearing on the right ($F_T = F_I \times H / L$) and a compressive force in the bearing on the left ($F_C = F_T$). Other sources of variation in axial load are the rocking of the vessel and the vertical component of ground motions. For model 2, the variation in axial load has the same periodicity as model 1 but a lower amplitude because the level arm (L) for resisting the overturning moment is longer due to the extended base. In the mid-height isolated vessel (M3), the normalized axial loads are nearly identical in the three bearings, per Figure 5-111c, with the variation due primarily to the vertical component of the earthquake shaking. For model 3, a) the isolation plane (at the mid-height) is at the same level as the center of gravity of the vessel ($H=0$ and hence $F_T = F_C = 0$), and b) rocking of the vessel is minimized as it is supported near its center of gravity.

Base isolation of tall, slender vessels is viable but may not be practical. Consideration must be given to the space needed (e.g., model 2 versus model 1) for base fixturing and support to prevent uplift under design basis and beyond design basis ground motions, unless the isolators are designed to resist tensile axial forces.

[1] Similar observations were made for the other seismic inputs and the results are the not presented here.

Isolating a tall, slender vessel at a level near its center of gravity, reduces (or eliminates) rocking response (and the variation of axial load between the bearings) and allows for a more compact design, noting that space is still required for the support frame (e.g., Figure 5-1).

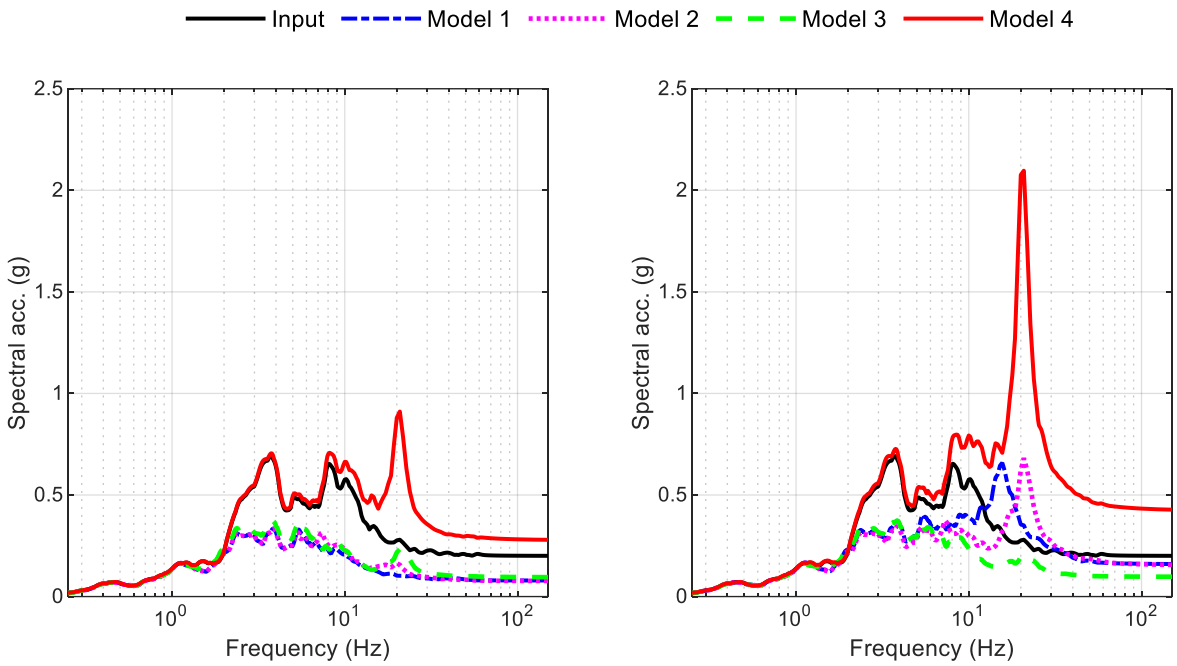

a) mid-height of vessel b) vessel top

Figure 5-105. Geomean horizontal acceleration response spectra, GM1A, 5% damping

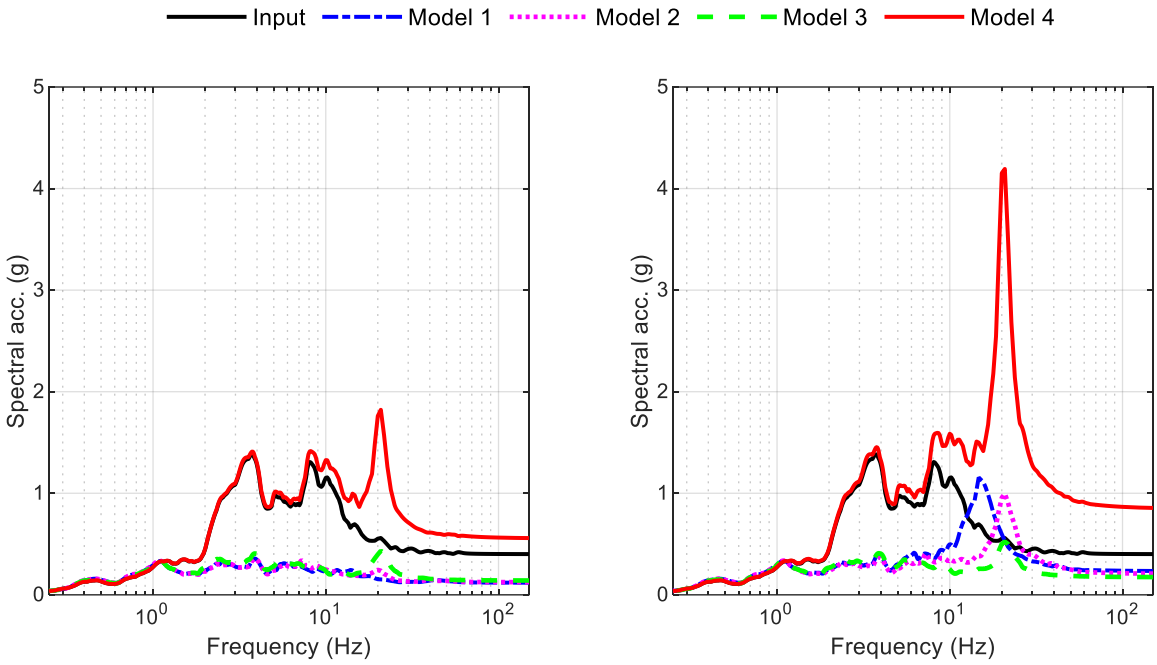

a) mid-height of vessel b) vessel top

Figure 5-106. Geomean horizontal acceleration response spectra, GM1B, 5% damping

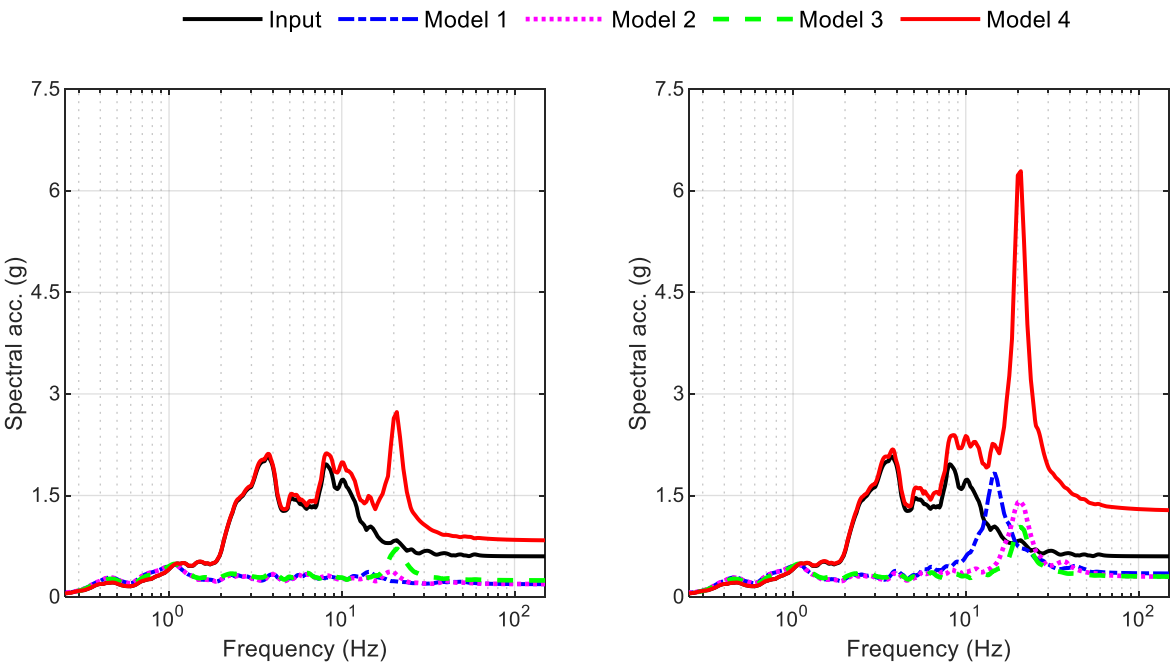

a) mid-height of vessel b) vessel top

Figure 5-107. Geomean horizontal acceleration response spectra, GM1C, 5% damping

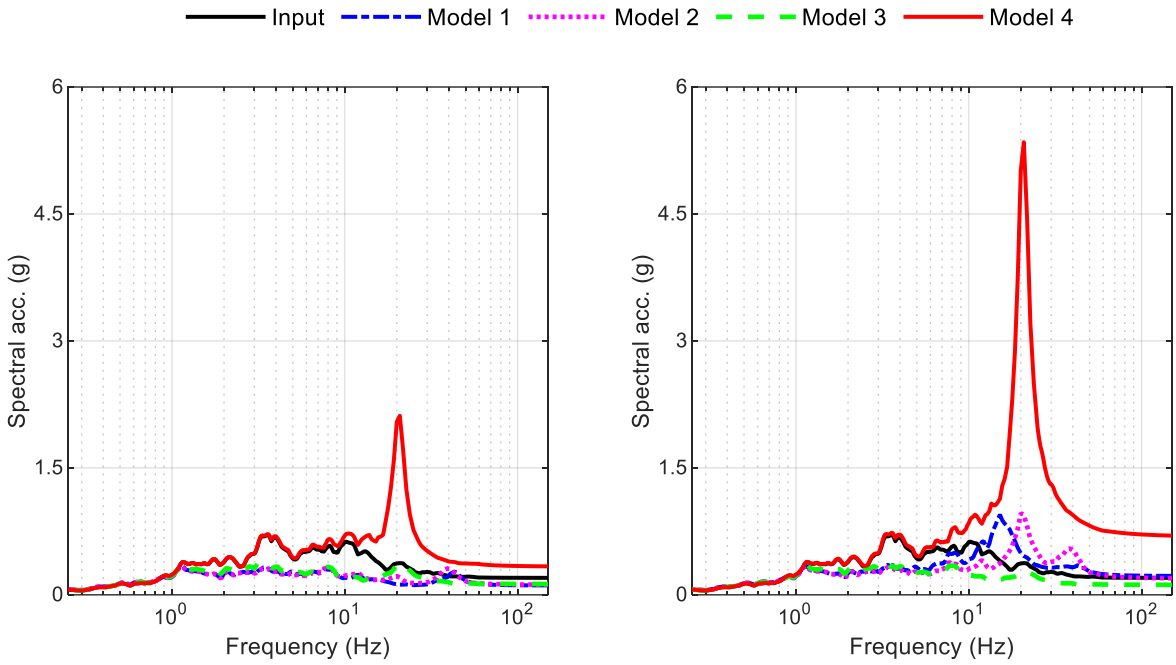

a) mid-height of vessel b) vessel top

Figure 5-108. Geomean horizontal acceleration response spectra, GM2A, 5% damping

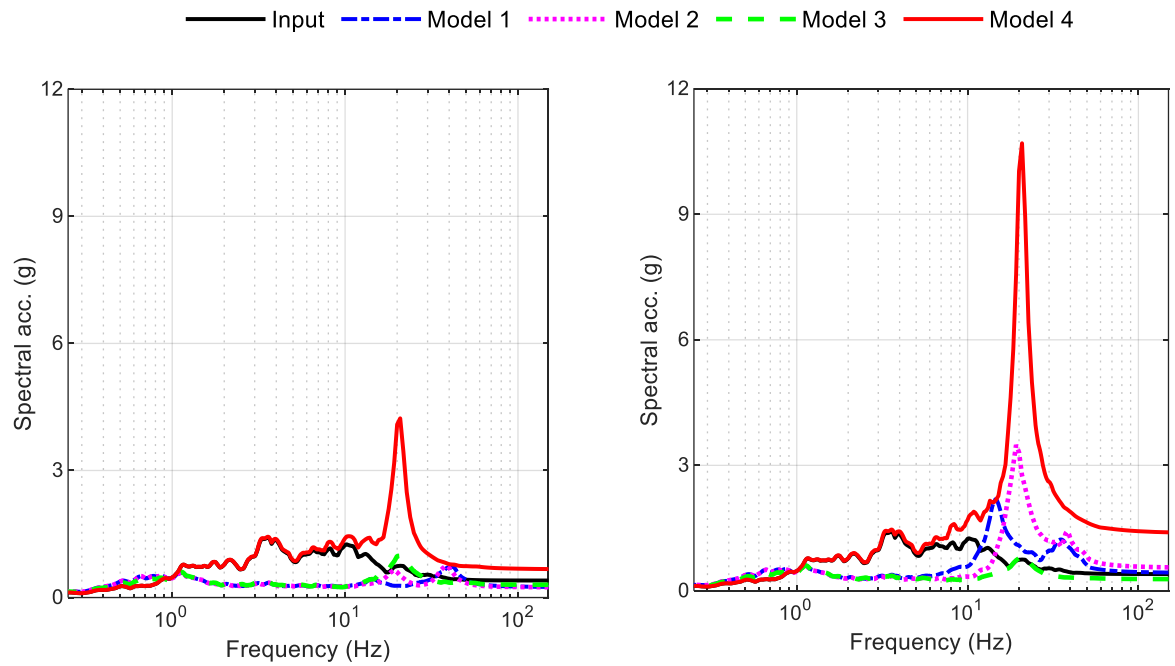

a) mid-height of vessel b) vessel top

Figure 5-109. Geomean horizontal acceleration response spectra, GM2B, 5% damping

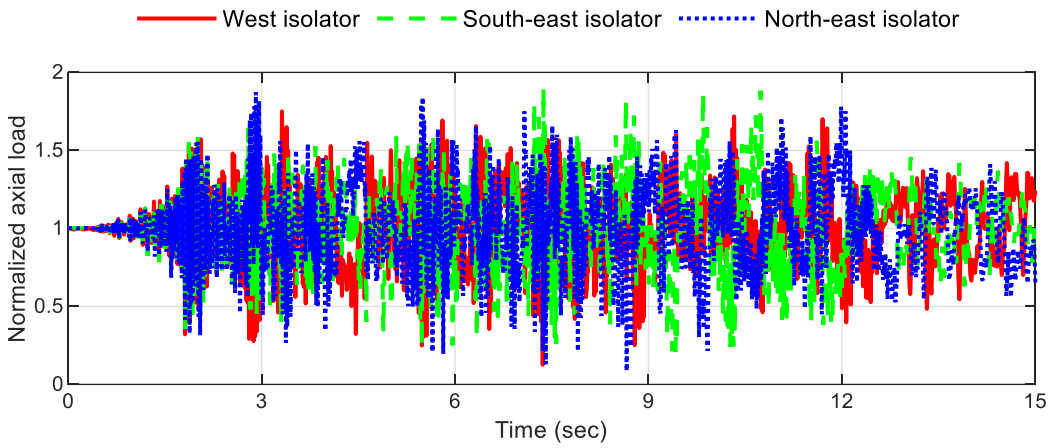

a) isolated, base

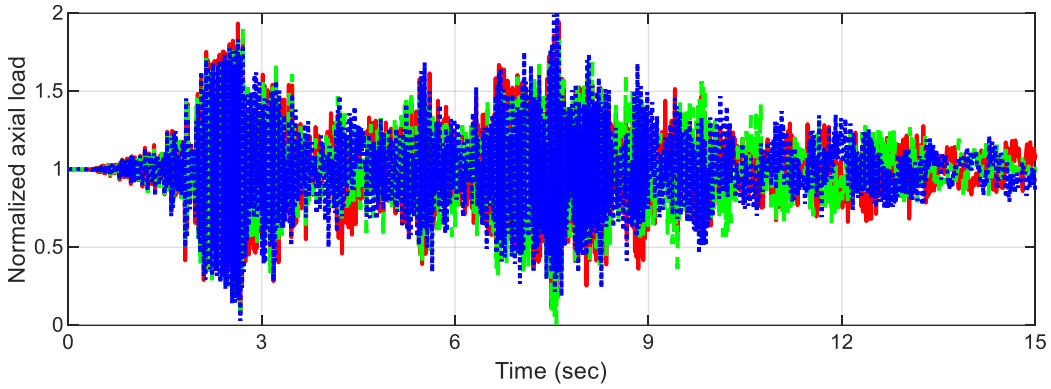

b) isolated, extended base

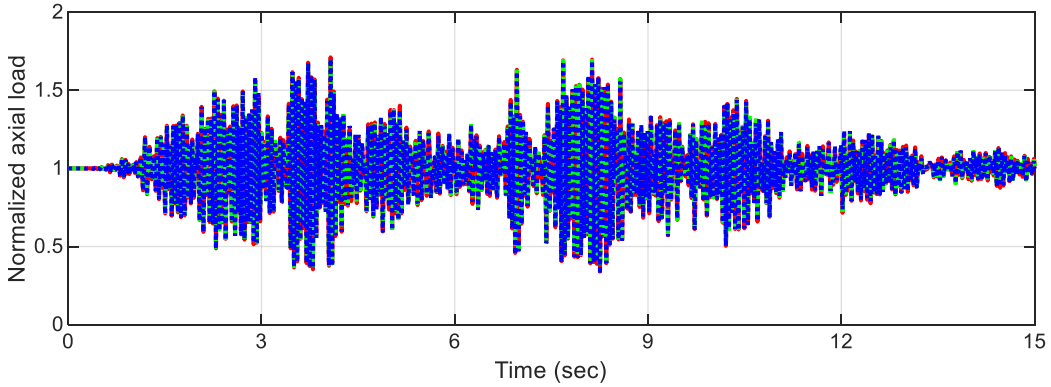

c) isolated, mid-height

Figure 5-110. Normalized axial loads in SFP bearings, GM2A

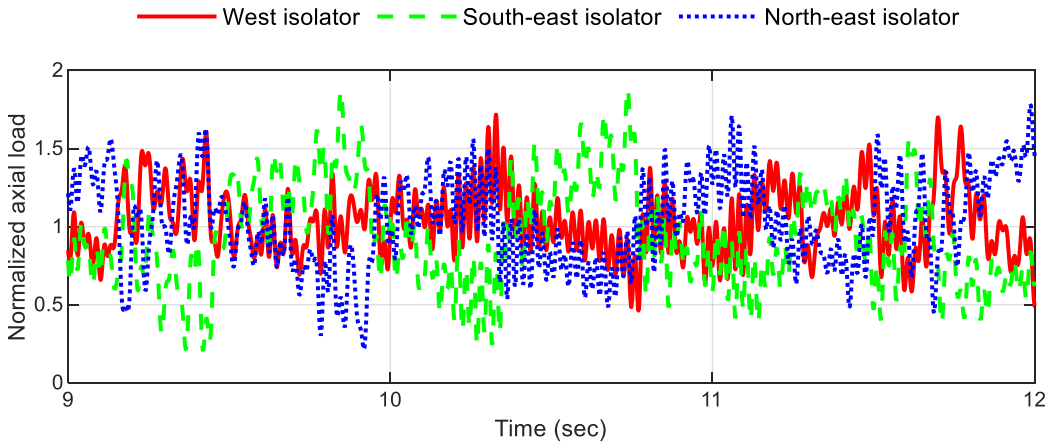

a) isolated, base

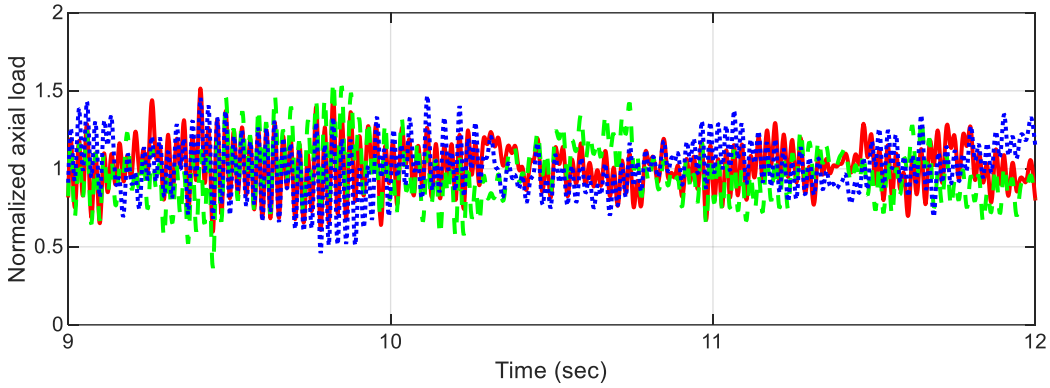

b) isolated, extended base

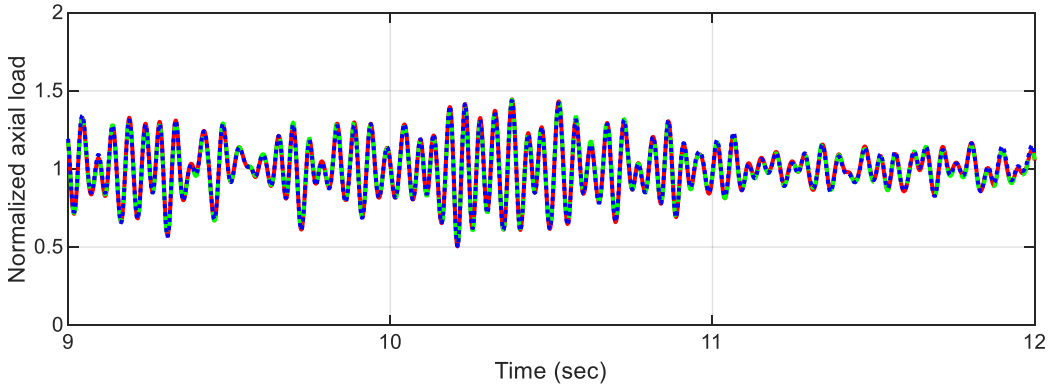

c) isolated, mid-height

Figure 5-111. Normalized axial loads in SFP bearings, GM2A (from 9 to 12 seconds)

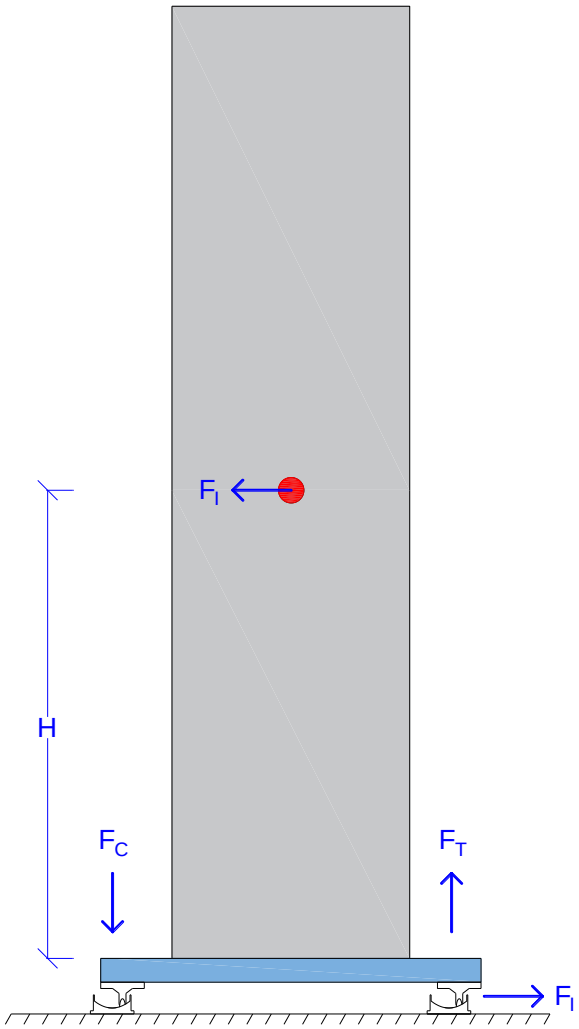

Figure 5-112. Sliding of the vessel on the bearings

5.6 Summary and conclusions

Numerical models were developed for the test specimen of Section 4 and benchmarked using the earthquake-simulator experiment data presented in Section 4.5. Shell and beam elements were used to model the vessel and its support frame. Link elements were utilized to model the Friction Pendulum bearings. Predicted acceleration responses at the top, bottom, and mid-height of the vessel, and the normalized force-displacements loops for the isolation systems were compared with the test data to benchmark the models: see Section 5.3. Good agreement was obtained between the predicted and recorded horizontal and rocking responses of the vessel. Differences in the vertical response were due in large part to the significant differences between the measured and predicted frequencies in the *z* direction: see Section 5.2.2. The predicted normalized force-displacement loops for the SFP and TFP isolation systems were in excellent agreement with the test data for the larger amplitude motions.

The benchmarked numerical were used to perform 84 response-history analyses to quantify the benefits of mid-height seismic isolation for different frame stiffnesses (*near rigid* or *flexible*) supporting the vessel, isolation system properties, and seismic inputs: see Section 5.4. Six SFP isolation systems were considered, with isolation periods of 1.06, 1.5, and 2.12 seconds and coefficients of friction of 6% and 10%. Two ground motion triplets, each with three intensities of shaking were utilized for analyses. The results demonstrated that mid-height seismic isolation of a tall, slender equipment is feasible and beneficial for a range of support structures stiffnesses, seismic inputs, and isolation-system properties, with very significant reductions in the horizontal accelerations possible with respect to those in non-isolated equipment. Importantly, the reductions in horizontal spectral accelerations in the mid-height isolated vessel are not affected by the stiffness of the support structure. The peak horizontal accelerations at the top of the isolated vessel were reduced by a factor of between 1.5 and 20 from those on the non-isolated vessel. The greatest reductions in horizontal accelerations were achieved using the more flexible isolation system but the tradeoff was the larger displacements in the bearings.

Requirements for seismic testing of isolators used for equipment protection were investigated by calculating the normalized energy dissipated by SFP bearings for different isolation systems, seismic inputs, and support conditions. The results confirm that five fully reversed cycles of loading to a user-computed maximum displacement impose sufficient earthquake-induced energy for prototype and production testing of isolators.

The benchmarked numerical models were also used to explore the practicality of base isolating a tall, slender vessel: section 5.5. Four models were analyzed, two isolated at the base, one fixed at the base, and one isolated at the mid-height, near its center of gravity. Although base isolation enabled a reduction in horizontal spectral accelerations with respect to those in the non-isolated vessel, the variation in axial load between the bearings was significant. Rocking of the base-isolated vessel contributed to the horizontal response at its top and bottom. Base isolation of tall, slender equipment is viable but may not be practical. Attention must be paid to prevent uplift in the bearings unless the isolators are designed to resist tensile axial forces. Numerical models should adequately capture the axial stiffness of individual bearings (see Section 3.6).

SECTION 6
SUMMARY, CONCLUSIONS, AND RECOMMENDATIONS

6.1 Introduction

Recent studies have made clear the pivotal role of nuclear energy in the rapid decarbonization of the global economy and meeting increasing energy demands. Standardized advanced nuclear reactors might be the only pathway to achieving these two goals by lowering capital cost and decreasing the time required to design, license, and construct plants. The near surface geology and the seismic hazard are different at each power plant site, thwarting the standardization of nuclear power plants (NPPs) by requiring site-specific soil-structure-interaction analysis, design, engineering, equipment qualification, licensing, and regulatory review.

Seismic isolation is a proven technology to mitigate the effects of earthquake shaking and could enable a rapid transition to standardization of advanced reactors. Standardized reactor buildings, once designed, qualified, and licensed, can be re-used at multiple sites by selecting an appropriate seismic isolation system, drastically reducing the scope of pre-construction activities and driving down construction cost. This report focuses on equipment isolation, an alternate implementation of seismic isolation where base isolation of reactor buildings is either impractical or cost prohibitive.

6.2 Summary

Although seismic isolation has not been used to protect individual pieces of safety-class equipment in a nuclear power plant, its use for non-nuclear applications has been studied, with a focus on power transformers. Electric power utilities have isolated existing and new high voltage transformers to reduce the impact of earthquake shaking, with the goal of providing electricity in the aftermath of an earthquake.

Herein a tall, slender vessel, which could represent a reactor vessel, a steam generator, or a heat exchanger, was used as the test specimen for proof-of-concept experiments of seismically isolated equipment. The half-length scale cylindrical, carbon steel vessel had an outer diameter of 60 inches, a height of 240 inches, and a wall thickness of 1 inch. The vessel was supported at its mid-height on a stiff steel frame using three equally spaced mounts. The steel frame was 10 ft by 10 ft in plan and approximately 10 ft tall. The vessel was filled with water to indirectly account for the fluid and internal equipment inside a prototype vessel. A rectangular plate was bolted to the top of the vessel to prevent loss of water and to attach two submerged

internals: a 6-ft long aluminum tube with a 3-inch outer diameter, and 6-ft long rectangular carbon steel plate, 0.5 in × 6 in in cross section. The weight of the vessel including water and its internals was 39.3 kips. Acceleration, displacement, strain, and pressure histories were recorded at various locations on the specimen. The test specimen and instrumentation plan are described in Section 4 and fabrication drawings are presented in Appendix B.

The proof-of-concept experiments were performed using a six degree-of-freedom earthquake simulator at the University at Buffalo. The specimen was tested in three configurations: 1) non-isolated, wherein the vessel was bolted directly to the load cells installed above the steel frame, 2) isolated using single Friction Pendulum (SFP) bearings, wherein the bearings were installed between the load cells and the vessel mounts, and 3) isolated using Triple Friction Pendulum (TFP) bearings, wherein the bearings were installed similar to that in the SFP-isolated configuration. The SFP and TFP bearings are described, and their force-displacement behavior characterized in Section 3. The SFP bearings had an average minimum and maximum coefficients of friction of 2.8% and 7.8%, respectively. The average minimum and maximum coefficients of friction for the outer (inner) surfaces of the TFP bearings was 6.7% (1.4%) and 11.3% (2.3%), respectively.

Three ground motions from the PEER NGA-West 2 database were utilized for the earthquake-simulator tests. The motions were selected to have a broad range of frequency content and were time scaled by a factor of 0.71, consistent with the assumed length scale of 0.5. The ground motions were amplitude scaled to achieve different intensities of earthquake shaking.

The amplitudes of the seismic inputs and simulator-specimen interaction were different for the non-isolated and isolated configurations and only a qualitative comparison of specimen response could be made to demonstrate the utility of the mid-height seismic isolation for tall, slender vessels. Numerical models in computer program SAP2000, benchmarked using the earthquake-simulator data, were used to investigate and quantify the benefits of mid-height seismic isolation for different support-frame stiffnesses, isolation-system properties, and seismic inputs. Requirements for prototype and production testing of bearings used for equipment isolation were investigated for different isolation systems, seismic inputs, and support conditions. Numerical models were further used to investigate the feasibility of base isolation for tall, slender vessels and compare vessel responses for base- and mid-height isolation.

6.3 Key results and conclusions

The overarching goal of this report was to provide isolation solutions for the designers of safety-class equipment inside nuclear reactor buildings. Three objectives were identified to achieve that goal, namely, 1) demonstrate experimentally the feasibility of a mid-height seismic isolation system for a tall, slender vessel, 2) numerically explore base isolation of tall, slender vessels, and 3) provide analysis and design recommendations for equipment isolation suitable for inclusion in the next revision of ASCE/SEI Standards 4 and 43. The key results and conclusions of this report, presented below, help meet the above three objectives:

1. The earthquake-simulator experiments demonstrated that mid-height seismic isolation of a tall, slender vessel is feasible and enables significant reductions in horizontal spectral accelerations (for frequencies greater than 3 Hz for the specimen herein) above the isolation plane, and at the top and the bottom of the vessel. The efficacy of the isolation systems and the corresponding reduction in horizontal accelerations from the non-isolated support condition was a function of the frequency content and amplitude of the seismic inputs.

2. Mid-height seismic isolation enables a reduction in seismic demands in vessel internals, characterized herein using peak horizontal accelerations at their bottom and axial strains near their points of attachment to the vessel head.

3. A stiff diaphragm must be provided above and below the isolation plane.

4. The global response of a mid-height isolated tall, slender vessel and its isolation system can be predicted accurately using currently available structural analysis software such as SAP2000. If the vessel is fully filled with fluid, as was the case herein, the fluid response can be treated as impulsive, and the weight of fluid can be distributed uniformly to the walls of the vessel along its height, for the purpose of predicting the global response of the vessel and its isolation system.

5. To capture the rocking and vertical responses of isolated equipment, numerical models must adequately capture the axial flexibility of individual bearings.

6. Results from response-history analyses, performed using benchmarked numerical models, demonstrated that mid-height seismic isolation of tall, slender equipment is practical and beneficial for a range of support structure stiffnesses, isolation-system properties, and seismic inputs. Substantial reductions in horizontal spectral accelerations from the non-isolated support condition

can be achieved. The peak horizontal accelerations at the top of the isolated vessel were lower, by a factor of between 1.5 and 20, than those in the non-isolated vessel.

7. Reductions in horizontal spectral accelerations enabled by mid-height seismic isolation are by-and-large independent of support structure stiffness: the reductions were similar for the vessel supported on a *rigid* and a *flexible* frame. (The horizontal stiffness of the *rigid* frame was 40 times that of the *flexible* frame.) Accordingly, an isolated piece of equipment could be seismically qualified once, but for multiple support conditions.
8. Five fully reversed cycles of loading to a user-calculated displacement is sufficient for prototype and production testing of bearings.
9. Base isolation of a tall, slender vessel is viable but may not be the *best* solution. Although, spectral accelerations were reduced in the base-isolated vessel with respect to the fixed-base configuration, rocking of the vessel contributed to its horizontal response and the variation in axial load between the bearings was significant. Unless bearings are designed to resist tensile axial forces, consideration must be given to the space needed for base fixturing to avoid uplift of bearings under extreme shaking. Isolating the vessel at its mid-height, near its center of gravity, virtually eliminated the rocking response and the variation of axial load between the bearings was tiny.

Although the focus herein was on safety-class equipment in advanced nuclear power plants, the results are applicable to tall, slender equipment regardless of industry sector. Although the experiments used only spherical sliding bearings, other types of seismic isolators, such as the lead-rubber bearing, could be used instead.

6.4 Recommendations for equipment isolation inside a nuclear facility

Consensus standards ASCE/SEI 4-16 and ASCE/SEI 43-19 provide criteria for seismic analysis and design of structures, systems, and components (SSCs) in seismically isolated, safety-related nuclear facilities, including nuclear power plants. Equipment isolation is not addressed in either ASCE/SEI 4-16 or ASCE 43-19 but will be included in their next revisions. Based on the results and conclusions in this report, three recommendations are provided for analysis and design of isolated equipment:

1. Provide a stiff diaphragm above and below the isolation plane.

2. The axial flexibility of individual bearings must be explicitly characterized and modeled to capture the rocking and vertical responses of isolated equipment.
3. Five fully reversed cycles of loading impose sufficient earthquake-induced energy demand on isolators for prototype and production testing of isolators, as currently proposed in ASCE/SEI 43-19 for building isolation.

SECTION 7
REFERENCES

Aiken, I. D., Clark, P. W., and Kelly, J. M. (2002). "Experimental testing of reduced-scale seismic isolation bearings for the advanced liquid metal reactor." *Proceedings: IAEA-TECDOC-1288, Verification of analysis methods for predicting the behaviour of seismically isolated nuclear structures*, International Atomic Energy Agency (IAEA), Vienna, Austria.

American Society of Civil Engineers (ASCE). (2017). "Seismic analysis of safety-related nuclear structures and commentary." *ASCE/SEI 4-16*, Reston VA.

American Society of Civil Engineers (ASCE). (2021). "Seismic design criteria for structures, systems, and components in nuclear facilities." *ASCE/SEI 43-19*, Reston VA.

Bolisetti, C., Yu, C.-C., Coleman, J. L., Kosbab, B., and Whittaker, A. S. (2016). "Characterizing the benefits of seismic isolation for nuclear structures: a framework for risk-based decision making." *Technical Report INL/EXT-16-40122*, Idaho National Laboratory, Idaho Falls, ID.

Buckle, I. G., and Mayes, R. L. (1990). "Seismic isolation: History, application, and performance - A world view." *Earthquake Spectra*, 6(2), 161-201.

Buongiorno, J., Corradini, M., Parsons, J., and Petti, D. (2018). "The future of nuclear energy in a carbon constrained world - an interdisciplinary MIT study." *MIT Energy Initiative*, Massachusetts Institute of Technology, Cambridge, MA.

Calugaru, V., and Mahin, S. A. (2009). "Experimental and analytical studies of fixed base and seismically isolated liquid storage tanks." *Proceedings: 3rd International Conference on Advances in Experimental Structural Engineering*, San Fransciso, CA.

Chalhoub, M. S., and Kelly, J. M. (1988). "Theoretical and experimental studies of cylindrical water tanks in base isolated structures." *UCB/EERC-88/07*, Earthquake Engineering Research Center, University of California, Berkeley, CA.

Chopra, A. K. (2007). "Dynamics of structures." Third Edition. Pearson.

Cilsalar, H., and Constantinou, M. C. (2019). "Development and validation of a seismic isolation system for lightweight construction." *Technical Report MCEER-19-0001*, University at Buffalo, State University of New York, Buffalo, NY.

Clark, P. W., Aiken, I. D., Kelly, J. M., Gluekler, E. L., and Tajirian, F. F. (1995). "Tests of reduced-scale seismic isolation bearings for the US advanced liquid metal reactor (ALMR) program." *Proceedings: Joint ASME/JSME Pressure Vessels and Piping Conference*, Honolulu, HI.

Cochran, R. (2015). "Seismic base isolation of a high voltage transformer." *Proceedings: Electrical Transmission and Substation Structures 2015*, Branson, Missouri, 413-425.

Constantinou, M. C., Mokha, A., and Reinhorn, A. (1990). "Teflon bearings in base isolation II: Modeling." *Journal of Structural Engineering*, 116(2), 455-474.

Constantinou, M. C., Whittaker, A. S., Kalpakidis, Y., Fenz, D. M., and Warn, G. P. (2007). "Performance of seismic isolation hardware under service and seismic loading." *Technical Report MCEER-07-0012*, University at Buffalo, State University of New York, Buffalo, NY.

Constantinou, M. C. (2022). *Personal Communication* to K. M. Lal

Constantinou, M. C., and Whittaker, A. S. (2022). *Personal Communication* to K. M. Lal

Computers and Structures Incorporated (CSI). (2019). Computer Program SAP2000 (Version 20.2.0), Berkeley, CA.

Computers and Structures Incorporated (CSI). (2021). Computer Program SAP2000 (Version 23.3.0), Berkeley, CA.

Dobrescu, S., and Marinescu, L. (2005). "Earthquake protection of the Bucharest FN tandem accelerator." *Electrostatic Accelerators*, Springer, Berlin, Germany, 374-377.

Doulgerakis, N., Tehrani, P. K., Talebinejad, I., Kosbab, B. D., Cohen, M., and Whittaker, A. S. (2021). "Software verification and validation guidance for nonlinear seismic analysis." *Report developed under DOE grant number DE-NE0008857*, United States Department of Energy, Washington, D.C.

Electric Power Research Institute (EPRI). (2013). "Seismic isolation of nuclear power plants." Report 3002000561, Palo Alto, CA.

Ersoy, S., Ala Saadeghvaziri, M., Liu, G.-Y., and Mau, S. T. (2001). "Analytical and experimental seismic studies of transformers isolated with friction pendulum system and design aspects." *Earthquake Spectra*, 17(4), 569-595.

Fenz, D. M., and Constantinou, M. C. (2008a). "Mechanical behavior of multi-spherical sliding bearings." *Technical Report MCEER-08-0007*, University at Buffalo, State University of New York, Buffalo, NY.

Fenz, D. M., and Constantinou, M. C. (2008b). "Development, implementation and verification of dynamic analysis models for multi-spherical sliding bearings." *Technical Report MCEER-08-0018*, University at Buffalo, State University of New York, Buffalo, NY.

Huang, Y.-N., Whittaker, A. S., and Luco, N. (2008). "Performance assessment of conventional and base-isolated nuclear power plants for earthquake and blast loadings." *Technical Report MCEER-08-0019*, University at Buffalo, State University of New York, Buffalo, NY.

Huang, Y.-N., Whittaker, A. S., Kennedy, R. P., and Mayes, R. L. (2009). "Assessment of base-isolated nuclear structures for design and beyond-design basis earthquake shaking." *Technical Report MCEER-09-0008*, University at Buffalo, State University of New York, Buffalo, NY.

Huang, Y.-N., Whittaker, A. S., and Luco, N. (2011a). "A seismic risk assessment procedure for nuclear power plants: (I) Methodology." *Nuclear Engineering and Design*, 241, 3996-4003.

Huang, Y.-N., Whittaker, A. S., and Luco, N. (2011b). "A seismic risk assessment procedure for nuclear power plants: (II) Application." *Nuclear Engineering and Design*, 241, 4004-4011.

International Atomic Energy Agency (IAEA). (2020a). "Nuclear power and the clean energy transition." *IAEA Bulletin, Volume 61-3*, Vienna, Austria.

International Atomic Energy Agency (IAEA). (2020b). "Driving deeper decarbonization with nuclear energy." *IAEA Bulletin, Volume 61-3*, Vienna, Austria.

International Atomic Energy Agency (IAEA). (2020c). "Climate change and nuclear power 2020." *STI/PUB/1911*, Vienna, Austria.

International Energy Agency (IEA). (2019). "Nuclear power in a clean energy system." Paris, France.

Ingersoll, E. D., and Gogan, K. (2020). "Missing link to a livable climate: How hydrogen-enabled synthetic fuels can help deliver the Paris goals." LucidCatalyst, Cambridge, MA.

Ipek, C., Wolff, E. D., and Constantinou, M. C. (2021). "Accuracy of analytical models to predict primary and secondary system response in seismically isolated buildings." *Soil Dynamics and Earthquake Engineering*, 150, 106944.

Kammerer, A. M., Whittaker, A. S., and Constantinou, M. C. (2019). "Technical considerations for seismic isolation of nuclear facilities." *NUREG/CR-7253*, United States Nuclear Regulatory Commission, Washington, D.C. (ML19050A422).

Kelly, J. M. (1983). "The use of base isolation and energy-absorbing restrainers for the seismic protection of a large power plant component." *EPRI-NP-2918*, Electric Power Research Institute, Palo Alto, CA.

Kelly, T. E., and Mayes, R. L. (1989). "Seismic isolation of storage tanks." *Proceedings: Seismic engineering: Research and Practice*, ASCE, 408-417.

Kircher, C. A., Delfosse, G. C., Schoof, C. C., Khemici, O., and Shah, H. (1979). "Performance of a 230 kV ATB 7 power circuit breaker mounted on GAPEC seismic isolation." *Report No. 40*, The John A. Blume Earthquake Engineering Center, Stanford University, Stanford, CA.

Kong, D. (2010). "Evaluation and protection of high voltage electrical equipment against severe shock and vibrations." *PhD dissertation*, University at Buffalo, State University of New York, Buffalo, NY.

Kumar, M., Whittaker, A. S., and Constantinou, M. C. (2015). "Response of base-isolated nuclear structures to extreme earthquake shaking." *Nuclear Engineering and Design*, 295, 860-874.

Kumar, M., Whittaker, A. S., and Constantinou, M. C. (2017a). "Extreme earthquake response of nuclear power plants isolated using sliding bearings." *Nuclear Engineering and Design*, 316, 9-25.

Kumar, M., Whittaker, A. S., Kennedy, R. P., Johnson, J. J., and Kammerer, A. (2017b). "Seismic probabilistic risk assessment for seismically isolated safety-related nuclear facilities." *Nuclear Engineering and Design*, 313, 386-400.

Kumar, M., Whittaker, A. S., and Constantinou, M. C. (2019a). "Seismic isolation of nuclear power plants using sliding bearings." *NUREG/CR-7254*, United States Nuclear Regulatory Commision, Washington, D.C. (ML19158A513).

Kumar, M., Whittaker, A. S., and Constantinou, M. C. (2019b). "Seismic isolation of nuclear power plants using elastomeric bearings." *NUREG/CR-7255*, United States Nuclear Regulatory Commision, Washington, D.C. (ML19063A541).

Lal, K. M., Parsi, S. S., and Whittaker, A. S. (2020). "Cost basis for utilizing seismic isolation for nuclear power plant design." *Report 03002018345*, Electric Power Research Institute, Palo Alto, C.A.

Lal, K. M., Parsi, S. S., Kosbab, B. D., Ingersoll, E. D., Charkas, H., and Whittaker, A. S. (2022). "Towards standardized nuclear reactors: Seismic isolation and the cost impact of the earthquake load case." *Nuclear Engineering and Design*, 386, (https://doi.org/10.1016/j.nucengdes.2021.111487).

Lal, K. M., Whittaker, A. S., and Constantinou, M. C. (2023). "Mid-height seismic isolation of tall, slender equipment." *Project number PRJ-3793*, DesignSafe-CI. (https://doi.org/10.17603/ds2-y9wd-8j58).

Lee, D., and Constantinou, M. C. (2017). "Development and validation of a combined horizontal-vertical seismic isolation system for high-voltage power transformers." *Technical Report MCEER-17-0007*, University at Buffalo, State University of New York, Buffalo, NY.

Lee, D., and Constantinou, M. C. (2018). "Combined horizontal–vertical seismic isolation system for high-voltage–power transformers: development, testing and validation." *Bulletin of Earthquake Engineering*, 16(9), 4273-4296.

Livermore Software Technology Corporation (LSTC). (2019). Computer Program LS-DYNA (Version R 9.3.1), Livermore, California.

Marinescu, L., Pascovici, G., Zoran, V., Dumitrescu, R., Sireteanu, T., Iordăchescu, E., Filimon, I., and Winkler, A. (1993). "Earthquake protection and other improvements to the Bucharest FN tandem accelerator." *Nuclear Instruments and Methods in Physics Research Section A: Accelerators, Spectrometers, Detectors and Associated Equipment*, 328(1-2), 90-96.

Masopust, R., Podrouzek, J., and Zach, J. (1993). "GERB viscous dampers in application for pipelines and other components in nuclear power plants." *Proceedings: Post SMiRT-12 Seminar No. 16*, Vienna, Austria.

McVitty, W. J., and Constantinou, M. C. (2015). "Property modification factors for seismic isolators: Design guidance for buildings." *Technical Report MCEER-15-0005*, University at Buffalo, State University of New York, Buffalo, NY.

Mir, F. U. H., Lal, K. M., Kosbab, B. D., Nguyen, N., Song, B., Clavelli, M., Tilow, K., and Whittaker, A. S. (2022a). "Earthquake-simulator experiments of a model of a seismically-isolated, fluoride-salt cooled high-temperature reactor." *Technical Report MCEER-22-0004*, University at Buffalo, State University of New York, Buffalo, NY.

Mir, F. U. H., Yu, C.-C., Whittaker, A. S., and Constantinou, M. C. (2022b). "Physical and numerical simulations of seismic fluid-structure interaction in advanced nuclear reactors." *Technical Report MCEER-22-0002*, University at Buffalo, State University of New York, Buffalo, NY.

Murota, N., Feng, M. Q., and Liu, G.-Y. (2005). "Experimental and analytical studies of base isolation systems for seismic protection of power transformers." *Technical Report MCEER-05-0008*, University at Buffalo, State University of New York, Buffalo, NY.

Oikonomou, K., Constantinou, M. C., Reinhorn, A. M., and Yenidogan, C. (2012). "Seismic isolation of electrical equipment - Seismic table simulation." *Proceedings: 15th World Conference on Earthquake Engineering (15WCEE)*, Lisbon, Portugal.

Oikonomou, K., Constantinou, M. C., Reinhorn, A. M., and Kemper Jr, L. (2016). "Seismic isolation of high voltage electrical power transformers." *Technical Report MCEER-16-0006*, University at Buffalo, State University of New York, Buffalo, NY.

Parsi, S. S. (2022). "Impedance-matching control design for shake-table testing and model-in-the-loop simulations." *Technical Report MCEER 22-0003*, University at Buffalo, State University of New York, Buffalo, NY.

Parsi, S. S., Lal, K. M., Kosbab, B. D., Ingersoll, E. D., Shirvan, K., and Whittaker, A. S. (2022). "Seismic isolation: A pathway to standardized advanced nuclear reactors." *Nuclear Engineering and Design*, 387, (https://doi.org/10.1016/j.nucengdes.2021.111445).

Partanen, R., Qvist, S., Gogan, K., and Ingersoll, E. (2019). "Sustainable nuclear: An assessment of the sustainability of nuclear power for the EU taxonomy consultation 2019." Prepared by LucidCatalyst and Think Atom for Électricité de France (EDF), United Kingdom.

Pecínka, L., Macák, P., Tanzer, M., Zeman, V., and Stych, J. (2001). "Seismic upgrading of WWER 440 and WWER 1000 primary coolant loops by means of viscous dampers GERB." *Proceedings: Workshop on the Seismic Re-evaluation of all Nuclear Facilities*, Ispra, Italy.

Sarlis, A. A., and Constantinou, M. C. (2010). "Modelling Triple Friction Pendulum isolators in program SAP2000." *Internal report*, University at Buffalo.

Sarlis, A. A., Constantinou, M. C., and Reinhorn, A. M. (2013). "Shake table testing of Triple Friction Pendulum isolators under extreme conditions." *Technical Report MCEER-13-0011*, University at Buffalo, State University of New York, Buffalo, NY.

Sivaselvan, M. V. (2022). *Personal Communication* to K. M. Lal

Tajirian, F. (1998). "Base isolation design for civil components and civil structures." *Proceedings: Structural Engineers World Congress*, San Francisco, California.

Tajirian, F. F., Kelly, J. M., and Gluekler, E. L. (1989). "Testing of seismic isolation bearings for the PRISM advanced liquid metal reactor under extreme loads." *Transactions: 10th International Conference on Structural Mechanics in Reactor Technology (SMiRT-10)*, Anaheim, CA.

Tajirian, F. F. (1992). "Seismic analysis for the ALMR." *Proceedings: International Atomic Energy Agency (IAES) Specialists' Meeting on Seismic Isolation Technology*, San Jose, CA.

Tajirian, F. F. (1993). "Seismic isolation of critical components and tanks." *Proceedings: ATC-17-1, Seminar on Seismic Isolation, Passive Energy Dissipation, and Active Control*, San Francisco, California, 223-244.

Tajirian, F. F., and Patel, M. R. (1993). "Response of seismic isolated facilities: a parametric study of the ALMR." *Transactions: 12th International Conference on Structural Mechanics in Reactor Technology (SMiRT-12)*, Stuttgart, Germany.

United States Nuclear Regulatory Commission (USNRC). (1973). "Design response spectra for seismic design of nuclear power plants." *Regulatory Guide 1.60*, Washington, D.C.

Warn, G. P., and Whittaker, A. S. (2006). "A study of the coupled horizontal-vertical behavior of elastomeric and lead-rubber seismic isolation bearings." *Technical Report MCEER-06-0011*, University at Buffalo, State University of New York, Buffalo, NY.

Warn, G. P., and Whittaker, A. S. (2007). "Performance estimates for seismically isolated bridges." *Technical Report MCEER-07-0024*, University at Buffalo, State University of New York, Buffalo, NY.

Whittaker, A. S., Sollogoub, P., and Kim, M. K. (2018). "Seismic isolation of nuclear power plants: Past, present and future." *Nuclear Engineering and Design*, 338, 290-299.

Yu, C.-C., Bolisetti, C., Coleman, J. L., Kosbab, B., and Whittaker, A. S. (2018). "Using seismic isolation to reduce risk and capital cost of safety-related nuclear structures." *Nuclear Engineering and Design*, 326, 268-284.

Yu, C. C., and Whittaker, A. S. (2020). "Analytical and numerical studies of seismic fluid-structure interaction in liquid-filled vessels." *Technical Report MCEER 20-0003*, University at Buffalo, State University of New York, Buffalo, NY.

Zayas, V. A., and Low, S. S. (1995). "Application of seismic isolation to industrial tanks." *Proceedings: Joint American Society of Mechanical Engineers (ASME)/Japan Society of Mechanical Engineers (JSME) Conference on Pressure Vessels and Piping*, Honolulu, HI.

APPENDIX A
TEST DATA FOR SFP AND TFP BEARINGS

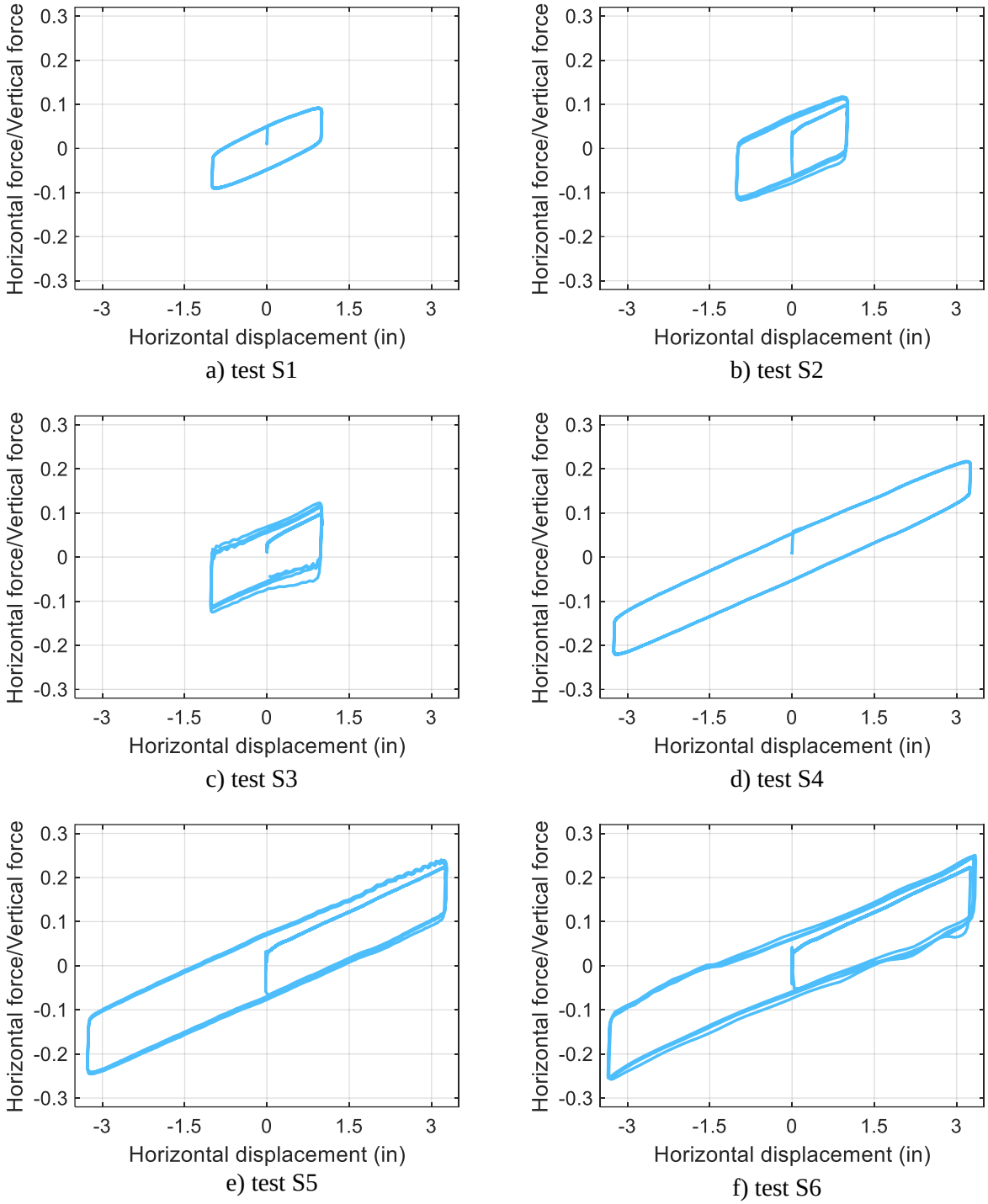

a) test S1

b) test S2

c) test S3

d) test S4

e) test S5

f) test S6

Figure A-1. Normalized force-displacement loops for bearing SF1, tests per Table 3-3

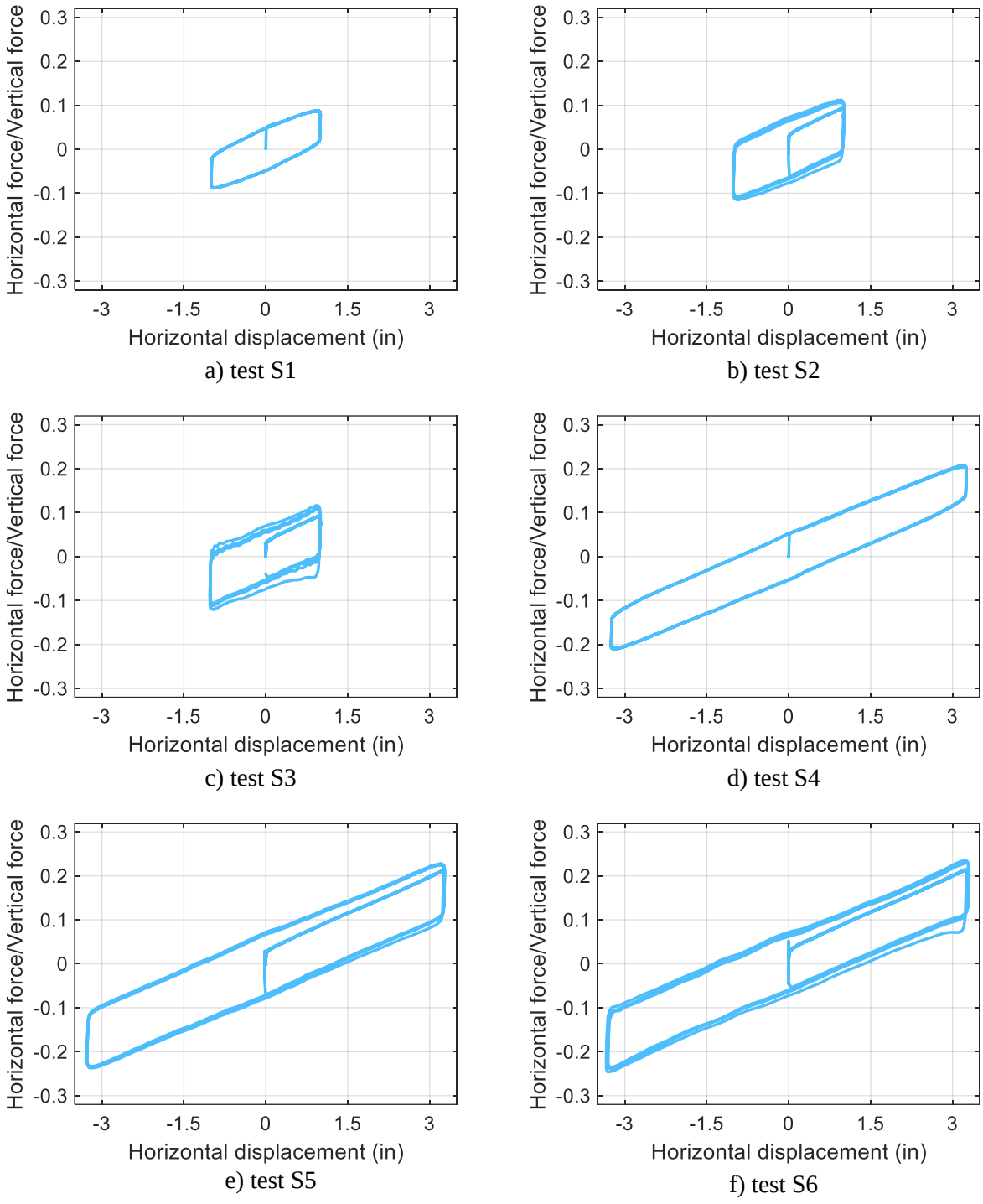

a) test S1

b) test S2

c) test S3

d) test S4

e) test S5

f) test S6

Figure A-2. Normalized force-displacement loops for bearing SF2, tests per Table 3-3

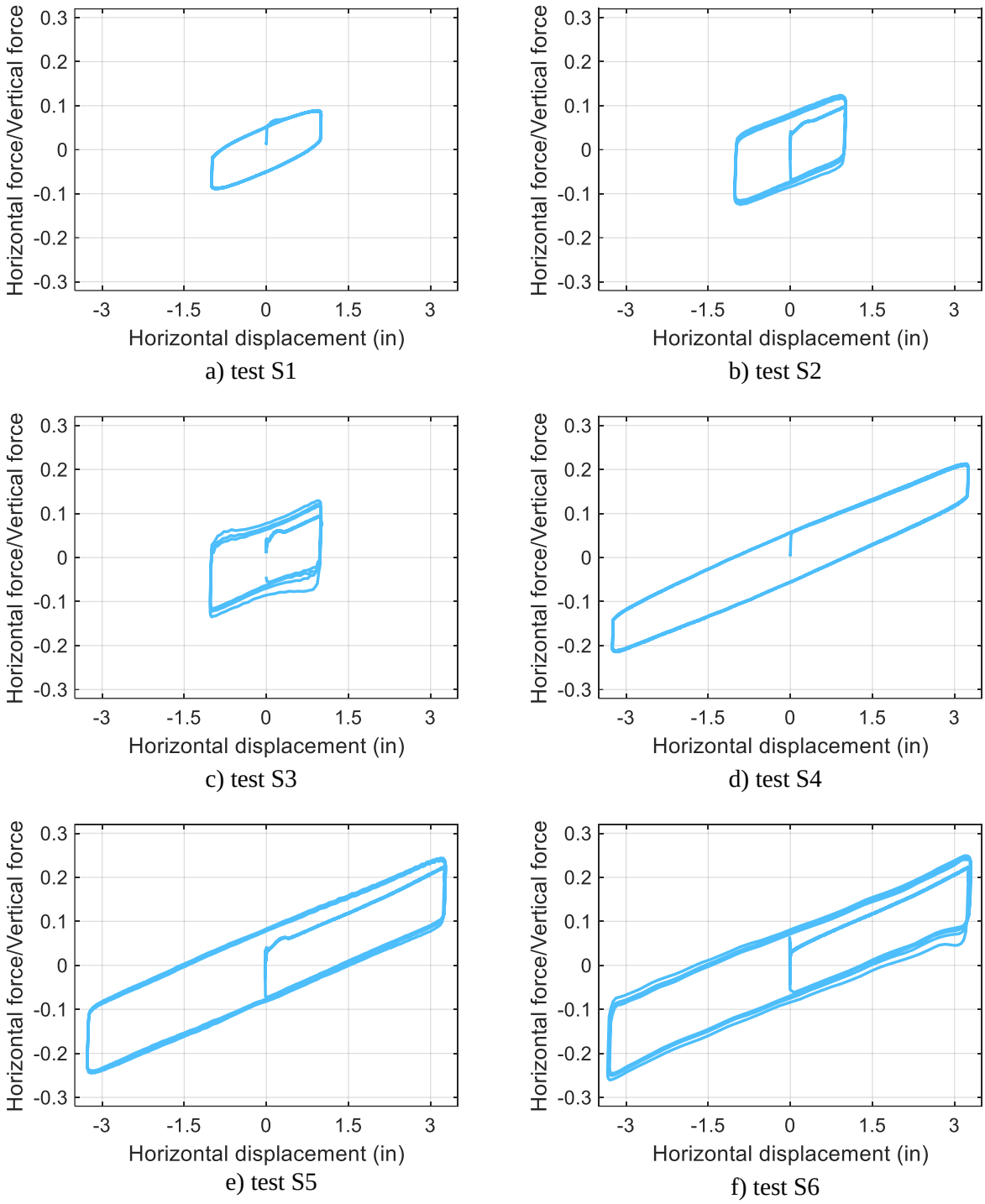

a) test S1

b) test S2

c) test S3

d) test S4

e) test S5

f) test S6

Figure A-3. Normalized force-displacement loops for bearing SF3, tests per Table 3-3

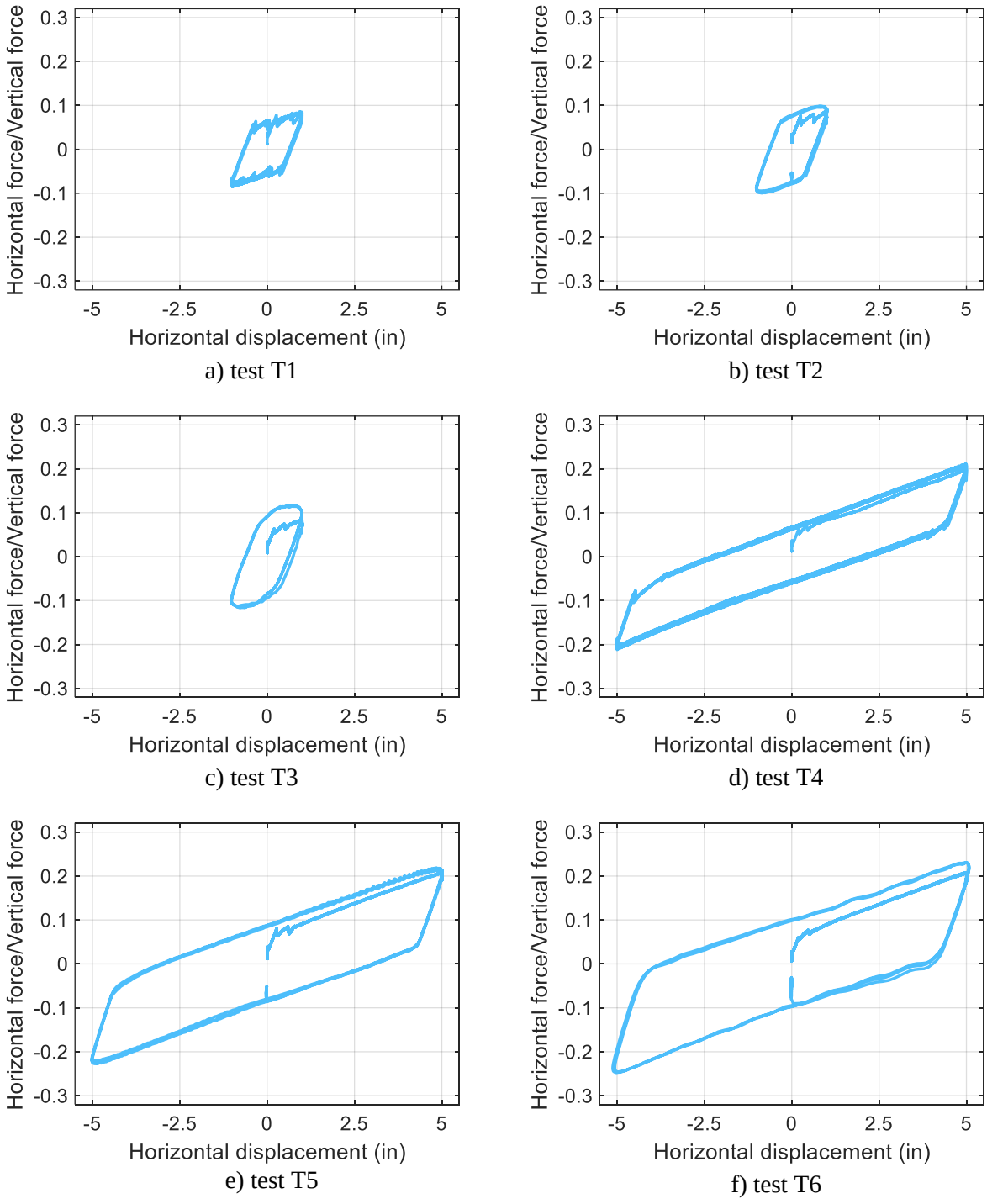

a) test T1

b) test T2

c) test T3

d) test T4

e) test T5

f) test T6

Figure A-4. Normalized force-displacement loops for bearing TF1, tests per Table 3-4

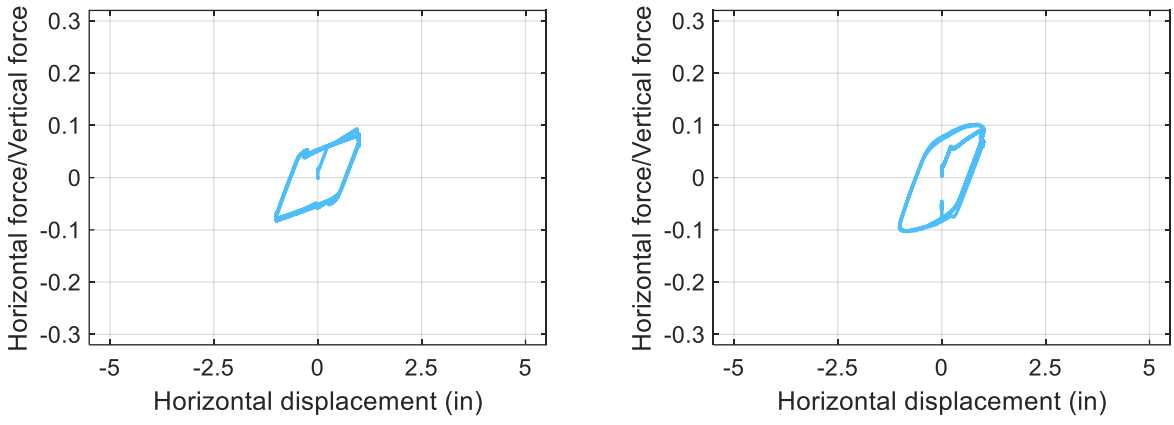

a) test T1

b) test T2

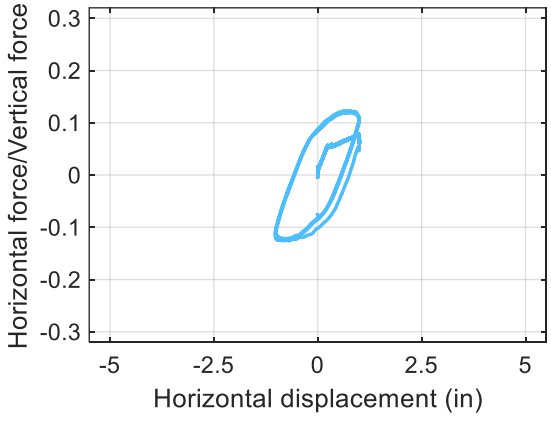

c) test T3

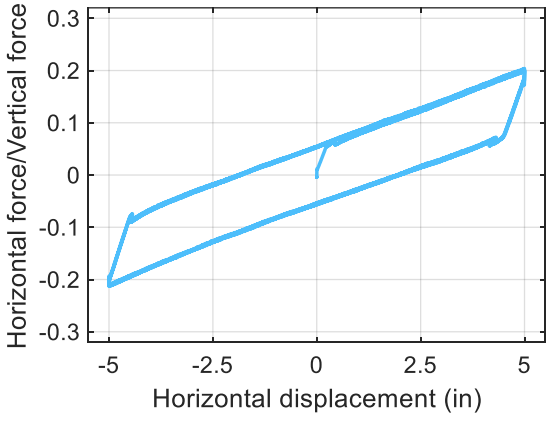

d) test T4

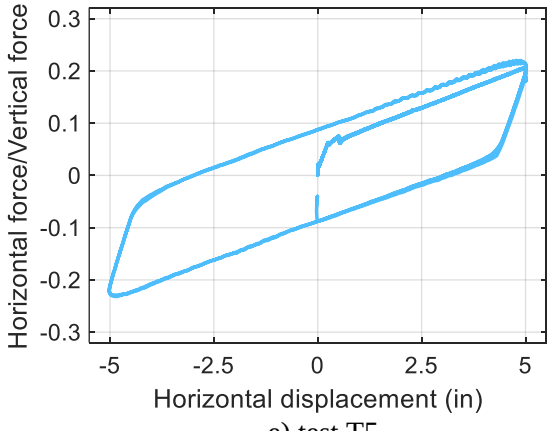

e) test T5

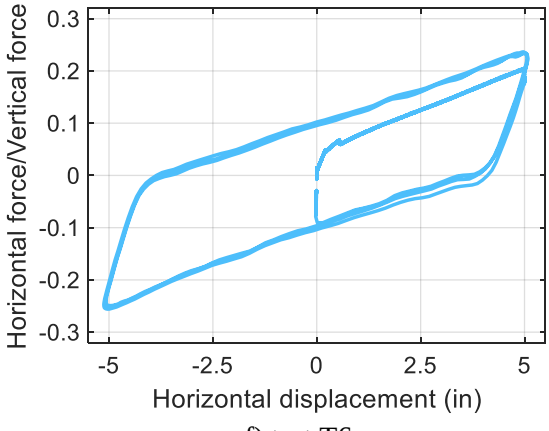

f) test T6

Figure A-5. Normalized force-displacement loops for bearing TF2, tests per Table 3-4

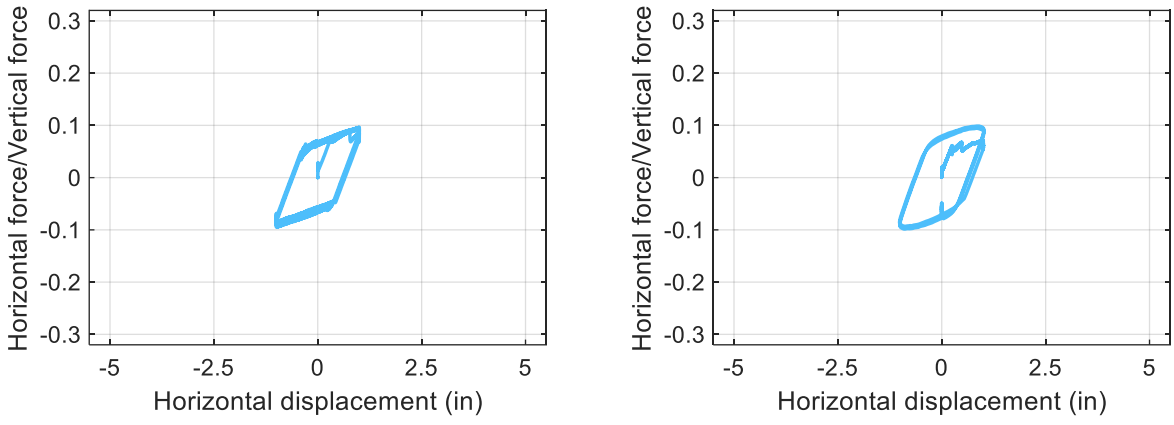

a) test T1

b) test T2

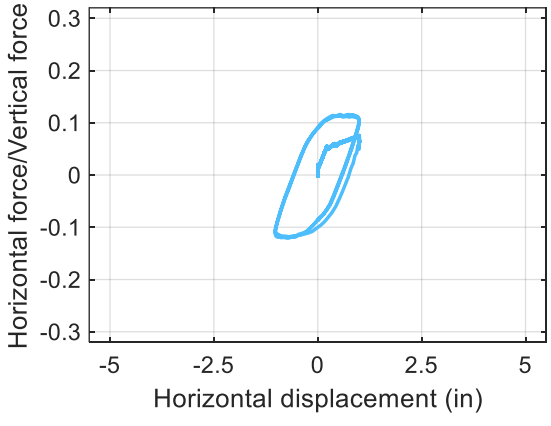

c) test T3

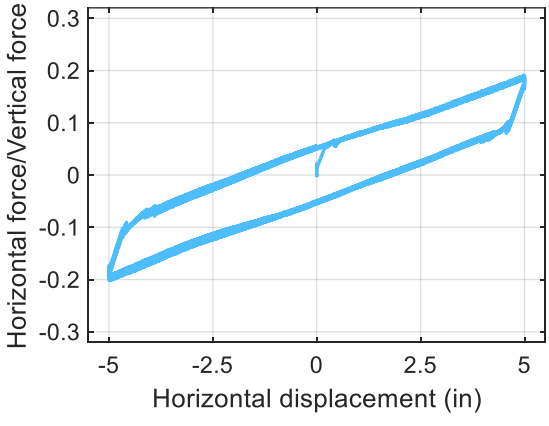

d) test T4

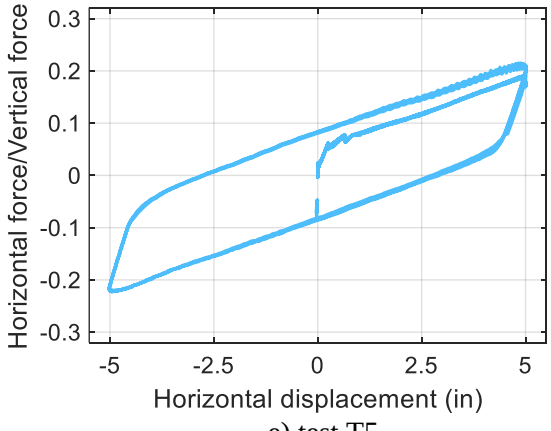

e) test T5

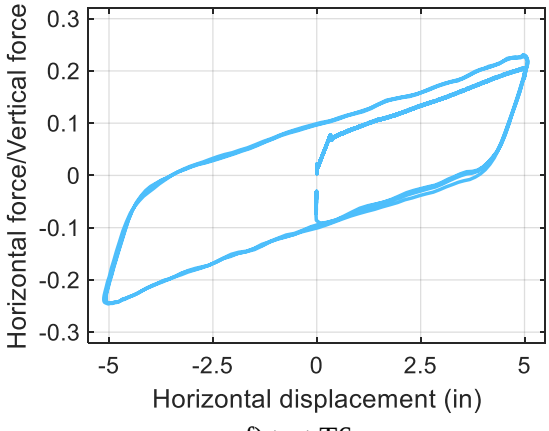

f) test T6

Figure A-6. Normalized force-displacement loops for bearing TF3, tests per Table 3-4

APPENDIX B
FABRICATION DRAWINGS

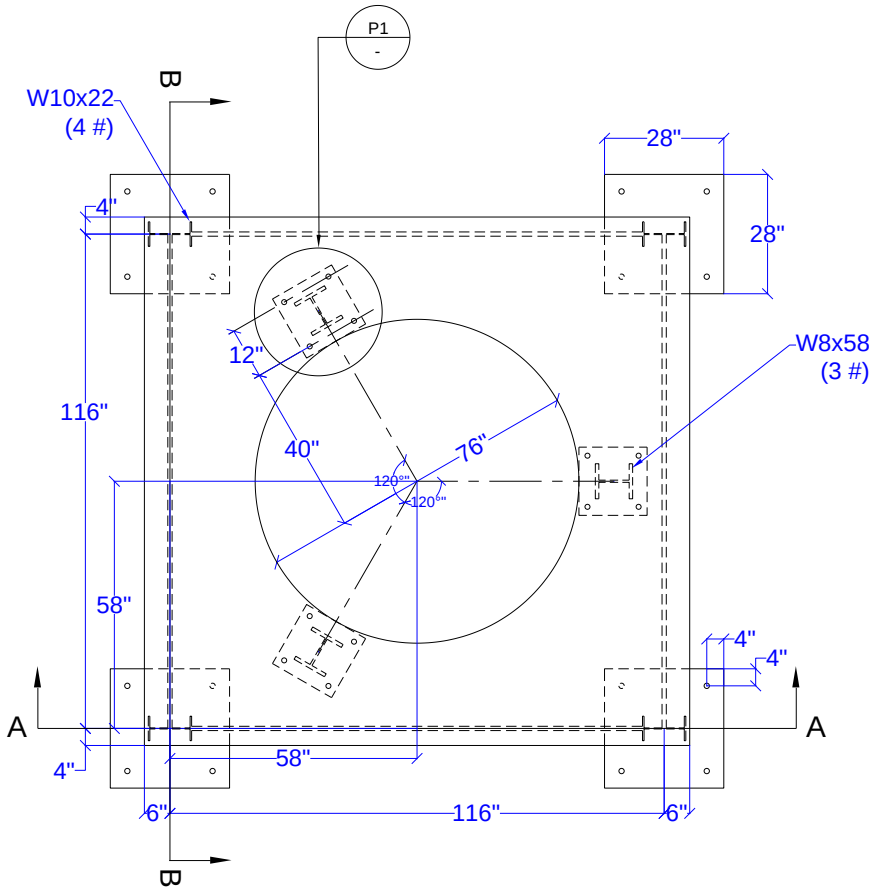

a) plan

Figure B-1. Fabrication drawings for support frame

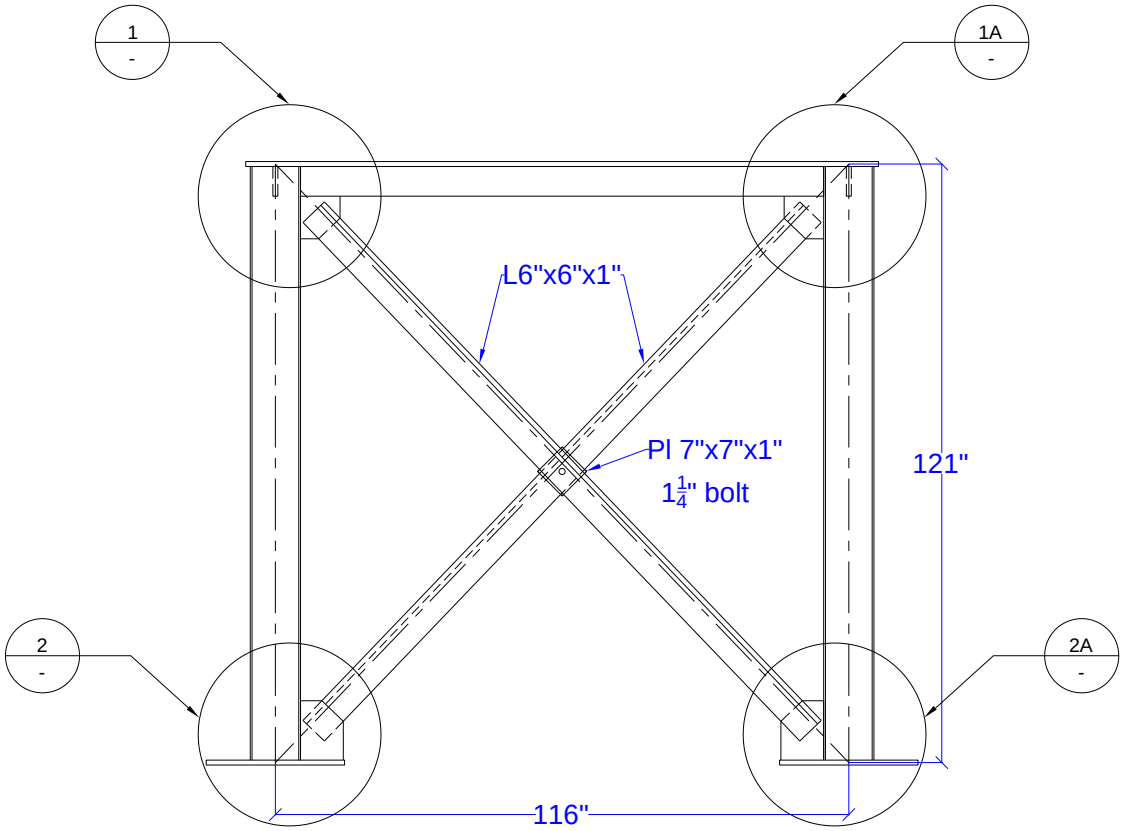

b) section A-A

Figure B-1. Fabrication drawings for support frame (cont.)

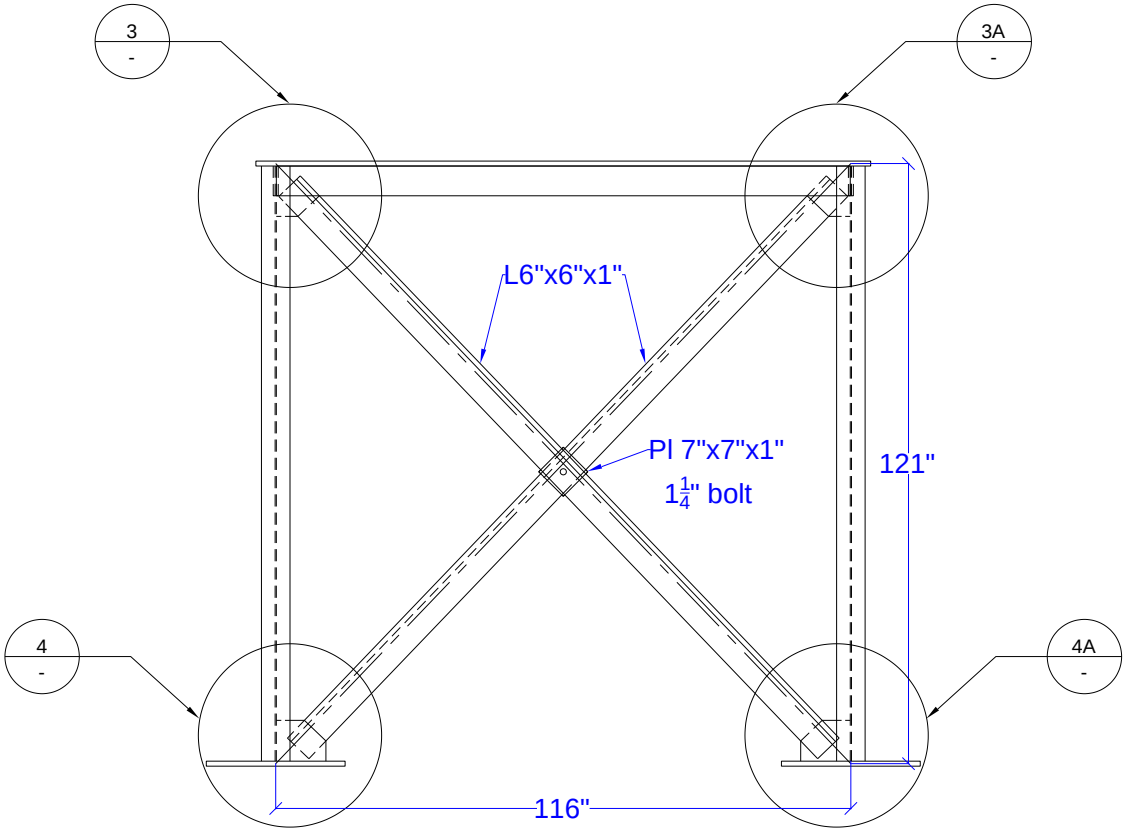

c) section B-B

Figure B-1. Fabrication drawings for support frame (cont.)

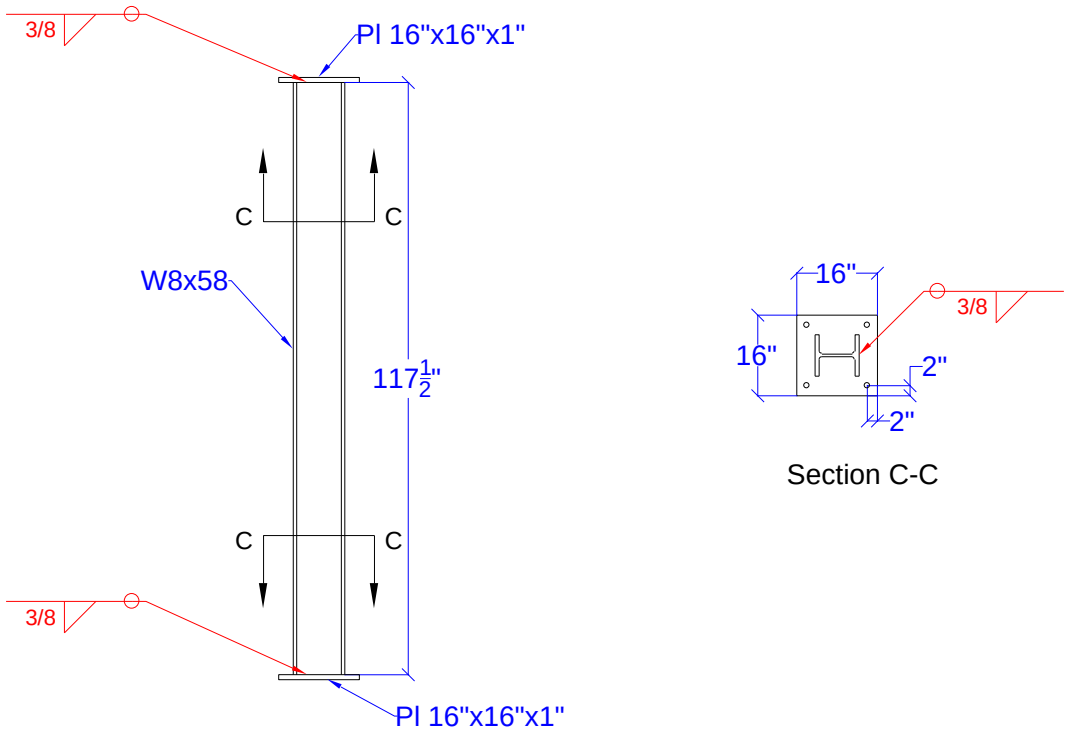

d) callout P1

Figure B-1. Fabrication drawings for support frame (cont.)

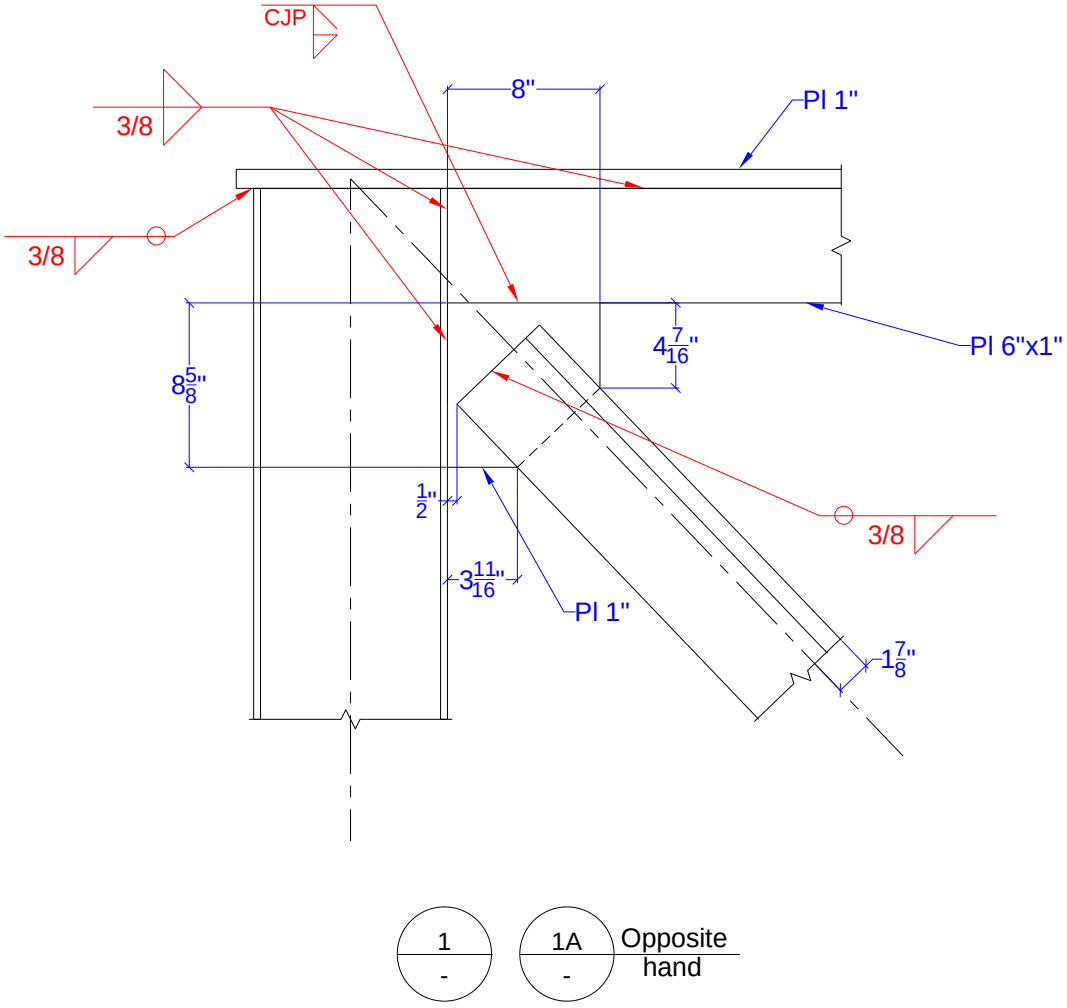

e) callout 1 and 1A

Figure B-1. Fabrication drawings for support frame (cont.)

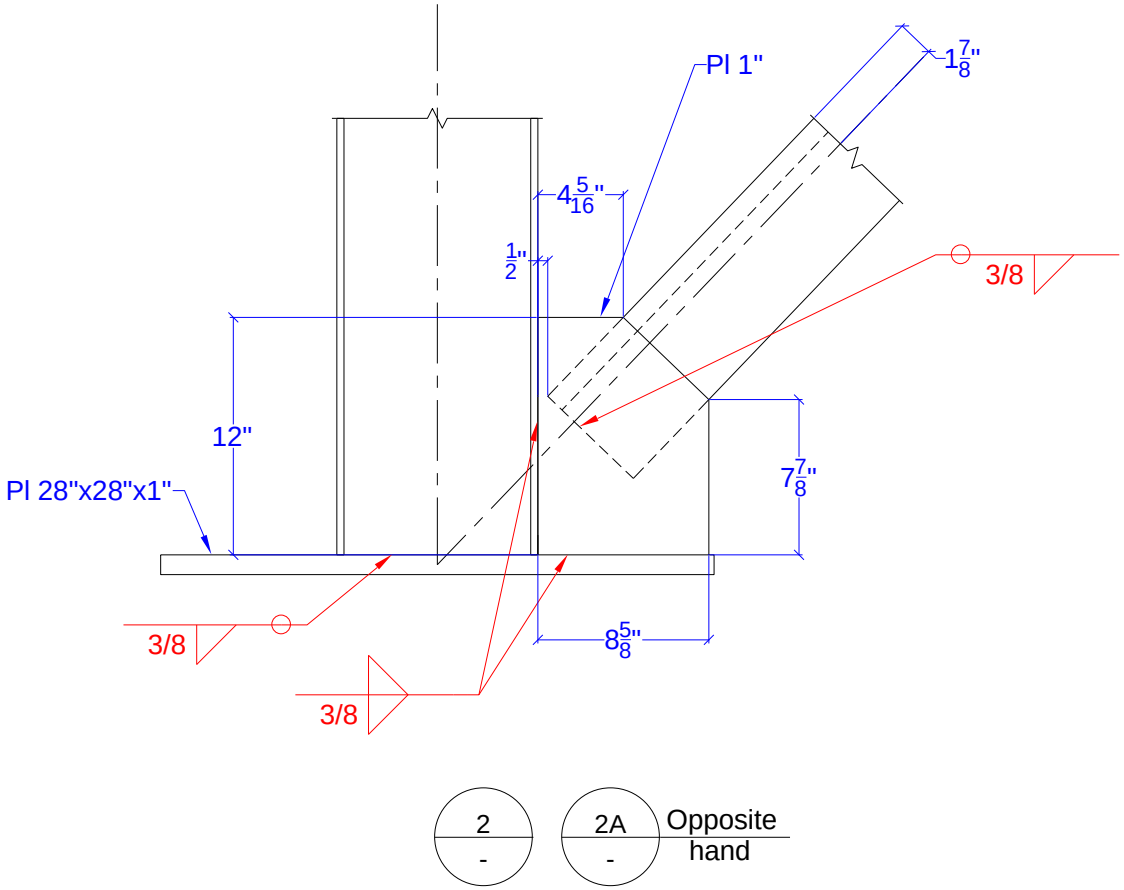

f) callout 2 and 2A

Figure B-1. Fabrication drawings for support frame (cont.)

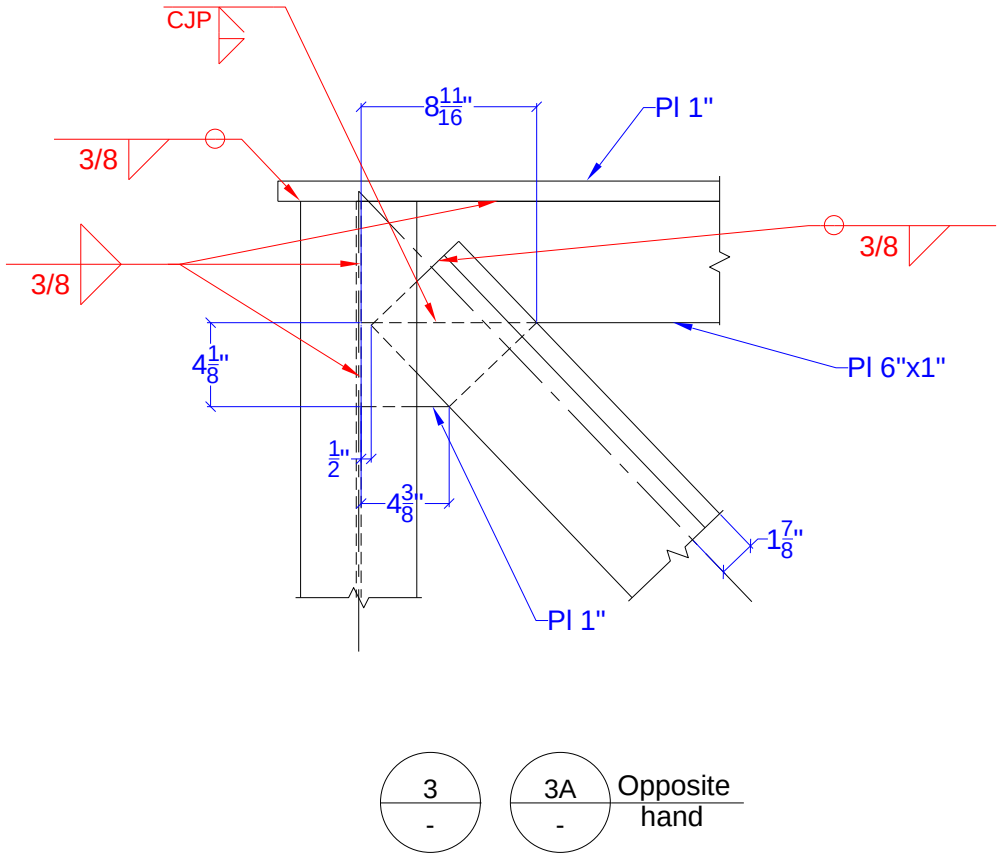

g) callout 3 and 3A

Figure B-1. Fabrication drawings for support frame (cont.)

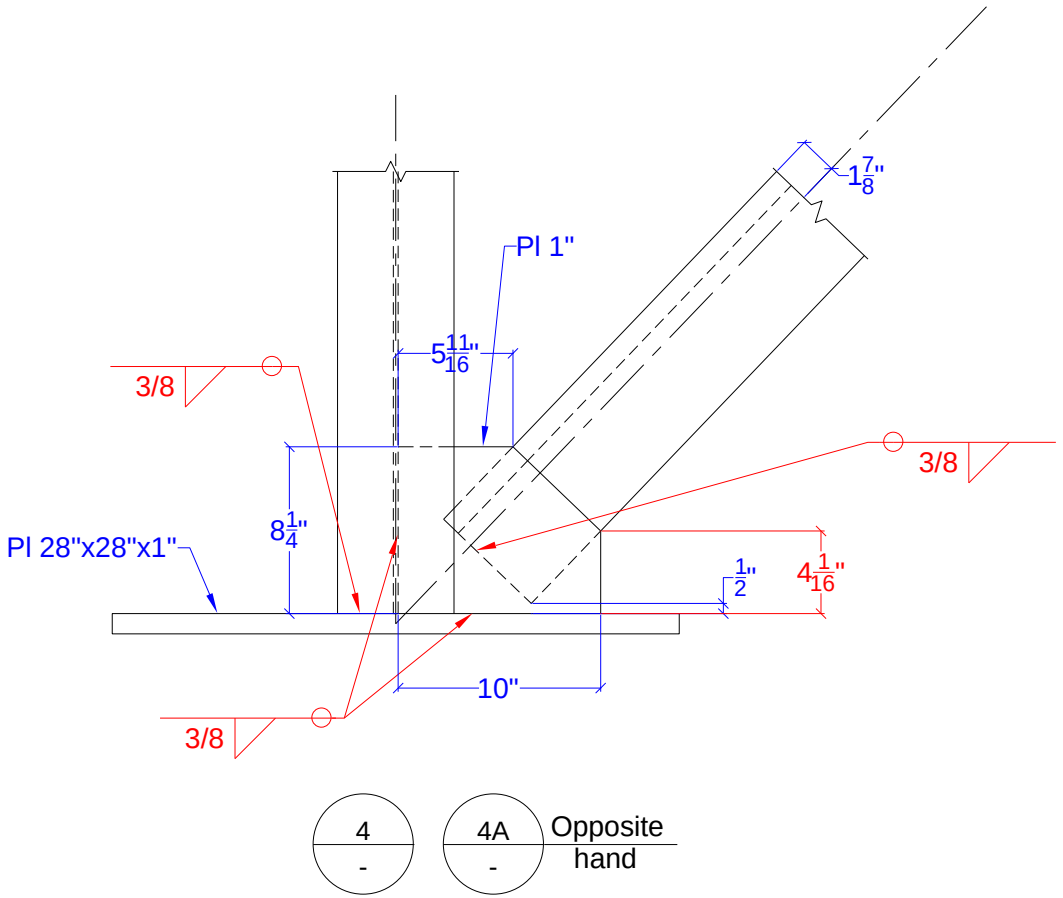

h) callout 4 and 4A

Figure B-1. Fabrication drawings for support frame (cont.)

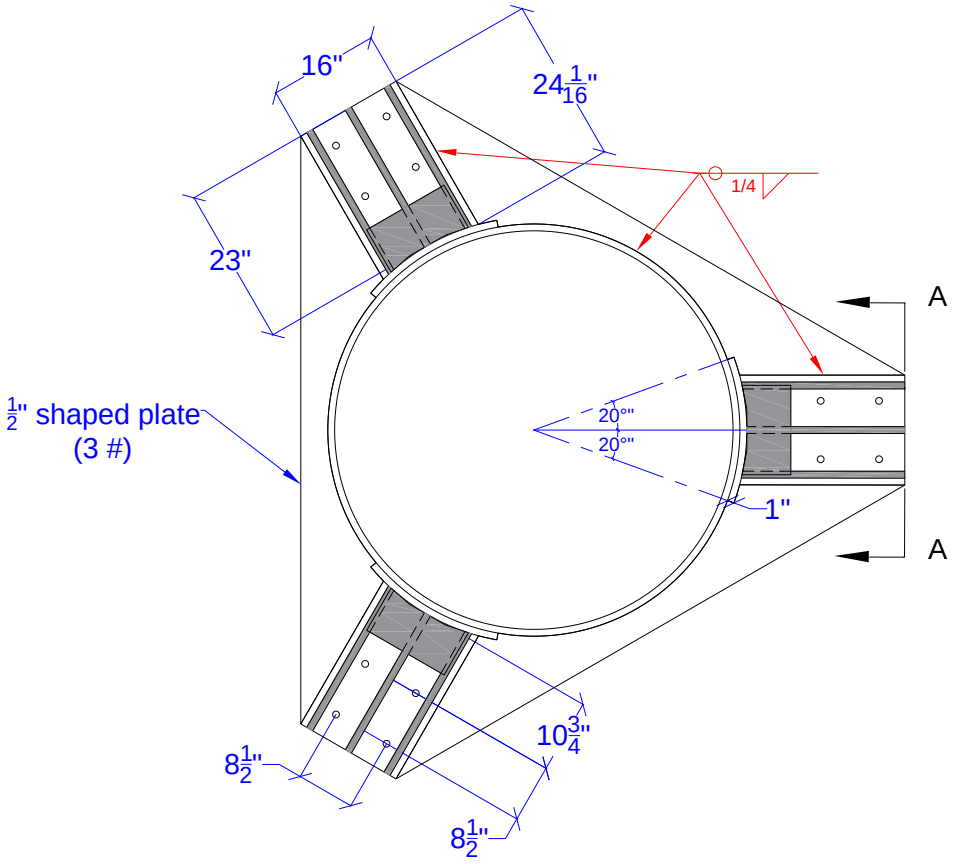

a) plan

Figure B-2. Fabrication drawings for vessel

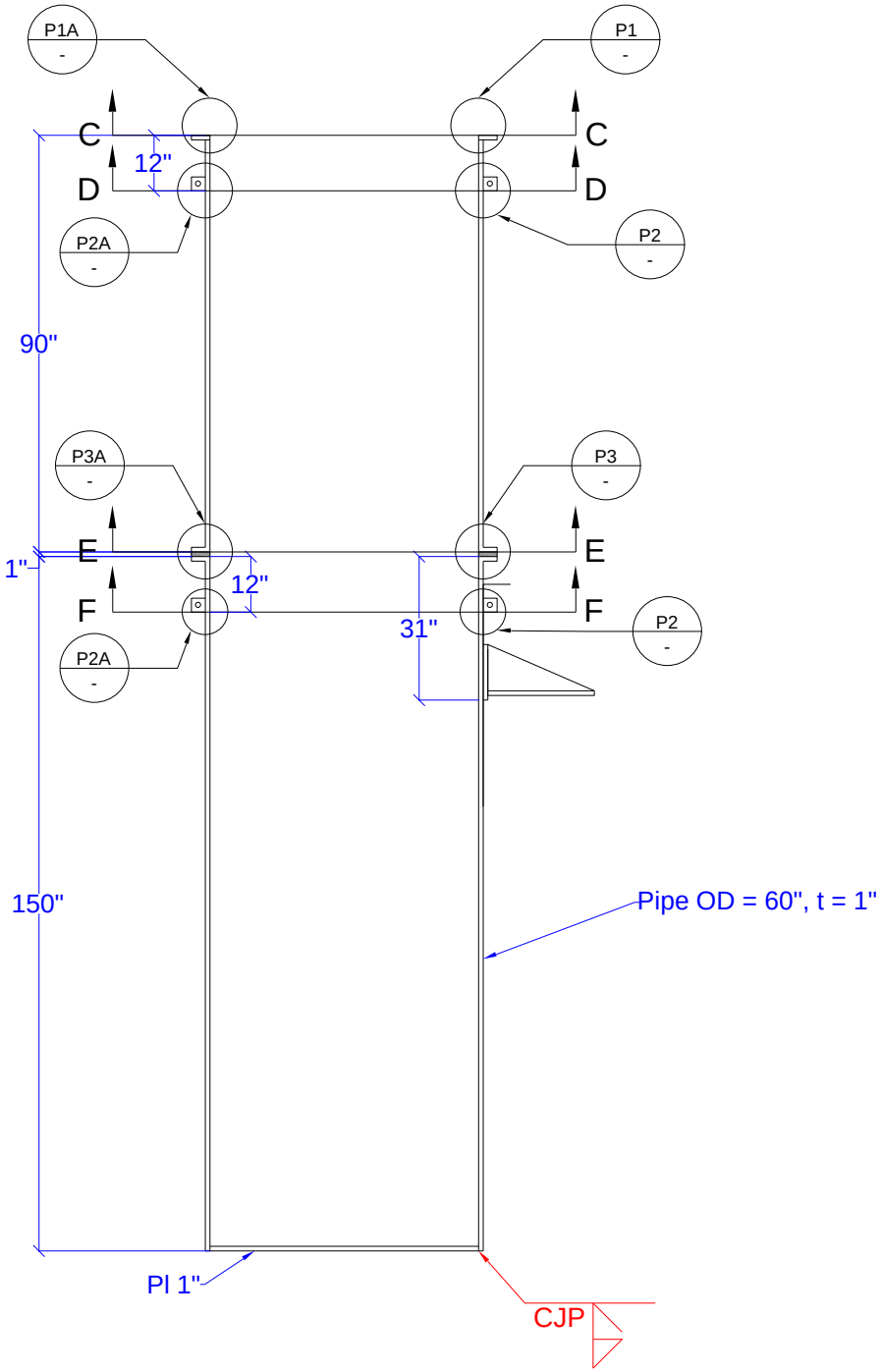

b) elevation

Figure B-2. Fabrication drawings for vessel (cont.)

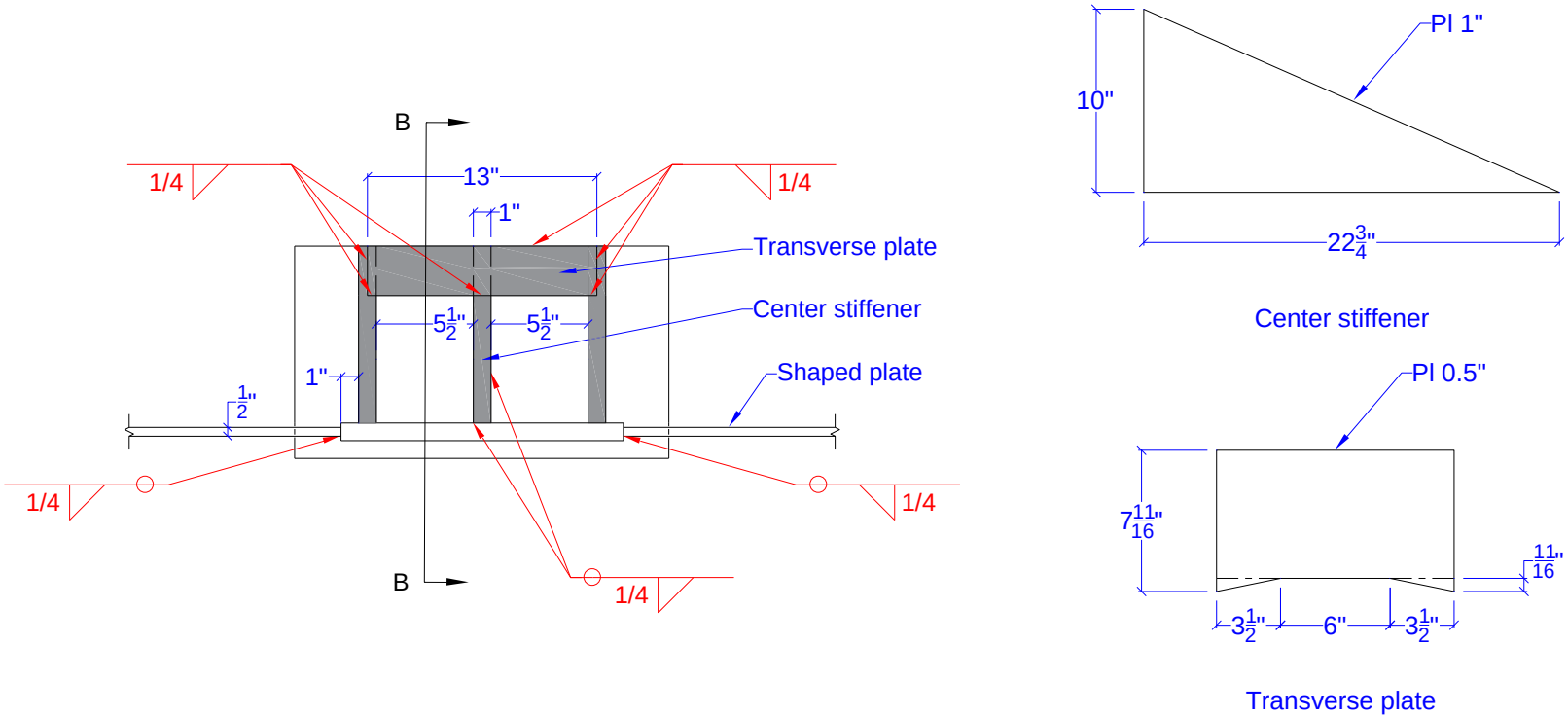

c) section A-A

Figure B-2. Fabrication drawings for vessel (cont.)

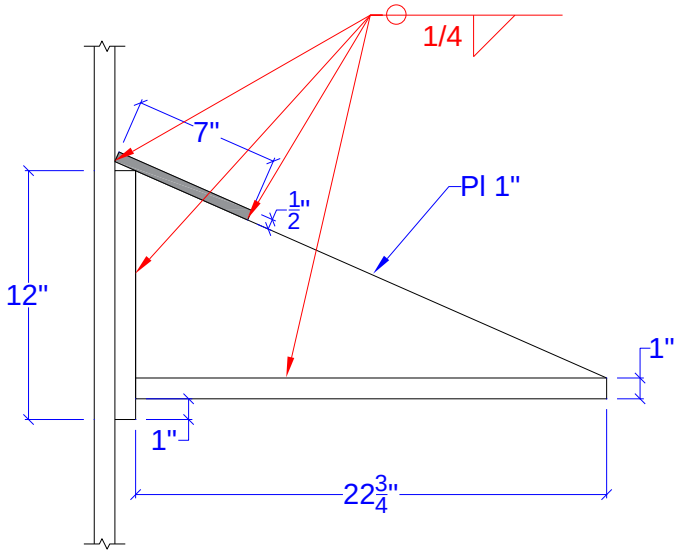

d) section B-B

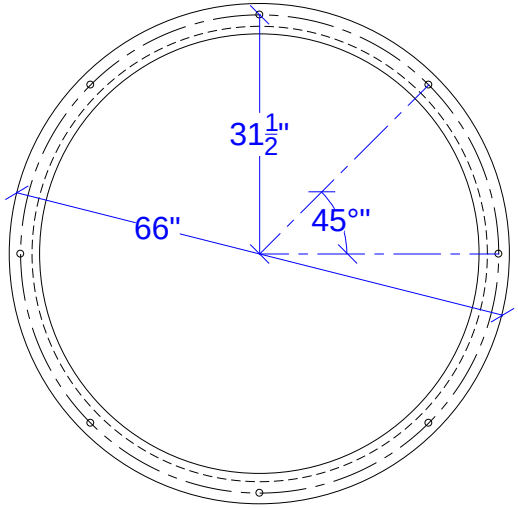

e) section C-C

Figure B-2. Fabrication drawings for vessel (cont.)

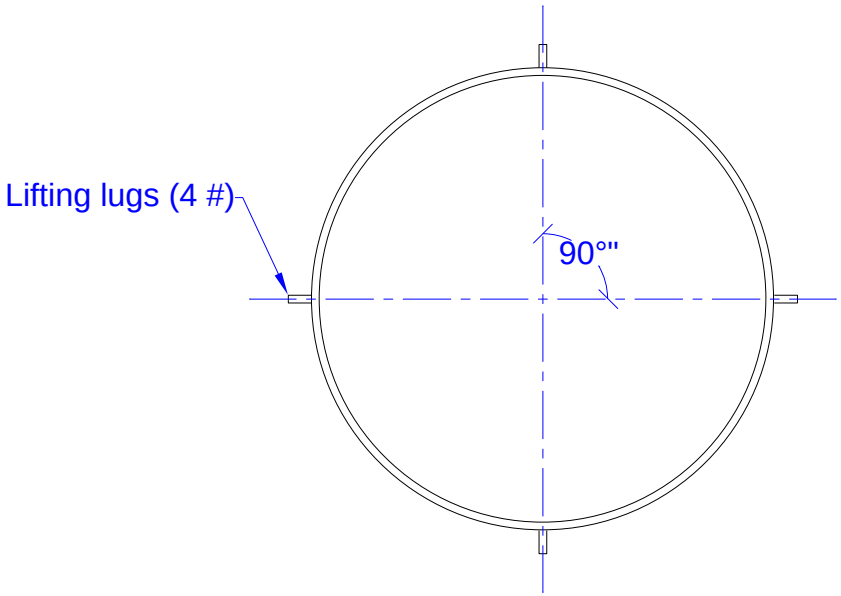

f) section D-D and F-F

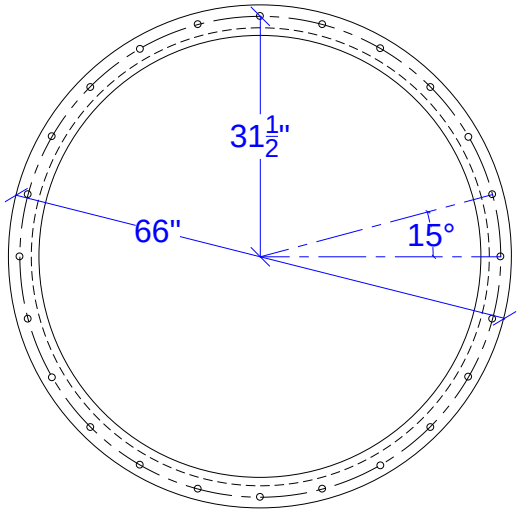

g) section E-E

Figure B-2. Fabrication drawings for vessel (cont.)

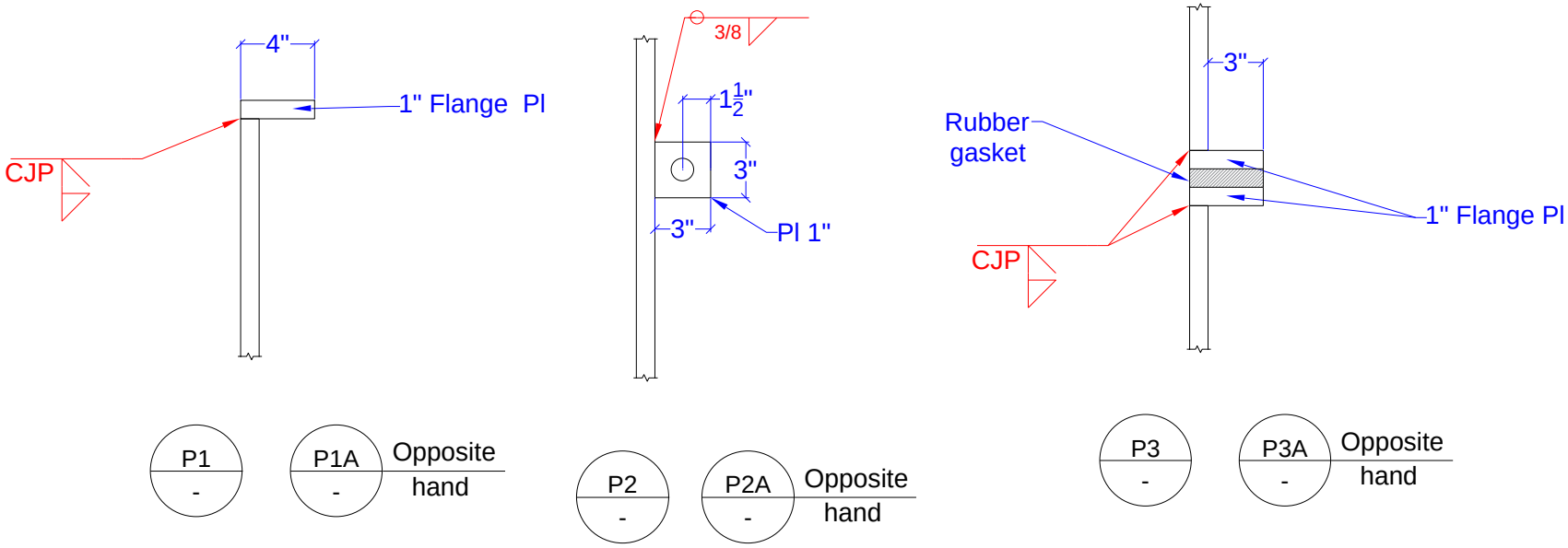

h) callout P1 i) callout P2 j) callout P3

Figure B-2. Fabrication drawings for vessel (cont.)

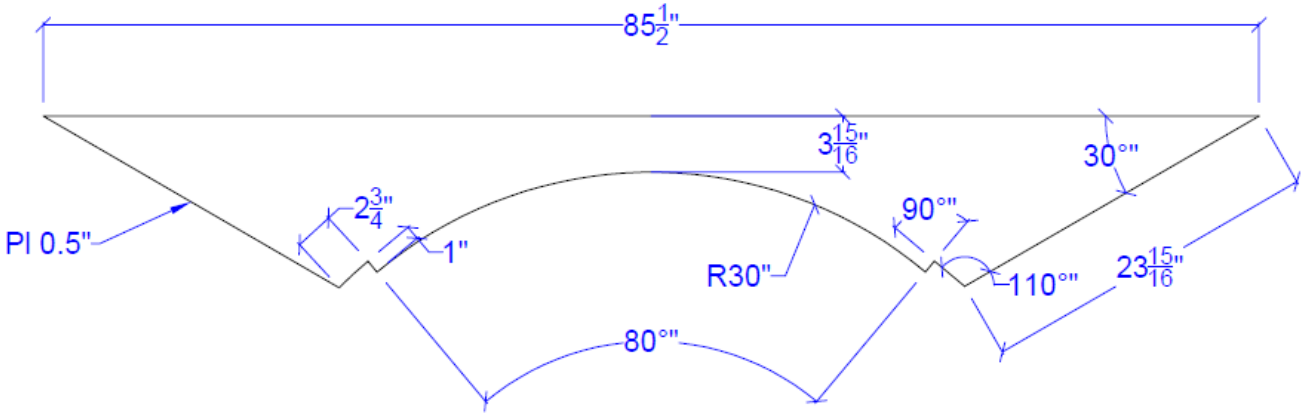

Figure B-3. Fabrication drawing for shaped plate

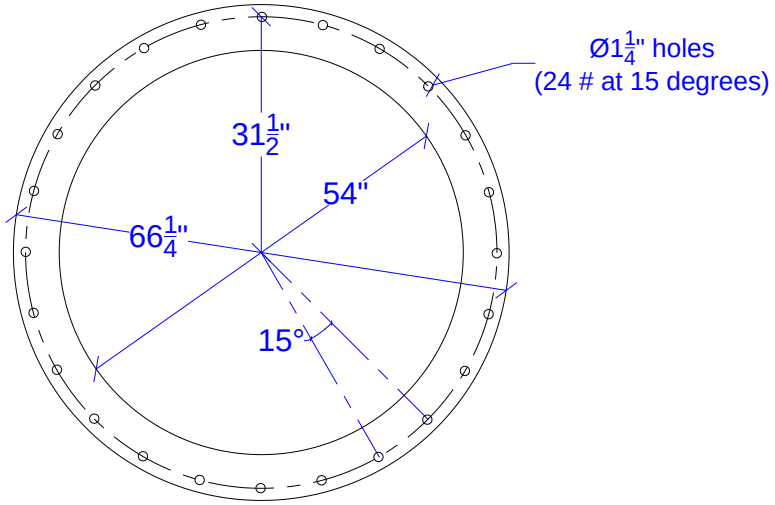

Figure B-4. Fabrication drawing for gasket

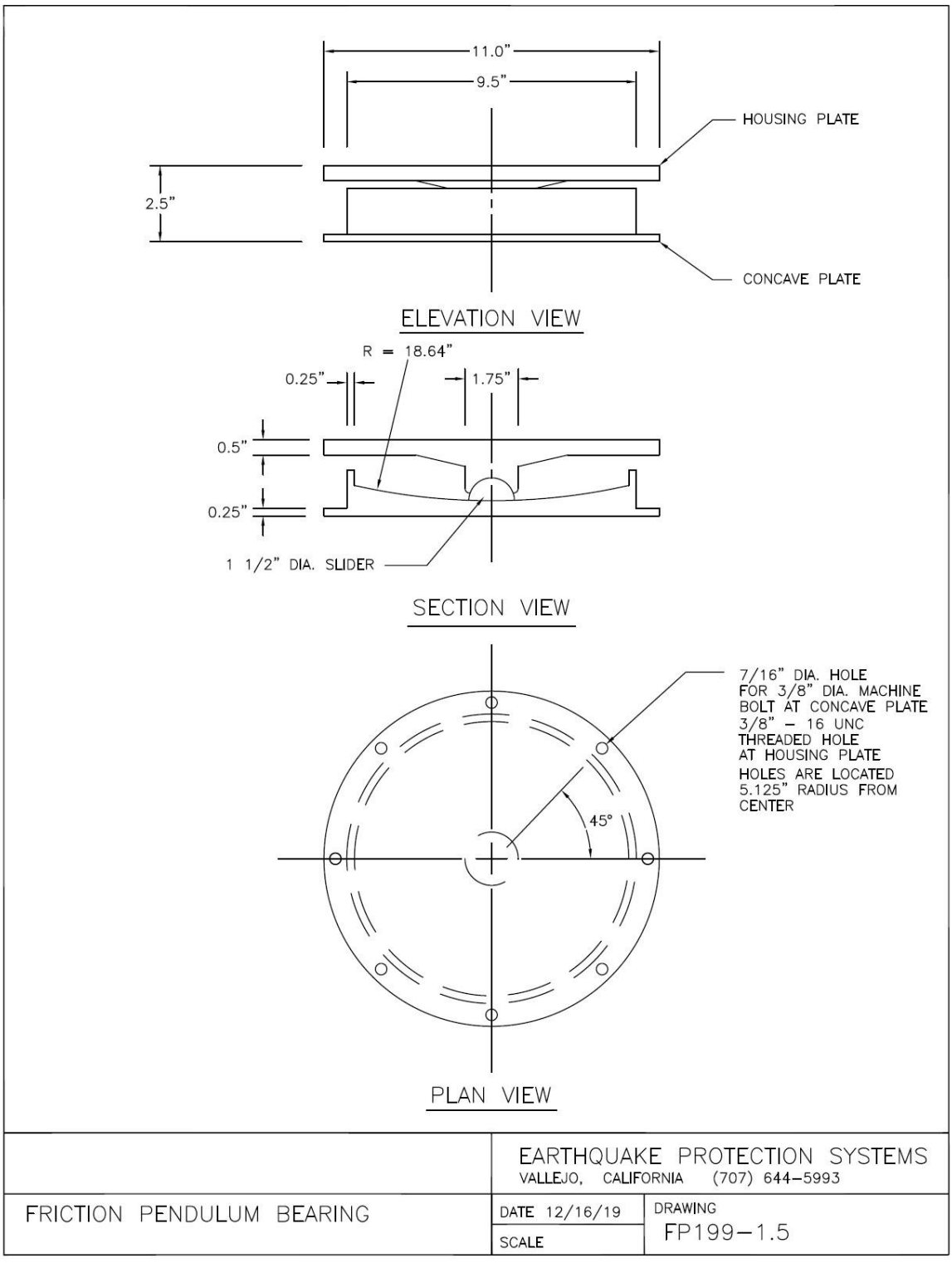

Figure B-5. Fabrication drawing for single Friction Pendulum bearings (courtesy of EPS)

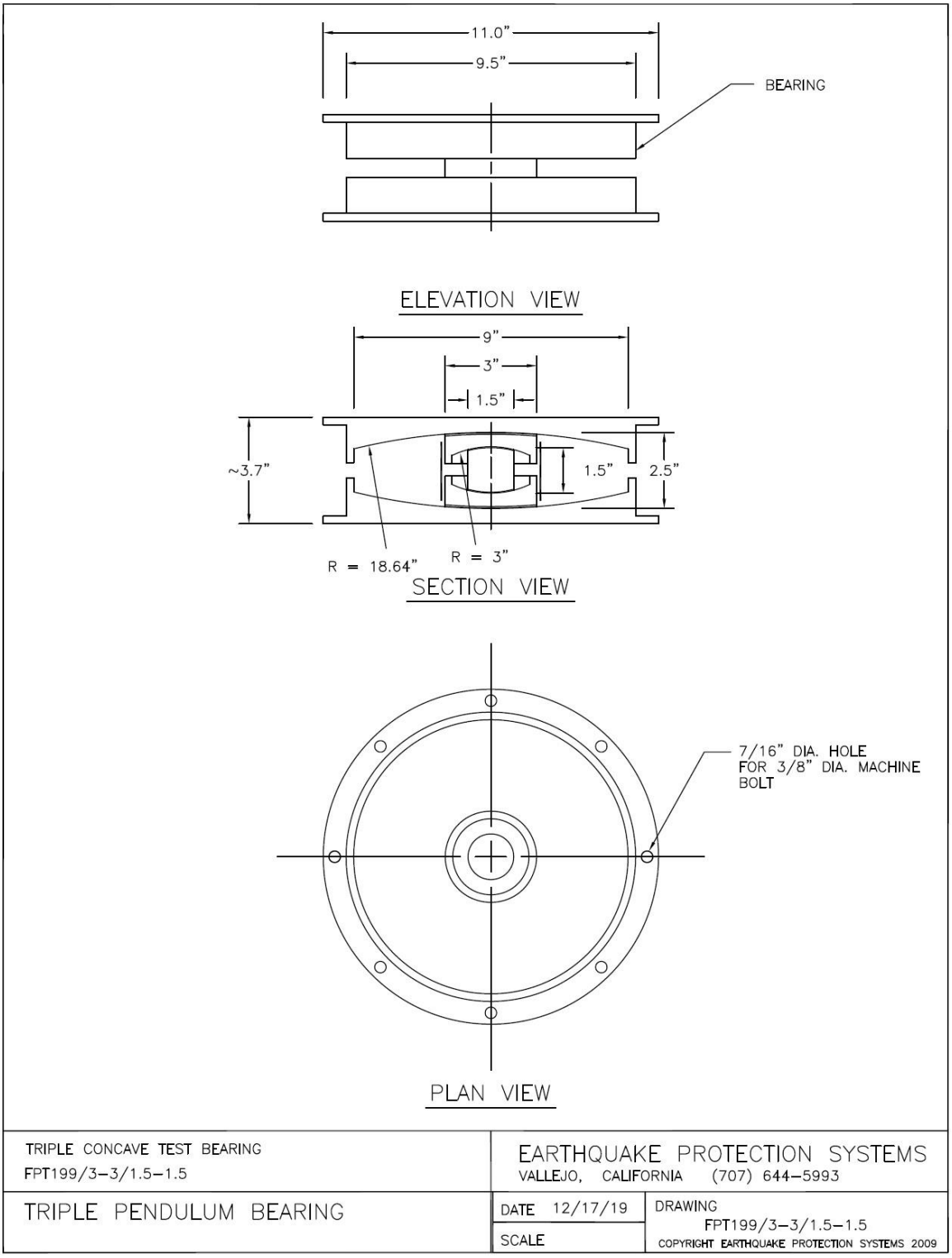

Figure B-6. Fabrication drawing for Triple Friction Pendulum bearings (courtesy of EPS)

APPENDIX C
VERTICAL ACCELERATIONS IN SFP BEARINGS

C.1 Introduction

Vertical accelerations in buildings or equipment isolated with single concave Friction Pendulum bearings can result from a number of sources, including: 1) vertical ground motion propagated through the bearing, and 2) change in height of the bearing as a result of its horizontal displacement. The second source of vertical acceleration is investigated and quantified in this appendix. Both sources of vertical acceleration will be filtered by the articulated slider, which has finite vertical stiffness, but that is not investigated here.

In a single Friction Pendulum (SFP) bearing, horizontal displacement of the articulated slider is accompanied by vertical displacement (i.e., change in bearing height) and acceleration. A *soft* limit on the maximum horizontal displacement is $0.2R$ (R is the radius of curvature of the sliding surface), which limits the vertical displacement to approximately $0.02R$. This is illustrated in Figure C-1 for the isolation systems of Section 5.4.3, with effective radii of curvature of 11, 22, and 44 inches and *soft* limits on the maximum horizontal displacement of 2.2, 4.4, and 8.8 inches, respectively. The green solid sliders in Figure C-1 locate the at-rest position. The solid blue slider identifies the $0.2R$ displacement. (The housing plate in which the slider rotates is not shown in the figure.) Upwards vertical displacement of the slider will increase the height of the SFP bearing. The increase in bearing height at a horizontal displacement of $0.2R$ is approximately 10% of the maximum horizontal displacement. Beyond a horizontal displacement of $0.2R$, the vertical displacement of the slider increases significantly as a percentage of the horizontal displacement. See the red solid slider in Figure C-1a: the vertical displacement is approximately $0.2R$ for a horizontal displacement of $0.6R$.

C.2 Calculation of vertical displacements and corresponding accelerations

Equation C-1 presents a relationship between the horizontal and vertical displacements of a slider in an SFP bearing, determined using Figure C-2.

$$R\sin(\theta) = H \tag{C-1a}$$

$$V = R - R\cos(\theta) \tag{C-1b}$$

where H is the horizontal displacement of the slider, V is its corresponding vertical displacement, R is the radius of curvature of the sliding surface, and θ is defined in Figure C-2; H, θ, and V vary with time during earthquake shaking. The vertical displacement history of the slider is a function of θ, which is a related to H for a bearing with a given R. The corresponding vertical acceleration history is calculated as the second time derivative of the vertical displacement history.

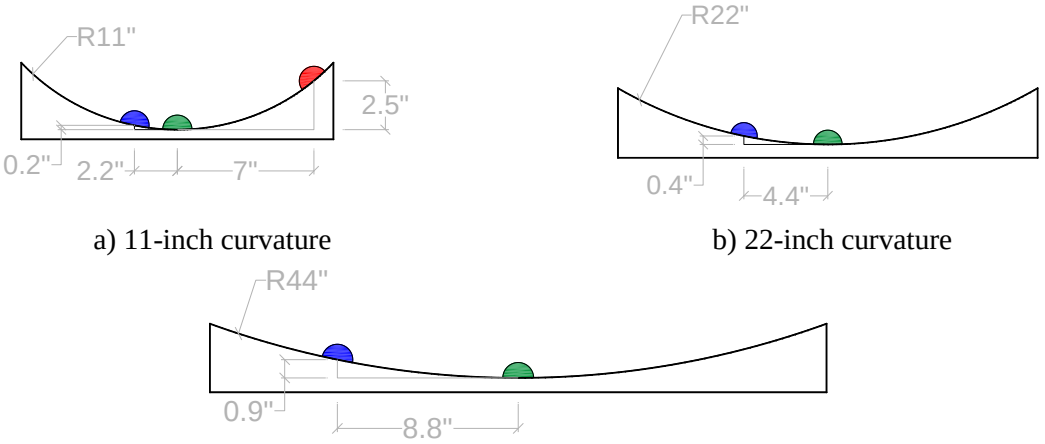

a) 11-inch curvature

b) 22-inch curvature

c) 44-inch curvature

Figure C-1. Cross section of SFP bearings with different curvatures

Although SAP2000 (CSI, 2021) implements a numerical model for the SFP bearing that does not track the change in bearing height as a function of horizontal displacement, the vertical displacement of the slider, and change in bearing height with time, can be computed easily given the vector sum of the horizontal displacement histories in the x and y directions: see Equation C-2. But is the vertical acceleration, resulting from horizontal movement of the slider, of engineering significance? The question is addressed, and practical solutions offered, in Section C.3. The focus here is safety-related equipment in advanced nuclear reactors, assumed, based on past construction of large light water reactors, to have frequencies of 5 Hz and greater at the prototype scale, which maps to approximately 7 Hz at the model scale (for a length scale of 2, see Section 4) for which results are presented below.

$$H = \sqrt{H_x^{\,2} + H_y^{\,2}} \tag{C-2a}$$

$$R\sin(\theta) = H \tag{C-2b}$$

$$V = R - R\cos(\theta) \tag{C-2c}$$

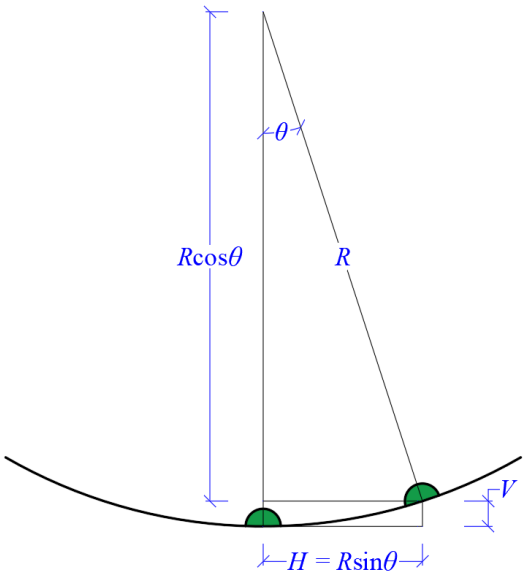

Figure C-2. Movement of slider in an SFP bearing

C.3 Analysis results and recommendations for design

Isolation-system horizontal displacement histories were processed in MATLAB to determine vertical displacement and acceleration histories of the sliders. The MATLAB code is presented in Figure C-3. The MATLAB code was first benchmarked by comparing results with a vertical displacement history computed using the material model MAT_SEISMIC_ISOLATOR available in LS-DYNA (LSTC, 2019). Calculations were performed for IS1 (see Section 5.4.3) and GM2B (see Section 5.4.4), and results are presented in Figure C-4. (The MAT_SEISMIC_ISOLATOR material model tracks vertical displacement of the slider as a function of horizonal displacement.) The displacement histories are identical. For information, Figure C-5 presents the vector sum of the normalized horizontal displacements of the slider for IS1 and GM1C and the normalized vertical displacement.

The horizontal displacement histories of isolation systems IS1, IS3, and IS5 of Section 5.4.3, determined by analysis of the isolated vessel supported on the *rigid* frame, were extracted from SAP2000 for the six seismic inputs of Section 5.4.4 and then processed in MATLAB to determine the vertical displacement and acceleration histories of the sliders. Figures C-6 through C-17 present results. Figures C-6, C-8, C-10, C-12, C-14, and C-16 present acceleration response spectra for the a) vertical acceleration component of the seismic input, black solid line, b) acceleration history due to the vertical displacement of the slider, red dashed line, and c) sum of the acceleration histories from a) and b), green dashed lines. The maximum

```
Dx = load('H_x.mat'); %load the x-direction horizontal displacement history of the isolation system
Dy = load('H_y.mat'); %load the y-direction horizontal displacement history of the isolation system

DH = sqrt(Dx.^2+Dy.^2); %SRSS of the x- and y-direction horizontal displacement histories, Equation C-2a

R = 11; %defining the radius of curvature of SFP bearings

theta = asind(DH/R); %finding the angle theta (in degrees) using Equation C-2b

Dz = R*(1-cosd(theta)); %finding the vertical displacement of the slider, Equation C-2c

dt = 0.001; %defining the time step of the displacement histories, 0.001 sec herein

Vel = gradient(Dz,dt); %first derivative of the vertical displacement history of the slider
Acc = gradient(Vel,dt); %second derivative of the vertical displacement history of the slider

AccZ_input = load('Input_Z.mat'); %load the vertical acceleration history of the input motion

Acc_total = AccZ_input + Acc; %sum of the input motion and the acceleration due to change in bearing
height
```

Figure C-3. MATLAB code used to calculate vertical displacement and accelerations of slider in a SFP bearing

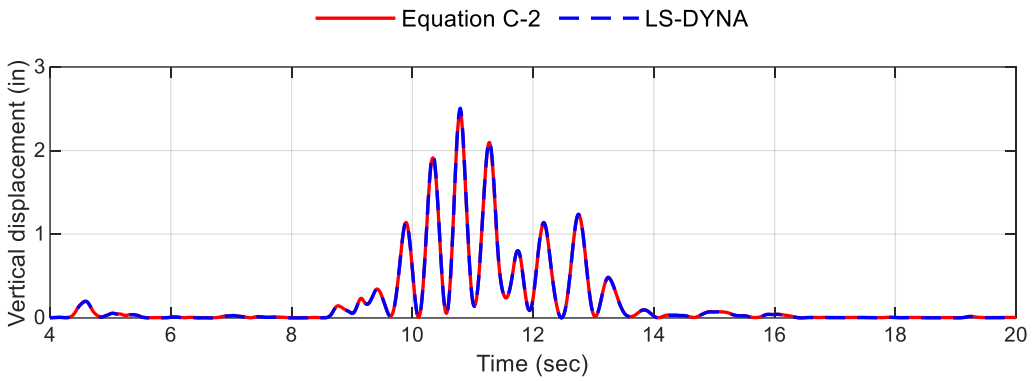

Figure C-4. Vertical displacement of slider in an SFP bearing, IS1 and GM2B

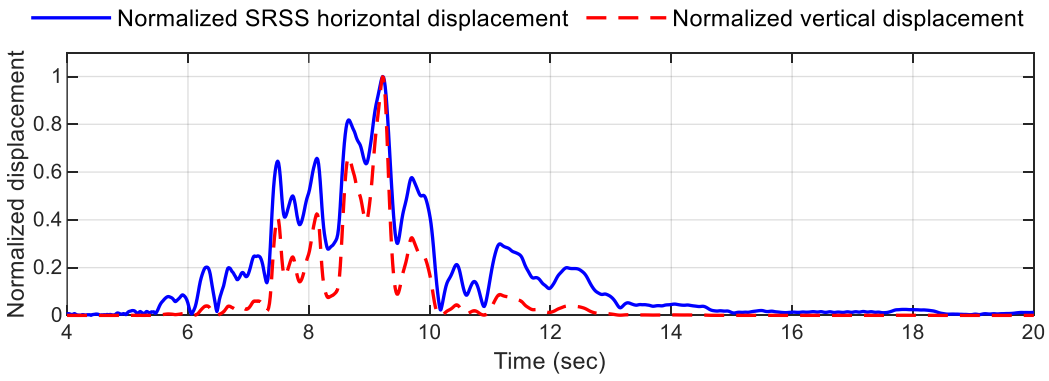

Figure C-5. Normalized displacements of slider in an SFP bearing, IS1 and GM1C

horizontal displacements of the slider are reported in the sub-figure captions. Figures C-7, C-9, C-11, C-13, C-15, and C-17 present the corresponding vertical displacement time series.

An additional set of analyses was performed using the three ground motions of Section 4.4. Results are presented in Figures C-18 through C-20. The ground motions were amplitude scaled such that the maximum horizontal displacement of the isolation systems was approximately 0.2*R*. All three components were scaled by the same factor, which is why the amplitude of the vertical spectrum (black solid line) for a given ground motion (e.g., GM1) is different in the three figures. The increase in vertical spectral acceleration due to the vertical displacement (acceleration) of the slider at this soft limit on horizontal displacement is sufficiently small to be ignored for the purpose of design unless the vertical component of earthquake shaking is tiny.

Focusing on safety-related equipment, with frequencies at the prototype (model) scale of 5 Hz (7 Hz) and greater, the effect of vertical displacement (and acceleration) of the slider on in-structure vertical spectra can be ignored if the maximum horizontal displacement of the slider is less than 0.2*R*. For example, compare the black solid and green dashed lines in Figures C-6b, C-10b, and C-16b. If the maximum horizontal displacement of the slider is greater than 0.2*R*, and the software being used for analysis does not account for vertical accelerations due to change in bearing height, the procedure introduced above could be used to correct the vertical input, namely, 1) generate a representative vertical displacement history for the isolation system, using for example the vector sum of the horizontal displacement histories at the center of stiffness of the isolated piece of equipment (or building), 2) differentiate the vertical displacement history twice to generate a vertical acceleration history (and baseline correct as needed), and 3) add the acceleration history of 2) to the vertical acceleration time series of the earthquake input at the support points (or the vertical component of ground motion at the base of the building) for analysis.

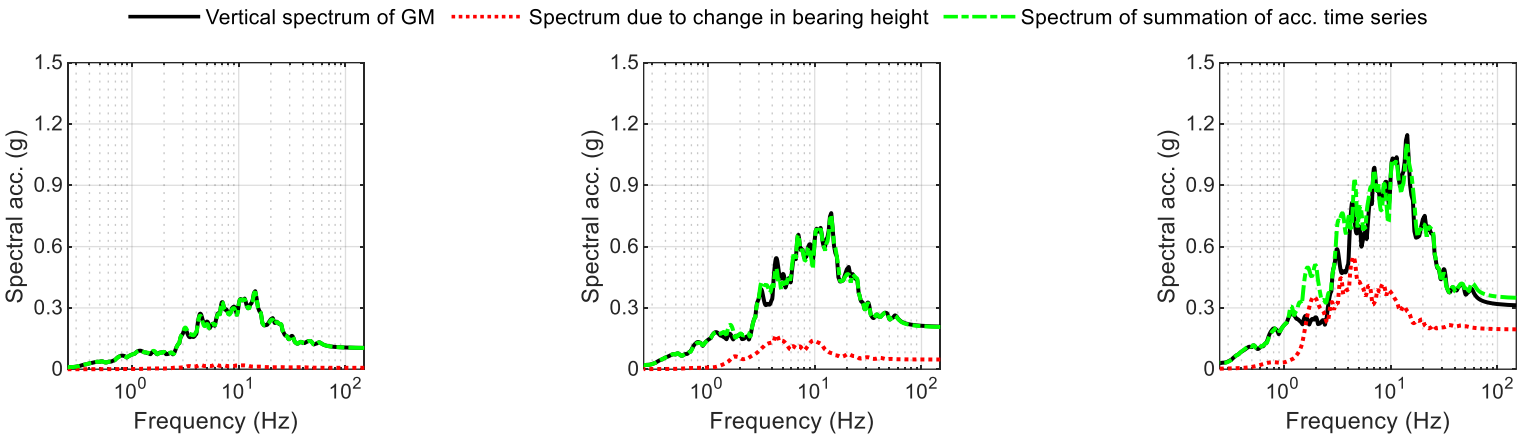

a) GM1A (H = 0.5”; 0.05R) b) GM1B (H = 1.4”; 0.13R) c) GM1C (H = 3.6”; 0.33R)

Figure C-6. Acceleration response spectra, IS1 isolated (R = 11 inches), 5% damping

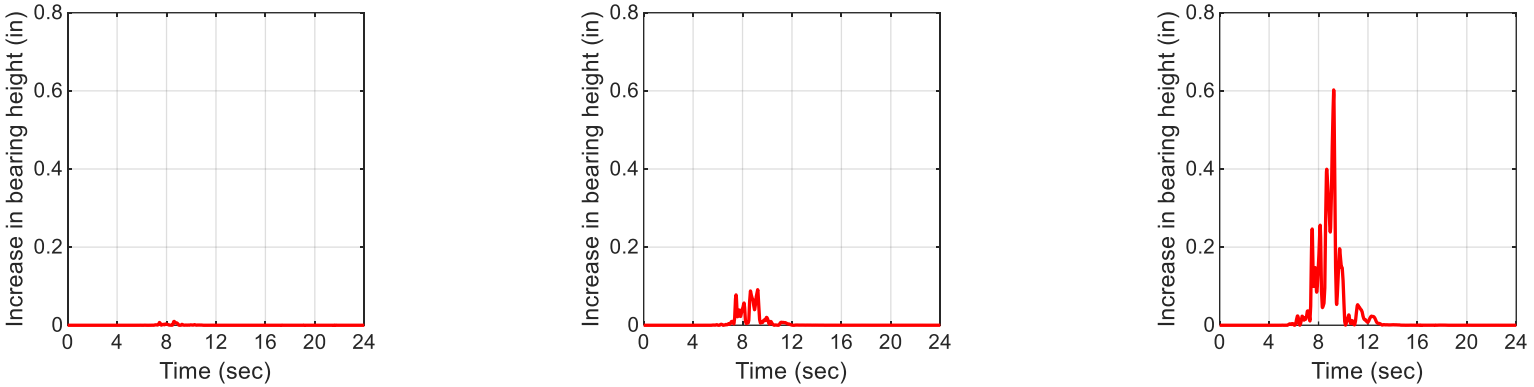

a) GM1A (H = 0.5”; 0.05R) b) GM1B (H = 1.4”; 0.13R) c) GM1C (H = 3.6”; 0.33R)

Figure C-7. Change in bearing height, IS1 isolated (R = 11 inches)

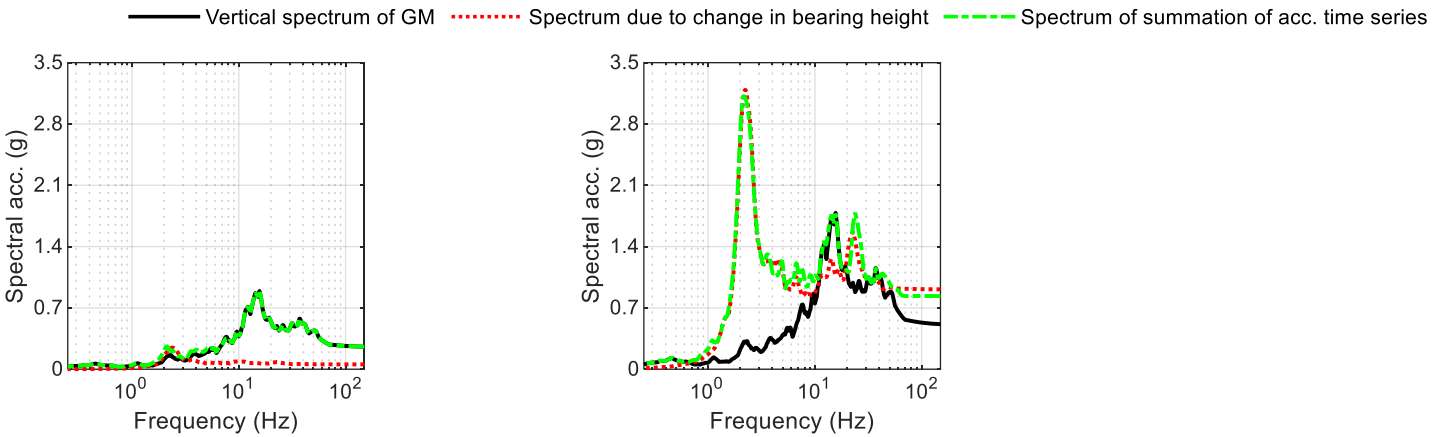

a) GM2A (H = 2”; 0.18R) b) GM2B (H = 7”; 0.64R) c) GM2C[1]

Figure C-8. Acceleration response spectra, IS1 isolated (R = 11 inches), 5% damping

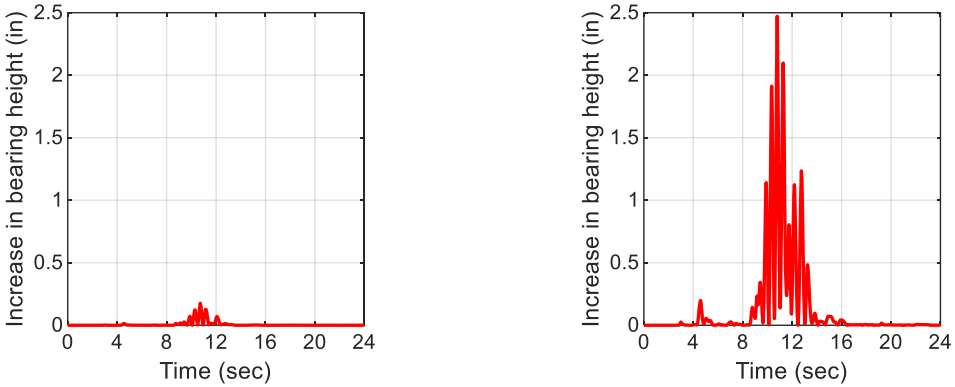

a) GM2A (H = 2”; 0.18R) b) GM2B (H = 7”; 0.64R) c) GM2C[1]

Figure C-9. Change in height of bearing, IS1 isolated (R = 11 inches)

1. Horizontal displacements exceed the capacity of the SFP bearings for this seismic input

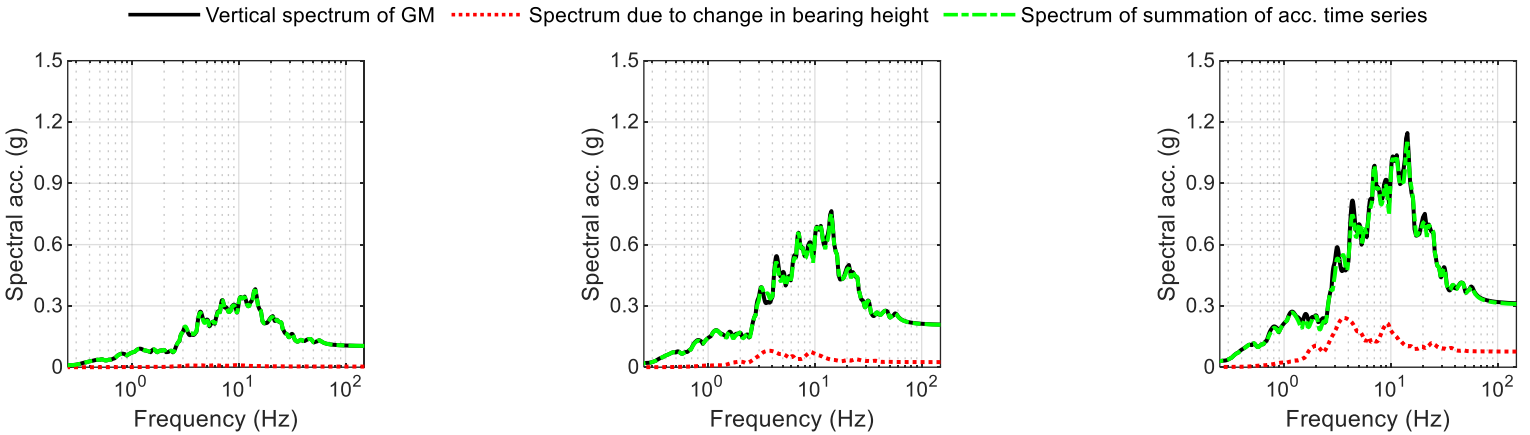

a) GM1A (H = 0.5”; 0.02R) b) GM1B (H = 1.5”; 0.07R) c) GM1C (H = 2.9”; 0.13R)

Figure C-10. Acceleration response spectra, IS3 isolated (R = 22 inches), 5% damping

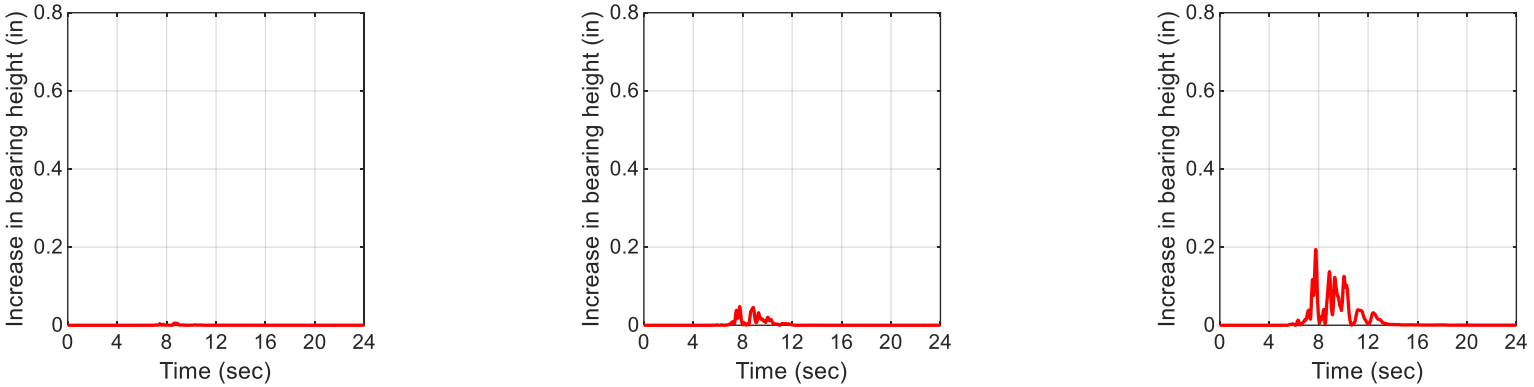

a) GM1A (H = 0.5”; 0.02R) b) GM1B (H = 1.5”; 0.07R) c) GM1C (H = 2.9”; 0.13R)

Figure C-11. Change in bearing height, IS3 isolated (R = 22 inches)

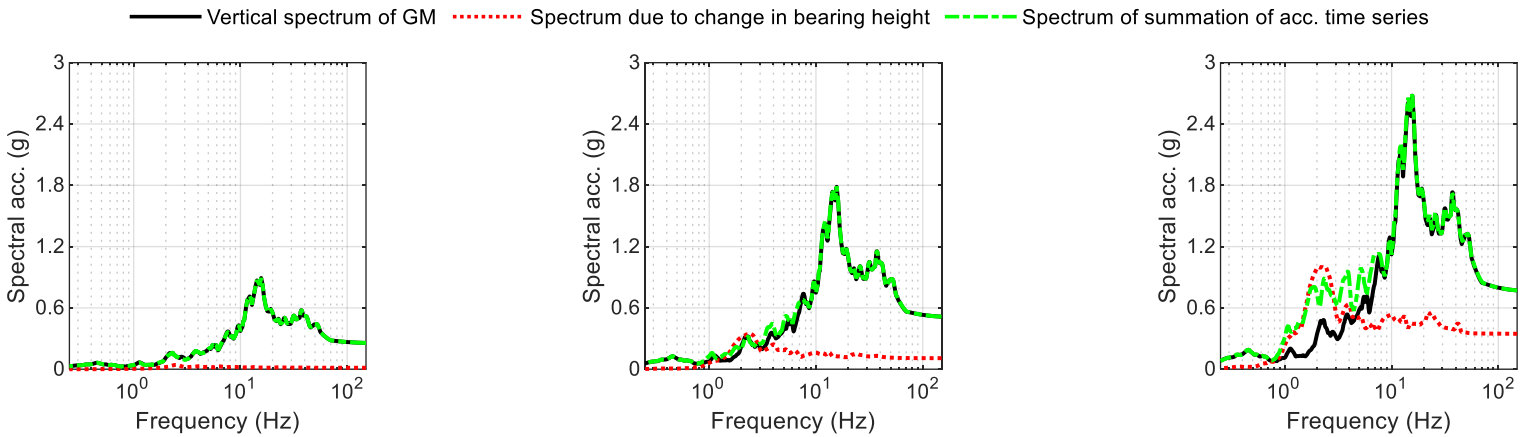

a) GM2A (H = 1.3”; 0.06R) b) GM2B (H = 4.2”; 0.19R) c) GM2C (H = 8”; 0.36R)

Figure C-12. Acceleration response spectra, IS3 isolated (R = 22 inches), 5% damping

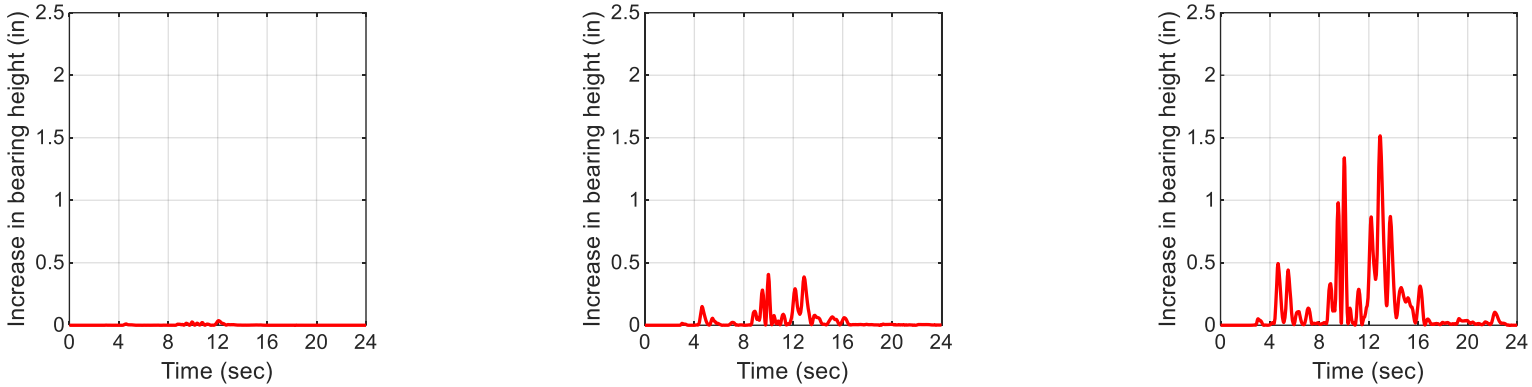

a) GM2A (H = 1.3”; 0.06R) b) GM2B (H = 4.2”; 0.19R) c) GM2C (H = 8”; 0.36R)

Figure C-13. Change in height of bearing, IS3 isolated (R = 22 inches)

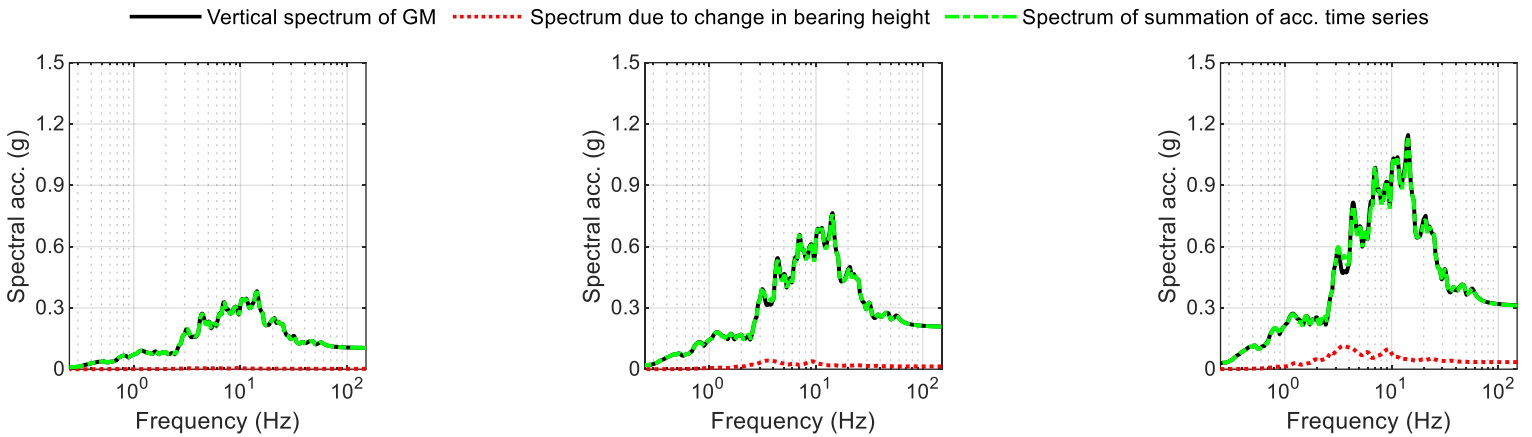

a) GM1A (H = 0.6”; 0.01R) b) GM1B (H = 1.7”; 0.04R) c) GM1C (H = 3.1”; 0.07R)

Figure C-14. Acceleration response spectra, IS5 isolated (R = 44 inches), 5% damping

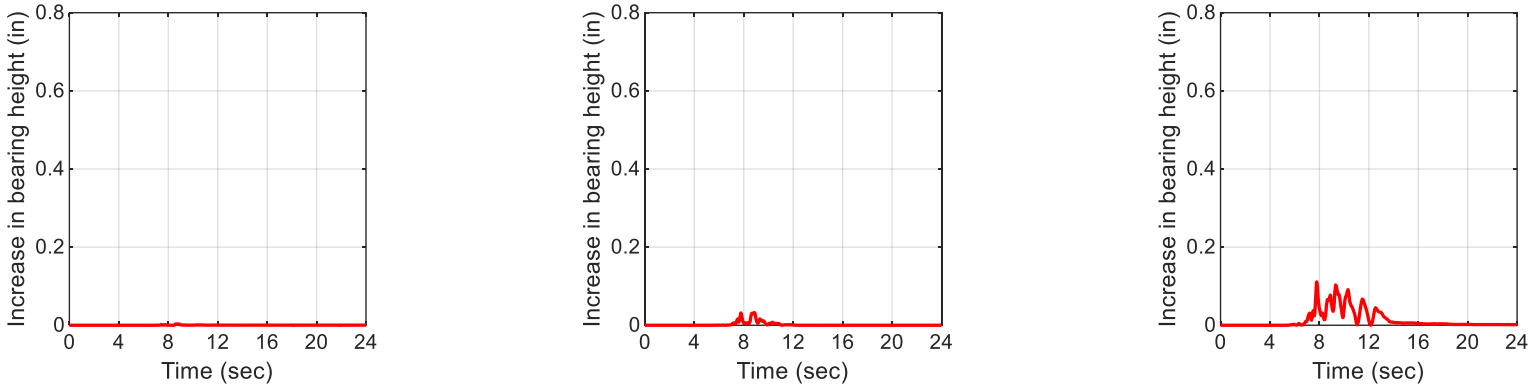

a) GM1A (H = 0.6”; 0.01R) b) GM1B (H = 1.7”; 0.04R) c) GM1C (H = 3.1”; 0.07R)

Figure C-15. Change in bearing height, IS5 isolated (R = 44 inches)

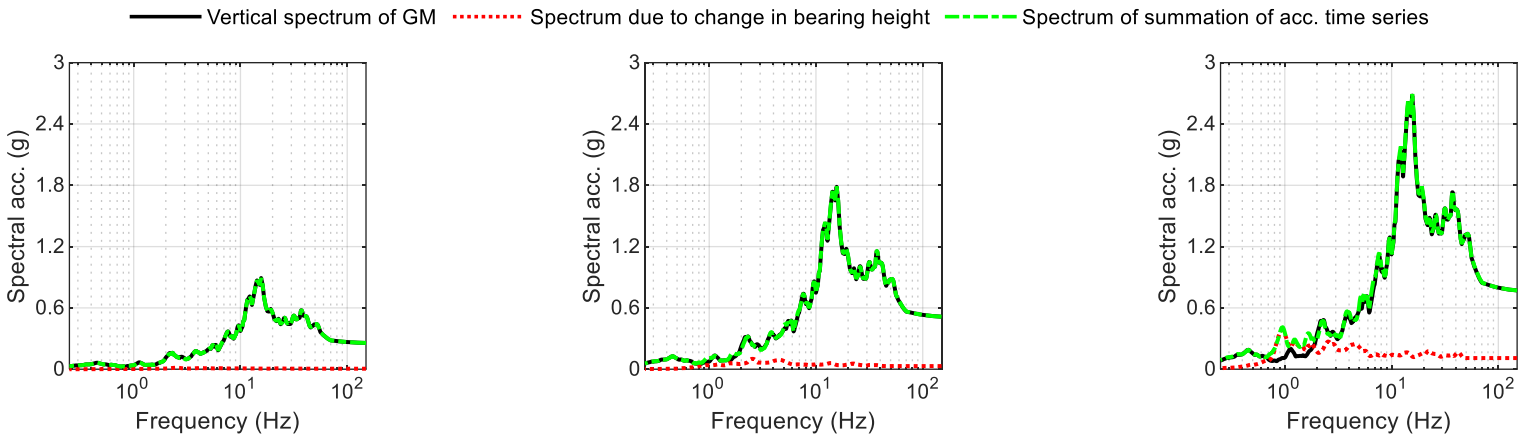

a) GM2A (H = 1.5”; 0.03R) b) GM2B (H = 4.6”; 0.10R) c) GM2C (H = 11.7”; 0.27R)

Figure C-16. Acceleration response spectra, IS5 isolated (R = 44 inches), 5% damping

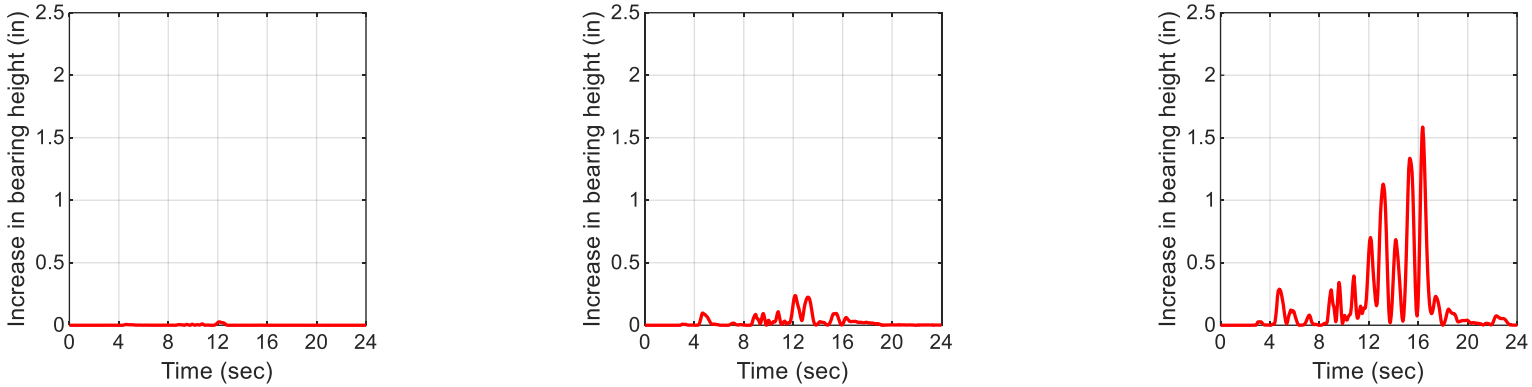

a) GM2A (H = 1.5”; 0.03R) b) GM2B (H = 4.6”; 0.10R) c) GM2C (H = 11.7”; 0.27R)

Figure C-17. Change in height of bearing, IS5 isolated (R = 44 inches)

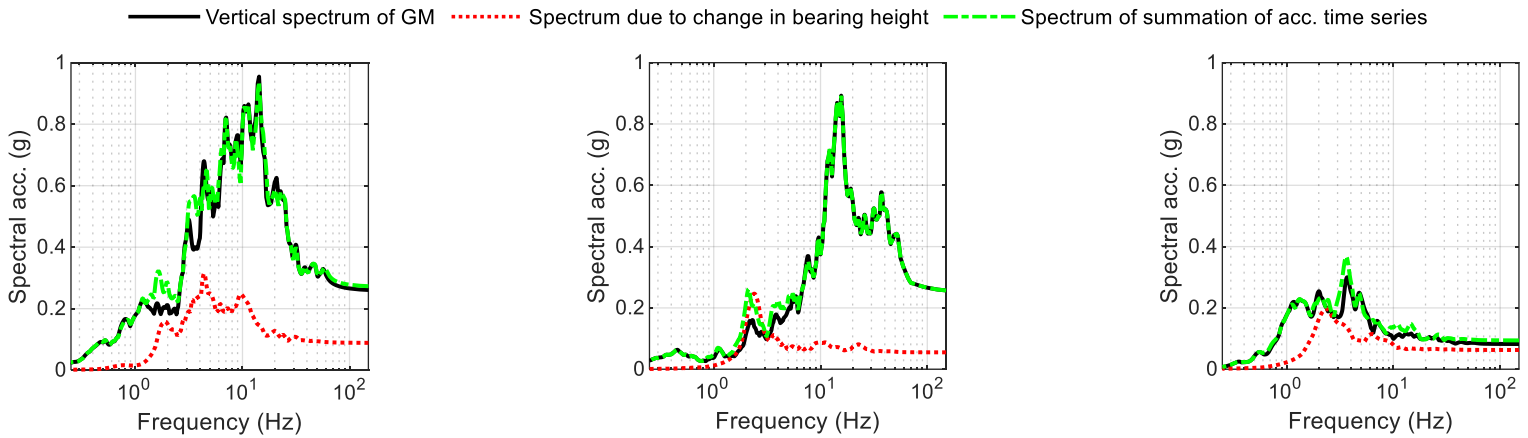

a) GM1 (H = 2.4”; 0.22R) b) GM2 (H = 2”; 0.18R) c) GM3 (H = 2.2”; 0.2R)

Figure C-18. Acceleration response spectra, IS1 isolated (R = 11 inches), 5% damping

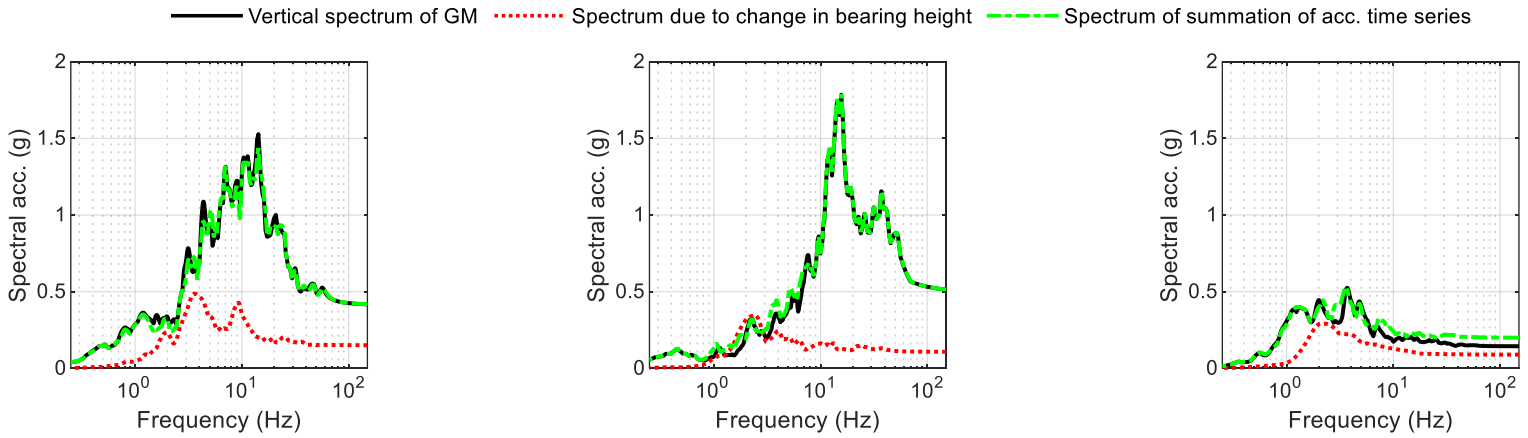

a) GM1 (H = 4.4”; 0.2R) b) GM2 (H = 4.2”; 0.19R) c) GM3 (H = 4.5”; 0.21R)

Figure C-19. Acceleration response spectra, IS3 isolated (R = 22 inches), 5% damping

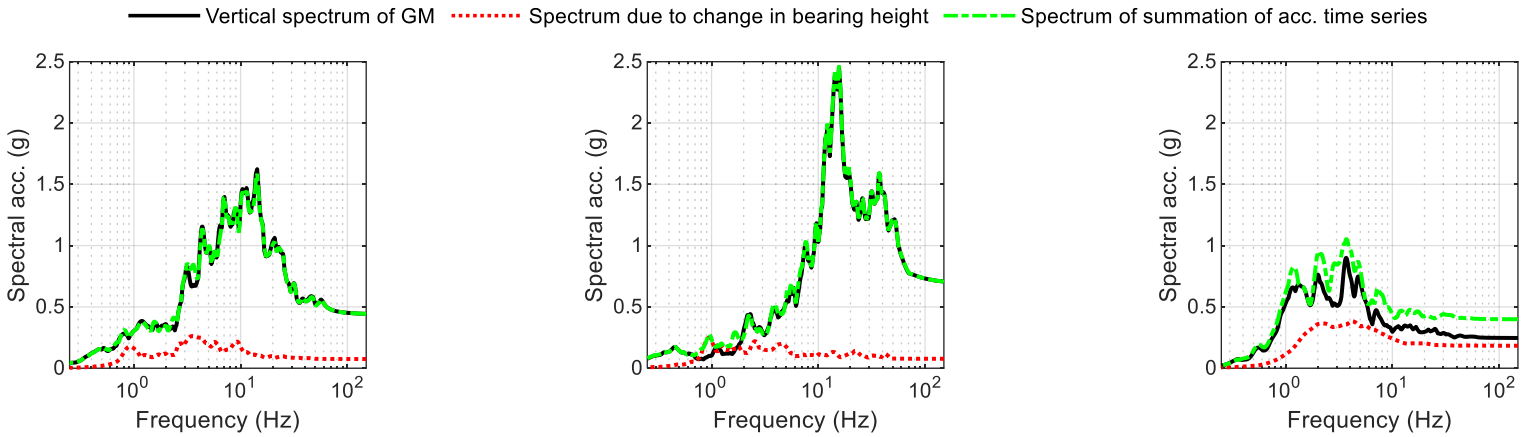

a) GM1 (H = 8.6”; 0.19R) b) GM2 (H = 9.1”; 0.21R) c) GM3 (H = 8.9”; 0.2R)

Figure C-20. Acceleration response spectra, IS5 isolated (R = 44 inches), 5% damping

MCEER Technical Reports

MCEER publishes technical reports on a variety of subjects written by authors funded through MCEER. These reports can be downloaded from the MCEER website at http://www.buffalo.edu/mceer. They can also be requested through NTIS, P.O. Box 1425, Springfield, Virginia 22151. NTIS accession numbers are shown in parenthesis, if available.

NCEER-87-0001 "First-Year Program in Research, Education and Technology Transfer," 3/5/87, (PB88-134275, A04, MF-A01).

NCEER-87-0002 "Experimental Evaluation of Instantaneous Optimal Algorithms for Structural Control," by R.C. Lin, T.T. Soong and A.M. Reinhorn, 4/20/87, (PB88-134341, A04, MF-A01).

NCEER-87-0003 "Experimentation Using the Earthquake Simulation Facilities at University at Buffalo," by A.M. Reinhorn and R.L. Ketter, not available.

NCEER-87-0004 "The System Characteristics and Performance of a Shaking Table," by J.S. Hwang, K.C. Chang and G.C. Lee, 6/1/87, (PB88-134259, A03, MF-A01). This report is available only through NTIS (see address given above).

NCEER-87-0005 "A Finite Element Formulation for Nonlinear Viscoplastic Material Using a Q Model," by O. Gyebi and G. Dasgupta, 11/2/87, (PB88-213764, A08, MF-A01).

NCEER-87-0006 "Symbolic Manipulation Program (SMP) - Algebraic Codes for Two and Three Dimensional Finite Element Formulations," by X. Lee and G. Dasgupta, 11/9/87, (PB88-218522, A05, MF-A01).

NCEER-87-0007 "Instantaneous Optimal Control Laws for Tall Buildings Under Seismic Excitations," by J.N. Yang, A. Akbarpour and P. Ghaemmaghami, 6/10/87, (PB88-134333, A06, MF-A01). This report is only available through NTIS (see address given above).

NCEER-87-0008 "IDARC: Inelastic Damage Analysis of Reinforced Concrete Frame - Shear-Wall Structures," by Y.J. Park, A.M. Reinhorn and S.K. Kunnath, 7/20/87, (PB88-134325, A09, MF-A01). This report is only available through NTIS (see address given above).

NCEER-87-0009 "Liquefaction Potential for New York State: A Preliminary Report on Sites in Manhattan and Buffalo," by M. Budhu, V. Vijayakumar, R.F. Giese and L. Baumgras, 8/31/87, (PB88-163704, A03, MF-A01). This report is available only through NTIS (see address given above).

NCEER-87-0010 "Vertical and Torsional Vibration of Foundations in Inhomogeneous Media," by A.S. Veletsos and K.W. Dotson, 6/1/87, (PB88-134291, A03, MF-A01). This report is only available through NTIS (see address given above).

NCEER-87-0011 "Seismic Probabilistic Risk Assessment and Seismic Margins Studies for Nuclear Power Plants," by Howard H.M. Hwang, 6/15/87, (PB88-134267, A03, MF-A01). This report is only available through NTIS (see address given above).

NCEER-87-0012 "Parametric Studies of Frequency Response of Secondary Systems Under Ground-Acceleration Excitations," by Y. Yong and Y.K. Lin, 6/10/87, (PB88-134309, A03, MF-A01). This report is only available through NTIS (see address given above).

NCEER-87-0013 "Frequency Response of Secondary Systems Under Seismic Excitation," by J.A. HoLung, J. Cai and Y.K. Lin, 7/31/87, (PB88-134317, A05, MF-A01). This report is only available through NTIS (see address given above).

NCEER-87-0014 "Modelling Earthquake Ground Motions in Seismically Active Regions Using Parametric Time Series Methods," by G.W. Ellis and A.S. Cakmak, 8/25/87, (PB88-134283, A08, MF-A01). This report is only available through NTIS (see address given above).

NCEER-87-0015 "Detection and Assessment of Seismic Structural Damage," by E. DiPasquale and A.S. Cakmak, 8/25/87, (PB88-163712, A05, MF-A01). This report is only available through NTIS (see address given above).

NCEER-87-0016 "Pipeline Experiment at Parkfield, California," by J. Isenberg and E. Richardson, 9/15/87, (PB88-163720, A03, MF-A01). This report is available only through NTIS (see address given above).

NCEER-87-0017 "Digital Simulation of Seismic Ground Motion," by M. Shinozuka, G. Deodatis and T. Harada, 8/31/87, (PB88-155197, A04, MF-A01). This report is available only through NTIS (see address given above).

NCEER-87-0018 "Practical Considerations for Structural Control: System Uncertainty, System Time Delay and Truncation of Small Control Forces," J.N. Yang and A. Akbarpour, 8/10/87, (PB88-163738, A08, MF-A01). This report is only available through NTIS (see address given above).

NCEER-87-0019 "Modal Analysis of Nonclassically Damped Structural Systems Using Canonical Transformation," by J.N. Yang, S. Sarkani and F.X. Long, 9/27/87, (PB88-187851, A04, MF-A01).

NCEER-87-0020 "A Nonstationary Solution in Random Vibration Theory," by J.R. Red-Horse and P.D. Spanos, 11/3/87, (PB88-163746, A03, MF-A01).

NCEER-87-0021 "Horizontal Impedances for Radially Inhomogeneous Viscoelastic Soil Layers," by A.S. Veletsos and K.W. Dotson, 10/15/87, (PB88-150859, A04, MF-A01).

NCEER-87-0022 "Seismic Damage Assessment of Reinforced Concrete Members," by Y.S. Chung, C. Meyer and M. Shinozuka, 10/9/87, (PB88-150867, A05, MF-A01). This report is available only through NTIS (see address given above).

NCEER-87-0023 "Active Structural Control in Civil Engineering," by T.T. Soong, 11/11/87, (PB88-187778, A03, MF-A01).

NCEER-87-0024 "Vertical and Torsional Impedances for Radially Inhomogeneous Viscoelastic Soil Layers," by K.W. Dotson and A.S. Veletsos, 12/87, (PB88-187786, A03, MF-A01).

NCEER-87-0025 "Proceedings from the Symposium on Seismic Hazards, Ground Motions, Soil-Liquefaction and Engineering Practice in Eastern North America," October 20-22, 1987, edited by K.H. Jacob, 12/87, (PB88-188115, A23, MF-A01). This report is available only through NTIS (see address given above).

NCEER-87-0026 "Report on the Whittier-Narrows, California, Earthquake of October 1, 1987," by J. Pantelic and A. Reinhorn, 11/87, (PB88-187752, A03, MF-A01). This report is available only through NTIS (see address given above).

NCEER-87-0027 "Design of a Modular Program for Transient Nonlinear Analysis of Large 3-D Building Structures," by S. Srivastav and J.F. Abel, 12/30/87, (PB88-187950, A05, MF-A01). This report is only available through NTIS (see address given above).

NCEER-87-0028 "Second-Year Program in Research, Education and Technology Transfer," 3/8/88, (PB88-219480, A04, MF-A01).

NCEER-88-0001 "Workshop on Seismic Computer Analysis and Design of Buildings With Interactive Graphics," by W. McGuire, J.F. Abel and C.H. Conley, 1/18/88, (PB88-187760, A03, MF-A01). This report is only available through NTIS (see address given above).

NCEER-88-0002 "Optimal Control of Nonlinear Flexible Structures," by J.N. Yang, F.X. Long and D. Wong, 1/22/88, (PB88-213772, A06, MF-A01).

NCEER-88-0003 "Substructuring Techniques in the Time Domain for Primary-Secondary Structural Systems," by G.D. Manolis and G. Juhn, 2/10/88, (PB88-213780, A04, MF-A01).

NCEER-88-0004 "Iterative Seismic Analysis of Primary-Secondary Systems," by A. Singhal, L.D. Lutes and P.D. Spanos, 2/23/88, (PB88-213798, A04, MF-A01).

NCEER-88-0005 "Stochastic Finite Element Expansion for Random Media," by P.D. Spanos and R. Ghanem, 3/14/88, (PB88-213806, A03, MF-A01).

NCEER-88-0006 "Combining Structural Optimization and Structural Control," by F.Y. Cheng and C.P. Pantelides, 1/10/88, (PB88-213814, A05, MF-A01).

NCEER-88-0007 "Seismic Performance Assessment of Code-Designed Structures," by H.H-M. Hwang, J-W. Jaw and H-J. Shau, 3/20/88, (PB88-219423, A04, MF-A01). This report is only available through NTIS (see address given above).

NCEER-88-0008 "Reliability Analysis of Code-Designed Structures Under Natural Hazards," by H.H-M. Hwang, H. Ushiba and M. Shinozuka, 2/29/88, (PB88-229471, A07, MF-A01). This report is only available through NTIS (see address given above).

NCEER-88-0009 "Seismic Fragility Analysis of Shear Wall Structures," by J-W Jaw and H.H-M. Hwang, 4/30/88, (PB89-102867, A04, MF-A01).

NCEER-88-0010 "Base Isolation of a Multi-Story Building Under a Harmonic Ground Motion - A Comparison of Performances of Various Systems," by F-G Fan, G. Ahmadi and I.G. Tadjbakhsh, 5/18/88, (PB89-122238, A06, MF-A01). This report is only available through NTIS (see address given above).

NCEER-88-0011 "Seismic Floor Response Spectra for a Combined System by Green's Functions," by F.M. Lavelle, L.A. Bergman and P.D. Spanos, 5/1/88, (PB89-102875, A03, MF-A01).

NCEER-88-0012 "A New Solution Technique for Randomly Excited Hysteretic Structures," by G.Q. Cai and Y.K. Lin, 5/16/88, (PB89-102883, A03, MF-A01).

NCEER-88-0013 "A Study of Radiation Damping and Soil-Structure Interaction Effects in the Centrifuge," by K. Weissman, supervised by J.H. Prevost, 5/24/88, (PB89-144703, A06, MF-A01).

NCEER-88-0014 "Parameter Identification and Implementation of a Kinematic Plasticity Model for Frictional Soils," by J.H. Prevost and D.V. Griffiths, not available.

NCEER-88-0015 "Two- and Three- Dimensional Dynamic Finite Element Analyses of the Long Valley Dam," by D.V. Griffiths and J.H. Prevost, 6/17/88, (PB89-144711, A04, MF-A01).

NCEER-88-0016 "Damage Assessment of Reinforced Concrete Structures in Eastern United States," by A.M. Reinhorn, M.J. Seidel, S.K. Kunnath and Y.J. Park, 6/15/88, (PB89-122220, A04, MF-A01). This report is only available through NTIS (see address given above).

NCEER-88-0017 "Dynamic Compliance of Vertically Loaded Strip Foundations in Multilayered Viscoelastic Soils," by S. Ahmad and A.S.M. Israil, 6/17/88, (PB89-102891, A04, MF-A01).

NCEER-88-0018 "An Experimental Study of Seismic Structural Response With Added Viscoelastic Dampers," by R.C. Lin, Z. Liang, T.T. Soong and R.H. Zhang, 6/30/88, (PB89-122212, A05, MF-A01). This report is available only through NTIS (see address given above).

NCEER-88-0019 "Experimental Investigation of Primary - Secondary System Interaction," by G.D. Manolis, G. Juhn and A.M. Reinhorn, 5/27/88, (PB89-122204, A04, MF-A01).

NCEER-88-0020 "A Response Spectrum Approach For Analysis of Nonclassically Damped Structures," by J.N. Yang, S. Sarkani and F.X. Long, 4/22/88, (PB89-102909, A04, MF-A01).

NCEER-88-0021 "Seismic Interaction of Structures and Soils: Stochastic Approach," by A.S. Veletsos and A.M. Prasad, 7/21/88, (PB89-122196, A04, MF-A01). This report is only available through NTIS (see address given above).

NCEER-88-0022 "Identification of the Serviceability Limit State and Detection of Seismic Structural Damage," by E. DiPasquale and A.S. Cakmak, 6/15/88, (PB89-122188, A05, MF-A01). This report is available only through NTIS (see address given above).

NCEER-88-0023 "Multi-Hazard Risk Analysis: Case of a Simple Offshore Structure," by B.K. Bhartia and E.H. Vanmarcke, 7/21/88, (PB89-145213, A05, MF-A01).

NCEER-88-0024 "Automated Seismic Design of Reinforced Concrete Buildings," by Y.S. Chung, C. Meyer and M. Shinozuka, 7/5/88, (PB89-122170, A06, MF-A01). This report is available only through NTIS (see address given above).

NCEER-88-0025 "Experimental Study of Active Control of MDOF Structures Under Seismic Excitations," by L.L. Chung, R.C. Lin, T.T. Soong and A.M. Reinhorn, 7/10/88, (PB89-122600, A04, MF-A01).

NCEER-88-0026 "Earthquake Simulation Tests of a Low-Rise Metal Structure," by J.S. Hwang, K.C. Chang, G.C. Lee and R.L. Ketter, 8/1/88, (PB89-102917, A04, MF-A01).

NCEER-88-0027 "Systems Study of Urban Response and Reconstruction Due to Catastrophic Earthquakes," by F. Kozin and H.K. Zhou, 9/22/88, (PB90-162348, A04, MF-A01).

NCEER-88-0028 "Seismic Fragility Analysis of Plane Frame Structures," by H.H-M. Hwang and Y.K. Low, 7/31/88, (PB89-131445, A06, MF-A01).

NCEER-88-0029 "Response Analysis of Stochastic Structures," by A. Kardara, C. Bucher and M. Shinozuka, 9/22/88, (PB89-174429, A04, MF-A01).

NCEER-88-0030 "Nonnormal Accelerations Due to Yielding in a Primary Structure," by D.C.K. Chen and L.D. Lutes, 9/19/88, (PB89-131437, A04, MF-A01).

NCEER-88-0031 "Design Approaches for Soil-Structure Interaction," by A.S. Veletsos, A.M. Prasad and Y. Tang, 12/30/88, (PB89-174437, A03, MF-A01). This report is available only through NTIS (see address given above).

NCEER-88-0032 "A Re-evaluation of Design Spectra for Seismic Damage Control," by C.J. Turkstra and A.G. Tallin, 11/7/88, (PB89-145221, A05, MF-A01).

NCEER-88-0033 "The Behavior and Design of Noncontact Lap Splices Subjected to Repeated Inelastic Tensile Loading," by V.E. Sagan, P. Gergely and R.N. White, 12/8/88, (PB89-163737, A08, MF-A01).

NCEER-88-0034 "Seismic Response of Pile Foundations," by S.M. Mamoon, P.K. Banerjee and S. Ahmad, 11/1/88, (PB89-145239, A04, MF-A01).

NCEER-88-0035 "Modeling of R/C Building Structures With Flexible Floor Diaphragms (IDARC2)," by A.M. Reinhorn, S.K. Kunnath and N. Panahshahi, 9/7/88, (PB89-207153, A07, MF-A01).

NCEER-88-0036 "Solution of the Dam-Reservoir Interaction Problem Using a Combination of FEM, BEM with Particular Integrals, Modal Analysis, and Substructuring," by C-S. Tsai, G.C. Lee and R.L. Ketter, 12/31/88, (PB89-207146, A04, MF-A01).

NCEER-88-0037 "Optimal Placement of Actuators for Structural Control," by F.Y. Cheng and C.P. Pantelides, 8/15/88, (PB89-162846, A05, MF-A01).

NCEER-88-0038 "Teflon Bearings in Aseismic Base Isolation: Experimental Studies and Mathematical Modeling," by A. Mokha, M.C. Constantinou and A.M. Reinhorn, 12/5/88, (PB89-218457, A10, MF-A01). This report is available only through NTIS (see address given above).

NCEER-88-0039 "Seismic Behavior of Flat Slab High-Rise Buildings in the New York City Area," by P. Weidlinger and M. Ettouney, 10/15/88, (PB90-145681, A04, MF-A01).

NCEER-88-0040 "Evaluation of the Earthquake Resistance of Existing Buildings in New York City," by P. Weidlinger and M. Ettouney, 10/15/88, not available.

NCEER-88-0041 "Small-Scale Modeling Techniques for Reinforced Concrete Structures Subjected to Seismic Loads," by W. Kim, A. El-Attar and R.N. White, 11/22/88, (PB89-189625, A05, MF-A01).

NCEER-88-0042 "Modeling Strong Ground Motion from Multiple Event Earthquakes," by G.W. Ellis and A.S. Cakmak, 10/15/88, (PB89-174445, A03, MF-A01).

NCEER-88-0043 "Nonstationary Models of Seismic Ground Acceleration," by M. Grigoriu, S.E. Ruiz and E. Rosenblueth, 7/15/88, (PB89-189617, A04, MF-A01).

NCEER-88-0044 "SARCF User's Guide: Seismic Analysis of Reinforced Concrete Frames," by Y.S. Chung, C. Meyer and M. Shinozuka, 11/9/88, (PB89-174452, A08, MF-A01).

NCEER-88-0045 "First Expert Panel Meeting on Disaster Research and Planning," edited by J. Pantelic and J. Stoyle, 9/15/88, (PB89-174460, A05, MF-A01).

NCEER-88-0046 "Preliminary Studies of the Effect of Degrading Infill Walls on the Nonlinear Seismic Response of Steel Frames," by C.Z. Chrysostomou, P. Gergely and J.F. Abel, 12/19/88, (PB89-208383, A05, MF-A01).

NCEER-88-0047 "Reinforced Concrete Frame Component Testing Facility - Design, Construction, Instrumentation and Operation," by S.P. Pessiki, C. Conley, T. Bond, P. Gergely and R.N. White, 12/16/88, (PB89-174478, A04, MF-A01).

NCEER-89-0001 "Effects of Protective Cushion and Soil Compliancy on the Response of Equipment Within a Seismically Excited Building," by J.A. HoLung, 2/16/89, (PB89-207179, A04, MF-A01).

NCEER-89-0002 "Statistical Evaluation of Response Modification Factors for Reinforced Concrete Structures," by H.H-M. Hwang and J-W. Jaw, 2/17/89, (PB89-207187, A05, MF-A01).

NCEER-89-0003 "Hysteretic Columns Under Random Excitation," by G-Q. Cai and Y.K. Lin, 1/9/89, (PB89-196513, A03, MF-A01).

NCEER-89-0004 "Experimental Study of `Elephant Foot Bulge' Instability of Thin-Walled Metal Tanks," by Z-H. Jia and R.L. Ketter, 2/22/89, (PB89-207195, A03, MF-A01).

NCEER-89-0005 "Experiment on Performance of Buried Pipelines Across San Andreas Fault," by J. Isenberg, E. Richardson and T.D. O'Rourke, 3/10/89, (PB89-218440, A04, MF-A01). This report is available only through NTIS (see address given above).

NCEER-89-0006 "A Knowledge-Based Approach to Structural Design of Earthquake-Resistant Buildings," by M. Subramani, P. Gergely, C.H. Conley, J.F. Abel and A.H. Zaghw, 1/15/89, (PB89-218465, A06, MF-A01).

NCEER-89-0007 "Liquefaction Hazards and Their Effects on Buried Pipelines," by T.D. O'Rourke and P.A. Lane, 2/1/89, (PB89-218481, A09, MF-A01).

NCEER-89-0008 "Fundamentals of System Identification in Structural Dynamics," by H. Imai, C-B. Yun, O. Maruyama and M. Shinozuka, 1/26/89, (PB89-207211, A04, MF-A01).

NCEER-89-0009 "Effects of the 1985 Michoacan Earthquake on Water Systems and Other Buried Lifelines in Mexico," by A.G. Ayala and M.J. O'Rourke, 3/8/89, (PB89-207229, A06, MF-A01).

NCEER-89-R010 "NCEER Bibliography of Earthquake Education Materials," by K.E.K. Ross, Second Revision, 9/1/89, (PB90-125352, A05, MF-A01). This report is replaced by NCEER-92-0018.

NCEER-89-0011 "Inelastic Three-Dimensional Response Analysis of Reinforced Concrete Building Structures (IDARC-3D), Part I - Modeling," by S.K. Kunnath and A.M. Reinhorn, 4/17/89, (PB90-114612, A07, MF-A01). This report is available only through NTIS (see address given above).

NCEER-89-0012 "Recommended Modifications to ATC-14," by C.D. Poland and J.O. Malley, 4/12/89, (PB90-108648, A15, MF-A01).

NCEER-89-0013 "Repair and Strengthening of Beam-to-Column Connections Subjected to Earthquake Loading," by M. Corazao and A.J. Durrani, 2/28/89, (PB90-109885, A06, MF-A01).

NCEER-89-0014 "Program EXKAL2 for Identification of Structural Dynamic Systems," by O. Maruyama, C-B. Yun, M. Hoshiya and M. Shinozuka, 5/19/89, (PB90-109877, A09, MF-A01).

NCEER-89-0015 "Response of Frames With Bolted Semi-Rigid Connections, Part I - Experimental Study and Analytical Predictions," by P.J. DiCorso, A.M. Reinhorn, J.R. Dickerson, J.B. Radziminski and W.L. Harper, 6/1/89, not available.

NCEER-89-0016 "ARMA Monte Carlo Simulation in Probabilistic Structural Analysis," by P.D. Spanos and M.P. Mignolet, 7/10/89, (PB90-109893, A03, MF-A01).

NCEER-89-P017 "Preliminary Proceedings from the Conference on Disaster Preparedness - The Place of Earthquake Education in Our Schools," Edited by K.E.K. Ross, 6/23/89, (PB90-108606, A03, MF-A01).

NCEER-89-0017 "Proceedings from the Conference on Disaster Preparedness - The Place of Earthquake Education in Our Schools," Edited by K.E.K. Ross, 12/31/89, (PB90-207895, A012, MF-A02). This report is available only through NTIS (see address given above).

NCEER-89-0018 "Multidimensional Models of Hysteretic Material Behavior for Vibration Analysis of Shape Memory Energy Absorbing Devices, by E.J. Graesser and F.A. Cozzarelli, 6/7/89, (PB90-164146, A04, MF-A01).

NCEER-89-0019 "Nonlinear Dynamic Analysis of Three-Dimensional Base Isolated Structures (3D-BASIS)," by S. Nagarajaiah, A.M. Reinhorn and M.C. Constantinou, 8/3/89, (PB90-161936, A06, MF-A01). This report has been replaced by NCEER-93-0011.

NCEER-89-0020 "Structural Control Considering Time-Rate of Control Forces and Control Rate Constraints," by F.Y. Cheng and C.P. Pantelides, 8/3/89, (PB90-120445, A04, MF-A01).

NCEER-89-0021 "Subsurface Conditions of Memphis and Shelby County," by K.W. Ng, T-S. Chang and H-H.M. Hwang, 7/26/89, (PB90-120437, A03, MF-A01).

NCEER-89-0022 "Seismic Wave Propagation Effects on Straight Jointed Buried Pipelines," by K. Elhmadi and M.J. O'Rourke, 8/24/89, (PB90-162322, A10, MF-A02).

NCEER-89-0023 "Workshop on Serviceability Analysis of Water Delivery Systems," edited by M. Grigoriu, 3/6/89, (PB90-127424, A03, MF-A01).

NCEER-89-0024 "Shaking Table Study of a 1/5 Scale Steel Frame Composed of Tapered Members," by K.C. Chang, J.S. Hwang and G.C. Lee, 9/18/89, (PB90-160169, A04, MF-A01).

NCEER-89-0025 "DYNA1D: A Computer Program for Nonlinear Seismic Site Response Analysis - Technical Documentation," by Jean H. Prevost, 9/14/89, (PB90-161944, A07, MF-A01). This report is available only through NTIS (see address given above).

NCEER-89-0026 "1:4 Scale Model Studies of Active Tendon Systems and Active Mass Dampers for Aseismic Protection," by A.M. Reinhorn, T.T. Soong, R.C. Lin, Y.P. Yang, Y. Fukao, H. Abe and M. Nakai, 9/15/89, (PB90-173246, A10, MF-A02). This report is available only through NTIS (see address given above).

NCEER-89-0027 "Scattering of Waves by Inclusions in a Nonhomogeneous Elastic Half Space Solved by Boundary Element Methods," by P.K. Hadley, A. Askar and A.S. Cakmak, 6/15/89, (PB90-145699, A07, MF-A01).

NCEER-89-0028 "Statistical Evaluation of Deflection Amplification Factors for Reinforced Concrete Structures," by H.H.M. Hwang, J-W. Jaw and A.L. Ch'ng, 8/31/89, (PB90-164633, A05, MF-A01).

NCEER-89-0029 "Bedrock Accelerations in Memphis Area Due to Large New Madrid Earthquakes," by H.H.M. Hwang, C.H.S. Chen and G. Yu, 11/7/89, (PB90-162330, A04, MF-A01).

NCEER-89-0030 "Seismic Behavior and Response Sensitivity of Secondary Structural Systems," by Y.Q. Chen and T.T. Soong, 10/23/89, (PB90-164658, A08, MF-A01).

NCEER-89-0031 "Random Vibration and Reliability Analysis of Primary-Secondary Structural Systems," by Y. Ibrahim, M. Grigoriu and T.T. Soong, 11/10/89, (PB90-161951, A04, MF-A01).

NCEER-89-0032 "Proceedings from the Second U.S. - Japan Workshop on Liquefaction, Large Ground Deformation and Their Effects on Lifelines, September 26-29, 1989," Edited by T.D. O'Rourke and M. Hamada, 12/1/89, (PB90-209388, A22, MF-A03).

NCEER-89-0033 "Deterministic Model for Seismic Damage Evaluation of Reinforced Concrete Structures," by J.M. Bracci, A.M. Reinhorn, J.B. Mander and S.K. Kunnath, 9/27/89, (PB91-108803, A06, MF-A01).

NCEER-89-0034 "On the Relation Between Local and Global Damage Indices," by E. DiPasquale and A.S. Cakmak, 8/15/89, (PB90-173865, A05, MF-A01).

NCEER-89-0035 "Cyclic Undrained Behavior of Nonplastic and Low Plasticity Silts," by A.J. Walker and H.E. Stewart, 7/26/89, (PB90-183518, A10, MF-A01).

NCEER-89-0036 "Liquefaction Potential of Surficial Deposits in the City of Buffalo, New York," by M. Budhu, R. Giese and L. Baumgrass, 1/17/89, (PB90-208455, A04, MF-A01).

NCEER-89-0037 "A Deterministic Assessment of Effects of Ground Motion Incoherence," by A.S. Veletsos and Y. Tang, 7/15/89, (PB90-164294, A03, MF-A01).

NCEER-89-0038 "Workshop on Ground Motion Parameters for Seismic Hazard Mapping," July 17-18, 1989, edited by R.V. Whitman, 12/1/89, (PB90-173923, A04, MF-A01).

NCEER-89-0039 "Seismic Effects on Elevated Transit Lines of the New York City Transit Authority," by C.J. Costantino, C.A. Miller and E. Heymsfield, 12/26/89, (PB90-207887, A06, MF-A01).

NCEER-89-0040 "Centrifugal Modeling of Dynamic Soil-Structure Interaction," by K. Weissman, Supervised by J.H. Prevost, 5/10/89, (PB90-207879, A07, MF-A01).

NCEER-89-0041 "Linearized Identification of Buildings With Cores for Seismic Vulnerability Assessment," by I-K. Ho and A.E. Aktan, 11/1/89, (PB90-251943, A07, MF-A01).

NCEER-90-0001 "Geotechnical and Lifeline Aspects of the October 17, 1989 Loma Prieta Earthquake in San Francisco," by T.D. O'Rourke, H.E. Stewart, F.T. Blackburn and T.S. Dickerman, 1/90, (PB90-208596, A05, MF-A01).

NCEER-90-0002 "Nonnormal Secondary Response Due to Yielding in a Primary Structure," by D.C.K. Chen and L.D. Lutes, 2/28/90, (PB90-251976, A07, MF-A01).

NCEER-90-0003 "Earthquake Education Materials for Grades K-12," by K.E.K. Ross, 4/16/90, (PB91-251984, A05, MF-A05). This report has been replaced by NCEER-92-0018.

NCEER-90-0004 "Catalog of Strong Motion Stations in Eastern North America," by R.W. Busby, 4/3/90, (PB90-251984, A05, MF-A01).

NCEER-90-0005 "NCEER Strong-Motion Data Base: A User Manual for the GeoBase Release (Version 1.0 for the Sun3)," by P. Friberg and K. Jacob, 3/31/90 (PB90-258062, A04, MF-A01).

NCEER-90-0006 "Seismic Hazard Along a Crude Oil Pipeline in the Event of an 1811-1812 Type New Madrid Earthquake," by H.H.M. Hwang and C-H.S. Chen, 4/16/90, (PB90-258054, A04, MF-A01).

NCEER-90-0007 "Site-Specific Response Spectra for Memphis Sheahan Pumping Station," by H.H.M. Hwang and C.S. Lee, 5/15/90, (PB91-108811, A05, MF-A01).

NCEER-90-0008 "Pilot Study on Seismic Vulnerability of Crude Oil Transmission Systems," by T. Ariman, R. Dobry, M. Grigoriu, F. Kozin, M. O'Rourke, T. O'Rourke and M. Shinozuka, 5/25/90, (PB91-108837, A06, MF-A01).

NCEER-90-0009 "A Program to Generate Site Dependent Time Histories: EQGEN," by G.W. Ellis, M. Srinivasan and A.S. Cakmak, 1/30/90, (PB91-108829, A04, MF-A01).

NCEER-90-0010 "Active Isolation for Seismic Protection of Operating Rooms," by M.E. Talbott, Supervised by M. Shinozuka, 6/8/9, (PB91-110205, A05, MF-A01).

NCEER-90-0011 "Program LINEARID for Identification of Linear Structural Dynamic Systems," by C-B. Yun and M. Shinozuka, 6/25/90, (PB91-110312, A08, MF-A01).

NCEER-90-0012 "Two-Dimensional Two-Phase Elasto-Plastic Seismic Response of Earth Dams," by A.N. Yiagos, Supervised by J.H. Prevost, 6/20/90, (PB91-110197, A13, MF-A02).

NCEER-90-0013 "Secondary Systems in Base-Isolated Structures: Experimental Investigation, Stochastic Response and Stochastic Sensitivity," by G.D. Manolis, G. Juhn, M.C. Constantinou and A.M. Reinhorn, 7/1/90, (PB91-110320, A08, MF-A01).

NCEER-90-0014 "Seismic Behavior of Lightly-Reinforced Concrete Column and Beam-Column Joint Details," by S.P. Pessiki, C.H. Conley, P. Gergely and R.N. White, 8/22/90, (PB91-108795, A11, MF-A02).

NCEER-90-0015 "Two Hybrid Control Systems for Building Structures Under Strong Earthquakes," by J.N. Yang and A. Danielians, 6/29/90, (PB91-125393, A04, MF-A01).

NCEER-90-0016 "Instantaneous Optimal Control with Acceleration and Velocity Feedback," by J.N. Yang and Z. Li, 6/29/90, (PB91-125401, A03, MF-A01).

NCEER-90-0017 "Reconnaissance Report on the Northern Iran Earthquake of June 21, 1990," by M. Mehrain, 10/4/90, (PB91-125377, A03, MF-A01).

NCEER-90-0018 "Evaluation of Liquefaction Potential in Memphis and Shelby County," by T.S. Chang, P.S. Tang, C.S. Lee and H. Hwang, 8/10/90, (PB91-125427, A09, MF-A01).

NCEER-90-0019 "Experimental and Analytical Study of a Combined Sliding Disc Bearing and Helical Steel Spring Isolation System," by M.C. Constantinou, A.S. Mokha and A.M. Reinhorn, 10/4/90, (PB91-125385, A06, MF-A01). This report is available only through NTIS (see address given above).

NCEER-90-0020 "Experimental Study and Analytical Prediction of Earthquake Response of a Sliding Isolation System with a Spherical Surface," by A.S. Mokha, M.C. Constantinou and A.M. Reinhorn, 10/11/90, (PB91-125419, A05, MF-A01).

NCEER-90-0021 "Dynamic Interaction Factors for Floating Pile Groups," by G. Gazetas, K. Fan, A. Kaynia and E. Kausel, 9/10/90, (PB91-170381, A05, MF-A01).

NCEER-90-0022 "Evaluation of Seismic Damage Indices for Reinforced Concrete Structures," by S. Rodriguez-Gomez and A.S. Cakmak, 9/30/90, PB91-171322, A06, MF-A01).

NCEER-90-0023 "Study of Site Response at a Selected Memphis Site," by H. Desai, S. Ahmad, E.S. Gazetas and M.R. Oh, 10/11/90, (PB91-196857, A03, MF-A01).

NCEER-90-0024 "A User's Guide to Strongmo: Version 1.0 of NCEER's Strong-Motion Data Access Tool for PCs and Terminals," by P.A. Friberg and C.A.T. Susch, 11/15/90, (PB91-171272, A03, MF-A01).

NCEER-90-0025 "A Three-Dimensional Analytical Study of Spatial Variability of Seismic Ground Motions," by L-L. Hong and A.H.-S. Ang, 10/30/90, (PB91-170399, A09, MF-A01).

NCEER-90-0026 "MUMOID User's Guide - A Program for the Identification of Modal Parameters," by S. Rodriguez-Gomez and E. DiPasquale, 9/30/90, (PB91-171298, A04, MF-A01).

NCEER-90-0027 "SARCF-II User's Guide - Seismic Analysis of Reinforced Concrete Frames," by S. Rodriguez-Gomez, Y.S. Chung and C. Meyer, 9/30/90, (PB91-171280, A05, MF-A01).

NCEER-90-0028 "Viscous Dampers: Testing, Modeling and Application in Vibration and Seismic Isolation," by N. Makris and M.C. Constantinou, 12/20/90 (PB91-190561, A06, MF-A01).

NCEER-90-0029 "Soil Effects on Earthquake Ground Motions in the Memphis Area," by H. Hwang, C.S. Lee, K.W. Ng and T.S. Chang, 8/2/90, (PB91-190751, A05, MF-A01).

NCEER-91-0001 "Proceedings from the Third Japan-U.S. Workshop on Earthquake Resistant Design of Lifeline Facilities and Countermeasures for Soil Liquefaction, December 17-19, 1990," edited by T.D. O'Rourke and M. Hamada, 2/1/91, (PB91-179259, A99, MF-A04).

NCEER-91-0002 "Physical Space Solutions of Non-Proportionally Damped Systems," by M. Tong, Z. Liang and G.C. Lee, 1/15/91, (PB91-179242, A04, MF-A01).

NCEER-91-0003 "Seismic Response of Single Piles and Pile Groups," by K. Fan and G. Gazetas, 1/10/91, (PB92-174994, A04, MF-A01).

NCEER-91-0004 "Damping of Structures: Part 1 - Theory of Complex Damping," by Z. Liang and G. Lee, 10/10/91, (PB92-197235, A12, MF-A03).

NCEER-91-0005 "3D-BASIS - Nonlinear Dynamic Analysis of Three Dimensional Base Isolated Structures: Part II," by S. Nagarajaiah, A.M. Reinhorn and M.C. Constantinou, 2/28/91, (PB91-190553, A07, MF-A01). This report has been replaced by NCEER-93-0011.

NCEER-91-0006 "A Multidimensional Hysteretic Model for Plasticity Deforming Metals in Energy Absorbing Devices," by E.J. Graesser and F.A. Cozzarelli, 4/9/91, (PB92-108364, A04, MF-A01).

NCEER-91-0007 "A Framework for Customizable Knowledge-Based Expert Systems with an Application to a KBES for Evaluating the Seismic Resistance of Existing Buildings," by E.G. Ibarra-Anaya and S.J. Fenves, 4/9/91, (PB91-210930, A08, MF-A01).

NCEER-91-0008 "Nonlinear Analysis of Steel Frames with Semi-Rigid Connections Using the Capacity Spectrum Method," by G.G. Deierlein, S-H. Hsieh, Y-J. Shen and J.F. Abel, 7/2/91, (PB92-113828, A05, MF-A01).

NCEER-91-0009 "Earthquake Education Materials for Grades K-12," by K.E.K. Ross, 4/30/91, (PB91-212142, A06, MF-A01). This report has been replaced by NCEER-92-0018.

NCEER-91-0010 "Phase Wave Velocities and Displacement Phase Differences in a Harmonically Oscillating Pile," by N. Makris and G. Gazetas, 7/8/91, (PB92-108356, A04, MF-A01).

NCEER-91-0011 "Dynamic Characteristics of a Full-Size Five-Story Steel Structure and a 2/5 Scale Model," by K.C. Chang, G.C. Yao, G.C. Lee, D.S. Hao and Y.C. Yeh," 7/2/91, (PB93-116648, A06, MF-A02).

NCEER-91-0012 "Seismic Response of a 2/5 Scale Steel Structure with Added Viscoelastic Dampers," by K.C. Chang, T.T. Soong, S-T. Oh and M.L. Lai, 5/17/91, (PB92-110816, A05, MF-A01).

NCEER-91-0013 "Earthquake Response of Retaining Walls; Full-Scale Testing and Computational Modeling," by S. Alampalli and A-W.M. Elgamal, 6/20/91, not available.

NCEER-91-0014 "3D-BASIS-M: Nonlinear Dynamic Analysis of Multiple Building Base Isolated Structures," by P.C. Tsopelas, S. Nagarajaiah, M.C. Constantinou and A.M. Reinhorn, 5/28/91, (PB92-113885, A09, MF-A02).

NCEER-91-0015 "Evaluation of SEAOC Design Requirements for Sliding Isolated Structures," by D. Theodossiou and M.C. Constantinou, 6/10/91, (PB92-114602, A11, MF-A03).

NCEER-91-0016 "Closed-Loop Modal Testing of a 27-Story Reinforced Concrete Flat Plate-Core Building," by H.R. Somaprasad, T. Toksoy, H. Yoshiyuki and A.E. Aktan, 7/15/91, (PB92-129980, A07, MF-A02).

NCEER-91-0017 "Shake Table Test of a 1/6 Scale Two-Story Lightly Reinforced Concrete Building," by A.G. El-Attar, R.N. White and P. Gergely, 2/28/91, (PB92-222447, A06, MF-A02).

NCEER-91-0018 "Shake Table Test of a 1/8 Scale Three-Story Lightly Reinforced Concrete Building," by A.G. El-Attar, R.N. White and P. Gergely, 2/28/91, (PB93-116630, A08, MF-A02).

NCEER-91-0019 "Transfer Functions for Rigid Rectangular Foundations," by A.S. Veletsos, A.M. Prasad and W.H. Wu, 7/31/91, not available.

NCEER-91-0020 "Hybrid Control of Seismic-Excited Nonlinear and Inelastic Structural Systems," by J.N. Yang, Z. Li and A. Danielians, 8/1/91, (PB92-143171, A06, MF-A02).

NCEER-91-0021 "The NCEER-91 Earthquake Catalog: Improved Intensity-Based Magnitudes and Recurrence Relations for U.S. Earthquakes East of New Madrid," by L. Seeber and J.G. Armbruster, 8/28/91, (PB92-176742, A06, MF-A02).

NCEER-91-0022 "Proceedings from the Implementation of Earthquake Planning and Education in Schools: The Need for Change - The Roles of the Changemakers," by K.E.K. Ross and F. Winslow, 7/23/91, (PB92-129998, A12, MF-A03).

NCEER-91-0023 "A Study of Reliability-Based Criteria for Seismic Design of Reinforced Concrete Frame Buildings," by H.H.M. Hwang and H-M. Hsu, 8/10/91, (PB92-140235, A09, MF-A02).

NCEER-91-0024 "Experimental Verification of a Number of Structural System Identification Algorithms," by R.G. Ghanem, H. Gavin and M. Shinozuka, 9/18/91, (PB92-176577, A18, MF-A04).

NCEER-91-0025 "Probabilistic Evaluation of Liquefaction Potential," by H.H.M. Hwang and C.S. Lee," 11/25/91, (PB92-143429, A05, MF-A01).

NCEER-91-0026 "Instantaneous Optimal Control for Linear, Nonlinear and Hysteretic Structures - Stable Controllers," by J.N. Yang and Z. Li, 11/15/91, (PB92-163807, A04, MF-A01).

NCEER-91-0027 "Experimental and Theoretical Study of a Sliding Isolation System for Bridges," by M.C. Constantinou, A. Kartoum, A.M. Reinhorn and P. Bradford, 11/15/91, (PB92-176973, A10, MF-A03).

NCEER-92-0001 "Case Studies of Liquefaction and Lifeline Performance During Past Earthquakes, Volume 1: Japanese Case Studies," Edited by M. Hamada and T. O'Rourke, 2/17/92, (PB92-197243, A18, MF-A04).

NCEER-92-0002 "Case Studies of Liquefaction and Lifeline Performance During Past Earthquakes, Volume 2: United States Case Studies," Edited by T. O'Rourke and M. Hamada, 2/17/92, (PB92-197250, A20, MF-A04).

NCEER-92-0003 "Issues in Earthquake Education," Edited by K. Ross, 2/3/92, (PB92-222389, A07, MF-A02).

NCEER-92-0004 "Proceedings from the First U.S. - Japan Workshop on Earthquake Protective Systems for Bridges," Edited by I.G. Buckle, 2/4/92, (PB94-142239, A99, MF-A06).

NCEER-92-0005 "Seismic Ground Motion from a Haskell-Type Source in a Multiple-Layered Half-Space," A.P. Theoharis, G. Deodatis and M. Shinozuka, 1/2/92, not available.

NCEER-92-0006 "Proceedings from the Site Effects Workshop," Edited by R. Whitman, 2/29/92, (PB92-197201, A04, MF-A01).

NCEER-92-0007 "Engineering Evaluation of Permanent Ground Deformations Due to Seismically-Induced Liquefaction," by M.H. Baziar, R. Dobry and A-W.M. Elgamal, 3/24/92, (PB92-222421, A13, MF-A03).

NCEER-92-0008 "A Procedure for the Seismic Evaluation of Buildings in the Central and Eastern United States," by C.D. Poland and J.O. Malley, 4/2/92, (PB92-222439, A20, MF-A04).

NCEER-92-0009 "Experimental and Analytical Study of a Hybrid Isolation System Using Friction Controllable Sliding Bearings," by M.Q. Feng, S. Fujii and M. Shinozuka, 5/15/92, (PB93-150282, A06, MF-A02).

NCEER-92-0010 "Seismic Resistance of Slab-Column Connections in Existing Non-Ductile Flat-Plate Buildings," by A.J. Durrani and Y. Du, 5/18/92, (PB93-116812, A06, MF-A02).

NCEER-92-0011 "The Hysteretic and Dynamic Behavior of Brick Masonry Walls Upgraded by Ferrocement Coatings Under Cyclic Loading and Strong Simulated Ground Motion," by H. Lee and S.P. Prawel, 5/11/92, not available.

NCEER-92-0012 "Study of Wire Rope Systems for Seismic Protection of Equipment in Buildings," by G.F. Demetriades, M.C. Constantinou and A.M. Reinhorn, 5/20/92, (PB93-116655, A08, MF-A02).

NCEER-92-0013 "Shape Memory Structural Dampers: Material Properties, Design and Seismic Testing," by P.R. Witting and F.A. Cozzarelli, 5/26/92, (PB93-116663, A05, MF-A01).

NCEER-92-0014 "Longitudinal Permanent Ground Deformation Effects on Buried Continuous Pipelines," by M.J. O'Rourke, and C. Nordberg, 6/15/92, (PB93-116671, A08, MF-A02).

NCEER-92-0015 "A Simulation Method for Stationary Gaussian Random Functions Based on the Sampling Theorem," by M. Grigoriu and S. Balopoulou, 6/11/92, (PB93-127496, A05, MF-A01).

NCEER-92-0016 "Gravity-Load-Designed Reinforced Concrete Buildings: Seismic Evaluation of Existing Construction and Detailing Strategies for Improved Seismic Resistance," by G.W. Hoffmann, S.K. Kunnath, A.M. Reinhorn and J.B. Mander, 7/15/92, (PB94-142007, A08, MF-A02).

NCEER-92-0017 "Observations on Water System and Pipeline Performance in the Limón Area of Costa Rica Due to the April 22, 1991 Earthquake," by M. O'Rourke and D. Ballantyne, 6/30/92, (PB93-126811, A06, MF-A02).

NCEER-92-0018 "Fourth Edition of Earthquake Education Materials for Grades K-12," Edited by K.E.K. Ross, 8/10/92, (PB93-114023, A07, MF-A02).

NCEER-92-0019 "Proceedings from the Fourth Japan-U.S. Workshop on Earthquake Resistant Design of Lifeline Facilities and Countermeasures for Soil Liquefaction," Edited by M. Hamada and T.D. O'Rourke, 8/12/92, (PB93-163939, A99, MF-E11).

NCEER-92-0020 "Active Bracing System: A Full Scale Implementation of Active Control," by A.M. Reinhorn, T.T. Soong, R.C. Lin, M.A. Riley, Y.P. Wang, S. Aizawa and M. Higashino, 8/14/92, (PB93-127512, A06, MF-A02).

NCEER-92-0021 "Empirical Analysis of Horizontal Ground Displacement Generated by Liquefaction-Induced Lateral Spreads," by S.F. Bartlett and T.L. Youd, 8/17/92, (PB93-188241, A06, MF-A02).

NCEER-92-0022 "IDARC Version 3.0: Inelastic Damage Analysis of Reinforced Concrete Structures," by S.K. Kunnath, A.M. Reinhorn and R.F. Lobo, 8/31/92, (PB93-227502, A07, MF-A02).

NCEER-92-0023 "A Semi-Empirical Analysis of Strong-Motion Peaks in Terms of Seismic Source, Propagation Path and Local Site Conditions, by M. Kamiyama, M.J. O'Rourke and R. Flores-Berrones, 9/9/92, (PB93-150266, A08, MF-A02).

NCEER-92-0024 "Seismic Behavior of Reinforced Concrete Frame Structures with Nonductile Details, Part I: Summary of Experimental Findings of Full Scale Beam-Column Joint Tests," by A. Beres, R.N. White and P. Gergely, 9/30/92, (PB93-227783, A05, MF-A01).

NCEER-92-0025 "Experimental Results of Repaired and Retrofitted Beam-Column Joint Tests in Lightly Reinforced Concrete Frame Buildings," by A. Beres, S. El-Borgi, R.N. White and P. Gergely, 10/29/92, (PB93-227791, A05, MF-A01).

NCEER-92-0026 "A Generalization of Optimal Control Theory: Linear and Nonlinear Structures," by J.N. Yang, Z. Li and S. Vongchavalitkul, 11/2/92, (PB93-188621, A05, MF-A01).

NCEER-92-0027 "Seismic Resistance of Reinforced Concrete Frame Structures Designed Only for Gravity Loads: Part I - Design and Properties of a One-Third Scale Model Structure," by J.M. Bracci, A.M. Reinhorn and J.B. Mander, 12/1/92, (PB94-104502, A08, MF-A02).

NCEER-92-0028 "Seismic Resistance of Reinforced Concrete Frame Structures Designed Only for Gravity Loads: Part II - Experimental Performance of Subassemblages," by L.E. Aycardi, J.B. Mander and A.M. Reinhorn, 12/1/92, (PB94-104510, A08, MF-A02).

NCEER-92-0029 "Seismic Resistance of Reinforced Concrete Frame Structures Designed Only for Gravity Loads: Part III - Experimental Performance and Analytical Study of a Structural Model," by J.M. Bracci, A.M. Reinhorn and J.B. Mander, 12/1/92, (PB93-227528, A09, MF-A01).

NCEER-92-0030 "Evaluation of Seismic Retrofit of Reinforced Concrete Frame Structures: Part I - Experimental Performance of Retrofitted Subassemblages," by D. Choudhuri, J.B. Mander and A.M. Reinhorn, 12/8/92, (PB93-198307, A07, MF-A02).

NCEER-92-0031 "Evaluation of Seismic Retrofit of Reinforced Concrete Frame Structures: Part II - Experimental Performance and Analytical Study of a Retrofitted Structural Model," by J.M. Bracci, A.M. Reinhorn and J.B. Mander, 12/8/92, (PB93-198315, A09, MF-A03).

NCEER-92-0032 "Experimental and Analytical Investigation of Seismic Response of Structures with Supplemental Fluid Viscous Dampers," by M.C. Constantinou and M.D. Symans, 12/21/92, (PB93-191435, A10, MF-A03). This report is available only through NTIS (see address given above).

NCEER-92-0033 "Reconnaissance Report on the Cairo, Egypt Earthquake of October 12, 1992," by M. Khater, 12/23/92, (PB93-188621, A03, MF-A01).

NCEER-92-0034 "Low-Level Dynamic Characteristics of Four Tall Flat-Plate Buildings in New York City," by H. Gavin, S. Yuan, J. Grossman, E. Pekelis and K. Jacob, 12/28/92, (PB93-188217, A07, MF-A02).

NCEER-93-0001 "An Experimental Study on the Seismic Performance of Brick-Infilled Steel Frames With and Without Retrofit," by J.B. Mander, B. Nair, K. Wojtkowski and J. Ma, 1/29/93, (PB93-227510, A07, MF-A02).

NCEER-93-0002 "Social Accounting for Disaster Preparedness and Recovery Planning," by S. Cole, E. Pantoja and V. Razak, 2/22/93, (PB94-142114, A12, MF-A03).

NCEER-93-0003 "Assessment of 1991 NEHRP Provisions for Nonstructural Components and Recommended Revisions," by T.T. Soong, G. Chen, Z. Wu, R-H. Zhang and M. Grigoriu, 3/1/93, (PB93-188639, A06, MF-A02).

NCEER-93-0004 "Evaluation of Static and Response Spectrum Analysis Procedures of SEAOC/UBC for Seismic Isolated Structures," by C.W. Winters and M.C. Constantinou, 3/23/93, (PB93-198299, A10, MF-A03).

NCEER-93-0005 "Earthquakes in the Northeast - Are We Ignoring the Hazard? A Workshop on Earthquake Science and Safety for Educators," edited by K.E.K. Ross, 4/2/93, (PB94-103066, A09, MF-A02).

NCEER-93-0006 "Inelastic Response of Reinforced Concrete Structures with Viscoelastic Braces," by R.F. Lobo, J.M. Bracci, K.L. Shen, A.M. Reinhorn and T.T. Soong, 4/5/93, (PB93-227486, A05, MF-A02).

NCEER-93-0007 "Seismic Testing of Installation Methods for Computers and Data Processing Equipment," by K. Kosar, T.T. Soong, K.L. Shen, J.A. HoLung and Y.K. Lin, 4/12/93, (PB93-198299, A07, MF-A02).

NCEER-93-0008 "Retrofit of Reinforced Concrete Frames Using Added Dampers," by A. Reinhorn, M. Constantinou and C. Li, not available.

NCEER-93-0009 "Seismic Behavior and Design Guidelines for Steel Frame Structures with Added Viscoelastic Dampers," by K.C. Chang, M.L. Lai, T.T. Soong, D.S. Hao and Y.C. Yeh, 5/1/93, (PB94-141959, A07, MF-A02).

NCEER-93-0010 "Seismic Performance of Shear-Critical Reinforced Concrete Bridge Piers," by J.B. Mander, S.M. Waheed, M.T.A. Chaudhary and S.S. Chen, 5/12/93, (PB93-227494, A08, MF-A02).

NCEER-93-0011 "3D-BASIS-TABS: Computer Program for Nonlinear Dynamic Analysis of Three Dimensional Base Isolated Structures," by S. Nagarajaiah, C. Li, A.M. Reinhorn and M.C. Constantinou, 8/2/93, (PB94-141819, A09, MF-A02).

NCEER-93-0012 "Effects of Hydrocarbon Spills from an Oil Pipeline Break on Ground Water," by O.J. Helweg and H.H.M. Hwang, 8/3/93, (PB94-141942, A06, MF-A02).

NCEER-93-0013 "Simplified Procedures for Seismic Design of Nonstructural Components and Assessment of Current Code Provisions," by M.P. Singh, L.E. Suarez, E.E. Matheu and G.O. Maldonado, 8/4/93, (PB94-141827, A09, MF-A02).

NCEER-93-0014 "An Energy Approach to Seismic Analysis and Design of Secondary Systems," by G. Chen and T.T. Soong, 8/6/93, (PB94-142767, A11, MF-A03).

NCEER-93-0015 "Proceedings from School Sites: Becoming Prepared for Earthquakes - Commemorating the Third Anniversary of the Loma Prieta Earthquake," Edited by F.E. Winslow and K.E.K. Ross, 8/16/93, (PB94-154275, A16, MF-A02).

NCEER-93-0016 "Reconnaissance Report of Damage to Historic Monuments in Cairo, Egypt Following the October 12, 1992 Dahshur Earthquake," by D. Sykora, D. Look, G. Croci, E. Karaesmen and E. Karaesmen, 8/19/93, (PB94-142221, A08, MF-A02).

NCEER-93-0017 "The Island of Guam Earthquake of August 8, 1993," by S.W. Swan and S.K. Harris, 9/30/93, (PB94-141843, A04, MF-A01).

NCEER-93-0018 "Engineering Aspects of the October 12, 1992 Egyptian Earthquake," by A.W. Elgamal, M. Amer, K. Adalier and A. Abul-Fadl, 10/7/93, (PB94-141983, A05, MF-A01).

NCEER-93-0019 "Development of an Earthquake Motion Simulator and its Application in Dynamic Centrifuge Testing," by I. Krstelj, Supervised by J.H. Prevost, 10/23/93, (PB94-181773, A-10, MF-A03).

NCEER-93-0020 "NCEER-Taisei Corporation Research Program on Sliding Seismic Isolation Systems for Bridges: Experimental and Analytical Study of a Friction Pendulum System (FPS)," by M.C. Constantinou, P. Tsopelas, Y-S. Kim and S. Okamoto, 11/1/93, (PB94-142775, A08, MF-A02).

NCEER-93-0021 "Finite Element Modeling of Elastomeric Seismic Isolation Bearings," by L.J. Billings, Supervised by R. Shepherd, 11/8/93, not available.

NCEER-93-0022 "Seismic Vulnerability of Equipment in Critical Facilities: Life-Safety and Operational Consequences," by K. Porter, G.S. Johnson, M.M. Zadeh, C. Scawthorn and S. Eder, 11/24/93, (PB94-181765, A16, MF-A03).

NCEER-93-0023 "Hokkaido Nansei-oki, Japan Earthquake of July 12, 1993, by P.I. Yanev and C.R. Scawthorn, 12/23/93, (PB94-181500, A07, MF-A01).

NCEER-94-0001 "An Evaluation of Seismic Serviceability of Water Supply Networks with Application to the San Francisco Auxiliary Water Supply System," by I. Markov, Supervised by M. Grigoriu and T. O'Rourke, 1/21/94, (PB94-204013, A07, MF-A02).

NCEER-94-0002 "NCEER-Taisei Corporation Research Program on Sliding Seismic Isolation Systems for Bridges: Experimental and Analytical Study of Systems Consisting of Sliding Bearings, Rubber Restoring Force Devices and Fluid Dampers," Volumes I and II, by P. Tsopelas, S. Okamoto, M.C. Constantinou, D. Ozaki and S. Fujii, 2/4/94, (PB94-181740, A09, MF-A02 and PB94-181757, A12, MF-A03).

NCEER-94-0003 "A Markov Model for Local and Global Damage Indices in Seismic Analysis," by S. Rahman and M. Grigoriu, 2/18/94, (PB94-206000, A12, MF-A03).

NCEER-94-0004 "Proceedings from the NCEER Workshop on Seismic Response of Masonry Infills," edited by D.P. Abrams, 3/1/94, (PB94-180783, A07, MF-A02).

NCEER-94-0005 "The Northridge, California Earthquake of January 17, 1994: General Reconnaissance Report," edited by J.D. Goltz, 3/11/94, (PB94-193943, A10, MF-A03).

NCEER-94-0006 "Seismic Energy Based Fatigue Damage Analysis of Bridge Columns: Part I - Evaluation of Seismic Capacity," by G.A. Chang and J.B. Mander, 3/14/94, (PB94-219185, A11, MF-A03).

NCEER-94-0007 "Seismic Isolation of Multi-Story Frame Structures Using Spherical Sliding Isolation Systems," by T.M. Al-Hussaini, V.A. Zayas and M.C. Constantinou, 3/17/94, (PB94-193745, A09, MF-A02).

NCEER-94-0008 "The Northridge, California Earthquake of January 17, 1994: Performance of Highway Bridges," edited by I.G. Buckle, 3/24/94, (PB94-193851, A06, MF-A02).

NCEER-94-0009 "Proceedings of the Third U.S.-Japan Workshop on Earthquake Protective Systems for Bridges," edited by I.G. Buckle and I. Friedland, 3/31/94, (PB94-195815, A99, MF-A06).

NCEER-94-0010 "3D-BASIS-ME: Computer Program for Nonlinear Dynamic Analysis of Seismically Isolated Single and Multiple Structures and Liquid Storage Tanks," by P.C. Tsopelas, M.C. Constantinou and A.M. Reinhorn, 4/12/94, (PB94-204922, A09, MF-A02).

NCEER-94-0011 "The Northridge, California Earthquake of January 17, 1994: Performance of Gas Transmission Pipelines," by T.D. O'Rourke and M.C. Palmer, 5/16/94, (PB94-204989, A05, MF-A01).

NCEER-94-0012 "Feasibility Study of Replacement Procedures and Earthquake Performance Related to Gas Transmission Pipelines," by T.D. O'Rourke and M.C. Palmer, 5/25/94, (PB94-206638, A09, MF-A02).

NCEER-94-0013 "Seismic Energy Based Fatigue Damage Analysis of Bridge Columns: Part II - Evaluation of Seismic Demand," by G.A. Chang and J.B. Mander, 6/1/94, (PB95-18106, A08, MF-A02).

NCEER-94-0014 "NCEER-Taisei Corporation Research Program on Sliding Seismic Isolation Systems for Bridges: Experimental and Analytical Study of a System Consisting of Sliding Bearings and Fluid Restoring Force/Damping Devices," by P. Tsopelas and M.C. Constantinou, 6/13/94, (PB94-219144, A10, MF-A03).

NCEER-94-0015 "Generation of Hazard-Consistent Fragility Curves for Seismic Loss Estimation Studies," by H. Hwang and J-R. Huo, 6/14/94, (PB95-181996, A09, MF-A02).

NCEER-94-0016 "Seismic Study of Building Frames with Added Energy-Absorbing Devices," by W.S. Pong, C.S. Tsai and G.C. Lee, 6/20/94, (PB94-219136, A10, A03).

NCEER-94-0017 "Sliding Mode Control for Seismic-Excited Linear and Nonlinear Civil Engineering Structures," by J. Yang, J. Wu, A. Agrawal and Z. Li, 6/21/94, (PB95-138483, A06, MF-A02).

NCEER-94-0018 "3D-BASIS-TABS Version 2.0: Computer Program for Nonlinear Dynamic Analysis of Three Dimensional Base Isolated Structures," by A.M. Reinhorn, S. Nagarajaiah, M.C. Constantinou, P. Tsopelas and R. Li, 6/22/94, (PB95-182176, A08, MF-A02).

NCEER-94-0019 "Proceedings of the International Workshop on Civil Infrastructure Systems: Application of Intelligent Systems and Advanced Materials on Bridge Systems," Edited by G.C. Lee and K.C. Chang, 7/18/94, (PB95-252474, A20, MF-A04).

NCEER-94-0020 "Study of Seismic Isolation Systems for Computer Floors," by V. Lambrou and M.C. Constantinou, 7/19/94, (PB95-138533, A10, MF-A03).

NCEER-94-0021 "Proceedings of the U.S.-Italian Workshop on Guidelines for Seismic Evaluation and Rehabilitation of Unreinforced Masonry Buildings," Edited by D.P. Abrams and G.M. Calvi, 7/20/94, (PB95-138749, A13, MF-A03).

NCEER-94-0022 "NCEER-Taisei Corporation Research Program on Sliding Seismic Isolation Systems for Bridges: Experimental and Analytical Study of a System Consisting of Lubricated PTFE Sliding Bearings and Mild Steel Dampers," by P. Tsopelas and M.C. Constantinou, 7/22/94, (PB95-182184, A08, MF-A02).

NCEER-94-0023 “Development of Reliability-Based Design Criteria for Buildings Under Seismic Load,” by Y.K. Wen, H. Hwang and M. Shinozuka, 8/1/94, (PB95-211934, A08, MF-A02).

NCEER-94-0024 “Experimental Verification of Acceleration Feedback Control Strategies for an Active Tendon System,” by S.J. Dyke, B.F. Spencer, Jr., P. Quast, M.K. Sain, D.C. Kaspari, Jr. and T.T. Soong, 8/29/94, (PB95-212320, A05, MF-A01).

NCEER-94-0025 “Seismic Retrofitting Manual for Highway Bridges,” Edited by I.G. Buckle and I.F. Friedland, published by the Federal Highway Administration (PB95-212676, A15, MF-A03).

NCEER-94-0026 “Proceedings from the Fifth U.S.-Japan Workshop on Earthquake Resistant Design of Lifeline Facilities and Countermeasures Against Soil Liquefaction,” Edited by T.D. O’Rourke and M. Hamada, 11/7/94, (PB95-220802, A99, MF-E08).

NCEER-95-0001 “Experimental and Analytical Investigation of Seismic Retrofit of Structures with Supplemental Damping: Part 1 - Fluid Viscous Damping Devices,” by A.M. Reinhorn, C. Li and M.C. Constantinou, 1/3/95, (PB95-266599, A09, MF-A02).

NCEER-95-0002 “Experimental and Analytical Study of Low-Cycle Fatigue Behavior of Semi-Rigid Top-And-Seat Angle Connections,” by G. Pekcan, J.B. Mander and S.S. Chen, 1/5/95, (PB95-220042, A07, MF-A02).

NCEER-95-0003 “NCEER-ATC Joint Study on Fragility of Buildings,” by T. Anagnos, C. Rojahn and A.S. Kiremidjian, 1/20/95, (PB95-220026, A06, MF-A02).

NCEER-95-0004 “Nonlinear Control Algorithms for Peak Response Reduction,” by Z. Wu, T.T. Soong, V. Gattulli and R.C. Lin, 2/16/95, (PB95-220349, A05, MF-A01).

NCEER-95-0005 “Pipeline Replacement Feasibility Study: A Methodology for Minimizing Seismic and Corrosion Risks to Underground Natural Gas Pipelines,” by R.T. Eguchi, H.A. Seligson and D.G. Honegger, 3/2/95, (PB95-252326, A06, MF-A02).

NCEER-95-0006 “Evaluation of Seismic Performance of an 11-Story Frame Building During the 1994 Northridge Earthquake,” by F. Naeim, R. DiSulio, K. Benuska, A. Reinhorn and C. Li, not available.

NCEER-95-0007 “Prioritization of Bridges for Seismic Retrofitting,” by N. Basöz and A.S. Kiremidjian, 4/24/95, (PB95-252300, A08, MF-A02).

NCEER-95-0008 "Method for Developing Motion Damage Relationships for Reinforced Concrete Frames," by A. Singhal and A.S. Kiremidjian, 5/11/95, (PB95-266607, A06, MF-A02).

NCEER-95-0009 "Experimental and Analytical Investigation of Seismic Retrofit of Structures with Supplemental Damping: Part II - Friction Devices," by C. Li and A.M. Reinhorn, 7/6/95, (PB96-128087, A11, MF-A03).

NCEER-95-0010 "Experimental Performance and Analytical Study of a Non-Ductile Reinforced Concrete Frame Structure Retrofitted with Elastomeric Spring Dampers," by G. Pekcan, J.B. Mander and S.S. Chen, 7/14/95, (PB96-137161, A08, MF-A02).

NCEER-95-0011 "Development and Experimental Study of Semi-Active Fluid Damping Devices for Seismic Protection of Structures," by M.D. Symans and M.C. Constantinou, 8/3/95, (PB96-136940, A23, MF-A04).

NCEER-95-0012 "Real-Time Structural Parameter Modification (RSPM): Development of Innervated Structures," by Z. Liang, M. Tong and G.C. Lee, 4/11/95, (PB96-137153, A06, MF-A01).

NCEER-95-0013 "Experimental and Analytical Investigation of Seismic Retrofit of Structures with Supplemental Damping: Part III - Viscous Damping Walls," by A.M. Reinhorn and C. Li, 10/1/95, (PB96-176409, A11, MF-A03).

NCEER-95-0014 "Seismic Fragility Analysis of Equipment and Structures in a Memphis Electric Substation," by J-R. Huo and H.H.M. Hwang, 8/10/95, (PB96-128087, A09, MF-A02).

NCEER-95-0015 "The Hanshin-Awaji Earthquake of January 17, 1995: Performance of Lifelines," Edited by M. Shinozuka, 11/3/95, (PB96-176383, A15, MF-A03).

NCEER-95-0016 "Highway Culvert Performance During Earthquakes," by T.L. Youd and C.J. Beckman, available as NCEER-96-0015.

NCEER-95-0017 "The Hanshin-Awaji Earthquake of January 17, 1995: Performance of Highway Bridges," Edited by I.G. Buckle, 12/1/95, not available.

NCEER-95-0018 "Modeling of Masonry Infill Panels for Structural Analysis," by A.M. Reinhorn, A. Madan, R.E. Valles, Y. Reichmann and J.B. Mander, 12/8/95, (PB97-110886, MF-A01, A06).

NCEER-95-0019 "Optimal Polynomial Control for Linear and Nonlinear Structures," by A.K. Agrawal and J.N. Yang, 12/11/95, (PB96-168737, A07, MF-A02).

NCEER-95-0020 "Retrofit of Non-Ductile Reinforced Concrete Frames Using Friction Dampers," by R.S. Rao, P. Gergely and R.N. White, 12/22/95, (PB97-133508, A10, MF-A02).

NCEER-95-0021 "Parametric Results for Seismic Response of Pile-Supported Bridge Bents," by G. Mylonakis, A. Nikolaou and G. Gazetas, 12/22/95, (PB97-100242, A12, MF-A03).

NCEER-95-0022 "Kinematic Bending Moments in Seismically Stressed Piles," by A. Nikolaou, G. Mylonakis and G. Gazetas, 12/23/95, (PB97-113914, MF-A03, A13).

NCEER-96-0001 "Dynamic Response of Unreinforced Masonry Buildings with Flexible Diaphragms," by A.C. Costley and D.P. Abrams," 10/10/96, (PB97-133573, MF-A03, A15).

NCEER-96-0002 "State of the Art Review: Foundations and Retaining Structures," by I. Po Lam, not available.

NCEER-96-0003 "Ductility of Rectangular Reinforced Concrete Bridge Columns with Moderate Confinement," by N. Wehbe, M. Saiidi, D. Sanders and B. Douglas, 11/7/96, (PB97-133557, A06, MF-A02).

NCEER-96-0004 "Proceedings of the Long-Span Bridge Seismic Research Workshop," edited by I.G. Buckle and I.M. Friedland, not available.

NCEER-96-0005 "Establish Representative Pier Types for Comprehensive Study: Eastern United States," by J. Kulicki and Z. Prucz, 5/28/96, (PB98-119217, A07, MF-A02).

NCEER-96-0006 "Establish Representative Pier Types for Comprehensive Study: Western United States," by R. Imbsen, R.A. Schamber and T.A. Osterkamp, 5/28/96, (PB98-118607, A07, MF-A02).

NCEER-96-0007 "Nonlinear Control Techniques for Dynamical Systems with Uncertain Parameters," by R.G. Ghanem and M.I. Bujakov, 5/27/96, (PB97-100259, A17, MF-A03).

NCEER-96-0008 "Seismic Evaluation of a 30-Year Old Non-Ductile Highway Bridge Pier and Its Retrofit," by J.B. Mander, B. Mahmoodzadegan, S. Bhadra and S.S. Chen, 5/31/96, (PB97-110902, MF-A03, A10).

NCEER-96-0009 "Seismic Performance of a Model Reinforced Concrete Bridge Pier Before and After Retrofit," by J.B. Mander, J.H. Kim and C.A. Ligozio, 5/31/96, (PB97-110910, MF-A02, A10).

NCEER-96-0010 "IDARC2D Version 4.0: A Computer Program for the Inelastic Damage Analysis of Buildings," by R.E. Valles, A.M. Reinhorn, S.K. Kunnath, C. Li and A. Madan, 6/3/96, (PB97-100234, A17, MF-A03).

NCEER-96-0011 "Estimation of the Economic Impact of Multiple Lifeline Disruption: Memphis Light, Gas and Water Division Case Study," by S.E. Chang, H.A. Seligson and R.T. Eguchi, 8/16/96, (PB97-133490, A11, MF-A03).

NCEER-96-0012 "Proceedings from the Sixth Japan-U.S. Workshop on Earthquake Resistant Design of Lifeline Facilities and Countermeasures Against Soil Liquefaction, Edited by M. Hamada and T. O'Rourke, 9/11/96, (PB97-133581, A99, MF-A06).

NCEER-96-0013 "Chemical Hazards, Mitigation and Preparedness in Areas of High Seismic Risk: A Methodology for Estimating the Risk of Post-Earthquake Hazardous Materials Release," by H.A. Seligson, R.T. Eguchi, K.J. Tierney and K. Richmond, 11/7/96, (PB97-133565, MF-A02, A08).

NCEER-96-0014 "Response of Steel Bridge Bearings to Reversed Cyclic Loading," by J.B. Mander, D-K. Kim, S.S. Chen and G.J. Premus, 11/13/96, (PB97-140735, A12, MF-A03).

NCEER-96-0015 "Highway Culvert Performance During Past Earthquakes," by T.L. Youd and C.J. Beckman, 11/25/96, (PB97-133532, A06, MF-A01).

NCEER-97-0001 "Evaluation, Prevention and Mitigation of Pounding Effects in Building Structures," by R.E. Valles and A.M. Reinhorn, 2/20/97, (PB97-159552, A14, MF-A03).

NCEER-97-0002 "Seismic Design Criteria for Bridges and Other Highway Structures," by C. Rojahn, R. Mayes, D.G. Anderson, J. Clark, J.H. Hom, R.V. Nutt and M.J. O'Rourke, 4/30/97, (PB97-194658, A06, MF-A03).

NCEER-97-0003 "Proceedings of the U.S.-Italian Workshop on Seismic Evaluation and Retrofit," Edited by D.P. Abrams and G.M. Calvi, 3/19/97, (PB97-194666, A13, MF-A03).

NCEER-97-0004 "Investigation of Seismic Response of Buildings with Linear and Nonlinear Fluid Viscous Dampers," by A.A. Seleemah and M.C. Constantinou, 5/21/97, (PB98-109002, A15, MF-A03).

NCEER-97-0005 "Proceedings of the Workshop on Earthquake Engineering Frontiers in Transportation Facilities," edited by G.C. Lee and I.M. Friedland, 8/29/97, (PB98-128911, A25, MR-A04).

NCEER-97-0006 "Cumulative Seismic Damage of Reinforced Concrete Bridge Piers," by S.K. Kunnath, A. El-Bahy, A. Taylor and W. Stone, 9/2/97, (PB98-108814, A11, MF-A03).

NCEER-97-0007 "Structural Details to Accommodate Seismic Movements of Highway Bridges and Retaining Walls," by R.A. Imbsen, R.A. Schamber, E. Thorkildsen, A. Kartoum, B.T. Martin, T.N. Rosser and J.M. Kulicki, 9/3/97, (PB98-108996, A09, MF-A02).

NCEER-97-0008 "A Method for Earthquake Motion-Damage Relationships with Application to Reinforced Concrete Frames," by A. Singhal and A.S. Kiremidjian, 9/10/97, (PB98-108988, A13, MF-A03).

NCEER-97-0009 "Seismic Analysis and Design of Bridge Abutments Considering Sliding and Rotation," by K. Fishman and R. Richards, Jr., 9/15/97, (PB98-108897, A06, MF-A02).

NCEER-97-0010 "Proceedings of the FHWA/NCEER Workshop on the National Representation of Seismic Ground Motion for New and Existing Highway Facilities," edited by I.M. Friedland, M.S. Power and R.L. Mayes, 9/22/97, (PB98-128903, A21, MF-A04).

NCEER-97-0011 "Seismic Analysis for Design or Retrofit of Gravity Bridge Abutments," by K.L. Fishman, R. Richards, Jr. and R.C. Divito, 10/2/97, (PB98-128937, A08, MF-A02).

NCEER-97-0012 "Evaluation of Simplified Methods of Analysis for Yielding Structures," by P. Tsopelas, M.C. Constantinou, C.A. Kircher and A.S. Whittaker, 10/31/97, (PB98-128929, A10, MF-A03).

NCEER-97-0013 "Seismic Design of Bridge Columns Based on Control and Repairability of Damage," by C-T. Cheng and J.B. Mander, 12/8/97, (PB98-144249, A11, MF-A03).

NCEER-97-0014 "Seismic Resistance of Bridge Piers Based on Damage Avoidance Design," by J.B. Mander and C-T. Cheng, 12/10/97, (PB98-144223, A09, MF-A02).

NCEER-97-0015 "Seismic Response of Nominally Symmetric Systems with Strength Uncertainty," by S. Balopoulou and M. Grigoriu, 12/23/97, (PB98-153422, A11, MF-A03).

NCEER-97-0016 "Evaluation of Seismic Retrofit Methods for Reinforced Concrete Bridge Columns," by T.J. Wipf, F.W. Klaiber and F.M. Russo, 12/28/97, (PB98-144215, A12, MF-A03).

NCEER-97-0017 "Seismic Fragility of Existing Conventional Reinforced Concrete Highway Bridges," by C.L. Mullen and A.S. Cakmak, 12/30/97, (PB98-153406, A08, MF-A02).

NCEER-97-0018 "Loss Asssessment of Memphis Buildings," edited by D.P. Abrams and M. Shinozuka, 12/31/97, (PB98-144231, A13, MF-A03).

NCEER-97-0019 "Seismic Evaluation of Frames with Infill Walls Using Quasi-static Experiments," by K.M. Mosalam, R.N. White and P. Gergely, 12/31/97, (PB98-153455, A07, MF-A02).

NCEER-97-0020 "Seismic Evaluation of Frames with Infill Walls Using Pseudo-dynamic Experiments," by K.M. Mosalam, R.N. White and P. Gergely, 12/31/97, (PB98-153430, A07, MF-A02).

NCEER-97-0021 "Computational Strategies for Frames with Infill Walls: Discrete and Smeared Crack Analyses and Seismic Fragility," by K.M. Mosalam, R.N. White and P. Gergely, 12/31/97, (PB98-153414, A10, MF-A02).

NCEER-97-0022 "Proceedings of the NCEER Workshop on Evaluation of Liquefaction Resistance of Soils," edited by T.L. Youd and I.M. Idriss, 12/31/97, (PB98-155617, A15, MF-A03).

MCEER-98-0001 "Extraction of Nonlinear Hysteretic Properties of Seismically Isolated Bridges from Quick-Release Field Tests," by Q. Chen, B.M. Douglas, E.M. Maragakis and I.G. Buckle, 5/26/98, (PB99-118838, A06, MF-A01).

MCEER-98-0002 "Methodologies for Evaluating the Importance of Highway Bridges," by A. Thomas, S. Eshenaur and J. Kulicki, 5/29/98, (PB99-118846, A10, MF-A02).

MCEER-98-0003 "Capacity Design of Bridge Piers and the Analysis of Overstrength," by J.B. Mander, A. Dutta and P. Goel, 6/1/98, (PB99-118853, A09, MF-A02).

MCEER-98-0004 "Evaluation of Bridge Damage Data from the Loma Prieta and Northridge, California Earthquakes," by N. Basoz and A. Kiremidjian, 6/2/98, (PB99-118861, A15, MF-A03).

MCEER-98-0005 "Screening Guide for Rapid Assessment of Liquefaction Hazard at Highway Bridge Sites," by T. L. Youd, 6/16/98, (PB99-118879, A06, not available on microfiche).

MCEER-98-0006 "Structural Steel and Steel/Concrete Interface Details for Bridges," by P. Ritchie, N. Kauhl and J. Kulicki, 7/13/98, (PB99-118945, A06, MF-A01).

MCEER-98-0007 "Capacity Design and Fatigue Analysis of Confined Concrete Columns," by A. Dutta and J.B. Mander, 7/14/98, (PB99-118960, A14, MF-A03).

MCEER-98-0008 “Proceedings of the Workshop on Performance Criteria for Telecommunication Services Under Earthquake Conditions,” edited by A.J. Schiff, 7/15/98, (PB99-118952, A08, MF-A02).

MCEER-98-0009 “Fatigue Analysis of Unconfined Concrete Columns,” by J.B. Mander, A. Dutta and J.H. Kim, 9/12/98, (PB99-123655, A10, MF-A02).

MCEER-98-0010 “Centrifuge Modeling of Cyclic Lateral Response of Pile-Cap Systems and Seat-Type Abutments in Dry Sands,” by A.D. Gadre and R. Dobry, 10/2/98, (PB99-123606, A13, MF-A03).

MCEER-98-0011 “IDARC-BRIDGE: A Computational Platform for Seismic Damage Assessment of Bridge Structures,” by A.M. Reinhorn, V. Simeonov, G. Mylonakis and Y. Reichman, 10/2/98, (PB99-162919, A15, MF-A03).

MCEER-98-0012 “Experimental Investigation of the Dynamic Response of Two Bridges Before and After Retrofitting with Elastomeric Bearings,” by D.A. Wendichansky, S.S. Chen and J.B. Mander, 10/2/98, (PB99-162927, A15, MF-A03).

MCEER-98-0013 “Design Procedures for Hinge Restrainers and Hinge Sear Width for Multiple-Frame Bridges,” by R. Des Roches and G.L. Fenves, 11/3/98, (PB99-140477, A13, MF-A03).

MCEER-98-0014 “Response Modification Factors for Seismically Isolated Bridges,” by M.C. Constantinou and J.K. Quarshie, 11/3/98, (PB99-140485, A14, MF-A03).

MCEER-98-0015 “Proceedings of the U.S.-Italy Workshop on Seismic Protective Systems for Bridges,” edited by I.M. Friedland and M.C. Constantinou, 11/3/98, (PB2000-101711, A22, MF-A04).

MCEER-98-0016 “Appropriate Seismic Reliability for Critical Equipment Systems: Recommendations Based on Regional Analysis of Financial and Life Loss,” by K. Porter, C. Scawthorn, C. Taylor and N. Blais, 11/10/98, (PB99-157265, A08, MF-A02).

MCEER-98-0017 “Proceedings of the U.S. Japan Joint Seminar on Civil Infrastructure Systems Research,” edited by M. Shinozuka and A. Rose, 11/12/98, (PB99-156713, A16, MF-A03).

MCEER-98-0018 “Modeling of Pile Footings and Drilled Shafts for Seismic Design,” by I. PoLam, M. Kapuskar and D. Chaudhuri, 12/21/98, (PB99-157257, A09, MF-A02).

MCEER-99-0001 "Seismic Evaluation of a Masonry Infilled Reinforced Concrete Frame by Pseudodynamic Testing," by S.G. Buonopane and R.N. White, 2/16/99, (PB99-162851, A09, MF-A02).

MCEER-99-0002 "Response History Analysis of Structures with Seismic Isolation and Energy Dissipation Systems: Verification Examples for Program SAP2000," by J. Scheller and M.C. Constantinou, 2/22/99, (PB99-162869, A08, MF-A02).

MCEER-99-0003 "Experimental Study on the Seismic Design and Retrofit of Bridge Columns Including Axial Load Effects," by A. Dutta, T. Kokorina and J.B. Mander, 2/22/99, (PB99-162877, A09, MF-A02).

MCEER-99-0004 "Experimental Study of Bridge Elastomeric and Other Isolation and Energy Dissipation Systems with Emphasis on Uplift Prevention and High Velocity Near-source Seismic Excitation," by A. Kasalanati and M. C. Constantinou, 2/26/99, (PB99-162885, A12, MF-A03).

MCEER-99-0005 "Truss Modeling of Reinforced Concrete Shear-flexure Behavior," by J.H. Kim and J.B. Mander, 3/8/99, (PB99-163693, A12, MF-A03).

MCEER-99-0006 "Experimental Investigation and Computational Modeling of Seismic Response of a 1:4 Scale Model Steel Structure with a Load Balancing Supplemental Damping System," by G. Pekcan, J.B. Mander and S.S. Chen, 4/2/99, (PB99-162893, A11, MF-A03).

MCEER-99-0007 "Effect of Vertical Ground Motions on the Structural Response of Highway Bridges," by M.R. Button, C.J. Cronin and R.L. Mayes, 4/10/99, (PB2000-101411, A10, MF-A03).

MCEER-99-0008 "Seismic Reliability Assessment of Critical Facilities: A Handbook, Supporting Documentation, and Model Code Provisions," by G.S. Johnson, R.E. Sheppard, M.D. Quilici, S.J. Eder and C.R. Scawthorn, 4/12/99, (PB2000-101701, A18, MF-A04).

MCEER-99-0009 "Impact Assessment of Selected MCEER Highway Project Research on the Seismic Design of Highway Structures," by C. Rojahn, R. Mayes, D.G. Anderson, J.H. Clark, D'Appolonia Engineering, S. Gloyd and R.V. Nutt, 4/14/99, (PB99-162901, A10, MF-A02).

MCEER-99-0010 "Site Factors and Site Categories in Seismic Codes," by R. Dobry, R. Ramos and M.S. Power, 7/19/99, (PB2000-101705, A08, MF-A02).

MCEER-99-0011 "Restrainer Design Procedures for Multi-Span Simply-Supported Bridges," by M.J. Randall, M. Saiidi, E. Maragakis and T. Isakovic, 7/20/99, (PB2000-101702, A10, MF-A02).

MCEER-99-0012 "Property Modification Factors for Seismic Isolation Bearings," by M.C. Constantinou, P. Tsopelas, A. Kasalanati and E. Wolff, 7/20/99, (PB2000-103387, A11, MF-A03).

MCEER-99-0013 "Critical Seismic Issues for Existing Steel Bridges," by P. Ritchie, N. Kauhl and J. Kulicki, 7/20/99, (PB2000-101697, A09, MF-A02).

MCEER-99-0014 "Nonstructural Damage Database," by A. Kao, T.T. Soong and A. Vender, 7/24/99, (PB2000-101407, A06, MF-A01).

MCEER-99-0015 "Guide to Remedial Measures for Liquefaction Mitigation at Existing Highway Bridge Sites," by H.G. Cooke and J. K. Mitchell, 7/26/99, (PB2000-101703, A11, MF-A03).

MCEER-99-0016 "Proceedings of the MCEER Workshop on Ground Motion Methodologies for the Eastern United States," edited by N. Abrahamson and A. Becker, 8/11/99, (PB2000-103385, A07, MF-A02).

MCEER-99-0017 "Quindío, Colombia Earthquake of January 25, 1999: Reconnaissance Report," by A.P. Asfura and P.J. Flores, 10/4/99, (PB2000-106893, A06, MF-A01).

MCEER-99-0018 "Hysteretic Models for Cyclic Behavior of Deteriorating Inelastic Structures," by M.V. Sivaselvan and A.M. Reinhorn, 11/5/99, (PB2000-103386, A08, MF-A02).

MCEER-99-0019 "Proceedings of the 7th U.S.- Japan Workshop on Earthquake Resistant Design of Lifeline Facilities and Countermeasures Against Soil Liquefaction," edited by T.D. O'Rourke, J.P. Bardet and M. Hamada, 11/19/99, (PB2000-103354, A99, MF-A06).

MCEER-99-0020 "Development of Measurement Capability for Micro-Vibration Evaluations with Application to Chip Fabrication Facilities," by G.C. Lee, Z. Liang, J.W. Song, J.D. Shen and W.C. Liu, 12/1/99, (PB2000-105993, A08, MF-A02).

MCEER-99-0021 "Design and Retrofit Methodology for Building Structures with Supplemental Energy Dissipating Systems," by G. Pekcan, J.B. Mander and S.S. Chen, 12/31/99, (PB2000-105994, A11, MF-A03).

MCEER-00-0001 "The Marmara, Turkey Earthquake of August 17, 1999: Reconnaissance Report," edited by C. Scawthorn; with major contributions by M. Bruneau, R. Eguchi, T. Holzer, G. Johnson, J. Mander, J. Mitchell, W. Mitchell, A. Papageorgiou, C. Scaethorn, and G. Webb, 3/23/00, (PB2000-106200, A11, MF-A03).

MCEER-00-0002 "Proceedings of the MCEER Workshop for Seismic Hazard Mitigation of Health Care Facilities," edited by G.C. Lee, M. Ettouney, M. Grigoriu, J. Hauer and J. Nigg, 3/29/00, (PB2000-106892, A08, MF-A02).

MCEER-00-0003 "The Chi-Chi, Taiwan Earthquake of September 21, 1999: Reconnaissance Report," edited by G.C. Lee and C.H. Loh, with major contributions by G.C. Lee, M. Bruneau, I.G. Buckle, S.E. Chang, P.J. Flores, T.D. O'Rourke, M. Shinozuka, T.T. Soong, C-H. Loh, K-C. Chang, Z-J. Chen, J-S. Hwang, M-L. Lin, G-Y. Liu, K-C. Tsai, G.C. Yao and C-L. Yen, 4/30/00, (PB2001-100980, A10, MF-A02).

MCEER-00-0004 "Seismic Retrofit of End-Sway Frames of Steel Deck-Truss Bridges with a Supplemental Tendon System: Experimental and Analytical Investigation," by G. Pekcan, J.B. Mander and S.S. Chen, 7/1/00, (PB2001-100982, A10, MF-A02).

MCEER-00-0005 "Sliding Fragility of Unrestrained Equipment in Critical Facilities," by W.H. Chong and T.T. Soong, 7/5/00, (PB2001-100983, A08, MF-A02).

MCEER-00-0006 "Seismic Response of Reinforced Concrete Bridge Pier Walls in the Weak Direction," by N. Abo-Shadi, M. Saiidi and D. Sanders, 7/17/00, (PB2001-100981, A17, MF-A03).

MCEER-00-0007 "Low-Cycle Fatigue Behavior of Longitudinal Reinforcement in Reinforced Concrete Bridge Columns," by J. Brown and S.K. Kunnath, 7/23/00, (PB2001-104392, A08, MF-A02).

MCEER-00-0008 "Soil Structure Interaction of Bridges for Seismic Analysis," I. PoLam and H. Law, 9/25/00, (PB2001-105397, A08, MF-A02).

MCEER-00-0009 "Proceedings of the First MCEER Workshop on Mitigation of Earthquake Disaster by Advanced Technologies (MEDAT-1), edited by M. Shinozuka, D.J. Inman and T.D. O'Rourke, 11/10/00, (PB2001-105399, A14, MF-A03).

MCEER-00-0010 "Development and Evaluation of Simplified Procedures for Analysis and Design of Buildings with Passive Energy Dissipation Systems, Revision 01," by O.M. Ramirez, M.C. Constantinou, C.A. Kircher, A.S. Whittaker, M.W. Johnson, J.D. Gomez and C. Chrysostomou, 11/16/01, (PB2001-105523, A23, MF-A04).

MCEER-00-0011 "Dynamic Soil-Foundation-Structure Interaction Analyses of Large Caissons," by C-Y. Chang, C-M. Mok, Z-L. Wang, R. Settgast, F. Waggoner, M.A. Ketchum, H.M. Gonnermann and C-C. Chin, 12/30/00, (PB2001-104373, A07, MF-A02).

MCEER-00-0012 "Experimental Evaluation of Seismic Performance of Bridge Restrainers," by A.G. Vlassis, E.M. Maragakis and M. Saiid Saiidi, 12/30/00, (PB2001-104354, A09, MF-A02).

MCEER-00-0013 "Effect of Spatial Variation of Ground Motion on Highway Structures," by M. Shinozuka, V. Saxena and G. Deodatis, 12/31/00, (PB2001-108755, A13, MF-A03).

MCEER-00-0014 "A Risk-Based Methodology for Assessing the Seismic Performance of Highway Systems," by S.D. Werner, C.E. Taylor, J.E. Moore, II, J.S. Walton and S. Cho, 12/31/00, (PB2001-108756, A14, MF-A03).

MCEER-01-0001 “Experimental Investigation of P-Delta Effects to Collapse During Earthquakes,” by D. Vian and M. Bruneau, 6/25/01, (PB2002-100534, A17, MF-A03).

MCEER-01-0002 “Proceedings of the Second MCEER Workshop on Mitigation of Earthquake Disaster by Advanced Technologies (MEDAT-2),” edited by M. Bruneau and D.J. Inman, 7/23/01, (PB2002-100434, A16, MF-A03).

MCEER-01-0003 “Sensitivity Analysis of Dynamic Systems Subjected to Seismic Loads,” by C. Roth and M. Grigoriu, 9/18/01, (PB2003-100884, A12, MF-A03).

MCEER-01-0004 “Overcoming Obstacles to Implementing Earthquake Hazard Mitigation Policies: Stage 1 Report,” by D.J. Alesch and W.J. Petak, 12/17/01, (PB2002-107949, A07, MF-A02).

MCEER-01-0005 “Updating Real-Time Earthquake Loss Estimates: Methods, Problems and Insights,” by C.E. Taylor, S.E. Chang and R.T. Eguchi, 12/17/01, (PB2002-107948, A05, MF-A01).

MCEER-01-0006 “Experimental Investigation and Retrofit of Steel Pile Foundations and Pile Bents Under Cyclic Lateral Loadings,” by A. Shama, J. Mander, B. Blabac and S. Chen, 12/31/01, (PB2002-107950, A13, MF-A03).

MCEER-02-0001 “Assessment of Performance of Bolu Viaduct in the 1999 Duzce Earthquake in Turkey” by P.C. Roussis, M.C. Constantinou, M. Erdik, E. Durukal and M. Dicleli, 5/8/02, (PB2003-100883, A08, MF-A02).

MCEER-02-0002 “Seismic Behavior of Rail Counterweight Systems of Elevators in Buildings,” by M.P. Singh, Rildova and L.E. Suarez, 5/27/02. (PB2003-100882, A11, MF-A03).

MCEER-02-0003 “Development of Analysis and Design Procedures for Spread Footings,” by G. Mylonakis, G. Gazetas, S. Nikolaou and A. Chauncey, 10/02/02, (PB2004-101636, A13, MF-A03, CD-A13).

MCEER-02-0004 “Bare-Earth Algorithms for Use with SAR and LIDAR Digital Elevation Models,” by C.K. Huyck, R.T. Eguchi and B. Houshmand, 10/16/02, (PB2004-101637, A07, CD-A07).

MCEER-02-0005 "Review of Energy Dissipation of Compression Members in Concentrically Braced Frames," by K.Lee and M. Bruneau, 10/18/02, (PB2004-101638, A10, CD-A10).

MCEER-03-0001 "Experimental Investigation of Light-Gauge Steel Plate Shear Walls for the Seismic Retrofit of Buildings" by J. Berman and M. Bruneau, 5/2/03, (PB2004-101622, A10, MF-A03, CD-A10).

MCEER-03-0002 "Statistical Analysis of Fragility Curves," by M. Shinozuka, M.Q. Feng, H. Kim, T. Uzawa and T. Ueda, 6/16/03, (PB2004-101849, A09, CD-A09).

MCEER-03-0003 "Proceedings of the Eighth U.S.-Japan Workshop on Earthquake Resistant Design f Lifeline Facilities and Countermeasures Against Liquefaction," edited by M. Hamada, J.P. Bardet and T.D. O'Rourke, 6/30/03, (PB2004-104386, A99, CD-A99).

MCEER-03-0004 "Proceedings of the PRC-US Workshop on Seismic Analysis and Design of Special Bridges," edited by L.C. Fan and G.C. Lee, 7/15/03, (PB2004-104387, A14, CD-A14).

MCEER-03-0005 "Urban Disaster Recovery: A Framework and Simulation Model," by S.B. Miles and S.E. Chang, 7/25/03, (PB2004-104388, A07, CD-A07).

MCEER-03-0006 "Behavior of Underground Piping Joints Due to Static and Dynamic Loading," by R.D. Meis, M. Maragakis and R. Siddharthan, 11/17/03, (PB2005-102194, A13, MF-A03, CD-A00).

MCEER-04-0001 "Experimental Study of Seismic Isolation Systems with Emphasis on Secondary System Response and Verification of Accuracy of Dynamic Response History Analysis Methods," by E. Wolff and M. Constantinou, 1/16/04 (PB2005-102195, A99, MF-E08, CD-A00).

MCEER-04-0002 "Tension, Compression and Cyclic Testing of Engineered Cementitious Composite Materials," by K. Kesner and S.L. Billington, 3/1/04, (PB2005-102196, A08, CD-A08).

MCEER-04-0003 "Cyclic Testing of Braces Laterally Restrained by Steel Studs to Enhance Performance During Earthquakes," by O.C. Celik, J.W. Berman and M. Bruneau, 3/16/04, (PB2005-102197, A13, MF-A03, CD-A00).

MCEER-04-0004 "Methodologies for Post Earthquake Building Damage Detection Using SAR and Optical Remote Sensing: Application to the August 17, 1999 Marmara, Turkey Earthquake," by C.K. Huyck, B.J. Adams, S. Cho, R.T. Eguchi, B. Mansouri and B. Houshmand, 6/15/04, (PB2005-104888, A10, CD-A00).

MCEER-04-0005 "Nonlinear Structural Analysis Towards Collapse Simulation: A Dynamical Systems Approach," by M.V. Sivaselvan and A.M. Reinhorn, 6/16/04, (PB2005-104889, A11, MF-A03, CD-A00).

MCEER-04-0006 "Proceedings of the Second PRC-US Workshop on Seismic Analysis and Design of Special Bridges," edited by G.C. Lee and L.C. Fan, 6/25/04, (PB2005-104890, A16, CD-A00).

MCEER-04-0007 "Seismic Vulnerability Evaluation of Axially Loaded Steel Built-up Laced Members," by K. Lee and M. Bruneau, 6/30/04, (PB2005-104891, A16, CD-A00).

MCEER-04-0008 "Evaluation of Accuracy of Simplified Methods of Analysis and Design of Buildings with Damping Systems for Near-Fault and for Soft-Soil Seismic Motions," by E.A. Pavlou and M.C. Constantinou, 8/16/04, (PB2005-104892, A08, MF-A02, CD-A00).

MCEER-04-0009 "Assessment of Geotechnical Issues in Acute Care Facilities in California," by M. Lew, T.D. O'Rourke, R. Dobry and M. Koch, 9/15/04, (PB2005-104893, A08, CD-A00).

MCEER-04-0010 "Scissor-Jack-Damper Energy Dissipation System," by A.N. Sigaher-Boyle and M.C. Constantinou, 12/1/04 (PB2005-108221).

MCEER-04-0011 "Seismic Retrofit of Bridge Steel Truss Piers Using a Controlled Rocking Approach," by M. Pollino and M. Bruneau, 12/20/04 (PB2006-105795).

MCEER-05-0001 "Experimental and Analytical Studies of Structures Seismically Isolated with an Uplift-Restraint Isolation System," by P.C. Roussis and M.C. Constantinou, 1/10/05 (PB2005-108222).

MCEER-05-0002 "A Versatile Experimentation Model for Study of Structures Near Collapse Applied to Seismic Evaluation of Irregular Structures," by D. Kusumastuti, A.M. Reinhorn and A. Rutenberg, 3/31/05 (PB2006-101523).

MCEER-05-0003 "Proceedings of the Third PRC-US Workshop on Seismic Analysis and Design of Special Bridges," edited by L.C. Fan and G.C. Lee, 4/20/05, (PB2006-105796).

MCEER-05-0004 "Approaches for the Seismic Retrofit of Braced Steel Bridge Piers and Proof-of-Concept Testing of an Eccentrically Braced Frame with Tubular Link," by J.W. Berman and M. Bruneau, 4/21/05 (PB2006-101524).

MCEER-05-0005 "Simulation of Strong Ground Motions for Seismic Fragility Evaluation of Nonstructural Components in Hospitals," by A. Wanitkorkul and A. Filiatrault, 5/26/05 (PB2006-500027).

MCEER-05-0006 "Seismic Safety in California Hospitals: Assessing an Attempt to Accelerate the Replacement or Seismic Retrofit of Older Hospital Facilities," by D.J. Alesch, L.A. Arendt and W.J. Petak, 6/6/05 (PB2006-105794).

MCEER-05-0007 "Development of Seismic Strengthening and Retrofit Strategies for Critical Facilities Using Engineered Cementitious Composite Materials," by K. Kesner and S.L. Billington, 8/29/05 (PB2006-111701).

MCEER-05-0008 "Experimental and Analytical Studies of Base Isolation Systems for Seismic Protection of Power Transformers," by N. Murota, M.Q. Feng and G-Y. Liu, 9/30/05 (PB2006-111702).

MCEER-05-0009 "3D-BASIS-ME-MB: Computer Program for Nonlinear Dynamic Analysis of Seismically Isolated Structures," by P.C. Tsopelas, P.C. Roussis, M.C. Constantinou, R. Buchanan and A.M. Reinhorn, 10/3/05 (PB2006-111703).

MCEER-05-0010 "Steel Plate Shear Walls for Seismic Design and Retrofit of Building Structures," by D. Vian and M. Bruneau, 12/15/05 (PB2006-111704).

MCEER-05-0011 "The Performance-Based Design Paradigm," by M.J. Astrella and A. Whittaker, 12/15/05 (PB2006-111705).

MCEER-06-0001 "Seismic Fragility of Suspended Ceiling Systems," H. Badillo-Almaraz, A.S. Whittaker, A.M. Reinhorn and G.P. Cimellaro, 2/4/06 (PB2006-111706).

MCEER-06-0002 "Multi-Dimensional Fragility of Structures," by G.P. Cimellaro, A.M. Reinhorn and M. Bruneau, 3/1/06 (PB2007-106974, A09, MF-A02, CD A00).

MCEER-06-0003 "Built-Up Shear Links as Energy Dissipators for Seismic Protection of Bridges," by P. Dusicka, A.M. Itani and I.G. Buckle, 3/15/06 (PB2006-111708).

MCEER-06-0004 "Analytical Investigation of the Structural Fuse Concept," by R.E. Vargas and M. Bruneau, 3/16/06 (PB2006-111709).

MCEER-06-0005 "Experimental Investigation of the Structural Fuse Concept," by R.E. Vargas and M. Bruneau, 3/17/06 (PB2006-111710).

MCEER-06-0006 "Further Development of Tubular Eccentrically Braced Frame Links for the Seismic Retrofit of Braced Steel Truss Bridge Piers," by J.W. Berman and M. Bruneau, 3/27/06 (PB2007-105147).

MCEER-06-0007 "REDARS Validation Report," by S. Cho, C.K. Huyck, S. Ghosh and R.T. Eguchi, 8/8/06 (PB2007-106983).

MCEER-06-0008 "Review of Current NDE Technologies for Post-Earthquake Assessment of Retrofitted Bridge Columns," by J.W. Song, Z. Liang and G.C. Lee, 8/21/06 (PB2007-106984).

MCEER-06-0009 "Liquefaction Remediation in Silty Soils Using Dynamic Compaction and Stone Columns," by S. Thevanayagam, G.R. Martin, R. Nashed, T. Shenthan, T. Kanagalingam and N. Ecemis, 8/28/06 (PB2007-106985).

MCEER-06-0010 "Conceptual Design and Experimental Investigation of Polymer Matrix Composite Infill Panels for Seismic Retrofitting," by W. Jung, M. Chiewanichakorn and A.J. Aref, 9/21/06 (PB2007-106986).

MCEER-06-0011 "A Study of the Coupled Horizontal-Vertical Behavior of Elastomeric and Lead-Rubber Seismic Isolation Bearings," by G.P. Warn and A.S. Whittaker, 9/22/06 (PB2007-108679).

MCEER-06-0012 "Proceedings of the Fourth PRC-US Workshop on Seismic Analysis and Design of Special Bridges: Advancing Bridge Technologies in Research, Design, Construction and Preservation," Edited by L.C. Fan, G.C. Lee and L. Ziang, 10/12/06 (PB2007-109042).

MCEER-06-0013 "Cyclic Response and Low Cycle Fatigue Characteristics of Plate Steels," by P. Dusicka, A.M. Itani and I.G. Buckle, 11/1/06 06 (PB2007-106987).

MCEER-06-0014 "Proceedings of the Second US-Taiwan Bridge Engineering Workshop," edited by W.P. Yen, J. Shen, J-Y. Chen and M. Wang, 11/15/06 (PB2008-500041).

MCEER-06-0015 "User Manual and Technical Documentation for the REDARS^{TM} Import Wizard," by S. Cho, S. Ghosh, C.K. Huyck and S.D. Werner, 11/30/06 (PB2007-114766).

MCEER-06-0016 "Hazard Mitigation Strategy and Monitoring Technologies for Urban and Infrastructure Public Buildings: Proceedings of the China-US Workshops," edited by X.Y. Zhou, A.L. Zhang, G.C. Lee and M. Tong, 12/12/06 (PB2008-500018).

MCEER-07-0001 "Static and Kinetic Coefficients of Friction for Rigid Blocks," by C. Kafali, S. Fathali, M. Grigoriu and A.S. Whittaker, 3/20/07 (PB2007-114767).

MCEER-07-0002 "Hazard Mitigation Investment Decision Making: Organizational Response to Legislative Mandate," by L.A. Arendt, D.J. Alesch and W.J. Petak, 4/9/07 (PB2007-114768).

MCEER-07-0003 "Seismic Behavior of Bidirectional-Resistant Ductile End Diaphragms with Unbonded Braces in Straight or Skewed Steel Bridges," by O. Celik and M. Bruneau, 4/11/07 (PB2008-105141).

MCEER-07-0004 "Modeling Pile Behavior in Large Pile Groups Under Lateral Loading," by A.M. Dodds and G.R. Martin, 4/16/07(PB2008-105142).

MCEER-07-0005 "Experimental Investigation of Blast Performance of Seismically Resistant Concrete-Filled Steel Tube Bridge Piers," by S. Fujikura, M. Bruneau and D. Lopez-Garcia, 4/20/07 (PB2008-105143).

MCEER-07-0006 "Seismic Analysis of Conventional and Isolated Liquefied Natural Gas Tanks Using Mechanical Analogs," by I.P. Christovasilis and A.S. Whittaker, 5/1/07, not available.

MCEER-07-0007 "Experimental Seismic Performance Evaluation of Isolation/Restraint Systems for Mechanical Equipment – Part 1: Heavy Equipment Study," by S. Fathali and A. Filiatrault, 6/6/07 (PB2008-105144).

MCEER-07-0008 "Seismic Vulnerability of Timber Bridges and Timber Substructures," by A.A. Sharma, J.B. Mander, I.M. Friedland and D.R. Allicock, 6/7/07 (PB2008-105145).

MCEER-07-0009 "Experimental and Analytical Study of the XY-Friction Pendulum (XY-FP) Bearing for Bridge Applications," by C.C. Marin-Artieda, A.S. Whittaker and M.C. Constantinou, 6/7/07 (PB2008-105191).

MCEER-07-0010 "Proceedings of the PRC-US Earthquake Engineering Forum for Young Researchers," Edited by G.C. Lee and X.Z. Qi, 6/8/07 (PB2008-500058).

MCEER-07-0011 "Design Recommendations for Perforated Steel Plate Shear Walls," by R. Purba and M. Bruneau, 6/18/07, (PB2008-105192).

MCEER-07-0012 "Performance of Seismic Isolation Hardware Under Service and Seismic Loading," by M.C. Constantinou, A.S. Whittaker, Y. Kalpakidis, D.M. Fenz and G.P. Warn, 8/27/07, (PB2008-105193).

MCEER-07-0013 "Experimental Evaluation of the Seismic Performance of Hospital Piping Subassemblies," by E.R. Goodwin, E. Maragakis and A.M. Itani, 9/4/07, (PB2008-105194).

MCEER-07-0014 "A Simulation Model of Urban Disaster Recovery and Resilience: Implementation for the 1994 Northridge Earthquake," by S. Miles and S.E. Chang, 9/7/07, (PB2008-106426).

MCEER-07-0015 "Statistical and Mechanistic Fragility Analysis of Concrete Bridges," by M. Shinozuka, S. Banerjee and S-H. Kim, 9/10/07, (PB2008-106427).

MCEER-07-0016 "Three-Dimensional Modeling of Inelastic Buckling in Frame Structures," by M. Schachter and AM. Reinhorn, 9/13/07, (PB2008-108125).

MCEER-07-0017 "Modeling of Seismic Wave Scattering on Pile Groups and Caissons," by I. Po Lam, H. Law and C.T. Yang, 9/17/07 (PB2008-108150).

MCEER-07-0018 "Bridge Foundations: Modeling Large Pile Groups and Caissons for Seismic Design," by I. Po Lam, H. Law and G.R. Martin (Coordinating Author), 12/1/07 (PB2008-111190).

MCEER-07-0019 "Principles and Performance of Roller Seismic Isolation Bearings for Highway Bridges," by G.C. Lee, Y.C. Ou, Z. Liang, T.C. Niu and J. Song, 12/10/07 (PB2009-110466).

MCEER-07-0020 "Centrifuge Modeling of Permeability and Pinning Reinforcement Effects on Pile Response to Lateral Spreading," by L.L Gonzalez-Lagos, T. Abdoun and R. Dobry, 12/10/07 (PB2008-111191).

MCEER-07-0021 "Damage to the Highway System from the Pisco, Perú Earthquake of August 15, 2007," by J.S. O'Connor, L. Mesa and M. Nykamp, 12/10/07, (PB2008-108126).

MCEER-07-0022 "Experimental Seismic Performance Evaluation of Isolation/Restraint Systems for Mechanical Equipment – Part 2: Light Equipment Study," by S. Fathali and A. Filiatrault, 12/13/07 (PB2008-111192).

MCEER-07-0023 "Fragility Considerations in Highway Bridge Design," by M. Shinozuka, S. Banerjee and S.H. Kim, 12/14/07 (PB2008-111193).

MCEER-07-0024 "Performance Estimates for Seismically Isolated Bridges," by G.P. Warn and A.S. Whittaker, 12/30/07 (PB2008-112230).

MCEER-08-0001 "Seismic Performance of Steel Girder Bridge Superstructures with Conventional Cross Frames," by L.P. Carden, A.M. Itani and I.G. Buckle, 1/7/08, (PB2008-112231).

MCEER-08-0002 "Seismic Performance of Steel Girder Bridge Superstructures with Ductile End Cross Frames with Seismic Isolators," by L.P. Carden, A.M. Itani and I.G. Buckle, 1/7/08 (PB2008-112232).

MCEER-08-0003 "Analytical and Experimental Investigation of a Controlled Rocking Approach for Seismic Protection of Bridge Steel Truss Piers," by M. Pollino and M. Bruneau, 1/21/08 (PB2008-112233).

MCEER-08-0004 "Linking Lifeline Infrastructure Performance and Community Disaster Resilience: Models and Multi-Stakeholder Processes," by S.E. Chang, C. Pasion, K. Tatebe and R. Ahmad, 3/3/08 (PB2008-112234).

MCEER-08-0005 "Modal Analysis of Generally Damped Linear Structures Subjected to Seismic Excitations," by J. Song, Y-L. Chu, Z. Liang and G.C. Lee, 3/4/08 (PB2009-102311).

MCEER-08-0006 "System Performance Under Multi-Hazard Environments," by C. Kafali and M. Grigoriu, 3/4/08 (PB2008-112235).

MCEER-08-0007 "Mechanical Behavior of Multi-Spherical Sliding Bearings," by D.M. Fenz and M.C. Constantinou, 3/6/08 (PB2008-112236).

MCEER-08-0008 "Post-Earthquake Restoration of the Los Angeles Water Supply System," by T.H.P. Tabucchi and R.A. Davidson, 3/7/08 (PB2008-112237).

MCEER-08-0009 "Fragility Analysis of Water Supply Systems," by A. Jacobson and M. Grigoriu, 3/10/08 (PB2009-105545).

MCEER-08-0010 "Experimental Investigation of Full-Scale Two-Story Steel Plate Shear Walls with Reduced Beam Section Connections," by B. Qu, M. Bruneau, C-H. Lin and K-C. Tsai, 3/17/08 (PB2009-106368).

MCEER-08-0011 "Seismic Evaluation and Rehabilitation of Critical Components of Electrical Power Systems," S. Ersoy, B. Feizi, A. Ashrafi and M. Ala Saadeghvaziri, 3/17/08 (PB2009-105546).

MCEER-08-0012 "Seismic Behavior and Design of Boundary Frame Members of Steel Plate Shear Walls," by B. Qu and M. Bruneau, 4/26/08 . (PB2009-106744).

MCEER-08-0013 "Development and Appraisal of a Numerical Cyclic Loading Protocol for Quantifying Building System Performance," by A. Filiatrault, A. Wanitkorkul and M. Constantinou, 4/27/08 (PB2009-107906).

MCEER-08-0014 "Structural and Nonstructural Earthquake Design: The Challenge of Integrating Specialty Areas in Designing Complex, Critical Facilities," by W.J. Petak and D.J. Alesch, 4/30/08 (PB2009-107907).

MCEER-08-0015 "Seismic Performance Evaluation of Water Systems," by Y. Wang and T.D. O'Rourke, 5/5/08 (PB2009-107908).

MCEER-08-0016 "Seismic Response Modeling of Water Supply Systems," by P. Shi and T.D. O'Rourke, 5/5/08 (PB2009-107910).

MCEER-08-0017 "Numerical and Experimental Studies of Self-Centering Post-Tensioned Steel Frames," by D. Wang and A. Filiatrault, 5/12/08 (PB2009-110479).

MCEER-08-0018 "Development, Implementation and Verification of Dynamic Analysis Models for Multi-Spherical Sliding Bearings," by D.M. Fenz and M.C. Constantinou, 8/15/08 (PB2009-107911).

MCEER-08-0019 "Performance Assessment of Conventional and Base Isolated Nuclear Power Plants for Earthquake Blast Loadings," by Y.N. Huang, A.S. Whittaker and N. Luco, 10/28/08 (PB2009-107912).

MCEER-08-0020 "Remote Sensing for Resilient Multi-Hazard Disaster Response – Volume I: Introduction to Damage Assessment Methodologies," by B.J. Adams and R.T. Eguchi, 11/17/08 (PB2010-102695).

MCEER-08-0021 "Remote Sensing for Resilient Multi-Hazard Disaster Response – Volume II: Counting the Number of Collapsed Buildings Using an Object-Oriented Analysis: Case Study of the 2003 Bam Earthquake," by L. Gusella, C.K. Huyck and B.J. Adams, 11/17/08 (PB2010-100925).

MCEER-08-0022 "Remote Sensing for Resilient Multi-Hazard Disaster Response – Volume III: Multi-Sensor Image Fusion Techniques for Robust Neighborhood-Scale Urban Damage Assessment," by B.J. Adams and A. McMillan, 11/17/08 (PB2010-100926).

MCEER-08-0023 "Remote Sensing for Resilient Multi-Hazard Disaster Response – Volume IV: A Study of Multi-Temporal and Multi-Resolution SAR Imagery for Post-Katrina Flood Monitoring in New Orleans," by A. McMillan, J.G. Morley, B.J. Adams and S. Chesworth, 11/17/08 (PB2010-100927).

MCEER-08-0024 "Remote Sensing for Resilient Multi-Hazard Disaster Response – Volume V: Integration of Remote Sensing Imagery and VIEWS^{TM} Field Data for Post-Hurricane Charley Building Damage Assessment," by J.A. Womble, K. Mehta and B.J. Adams, 11/17/08 (PB2009-115532).

MCEER-08-0025 "Building Inventory Compilation for Disaster Management: Application of Remote Sensing and Statistical Modeling," by P. Sarabandi, A.S. Kiremidjian, R.T. Eguchi and B. J. Adams, 11/20/08 (PB2009-110484).

MCEER-08-0026 "New Experimental Capabilities and Loading Protocols for Seismic Qualification and Fragility Assessment of Nonstructural Systems," by R. Retamales, G. Mosqueda, A. Filiatrault and A. Reinhorn, 11/24/08 (PB2009-110485).

MCEER-08-0027 "Effects of Heating and Load History on the Behavior of Lead-Rubber Bearings," by I.V. Kalpakidis and M.C. Constantinou, 12/1/08 (PB2009-115533).

MCEER-08-0028 "Experimental and Analytical Investigation of Blast Performance of Seismically Resistant Bridge Piers," by S.Fujikura and M. Bruneau, 12/8/08 (PB2009-115534).

MCEER-08-0029 "Evolutionary Methodology for Aseismic Decision Support," by Y. Hu and G. Dargush, 12/15/08.

MCEER-08-0030 "Development of a Steel Plate Shear Wall Bridge Pier System Conceived from a Multi-Hazard Perspective," by D. Keller and M. Bruneau, 12/19/08 (PB2010-102696).

MCEER-09-0001 "Modal Analysis of Arbitrarily Damped Three-Dimensional Linear Structures Subjected to Seismic Excitations," by Y.L. Chu, J. Song and G.C. Lee, 1/31/09 (PB2010-100922).

MCEER-09-0002 "Air-Blast Effects on Structural Shapes," by G. Ballantyne, A.S. Whittaker, A.J. Aref and G.F. Dargush, 2/2/09 (PB2010-102697).

MCEER-09-0003 "Water Supply Performance During Earthquakes and Extreme Events," by A.L. Bonneau and T.D. O'Rourke, 2/16/09 (PB2010-100923).

MCEER-09-0004 "Generalized Linear (Mixed) Models of Post-Earthquake Ignitions," by R.A. Davidson, 7/20/09 (PB2010-102698).

MCEER-09-0005 "Seismic Testing of a Full-Scale Two-Story Light-Frame Wood Building: NEESWood Benchmark Test," by I.P. Christovasilis, A. Filiatrault and A. Wanitkorkul, 7/22/09 (PB2012-102401).

MCEER-09-0006 "IDARC2D Version 7.0: A Program for the Inelastic Damage Analysis of Structures," by A.M. Reinhorn, H. Roh, M. Sivaselvan, S.K. Kunnath, R.E. Valles, A. Madan, C. Li, R. Lobo and Y.J. Park, 7/28/09 (PB2010-103199).

MCEER-09-0007 "Enhancements to Hospital Resiliency: Improving Emergency Planning for and Response to Hurricanes," by D.B. Hess and L.A. Arendt, 7/30/09 (PB2010-100924).

MCEER-09-0008 "Assessment of Base-Isolated Nuclear Structures for Design and Beyond-Design Basis Earthquake Shaking," by Y.N. Huang, A.S. Whittaker, R.P. Kennedy and R.L. Mayes, 8/20/09 (PB2010-102699).

MCEER-09-0009 "Quantification of Disaster Resilience of Health Care Facilities," by G.P. Cimellaro, C. Fumo, A.M Reinhorn and M. Bruneau, 9/14/09 (PB2010-105384).

MCEER-09-0010 "Performance-Based Assessment and Design of Squat Reinforced Concrete Shear Walls," by C.K. Gulec and A.S. Whittaker, 9/15/09 (PB2010-102700).

MCEER-09-0011 "Proceedings of the Fourth US-Taiwan Bridge Engineering Workshop," edited by W.P. Yen, J.J. Shen, T.M. Lee and R.B. Zheng, 10/27/09 (PB2010-500009).

MCEER-09-0012 "Proceedings of the Special International Workshop on Seismic Connection Details for Segmental Bridge Construction," edited by W. Phillip Yen and George C. Lee, 12/21/09 (PB2012-102402).

MCEER-10-0001 "Direct Displacement Procedure for Performance-Based Seismic Design of Multistory Woodframe Structures," by W. Pang and D. Rosowsky, 4/26/10 (PB2012-102403).

MCEER-10-0002 "Simplified Direct Displacement Design of Six-Story NEESWood Capstone Building and Pre-Test Seismic Performance Assessment," by W. Pang, D. Rosowsky, J. van de Lindt and S. Pei, 5/28/10 (PB2012-102404).

MCEER-10-0003 "Integration of Seismic Protection Systems in Performance-Based Seismic Design of Woodframed Structures," by J.K. Shinde and M.D. Symans, 6/18/10 (PB2012-102405).

MCEER-10-0004 "Modeling and Seismic Evaluation of Nonstructural Components: Testing Frame for Experimental Evaluation of Suspended Ceiling Systems," by A.M. Reinhorn, K.P. Ryu and G. Maddaloni, 6/30/10 (PB2012-102406).

MCEER-10-0005 "Analytical Development and Experimental Validation of a Structural-Fuse Bridge Pier Concept," by S. El-Bahey and M. Bruneau, 10/1/10 (PB2012-102407).

MCEER-10-0006 "A Framework for Defining and Measuring Resilience at the Community Scale: The PEOPLES Resilience Framework," by C.S. Renschler, A.E. Frazier, L.A. Arendt, G.P. Cimellaro, A.M. Reinhorn and M. Bruneau, 10/8/10 (PB2012-102408).

MCEER-10-0007 "Impact of Horizontal Boundary Elements Design on Seismic Behavior of Steel Plate Shear Walls," by R. Purba and M. Bruneau, 11/14/10 (PB2012-102409).

MCEER-10-0008 "Seismic Testing of a Full-Scale Mid-Rise Building: The NEESWood Capstone Test," by S. Pei, J.W. van de Lindt, S.E. Pryor, H. Shimizu, H. Isoda and D.R. Rammer, 12/1/10 (PB2012-102410).

MCEER-10-0009 "Modeling the Effects of Detonations of High Explosives to Inform Blast-Resistant Design," by P. Sherkar, A.S. Whittaker and A.J. Aref, 12/1/10 (PB2012-102411).

MCEER-10-0010 "L'Aquila Earthquake of April 6, 2009 in Italy: Rebuilding a Resilient City to Withstand Multiple Hazards," by G.P. Cimellaro, I.P. Christovasilis, A.M. Reinhorn, A. De Stefano and T. Kirova, 12/29/10.

MCEER-11-0001 "Numerical and Experimental Investigation of the Seismic Response of Light-Frame Wood Structures," by I.P. Christovasilis and A. Filiatrault, 8/8/11 (PB2012-102412).

MCEER-11-0002 "Seismic Design and Analysis of a Precast Segmental Concrete Bridge Model," by M. Anagnostopoulou, A. Filiatrault and A. Aref, 9/15/11.

MCEER-11-0003 'Proceedings of the Workshop on Improving Earthquake Response of Substation Equipment," Edited by A.M. Reinhorn, 9/19/11 (PB2012-102413).

MCEER-11-0004 "LRFD-Based Analysis and Design Procedures for Bridge Bearings and Seismic Isolators," by M.C. Constantinou, I. Kalpakidis, A. Filiatrault and R.A. Ecker Lay, 9/26/11.

MCEER-11-0005 "Experimental Seismic Evaluation, Model Parameterization, and Effects of Cold-Formed Steel-Framed Gypsum Partition Walls on the Seismic Performance of an Essential Facility," by R. Davies, R. Retamales, G. Mosqueda and A. Filiatrault, 10/12/11.

MCEER-11-0006 "Modeling and Seismic Performance Evaluation of High Voltage Transformers and Bushings," by A.M. Reinhorn, K. Oikonomou, H. Roh, A. Schiff and L. Kempner, Jr., 10/3/11.

MCEER-11-0007 "Extreme Load Combinations: A Survey of State Bridge Engineers," by G.C. Lee, Z. Liang, J.J. Shen and J.S. O'Connor, 10/14/11.

MCEER-12-0001 "Simplified Analysis Procedures in Support of Performance Based Seismic Design," by Y.N. Huang and A.S. Whittaker.

MCEER-12-0002 "Seismic Protection of Electrical Transformer Bushing Systems by Stiffening Techniques," by M. Koliou, A. Filiatrault, A.M. Reinhorn and N. Oliveto, 6/1/12.

MCEER-12-0003 "Post-Earthquake Bridge Inspection Guidelines," by J.S. O'Connor and S. Alampalli, 6/8/12.

MCEER-12-0004 "Integrated Design Methodology for Isolated Floor Systems in Single-Degree-of-Freedom Structural Fuse Systems," by S. Cui, M. Bruneau and M.C. Constantinou, 6/13/12.

MCEER-12-0005 "Characterizing the Rotational Components of Earthquake Ground Motion," by D. Basu, A.S. Whittaker and M.C. Constantinou, 6/15/12.

MCEER-12-0006 "Bayesian Fragility for Nonstructural Systems," by C.H. Lee and M.D. Grigoriu, 9/12/12.

MCEER-12-0007 "A Numerical Model for Capturing the In-Plane Seismic Response of Interior Metal Stud Partition Walls," by R.L. Wood and T.C. Hutchinson, 9/12/12.

MCEER-12-0008 "Assessment of Floor Accelerations in Yielding Buildings," by J.D. Wieser, G. Pekcan, A.E. Zaghi, A.M. Itani and E. Maragakis, 10/5/12.

MCEER-13-0001 "Experimental Seismic Study of Pressurized Fire Sprinkler Piping Systems," by Y. Tian, A. Filiatrault and G. Mosqueda, 4/8/13.

MCEER-13-0002 "Enhancing Resource Coordination for Multi-Modal Evacuation Planning," by D.B. Hess, B.W. Conley and C.M. Farrell, 2/8/13.

MCEER-13-0003 "Seismic Response of Base Isolated Buildings Considering Pounding to Moat Walls," by A. Masroor and G. Mosqueda, 2/26/13.

MCEER-13-0004 "Seismic Response Control of Structures Using a Novel Adaptive Passive Negative Stiffness Device," by D.T.R. Pasala, A.A. Sarlis, S. Nagarajaiah, A.M. Reinhorn, M.C. Constantinou and D.P. Taylor, 6/10/13.

MCEER-13-0005 "Negative Stiffness Device for Seismic Protection of Structures," by A.A. Sarlis, D.T.R. Pasala, M.C. Constantinou, A.M. Reinhorn, S. Nagarajaiah and D.P. Taylor, 6/12/13.

MCEER-13-0006 "Emilia Earthquake of May 20, 2012 in Northern Italy: Rebuilding a Resilient Community to Withstand Multiple Hazards," by G.P. Cimellaro, M. Chiriatti, A.M. Reinhorn and L. Tirca, June 30, 2013.

MCEER-13-0007 "Precast Concrete Segmental Components and Systems for Accelerated Bridge Construction in Seismic Regions," by A.J. Aref, G.C. Lee, Y.C. Ou and P. Sideris, with contributions from K.C. Chang, S. Chen, A. Filiatrault and Y. Zhou, June 13, 2013.

MCEER-13-0008 "A Study of U.S. Bridge Failures (1980-2012)," by G.C. Lee, S.B. Mohan, C. Huang and B.N. Fard, June 15, 2013.

MCEER-13-0009 "Development of a Database Framework for Modeling Damaged Bridges," by G.C. Lee, J.C. Qi and C. Huang, June 16, 2013.

MCEER-13-0010 "Model of Triple Friction Pendulum Bearing for General Geometric and Frictional Parameters and for Uplift Conditions," by A.A. Sarlis and M.C. Constantinou, July 1, 2013.

MCEER-13-0011 "Shake Table Testing of Triple Friction Pendulum Isolators under Extreme Conditions," by A.A. Sarlis, M.C. Constantinou and A.M. Reinhorn, July 2, 2013.

MCEER-13-0012 "Theoretical Framework for the Development of MH-LRFD," by G.C. Lee (coordinating author), H.A Capers, Jr., C. Huang, J.M. Kulicki, Z. Liang, T. Murphy, J.J.D. Shen, M. Shinozuka and P.W.H. Yen, July 31, 2013.

MCEER-13-0013 "Seismic Protection of Highway Bridges with Negative Stiffness Devices," by N.K.A. Attary, M.D. Symans, S. Nagarajaiah, A.M. Reinhorn, M.C. Constantinou, A.A. Sarlis, D.T.R. Pasala, and D.P. Taylor, September 3, 2014.

MCEER-14-0001 "Simplified Seismic Collapse Capacity-Based Evaluation and Design of Frame Buildings with and without Supplemental Damping Systems," by M. Hamidia, A. Filiatrault, and A. Aref, May 19, 2014.

MCEER-14-0002 "Comprehensive Analytical Seismic Fragility of Fire Sprinkler Piping Systems," by Siavash Soroushian, Emmanuel "Manos" Maragakis, Arash E. Zaghi, Alicia Echevarria, Yuan Tian and Andre Filiatrault, August 26, 2014.

MCEER-14-0003 "Hybrid Simulation of the Seismic Response of a Steel Moment Frame Building Structure through Collapse," by M. Del Carpio Ramos, G. Mosqueda and D.G. Lignos, October 30, 2014.

MCEER-14-0004 "Blast and Seismic Resistant Concrete-Filled Double Skin Tubes and Modified Steel Jacketed Bridge Columns," by P.P. Fouche and M. Bruneau, June 30, 2015.

MCEER-14-0005 "Seismic Performance of Steel Plate Shear Walls Considering Various Design Approaches," by R. Purba and M. Bruneau, October 31, 2014.

MCEER-14-0006 "Air-Blast Effects on Civil Structures," by Jinwon Shin, Andrew S. Whittaker, Amjad J. Aref and David Cormie, October 30, 2014.

MCEER-14-0007 "Seismic Performance Evaluation of Precast Girders with Field-Cast Ultra High Performance Concrete (UHPC) Connections," by G.C. Lee, C. Huang, J. Song, and J. S. O'Connor, July 31, 2014.

MCEER-14-0008 "Post-Earthquake Fire Resistance of Ductile Concrete-Filled Double-Skin Tube Columns," by Reza Imani, Gilberto Mosqueda and Michel Bruneau, December 1, 2014.

MCEER-14-0009 "Cyclic Inelastic Behavior of Concrete Filled Sandwich Panel Walls Subjected to In-Plane Flexure," by Y. Alzeni and M. Bruneau, December 19, 2014.

MCEER-14-0010 "Analytical and Experimental Investigation of Self-Centering Steel Plate Shear Walls," by D.M. Dowden and M. Bruneau, December 19, 2014.

MCEER-15-0001 "Seismic Analysis of Multi-story Unreinforced Masonry Buildings with Flexible Diaphragms," by J. Aleman, G. Mosqueda and A.S. Whittaker, June 12, 2015.

MCEER-15-0002 "Site Response, Soil-Structure Interaction and Structure-Soil-Structure Interaction for Performance Assessment of Buildings and Nuclear Structures," by C. Bolisetti and A.S. Whittaker, June 15, 2015.

MCEER-15-0003 "Stress Wave Attenuation in Solids for Mitigating Impulsive Loadings," by R. Rafiee-Dehkharghani, A.J. Aref and G. Dargush, August 15, 2015.

MCEER-15-0004 "Computational, Analytical, and Experimental Modeling of Masonry Structures," by K.M. Dolatshahi and A.J. Aref, November 16, 2015.

MCEER-15-0005 "Property Modification Factors for Seismic Isolators: Design Guidance for Buildings," by W.J. McVitty and M.C. Constantinou, June 30, 2015.

MCEER-15-0006 "Seismic Isolation of Nuclear Power Plants using Sliding Bearings," by Manish Kumar, Andrew S. Whittaker and Michael C. Constantinou, December 27, 2015.

MCEER-15-0007 "Quintuple Friction Pendulum Isolator Behavior, Modeling and Validation," by Donghun Lee and Michael C. Constantinou, December 28, 2015.

MCEER-15-0008 "Seismic Isolation of Nuclear Power Plants using Elastomeric Bearings," by Manish Kumar, Andrew S. Whittaker and Michael C. Constantinou, December 29, 2015.

MCEER-16-0001 "Experimental, Numerical and Analytical Studies on the Seismic Response of Steel-Plate Concrete (SC) Composite Shear Walls," by Siamak Epackachi and Andrew S. Whittaker, June 15, 2016.

MCEER-16-0002 "Seismic Demand in Columns of Steel Frames," by Lisa Shrestha and Michel Bruneau, June 17, 2016.

MCEER-16-0003 "Development and Evaluation of Procedures for Analysis and Design of Buildings with Fluidic Self-Centering Systems" by Shoma Kitayama and Michael C. Constantinou, July 21, 2016.

MCEER-16-0004 "Real Time Control of Shake Tables for Nonlinear Hysteretic Systems," by Ki Pung Ryu and Andrei M. Reinhorn, October 22, 2016.

MCEER-16-0006 "Seismic Isolation of High Voltage Electrical Power Transformers," by Kostis Oikonomou, Michael C. Constantinou, Andrei M. Reinhorn and Leon Kemper, Jr., November 2, 2016.

MCEER-16-0007 "Open Space Damping System Theory and Experimental Validation," by Erkan Polat and Michael C. Constantinou, December 13, 2016.

MCEER-16-0008 "Seismic Response of Low Aspect Ratio Reinforced Concrete Walls for Buildings and Safety-Related Nuclear Applications," by Bismarck N. Luna and Andrew S. Whittaker.

MCEER-16-0009 "Buckling Restrained Braces Applications for Superstructure and Substructure Protection in Bridges," by Xiaone Wei and Michel Bruneau, December 28, 2016.

MCEER-16-0010 "Procedures and Results of Assessment of Seismic Performance of Seismically Isolated Electrical Transformers with Due Consideration for Vertical Isolation and Vertical Ground Motion Effects," by Shoma Kitayama, Michael C. Constantinou and Donghun Lee, December 31, 2016.

MCEER-17-0001 "Diagonal Tension Field Inclination Angle in Steel Plate Shear Walls," by Yushan Fu, Fangbo Wang and Michel Bruneau, February 10, 2017.

MCEER-17-0002 "Behavior of Steel Plate Shear Walls Subjected to Long Duration Earthquakes," by Ramla Qureshi and Michel Bruneau, September 1, 2017.

MCEER-17-0003 "Response of Steel-plate Concrete (SC) Wall Piers to Combined In-plane and Out-of-plane Seismic Loadings," by Brian Terranova, Andrew S. Whittaker, Siamak Epackachi and Nebojsa Orbovic, July 17, 2017.

MCEER-17-0004 "Design of Reinforced Concrete Panels for Wind-borne Missile Impact," by Brian Terranova, Andrew S. Whittaker and Len Schwer, July 18, 2017.

MCEER-17-0005 "A Simple Strategy for Dynamic Substructuring and its Application to Soil-Foundation-Structure Interaction," by Aikaterini Stefanaki and Metttupalayam V. Sivaselvan, December 15, 2017.

MCEER-17-0006 "Dynamics of Cable Structures: Modeling and Applications," by Nicholas D. Oliveto and Mettupalayam V. Sivaselvan, December 1, 2017.

MCEER-17-0007 "Development and Validation of a Combined Horizontal-Vertical Seismic Isolation System for High-Voltage-Power Transformers," by Donghun Lee and Michael C. Constantinou, November 3, 2017.

MCEER-18-0001 "Reduction of Seismic Acceleration Parameters for Temporary Bridge Design," by Conor Stucki and Michel Bruneau, March 22, 2018.

MCEER-18-0002 "Seismic Response of Low Aspect Ratio Reinforced Concrete Walls," by Bismarck N. Luna, Jonathan P. Rivera, Siamak Epackachi and Andrew S. Whittaker, April 21, 2018.

MCEER-18-0003 "Seismic Damage Assessment of Low Aspect Ratio Reinforced Concrete Shear Walls," by Jonathan P. Rivera, Bismarck N. Luna and Andrew S. Whittaker, April 16, 2018.

MCEER-18-0004 "Seismic Performance Assessment of Seismically Isolated Buildings Designed by the Procedures of ASCE/ SEI 7," by Shoma Kitayama and Michael C. Constantinou, April 14, 2018.

MCEER-19-0001 MCEER-19-0001 "Development and Validation of a Seismic Isolation System for Lightweight Residential Construction," by Huseyin Cisalar and Michael C. Constantinou, March 24, 2019.

MCEER-20-0001 "A Multiscale Study of Reinforced Concrete Shear Walls Subjected to Elevated Temperatures," by Alok Deshpande and Andrew S. Whittaker, June 26, 2020.

MCEER-20-0002 "Further Results on the Assessment of Performance of Seismically Isolated Electrical Transformers," by Shoma Kitayama and Michael C. Constantinou, June 30, 2020.

MCEER-20-0003 "Analytical and Numerical Studies of Seismic Fluid-Structure Interaction in Liquid-Filled Vessels," by Ching-Ching Yu and Andrew S. Whittaker, August 1, 2020.

MCEER-22-0001 "Modeling Triple Friction Pendulum Bearings in Program OpenSees Including Frictional Heating Effects," by Hyun-Myung Kim and Michael C. Constantinou, April 18, 2022.

MCEER-22-0002 "Physical and Numerical Simulations of Seismic Fluid-Structure Interaction in Advanced Nuclear Reactors," by Faizan Ul Haq Mir, Ching-Ching Yu, Andrew S. Whittaker and Michael C. Constantinou, July 8, 2022.

MCEER-22-0003 "Impedance-Matching Control Design for Shake-Table Testing and Model-in-the-Loop Simulations," by Sai Sharath Parsi, Mettupalayam V. Sivaselvan and Andrew S. Whittaker, September 30, 2022.

MCEER-22-0004 "Earthquake-Simulator Experiments of a Model of a Seismically-Isolated, Fluoride-Salt Cooled High-Temperature Reactor," by Faizan Ul Haq Mir, Kaivalya M. Lal, Benjamin D. Kosbab, Nam Nguyen, Brian Song, Matthew Clavelli, Kaniel Z. Tilow and Andrew S. Whittaker, October 24, 2022.

MCEER-23-0001 “Mid-height Seismic Isolation of Tall, Slender Equipment in Advanced Nuclear Power Plants,” by Kaivalya M. Lal, Andrew S. Whittaker and Michael C. Constantinou, February 4, 2023.

MCEER: Earthquake Engineering to Extreme Events

University at Buffalo, The State University of New York
133A Ketter Hall | Buffalo, NY 14260
mceer@buffalo.edu; buffalo.edu/mceer

ISSN 1520-295X